

Covid-19: Targeting essential sars-cov-2 proteins for drug discovery

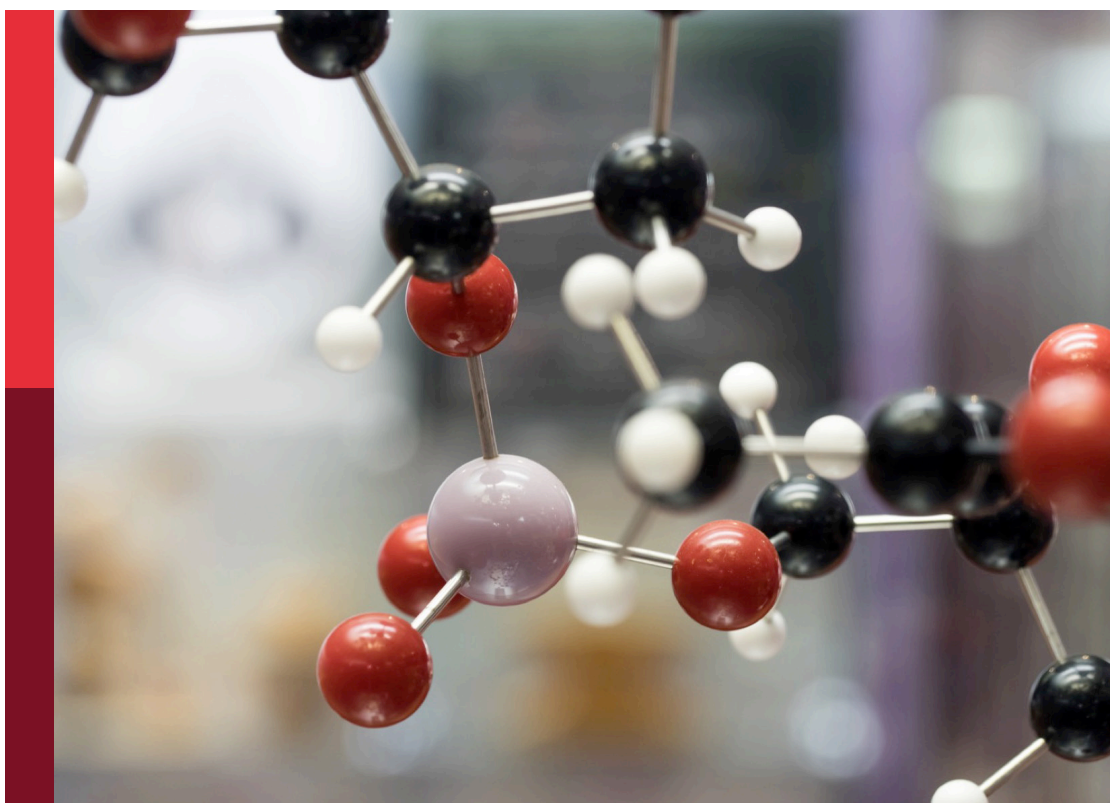
Edited by

Wenshe Ray Liu, Matthew Bogyo, Jun Wang and Andrzej Joachimiak

Published in

Frontiers in Chemistry

Frontiers in Molecular Biosciences



FRONTIERS EBOOK COPYRIGHT STATEMENT

The copyright in the text of individual articles in this ebook is the property of their respective authors or their respective institutions or funders. The copyright in graphics and images within each article may be subject to copyright of other parties. In both cases this is subject to a license granted to Frontiers.

The compilation of articles constituting this ebook is the property of Frontiers.

Each article within this ebook, and the ebook itself, are published under the most recent version of the Creative Commons CC-BY licence. The version current at the date of publication of this ebook is CC-BY 4.0. If the CC-BY licence is updated, the licence granted by Frontiers is automatically updated to the new version.

When exercising any right under the CC-BY licence, Frontiers must be attributed as the original publisher of the article or ebook, as applicable.

Authors have the responsibility of ensuring that any graphics or other materials which are the property of others may be included in the CC-BY licence, but this should be checked before relying on the CC-BY licence to reproduce those materials. Any copyright notices relating to those materials must be complied with.

Copyright and source acknowledgement notices may not be removed and must be displayed in any copy, derivative work or partial copy which includes the elements in question.

All copyright, and all rights therein, are protected by national and international copyright laws. The above represents a summary only. For further information please read Frontiers' Conditions for Website Use and Copyright Statement, and the applicable CC-BY licence.

ISSN 1664-8714
ISBN 978-2-83251-703-1
DOI 10.3389/978-2-83251-703-1

About Frontiers

Frontiers is more than just an open access publisher of scholarly articles: it is a pioneering approach to the world of academia, radically improving the way scholarly research is managed. The grand vision of Frontiers is a world where all people have an equal opportunity to seek, share and generate knowledge. Frontiers provides immediate and permanent online open access to all its publications, but this alone is not enough to realize our grand goals.

Frontiers journal series

The Frontiers journal series is a multi-tier and interdisciplinary set of open-access, online journals, promising a paradigm shift from the current review, selection and dissemination processes in academic publishing. All Frontiers journals are driven by researchers for researchers; therefore, they constitute a service to the scholarly community. At the same time, the *Frontiers journal series* operates on a revolutionary invention, the tiered publishing system, initially addressing specific communities of scholars, and gradually climbing up to broader public understanding, thus serving the interests of the lay society, too.

Dedication to quality

Each Frontiers article is a landmark of the highest quality, thanks to genuinely collaborative interactions between authors and review editors, who include some of the world's best academicians. Research must be certified by peers before entering a stream of knowledge that may eventually reach the public - and shape society; therefore, Frontiers only applies the most rigorous and unbiased reviews. Frontiers revolutionizes research publishing by freely delivering the most outstanding research, evaluated with no bias from both the academic and social point of view. By applying the most advanced information technologies, Frontiers is catapulting scholarly publishing into a new generation.

What are Frontiers Research Topics?

Frontiers Research Topics are very popular trademarks of the *Frontiers journals series*: they are collections of at least ten articles, all centered on a particular subject. With their unique mix of varied contributions from Original Research to Review Articles, Frontiers Research Topics unify the most influential researchers, the latest key findings and historical advances in a hot research area.

Find out more on how to host your own Frontiers Research Topic or contribute to one as an author by contacting the Frontiers editorial office: frontiersin.org/about/contact

Covid-19: Targeting essential sars-cov-2 proteins for drug discovery

Topic editors

Wenshe Ray Liu — Texas A&M University, United States

Matthew Bogyo — Stanford University, United States

Jun Wang — The State University of New Jersey, United States

Andrzej Joachimiak — Argonne National Laboratory (DOE), United States

Citation

Liu, W. R., Bogyo, M., Wang, J., Joachimiak, A., eds. (2023). *Covid-19: Targeting essential sars-cov-2 proteins for drug discovery*. Lausanne: Frontiers Media SA.
doi: 10.3389/978-2-83251-703-1

Table of contents

- 05 **Structure-Based Virtual Screening and Identification of Potential Inhibitors of SARS-CoV-2 S-RBD and ACE2 Interaction**
Jiacheng Xiong, Yusen Xiang, Ziming Huang, Xiaohong Liu, Mengge Wang, Guangbo Ge, Hongzhuan Chen, Jianrong Xu, Mingyue Zheng and Lili Chen
- 17 **Inhibition of SARS-CoV-2 by Targeting Conserved Viral RNA Structures and Sequences**
Shalakha Hegde, Zhichao Tang, Junxing Zhao and Jingxin Wang
- 28 **Corrigendum: Inhibition of SARS-CoV-2 by Targeting Conserved Viral RNA Structures and Sequences**
Shalakha Hegde, Zhichao Tang, Junxing Zhao and Jingxin Wang
- 30 **Targeting SARS-CoV-2 Proteases for COVID-19 Antiviral Development**
Zongyang Lv, Kristin E. Cano, Lijia Jia, Marcin Drag, Tony T. Huang and Shaun K. Olsen
- 61 **An Enhanced Hybrid Screening Approach to Identify Potent Inhibitors for the SARS-CoV-2 Main Protease From the NCI Compound Library**
Shuhua G. Li, Kai S. Yang, Lauren R. Blankenship, Chia-Chuan D. Cho, Shiqing Xu, Hongbin Wang and Wenshe Ray Liu
- 70 **Potential Inhibitors Targeting Papain-Like Protease of SARS-CoV-2: Two Birds With One Stone**
Haihai Jiang, Peiyao Yang and Jin Zhang
- 84 **Crystallization of Feline Coronavirus M^{pro} With GC376 Reveals Mechanism of Inhibition**
Jimmy Lu, Sizhu Amelia Chen, Muhammad Bashir Khan, Raelynn Brassard, Elena Arutyunova, Tess Lamer, Wayne Vuong, Conrad Fischer, Howard S. Young, John C. Vederas and M. Joanne Lemieux
- 94 **The Molecular Basis of the Effect of Temperature on the Structure and Function of SARS-CoV-2 Spike Protein**
Faez Iqbal Khan, Kevin A. Lobb and Dakun Lai
- 103 **Hydrazones and Thiosemicarbazones Targeting Protein-Protein-Interactions of SARS-CoV-2 Papain-like Protease**
Wiebke Ewert, Sebastian Günther, Francesca Miglioli, Sven Falke, Patrick Y. A. Reinke, Stephan Niebling, Christian Günther, Huijong Han, Vasundara Srinivasan, Hévila Brognaro, Julia Lieske, Kristina Lorenzen, Maria M. Garcia-Alai, Christian Betzel, Mauro Carcelli, Winfried Hinrichs, Dominga Rogolino and Alke Meents

- 116 Insights Into Drug Repurposing, as Well as Specificity and Compound Properties of Piperidine-Based SARS-CoV-2 PL^{pro} Inhibitors**
Dale J. Calleja, Nathan Kuchel, Bernadine G. C. Lu, Richard W. Birkinshaw, Theresa Klemm, Marcel Doerflinger, James P. Cooney, Liana Mackiewicz, Amanda E. Au, Yu Q. Yap, Timothy R Blackmore, Kasiram Katneni, Elly Crighton, Janet Newman, Kate E. Jarman, Melissa J. Call, Bernhard C. Lechtenberg, Peter E. Czabotar, Marc Pellegrini, Susan A. Charman, Kym N. Lowes, Jeffrey P. Mitchell, Ueli Nachbur, Guillaume Lessene and David Komander
- 137 Inhibitors of SARS-CoV-2 PL^{pro}**
Dale J. Calleja, Guillaume Lessene and David Komander
- 157 Self-Masked Aldehyde Inhibitors of Human Cathepsin L Are Potent Anti-CoV-2 Agents**
Jiyun Zhu, Linfeng Li, Aleksandra Drelich, Bala C. Chenna, Drake M. Mellott, Zane W. Taylor, Vivian Tat, Christopher Z. Garcia, Ardala Katzfuss, Chien-Te K. Tseng and Thomas D. Meek
- 168 Druggable targets and therapeutic development for COVID-19**
Xiaohua Duan, Laurretta A. Lacko and Shuibing Chen
- 185 Structural similarities between SARS-CoV2 3CL^{pro} and other viral proteases suggest potential lead molecules for developing broad spectrum antivirals**
Khushboo Bafna, Christopher L. Cioffi, Robert M. Krug and Gaetano T. Montelione



Structure-Based Virtual Screening and Identification of Potential Inhibitors of SARS-CoV-2 S-RBD and ACE2 Interaction

Jiacheng Xiong^{1,2†}, Yusen Xiang^{3†}, Ziming Huang^{1,2}, Xiaohong Liu^{1,2,4}, Mengge Wang³, Guangbo Ge³, Hongzhan Chen³, Jianrong Xu^{5,6*}, Mingyue Zheng^{1,2*} and Lili Chen^{3*}

¹State Key Laboratory of Drug Research, Drug Discovery and Design Center, Shanghai Institute of Materia Medica, Chinese Academy of Sciences, Shanghai, China, ²College of Pharmacy, University of Chinese Academy of Sciences, Beijing, China, ³Institute of Interdisciplinary Integrative Medicine Research, Shanghai University of Traditional Chinese Medicine, Shanghai, China, ⁴Shanghai Institute for Advanced Immunochemical Studies, School of Life Science and Technology, ShanghaiTech University, Shanghai, China, ⁵Academy of Integrative Medicine, Shanghai University of Traditional Chinese Medicine, Shanghai, China, ⁶Department of Pharmacology and Chemical Biology, Shanghai Jiao Tong University School of Medicine, Shanghai, China

OPEN ACCESS

Edited by:

Wenshe Ray Liu,
Texas A&M University, United States

Reviewed by:

Kai S. Yang,
Texas A&M University, United States
Nand Kishore,
Indian Institute of Technology
Bombay, India

*Correspondence:

Lili Chen
lchen@shutcm.edu.cn
Mingyue Zheng
myzheng@simm.ac.cn
Jianrong Xu
janker.xu@gmail.com

[†]These authors have contributed
equally to this work

Specialty section:

This article was submitted to
Chemical Biology,
a section of the journal
Frontiers in Chemistry

Received: 13 July 2021

Accepted: 09 September 2021

Published: 27 September 2021

Citation:

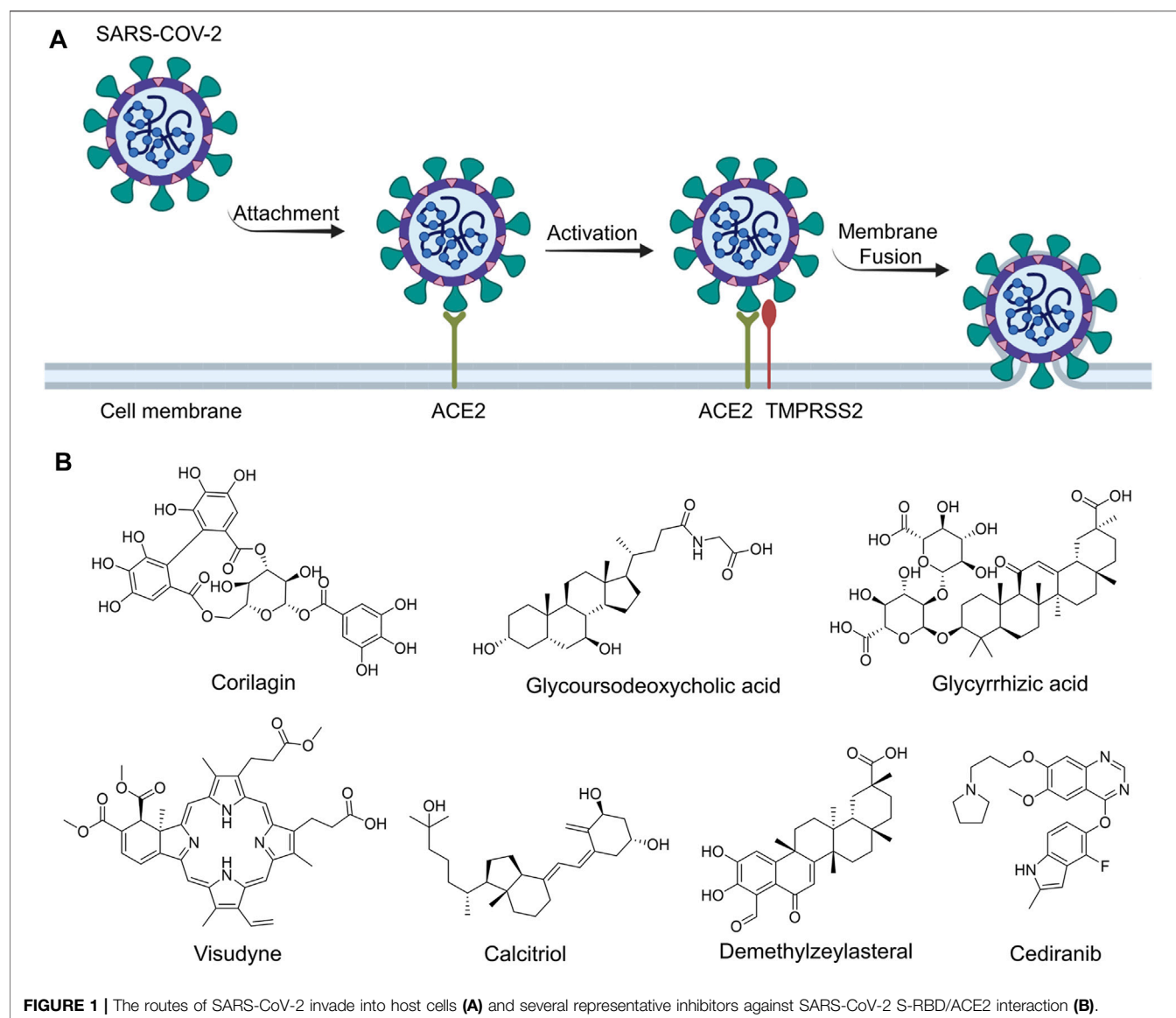
Xiong J, Xiang Y, Huang Z, Liu X, Wang M, Ge G, Chen H, Xu J, Zheng M and Chen L (2021) Structure-Based Virtual Screening and Identification of Potential Inhibitors of SARS-CoV-2 S-RBD and ACE2 Interaction. *Front. Chem.* 9:740702. doi: 10.3389/fchem.2021.740702

The emergence and rapid spread of SARS-CoV-2 have caused a worldwide public health crisis. Designing small molecule inhibitors targeting SARS-CoV-2 S-RBD/ACE2 interaction is considered as a potential strategy for the prevention and treatment of SARS-CoV-2. But to date, only a few compounds have been reported as SARS-CoV-2 S-RBD/ACE2 interaction inhibitors. In this study, we described the virtual screening and experimental validation of two novel inhibitors (DC-RA016 and DC-RA052) against SARS-CoV-2 S-RBD/ACE2 interaction. The NanoBiT assays and surface plasmon resonance (SPR) assays demonstrated their capabilities of blocking SARS-CoV-2 S-RBD/ACE2 interaction and directly binding to both S-RBD and ACE2. Moreover, the pseudovirus assay revealed that these two compounds possessed significant antiviral activity (about 50% inhibition rate at maximum non-cytotoxic concentration). These results indicate that the compounds DC-RA016 and DC-RA052 are promising inhibitors against SARS-CoV-2 S-RBD/ACE2 interaction and deserve to be further developed.

Keywords: SARS-CoV-2, angiotensin-converting enzyme 2 (ACE2), spike protein receptor-binding domain (S-RBD), structure-based virtual screening, protein-protein interaction (PPI) inhibitors

INTRODUCTION

There is an ongoing pandemic of coronavirus disease 2019 (COVID-19) caused by severe acute respiratory syndrome coronavirus 2 (SARS-CoV-2). SARS-CoV-2 is a kind of positive single-stranded RNA virus with an envelope structure (Gorbalenya et al., 2020; Yao et al., 2020). It was the seventh known coronavirus able to infect humans (Chen et al., 2020). The human infection caused by SARS-CoV-2 can induce severe pulmonary disease and complications with significant morbidities and mortalities (Sun et al., 2020; Yang X. et al., 2020; Zhang J.-j. et al., 2020). According to the released statistics from the World Health Organization (WHO), the numbers of confirmed cases and deaths of COVID-19 worldwide have so far exceeded 180 million and four million with a continuous upward tendency (<https://covid19.who.int/table>). Despite the disastrous effect of COVID-19 on public health, civil society, and the global economy, there is currently still no specific drug available



against it. Hence, the search for effective treatment strategies for SARS-CoV-2 infections is in urgent demand.

The invasion of SARS-CoV-2 into host cells relies on the spike protein on the surface of its envelope (Walls et al., 2020). In humans, the primary receptor of the SARS-CoV-2 spike protein is angiotensin-converting enzyme 2 (ACE2) (Wang et al., 2020; Zhang H. et al., 2020). SARS-CoV-2 spike protein recognizes and binds to ACE2 through the receptor-binding domain (Xu et al., 2021). Then it is hydrolytically activated by transmembrane protease serine 2 (TMPRSS2) and mediates subsequent virus-host cell membrane fusion (Figure 1A) (Hoffmann et al., 2020). The binding affinity between spike protein of SARS-CoV-2 and ACE2 has been determined to be low to ~15 nM and 10 to 20 fold higher than that reported in SARS-CoV in 2002, which may be an important cause of the extremely high transmissibility of SARS-CoV-2 (Wrapp et al., 2020). Considering such a critical role of the interaction between spike protein receptor-binding domain

(S-RBD) and ACE2 in the entry of the SARS-CoV-2 into host cells, the inhibition of such interaction is considered as a particularly attractive strategy for the development of treatments for SARS-CoV-2 infections (Li et al., 2020; Monteil et al., 2020; Yang J. et al., 2020).

Recently, virtual screening and high throughput screening studies targeting SARS-CoV-2 S-RBD/ACE2 interaction have discovered several small molecule inhibitors (Figure 1B) (Carino et al., 2020; Fu et al., 2020; Hanson et al., 2020; Yu et al., 2020; Zhu et al., 2021). Nevertheless, the antiviral activities of some compounds, such as corilagin, glycoursodeoxycholic acid, and glycyrrhizic acid, are not clear (Carino et al., 2020; Hanson et al., 2020; Yu et al., 2020). Visudyne shows intense antiviral activity against SARS-CoV-2 pseudovirus. However, its cytotoxicity data is not reported (Fu et al., 2020). Besides, demethylzeylasteral and cediranib have undergone pseudovirus and cytotoxicity tests, but only demethylzeylasteral shows slight

inhibitory activity (approximately 7%) against SARS-CoV-2 pseudovirus under nontoxic concentration (Zhu et al., 2021). Hence, there remains a critical need and challenge to discover safe and effective inhibitors against the interaction between S-RBD and ACE2.

In this study, we identified two novel inhibitors (named DC-RA016 and DC-RA052) against SARS-CoV-2 S-RBD/ACE2 interaction through structure-based virtual screening and biological experiments. NanoLuc binary technology (NanoBiT)-based binding and surface plasmon resonance (SPR) assay demonstrated that DC-RA016 and DC-RA052 could bind to both S-RBD and ACE2, blocking the interaction between them. Additionally, the pseudovirus assay and cytotoxicity experiment showed that both DC-RA016 and DC-RA052 have moderate inhibition ability to SARS-CoV-2-S pseudovirus and low cytotoxicity. In addition, the preliminary pharmacophore analysis and the mechanism action study of DC-RA016 were carried out to further uncover the inhibitory mechanism of the compound on SARS-CoV-2 S-RBD/ACE2 interaction. Therefore, these two compounds are promising new inhibitors of SARS-CoV-2 S-RBD/ACE2 interaction and worth further development.

MATERIALS AND METHODS

Structure-based Virtual Screening and 2D Similarity Search

The whole virtual screening process was carried out using Schrödinger Suite 2017 on a Linux server with four 6-core Intel Xeon E5-4607 CPUs and 32 GB of memory. The crystal structure of the SARS-CoV-2 S-RBD bound to ACE2 (PDB code: 6M0J) was obtained from the Protein Data Bank (PDB) for the docking studies. This crystal structure was prepared using the Protein Preparation Wizard module with default parameters. The process of protein preparation included the determination of valence bonds, the addition of hydrogen atom, removal of water molecule and heteroatom, optimization of hydrogen bond network, optimization of the orientation of Asn, Gln, and His, and restrained structural optimization. Finally, a grid box containing the contact interface of SARS-CoV-2 S-RBD/ACE2 complexes was generated with the Receptor Grid Generation module by manually setting the central coordinate. The size of the grid box was defined as $30 \times 30 \times 30$ Å.

Small molecules in the SPECS commercial compound database were selected for virtual screening. In order to avoid false positives caused by pan assay interference compounds (PAINS), the compounds containing PAINS structural alert were removed with the Structure Filter module in Canvas. Subsequently, the three-dimensional coordinates, different stereoisomers, and protonation states at $\text{pH } 7.0 \pm 2.0$ of remaining compounds were generated with LigPred Module. The resulting structures were used for docking.

The final molecular docking was performed with the Virtual Screening Workflow module. All treated molecules were first docked into the defined interface pocket in standard precision

mode. Then the top poses were further docked in extra precision mode.

The structural similarity between the two molecules was calculated using the 1024-dimensional Morgan fingerprints with radius two and the Tanimoto coefficient. The calculation of fingerprints and the Tanimoto coefficient were both implemented with the RDkit python package.

Compounds

The tested compounds were purchased from SPECS (Zoetermeer, Netherlands) and used directly without further purification. All compounds were first dissolved in DMSO and subsequently diluted to the final bioassay concentration.

Determination of SARS-CoV-2 S-RBD/ACE2 Inhibitors by NanoBiT-Based Assay

The initial screening and 50% inhibitory concentration (IC_{50}) determination of SARS-CoV-2 S-RBD/ACE2 interaction inhibitors were conducted as previously described (Yu et al., 2020). Briefly, SARS-CoV-2 S-RBD-LgBiT (S residues 319–591) and SmBiT-ACE2 (ACE2 residues 19–615) fusion plasmids were transiently co-transfected into HEK293 cells in a 6-well plate using FuGENE HD transfection reagent (Promega, Madison, WI). After 6 h, the HEK293 cells were reseeded into a 384-well plate for screening the active compounds. The compounds were added at indicated concentrations and plates were incubated for 3 h. After the addition of Nano-Glo live Cell Assay reagent, luminescence was determined using the Envision plate reader (EnVision, Perkin Elmer, Waltham, MA, United States). To exclude the false positives, the cytotoxicity of the compounds on the HEK293 cells and the inhibitory effects of the compounds on NanoLuc (HEK293/Nanoluc stable cells) were also measured, respectively. The activities of the compounds were evaluated using the inhibitory effects on SARS-CoV-2 S-RBD/ACE2 interaction (NanoBiT inh%), NanoLuc luciferase (NanoLuc inh%) and the cell proliferation (Cytotox inh%, CC_{50}) on HEK293 cells.

SARS-CoV-2-S Pseudovirus-Based Inhibition Assay

Three separate plasmids including pAX2, pHB-Rluc and pcDNA3.1-SARS-CoV-2-S were obtained from Precodo (Anhui, China). HEK293T cells were grown in Dulbecco's modified Eagle's medium (DMEM) (Corning Inc., Corning, NY, United States) supplemented with 10% heat-inactivated fetal bovine serum (FBS) (ExCell Bio, Shanghai, China) and 1% penicillin-streptomycin under a humidified atmosphere containing 5% CO_2 at 37°C . HEK293T cells grown to 70% confluency were co-transfected with the above-mentioned plasmids using Lipofiter 3.0 transfection reagent (Hanbio, Shanghai, China) according to the manufacturer's instruction. After 6 h of transfection, HEK293T cells were refreshed with DMEM containing 10% FBS and SARS-CoV-2-S pseudoviruses in the supernatant was harvested at 48 h, filtered using a $0.45 \mu\text{m}$ membrane (Jet Bio-Filtration, Guangzhou, China) and stored in

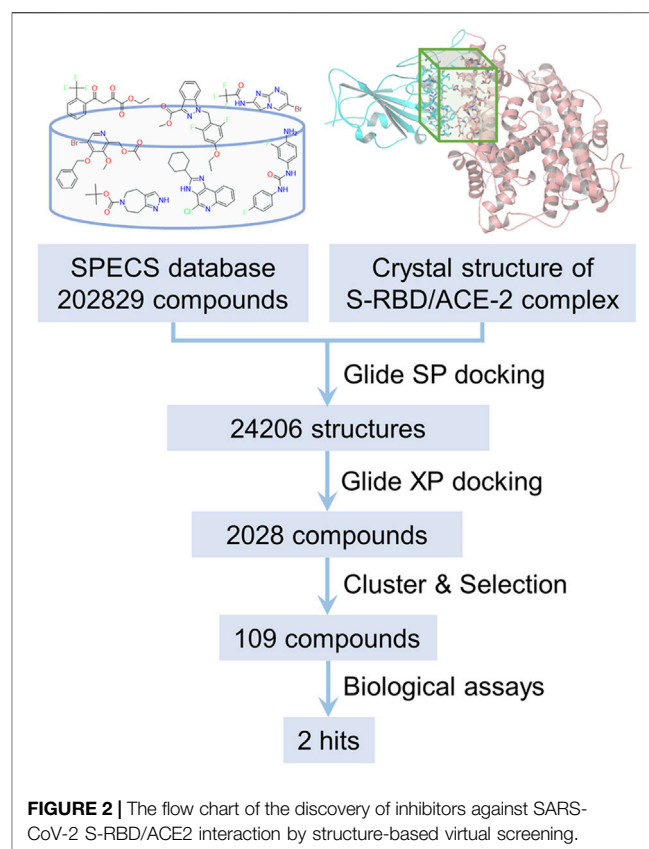
aliquots at -80°C until use. Subsequently, HEK293T cells were transiently transfected with pcDNA3.1-ACE2 (Precedo, Anhui, China) or with vector alone. Transfected HEK293T cells were incubated with the indicated concentrations of test compounds at 37°C for 1 h. Then, SARS-CoV-2-S pseudovirus and Polybrene ($6\text{ }\mu\text{g/ml}$) (Absin, Shanghai, China) were added to infect the cells for 24 h. After that, the cells were further cultured with fresh DMEM containing 10% FBS for an additional 24 h. Then cells were lysed with Cell Lysis Buffer (Promega, Madison, WI, United States), and the luciferase activity was detected using a Multilabel Reader (SpectraMax Paradigm, Molecular Devices, CA, United States). The inhibition rate (%) was calculated by the equation: (the luminescence of the test compounds/the maximum luminescence after transfection for SARS-CoV-2-S pseudovirus) \times 100%. IC_{50} values were determined via nonlinear regression analysis using GraphPad Prism software 8.0 (GraphPad Software, Inc., San Diego, CA, United States). The cytotoxicity of the test compounds was determined using the CellTiter-Glo (CTG) Luminescent Cell Viability Assay (Promega, Madison, WI, United States) according to the manufacturer's protocols. Selectivity index (SI) for each compound was calculated by dividing CC_{50} (cytotoxicity on HEK293T cells) by IC_{50} (the inhibitory activity against SARS-CoV-2-S pseudovirus). The maximum non-cytotoxic concentration (MNCC) was defined as the concentration required to retain cell viability by 90% and calculated according to the previously published method (Cheng et al., 2013). The inhibition of the compounds to SARS-CoV-2-S pseudovirus infectivity at MNCC was fitted based on the inhibition curve and expressed as the inhibition ratio (%I).

SPR-Based Assay

A BIAcore T200 instrument (GE Healthcare Life Sciences, United States) was used to evaluate the binding affinity of the test compounds to human ACE2 or SARS-CoV-2 S-RBD as previously described (Li et al., 2017). Briefly, both proteins were respectively immobilized on the different channels of CM5 sensor chip by a standard amine-coupling approach at a flow rate of $10\text{ }\mu\text{L/min}$ in 10 mM sodium acetate buffer (pH 4.0). The sensor surface was activated with a 7 min injection of the mixture of 50 mM N-hydroxysuccinimide (NHS) and 200 mM 1-ethyl-3-(3-dimethylaminopropyl) carbodiimide (EDC). Then $10\text{ }\mu\text{g/ml}$ of human ACE2 or $50\text{ }\mu\text{g/ml}$ of SARS-CoV-2 S-RBD was injected for 420 s and the surface was blocked with 1 M ethanolamine, pH 8.5. Series concentrations of the test compounds were injected into the flow system at a flow rate of $30\text{ }\mu\text{L/min}$ for 90 s, and the dissociation was 120 s. All binding analysis was performed in phosphate buffered saline (PBS) with 0.05% (v/v) Tween-20 and 1% DMSO (pH 7.4) at 25°C . Prior to analysis, double reference subtractions and solvent corrections were made to eliminate bulk refractive index changes, injection noise, and data drift. The binding affinity was determined by fitting to a Langmuir 1:1 binding model within the BIAcore Evaluation software (GE Healthcare Life Sciences, United States).

Statistical Analysis

Statistical analyses were performed using GraphPad Prism software 8.0. One-way ANOVA was used to determine the



statistical significance between different groups (* $p < 0.05$, ** $p < 0.01$, and *** $p < 0.001$).

RESULTS AND DISCUSSION

Structure-based Virtual Screening

In structure-based virtual screening, the primary thing is to choose the appropriate docking pocket and protein crystal structure. However, according to our observation, the SARS-CoV-2 S-RBD and human ACE2 don't have druggable pockets near the contact interface in their unbound forms. Only when they are bound together, there is a well-defined pocket presented on their contact interface, which is hence defined as the docking pocket in the current study. A crystal structure of the SARS-CoV-2 S-RBD/human ACE2 complex was obtained from PDB and pretreated for virtual screening. The compounds for virtual screening were obtained from the SPECS database and first filtered by PAINS rules. The 202,829 remaining compounds were docking to the previously selected pocket after ligand preparation. The molecular docking was first carried out in standard precision mode. The top 10% poses ranked by SP score were redocked in extra precision mode. The top 20% candidates ranked by XP score were subsequently subjected to cluster analysis and visual inspection to pick the compounds with diversity and reasonable binding mode. Finally, 109 candidate compounds were selected and then purchased for follow-up biological testing. The whole process of

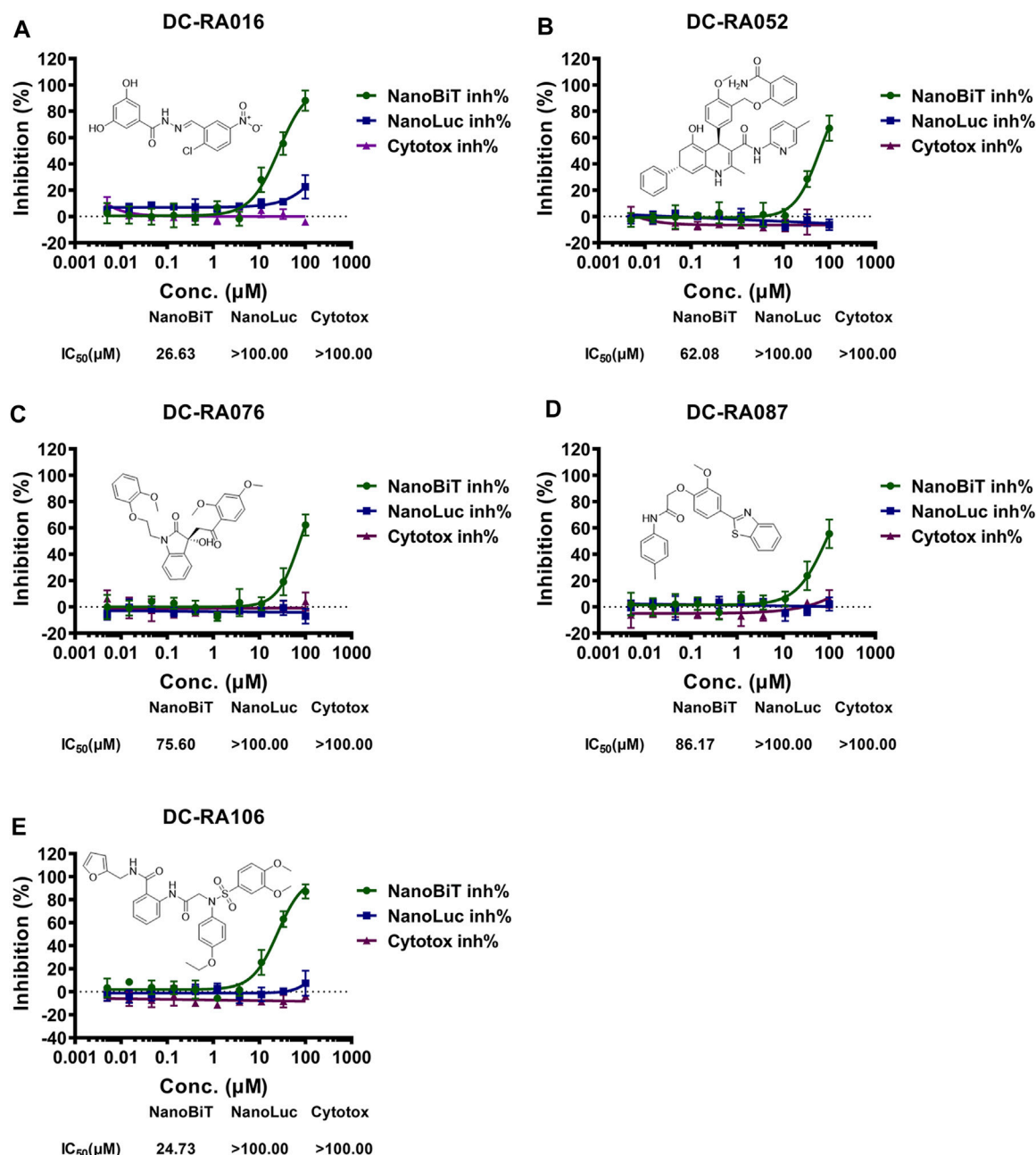


FIGURE 3 | NanoBiT-based SARS-CoV-2 S-RBD/ACE2 interaction assays for five compounds: **(A)** DC-RA016; **(B)** DC-RA052; **(C)** DC-RA076; **(D)** DC-RA087; **(E)** DC-RA106. NanoBiT inh%: the inhibition rates against SARS-CoV-2 S-RBD/ACE2 interaction; NanoLuc inh%: the inhibition rates against NanoLuc luciferase; Cytotox inh%: the inhibition rates against the transfected HEK293 cell proliferation. $n = 3$.

the discovery of inhibitors against the interaction between S-RBD and ACE2 protein is schematically depicted in **Figure 2**.

Identification of SARS-CoV-2 S-RBD/ACE2 Interaction Inhibitors Based on NanoBiT Assay

To discover SARS-CoV-2 S-RBD/ACE2 interaction inhibitors, a NanoBiT-based assay was applied for preliminary screening. 24

of 109 compounds showed the primary inhibitory activities against SARS-CoV-2 S-RBD/ACE2 interaction under 20 and 50 μM concentration, no inhibitory effects on NanoLuc luciferase and cytotoxicity (**Supplementary Figure S1**). We next assessed these compounds for their antiviral activities against SARS-CoV-2-S pseudovirus. Among of them, five compounds were identified as potential inhibitors against SARS-CoV-2-S pseudovirus (**Figure 4A**). We further determined IC₅₀ values of these compounds with serially-

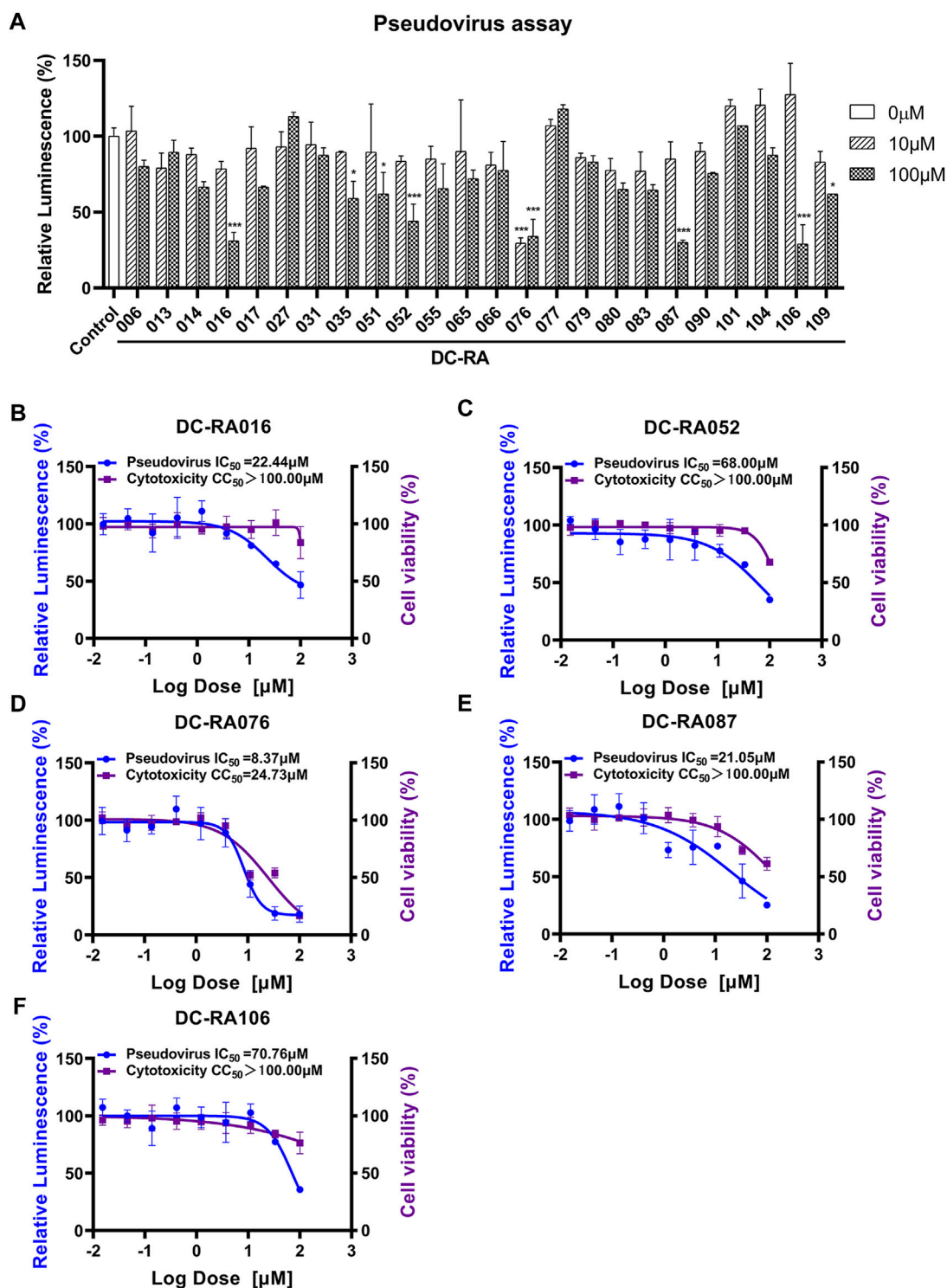


FIGURE 4 | Anti-SARS-CoV-2-S pseudovirus activities and cytotoxicities of several compounds. **(A)** Determining Anti-SARS-CoV-2-S pseudovirus activities of 24 compounds showing the potent blocking activities against SARS-CoV-2 S-RBD/ACE2 interaction in the initial NanoBiT assay using the two concentrations (10, 100 μ M); **(B-F)** IC_{50} and CC_{50} values of five compounds: **(B)** DC-RA016, **(C)** DC-RA052, **(D)** DC-RA076, **(E)** DC-RA087, **(F)** DC-RA106; Relative Luminescence (%) standing for the infection of SARS-CoV-2-S pseudovirus (blue), cell viability (purple).

TABLE 1 | Summary of Anti-SARS-CoV-2-S pseudovirus activities and cytotoxicities of five compounds.

Compounds	IC ₅₀ (μM)	CC ₅₀ (μM)	MNCC (μM)	%I	SI
DC-RA016	22.44	>100.00	95.81	52.08	>4.46
DC-RA052	68.00	>100.00	48.45	45.30	>1.47
DC-RA076	8.37	24.73	2.64	5.75	2.95
DC-RA087	21.05	>100.00	14.01	36.74	>4.75
DC-RA106	70.76	>100.00	13.24	0.14	>1.41

IC₅₀: the 50% inhibitory concentration of Anti-SARS-CoV-2-S pseudovirus; CC₅₀: cytotoxicities on ACE2-expressing HEK293T cells; MNCC: maximum non-cytotoxic concentration; %I: SARS-CoV-2-S pseudovirus inhibition ratio at MNCC; SI: selectivity index.

diluted concentrations for SARS-CoV-2 S-RBD/ACE2 interaction (NanoBiT inh%), NanoLuc luciferase (NanoLuc inh%) and CC₅₀ values for the cytotoxicity (Cytotox inh%) on HEK293 cells (Figure 3). It was shown that DC-RA016, DC-RA052, DC-RA076, DC-RA087 and DC-RA106 exhibited dose-dependent inhibition against SARS-CoV-2 S-RBD/ACE2 interaction, and their IC₅₀ values were 26.63, 62.08, 75.60, 86.17 and 24.73 μM, respectively. These compounds had no obvious inhibitory activities against NanoLuc luciferase (IC₅₀ > 100 μM). It was observed that these compounds were low cytotoxicity with CC₅₀ greater than 100 μM. Thus, the five compounds could disrupt the interaction between SARS-CoV-2 S-RBD and ACE2.

Evaluation of Viral Attachment Inhibitors Using a SARS-CoV-2-S Pseudovirus-Based Inhibition Assay

To evaluate whether the compounds can inhibit the attachment of SARS-CoV-2, a pseudovirus based inhibition assay was established. Due to 24 compounds showing the potent blocking activities against SARS-CoV-2 S-RBD/ACE2 interaction in the initial NanoBiT assay, we next detected the inhibitory activities of these compounds in SARS-CoV-2-S pseudovirus based inhibition assay with the final concentrations of 10 and 100 μM. As shown in Figure 4A, five compounds significantly inhibited SARS-CoV-2-S pseudovirus attachment to ACE2-expressing HEK293T cells at a concentration of 100 μM ($p < 0.001$). Further experiments showed that DC-RA016, DC-RA052, DC-RA076, DC-RA087, and DC-RA106 exhibited dose-dependent inhibitory activities against pseudovirus attachment with IC₅₀ values of 22.44, 68.00, 8.37, 21.05 and 70.76 μM, respectively (Figures 4B–F). Along with the pseudovirus assay, the cytotoxicity of the five compounds to ACE2-expressing HEK293T cells was also investigated (Figures 4B–F). It could be noted that the compound DC-RA076 showed obvious cytotoxicity (CC₅₀ = 24.73 μM) to ACE2-expressing HEK293T cells with SI of 2.95 and MNCC of 2.64 μM (Table 1), while other four compounds displayed the inhibitory effects on SARS-CoV-2-S pseudovirus attachment without obvious cytotoxicity (CC₅₀ > 100 μM) with SI ranging from 1.41 to 4.75 and MNCC ranging from 13.24 to 95.81 μM (Table 1). It is worth noting that the %I of DC-RA016

(52.08%), DC-RA052 (45.30%), and DC-RA087 (36.74%) is much larger than DC-RA076 (5.75%) and DC-RA106 (0.14%), indicating that the three compounds may have the potential for further structural optimization and fight against SARS-CoV-2. Thus, among the five compounds, DC-RA016, DC-RA052, and DC-RA087 demonstrated the relatively good antiviral effects with low cytotoxicity.

Determination of Interactions Between the Five Compounds and SARS-CoV-2 S-RBD or ACE2 by SPR Assay

To further validate the inhibitory mechanism of the five compounds against SARS-CoV-2-S pseudovirus attachment, SPR assay was carried out to investigate whether these compounds could directly bind to SARS-CoV-2 S-RBD or ACE2. As shown in Figure 5, DC-RA016, DC-RA052, DC-RA087 and DC-RA106 could bind to human ACE2 (Figures 5A,C,G,I); while DC-RA016, DC-RA052 and DC-RA106 showed binding to SARS-CoV-2 S-RBD (Figures 5B,D,J). All these binding displayed fast kinetics, except for DC-RA087 to human ACE2 (Figure 5G). For DC-RA076, no binding was observed for both targets. DC-RA052 exhibited high affinities to both SARS-CoV-2 S-RBD and ACE2 and the KD values were 21.66 and 34.71 μM, respectively. In spite of concentration-dependent binding curves, saturated binding seemed not reached for DC-RA106, which could lead to poor quality of affinity regression (KD > 100.00 μM). In view of the previous results of the SARS-CoV-2-S pseudovirus-based inhibition assay, compounds DC-RA016 and DC-RA052 were ultimately identified as the two most promising hits blocking the interaction between SARS-CoV-2 S-RBD and ACE2 and SARS-CoV-2 virus attachment.

Similarity Search and Structure-activity Relationship

Through the 2D similarity search, we found there were a few molecules similar to DC-RA016 in the SPECS database. Hence, 12 analogues of DC-RA016 were purchased to explore the structure-activity relationship of it. Their inhibition ability to the interaction of SARS-CoV-2 S-RBD and human ACE2 were tested by NanoBiT assay. As shown in Table 2, those compounds whose R1 groups were not 3,5-dihydroxy phenyl group all displayed no inhibitory activity against SARS-CoV-2 S-RBD and ACE2 interaction. Among the four compounds having the same R1 group with DC-RA016, two compounds (DC-RA016-9 and DC-RA016-12) could disrupt the interaction between SARS-CoV-2 S-RBD and ACE2 under the concentration of 50 and 20 μM. We further determined their dose-dependent inhibition against SARS-CoV-2 S-RBD/ACE2 interaction, NanoLuc luciferase and cytotoxicity on HEK293 cells. It was found that DC-RA016-12 exhibited the similar activity (IC₅₀ = 26.06 μM) (Supplementary Figure S2A) to DC-RA016 (IC₅₀ = 26.63 μM), while DC-RA016-9 displayed less inhibitory activity (IC₅₀ = 73.84 μM) (Supplementary Figure S2B) than DC-RA016.

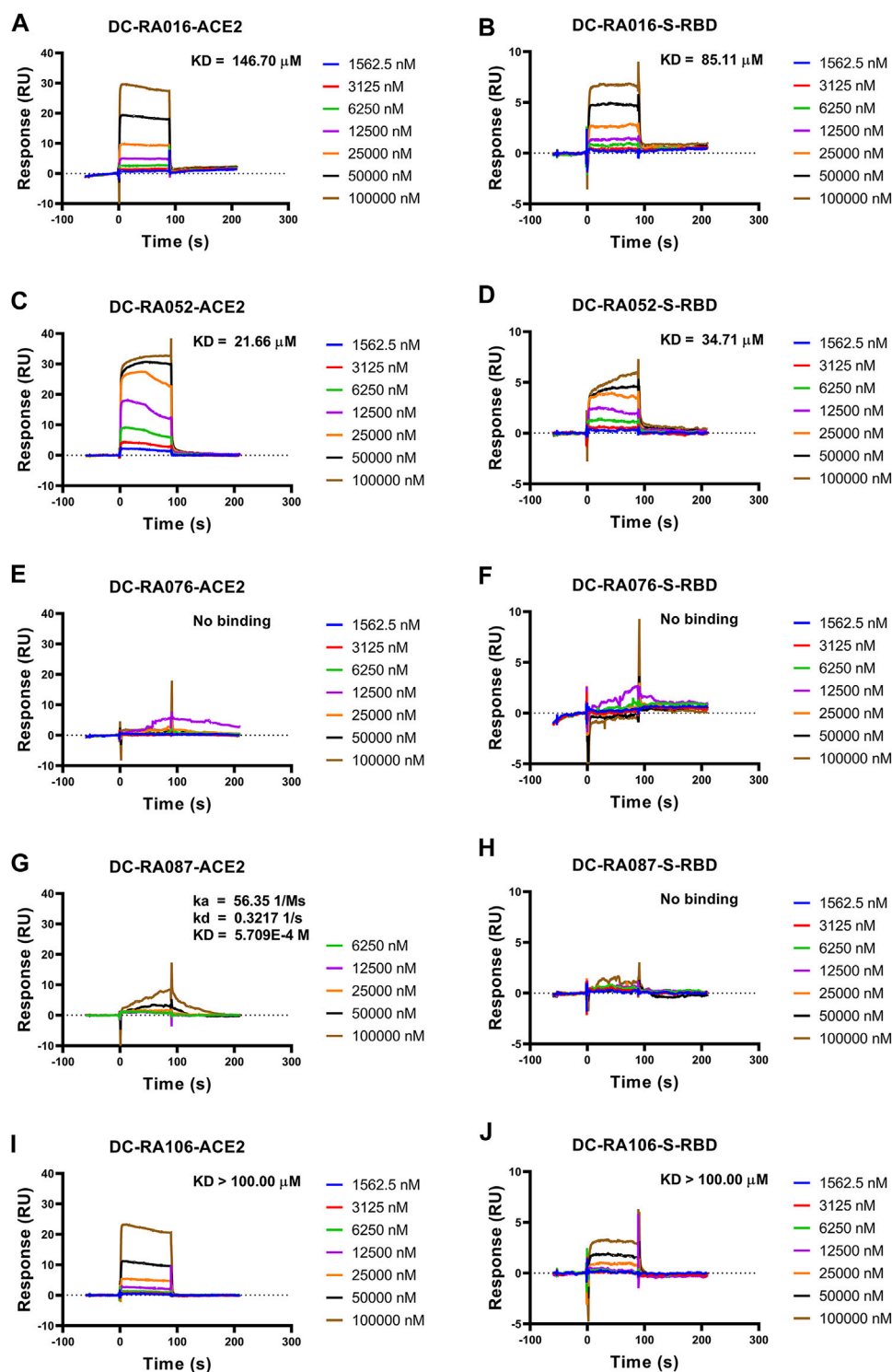


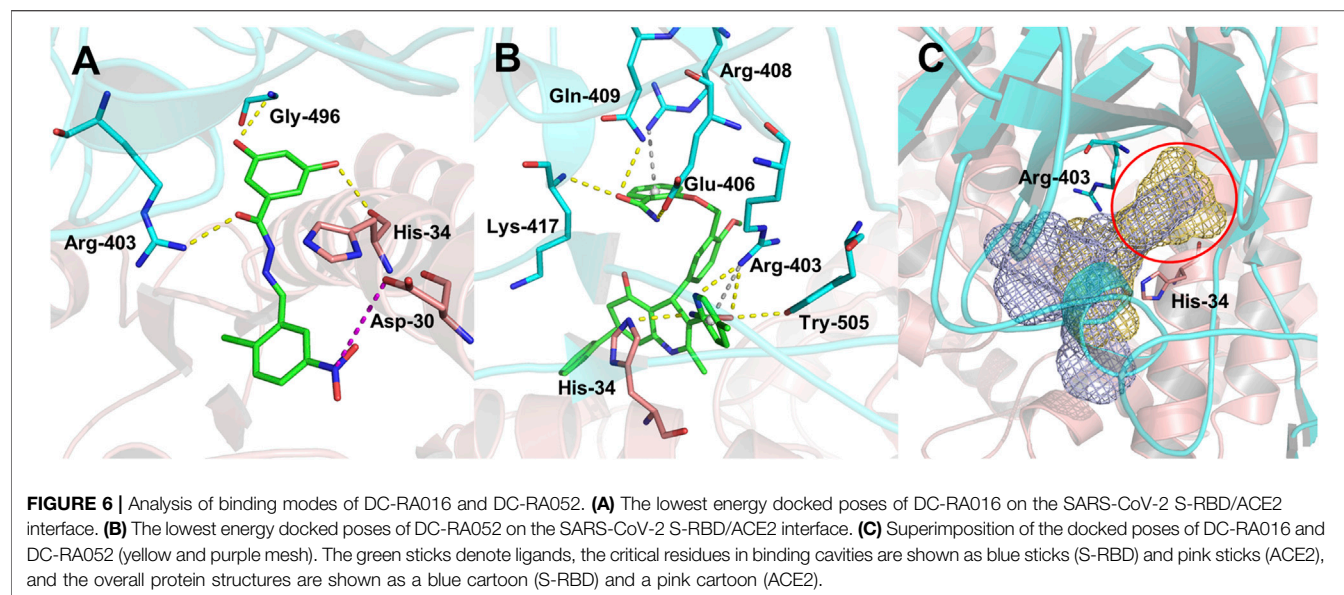
FIGURE 5 | The binding affinity between the five compounds and SARS-CoV-2 S-RBD or ACE2. Compounds bound to SARS-CoV-2 S-RBD or ACE2. Interactions of SARS-CoV-2 S-RBD or ACE2 with compounds measured by SPR. The SARS-CoV-2 S-RBD or ACE2 was coated on the CM5 sensor chip and serial dilutions of compounds (typically, 1,562.5, 3,125, 6,250, 12,500, 25,000, 50,000 and 100,000 nM) were used as analytes. Changes in plasmon resonance are shown as response units. **(A)** Binding curves (colored lines) obtained by passing different concentrations of DC-RA016 over immobilized ACE2. **(B)** Binding curves (colored lines) obtained by passing different concentrations of DC-RA016 over immobilized S-RBD. **(C)** Binding curves (colored lines) obtained by passing different concentrations of DC-RA052 over immobilized ACE2. **(D)** Binding curves (colored lines) obtained by passing different concentrations of DC-RA052 over immobilized S-RBD. **(E)** Binding curves (colored lines) obtained by passing different concentrations of DC-RA076 over immobilized ACE2. **(F)** Binding curves (colored lines) obtained by passing different concentrations of DC-RA076 over immobilized S-RBD. **(G)** Binding curves (colored lines) obtained by passing different concentrations of DC-RA087 over immobilized ACE2. **(H)** Binding curves (colored lines) obtained by passing different concentrations of DC-RA087 over immobilized S-RBD. **(I)** Binding curves (colored lines) obtained by passing different concentrations of DC-RA106 over immobilized ACE2. **(J)** Binding curves (colored lines) obtained by passing different concentrations of DC-RA106 over immobilized S-RBD. (Continued)

FIGURE 5 | concentrations of DC-RA076 over immobilized S-RBD. **(G)** Binding curves (colored lines) obtained by passing different concentrations of DC-RA087 over immobilized ACE2. **(H)** Binding curves (colored lines) obtained by passing different concentrations of DC-RA087 over immobilized S-RBD. **(I)** Binding curves (colored lines) obtained by passing different concentrations of DC-RA106 over immobilized ACE2. **(J)** Binding curves (colored lines) obtained by passing different concentrations of DC-RA106 over immobilized S-RBD.

TABLE 2 | The activities of DC-RA016 analogues in NanoBIT-based assay.

Cmpd name	R ₁	R ₂	SARS-CoV-2 S-RBD/ ACE2 inhibition %		NanoLuc inhibition %	
			50 μM	20 μM	50 μM	20 μM
DC-RA016			73.1	73.1	38.4	32.8
DC-RA016-1			7.4	3.1	-2.2	0.6
DC-RA016-2			22.5	0.8	16.4	16.4
DC-RA016-3			24.2	1.7	20.2	19.3
DC-RA016-4			-24.9	-3.8	9.0	8.2
DC-RA016-5			24.9	8.7	11.2	9.8
DC-RA016-6			2.9	1.9	3.5	0.9
DC-RA016-7			20.2	10.6	16.0	14.6
DC-RA016-8			-18.3	6.7	5.7	0.0
DC-RA016-9			88.6	0.6	27.7	14.0
DC-RA016-10			-17.7	-6.5	3.8	4.1
DC-RA016-11			12.7	4.8	15.5	13.4
DC-RA016-12			88.9	61.3	26.1	18.1

SARS-CoV-2 S-RBD/ACE2 Inhibition %: the inhibition rates against SARS-CoV-2 S-RBD/ACE2 interaction; NanoLuc Inhibition %: the inhibition rates against NanoLuc luciferase.



To analyze the mechanism of action of DC-RA016, the binding pose of the compound DC-RA016 on the SARS-CoV-2 S-RBD/ACE2 interface was generated by XP docking. As shown in **Figure 6A**, DC-RA016 could form strong interactions with the SARS-CoV-2 S-RBD/ACE2 complex interface. The two phenolic hydroxyls of DC-RA016 respectively formed H-bonds with the His-34 of ACE2 and Gly496 of S-RBD. The replacement of the R1 group of DC-RA016 with other structures would disrupt such interaction, which provided the structural explanation for the impaired activity of compounds DC-RA016-1 to DC-RA016-8. Additionally, an electrostatic interaction also occurred between the nitro of DC-RA016 and Asp-30 of ACE2, which accounted for the stronger inhibitory activity of compounds DC-RA016 and DC-RA016-12 than compounds DC-RA016-9, DC-RA016-10, and DC-RA016-11. Compared with DC-RA016, the change of the position of chlorine substitution in DC-RA016-12 didn't have obvious effects on its inhibitory activity. Moreover, although its R₂ group was quite different from that of DC-RA016, DC-RA016-9 still displayed certain inhibitory activity. These results suggested that the R₂ group was not the essential pharmacophore of DC-RA016, so we plan to carry further structural modification on this group in the future.

The docking analysis on DC-RA052, another important inhibitor, was also carried out. As shown in **Figure 6B**, Lys-417, Gln-409, Glu-406, Arg-403, Tyr-505 of SARS-CoV-2 S-RBD, and His-34 of ACE2 were found to form H-bonds with DC-RA052. Moreover, the benzene ring and pyridine ring of DC-RA052 formed π -cation interaction with the Arg-408 and Arg-403 of S-RBD. Comparing the binding modes of DC-RA016 and DC-RA052, it could be noted that both DC-RA016 and DC-RA052 interacted with the Arg-403 of S-RBD and His-34 of ACE2. Then, based on the docked complex structures, we calculated the per-residue interaction scores with glide. The results indicated the strong interaction of Arg-403 of S-RBD and His-34 of ACE2 to DC-RA016 and DC-RA052

(**Supplementary Table S1**). Moreover, as shown in **Figure 6C**, there was a deep pocket (marked with the red circle) on the SARS-CoV-2 S-RBD/ACE2 interface. Arg-403 of S-RBD and His-34 of ACE2 were both at the edge of this pocket. Hence, we considered Arg-403 of S-RBD and His-34 of ACE2 as two key residues responsible for the binding of ligands to the SARS-CoV-2 S-RBD/ACE2 interface. To explore the reason why the binding of identified inhibitors can influence SARS-CoV-2 S-RBD/ACE2 interaction, the mean effects of mutation of each residue within 5 Å of DC-RA016 and DC-RA052 on the binding affinity of SARS-CoV-2 S-RBD to ACE2 were visualized. The data for visualization was obtained from a previous study, where Starr et al. systematically changed every amino acid in the SARS-CoV-2 S-RBD and determined the effects of the substitutions on ACE2 binding. The mean effects per site were calculated from the set of $\Delta\log_{10}(K_D, \text{app})$ measurements of all missense mutations at a site (Starr et al., 2020). $\Delta\log_{10}(K_D, \text{app})$ represents the log binding constants relative to the wild-type SARS-CoV-2 RBD. As shown in **Supplementary Figure S3**, the mutations of many residues around DC-RA016 and DC-RA052 such as Ile-418 and Phe-497 could significantly reduce the binding affinity of SARS-CoV-2 S-RBD to ACE2, which mean these residues played key roles in the binding of SARS-CoV-2 S-RBD to ACE2. And yet, binding to the SARS-CoV-2 S-RBD/ACE2 interface, DC-RA016 and DC-RA052 would contact with these residues and interfere with their functions, disrupting the interaction between SARS-CoV-2 S-RBD and ACE2.

CONCLUSION

Prior work has demonstrated that the interaction of SARS-CoV-2 S-RBD and the ACE2 receptor plays a critical role in the virus invasion into the host cell. Hence interference of SARS-CoV-2 S-RBD/ACE2 interaction is regarded as a promising antiviral

strategy for SARS-CoV-2. However, only fewer small molecule inhibitors targeting such interaction have been reported so far. In this study, the structural-based virtual screening was conducted to search for the compounds that can inhibit the SARS-CoV-2 S-RBD/ACE2 interaction. The screened compounds were docked by targeting the SARS-CoV-2 S-RBD/ACE2 interface. Subsequently, A NanoBiT-based binding assay was performed to evaluate the inhibition effect of those compounds on SARS-CoV-2 S-RBD/ACE2 interaction resulting in 24 potential inhibitor candidates. Among them, DC-RA016, DC-RA052, and DC-RA087 displayed low cytotoxicity and moderate inhibition ability to SARS-CoV-2-S pseudovirus. Furthermore, the SPR assays identified that DC-RA016 and DC-RA052 could directly bond to both ACE2 and S-RBD. Taken together, the compounds DC-RA016 and DC-RA052 obtained in this study can serve as an ideal starting point for drug design against SARS-CoV-2 S-RBD/ACE2 interaction and SARS-CoV-2 infection. In addition, two biological active analogues of DC-RA016 were discovered through the 2D similarity search. Among them, DC-RA016-12 exhibited similar activity to DC-RA016 in NanoBiT-based assay.

DATA AVAILABILITY STATEMENT

The original contributions presented in the study are included in the article/**Supplementary Files**, further inquiries can be directed to the corresponding authors.

REFERENCES

- Carino, A., Moraca, F., Fiorillo, B., Marchianò, S., Sepe, V., Biagioli, M., et al. (2020). Hijacking SARS-Cov-2/ace2 Receptor Interaction by Natural and Semi-synthetic Steroidal Agents Acting on Functional Pockets on the Receptor Binding Domain. *Front. Chem.* 8 (846), 572885. doi:10.3389/fchem.2020.572885
- Chen, B., Tian, E.-K., He, B., Tian, L., Han, R., Wang, S., et al. (2020). Overview of Lethal Human Coronaviruses. *Sig. Transduct. Target. Ther.* 5 (1), 89. doi:10.1038/s41392-020-0190-2
- Cheng, J., Sun, N., Zhao, X., Niu, L., Song, M., Sun, Y., et al. (2013). In Vitro screening for Compounds Derived from Traditional Chinese Medicines with Antiviral Activities against Porcine Reproductive and Respiratory Syndrome Virus. *J. Microbiol. Biotechnol.* 23 (8), 1076–1083. doi:10.4014/jmb.1303.03074
- Fu, W., Chen, Y., Wang, K., Hettighouse, A., Hu, W., Wang, J.-Q., et al. (2020). Repurposing FDA-Approved Drugs for SARS-CoV-2 through an ELISA-Based Screening for the Inhibition of RBD/ACE2 Interaction. *Protein Cell* 12 (7), 586–591. doi:10.1007/s13238-020-00803-w
- Gorbalenya, A. E., Baker, S. C., Baric, R. S., de Groot, R. J., Drosten, C., Gulyaeva, A. A., et al. (2020). The Species Severe Acute Respiratory Syndrome-Related Coronavirus: Classifying 2019-nCoV and Naming it SARS-CoV-2. *Nat. Microbiol.* 5 (4), 536–544. doi:10.1038/s41564-020-0695-z
- Hanson, Q. M., Wilson, K. M., Shen, M., Itkin, Z., Eastman, R. T., Shinn, P., et al. (2020). Targeting ACE2-RBD Interaction as a Platform for COVID-19 Therapeutics: Development and Drug-Repurposing Screen of an AlphaLISA Proximity Assay. *ACS Pharmacol. Transl. Sci.* 3 (6), 1352–1360. doi:10.1021/acspstsci.0c00161
- Hoffmann, M., Kleine-Weber, H., Schroeder, S., Krüger, N., Herrler, T., Erichsen, S., et al. (2020). SARS-CoV-2 Cell Entry Depends on ACE2 and TMPRSS2 and Is Blocked by a Clinically Proven Protease Inhibitor. *cell* 181 (2), 271–280. doi:10.1016/j.cell.2020.02.052

AUTHOR CONTRIBUTIONS

LC, MZ, and JXu conceived and designed the experiments. JXi, YX, ZH, XL, and MW carried out the experiments and data analysis. JXi and YX wrote the manuscript. LC, MZ, HC, and GG critically revised the manuscript.

FUNDING

This work was supported by Scientific Research Project of Shanghai Municipal Health Commission on Traditional Chinese Medicine for Prevention and Treatment of COVID-19 (2020XGKY07), Emergency Scientific Research Program of Shanghai University of Traditional Chinese Medicine (2019YJ 06-01), the National Natural Science Foundation of China (81773634 to MZ), Tencent AI Lab Rhino-Bird Focused Research Program (No. JR202002), and Shanghai Science and Technology Innovation Action Plans (20S21901500, 20S21900900) supported by Shanghai Science and Technology Committee.

SUPPLEMENTARY MATERIAL

The Supplementary Material for this article can be found online at: <https://www.frontiersin.org/articles/10.3389/fchem.2021.740702/full#supplementary-material>

- Li, J., Yu, C., Wang, R., Xu, J., Chi, Y., Qin, J., et al. (2017). The ω -carboxyl Group of 7-Ketocholesteryl-9-Carboxynonanoate Mediates the Binding of oxLDL to CD36 Receptor and Enhances Caveolin-1 Expression in Macrophages. *Int. J. Biochem. Cel Biol.* 90, 121–135. doi:10.1016/j.biocel.2017.07.022
- Li, J., Zhan, P., and Liu, X. (2020). Targeting the Entry Step of SARS-CoV-2: a Promising Therapeutic Approach. *Sig. Transduct. Target. Ther.* 5 (1), 98. doi:10.1038/s41392-020-0195-x
- Monteil, V., Kwon, H., Prado, P., Hagelkrüys, A., Wimmer, R. A., Stahl, M., et al. (2020). Inhibition of SARS-CoV-2 Infections in Engineered Human Tissues Using Clinical-Grade Soluble Human ACE2. *Cell* 181 (4), 905–913. doi:10.1016/j.cell.2020.04.004
- Starr, T. N., Greaney, A. J., Hilton, S. K., Ellis, D., Crawford, K. H. D., Dingens, A. S., et al. (2020). Deep Mutational Scanning of SARS-CoV-2 Receptor Binding Domain Reveals Constraints on Folding and ACE2 Binding. *Cell* 182 (5), 1295–1310. doi:10.1016/j.cell.2020.08.012
- Sun, S.-H., Chen, Q., Gu, H.-J., Yang, G., Wang, Y.-X., Huang, X.-Y., et al. (2020). A Mouse Model of SARS-CoV-2 Infection and Pathogenesis. *Cell Host Microbe* 28 (1), 124–133. doi:10.1016/j.chom.2020.05.020
- Walls, A. C., Park, Y.-J., Tortorici, M. A., Wall, A., McGuire, A. T., and Velesler, D. (2020). Structure, Function, and Antigenicity of the SARS-CoV-2 Spike Glycoprotein. *Cell* 181 (2), 281–292. doi:10.1016/j.cell.2020.02.058
- Wang, Q., Zhang, Y., Wu, L., Niu, S., Song, C., Zhang, Z., et al. (2020). Structural and Functional Basis of SARS-CoV-2 Entry by Using Human ACE2. *Cell* 181 (4), 894–904. doi:10.1016/j.cell.2020.03.045
- Wrapp, D., Wang, N., Corbett, K. S., Goldsmith, J. A., Hsieh, C.-L., Abiona, O., et al. (2020). Cryo-EM Structure of the 2019-nCoV Spike in the Prefusion Conformation. *Science* 367 (6483), 1260–1263. doi:10.1126/science.abb2507
- Xu, C., Wang, Y., Liu, C., Zhang, C., Han, W., Hong, X., et al. (2021). Conformational Dynamics of SARS-CoV-2 Trimeric Spike Glycoprotein in Complex with Receptor ACE2 Revealed by Cryo-EM. *Sci. Adv.* 7 (1), eabe5575. doi:10.1126/sciadv.abe5575

- Yang, J., Petitjean, S. J. L., Koehler, M., Zhang, Q., Dumitru, A. C., Chen, W., et al. (2020a). Molecular Interaction and Inhibition of SARS-CoV-2 Binding to the ACE2 Receptor. *Nat. Commun.* 11 (1), 1–10. doi:10.1038/s41467-020-18319-6
- Yang, X., Yu, Y., Xu, J., Shu, H., Xia, J. a., Liu, H., et al. (2020b). Clinical Course and Outcomes of Critically Ill Patients with SARS-CoV-2 Pneumonia in Wuhan, China: a Single-Centered, Retrospective, Observational Study. *Lancet Respir. Med.* 8 (5), 475–481. doi:10.1016/S2213-2600(20)30079-5
- Yao, H., Song, Y., Chen, Y., Wu, N., Xu, J., Sun, C., et al. (2020). Molecular Architecture of the SARS-CoV-2 Virus. *Cell* 183 (3), 730–738. doi:10.1016/j.cell.2020.09.018
- Yu, S., Zhu, Y., Xu, J., Yao, G., Zhang, P., Wang, M., et al. (2021). Glycyrrhizic Acid Exerts Inhibitory Activity against the Spike Protein of SARS-CoV-2. *Phytomedicine* 85, 153364. doi:10.1016/j.phymed.2020.153364
- Zhang, H., Penninger, J. M., Li, Y., Zhong, N., and Slutsky, A. S. (2020a). Angiotensin-converting Enzyme 2 (ACE2) as a SARS-CoV-2 Receptor: Molecular Mechanisms and Potential Therapeutic Target. *Intensive Care Med.* 46 (4), 586–590. doi:10.1007/s00134-020-05985-9
- Zhang, J.-j., Dong, X., Cao, Y.-y., Yuan, Y.-d., Yang, Y.-b., Yan, Y.-q., et al. (2020b). Clinical Characteristics of 140 Patients Infected with SARS-CoV-2 in Wuhan, China. *Allergy* 75 (7), 1730–1741. doi:10.1111/all.14238
- Zhu, Z.-L., Qiu, X.-D., Wu, S., Liu, Y.-T., Zhao, T., Sun, Z.-H., et al. (2021). Blocking Effect of Demethylzeylasteral on the Interaction between

Human ACE2 Protein and SARS-CoV-2 RBD Protein Discovered Using SPR Technology. *Molecules* 26 (1), 57. doi:10.3390/molecules26010057

Conflict of Interest: The authors declare that the research was conducted in the absence of any commercial or financial relationships that could be construed as a potential conflict of interest.

Publisher's Note: All claims expressed in this article are solely those of the authors and do not necessarily represent those of their affiliated organizations, or those of the publisher, the editors and the reviewers. Any product that may be evaluated in this article, or claim that may be made by its manufacturer, is not guaranteed or endorsed by the publisher.

Copyright © 2021 Xiong, Xiang, Huang, Liu, Wang, Ge, Chen, Xu, Zheng and Chen. This is an open-access article distributed under the terms of the Creative Commons Attribution License (CC BY). The use, distribution or reproduction in other forums is permitted, provided the original author(s) and the copyright owner(s) are credited and that the original publication in this journal is cited, in accordance with accepted academic practice. No use, distribution or reproduction is permitted which does not comply with these terms.



Inhibition of SARS-CoV-2 by Targeting Conserved Viral RNA Structures and Sequences

Shalakha Hegde[†], Zhichao Tang[†], Junxing Zhao and Jingxin Wang^{*}

Department of Medicinal Chemistry, University of Kansas, Lawrence, KS, United States

OPEN ACCESS

Edited by:

Jun Wang,
Rutgers, The State University of New
Jersey, United States

Reviewed by:

Tao Liu,
Peking University, China
Liqiang Chen,
University of Minnesota Twin Cities,
United States

*Correspondence:

Jingxin Wang
wang.jingxin@ku.edu

[†]These authors have contributed
equally to this work.

Specialty section:

This article was submitted to
Chemical Biology,
a section of the journal
Frontiers in Chemistry

Received: 27 October 2021

Accepted: 29 November 2021

Published: 23 December 2021

Citation:

Hegde S, Tang Z, Zhao J and Wang J
(2021) Inhibition of SARS-CoV-2 by
Targeting Conserved Viral RNA
Structures and Sequences.
Front. Chem. 9:802766.
doi: 10.3389/fchem.2021.802766

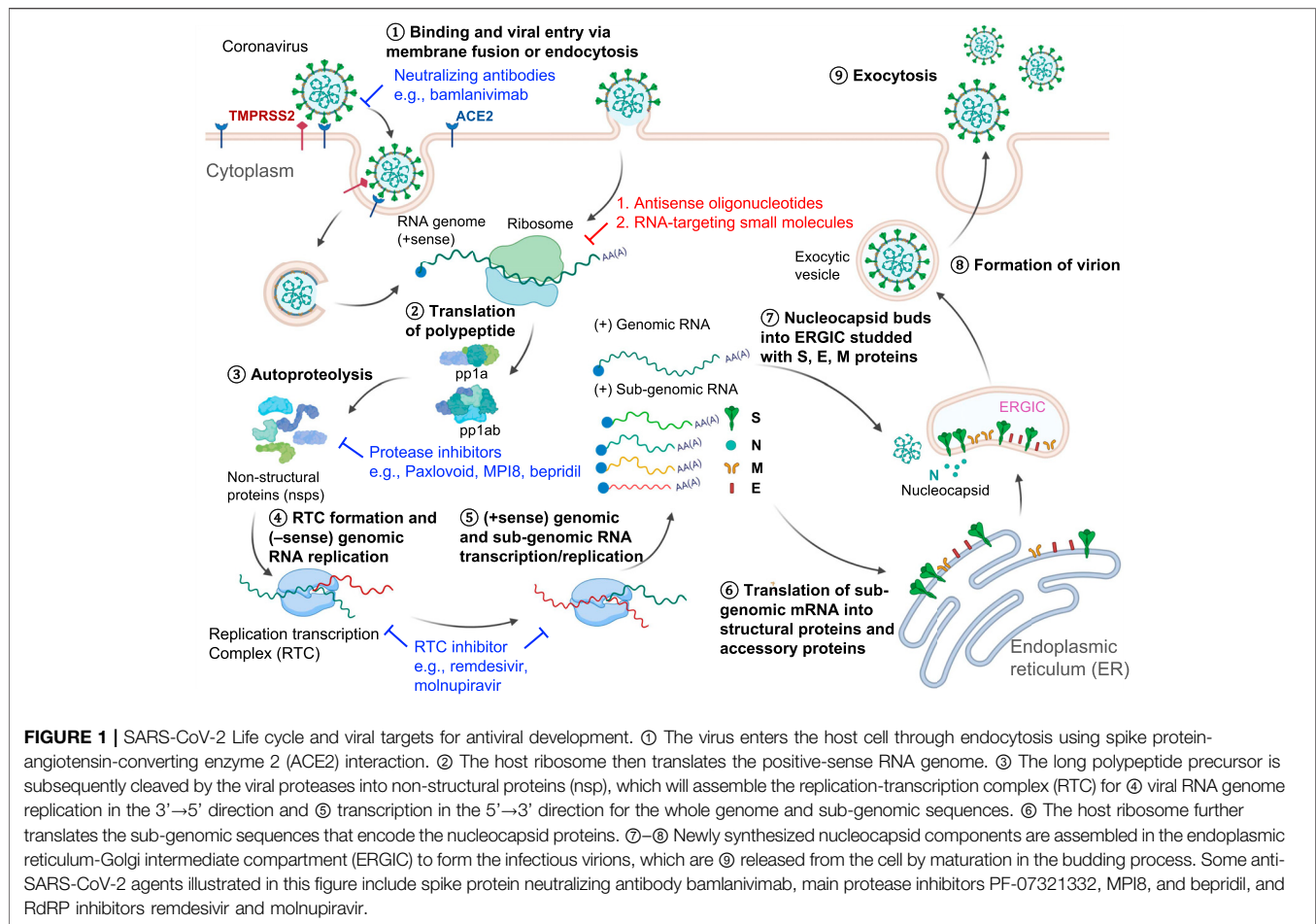
The ongoing COVID-19/Severe Acute Respiratory Syndrome CoV-2 (SARS-CoV-2) pandemic has become a significant threat to public health and has hugely impacted societies globally. Targeting conserved SARS-CoV-2 RNA structures and sequences essential for viral genome translation is a novel approach to inhibit viral infection and progression. This new pharmacological modality compasses two classes of RNA-targeting molecules: 1) synthetic small molecules that recognize secondary or tertiary RNA structures and 2) antisense oligonucleotides (ASOs) that recognize the RNA primary sequence. These molecules can also serve as a “bait” fragment in RNA degrading chimeras to eliminate the viral RNA genome. This new type of chimeric RNA degrader is recently named ribonuclease targeting chimera or RIBOTAC. This review paper summarizes the sequence conservation in SARS-CoV-2 and the current development of RNA-targeting molecules to combat this virus. These RNA-binding molecules will also serve as an emerging class of antiviral drug candidates that might pivot to address future viral outbreaks.

Keywords: SARS-CoV-2, antiviral, RNA-targeting, small molecule, antisense oligonucleotide, untranslated region, programmed frameshift, RIBOTAC

INTRODUCTION

SARS-CoV-2's Life Cycle and “Druggable” Targets

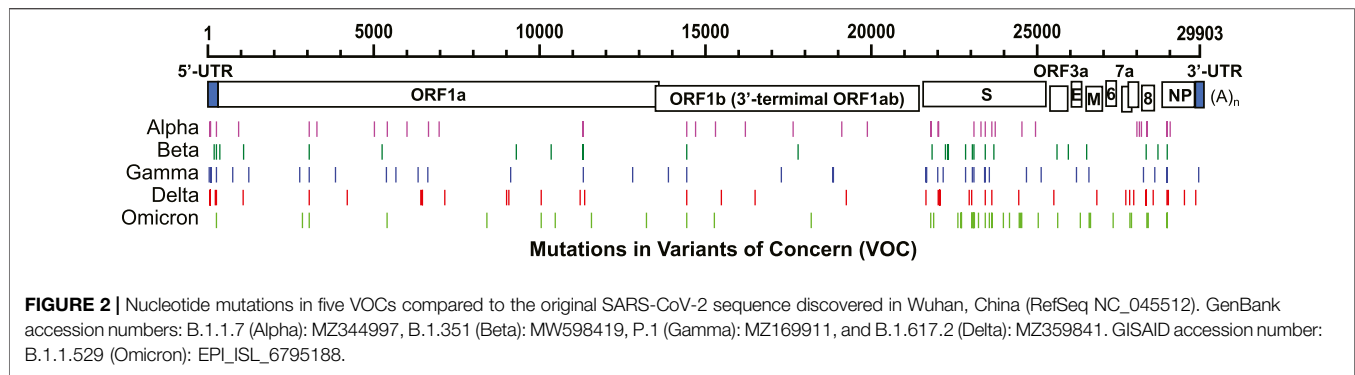
SARS-CoV-2 belongs to the betacoronavirus genus and is an enveloped ssRNA (+) virus with a genome length of about 30,000 nucleotides (RefSeq NC_045512) (Wu et al., 2020). The viral genome is 5' capped and 3' polyadenylated (Robson et al., 2020) so that it is recognized and treated as an mRNA by the host cell ribosome. Two-thirds of the viral genome at the 5'-end have two long open reading frames (ORFs), ORF1a and ORF1ab, encoding two replicase-associated polyprotein precursors, pp1a and pp1ab (Figure 1). These polyprotein precursors are cleaved by viral proteases into 16 non-structural proteins (nsps) (Kim et al., 2020), some of which have essential viral functions (Figure 1). For example, an RNA-dependent RNA polymerase (RdRP) complex consisting of nsp12 in pp1ab and nsps7 and 8 in pp1a is required for viral transcription and replication (Hillen et al., 2020). RdRP is the core enzyme in the viral “replication-transcription complex” (RTC) (Fung and Liu, 2019). The RTC then promotes 3'→5' replication of the (–) viral genome to form a full-length double-stranded (ds) RNA in the endoplasmic reticulum (ER) membrane invaginations (Knoops et al., 2008). This dsRNA then serves as a template for transcribing the genomic and subgenomic RNAs by RTC-mediated transcription in the 5'→3' direction (Wu and Brian, 2010) (Figure 1). RNA transcription for each coronavirus structural protein is accomplished through a “discontinuous” mechanism. The RTC binds to the leader



transcriptional regulatory sequences (TRS-L) in the 5' UTR and then “hops” onto the body TRS (TRS-B) sequence. These TRS-B sequences locate at the 5'-end of each structural gene for transcription (Zúñiga et al., 2004; Sola et al., 2015). After completing structural protein synthesis and genomic RNA replication, new coronavirus particles are assembled at the host ER and released through the Golgi apparatus to complete the viral life cycle (Sawicki et al., 2007).

Current drug development pipelines have tackled different steps in the life cycle of SARS-CoV-2 (**Figure 1**). Spike protein-targeting antibodies (e.g., bamlanivimab) can effectively neutralize the virus and prevent viral entry (Gottlieb et al., 2021). RNA-targeting antisense oligonucleotides (ASO) or small molecules will degrade the viral RNA genome or hinder RNA translation (Li et al., 2021b; Li et al., 2021a; Lulla et al., 2021; Rosenke et al., 2021; Sun et al., 2021a; Zhang et al., 2021; Zhu et al., 2021). The SARS-CoV-2 main protease (M^{pro}) is also an attractive drug target. PF-07321332 (Paxlovid) was developed as an oral drug targeting M^{pro} and is being tested in a Phase 3 clinical trial (ClinicalTrials.gov Identifier: NCT04960202) (Owen et al., 2021). Other reported M^{pro} inhibitors such as an FDA-approved drug, bepridil, and a peptoid MPI8 were demonstrated to have

efficacy in virus-infected cells (Ma et al., 2021; Vatansever et al., 2021). RdRP inhibitors remdesivir and molnupiravir, which impede the RNA replication/transcription processes, both showed clinical improvement in the COVID-19 patients (Wang et al., 2020; Fischer et al., 2021). In this review, we focused on the RNA-targeting approach, an emerging antiviral pharmacological modality that is complementary to traditional protein-targeting methods. An advantage of ASO-based drug development is the ability to rapidly generate drug candidates, which recognize the primary sequences of viral RNAs. The off-targets of the ASOs can also be quickly identified through experiments or predictive algorithms based on the primary sequences (Hagedorn et al., 2018; Yoshida et al., 2019). Compared to the ASO-based drug discovery, RNA-targeting small molecules are a relatively underdeveloped field. To date, only one non-ribosomal RNA binding molecule, risdiplam, has been approved by the FDA (Jaklevic, 2020). We envision that the chemical space, potency, off-targets for RNA-binding small molecules will be further investigated as therapeutics to antivirals and other human diseases (Hargrove, 2020; Meyer et al., 2020; Ursu et al., 2020). RNA-targeting molecules will probably synergically inhibit viral replication when combined with protein-targeting drugs in cocktail therapies.



Conserved RNA Sequences and Structures in SARS-CoV-2

The mutation rate of SARS-CoV-2 is estimated at 1×10^{-3} substitutions per base (30 nucleotides/genome) per year under neutral genetic drift conditions (van Dorp et al., 2020), or 1×10^{-5} – 1×10^{-4} substitutions per base (0.3–3 nucleotides/genome) in each transmission events from population phylodynamic studies (Van Egeren et al., 2021). This rate is much slower than some other RNA viruses, such as influenza A virus (Manzanares-Meza and Medina-Contreras, 2020) and human immunodeficiency virus (HIV) (Van Egeren et al., 2021). As of December 2, 2021, five circulating variants of SARS-CoV-2 are classified as variants of concern (VOC) in the World Health Organization (<https://www.who.int/en/activities/tracking-SARS-CoV-2-variants/>), including B.1.1.7 (Alpha), B.1.351 (Beta), P.1 (Gamma), B.1.617.2 (Delta), and B.1.1.529 (Omicron) variants. Among these variants, the spike protein (S) harbors most of the nucleotide mutations compared to the original genomic sequence isolated from Wuhan, China, in December 2019 (Figure 2). Some mutations occur beyond the protein-coding region. For example, a prevalent mutation C241U (c.-63C>U) exists in the 5' untranslated region (UTR) of all four VOCs (Figure 3A).

By phylogenetic comparison of SARS-CoV-2, SARS-CoV, and SARS-related bat coronavirus sequences (Ceraolo and Giorgi, 2020), an earlier bioinformatics work from the Das group in 2020 identified 30 RNA regions as SARS-related conserved sequences and predicted 106 regions as SARS-CoV-2 conserved structures (Rangan et al., 2020). Shortly afterward, the RNA structures of SARS-CoV-2 were interrogated by chemical probing (Lan et al., 2020; Manfredonia et al., 2020; Sanders et al., 2020; Zhao et al., 2020; Sun et al., 2021a; Huston et al., 2021), psoralen crosslinking (Ziv et al., 2020), and NMR spectroscopy experiments (Wacker et al., 2020). Among all SARS-CoV-2 RNA structures identified, the 5' and 3' UTRs and a region named programmed -1 frameshift (PFS) element (13,459–13,546) in the ORF1a/ab have been intensively studied for their structures, functions, and druggability.

SARS-CoV-2 PFS Element

ORF1a is the 5'-terminal fraction of ORF1ab and has an in-frame stop codon at nucleotide 13,481. The correct translation of

ORF1b (3'-terminal ORF1ab), which encodes the viral RdRP (nsp12), requires a PFS that shifts the ORF by -1 nucleotide via a "slippery sequence" to circumvent the ORF1a stop codon (Hagemeijer et al., 2012) (Figure 3A). Although the PFS element was not shown as a conserved structure in Das' bioinformatics algorithm (Rangan et al., 2020), this region has demonstrated high-degree conservation among SARS-CoV and four VOC of CoV-2 (Figure 3A). The PFS element contains an attenuator hairpin (a negative regulator of the PFS), a slippery sequence (U_UUA_AAC motif), and a pseudoknot structure in betacoronavirus (Hagemeijer et al., 2012; Rangan et al., 2020) (Figure 3A). Once the ribosome recognizes the pseudoknotted structure, tRNAs in the ribosomal P- and A-sites re-bind to the -1 reading frame at the slippery sequence, and the ribosome starts to translate within the new reading frame (Bhatt et al., 2021) (Figure 3A). Without PFS, viral RNA translation would halt at the stop codon (13,481–13,483) within the pseudoknot (Figure 3A). It was demonstrated that the PFS element sequence alone could recapitulate the PFS activity without a protein cofactor in SARS-CoV (Baranov et al., 2005). The pseudoknotted structure was observed in NMR (Liphardt et al., 1999), chemical probing (Huston et al., 2021), cryo-EM (complexed with an elongating ribosome) (Bhatt et al., 2021), and X-ray crystallography (Roman et al., 2021).

SARS-CoV-2 UTRs

In the 5' UTR (1–265), there are five stem-loops identified, SL1–5 (Figure 3B). SL1 was demonstrated to bind to nsp1 protein and cooperate in recruiting the human ribosome (Vankadari et al., 2020). SL5, which includes the genome start codon, is a four-helix junction essential for viral packaging (Escors et al., 2003) (Figure 3C). It is proposed that the structures of SL1, SL2, and SL4, but not the exact nucleotide sequences, play a more critical role in betacoronavirus function (Yang and Leibowitz, 2015).

In the 3' UTR, three main secondary structures were elucidated by chemical probing: bulged stem-loop (BSL), SL-1, and the highly variable region (HVR) (Figure 3C). Bioinformatics analysis and reverse genetics suggested the pseudoknotted structure formation at the base stem of BSL and the SL-1 loop in SARS-CoV (Goebel et al., 2004) (Figure 3B). The equilibrium between the double stem-loop

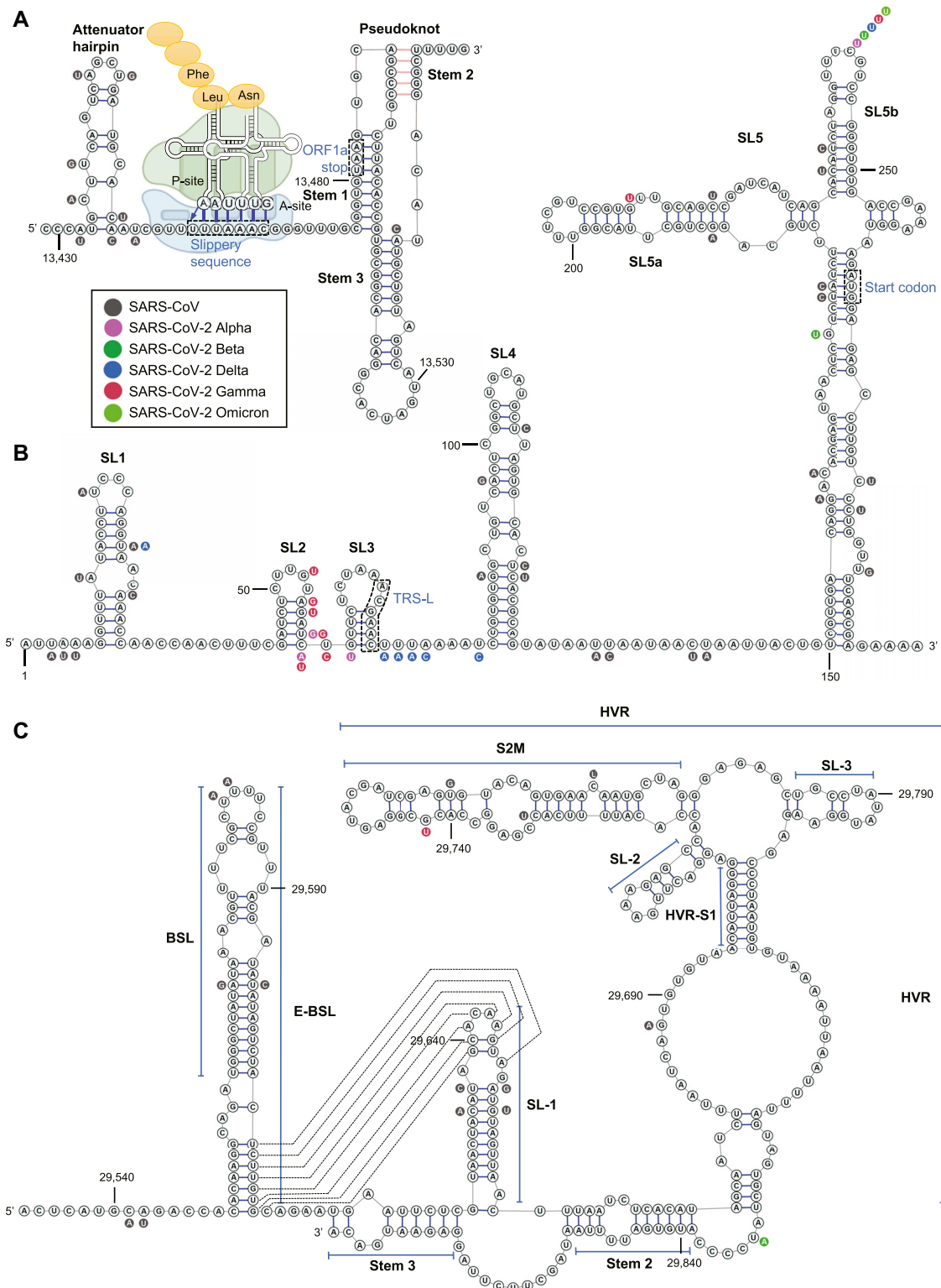


FIGURE 3 | The RNA structure and nucleotide conservation of the (A) PFS element in SARS-CoV-2, (B) 5' UTR, and (C) 3' UTR. The ribosome acts on the slippery sequence to produce a -1 PFS is illustrated in (A).

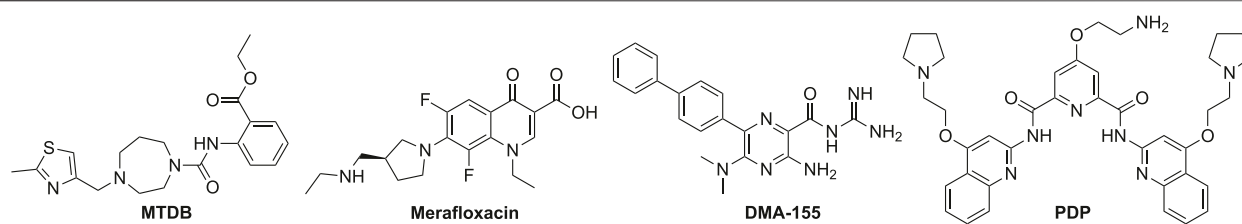


FIGURE 4 | The small molecules with antiviral activities targeting the SARS-CoV-2 RNA genome.

and pseudoknot was proposed to be a molecular switch in SARS-CoV RNA transcription (Yang and Leibowitz, 2015). This equilibrium model is also supported by quantitative covariation analysis (Rfam: RF11065) (Mathews et al., 2004). However, the pseudoknot was not observed as a stable structure at 37°C in NMR experiments in a model betacoronavirus, mouse hepatitis virus (MHV) (Stammler et al., 2011). Chemical probing experiments also suggested the unfavorable formation of pseudoknot (Zhao et al., 2020; Huston et al., 2021).

The HVR in the 3' UTR is not essential to betacoronavirus. The HVR can be deleted without affecting viral propagation in cell culture, albeit the HVR-deleted MHV strain has lower pathogenicity in mice (Goebel et al., 2007). Nevertheless, some sub-region of the HVR is highly conserved among betacoronavirus, such as the stable S2M (Rangan et al., 2020) (Figure 3C). The Stem 3 region duplexed by a sequence at the 3'-end of the viral genome and that between BSL and SL-1 (Figure 3C) was shown to be essential for the MHV viability (Goebel et al., 2007; Liu et al., 2013) and phylogenetically conserved (Züst et al., 2008), although chemical probing result suggested that the formation of Stem 3 is not favorable (Zhao et al., 2020). It was demonstrated by psoralen crosslinking that the 3'-end of the genome in the Stem 3 region can bind to the viral 5' UTR and cyclize the SARS-CoV-2 genome (Ziv et al., 2020).

Among the 106 predicted conserved structured RNA regions by the Das group (Rangan et al., 2020), two locate in the 5' UTR: SL2-4 and SL5 (SARS-CoV-2-conserved structure-8 and -16), and one reside in the 3' UTR: BSL-SL-1 region (SARS-CoV-2-conserved structure-33) (structure numbers provided in Rangan et al., 2020).

VIRAL RNA-TARGETING STRATEGIES

RNA-Binding Small Molecules Targeting the SARS-CoV-2 RNA Genome

De novo design of nucleic acid ligands has been pursued for more than 35 years. The field was first pioneered by the Dervan group in optimizing DNA-binding molecules (Dervan, 1986), and then by the Disney group to identify selective RNA-binding molecules. In the recent 15 years, Disney and others have established that "the right" synthetic small molecules can indeed bind to RNA structures, but not the primary sequences, with a high degree of selectivity (Fedorova et al., 2018; Warner et al., 2018; Hargrove, 2020; Ursu et al., 2020).

Viruses make use of their RNA structures to hijack host cell functions and promote viral life cycle progression. These viral RNA structures have been chosen as druggable targets in small-molecule drug development. For example, HIV-1 uses transactivator protein (Tat) to interact with a highly structured transactivation response (TAR) hairpin in its RNA to enhance the viral transcription (Sophie et al., 1990; Schulze-Gahmen and Hurley, 2018). Peptoid inhibitors targeting the TAR-Tat interaction have been shown to inhibit HIV-1 replication *in vitro* and *in vivo* (Hamy et al., 1997).

The discovery of RNA-targeting anti-SARS-CoV or CoV-2 small molecules primarily focused on the PFS element. MTDB was first identified by virtual screening and 3-dimensional (3D) modeling. MTDB can potentially bind to the pseudoknot in the SARS-CoV PFS element and inhibit the PFS function in a dual luciferase system (Park et al., 2011) (Figure 4). The dual luciferase assay is widely used in discovering and validating PFS regulators. In this assay, the PFS element was placed in the junction of a Renilla/firefly fusion luciferase, and the fusion luciferase could only be produced when the PFS occurred (Harger and Dinman, 2003). It was demonstrated by small-angle X-ray scattering analysis and reverse genetics that the conformation and function of the pseudoknot in the PFS element between SARS-CoV and SARS-CoV-2 are highly similar (Kelly et al., 2020). Indeed, MTDB can also reduce the SARS-CoV-2 PFS activity by 60% (Kelly et al., 2020).

A mCherry/GFP dual fluorescent protein assay was used in a high-content imaging screen, which identified a novel small-molecule PFS inhibitor, merafloxacin (Figure 4). Merafloxacin had a half-maximal inhibitory concentration (IC₅₀) in the dual fluorescent protein reporter cells at 19 μM and SARS-CoV-2-infected cells at 2.4 μM (Sun et al., 2021b). Merafloxacin belongs to the fluoroquinolone class known to interact with bacterial DNA and gyrase/topoisomerases (Aldred et al., 2014). Merafloxacin had a similar inhibitory effect to the reporter cells with mutated PFS elements, further suggesting that merafloxacin recognizes shape but not the primary sequence of the RNA (Sun et al., 2021b). Comparing MTDB and merafloxacin side-by-side, it was demonstrated that merafloxacin was a more potent inhibitor against PFS in SARS-CoV-2-infected Vero E6 cells (Bhatt et al., 2021).

Amiloride analogs (e.g., DMA-155, Figure 4) targeting the SARS-CoV-2 5' UTR also exhibited antiviral activity in SARS-CoV-2-infected cells (Zafferani et al., 2020). NMR studies uncovered that SL4, SL5a, and SL6 could all bind to the amilorides (Zafferani et al., 2020). An RNA sequence (RG-1)

having a high propensity to form a G-quadruplex (G4) in the SARS-CoV-2 genome was validated in the coding sequence of nucleocapsid phosphoprotein (N) in cells (Zhao et al., 2021). PDP was demonstrated to stabilize RG-1 G4 and reduce the protein levels of the viral N protein by inhibiting its translation both *in vitro* and *in vivo* (Zhao et al., 2021).

Several RNA-binding proteins (RBPs) in the host cells (e.g., IGF2BP1, hnRNP A1, and TIA1) were predicted to bind to the SARS-CoV-2 RNA genome (Sun et al., 2021a). Some FDA-approved small-molecule drugs, such as nilotinib, sorafenib, and deguelin, were demonstrated to interfere with essential RBP-viral RNA interactions and reduce the viral titer (Sun et al., 2021a). Strictly speaking, the targets of these drugs are host factors rather than viral RNA structures.

RNA-Binding ASOs Targeting the SARS-CoV-2 RNA Genome

Pharmacological Mechanisms of ASOs

ASOs are RNA or DNA sequences with 15–25 natural or modified nucleotides (Dhuri et al., 2020), which hybridize specifically *via* Watson-Crick base-pairing to a target RNA and modulate RNA splicing or gene expression (Roberts et al., 2020). ASOs generally act through two mechanisms in human cells: 1) cleaving of the target RNA *via* ASO-induced ribonuclease (RNase) H1 activity and 2) masking the target RNA from interaction with the human RBPs or the ribosome.

The ASOs used to induce RNase H1 activation are also termed “gapmers”. Gapmers usually contain a central DNA sequence (> 6 nucleotides) that hybridizes with the target RNA (Papargyri et al., 2020). RNase H1 is a ubiquitous ribonuclease found in the nucleus and the cytoplasm of all human cells (Crooke, 2017). RNase H1 specifically recognizes and hydrolyzes the RNA strand of the RNA-DNA heteroduplexes formed between the DNA block in the gapmer and the target RNA. Therefore, gapmers can be used to reduce the unwanted RNA level (i.e., gene knockdown) in a catalytic manner (Meng et al., 2015; Crooke, 2017). The DNA block in a gapmer is usually flanked (capped) by a short sequence of modified nucleotides to prevent exonuclease degradation.

“Masking” ASOs are commonly used as a steric block in the target RNA and, thereby, to modulate RNA splicing and suppress translation. The FDA has approved several ASOs acting through this mechanism to treat a variety of human diseases (Roberts et al., 2020; Tang et al., 2021a). For example, fomivirsen was the first FDA-approved ASO drug to treat cytomegalovirus (CMV) retinitis (approved in 1998; withdrawn in 2006 for lack of medical need) (Stein and Castanotto, 2017). Fomivirsen binds to the immediate early region 2 in the human CMV mRNA, halting the RNA translation of (IE)-2 protein which is crucial for viral replication (Geary et al., 2002). ASOs are also widely used for modulating RNA splicing in rare genetic diseases, such as Duchenne muscular dystrophy (DMD) and spinal muscular atrophy (SMA) (Tang et al., 2021b).

Chemical Modification in ASOs

Several chemical modifications of ASOs have been developed to improve their stability and cellular uptake (Crooke, 2017). For

example, replacing the natural phosphodiester bridge with a phosphorothioate group in the ASO would significantly increase its half-life *in vivo* due to high serum protein binding and nuclease resistance (Temsamani et al., 1993). Phosphorothioate linkage in ASOs retains the RNase H1 recognition and is usually used throughout gapmers (Lulla et al., 2021). Alkylation of the 2'-OH in the ribose with a methoxyethyl group (MOE) in the ASO would enhance the hybridization stability and lessen the nonspecific binding (Dhuri et al., 2020). It is estimated that each MOE substitution increases the melting temperature (T_m) by 2 °C (Freier and Altmann, 1997). Locked nucleic acid (LNA) is a class of modified ribose where the 2'-OH is linked to the 4'-CH *via* a constrained methylene bridge (Singh et al., 1998). The constrained LNA maintains a preferable conformation in RNA binding and, therefore, would significantly increase the hybridization stability in ASOs (+2–4 °C in T_m per LNA substitution) (Koshkin et al., 1998). One or more LNAs can be used in ASOs, and the ASOs with interspersed combination of LNA and DNA nucleotides are also termed “mixmers” (Bernardo et al., 2012). A popular ASO form in clinical use is based on a phosphorodiamidate morpholino oligomer (PMO) skeleton. PMOs have morpholine subunits instead of ribose/deoxyribose and are linked by the phosphorodiamidate group (Dhuri et al., 2020). PMOs have various advantages, including reduced nonspecific binding imparted by the neutral charge and complete nuclease resistance (Dhuri et al., 2020).

Anti-SARS-CoV-2 ASOs

By using 3D antisense modeling, a PMO named PRF3p was optimized to target the Stem 3 region in the PFS element (Li et al., 2021b) (Figure 5). The PRF3p binding disrupted the pseudoknotted structure in the PFS element and inhibited the frameshift, eventually leading to a knockdown of the genes encoded by the ORF1b in the virus-infected 293T cells (Li et al., 2021b). Gapmers S2D, S3D-1, S2D-2, and Slp-2 targeting PFS elements were reported to have efficacy in Huh-7 inoculated with SARS-CoV-2 with a luciferase reporter (Zhang et al., 2021).

A PMO named SBD1 was designed to target the conserved TRS-L region in the SARS-CoV 5' UTR (Figure 5), and thereby inhibited the “discontinuous” transcription (Li et al., 2021b). The suppression of sub-genomic RNA transcription ultimately led to the reduction of viral structural protein levels and virus titer (Li et al., 2021). Two PMOs, 5'END-1 and 5'END-2, targeted the viral 5' UTR and were shown to inhibit the translation pre-initiation complex (Rosenke et al., 2021). The 5'-end of ORF1a is also a region for ASO-binding to have antiviral effects. Two 2'-MOE/phosphorothioate-modified ASOs targeting this region, SE_ORF1ab_6449 and SE_ORF1ab_9456, were reported to effectively inhibit SARS-CoV infection in Vero E6 cells (Figure 5) (Sun et al., 2021a). Gapmers 2 and 5 targeting the conserved S2M sequences in the 3' UTR were demonstrated to have efficacy in degrading the viral RNA genome (Figure 5) (Lulla et al., 2021). The current development of ASO-based anti-SARS-CoV-2 agents is summarized in Table 1.

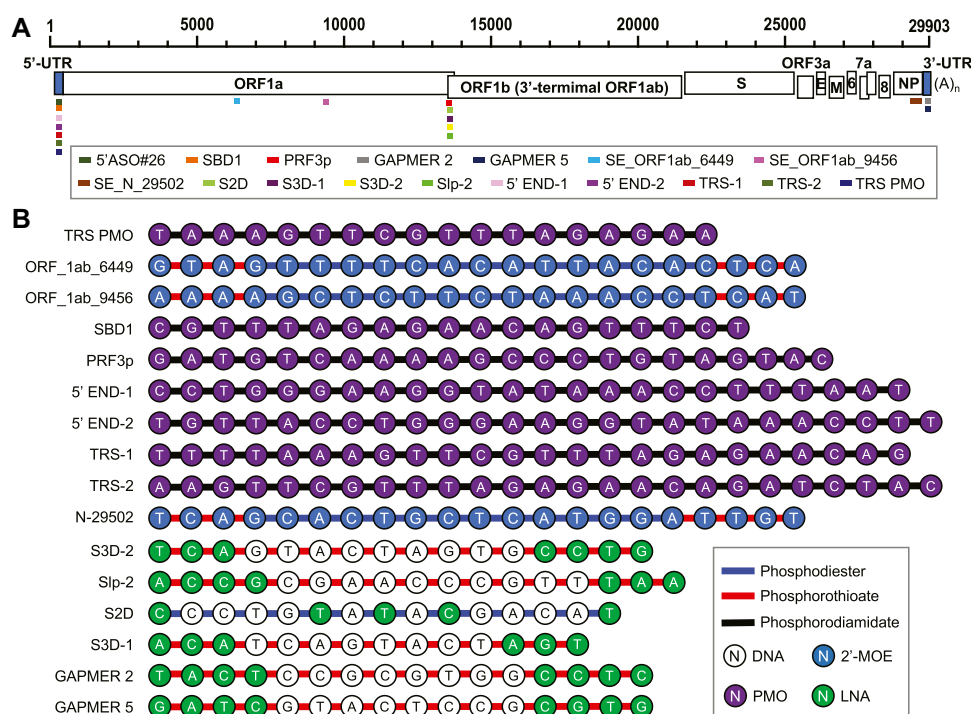


FIGURE 5 | (A) Antiviral ASO binding sites in the SARS-CoV-2 genome. **(B)** Chemical composition of the anti-SARS-CoV-2 ASOs.

TABLE 1 | ASO-based anti-SARS-CoV-2 agents that target the viral RNA genome.

Name	Chemistry ^a	Target gene	Target or ASO sequences	Length	References
5'ASO#26	Mixmer/PS	5' UTR	29–44	16	Zhu et al. (2021)
SE_ORF1ab_6449	2'-MOE/PS	ORF1ab	6,451–6,471	21	Sun et al. (2021a)
SE_ORF1ab_9456	2'-MOE/PS	ORF1ab	9,458–9,478	21	Sun et al. (2021a)
SE_N_29502	2'-MOE/PS	ORF1ab	29,497–29,517	21	Sun et al. (2021a)
SBD1	PMO	5'UTR, TRS	59–72 & 79–85 ^b	19	Li et al. (2021b)
PRF3p	PMO	PFS Element	13,503–13,506 and 13,534–13,551 ^b	22	Li et al. (2021b)
GAPMER 2	Gapmer/PS	S2M, 3'UTR	29,734–29,749	16	Lulla et al. (2021)
GAPMER 5	Gapmer/PS	S2M, 3'UTR	29,739–29,754	16	Lulla et al. (2021)
S2D	Mixmer	PFS Element	13,526–13,540	15	Zhang et al. (2021)
S3D-1	Gapmer/PS	PFS Element	13,516–13,529	14	Zhang et al. (2021)
S3D-2	Gapmer/PS	PFS Element	13,511–13,526	16	Zhang et al. (2021)
Slp-2	Gapmer/PS	PFS element	13,463–13,479	17	Zhang et al. (2021)
5'END-1	PMO	5'UTR	1–24	24	Rosenke et al. (2021)
5'END-2	PMO	5'UTR	5–29	25	Rosenke et al. (2021)
TRS1	PMO	5'UTR, TRS	59–82	24	Rosenke et al. (2021)
TRS2	PMO	5'UTR, TRS	53–77	25	Rosenke et al. (2021)
TRS PMO	PMO	5'UTR, TRS	62–79	18	Li et al. (2021a)

^aPS, phosphorothioate.

^b3D-ASOs.

RNA-Degrading Chimeras

The RNA-degrading chimeras follow a well-established precedent from the protein field, namely, the proteolysis targeting chimera or PROTAC. PROTACs bind to their target protein using a guide arm as “bait”. The effector

arm of PROTACs recruits an endogenous E3 ubiquitin ligase resulting in polyubiquitination and subsequent proteasomal degradation of the target protein (Schapira et al., 2019). The Disney group first extended this chimeric degrader concept to the RNA field by creating a ribonuclease

understanding of the RNA-ligand interactions, the RNA-targeting drug discovery platforms have the potential to quickly generate antiviral candidates to address future viral outbreaks.

AUTHOR CONTRIBUTIONS

SH, ZT, JZ, and JW wrote the manuscript. ZT analyzed the sequencing data.

REFERENCES

- Aldred, K. J., Kerns, R. J., and Osherooff, N. (2014). Mechanism of Quinolone Action and Resistance. *Biochemistry* 53, 1565–1574. doi:10.1021/bi5000564
- Baranov, P. V., Henderson, C. M., Anderson, C. B., Gesteland, R. F., Atkins, J. F., and Howard, M. T. (2005). Programmed Ribosomal Frameshifting in Decoding the SARS-CoV Genome. *Virology* 332, 498–510. doi:10.1016/j.virol.2004.11.038
- Berber, B., Aydin, C., Kocabas, F., Guney-Esken, G., Yilancioglu, K., Karadag-Alpaslan, M., et al. (2021). Gene Editing and RNAi Approaches for COVID-19 Diagnostics and Therapeutics. *Gene Ther.* 28, 290–305. doi:10.1038/s41434-020-00209-7
- Bernardo, B. C., Gao, X.-M., Winbanks, C. E., Boey, E. J. H., Tham, Y. K., Kiriazis, H., et al. (2012). Therapeutic Inhibition of the miR-34 Family Attenuates Pathological Cardiac Remodeling and Improves Heart Function. *Proc. Natl. Acad. Sci.* 109, 17615–17620. doi:10.1073/pnas.1206432109
- Bhatt, P. R., Scaiola, A., Loughran, G., Leibundgut, M., Kratzel, A., Meurs, R., et al. (2021). Structural Basis of Ribosomal Frameshifting during Translation of the SARS-CoV-2 RNA Genome. *Science* 372, 1306–1313. doi:10.1126/science.abf3546
- Ceraolo, C., and Giorgi, F. M. (2020). Genomic Variance of the 2019-nCoV Coronavirus. *J. Med. Virol.* 92, 522–528. doi:10.1002/jmv.25700
- Costales, M. G., Aikawa, H., Li, Y., Childs-Disney, J. L., Abegg, D., Hoch, D. G., et al. (2020). Small-molecule Targeted Recruitment of a Nuclease to Cleave an Oncogenic RNA in a Mouse Model of Metastatic Cancer. *Proc. Natl. Acad. Sci. USA* 117, 2406–2411. doi:10.1073/pnas.1914286117
- Costales, M. G., Matsumoto, Y., Velagapudi, S. P., and Disney, M. D. (2018). Small Molecule Targeted Recruitment of a Nuclease to RNA. *J. Am. Chem. Soc.* 140, 6741–6744. doi:10.1021/jacs.8b01233
- Crooke, S. T. (2017). Molecular Mechanisms of Antisense Oligonucleotides. *Nucleic Acid Ther.* 27, 70–77. doi:10.1089/nat.2016.0656
- Crosby, J. R., Zhao, C., Jiang, C., Bai, D., Katz, M., Greenlee, S., et al. (2017). Inhaled ENaC Antisense Oligonucleotide Ameliorates Cystic Fibrosis-like Lung Disease in Mice. *J. Cystic Fibrosis* 16, 671–680. doi:10.1016/j.jcf.2017.05.003
- Dervan, P. B. (1986). Design of Sequence-specific DNA-Binding Molecules. *Science* 232, 464–471. doi:10.1126/science.2421408
- Dhuri, K., Bechtold, C., Quijano, E., Pham, H., Gupta, A., Vikram, A., et al. (2020). Antisense Oligonucleotides: An Emerging Area in Drug Discovery and Development. *J. Clin. Med.* 9, 2004–1373. doi:10.3390/jcm9062004
- Disney, M. D. (2019). Targeting RNA with Small Molecules to Capture Opportunities at the Intersection of Chemistry, Biology, and Medicine. *J. Am. Chem. Soc.* 141, 6776–6790. doi:10.1021/jacs.8b13419
- Escors, D., Izeta, A., Capiscol, C., and Enjuanes, L. (2003). Transmissible Gastroenteritis Coronavirus Packaging Signal Is Located at the 5' End of the Virus Genome. *J. Virol.* 77, 7890–7902. doi:10.1128/jvi.77.14.7890-7902.2003
- Fedorova, O., Jagdmann, G. E., Adams, R. L., Yuan, L., Van Zandt, M. C., and Pyle, A. M. (2018). Small Molecules that Target Group II Introns Are Potent Antifungal Agents. *Nat. Chem. Biol.* 14, 1073–1078. doi:10.1038/s41589-018-0142-0
- Fischer, W., Eron, J. J., Holman, W., Cohen, M. S., Fang, L., Szcwzyk, L. J., et al. (2021). *Molnupiravir, an Oral Antiviral Treatment for COVID-19*. medRxiv. doi:10.1101/2021.06.17.21258639

FUNDING

This review was supported by the National Institute of General Medical Sciences (NIGMS) of the National Institutes of Health under award number P20GM113117 and the University of Kansas (KU) One University Open Access Author Fund sponsored jointly by the KU Provost, KU Vice Chancellor for Research & Graduate Studies, and KUMC Vice Chancellor for Research and managed jointly by the Libraries at the Medical Center and KU – Lawrence.

- Floyd-Smith, G., Slattery, E., and Lengyel, P. (1981). Interferon Action: RNA Cleavage Pattern of a (2'-5')Oligoadenylate-dependent Endonuclease. *Science* 212, 1030–1032. doi:10.1126/science.6165080
- Freier, S., and Altmann, K. H. (1997). The Ups and downs of Nucleic Acid Duplex Stability: Structure-Stability Studies on Chemically-Modified DNA:RNA Duplexes. *Nucleic Acids Res.* 25, 4429–4443. doi:10.1093/nar/25.22.4429
- Fung, T. S., and Liu, D. X. (2019). Human Coronavirus: Host-Pathogen Interaction. *Annu. Rev. Microbiol.* 73, 529–557. doi:10.1146/annurev-micro-020518-115759
- Garbuzenko, O. B., Saad, M., Pozharov, V. P., Reuhl, K. R., Mainelis, G., and Minko, T. (2010). Inhibition of Lung Tumor Growth by Complex Pulmonary Delivery of Drugs with Oligonucleotides as Suppressors of Cellular Resistance. *Proc. Natl. Acad. Sci.* 107, 10737–10742. doi:10.1073/pnas.1004604107
- Geary, R. S., Henry, S. P., and Grillone, L. R. (2002). Fomivirsen. *Clin. Pharmacokinet.* 41, 255–260. doi:10.2165/00003088-200241040-00002
- Geary, R. S., Norris, D., Yu, R., and Bennett, C. F. (2015). Pharmacokinetics, Biodistribution and Cell Uptake of Antisense Oligonucleotides. *Adv. Drug Deliv. Rev.* 87, 46–51. doi:10.1016/j.addr.2015.01.008
- Goebel, S. J., Hsue, B., Dombrowski, T. F., and Masters, P. S. (2004). Characterization of the RNA Components of a Putative Molecular Switch in the 3' Untranslated Region of the Murine Coronavirus Genome. *J. Virol.* 78, 669–682. doi:10.1128/jvi.78.2.669-682.2004
- Goebel, S. J., Miller, T. B., Bennett, C. J., Bernard, K. A., and Masters, P. S. (2007). A Hypervariable Region within the 3' Cis -Acting Element of the Murine Coronavirus Genome Is Nonessential for RNA Synthesis but Affects Pathogenesis. *J. Virol.* 81, 1274–1287. doi:10.1128/JVI.00803-06
- Gottlieb, R. L., Nirula, A., Chen, P., Boscia, J., Heller, B., Morris, J., et al. (2021). Effect of Bamlanivimab as Monotherapy or in Combination with Etesevimab on Viral Load in Patients with Mild to Moderate COVID-19. *JAMA* 325, 632–644. doi:10.1001/jama.2021.0202
- Hagedorn, P. H., Pontoppidan, M., Bisgaard, T. S., Berrera, M., Dieckmann, A., Ebeling, M., et al. (2018). Identifying and Avoiding Off-Target Effects of RNase H-dependent Antisense Oligonucleotides in Mice. *Nucleic Acids Res.* 46, 5366–5380. doi:10.1093/nar/gky397
- Hagemeyer, M., Rottier, P., and Haan, C. (2012). Biogenesis and Dynamics of the Coronavirus Replicative Structures. *Viruses* 4, 3245–3269. doi:10.3390/v4113245
- Hamy, F., Felder, E. R., Heizmann, G., Lazdins, J., Aboul-ela, F., Varani, G., et al. (1997). An Inhibitor of the Tat/TAR RNA Interaction that Effectively Suppresses HIV-1 Replication. *Proc. Natl. Acad. Sci.* 94, 3548–3553. doi:10.1073/pnas.94.8.3548
- Haniff, H. S., Tong, Y., Liu, X., Chen, J. L., Suresh, B. M., Andrews, R. J., et al. (2020). Targeting the SARS-CoV-2 RNA Genome with Small Molecule Binders and Ribonuclease Targeting Chimera (RIBOTAC) Degradable. *ACS Cent. Sci.* 6, 1713–1721. doi:10.1021/acscentsci.0c00984
- Harger, J. W., and Dinman, J. D. (2003). An *In Vivo* Dual-Luciferase Assay System for Studying Translational Recoding in the Yeast *Saccharomyces cerevisiae*. *RNA* 9, 1019–1024. doi:10.1261/rna.5930803
- Hargrove, A. E. (2020). Small Molecule-RNA Targeting: Starting with the Fundamentals. *Chem. Commun.* 56, 14744–14756. doi:10.1039/D0CC06796B
- Hillen, H. S., Kokic, G., Farnung, L., Dienemann, C., Tegunov, D., and Cramer, P. (2020). Structure of Replicating SARS-CoV-2 Polymerase. *Nature* 584, 154–156. doi:10.1038/s41586-020-2368-8

- Huston, N. C., Wan, H., Strine, M. S., de Cesaris Araujo Tavares, R., Wilen, C. B., and Pyle, A. M. (2021). Comprehensive *In Vivo* Secondary Structure of the SARS-CoV-2 Genome Reveals Novel Regulatory Motifs and Mechanisms. *Mol. Cell* 81, 584–598. e5. doi:10.1016/j.molcel.2020.12.041
- Jaklevic, M. C. (2020). Oral Drug Approved for Spinal Muscular Atrophy. *JAMA* 324, 1026. doi:10.1001/jama.2020.16783
- Kelly, J. A., Olson, A. N., Neupane, K., Munshi, S., San Emeterio, J., Pollack, L., et al. (2020). Structural and Functional Conservation of the Programmed –1 Ribosomal Frameshift Signal of SARS Coronavirus 2 (SARS-CoV-2). *J. Biol. Chem.* 295, 10741–10748. doi:10.1074/jbc.AC120.013449
- Kim, D., Lee, J.-Y., Yang, J.-S., Kim, J. W., Kim, V. N., and Chang, H. (2020). The Architecture of SARS-CoV-2 Transcriptome. *Cell* 181, 914–921. e10. doi:10.1016/j.cell.2020.04.011
- Knoops, K., Kikkert, M., Worm, S. H. E. v. d., Zevenhoven-Dobbe, J. C., van der Meer, Y., Koster, A. J., et al. (2008). SARS-coronavirus Replication Is Supported by a Reticulovesicular Network of Modified Endoplasmic Reticulum. *Plos Biol.* 6, e226. doi:10.1371/journal.pbio.0060226
- Koshkin, A. A., Singh, S. K., Nielsen, P., Rajwanshi, V. K., Kumar, R., Meldgaard, M., et al. (1998). LNA (Locked Nucleic Acids): Synthesis of the Adenine, Cytosine, Guanine, 5-methylcytosine, Thymine and Uracil Bicyclonucleoside Monomers, Oligomerisation, and Unprecedented Nucleic Acid Recognition. *Tetrahedron* 54, 3607–3630. doi:10.1016/S0040-4020(98)00094-5
- Lan, T. C. T., Allan, M. F., Malsick, L. E., Khandwala, S., Nyeo, S. S. Y., Sun, Y., et al. (2020). Insights into the Secondary Structural Ensembles of the Full SARS-CoV-2 RNA Genome in Infected Cells. *bioRxiv*. doi:10.1101/2020.06.29.178343
- Li, C., Callahan, A. J., Simon, M. D., Totaro, K. A., Mijalis, A. J., Phadke, K.-S., et al. (2021a). Fully Automated Fast-Flow Synthesis of Antisense Phosphorodiamidate Morpholino Oligomers. *Nat. Commun.* 12, 4396. doi:10.1038/s41467-021-24598-4
- Li, G., Xiang, Y., Sabapathy, K., and Silverman, R. H. (2004). An Apoptotic Signaling Pathway in the Interferon Antiviral Response Mediated by RNase L and C-Jun NH2-terminal Kinase. *J. Biol. Chem.* 279, 1123–1131. doi:10.1074/jbc.M305893200
- Li, Y., Garcia, G., Arumugaswami, V., and Guo, F. (2021b). Structure-based Design of Antisense Oligonucleotides that Inhibit SARS-CoV-2 Replication. *bioRxiv*. doi:10.1101/2021.08.23.457434
- Liphardt, J., Naphthine, S., Kontos, H., and Brierley, I. (1999). Evidence for an RNA Pseudoknot Loop-helix Interaction Essential for Efficient –1 Ribosomal Frameshifting. *J. Mol. Biol.* 288, 321–335. doi:10.1006/jmbi.1999.2689
- Liu, P., Yang, D., Carter, K., Masud, F., and Leibowitz, J. L. (2013). Functional Analysis of the Stem Loop S3 and S4 Structures in the Coronavirus 3'UTR. *Virology* 443, 40–47. doi:10.1016/j.virol.2013.04.021
- Liu, X., Haniff, H. S., Childs-Disney, J. L., Shuster, A., Aikawa, H., Adibekian, A., et al. (2020). Targeted Degradation of the Oncogenic MicroRNA 17-92 Cluster by Structure-Targeting Ligands. *J. Am. Chem. Soc.* 142, 6970–6982. doi:10.1021/jacs.9b13159
- Lulla, V., Wandel, M. P., Bandyra, K. J., Ulferts, R., Wu, M., Dendooven, T., et al. (2021). Targeting the Conserved Stem Loop 2 Motif in the SARS-CoV-2 Genome. *J. Virol.* 95, e0066321. doi:10.1128/JVI.00663-21
- Ma, X. R., Alugubelli, Y. R., Ma, Y., Vatansever, E. C., Scott, D. A., Qiao, Y., et al. (2021). MPI8 Is Potent against SARS-CoV-2 by Inhibiting Dually and Selectively the SARS-CoV-2 Main Protease and the Host Cathepsin L. *ChemMedChem*. doi:10.1002/cmdc.202100456
- Manfredonia, I., Nithin, C., Ponce-Salvatierra, A., Ghosh, P., Wirecki, T. K., Marinus, T., et al. (2020). Genome-wide Mapping of SARS-CoV-2 RNA Structures Identifies Therapeutically-Relevant Elements. *Nucleic Acids Res.* 48, 12436–12452. doi:10.1093/nar/gkaa1053
- Manzanares-Meza, L. D., and Medina-Contreras, O. (2020). SARS-CoV-2 and Influenza: a Comparative Overview and Treatment Implications. *Boletín Médico Del Hosp. Infantil de México* 77, 262–273. doi:10.24875/BMHIM.20000183
- Mathews, D. H., Disney, M. D., Childs, J. L., Schroeder, S. J., Zuker, M., and Turner, D. H. (2004). Incorporating Chemical Modification Constraints into a Dynamic Programming Algorithm for Prediction of RNA Secondary Structure. *Proc. Natl. Acad. Sci.* 101, 7287–7292. doi:10.1073/pnas.0401799101
- McCloy, G., and Banerjee, S. (2018). Cell-Penetrating Peptides to Enhance Delivery of Oligonucleotide-Based Therapeutics. *Biomedicine* 6, 51. doi:10.3390/biomedicine6020051
- Meng, L., Ward, A. J., Chun, S., Bennett, C. F., Beaudet, A. L., and Rigo, F. (2015). Towards a Therapy for Angelman Syndrome by Targeting a Long Non-coding RNA. *Nature* 518, 409–412. doi:10.1038/nature13975
- Meyer, S. M., Williams, C. C., Akahori, Y., Tanaka, T., Aikawa, H., Tong, Y., et al. (2020). Small Molecule Recognition of Disease-Relevant RNA Structures. *Chem. Soc. Rev.* 49, 7167–7199. doi:10.1039/d0cs00560f
- Moschos, S. A., Frick, M., Taylor, B., Turnpenny, P., Graves, H., Spink, K. G., et al. (2011). Uptake, Efficacy, and Systemic Distribution of Naked, Inhaled Short Interfering RNA (siRNA) and Locked Nucleic Acid (LNA) Antisense. *Mol. Ther.* 19, 2163–2168. doi:10.1038/mt.2011.206
- Naik, S., Paranjape, J. M., and Silverman, R. H. (1998). RNase L Dimerization in a Mammalian Two-Hybrid System in Response to 2',5'-oligoadenylates. *Nucleic Acids Res.* 26, 1522–1527. doi:10.1093/nar/26.6.1522
- Owen, D. R., Allerton, C. M. N., Anderson, A. S., Aschenbrenner, L., Avery, M., Berritt, S., et al. (2021). An Oral SARS-CoV-2 M Pro Inhibitor Clinical Candidate for the Treatment of COVID-19. *Science*, eabl4784. doi:10.1126/science.abl4784
- Papargyri, N., Pontoppidan, M., Andersen, M. R., Koch, T., and Hagedorn, P. H. (2020). Chemical Diversity of Locked Nucleic Acid-Modified Antisense Oligonucleotides Allows Optimization of Pharmaceutical Properties. *Mol. Ther. - Nucleic Acids* 19, 706–717. doi:10.1016/j.omtn.2019.12.011
- Park, S.-J., Kim, Y.-G., and Park, H.-J. (2011). Identification of RNA Pseudoknot-Binding Ligand that Inhibits the –1 Ribosomal Frameshifting of SARS-Coronavirus by Structure-Based Virtual Screening. *J. Am. Chem. Soc.* 133, 10094–10100. doi:10.1021/ja1098325
- Rangan, R., Zheludev, I. N., Hagey, R. J., Pham, E. A., Wayment-Steele, H. K., Glenn, J. S., et al. (2020). RNA Genome Conservation and Secondary Structure in SARS-CoV-2 and SARS-Related Viruses: a First Look. *RNA* 26, 937–959. doi:10.1261/rna.076141.120
- Roberts, T. C., Langer, R., and Wood, M. J. A. (2020). Advances in Oligonucleotide Drug Delivery. *Nat. Rev. Drug Discov.* 19, 673–694. doi:10.1038/s41573-020-0075-7
- Robson, F., Khan, K. S., Le, T. K., Paris, C., Demirbag, S., Barfuss, P., et al. (2020). Coronavirus RNA Proofreading: Molecular Basis and Therapeutic Targeting. *Mol. Cell* 79, 710–727. doi:10.1016/j.molcel.2020.07.027
- Roman, C., Lewicka, A., Koirala, D., Li, N.-S., and Piccirilli, J. A. (2021). The SARS-CoV-2 Programmed –1 Ribosomal Frameshifting Element Crystal Structure Solved to 2.09 Å Using Chaperone-Assisted RNA Crystallography. *ACS Chem. Biol.* 16, 1469–1481. doi:10.1021/acscchembio.1c00324
- Rosenke, K., Leventhal, S., Moulton, H. M., Hatlevig, S., Hawman, D., Feldmann, H., et al. (2021). Inhibition of SARS-CoV-2 in Vero Cell Cultures by Peptide-Conjugated Morpholino Oligomers. *J. Antimicrob. Chemother.* 76, 413–417. doi:10.1093/jac/dkaa460
- Roy, S., Delling, U., Chen, C. H., Rosen, C. A., and Sonenberg, N. (1990). A Bulge Structure in HIV-1 TAR RNA Is Required for Tat Binding and Tat-Mediated Trans-activation. *Genes Dev.* 4, 1365–1373. doi:10.1101/GAD.4.8.1365
- Sanders, W., Fritch, E. J., Madden, E. A., Graham, R. L., Vincent, H. A., Heise, M. T., et al. (2020). Comparative Analysis of Coronavirus Genomic RNA Structure Reveals Conservation in SARS-like Coronaviruses. *bioRxiv*. doi:10.1101/2020.06.15.153197
- Sawicki, S. G., Sawicki, D. L., and Siddell, S. G. (2007). A Contemporary View of Coronavirus Transcription. *J. Virol.* 81, 20–29. doi:10.1128/JVI.01358-06
- Schapira, M., Calabrese, M. F., Bullock, A. N., and Crews, C. M. (2019). Targeted Protein Degradation: Expanding the Toolbox. *Nat. Rev. Drug Discov.* 18, 949–963. doi:10.1038/s41573-019-0047-y
- Schulze-Gahmen, U., and Hurley, J. H. (2018). Structural Mechanism for HIV-1 TAR Loop Recognition by Tat and the Super Elongation Complex. *Proc. Natl. Acad. Sci. USA* 115, 12973–12978. doi:10.1073/pnas.1806438115
- Singh, S. K., Koshkin, A. a., Wengel, J., and Nielsen, P. (1998). LNA (Locked Nucleic Acids): Synthesis and High-Affinity Nucleic Acid Recognition. *Chem. Commun.* 1998, 455–456. doi:10.1039/a708608c
- Sola, I., Almazán, F., Zúñiga, S., and Enjuanes, L. (2015). Continuous and Discontinuous RNA Synthesis in Coronaviruses. *Annu. Rev. Virol.* 2, 265–288. doi:10.1146/annurev-virology-100114-055218
- Stammler, S. N., Cao, S., Chen, S.-J., and Giedroc, D. P. (2011). A Conserved RNA Pseudoknot in a Putative Molecular Switch Domain of the 3'-untranslated Region of Coronaviruses Is Only Marginally Stable. *RNA* 17, 1747–1759. doi:10.1261/rna.2816711

- Stein, C. A., and Castanotto, D. (2017). FDA-approved Oligonucleotide Therapies in 2017. *Mol. Ther.* 25, 1069–1075. doi:10.1016/j.yymthe.2017.03.023
- Su, X., Ma, W., Feng, D., Cheng, B., Wang, Q., Guo, Z., et al. (2021). Efficient Inhibition of SARS-CoV-2 Using Chimeric Antisense Oligonucleotides through RNase L Activation. *Angew. Chem. Int. Ed.* 60, 21662–21667. doi:10.1002/anie.202105942
- Sun, L., Li, P., Ju, X., Rao, J., Huang, W., Ren, L., et al. (2021a). *In Vivo* structural Characterization of the SARS-CoV-2 RNA Genome Identifies Host Proteins Vulnerable to Repurposed Drugs. *Cell* 184, 1865–1883. e20. doi:10.1016/j.cell.2021.02.008
- Sun, Y., Abriola, L., Niederer, R. O., Pedersen, S. F., Alfajaro, M. M., Silva Monteiro, V., et al. (2021b). Restriction of SARS-CoV-2 Replication by Targeting Programmed -1 Ribosomal Frameshifting. *Proc. Natl. Acad. Sci. USA* 118, e2023051118. doi:10.1073/pnas.2023051118
- Tang, Z., Zhao, J., Pearson, Z. J., Boskovic, Z. V., and Wang, J. (2021a). RNA-targeting Splicing Modifiers: Drug Development and Screening Assays. *Molecules* 26, 2263. doi:10.3390/molecules26082263
- Tang, Z., Zhao, J., Pearson, Z. J., Boskovic, Z. V., and Wang, J. (2021b). RNA-targeting Splicing Modifiers: Drug Development and Screening Assays. *Molecules* 26, 2263. doi:10.3390/molecules26082263
- Temsamani, J., Tang, J.-Y., Padmapriya, A., Kubert, M., and Agrawal, S. (1993). Pharmacokinetics, Biodistribution, and Stability of Capped Oligodeoxynucleotide Phosphorothioates in Mice. *Antisense Res. Dev.* 3, 277–284. doi:10.1089/ard.1993.3.277
- Thakur, C. S., Jha, B. K., Dong, B., Das Gupta, J., Silverman, K. M., Mao, H., et al. (2007). Small-molecule Activators of RNase L with Broad-Spectrum Antiviral Activity. *Proc. Natl. Acad. Sci.* 104, 9585–9590. doi:10.1073/pnas.0700590104
- Ursu, A., Childs-Disney, J. L., Andrews, R. J., O'Leary, C. A., Meyer, S. M., Angelbello, A. J., et al. (2020). Design of Small Molecules Targeting RNA Structure from Sequence. *Chem. Soc. Rev.* 49, 7252–7270. doi:10.1039/d0cs00455c
- van Dorp, L., Acman, M., Richard, D., Shaw, L. P., Ford, C. E., Ormond, L., et al. (2020). Emergence of Genomic Diversity and Recurrent Mutations in SARS-CoV-2. *Infect. Genet. Evol.* 83, 104351. doi:10.1016/j.meegid.2020.104351
- Van Egeren, D., Novokhodko, A., Stoddard, M., Tran, U., Zetter, B., Rogers, M., et al. (2021). Risk of Rapid Evolutionary Escape from Biomedical Interventions Targeting SARS-CoV-2 Spike Protein. *PLoS One* 16, e0250780. doi:10.1371/journal.pone.0250780
- Vankadari, N., Jeyasankar, N. N., and Lopes, W. J. (2020). Structure of the SARS-CoV-2 Nsp1/5'-Untranslated Region Complex and Implications for Potential Therapeutic Targets, a Vaccine, and Virulence. *J. Phys. Chem. Lett.* 11, 9659–9668. doi:10.1021/acs.jpclett.0c02818
- Vatansever, E. C., Yang, K. S., Drelich, A. K., Kratch, K. C., Cho, C.-C., Kempaiah, K. R., et al. (2021). Bepridil Is Potent against SARS-CoV-2 *In Vitro*. *Proc. Natl. Acad. Sci. USA* 118, e2012201118. doi:10.1073/pnas.2012201118
- Wacker, A., Weigand, J. E., Akabayov, S. R., Altincekic, N., Bains, J. K., Banijamali, E., et al. (2020). Secondary Structure Determination of Conserved SARS-CoV-2 RNA Elements by NMR Spectroscopy. *Nucleic Acids Res.* 48, 12415–12435. doi:10.1093/nar/gkaa1013
- Wang, Y., Zhang, D., Du, G., Du, R., Zhao, J., Jin, Y., et al. (2020). Remdesivir in Adults with Severe COVID-19: a Randomised, Double-Blind, Placebo-Controlled, Multicentre Trial. *The Lancet* 395, 1569–1578. doi:10.1016/S0140-6736(20)31022-9
- Warner, K. D., Hajdin, C. E., and Weeks, K. M. (2018). Principles for Targeting RNA with Drug-like Small Molecules. *Nat. Rev. Drug Discov.* 17, 547–558. doi:10.1038/nrd.2018.93
- Wreschner, D. H., McCauley, J. W., Skehel, J. J., and Kerr, I. M. (1981). Interferon Action-Sequence Specificity of the ppp(A2'p)nA-dependent Ribonuclease. *Nature* 289, 414–417. doi:10.1038/289414a0
- Wu, F., Zhao, S., Yu, B., Chen, Y.-M., Wang, W., Song, Z.-G., et al. (2020). A New Coronavirus Associated with Human Respiratory Disease in China. *Nature* 579, 265–269. doi:10.1038/s41586-020-2008-3
- Wu, H.-Y., and Brian, D. A. (2010). Subgenomic Messenger RNA Amplification in Coronaviruses. *Proc. Natl. Acad. Sci.* 107, 12257–12262. doi:10.1073/pnas.1000378107
- Yang, D., and Leibowitz, J. L. (2015). The Structure and Functions of Coronavirus Genomic 3' and 5' Ends. *Virus. Res.* 206, 120–133. doi:10.1016/j.virusres.2015.02.025
- Yoshida, T., Naito, Y., Yasuhara, H., Sasaki, K., Kawaji, H., Kawai, J., et al. (2019). Evaluation of Off-target Effects of Gapmer Antisense Oligonucleotides Using Human Cells. *Genes Cells* 24, 827–835. doi:10.1111/gtc.12730
- Zafferani, M., Haddad, C., Luo, L., Davila-Calderon, J., Yuan-Chiu, L., et al. (2021). Amilorides Inhibit SARS-CoV-2 Replication *in vitro* by Targeting RNA Structures. *Sci. Adv.* 7, eabl6096. doi:10.1126/sciadv.abl6096
- Zhang, K., Zheludev, I. N., Hagey, R. J., Haslecker, R., Hou, Y. J., Kretsch, R., et al. (2021). Cryo-EM and Antisense Targeting of the 28-kDa Frameshift Stimulation Element from the SARS-CoV-2 RNA Genome. *Nat. Struct. Mol. Biol.* 28, 747–754. doi:10.1038/s41594-021-00653-y
- Zhao, C., Qin, G., Niu, J., Wang, Z., Wang, C., Ren, J., et al. (2021). Targeting RNA G-Quadruplex in SARS-CoV-2: A Promising Therapeutic Target for COVID-19? *Angew. Chem. Int. Ed.* 60, 432–438. doi:10.1002/anie.202011419
- Zhao, J., Qiu, J., Aryal, S., Hackett, J., and Wang, J. (2020). The RNA Architecture of the SARS-CoV-2 3'-Untranslated Region. *Viruses* 12, 1473. doi:10.3390/v12121473
- Zhu, C., Lee, J. Y., Woo, J. Z., Xu, L., Nguyen, X., Yamashiro, L. H., et al. (2021). An Intranasal ASO Therapeutic Targeting SARS-CoV-2. *bioRxiv*. doi:10.1101/2021.05.17.444397
- Ziv, O., Price, J., Shalamova, L., Kamenova, T., Goodfellow, I., Weber, F., et al. (2020). The Short- and Long-Range RNA-RNA Interactome of SARS-CoV-2. *Mol. Cell* 80, 1067–1077. doi:10.1016/j.molcel.2020.11.004
- Zuñiga, S., Sola, I., Alonso, S., and Enjuanes, L. (2004). Sequence Motifs Involved in the Regulation of Discontinuous Coronavirus Subgenomic RNA Synthesis. *J. Virol.* 78, 980–994. doi:10.1128/jvi.78.2.980-994.2004
- Züst, R., Miller, T. B., Goebel, S. J., Thiel, V., and Masters, P. S. (2008). Genetic Interactions between an Essential 3' Cis-Acting RNA Pseudoknot, Replicase Gene Products, and the Extreme 3' End of the Mouse Coronavirus Genome. *J. Virol.* 82, 1214–1228. doi:10.1128/JVI.01690-07

Conflict of Interest: The authors declare that the research was conducted in the absence of any commercial or financial relationships that could be construed as a potential conflict of interest.

Publisher's Note: All claims expressed in this article are solely those of the authors and do not necessarily represent those of their affiliated organizations, or those of the publisher, the editors and the reviewers. Any product that may be evaluated in this article, or claim that may be made by its manufacturer, is not guaranteed or endorsed by the publisher.

Copyright © 2021 Hegde, Tang, Zhao and Wang. This is an open-access article distributed under the terms of the Creative Commons Attribution License (CC BY). The use, distribution or reproduction in other forums is permitted, provided the original author(s) and the copyright owner(s) are credited and that the original publication in this journal is cited, in accordance with accepted academic practice. No use, distribution or reproduction is permitted which does not comply with these terms.



Corrigendum: Inhibition of SARS-CoV-2 by Targeting Conserved Viral RNA Structures and Sequences

OPEN ACCESS

Edited and reviewed by:

Jun Wang,
Rutgers, The State University of New
Jersey, United States

*Correspondence:

Jingxin Wang
wang.jingxin@ku.edu

[†]These authors have contributed
equally to this work

Specialty section:

This article was submitted to
Chemical Biology,
a section of the journal
Frontiers in Chemistry

Received: 23 December 2021

Accepted: 11 January 2022

Published: 04 February 2022

Citation:

Hegde S, Tang Z, Zhao J and Wang J
(2022) Corrigendum: Inhibition of
SARS-CoV-2 by Targeting Conserved
Viral RNA Structures and Sequences.
Front. Chem. 10:842171.
doi: 10.3389/fchem.2022.842171

Shalakha Hegde[†], Zhichao Tang[†], Junxing Zhao and Jingxin Wang*

Department of Medicinal Chemistry, University of Kansas, Lawrence, KS, United States

Keywords: SARS-CoV-2, antiviral, RNA-targeting, small molecule, antisense oligonucleotide, untranslated region, programmed frameshift, RIBOTAC

A Corrigendum on

Inhibition of SARS-CoV-2 by Targeting Conserved Viral RNA Structures and Sequences
by Hegde, S., Tang, Z., Zhao, J., and Wang, J. (2021). *Front. Chem.* 9:802766. doi:10.3389/fchem.2021.802766

In the original article, there was a mistake in **Figure 4** as published. **Figure 4** was a duplication of **Figure 6**. The corrected **Figure 4** appears below.

The authors apologize for this error and state that this does not change the scientific conclusions of the article in any way. The original article has been updated.

Publisher's Note: All claims expressed in this article are solely those of the authors and do not necessarily represent those of their affiliated organizations, or those of the publisher, the editors and the reviewers. Any product that may be evaluated in this article, or claim that may be made by its manufacturer, is not guaranteed or endorsed by the publisher.

Copyright © 2022 Hegde, Tang, Zhao and Wang. This is an open-access article distributed under the terms of the Creative Commons Attribution License (CC BY). The use, distribution or reproduction in other forums is permitted, provided the original author(s) and the copyright owner(s) are credited and that the original publication in this journal is cited, in accordance with accepted academic practice. No use, distribution or reproduction is permitted which does not comply with these terms.

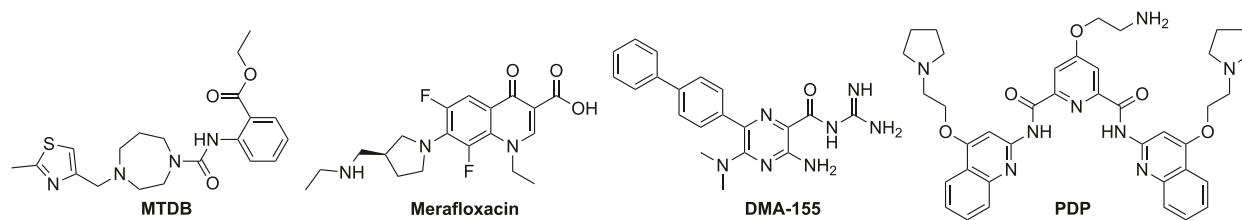


FIGURE 4 | The small molecules with antiviral activities targeting the SARS-CoV-2 RNA genome.



Targeting SARS-CoV-2 Proteases for COVID-19 Antiviral Development

Zongyang Lv^{1†}, Kristin E. Cano^{1†}, Lijia Jia¹, Marcin Drag², Tony T. Huang³ and Shaun K. Olsen^{1*}

¹Department of Biochemistry and Structural Biology, University of Texas Health Science Center at San Antonio, San Antonio, TX, United States, ²Department of Chemical Biology and Bioimaging, Wroclaw University of Science and Technology, Wroclaw, Poland, ³Department of Biochemistry and Molecular Pharmacology, New York University School of Medicine, New York, NY, United States

OPEN ACCESS

Edited by:

Wenshe Ray Liu,
Texas A&M University, United States

Reviewed by:

Kai S. Yang,
Texas A&M University, United States

Jun Wang,
Rutgers, The State University of New
Jersey, United States

*Correspondence:

Shaun K. Olsen
olsens@uthscsa.edu

[†]These authors have contributed
equally to this work

Specialty section:

This article was submitted to
Chemical Biology,
a section of the journal
Frontiers in Chemistry

Received: 20 November 2021

Accepted: 20 December 2021

Published: 03 February 2022

Citation:

Lv Z, Cano KE, Jia L, Drag M,
Huang TT and Olsen SK (2022)
Targeting SARS-CoV-2 Proteases for
COVID-19 Antiviral Development.
Front. Chem. 9:819165.
doi: 10.3389/fchem.2021.819165

The emergence of severe acute respiratory syndrome (SARS-CoV-2) in 2019 marked the third occurrence of a highly pathogenic coronavirus in the human population since 2003. As the death toll surpasses 5 million globally and economic losses continue, designing drugs that could curtail infection and disease progression is critical. In the US, three highly effective Food and Drug Administration (FDA)-authorized vaccines are currently available, and Remdesivir is approved for the treatment of hospitalized patients. However, moderate vaccination rates and the sustained evolution of new viral variants necessitate the ongoing search for new antivirals. Several viral proteins have been prioritized as SARS-CoV-2 antiviral drug targets, among them the papain-like protease (PLpro) and the main protease (Mpro). Inhibition of these proteases would target viral replication, viral maturation, and suppression of host innate immune responses. Knowledge of inhibitors and assays for viruses were quickly adopted for SARS-CoV-2 protease research. Potential candidates have been identified to show inhibitory effects against PLpro and Mpro, both in biochemical assays and viral replication in cells. These results encourage further optimizations to improve prophylactic and therapeutic efficacy. In this review, we examine the latest developments of potential small-molecule inhibitors and peptide inhibitors for PLpro and Mpro, and how structural biology greatly facilitates this process.

Keywords: SARS-CoV-2, COVID-19, PLpro, Mpro, 3CLpro, papain-like protease, main protease, protease inhibitors

INTRODUCTION

In the past 2 decades, humans have experienced three major coronavirus outbreaks: severe acute respiratory syndrome (SARS) in 2003, Middle East respiratory syndrome (MERS) in 2012–2013 and, currently, coronavirus disease 2019 (COVID-19) since 2019. Since the first case of COVID-19 was reported in December 2019 in Wuhan, China, this disease has rapidly spread in China and around the world. In early 2020, the novel coronavirus SARS-CoV-2 was identified as the causative agent, and by March 2020, WHO characterized COVID-19 as a pandemic. This outbreak has resulted in over 240 million confirmed cases and over 5 million related deaths to date. The virus has caused huge economic loss globally due to mandatory lockdowns and quarantines.

Two major efforts from the drug discovery industry battling COVID-19 focused on developing vaccines to prevent infection and drugs to treat patients. Currently, there are three vaccines that are being administered in the United States: Johnson and Johnson's Janssen, Pfizer-BioNTech, and Moderna. The vaccines were shown to be effective in preventing infection and alleviating symptoms.

However, a significant number of people remain unvaccinated. At the time of preparation of this manuscript, new cases and new variants are still emerging.

Several treatments like fever treatment, oxygen supplementation, and mechanical ventilation are used as supportive care, but a SARS-CoV-2-specific antiviral has been the focus of scientists worldwide. Activity assays, drug screening, computational analysis, and structure determination techniques have all been well developed since 2003. Drug development for COVID-19 had built upon knowledge and experience from SARS research and quickly generated exciting prospects, which will be discussed extensively below (Ho, 2003; Lapinsky and Hawryluck, 2003).

Currently, there are over 6,500 records of clinical trials on the official website (clinicaltrials.gov). However, drugs that are approved to treat COVID-19 are scarce. Veklury (Remdesivir) is a Food and Drug Administration (FDA)-approved antiviral drug that interferes with the activity of RNA-dependent RNA polymerase and is approved for use in adults and pediatric patients [12 years of age and older and weighing at least 40 kg (about 88 pounds)] for the treatment of COVID-19 requiring hospitalization (Warren et al., 2016; Siegel et al., 2017; Gupta et al., 2019; Li et al., 2020). The FDA has issued Emergency Use Authorization (EUA) for several monoclonal antibody treatments for COVID-19 for the treatment of mild or moderate COVID-19 in adults and pediatric patients (ages 12 and up) (Baum et al., 2020). In addition, now, Pfizer has announced an oral therapeutic called Paxlovid that inhibits the activity of SARS-CoV-2 main protease (Mpro) and can reduce the risk of hospitalization or death by 89% (Owen et al., 2021; Pfizer 2021). Merck has also recently announced an oral therapeutic called Molnupiravir that interferes with RNA-dependent RNA polymerase and reduces the risk of hospitalization or death by approximately 50% (Sheahan et al., 2020). Merck and Pfizer are pursuing EUA, and if granted, Paxlovid and Molnupiravir would be the first orally administered COVID-19 antiviral treatments with game changing potential in the battle against the pandemic.

Despite these many advances, the search for COVID-19-specific treatments is far from over. New SARS-CoV-2 virus strains are emerging, and some showed an increase in transmissibility and severity in infections. Development of new drugs targeting different components of the virus can potentially override the risk of new mutations. Structure-guided drug discovery has been a useful method for many viruses. Ongoing efforts to identify antivirals for SARS-CoV-2 have focused on three NSPs (nonstructural proteins): nsp3 papain-like protease (PLpro), nsp5 Mpro, and nsp12 RNA-dependent RNA polymerase. From here, we are going to look at the function and structure of the two SARS-CoV-2 proteases essential for viral replication (PLpro and Mpro) and how structural biology facilitates the development of inhibitors targeting these two proteases.

PAPAIN-LIKE PROTEASE AND MAIN PROTEASE ARE TWO IMPORTANT PROTEASES FOR SARS-COV-2

SARS-CoV-2 belongs to the clade B of genus betacoronavirus. The viral genome is made up of a single-stranded positive-sense

RNA of about 29.8–29.9 kbp in size. At 5' of SARS-CoV-2 genome, there are two overlapping ORFs: ORF1a and ORF1b. ORF1b utilizes a programmed –1 ribosomal frameshift that allows translation of nsp11–nsp16 after the stop codon of ORF1a (**Figure 1**) (Kelly et al., 2020; Giri et al., 2021). Other ORFs encode four conserved structural proteins—spike (S), envelope (E), membrane (M), and nucleocapsid (N)—and six accessory proteins (Kim et al., 2020). ORF1a and ORF1b encode polyprotein 1a and 1b (pp1a and pp1b), which are cleaved into 16 NSPs by protease activity of two cysteine proteases: PLpro and Mpro.

PLpro specifically identifies and cleaves peptide bonds between nsp1 and nsp2 (LNGG↓AYTR), nsp2 and nsp3 (LKGG↓APTK), and nsp3 and nsp4 (LKGG↓KIVN), liberating three proteins: nsp1, nsp2, and nsp3 (**Figure 1**) (Harcourt et al., 2004). In SARS-CoV-2, nsp3 contains 1,945 residues with a mass of ~212 kDa. PLpro is a domain of nsp3—a large multi-domain protein (amino acid residues 746–1,060) that is an essential component of the replication and transcription complex (RTC) (Lei et al., 2018). The enzyme is located in nsp3 between the SARS unique domain and a nucleic acid-binding domain. It is highly conserved and found in all coronaviruses (Lei et al., 2018). When two copies are present in MERS, a single PLpro was found in SARS-CoV-1 and SARS-CoV-2 (Woo et al., 2010; Mielech et al., 2014).

In addition to its ability to hydrolyze the peptide bonds linking nsp1/nsp2, nsp2/nsp3, and nsp3/nsp4, PLpro also cleaves ubiquitin (Ub) and ISG15 [interferon (IFN)-stimulated gene 15] substrates (**Figure 1**) (Ratia et al., 2014; Li et al., 2016). Ub is a small regulatory protein found in most eukaryotic organisms (Komander and Rape 2012). It affects most eukaryotic cellular pathways by covalently modifying an amino group on substrates by a cascade of three enzymes: E1, E2, and E3 (Komander and Rape, 2012; Lv et al., 2017; Yuan et al., 2017; Lv et al., 2018). Ub can also serve as a substrate of ubiquitination modification on one of its amino groups and, most importantly, on the side chains of K48 and K63 forming K48-linked and K63-linked poly-Ub chains. These chains interact with different Ub binding domains and lead to protein degradation and various cellular signaling events, including innate immunity (Komander and Rape 2012). K63-linked poly-Ub was shown to activate the TAK1 kinase complex, which, in turn, phosphorylates and activates IKK (Deng et al., 2000; Wang et al., 2001). IKK phosphorylates NF-κB inhibitory proteins IκB (Karin 1999). Phosphorylated IκB is ubiquitinated by SCF complex, forming K48-linked poly-Ub chains, which is the signal for proteasome degradation. Freed NF-κB translocates into nucleus and activates transcription of a plethora of genes (Hayden and Ghosh, 2008).

ISG15 is a ubiquitin-like modifier. It is conjugated to substrate with an enzyme cascade similar to Ub (Perng and Lenschow, 2018). ISG15 is induced by type I IFN, and ISG15 can directly inhibit viral replication and modulate host immunity (Perng and Lenschow, 2018). The protease activity of SARS-CoV-2 PLpro toward K48-linked poly-Ub chains and ISG15 is important in restricting innate immunity (Perng and Lenschow, 2018; Klemm et al., 2020). With the presence of the protease activity of SARS-CoV-2 PLpro, there is a decrease in ISGylation of IFN regulatory

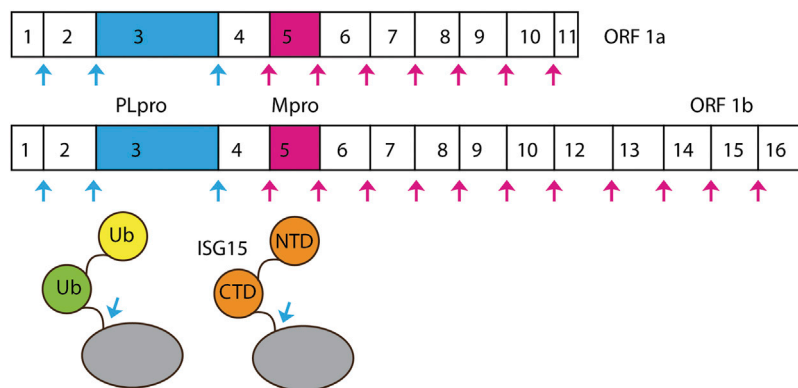


FIGURE 1 | Cleavage sites of PLpro and Mpro. SARS-CoV-2 ORF1a is processed by PLpro and Mpro into Nsp1–Nsp11.

factor 3, and decreases in phosphorylation of TBK1, which is an activation event of the NF- κ B pathway (Shin et al., 2020).

Mpro is the protein encoded from nsp5. Mpro cleaves two large overlapping polyproteins pp1a and pp1ab at 11 conserved sites, including its own N-terminal and C-terminal autoprocessing sites. SARS-CoV-1 Mpro and SARS-CoV-2 Mpro exhibit highly overlapping substrate specificities (Rut et al., 2021). The enzyme has a recognition sequence of Leu-Gln↓(Ser, Ala, Gly), where ↓ marks the cleavage site (**Figure 1**) (Anand et al., 2003; Hilgenfeld, 2014). It is responsible for the cleavage of pp1a/1ab to produce the mature of nsp4–16. This protease is called the Mpro because it plays a major role in processing replicase polyproteins and thus facilitates viral gene expression and replication.

SARS-COV-2 PAPAIN-LIKE PROTEASE STRUCTURE

PLpro is a cysteine protease with rich cysteine content; in addition to catalytic C111, there are 10 other cysteines, of which four coordinate a structural zinc atom. Mutation of the cysteines coordinating zinc causes loss of activity (Barretto et al., 2005). A high concentration of reducing reagent is usually applied to keep the protein in the active state (Rut et al., 2020a); otherwise, oxidation of the catalytic cysteine is observed (Lin et al., 2018). Wild-type (WT) PLpro was also reported to have a poor crystallization property (Osipiuk et al., 2021a).

SARS-CoV-2 PLpro lacks the N-terminal M1 residue compared to SARS-CoV-1 PLpro, which results in being smaller by one residue (Patchett et al., 2021), but maintains 83% sequence identity to SARS-CoV-1 PLpro. Several structures of apo SARS-CoV-2 PLpro have been reported, including WT structures (PDB: 6WZU, 7JRN, and 7NFV) (Osipiuk et al., 2021a) and C111S mutant structures (PDB: 7CJD, 6WRH, 6XG3, 7D47, 7M1Y, and 7K7K) (Osipiuk et al., 2021a; Gao et al., 2021; Zhao et al., 2021). The overall structure SARS-CoV-2 PLpro is similar to PLpro from SARS-CoV-1. It has

a Ubl domain whose function is unknown, and a catalytic unit with a right-hand scaffold that is comprised of three domains Finger, Palm, and Thumb (**Figure 2A**). The Thumb–Palm–Fingers catalytic unit and the conserved catalytic triad resemble the structure of Ub-specific proteases (USPs), although with low sequence identity, whereas the Ubl domain is not present in USPs (Mielech et al., 2014; Hilgenfeld, 2014). Thumb domain is comprised of six α -helices and a small β -hairpin. The Finger subdomain is made of six β -strands and two α -helices and includes a zinc-binding site formed by four cysteine residues (C189, C192, C224, and C226). Zinc binding is essential for structural integrity and protease activity (Barretto et al., 2005). The Palm domain is comprised of six β -strands. The catalytic residues C111, H272, and D286 are located at the interface between the Thumb and Palm domains. Most variations in the structures are at Finger domain and G266–G271 loop (also named BL2 loop or BL loop) containing Y268 and Q269 (**Figure 2A**) (Rut et al., 2020a; Shin et al., 2020; Smith et al., 2020; Ma et al., 2021a; Osipiuk et al., 2021a; Fu et al., 2021; Gao et al., 2021; Shan et al., 2021; Shen et al., 2021). This loop adopts different conformations in structures of the PLpro in different states: apo, substrate bound, and different inhibitor bound.

SARS2-COV-2 PAPAIN-LIKE PROTEASE INTERACTS WITH UBIQUITIN AND UBIQUITIN-LIKE MODIFIER ISG15 AT S1 AND S2 SITES

Like the three Ub binding sites (S1', S1, and S2) arrangement observed in the USP family of deubiquitinases (DUBs), S1–S2 sites of SARS-CoV-1 PLpro have been well characterized to interact with Ub and ISG15. Although the K48-linked diUb and two tandem Ubl domains of a single ISG15 sit on the S1 and S2 sites share the same arrangement, there are significant differences in how the Ubl domains sit on the enzyme.

At S1 of SARS-CoV-2 PLpro, both hydrophobic and hydrophilic interactions are involved in the contact with Ub

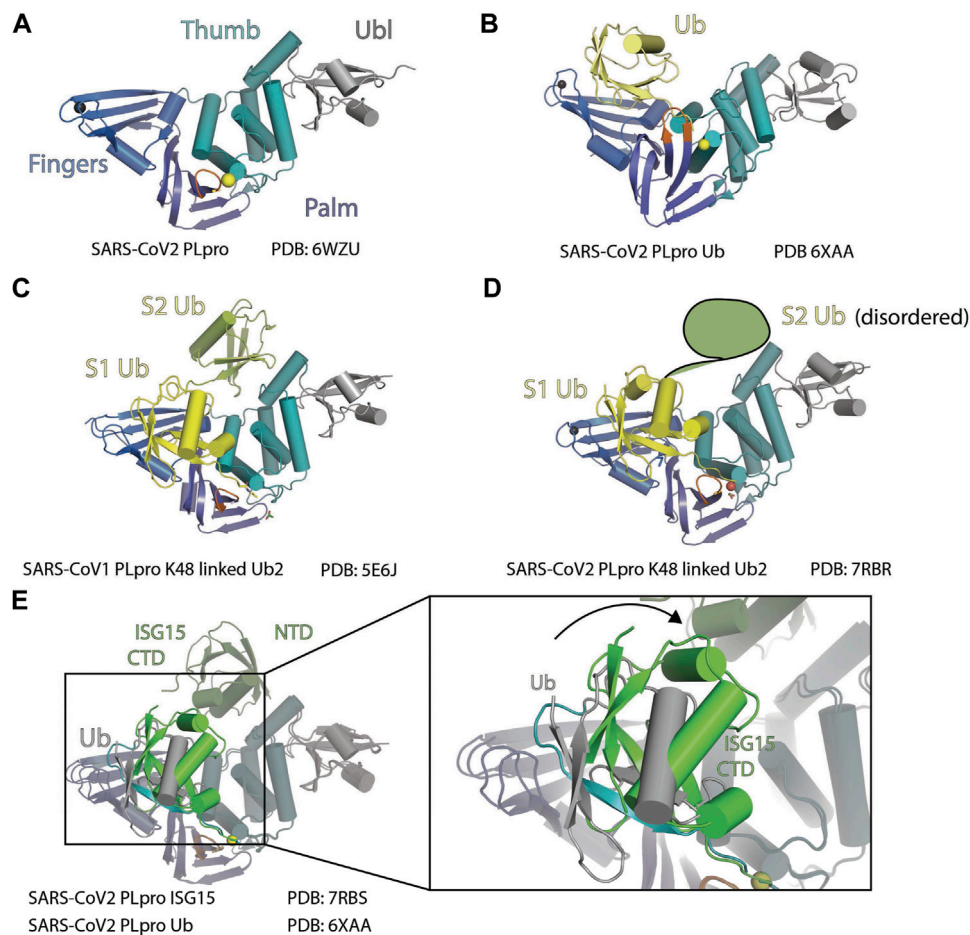


FIGURE 2 | Structure of PLpro with Ub. **(A)** Crystal structure of SARS-CoV-2 PLpro is shown as cartoon to demonstrate its four domains (PDB: 6WZU): Ubiquitin-like domain Ubl (gray), Thumb domain (teal), Palm domain (slate), and Finger domain (marine). BL loop is colored orange. Sulfur atom of C111 and Zinc ion are shown as spheres. **(B)** Crystal structure of SARS-CoV-2 PLpro in complex with ubiquitin is shown as cartoon (PDB: 6XAA). PLpro is colored as in panel A and ubiquitin is colored yellow. **(C)** Crystal structure of SARS-CoV-1 PLpro in complex with K48-linked diUb is shown as cartoon (PDB: 5E6J). S1 (proximal) Ub is colored yellow, and S2 (distal) Ub is colored lime. **(D)** Crystal structure of SARS-CoV-2 PLpro in complex with K48-linked diUb is shown as cartoon (PDB: 7RBR). S1 Ub is colored yellow. S2 (distal) Ub is disordered, and its position is outlined. **(E)** Crystal structure of SARS-CoV-2 with Ub (PDB: 6XAA) is superimposed with the crystal structure of SARS-CoV-2 with ISG15 (PDB: 7RBS). The rotation of ISG15 CTD compared to Ub at S1 site is highlighted.

(Figure 2B) (PDB: 6WZU). L199 and Y207 from Finger domain of PLpro make hydrophobic contacts with Ub globular domain. E167 from Thumb domain forms salt bridge with R42, T225, and R232 from Finger domain, M208 from Palm domain, and R166 from Thumb domain are involved in hydrogen bonds (H bonds) contacts with Ub (Chou et al., 2014; Ratia et al., 2014). E168A and E168R mutants from SARS-CoV-1, which have equivalent position of E167 of SARS-CoV-2, do not affect peptide substrate cleavage and greatly decreased DUB activity in SARS-CoV-1 PLpro (Chou et al., 2014). This validates the S1 site interaction between PLpro and Ub yet indicates that the ORF1a peptide cleavage utilizes an alternative binding mechanism independent of S1.

The structure of a K48-linked di-Ub with SARS-CoV-1 PLpro complex reveals an extended di-Ub binding and conformation across both S1 and S2 sites, rather than sitting across the S1–S1' position; this makes SARS PLpro specific for cleavage of K48-

linked polyubiquitin chains (Figure 2C) (Békés et al., 2016). This is consistent with the observation that di-Ub K48-linked chain by itself is a competing substrate and is resistant to cleavage by PLpro (Ratia et al., 2014). The position of S1 Ub in this structure is similar to the mono-Ub SARS PLpro structures. At the S2 site, Ub contacts the residues 62–74 from the α -helix following Ubl domain with the hydrophobic I44 patch. As a result, the K48-linked di-Ub bound to SARS PLpro is stabilized in an extended conformation that is different from prior structures of K48-linked poly-Ub chains (Cook et al., 1992).

On the basis of the high sequence similarity between PLpro from SARS-CoV-1 and SARS-CoV-2, it was expected that the two proteases process K48-linked poly-Ub chains and ISG15 modification similarly. However, several research groups independently reported PLpro from the two viruses have differences in their activity toward K48-linked poly-Ub chains (Klemm et al., 2020; Shin et al., 2020; Rut et al., 2020a; Patchett

et al., 2021; Osipiuk et al., 2021b). Interestingly, Ub interacts with SARS-CoV-1 and SARS-CoV-2 PLpro at S2 and S1 sites very similarly besides minor differences caused by sequence variation between SARS-CoV-1 and SARS-CoV-2 PLpro (Shin et al., 2020; Rut et al., 2020a; Patchett et al., 2021). A recent structure of SARS-CoV-2 PLpro with Lys48-linked di-Ub shows a highly similar structure (**Figure 2D**) (Osipiuk et al., 2021b). A S2 site mutation (F69S/E70K/H73G) was shown to greatly reduce Ub chain cleavage activity by SARS PLpro (Patchett et al., 2021).

At S1, SARS-CoV-2 has T225 compared to V226 in SARS-CoV-1, and SARS-CoV-2 has K232 compared to Q233 in SARS-CoV-1 (Patchett et al., 2021). SARS-CoV-1 PLpro amide nitrogen from the side chain of Q233 forms an H bond with the backbone carboxylate of A46, and in SARS-CoV-2, PLpro side chain amine group of K232 also forms H bond with backbone carboxylate of A46. SARS-CoV-1 PLpro V226 forms hydrophobic contacts with the backbone of E64 and S65, whereas SARS-CoV-2 PLpro T225 forms hydrophobic contact with the side chain of Q62 and the main chain of E64 and S65. Swapping residue between SARS-CoV-1 and SARS-CoV-2 PLpro changes the features of these two proteases, proving that these minor differences in contacts are important for accounting the difference in activities toward K48-linked Ub chain between PLpro from SARS-CoV-2 and SARS-CoV-1 (Patchett et al., 2021). Shin et al. found a T75L mutant partially recovered cleavage by SARS-CoV-2 PLpro toward K48-linked poly-Ub chains (Shin et al., 2020). Our research shows that the S2 mutant T75L/D179E only partially recovers SARS-CoV-2 PLpro activity toward K48-linked poly-Ub cleavage, whereas the S1 mutant T225V/K232Q significantly improves SARS-CoV-2 PLpro cleavage of K48-linked poly-Ub chains. The corresponding swapped mutant in SARS-CoV-1 PLpro (V226T/Q233K) has reduced activity (Patchett et al., 2021). These results indicated that the differences in the primary sequence at both S1 and S2 both contributed to the difference in the activity of SARS-CoV-1 and SARS-CoV-2 PLpro toward K48-linked Ub, and variation in S1 may take a dominant role. In the recent structure of SARS-CoV-2 PLpro with K48-diUb, only weak electron density is observed for the distal domain (Osipiuk et al., 2021b). This also supports the concept of the S1 site as a major driver for Ub chain substrate recruitment.

ISG15 has two tandem Ub-like folds: NTD and CTD. ISG15 binds to PLpro in a S1–S2 arrangement similar to K48-linked diUb, with the CTD occupying S1 and NTD occupying S2, yet there are apparent differences. At S1 site, ISG15 CTD has different binding modes with PLpro compared to Ub (5TL6 (Daczkowski et al., 2017), 6XA9 (Klemm et al., 2020), and 6YVA (Shin et al., 2020)). When crystalized with SARS-CoV-2 PLpro, ISG15 CTD shows a ~40° rotation compared to S1 Ub (**Figure 2E**) (Klemm et al., 2020; Shin et al., 2020). As a result, ISG15 CTD loses contact with the Finger domain and gains contact with the Thumb domain, where a new set of contacts is formed including PLpro S170, Y171, and Q174, contacting G126, P128, and E130 from ISG15 (Klemm et al., 2020; Shin et al., 2020; Patchett et al., 2021). MERS PLpro, SARS-CoV-1, and SARS-CoV-2 PLpro share the same binding mode to the ISG15 CTD (Daczkowski et al., 2017; Clasman et al., 2020; Shin et al., 2020). In SARS-CoV-1, based on different binding modes of Ub and ISG15, PLpro N156E resulted in selective decrease of

activity in ISG15 cleavage assays, with minor impact on Ub cleavage (Békés et al., 2016). We recently found that S170A/Y171A/Q174A triple mutant is active on mono-Ub but deficient in ISG15-VS labeling (Patchett et al., 2021).

At S2, the structure of SARS-CoV-2 PLpro engages ISG15 NTD. In comparison to the free ISG15 structure, ISG15 NTD rotates about 90°, similar to the conformation when bound to MERS PLpro (Daczkowski et al., 2017; Shin et al., 2020). Comparison of binding modes at the S2 site of ISG15 and K48-linked diUb shows both Ub1 domains sit on a hydrophobic site around F69 for SARS-CoV-2 and F70 for SARS-CoV. Distal Ub uses its I44 patch to interact with F70 and flanked by L8 and H68, whereas ISG15 uses M23 and an aliphatic part of E27 side chain to interact with F70. As a result, the globular domain of ISG15 NTD and distal Ub are rotated relative to each other (Békés et al., 2016; Shin et al., 2020).

P1–P4 Sites

Close to the catalytic site, four C-terminal residues (73–76) of Ub are bound to the narrow active site channel of PLpro (Chou et al., 2014). The positions occupied by the last four residues of Ub were named P4 (L73), P3 (R74), P2 (G75), and P1 (G76) sites. Amino acid residues around the P4–P1 sites are conserved between SARS-CoV-1 and SARS-CoV-2, including the conserved catalytic triad of PLpro. The substrate binding channel is very narrow at the P1 and P2 sites, consistent with the high specificity of glycine residues at these two sites (**Figure 3A**) (Rut et al., 2020a). The P1 and P2 sites have polar interactions with substrate, including H bond with G271 and G163, and van der Waals contacts to L163 and Y164. The substrate binding channel becomes solvent exposed at P3 site and wide at the P4 site to accommodate larger side chains of leucine and arginine. Importantly, the loop β 11–12 strand or BL loop forms the boundary of P3–P4 sites (**Figure 3A**) (Hu et al., 2005). The BL loop is highly dynamic among apo structures, and it adopts different conformations, including its movement in both backbone and side chains. In PDB accessions 7D47 and 6W9C, BL loops are in an open conformation, whereas in PDB accessions 6WZU, 6WRH, 6XG3, 7NFV, 7D6H, and 7D7K, the BL loops are closed (**Figure 3B**). Adding to the backbone movement, the side chains of two residues Y268 and Q269 adopt various rotamers. Upon binding of substrate, BL loop closes and locks substrate in position for catalysis. G271 forms H bond with G76 from Ub. Y268 and Q269 are involved in van der Waals contact with L71, R72, L73, and R74 from Ub. The plasticity of Y269 from SARS PLpro was exploited for drug discovery targeting Baez-Santos et al. (Báez-Santos et al., 2014a; Báez-Santos et al., 2015). New inhibitors targeting SARS-CoV-2 also take advantage of plasticity in this region involving corresponding residue Y268, which will be discussed in the following sections.

Catalytic Triad

Next to the P1 site, SARS-CoV-2 PLpro has a canonical cysteine protease catalytic triad comprising C111, H272, and D286 (Báez-Santos et al., 2015; Rut et al., 2020a; Shin et al., 2020; Osipiuk et al., 2021a) (**Figure 3C**) D286 forms an H bond with the side chain of H272, therefore, restricting its rotation. This action aligns H272, so its side chain faces C111 for catalysis. In the first step, C111 is deprotonated by the basic side chain of H272 to increase its reactivity. Then the amide bond of substrate is

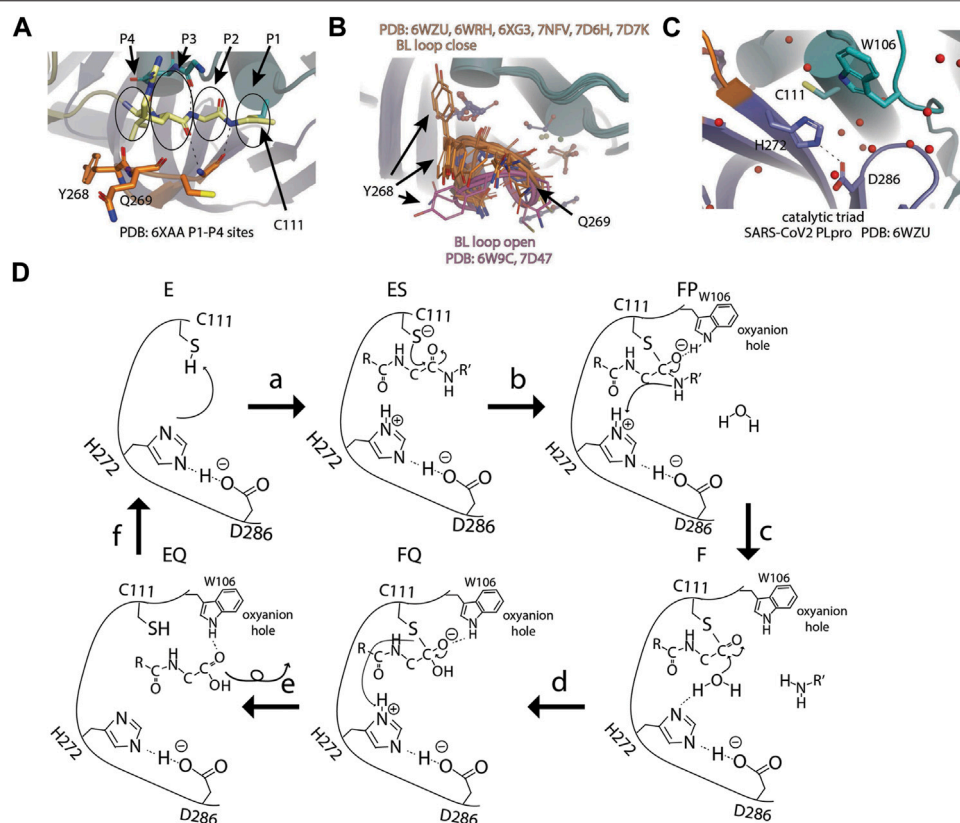


FIGURE 3 | Active site and catalysis. **(A)** Close-up view of catalytic pocket PLpro with Ub bound. The last four residues of Ub occupy P1–P4 sites of the substrate binding pocket: P1 by G76, P2 by G75, P3 by R74, and P4 by L73. P1–P4 sites are highlighted by circles. **(B)** Apo structures of SARS-CoV-2 PLpro are superimposed and shown as cartoon (PDB open: 6W9C and 7D47; close: 6WZU, 6WRH, 6XG3, 7NFV, 7D6H, and 7D7K). Side chains of residue Y268 and Q269 are shown as thin sticks. BL loops in open conformation are colored pink and closed. Conformations are colored orange. **(C)** Close-up view of catalytic triad of SARS-CoV-2 PLpro (PDB 6WZU). **(D)** Schematic drawing of catalytic cycle of SARS-CoV-2 PLpro. In unliganded "E" state, the imidazole group of H272 attacks C111 thiol group to lower its pKa. In the "ES" state, when substrate enters the active site, thiolate attacks the carbon atom of amide bond and forms the first tetrahedral intermediate ("FP" state). The negative charge is transferred to amide oxygen and is stabilized by the oxyanion hole. The amine product is released upon breakage of peptide bond ("F" state). A water molecule attacks the carbonyl and forms the second tetrahedral intermediate ("FQ" state). Lastly, the elimination of cysteine from the intermediate frees the N-terminus of the substrate ("EQ" state) and the enzyme is restored to the "E" state.

nucleophilic attacked by the deprotonated C111. This results in the formation of tetrahedral intermediate and subsequent breakage of amide bond. C111 forms a thioester intermediate with the carboxyl-terminus (C-terminus) of the substrate. The carboxyl oxygen under attack now has a negative charge and is stabilized by the oxyanion hole including W106. H272 protonates the amine and restores its deprotonated form. The thioester bond is subsequently hydrolyzed, releasing the carboxylic acid substrate fragment, and the enzyme is restored (Figure 3D).

INHIBITORS AGAINST SARS-COV-2 PAPAIN-LIKE PROTEASE

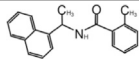
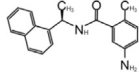
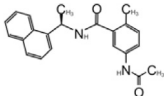
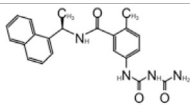
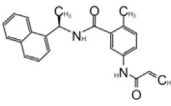
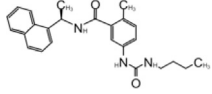
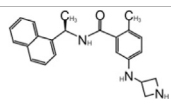
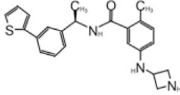
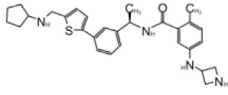
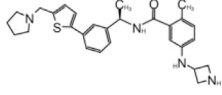
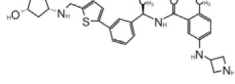
GRL0617 and Its Analogs Inhibit SARS-CoV-1 Papain-Like Protease

In 2008, Ratia et al. screened a structurally diverse library of 50,080 compounds for inhibitors of PLpro with RLRGG-AMC (7-amido-4-methylcoumarin) fluorescent substrate. Authors

included 5 mM DTT in the assay to prevent electrophiles from non-specifically binding the catalytic cysteine (Ratia et al., 2008). This screening campaign found compound 7724772 that inhibited PLpro with an IC_{50} (half-maximal inhibitory concentration) value of $20.1 \pm 1.1 \mu M$ (Table 1). A series of derivatives were synthesized and tested for potency. Refinement by the addition of a naphthyl group and an amino group to the ortho-methyl benzene ring resulted in the more potent compound GRL0617 (Table 1). It has an $IC_{50} = 0.6 \pm 0.1 \mu M$ toward SARS-CoV-1 PLpro. Compound 6 has one more Ac group than GRL0617, and it has decent potency with $IC_{50} = 2.6 \mu M$ and EC_{50} (half-maximal effective concentration) = $13.1 \mu M$ (Table 1) (Ratia et al., 2008). Both GRL0617 and compound 6 inhibited SARS-CoV-1 viral replication in Vero E6 cells with an EC_{50} value of 14.5 and $13.1 \mu M$, respectively. It is also encouraging that they had no associated cytotoxicity (Ratia et al., 2008).

X-ray structure of the SARS-CoV-1 PLpro-GRL0617 complex was solved at a resolution of 2.5 \AA (Figure 4A). The structure

TABLE 1 | GRL0617-like inhibitors I.

Compound Name	Chemical Structure	IC ₅₀	EC ₅₀	References
7724772		20.1 ± 1.1 μM	—	Ratia et al. (2008)
GRL0617		~2 μM	~20 μM	Barretto et al. (2005); Beigel et al. (2020); Fu et al. (2020); Hoffman et al. (2020); Ahmad et al. (2021); Ampornpanai et al. (2021); Fu et al. (2021)
Compound 6		11 ± 3 μM	—	Ahmad et al. (2021)
Compound 2		5.1 ± 0.7 μM	Failed	Ospiuk et al. (2021a)
Compound 3		6.4 ± 0.6 μM	Failed	
Compound 5		16.8 ± 2.9 μM	2.5 μM	
ZN2-184		1.01 ± 0.15 μM	—	Shen et al. (2021)
ZN-3-80		0.59 ± 0.04 μM	—	
XR8-23		0.39 ± 0.05 μM	2.8 ± 0.4 μM	
XR8-24		0.56 ± 0.03 μM	2.5 ± 0.3 μM	
XR8-89		0.113 ± 0.004 μM	11.3 ± 1.6 μM	

shows that the GRL0617 binds at P3–P4 position, in proximity but not within the catalytic site. The interaction between GRL0617 and PLpro is stabilized through H bonds and hydrophobic interactions. The 1-naphthyl group forms hydrophobic interactions with the aromatic rings of Y265 and Y269. P248 and P249 residues line the substrate binding pocket, and they are known to accommodate the leucine residue at the P4 position of PLpro substrates (**Figure 4A**) (Ratia et al., 2006). The di-substituted benzene ring occupies the putative P3 position and

stacks against the aliphatic portions of G164, D165, and Q270. The ortho-methyl group is lined by the side chains of Y265, Y274, and L163, and the amino group is surrounded by the side chain oxygen of Q270 and E168 and the hydroxyl of Y269 (**Figure 4A**) (Ratia et al., 2008). Comparison of the unbound and inhibitor-bound structures reveals a significant conformational difference in the BL loop that it moves toward GRL0617 and gains contacts with the inhibitor. Along with the movement of backbone, the side chains of Y269 and Q270 close over the inhibitor (**Figure 4A**)

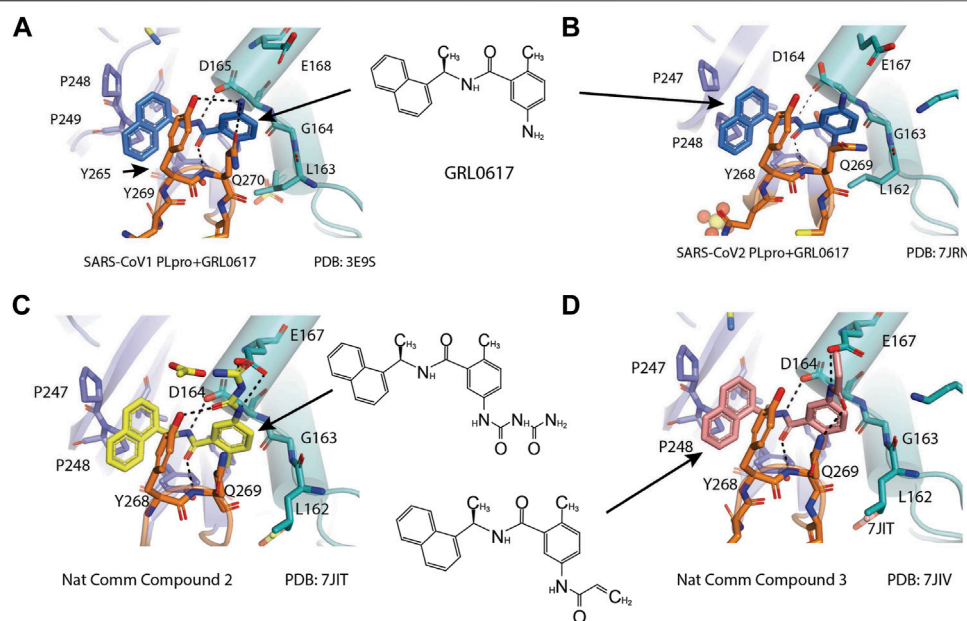


FIGURE 4 | Close-up view of interaction between SARS-CoV-1 PLpro and inhibitors in crystal structures. PLpro is shown as cartoon with sticks representation shown for residues involving contact with inhibitors. Inhibitors are shown as sticks. Hydrogen bonds are labeled with dashed lines. **(A)** SARS-CoV-1 PLpro with GRL0617 (PDB: 3E9S). **(B)** SARS-CoV-2 PLpro with GRL0617 (PDB: 7JRN). **(C)** SARS-CoV-2 PLpro with compound 2 (PDB: 7JIT). **(D)** SARS-CoV-2 PLpro with compound 3 (PDB: 7JIV).

(Ratia et al., 2008). Importantly, GRL0617 was unable to inhibit HAUSP, USP18, UCH-L1, UCH-L3, and a papain-like protease (PLP2) from the human coronavirus NL63. The high specificity and low cytotoxicity make GRL0617 an ideal lead for future refinement (Ratia et al., 2008; Ghosh et al., 2009).

GRL0617 is Also a Good Inhibitor for SARS-CoV-2 Papain-Like Protease

As the catalytic site including P1–P4 is strictly conserved between S1 and SARS-CoV-2 PLpro, Brendan et al. tested five inhibitors including 7724772 and GRL0617. It was found that GRL0617 inhibited SARS-CoV-2 PLpro IC_{50} value of 2.4 μM (Freitas et al., 2020). Inhibition of PLpro by GRL0617 was used to confirm the role of PLpro in modulating host immunity through IFN and NF- κB pathways (Shin et al., 2020). Freitas et al. also used GRL0617 directly and found it inhibited SARS-CoV-2 PLpro with $IC_{50} = 2.4 \mu M$ (Freitas et al., 2020). GRL0617 is often among the best hits from high-throughput screening campaigns or used effectively as a positive control (Smith et al., 2020; Zhao et al., 2021; Shen et al., 2021; Shan et al., 2021; Fu et al., 2021). Smith et al. (2020) screened several libraries and found disulfiram and GRL0617 as the best leads (Smith et al., 2020). Fu et al. (2021) showed that GRL0617 inhibited the deISGylation activity of PLpro in a cell-based assay. The *in vitro* IC_{50} values of GRL0617 against SARS-CoV-2 PLpro were $2.1 \pm 0.2 \mu M$ (Fu et al., 2021). Shen et al. used an unbiased ChemDiv library (10,000-compound SMART library subset excluding PAINS compounds) and a biased, annotated TargetMol Bioactive library (5,370 compounds) to

screen for inhibitors against SARS-CoV-2 PLpro. This screen resulted in a low hit rate, identifying only CPI-169 and the positive control GRL0617 (Table 1) (Shen et al., 2021). Jerzy et al. tested GRL0617 (named compound 1 in their paper) at IC_{50} value of 2.3 μM *in vitro* (Osipiuk et al., 2021a). Shan et al. first screened 25 DUB inhibitors and only found GRL0617 (Shan et al., 2021). Authors then screened 35,360 diverse compounds, including lead-like fragments, FDA-approved drugs, and small molecules with reported biological activities and follow-up assays, and found that GRL0617 was the best hit in potency, selectivity, and molecular complexity (Shan et al., 2021). These efforts show GRL0617 is indeed a good lead for inhibition of SARS-CoV-2 PLpro.

The mechanism of inhibition by GRL0617 has been investigated, and Shin et al. showed GRL0617 is ineffective against MERS-PLpro; authors hypothesized that this could be due to the presence of threonine instead of tyrosine at this conserved position (Y268 in SARS-CoV-2 PLpro) (Shin et al., 2020). Accordingly, the mutation of Y268 to either threonine (Y269T) or glycine (Y268G) in SARS-CoV-2 PLpro strongly reduced the inhibitory effect of GRL0617 (Shin et al., 2020). It was believed that GRL0617 functions by blocking the entry of the Ub and ISG15 C-terminus toward the catalytic cleft of the protease, as it occupies the P3–P4 position (Ratia et al., 2008; Shin et al., 2020). Indeed, Fu et al. used NMR to show that ^{15}N -ISG15 caused drastic peak broadening and intensity loss in the 1H , ^{15}N -HSQC NMR spectrum with PLpro, and it was recovered by titration of GRL0617, proving the concept that GRL0617 competes with ISG15 for the binding site in PLpro and blocks the binding of Ubl to PLpro (Fu et al., 2021).

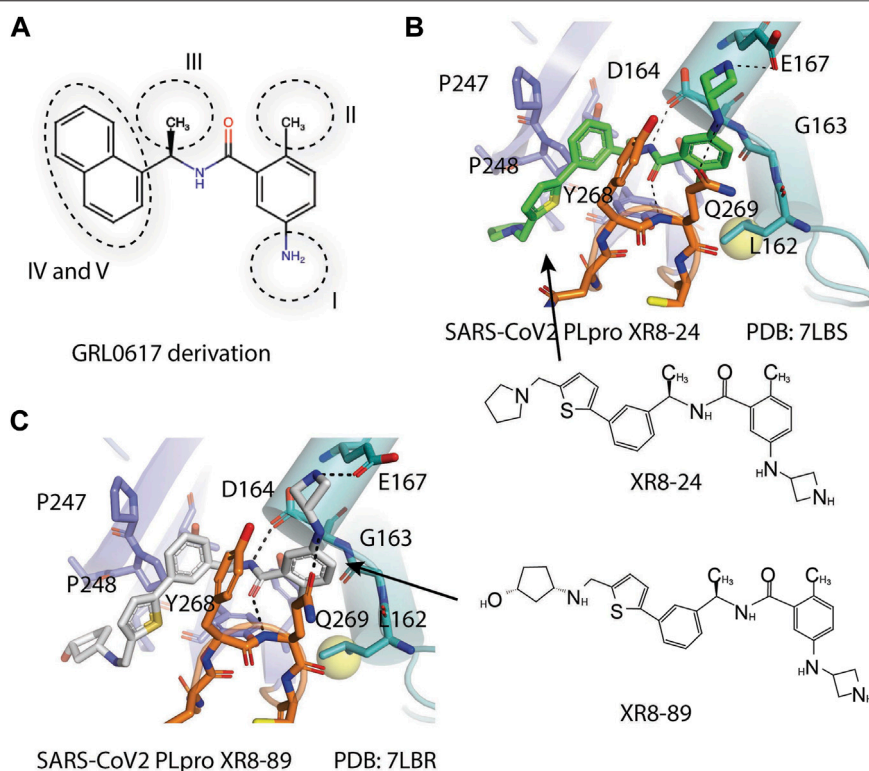


FIGURE 5 | (A) Five regions that were derivatized for refinement of GRL0617. **(B and C)** Close-up view of interaction between SARS-CoV-1 PLpro and inhibitors in crystal structures. PLpro is shown as cartoon with sticks representation shown for residues involving contact with inhibitors. Inhibitors are shown as sticks. Hydrogen bonds were labeled with dashed lines. **(B)** SARS-CoV-2 PLpro with XR8-24 (PDB: 7LBS). **(C)** SARS-CoV-2 PLpro with XR8-89 (PDB: 7LBR).

Four structures of SARS-CoV-2 PLpro with GRL0617 were reported (Osipiuk et al., 2021a; Gao et al., 2021; Ma et al., 2021a; Fu et al., 2021). Compared to the apo-structure of PLpro C111S (PDB: 6WRH), consistent with previous observations in SARS-CoV-1 PLpro, there is an apparent conformational change of the BL loop that stabilizes GRL0617 binding. The structures show consistent binding mode that GRL0617 occupies the P3–P4 positions of the substrate cleft near the active site (**Figure 4A**). The BL loop connecting $\alpha 3$ and $\alpha 4$ forms one side of the boundary of this pocket and closes toward the inhibitor compared to apo conformation. This movement is consistent with the observation from SARS-CoV-1 PLpro structures (Ratia et al., 2008). Side chains of both Y268 and Q269 close toward GRL0617 (**Figure 4A**). The movement of both backbone and side chains of residues uncover hydrophobic region and form polar and hydrophobic interactions with GRL0617. Y269 wedges between substituted benzene group and 1-naphthyl group (**Figure 4A**). Aliphatic region of Q269 forms van der Waals contact with the benzene ring. The H bonds and hydrophobic interactions between GRL0617 and PLpro are conserved from SARS-CoV-1 to SARS-CoV-2. The 1-naphthyl group forms hydrophobic interactions with the aromatic rings of Y264 and Y268, and it is partially solvent-exposed. P247 and P248 residues set important boundaries for the substrate binding pocket (**Figure 4A**). The (R)-methyl group points toward Y264 and T301. The carbonyl oxygen of GRL0617 forms an H bond with

the backbone nitrogen of N269 (**Figure 4A**). The di-substituted benzene ring occupies the putative P3 position and stacks against the aliphatic portions of G163, D164, and Q269. The ortho-methyl group is lined by the side chains of Y264, Y273, and L162, and the amino group of aniline is surrounded by the side chain oxygen of Q269 and E167 and the hydroxyl of Y268, forming H bonds with side chain of Y268 and potentially E167 (**Figure 4A**) (Ma et al., 2021a; Osipiuk et al., 2021a; Fu et al., 2021; Gao et al., 2021). Some minor differences are observed in the three GRL0617 bound CoV-2 PLpro structures. In PDB accessions 7CMD and 7JRN, the side chain of L162 is about 3.7 Å away from ortho-methyl group, whereas in PDB accessions 7JIR and 7CJM, L162 is an outlier that its side chain flips away from GRL0617 and has no contact with the inhibitor. Another amino acid residue that shows a difference is E167 from PDB 7JIR and 7CJM, whose side chain oxygen is ~3.7 Å from the aniline amine group of GRL0617, likely forming a weak H bond, whereas the same side chains from the other PDBs indicate side chains of E167 flipping away from inhibitor (Ma et al., 2021a; Osipiuk et al., 2021a; Fu et al., 2021; Gao et al., 2021).

Development of GRL0617 Derivatives

The inhibition, structure, and effectiveness of GRL0617 against SARS-CoV-2 PLpro are all in agreement with previously observations with SARS-CoV-1 PLpro. GRL0617 is a promising platform for further development, especially

considering its low cytotoxicity and good potency. Some representative compounds are discussed below. Compound 6 (**Table 1**) was initially reported among a series of derivatives of the initial hit 7724772, along with GRL0617 (Ratia et al., 2008). It was generated by adding an acetyl group to GRL0617. For SARS-CoV-1 PLpro, Compound 6 has similar IC_{50} value with GRL0617, whereas its EC_{50} at 13.1 μM is similar to GRL0617 (Ratia et al., 2008). Freitas et al. report that compound 6 has an IC_{50} value of 5 μM (Freitas et al., 2020). More recently, Fu et al. showed that the *in vitro* IC_{50} values of compound 6 against SARS-CoV-2 PLpro were $11 \pm 3 \mu M$ (Fu et al., 2021).

D164 and E167 are in proximity of the amine of four methyl aniline groups from GRL0617, and Jerzy et al. generated a series of GRL0617 derivatives to derivatize in this region (Osipiuk et al., 2021a). Crystal structures of SARS-CoV-2 PLpro with compounds 2 and 3 were achieved (**Table 1**) (**Figures 4C,D**) (PDB: 7JIT, 7JIV, and 7JIW). As expected, the inhibitors bind to the same site in the enzyme as GRL0617, located 8–10 Å away from the catalytic cysteine. Some of the newly designed inhibitors had additional contacts. For example, compound 2 has interactions with its carbamylurea moiety, forming H bonds with Glu167, Tyr268, and water-mediated H bond with K157 (**Figure 4C**), yet these derivatives including compound 2 had decreased potency (IC_{50} in the range of 5.1–32.8 μM) for unknown reasons. The new inhibitors were also tested in Vero E6 cells for the SARS-CoV-2 replication. Interestingly, the viral replication assay shows different comparison of potency among inhibitors with biochemical assay. Compounds 2 and 3 are good PLpro inhibitors with IC_{50} values of 5.1 and 6.4 μM , respectively, but failed in the viral replication assay. Compound 5 was the weakest inhibitor *in vitro* with IC_{50} values of 32.8 μM , but it was one of the best performers in the live viral replication assay ($EC_{50} = 2.5 \mu M$). The authors speculated that the differences in cell permeability and solubility could account for the differences (Osipiuk et al., 2021a).

Shen et al. used a more systematic approach that derivatized five regions of GRL0617 (**Figure 5**) (Shen et al., 2021). Region I is from the amine group of aniline; region II is from the ortho methyl group on derivatized benzene group; region III is from the R methyl group; region IV and region V are achieved by replacing the naphthalene group and further extensions (**Figure 5A**) (Shen et al., 2021). Refinement at region II (replacing ortho methyl group with -Cl, -Br, -CH = CH, -CF₃, or -F) was not successful. Although extra room at region III suggested room for refinement (Ratia et al., 2008), replacing the (R)-methyl group with -Et, -CH₂CH₂OH, or -CH₂CONHCH₃ group decreased potency (Shen et al., 2021). The generated derivatives show lower potency than GRL0617. At region I, adding azetidine group to derivatize the amine group from aniline yielded ZN2-184 that has two-fold increase in potency (**Table 1**). The rationale of this modification is the same as Jerzy et al., to gain contact with E167, and Shen et al. found more a favorable group at this site (Shen et al., 2021). At region IV, replacing naphthalene ring with fused heteroaryls, such as benzothiophene, indole, and carbazole with various linkages, had lower potency, likely due to spatial restraints. Replacement of naphthalene with bi-aryl groups like 2-phenylthiophene (ZN-3-80; $IC_{50} = 0.59 \mu M$) increased potency

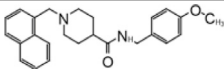
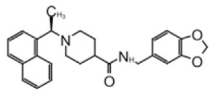
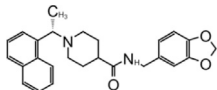
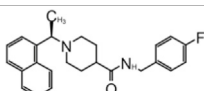
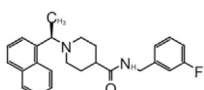
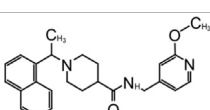
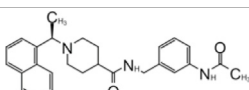
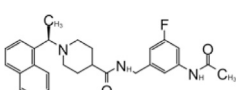
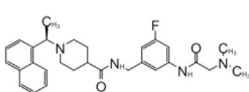
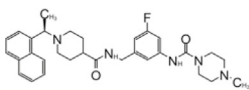
(**Table 1**). Taking advantage of the extra space next to the naphthalene group, which features hydrophobic residues like P248 and P299, and backbone of G266 (named BL groove), adding basic groups from phenylthiophene significantly improved potency, dropping IC_{50} to below 500 nM. XR8-89 is the best in the series and has an IC_{50} value of 0.11 μM (**Table 1**).

SPR assays show the extended ligands with basic side chain have significant decreased dissociation rates of XR8-89 and XR8-23 (Shen et al., 2021). To examine the binding mode of the novel PLpro inhibitors, authors obtained co-crystal structures of XR8-24, XR8-65, XR8-69, XR8-83, and XR8-89 with SARS-CoV-2 PLpro (PDB: 7LBR, 7LBS, 7LLE, 7LLZ, and 7LOS) (**Table 1**). Superposition of the ligand-bound structures shows all inhibitors utilized the same binding mode similar to GRL0617, including closure of BL loop and H bond between amide of inhibitor and D164 and Q269 (Osipiuk et al., 2021a; Gao et al., 2021; Ratia et al., 2008; Ahmad et al., 2021). The analysis of the representative co-crystal structures of XR8-24 and XR8-89 found that the azetidine ring extends into Site I to interact with side chain of E168 (**Figures 5B,C**) (Shen et al., 2021). The amide group of XR8-24 and XR8-89 is aligned closely with that of GRL0617 in SARS-CoV-2 PLpro (PDB: 7JRN) with the expected two H bonds between amide and the main chain of Q269 on the BL loop and with side chain of D164. In Site IV, the phenylthiophene group sits between P248 and side chain of Y268 at a similar position of naphthalene ring of GRL0617 (**Figures 5B,C**) (Shen et al., 2021). The thiophene extends further compared to naphthalene group of GRL0618 (Site V), where it takes part in van der Waals interactions with residues P248, Y264, and (Shen et al., 2021). The additional groups that derivatized from phenylthiophene have mostly poor electron density in crystal structures (Shen et al., 2021). Indeed, this region is open to solvent and authors conjectured that crystal packing forces might also contribute to it. However, the pyrrolidine ring of XR8-24 is better defined, with putative interaction with P248, G266, and Y265 (**Figure 5B**). In a plaque formation assay using the SARS-CoV-2 USA/WA1/2020 strain and Vero E6 cells, GRL0617 has an EC_{50} value of $21.7 \pm 1.6 \mu M$, whereas both XR8-23 and XR8-24 were significantly more potent than GRL0617 with EC_{50} at $2.8 \pm 0.4 \mu M$ and $2.5 \pm 1.9 \mu M$, respectively. XR8-89 also demonstrated superior antiviral potency compared to GRL0617, yet with higher EC_{50} value at $11.3 \pm 1.6 \mu M$. In this study, antiviral potency does not strictly correlate with the superior potency of this inhibitor in biochemical assays for unknown reasons. The lack of observable cytotoxicity for XR8-89 might indicate attenuated cell permeability as a cause of lower antiviral potency (Shen et al., 2021). No toxicity was observed under assay conditions in Vero E6 cells for these compounds at concentrations lower than 50 μM (Shen et al., 2021).

GRL0667, Compound 3, Compound 15g, and Compound 15h

Another lead compound 3 (6577871) was found *via* high-throughput screening of a diverse chemical library where GRL0617 was identified, but with lower potency $IC_{50} = 59 \mu M$ (**Table 2**) (Ratia et al., 2008; Ghosh et al., 2010). Subsequent lead

TABLE 2 | GRL0667-like inhibitors II.

Compound Name	Chemical Structure	IC ₅₀	EC ₅₀	References
6577871 (Compound 3)		59.2 ± 7.8 μM (SARS-CoV-1)	—	Ghosh et al. (2010)
CP15g (GRL0667)		0.32 ± 0.01 μM (SARS-CoV-1)	—	
CP15 h		0.56 ± 0.03 μM (SARS-CoV-1)	—	
3J		0.49 μM (SARS-CoV-1)	—	Báez-Santos et al. (2014b)
3K		0.15 μM (SARS-CoV-1)	—	
rac5c		0.81 μM	—	Klemm et al. (2020)
Compound 12		2.69 ± 0.34 μM	—	Shan et al. (2021)
Compound 14		1.76 ± 0.06 μM	—	
Compound 18		0.80 ± 0.29 μM	—	
Compound 19		0.44 ± 0.05 μM	—	

optimization efforts led to the design of potent inhibitor 15g (GRL0667, IC₅₀ = 0.32 μM) which inhibited SARS-CoV-1 viral replication in Vero cells with an EC₅₀ value of 9.1 μM, and its enantiomer 15 h has IC₅₀ = 0.56 μM and similar antiviral potency (Table 2). The crystal structure shows that the naphthyl ring of 15g aligns in a similar fashion in the hydrophobic pocket formed by residues Y269, Y265, P248, P249, and T302, whereas the rest of the inhibitors exhibit different binding modes (Figure 6A) (note that GRL0617 was named compound 2 in this paper; PDB: 5MJ5) (Ghosh et al., 2010). The piperidyl group and the carboxamide group of 15g occupies similar position of methyl-aniline group of GRL0617, yet less bulky, so it allows side chain of Y269 to be slightly closer. The conformation of BL loop at Q270 is very

different induced by binding of different inhibitors. Both the main chain and side chain of Q270 flip away from 15g, to make room for its benzodioxolane group that rests on the aliphatic region of Q270 side chain (Ghosh et al., 2010). The flexibility of BL loop is exploited by 15g.

In 2014, the same authors used SAR (structure–activity relationship) to show that adding additional groups to (R)-methyl group cause decreased potency, which is consistent with refinement of GRL0617 (Shen et al., 2021). Replacing benzodioxolane with 3-F-benzene or 4-F-benzene slightly increase potency (3j: 4-F IC₅₀ = 0.49 μM; 3k: 3-F IC₅₀ = 0.15 μM) (Table 2). The structural comparison of 3j and 3k with 15g shows that the binding modes to SARS-CoV-1 PLpro are

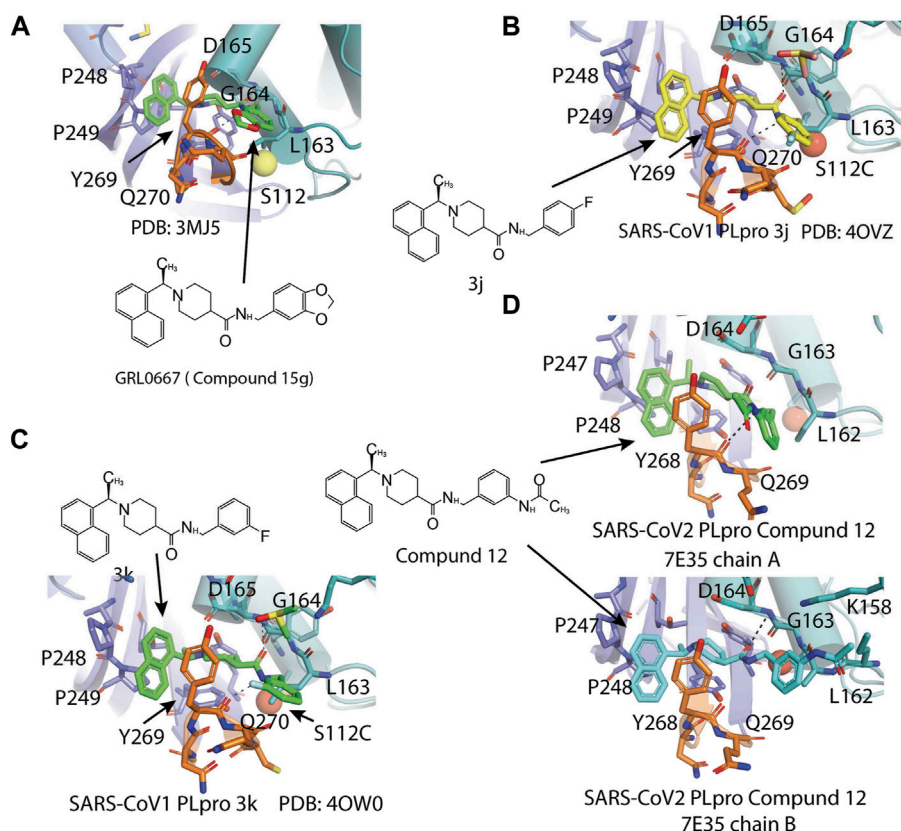


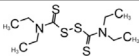
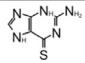
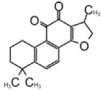
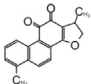
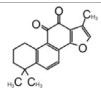
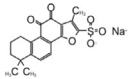
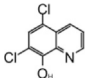
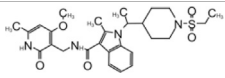
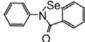
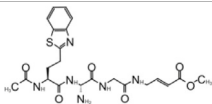
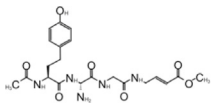
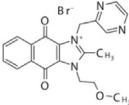
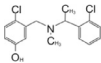
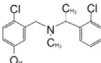
FIGURE 6 | Close-up view of interaction between SARS-CoV-1 PLpro and inhibitors in crystal structures. PLpro is shown as cartoon with sticks representation shown for residues involving contact with inhibitors. Inhibitors are shown as sticks. Hydrogen bonds were labeled with dashed lines. **(A)** SARS-CoV-1 PLpro with GRL0667 (PDB: 3MJ5). **(B)** SARS-CoV-1 PLpro with 3j (PDB: 4OVZ). **(C)** SARS-CoV PLpro with 3k (PDB: 3OW0). **(D)** SARS-CoV-2 PLpro with compound 12 from the two copies in the asymmetric unit (PDB: 7E35).

almost identical with minor translation compared to GRL0617 (PDB: 4OVZ and 4OW0) (Figures 6B,C) (Báez-Santos et al., 2014b). Klemm et al. synthesized racemic forms of compounds reported in 2014: rac3j, rac3k, and rac5c (Table 2) (Báez-Santos et al., 2015; Klemm et al., 2020). Each compound had low or sub-micromolar inhibitory activity against SARS-CoV-2 PLpro. Rac5c is the best among the list, and it has IC_{50} value of $0.81 \mu M$. It inhibited protease activity in the context of full NSP3 and inhibited viral replication at $11 \mu M$ concentration (Klemm et al., 2020).

Hengyue et al. prepared a series of reported SARS-CoV-1 PLpro inhibitors that share a naphthyl group with GRL0617 resembling GRL0667 (Shan et al., 2021; Ghosh et al., 2010; Báez-Santos et al., 2014b). These inhibitors showed better potency than GRL0617 in an *in vitro* fluorescence-based assay with IC_{50} values ranging between 2.6 and $4.3 \mu M$. Authors solved the co-crystal structure of the SARS-CoV-2 PLpro C112S with compound 12 at 2.4 \AA resolution (PDB: 7E35) (Table 2). In comparison with the apo structure, the BL loop adopts the same conformation as with complex with GRL0617 that both backbone of the BL loop and side chain of Y269 bends toward 12 (Figure 6D) (Gao et al., 2021; Ma et al., 2021a; Fu

et al., 2021). Interestingly, the electron density maps indicated distinct binding modes of inhibitor for each asymmetric unit. In chain A, the phenyl ring of Y269 simultaneously engages with all three hydrophobic rings of 12, acting as a latch of the binding pocket. The carbonyl of Y269 forms an H bond with the backbone amide of 12 (Figure 6D). The derivatized cyclohexane extends into a small pocket formed by P248, R167, A247, and M209. This is different from compound 12 in chain B, where the same group is sandwiched by E162, L163, and the side chain of M209 from crystal packed molecule nearby (Shan et al., 2021). On the basis of the structure, further refinement of inhibitors was done with SAR. Piperidyl ring is tightly surrounded, so it is not an ideal candidate for refinement. Addition of 5-fluorine to benzene group of 12 potentially increased favorable contact with Q270, thereby increased potency of 14. Replacement of benzyl ring with piperidine ring were not successful, yet acetamide group extended by tertiary amine show increased potency: compounds 18 and 19 (Table 2). According to SPR results, 19 bound to SARS-CoV-2 PLpro with a K_d value of 2.6 mM , compared to that of GRL0617 at 10.8 mM . In addition, 19 is also shown not to inhibit DUBs at $10 \mu M$ and, at 10 mM 19, significantly inhibited

TABLE 3 | Other PLpro inhibitors.

Compound Name	Chemical Structure	IC ₅₀	EC ₅₀	References
Disulfiram		2 μ M	—	Smith et al. (2020)
6-TG		72 \pm 12 μ M	—	Fu et al. (2021)
Cryptotanshinone		~1–5 μ M	~1–5 μ M	Yang et al. (2005); Park et al. (2012)
Dihydrotanshinone I		2.21 \pm 0.10 μ M	2.26 \pm 0.11 μ M	Yang et al. (2005)
Tanshinone IIA		1.57 μ M	—	Lim et al. (2021)
Tanshinone IIA sulfonate sodium		1.65 \pm 0.13 μ M	—	Xu et al. (2021)
Chloroxine		7.24 \pm 0.68 μ M	—	—
CPI-169		7.3 μ M	—	Shen et al. (2021)
Ebselen		2.26 \pm 1.05 μ M	—	Weglarz-Tomczak et al. (2021)
VIR250		—	—	Rut et al. (2020a); Patchett et al. (2021)
VIR251		—	—	—
YM155		2.47 \pm 0.46 μ M	—	Zhao et al. (2021)
Jun9-13-7		7.29 \pm 1.03 μ M	—	Ma et al. (2021a)
Jun9-13-9		6.67 \pm 0.05 μ M	—	—

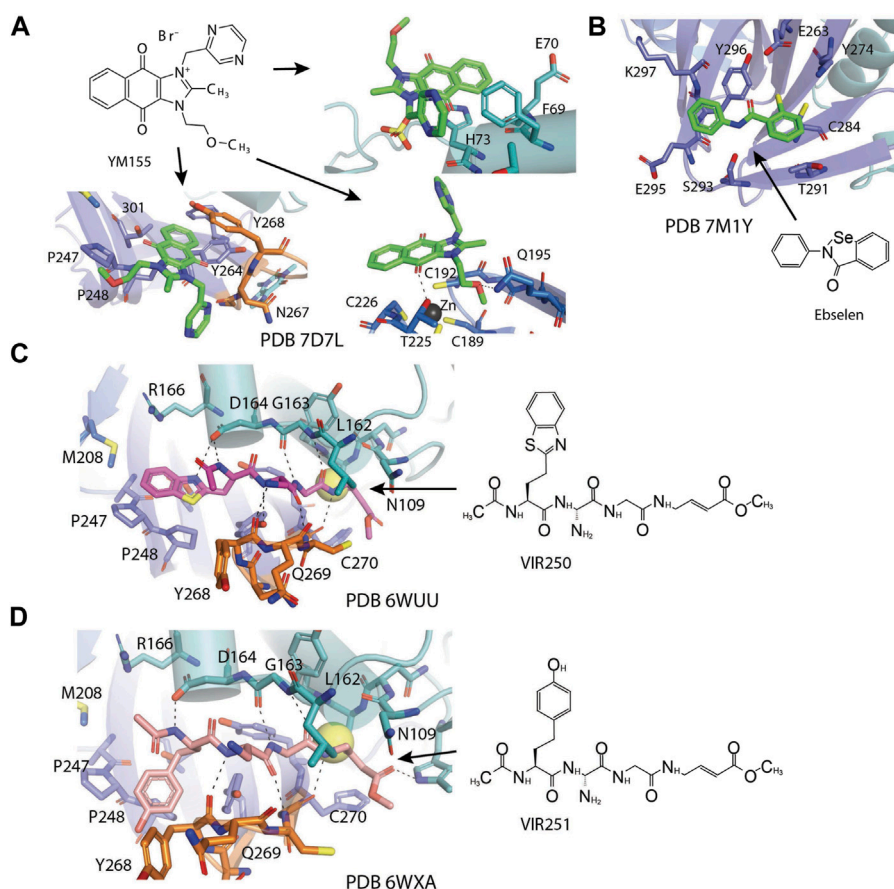


FIGURE 7 | Close-up view of interaction between SARS-CoV-1 PLpro and inhibitors in crystal structures. PLpro is shown as cartoon with sticks representation shown for residues involving contact with inhibitors. Inhibitors are shown as sticks. Hydrogen bonds were labeled with dashed lines. **(A)** Three binding sites of YM155 on SARS-CoV-2 PLpro (PDB: 7D7L). **(B)** SARS-CoV-2 PLpro with ebselen (PDB: 7M1Y). **(C)** SARS-CoV-2 PLpro with VIR250 (PDB: 6WUU). **(D)** SARS-CoV-2 PLpro with VIR251 (PDB: 6WXA).

SARS-CoV-2 PLpro in 293T cells and significantly recover the activation level of NF- κ B that can be inhibited by PLpro. 19 could significantly inhibit SARS-CoV-2 replication even at 400 nM. At 10 mM, 19 did not show detectable cytotoxicity in hACE2-HeLa cells. 19 was the best in the series with an IC_{50} value of 182 nM and a therapeutic index (CC_{50}/IC_{50}) over 55 (Shan et al., 2021).

Disulfiram

Disulfiram is a drug which was approved by the US FDA for use in alcohol aversion therapy (Lin et al., 2018). Disulfiram was first shown to inhibit SARS-CoV-1 PLpro at $IC_{50} = 24.1 \pm 1.8 \mu M$ by Lin et al., in 2018 (Table 3) (Lin et al., 2018). With a zinc-specific fluorophore, FluoZin-3, it was found that Zn^{2+} ion was released upon addition of disulfiram (Lin et al., 2018). The study by Karan et al. is in agreement with disulfiram functioning as a zinc ejector and confirmed the addition of disulfiram on PLpro with molecular weight calculated by mass spectrometry (Sargsyan et al., 2020). Another proposed mechanism of inhibition is the formation of a covalent adduct to catalytic cysteine, as BME treatment can partially restore PLpro activity inhibited by

disulfiram (Lin et al., 2018). Efforts in obtaining the structure of disulfiram have not been successful. Lin et al. only observed BME like electron density projecting off SARS-CoV-1 PLpro C112 but not cysteines coordinating Zn^{2+} , which supports the hypothesis that disulfiram inhibits PLpro by forming covalent adduct to catalytic cysteine. Smith et al. screened several libraries and found disulfiram and GRL0617 as the best leads (Smith et al., 2020), yet Gao et al. did not detect inhibition by disulfiram (Lin et al., 2018). The discrepancy may stem from different substrates used in assessing inhibitor efficacy or the presence of reducing reagents that neutralized the inhibitory effect. The inhibitory effect of disulfiram is greatly limited by the oxidation-reduction environment. Considering disulfiram is known to be promiscuous, the application and development of disulfiram for PLpro could be restricted.

6-Thioguanine

6-Thioguanine (6-TG) is an FDA-approved drug that has been used in the clinic since the 1950s, originally for the treatment of childhood leukemias and subsequently for treatment of inflammatory bowel and Crohn's disease (Bayoumy et al.,

2020). Chou et al. discovered 6-TG as a reversible and slow-binding inhibitor for SARS-CoV-1 PLpro with $IC_{50} = 5.0 \pm 1.7 \mu M$ (Table 3) (Chou et al., 2008). Cheng found that 6-TG is an inhibitor for MERS PLpro (Cheng et al., 2015). Fu et al. used 6-TG, determined its potency against SARS-CoV-2 PLpro ($IC_{50} = 72 \pm 12 \mu M$), and used it as a positive control for inhibitor screening (Fu et al., 2021). Gao et al. found that only 6-TG inhibited PLpro weakly with $IC_{50} = 103.7 \pm 49.4 \mu M$ (Gao et al., 2021). This preprint publication describes that an increasing concentration of 6-TG inhibited PLpro-mediated processing of the TAP-nsp123 WT polyprotein and blocked cleavage of ISG15 in HEK293T cells (Swaim et al., 2021). 6-TG inhibited viral replication in Vero-E6 cells with an EC_{50} value of $0.647 \pm 0.374 \mu M$, which is comparable to that of Remdesivir at $0.77 \mu M$. 6-TG inhibited virus replication in Calu3 cells at a lower EC_{50} , $0.061 \pm 0.049 \mu M$. 6-TG did not elicit significant cellular toxicity in either Vero-E6 or Calu3 cells ($CC_{50} > 50 \mu M$) (Swaim et al., 2021). Despite previous positive results in inhibition, in a recent study, 6-TG did not show binding in a TSA assay or inhibition in FlipGFP assay, therefore invalidating 6-TG as a PLpro inhibitor (Ma et al., 2021b).

Tanshinone

Tanshinone is a class of compounds that was originally extracted from *Salvia miltiorrhiza* (Zhou et al., 2005). Tanshinone was identified as an inhibitor for SARS-CoV-1 PLpro in 2012 (Park et al., 2012). Authors extracted and tested a series of tanshinones with cryptotanshinone displayed the most potent inhibitory activity ($IC_{50} = 0.8 \mu M$) toward SARS-CoV-1 PLpro and weak inhibition for Mpro ($IC_{50} = 226.7 \pm 6.2 \mu M$) (Table 3). The IC_{50} values demonstrated that the presence of naphthalene in tanshinone I ($IC_{50} = 0.7 \mu M$) provide a greater inhibitory effect than the other tanshinone derivatives. No detectable inhibition was observed for other proteases tested, including chymotrypsin, papain, and HIV protease (Park et al., 2012).

Zhao et al. (2021) found tanshinone while screening libraries against SARS-CoV-2 PLpro and determined that cryptotanshinone inhibited with an $IC_{50} = 5.63 \pm 1.45 \mu M$ and $EC_{50} = 0.70 \pm 0.09 \mu M$, and tanshinone I has IC_{50} values of $2.21 \pm 0.10 \mu M$ and $EC_{50} = 2.26 \pm 0.11$ (Table 3) (Zhao et al., 2021).

Lim et al. found that dihydrotanshinone I inhibits SARS-CoV-2 PLpro with $IC_{50} = 0.586 \mu M$, in comparison to the IC_{50} values of $1.79 \mu M$ for GRL0617, $1.57 \mu M$ for tanshinone IIA, and $1.34 \mu M$ cryptotanshinone (Lim et al., 2021). Authors also found that dihydrotanshinone I has good specificity that it did not inhibit 3CLpro (Lim et al., 2021).

Yunxia et al. used ALKGG-AMC as substrate to screen a compound library with 1971 clinically approved compounds. Tanshinone IIA sulfonate sodium, a more water-soluble form of tanshinone was found to be a potent inhibitor. It has an IC_{50} value of $1.65 \pm 0.13 \mu M$, and the K_D value is $145 \pm 8.5 \mu M$ (Table 3) (Xu et al., 2021). Tanshinone was found to directly interact with PLpro in biolayer interferometry (BLI) assay. Thermal shifting assay using SYPRO Orange found tanshinone IIA sulfonate sodium gently increased the thermo stability of PLpro by $1^\circ C$ (Xu et al., 2021). As crystal structure of tanshinone with PLpro is not available, docking and molecular dynamics

simulations were applied to indicate tanshinone IIA sulfonate sodium binds to P3–P4 sites and interacts with Y268, which is similar to the binding pocket of GRL0617 (Xu et al., 2021).

Chloroxine

Along with tanshinone, chloroxine is also found to be a direct-interacting inhibitor for SARS-CoV-2 PLpro (Table 3) (Xu et al., 2021). It has IC_{50} value of $7.24 \pm 0.68 \mu M$, and the K_D value is $4.6 \pm 0.29 \mu M$. Thermal shifting assay using SYPRO Orange found mixing chloroxine compounds with PLpro increase T_m by $2.5^\circ C$. There is no crystal structure of chloroxine with PLpro available, so the mode of binding was illustrated by docking and molecular dynamics simulations (Xu et al., 2021). Chloroxine did not show stable binding to the active pocket but has a unique binding site at the PLpro-ISG15 binding interface, near residue R65. It was proposed that the binding of chloroxine could have a direct impact on interrupting the PLpro-ISG15 binding interface; however, it does not explain the inhibition of peptide-based substrate ALKGG-AMC as it is not expected to interact at S2 site (Xu et al., 2021). R65 is $\sim 38 \text{ \AA}$ away from the catalytic triad, so this binding mode awaits validation.

CPI-169

A screening campaign using unbiased ChemDiv library (10,000-compound) and a biased, annotated TargetMol Bioactive library (5,370 compounds) for inhibitors only identified CPI-169 as a new inhibitor for SARS-CoV-2 PLpro (Table 3) (Shen et al., 2021). CPI-169 inhibits SARS-CoV-2 with an IC_{50} value of $7.3 \mu M$. CPI-169 binds to PLpro moderately with $K_D = 10.2 \mu M$. In comparison, GRL0617 is slightly more potent with $IC_{50} = 1.6 \mu M$ and $K_D = 1.9 \mu M$ (Shen et al., 2021). Authors computationally docked to the BL loop of PLpro however were unable to obtain co-crystal structures. The SAR of CPI-169 is yet to be reported (Shen et al., 2021).

YM155

Zhao et al. (2021) found YM155 while screening 6,000 compounds from libraries consisting of approved drugs, drug candidates in clinical trials, and pharmacologically active compounds against SARS-CoV-2 PLpro (Table 3) (Zhao et al., 2021). YM155 is an antineoplastic drug in clinical trials, inhibited PLpro with an IC_{50} value of $2.47 \mu M$ (Zhao et al., 2021). YM155 also exhibits strong antiviral activities in cell-based assays with an EC_{50} value of 170 nmol/L (Zhao et al., 2021). The crystal structure of YM155 with SARS-CoV-2 PLpro reveals three YM155 binding sites on SARS-CoV-2 PLpro (Figure 7A). The first YM155 molecule binds at the substrate binding pocket. Different from GRL0617, which occupies both P3 and P4 sites, YM155 only occupies P4 position (Figure 7A). The naphthoquinone aromatic group of YM155 forms hydrophobic interactions with the side chains of P248 and with the aromatic rings of Y264, Y268, and Y273. The plane of naphthoquinone group is tilted compared to naphthalene group of GRL0617. Importantly, binding of YM155 induced a unique conformation of BL loop. As previously described, BL loop closes upon GRL0617 binding, and Y268 flips toward GRL0617 and wedges between the two aromatic rings of GRL0617. When

bound to YM155, Q269 flips away from body of the protease, making room for Y268 to shift toward the direction of thumb and Ubl domains. The side chain of Y269 forms π -stacking interaction with YM155, thus clamping the inhibitor to the protease (Zhao et al., 2021). On the basis of this binding site of YM155, the inhibitory effect can be rationalized by competition with the substrate.

The second YM155 binding site was observed near the thumb domain, interacting with F69 and H73 (**Figure 7A**). Interestingly, PLpro F69 is a critical residue at S2 involved in hydrophobic interactions to both distal Ub and NTD of ISG15 (Shin et al., 2020; Békés et al., 2016). YM155 here could function as a blocker for Ubl at S2 site. A third YM155 molecule is bound at the zinc-finger motif (**Figure 7A**). The methoxyethane group of the inhibitor inserts into the cleft, forming an H bond with Q195. A second H bond is formed between YM155 naphthoquinone group and T225. Binding of YM155 distorted the region containing C224 and C226, compared to apo structure (PDB: 7D7L) (Zhao et al., 2021). The Finger domain is important for the proteolytic and deubiquitinating activity of PLpro, so this YM155 binding site may also significantly contribute to its inhibitory effects (Herold et al., 1999; Klemm et al., 2020). The inhibitory effects of three individual binding sites for YM155, and SAR of YM155 derivatives need to be investigated.

Ebselen

Ebselen is a low-molecular weight organoselenium drug that has low toxicity to use in humans (**Table 3**) (Azad and Tomar 2014). Karen et al. found that ebselen inhibits PLpro with the similar mechanism of disulfiram that it covalently adds to cysteines of SARS-CoV-2 PLpro and ejects Zn^{2+} . It has an IC_{50} value of $0.67 \pm 0.09 \mu\text{M}$ measured by fluorogenic peptide substrate (Sargsyan et al., 2020). Ebselen is a dual inhibitor for both PLpro and Mpro with higher potency toward Mpro (Jin et al., 2020a; Zmudzinski et al., 2020; Weglarz-Tomczak et al., 2021). Jin et al. proposed a reaction mechanism for ebselen inhibiting Mpro, and the same mechanism might account for its inhibition to PLpro (described in the Mpro section) (Jin et al., 2020a). In our preprint publication on BioRxiv, the best inhibitor among a series of ebselen derivatives, Compound 7, has an IC_{50} value of $0.58 \pm 0.04 \mu\text{M}$. However, Gao et al. found ebselen not to be inhibitory in their assay (**Table 3**) (Gao et al., 2021). The discrepancy may stem from different substrates used for assessing inhibitor efficacy or the assay condition, e.g., reducing reagent.

The mechanism of inhibition by ebselen to Mpro is by the formation an adduct at the catalytic cysteine to form a seleno sulfide bond. (Ampornnanai et al., 2021). Both Mpro and PLpro are cysteine proteases, and ebselen may inhibit PLpro in the same way. However, the analysis of a recent unpublished PDB accession 7M1Y found that, when crystallized with PLpro C111S mutant, weak electron density demonstrates ebselen bound at a shallow pocket on palm domain. Selenium phenyl group is surrounded by side chains of residues E263, K274, C284, T291, and Y296, and at the other end, phenyl group is lined by backbone of E295 and Y296 (**Figure 7B**). Ebselen inhibited viral replication with $\text{EC}_{50} = 4.67 \mu\text{M}$, which could a combined effect of targeting both Mpro and PLpro (Jin et al., 2020a).

Peptide Inhibitors: VIR250 and VIR251

Hybrid combinatorial substrate library (HyCoSuL) is a combinatorial library of tetra-peptides containing natural and unnatural amino acid mixtures at the P4–P2 positions, a fixed amino acid at the P1 position, and an ACC (7-amino-4-carbamoylmethylcoumarin) fluorescent tag occupying the P1' position (Drag et al., 2008; Rut et al., 2020b). Once the peptide is recognized and cleaved by a protease, the ACC is released and produces a readable fluorescence signal. This method was used to investigate DUBs' activity (Drag et al., 2008; Rut et al., 2020b). A series of tetrapeptide-ACC including natural and unnatural amino acid residues was designed and synthesized, and the best amino acid composition to target SARS-CoV-2 PLpro was determined (Poreba et al., 2017). The preferred substrates [Ac-hTyr-Dap-Gly-Gly-ACC, VIR251, and Ac-Abu (Bth)-Dap-Gly-Gly-ACC, VIR250] were converted into inhibitors by exchanging the fluorescent tag to a vinylmethyl ester (VME) group (**Table 3**) (Rut et al., 2020a). Both VIR250 and VIR251 exhibit high selectivity and robust inhibition toward both SARS-CoV-1 PLpro and SARS-CoV-2 PLpro, whereas no inhibition of human DUB (UCH-L3) was observed in biochemical assay and cell lysate-based assay (Rut et al., 2020a). This high specificity is important for drug discovery purposes.

The crystal structures of VIR250 and VIR251 in complex with both SARS-CoV-1 and SARS-CoV-2 PLpro in combination were determined, in collaboration with our lab, for the purpose of understanding the binding mode and future refinement of the inhibitors (**Figures 7C,D**) (Rut et al., 2020a; Patchett et al., 2021). As expected, the catalytic C111 is covalently linked to the β carbon of the vinyl group of the VME warheads of inhibitors with thioether linkages. Both inhibitors occupy the P1–P4 pockets of SARS-CoV-2 PLpro. P1 and P2 sites of inhibitors are Gly residues, which are the same as Ub and ISG15. At P3, inhibitors have Dap, which is an unnatural amino acid residue, whereas in Ub, it is Arg, and, in ISG15, it is Pro. Dap of VIR250 participates in a backbone–backbone H bond with G271 and Y268, whereas that of VIR251 engages in the backbone–backbone H bond with Y268 (**Figures 7C,D**). More importantly, whereas P1–P3 residues engage very similar contacts with PLpros of both species, P4 residues show significant diverse conformations. When crystallized with SARS-CoV-2, VIR250 P4 Abu (Bth) projects toward Finger domain and engages in a network of van der Waals interactions with M208, P247, P248, and T301, this contrasts its conformation when crystallized with SARS-CoV-1, which the side chain flips about 90° pointing in the direction of palm domain. Interestingly, SARS-CoV-2 VIR251 hTyr at the P4 position projects toward the palm domain, which is same as SARS-CoV-1 VIR250 P4 side chain, and opposite of SARS-CoV-2 VIR251 P4, whereas SARS-CoV-2 VIR250 P4 side chain is pointing to similar direction as SARS-CoV-2 VIR251 P4 (**Figures 7C,D**).

The significant freedom of P4 site is consistent with the observation that P1–P2 sites are narrow and less accessible, P3 site is half exposed, whereas P4 site is broad and well solvent exposed. The P3–P4 sites are exploited by both small-molecule

inhibitors and peptide inhibitors. The different conformations of P4 side chain of inhibitors are accompanied by slight shift of the BL loop and different rotamers of key residues including Y268 and Q269. Interestingly, when compared with the GRL0617-bound PLpro structure, the side chains of P4 of inhibitors partially overlap with naphthalene group from GRL0617 (**Figures 7C,D**). With the previous success in replacing naphthalene with longer biaryls (Shen et al., 2021), it is possible to elongate the side chain of P4 position of peptide inhibitor in future refinement.

Jun9-13-7 and Jun9-13-9

Ma et al. found two new inhibitors Jun9-13-7 and Jun9-13-9 screening against the Enamine 50K diversity compound library and subsequent lead optimization (**Table 3**) (Ma et al., 2021a). Jun9-13-7 and Jun9-13-9 had IC_{50} values of 7.29 ± 1.03 and $6.67 \pm 0.05 \mu M$, respectively (Ma et al., 2021a). The two inhibitors also increased the thermal stability of SARS-CoV-2 PLpro by $2.98 \pm 0.09^{\circ}C$ and $2.18 \pm 0.29^{\circ}C$. The inhibition by these two hits is slightly weaker than GRL0617 tested under same conditions: IC_{50} value of $2.05 \pm 0.12 \mu M$.

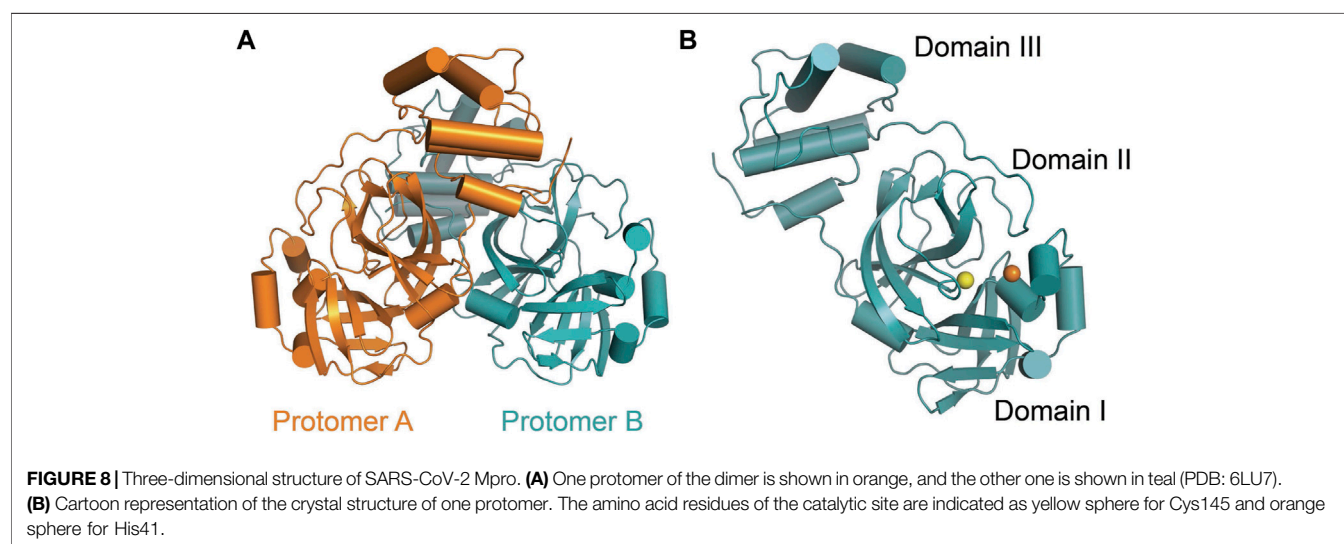
Subsequent lead optimization led to the discovery of several inhibitors with sub-micromolar potency in the enzymatic assay. Among them, Jun9-75-4 was the most potent PLpro inhibitor with an IC_{50} value of $0.62 \mu M$, a 10-fold increase compared to original hit, and three-fold more potent than GRL0617. Without a structure of the new inhibitors with PLpro, the authors used molecular dynamics method to analyze how the inhibitors interact with SARS-CoV-2 PLpro (Ma et al., 2021a).

STRUCTURAL BIOLOGY OF SARS-COV-2 MAIN PROTEASE

SARS-CoV-2 Mpro (nsp5, also referred to as 3CLpro) is a cysteine protease that is widely conserved among coronaviruses. Mpro operates at the recognition sequence Leu-

Gln↓ (Ser, Ala, Gly) (↓ marks the cleavage site) to mediate the maturation cleavage of polyproteins nsp4–16 during virus replication. There is no known human protease with a specificity for Gln at the cleavage site of the substrate (Zhang et al., 2020a). This feature along with its essential function in viral cell cycle makes Mpro a promising target for COVID-19 treatment development. The active version of Mpro is a homodimer, and each protomer is comprised of three domains (domains I, II, and III) (**Figure 8**). The domains I (residues 8–101) and II (residues 102–184) consist of antiparallel β -barrels, and together, they form the chymotrypsin-like structure. The domain III (201–306), which is mostly composed by α -helices, is responsible for the dimerization process. SARS-CoV-2 Mpro has 96% primary sequence identity to that from SARS-CoV-1. A notable difference in SARS-CoV-2 Mpro is the mutation of T285 and I286 to Ala and Leu, respectively, when compared to that from SARS-CoV-1 (Zhang et al., 2020b). These changes keep the two domains III closer, leading to an increase in catalytic turnover.

The substrate-binding pocket lies in the cleft between domains I and II. The active site of the enzyme consists of four pockets (S1', S1, S2, and S3), with the S1 pocket containing a catalytic dyad (**Figure 9A**). This catalytic dyad is composed of the C145 and H41 residues. The absence of the standard third catalytic element is compensated by the presence of a buried water molecule, which forms H bonds with the residue of H41 and the surrounding amino acids (**Figure 9B**) (Anand et al., 2003; Kneller et al., 2020a; Kneller et al., 2020b; Citarella et al., 2021). The active site of Mpro is favored by strong H bond interactions with an "oxyanion hole" formed by G143, S144, and C145 (Świderek and Moliner, 2020). The stabilization of the oxyanion by the H bonds in the transition state should contribute to the catalytic activity (Simón and Goodman, 2010). Another water molecule is located within the active site of the enzyme and establishes H bonds with F140, H163, and E166, further stabilizing the oxyanion hole.



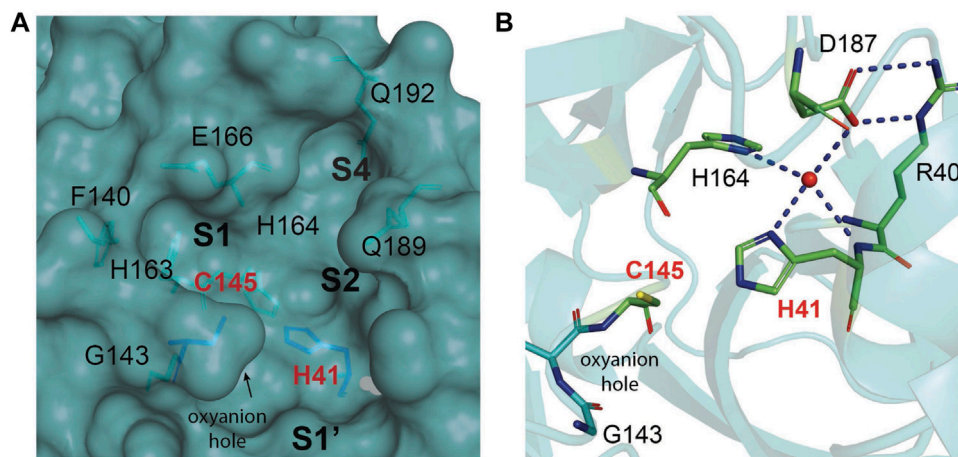


FIGURE 9 | The substrate-binding cleft located between domains I and II of Mpro. **(A)** The active site cavity is located on the surface of Mpro. Subsites S1, S2, and S4 are shaped into well-formed binding pockets. The catalytic dyad is highlighted in red with the residues that flank the cavity. The oxyanion hole created by residues 140–144 is highlighted. **(B)** A close-up view of the catalytic site cavity in which the catalytic residues (Cys145 and His41) are highlighted in red. The catalytic water molecule is shown as a red sphere. Hydrogen bonds are shown as black dashed lines.

The thiol group of C145 is responsible for hydrolysis. The initial step in the process is deprotonation of Cys-thiol and followed by nucleophilic attack of resulting anionic sulfur on the substrate carbonyl carbon. In this step, a peptide product is released, whereas H41 is restored to its deprotonated form. The resulting thioester is hydrolyzed to release a carboxylic acid, and the free enzyme is regenerated in the final step (**Figure 10**)

(Pillaiyar et al., 2016). The interaction of the amino-terminus (N-terminus) of one protomer with domain II of the other *via* H bonding helps shape the S1 pocket of the active site (Zhang et al., 2020a; Zhang et al., 2020b). Simulations showed that the active site residues and the substrate binding pocket are not in the proper conformation for catalysis in the monomers (Chen et al., 2006). Therefore, the dimer is the active form, whereas the

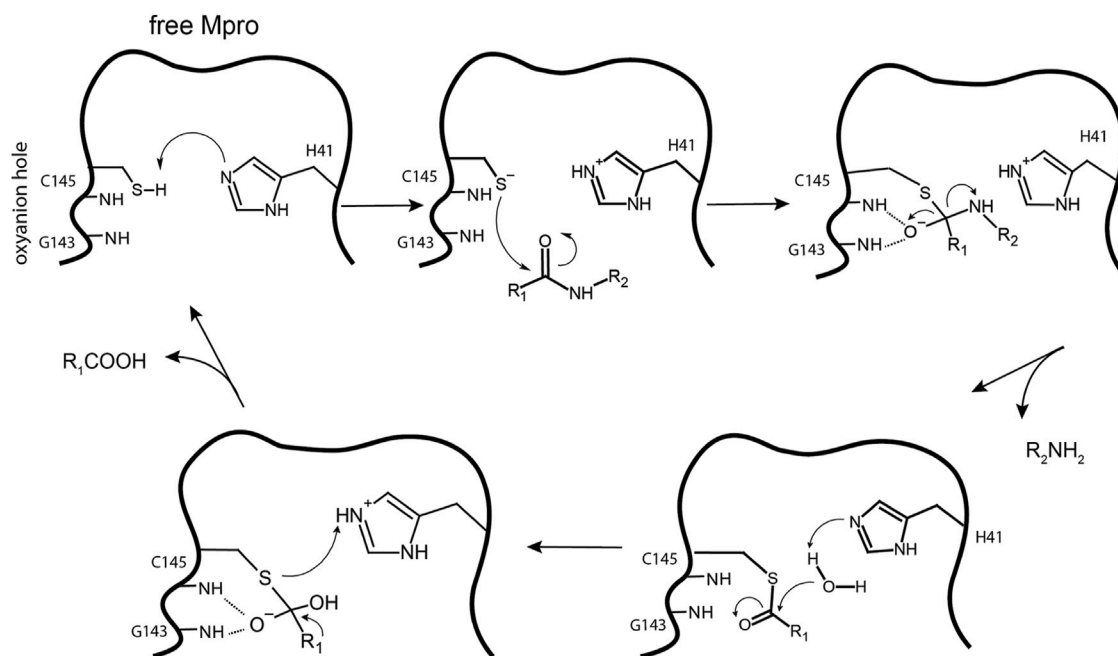
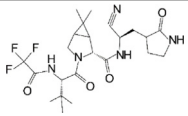
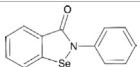
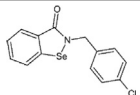
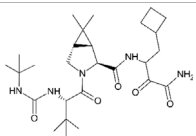
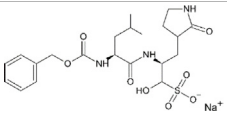
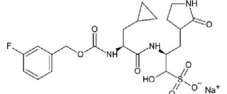
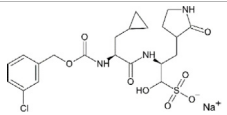
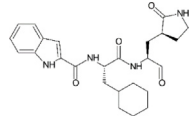
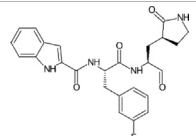
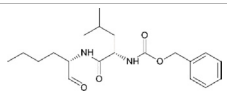
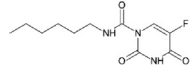


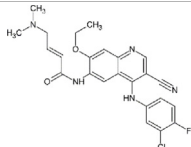
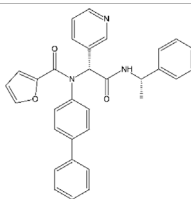
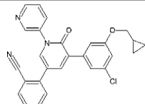
FIGURE 10 | Hydrolysis mechanism of SARS-CoV-2 Mpro. In the free state, H41 of Mpro deprotonates the thiol of C145. The next step is nucleophilic attack by the deprotonated C145 sulfur on the peptide carbonyl carbon. Then, a fragment of the substrate (R_2) is released, and the histidine is restored to its deprotonated form. The new carboxyl-moiety undergoes nucleophilic attack by water, which results in H41 becoming protonated. The thioester bond is subsequently hydrolyzed to generate a C-terminus on the remaining substrate fragment while regenerating the free enzyme.

TABLE 4 | Mpro inhibitors.

Compound Name	Chemical Structure	IC ₅₀	EC ₅₀	References
PF-07321332			74.5 nM	Owen et al. (2021)
Ebselen		0.67–2.1 μM	4.67 μM	Jin et al. (2020a); Ma et al. (2020a); Banerjee et al. (2021)
MR6-31-2			1.8 μM	Ampornpanai et al. (2021)
Boceprevir		1.59–8 μM	1.90–15.57 μM	Ma et al. (2020b); Fu et al. (2020); Oerlemans et al. (2021)
GC-376		0.03–0.19 μM	0.7–0.92 μM	(Ma et al. (2020b); Fu et al. (2020); Vuong et al. (2020)
GC-376 derivative 2c		0.07 μM	0.57 μM	Vuong et al. (2021)
GC-376 derivative 2d		0.08 μM	0.7 μM	Vuong et al. (2021)
N3 derivative 11a		0.053 μM	0.53 μM	Dai et al. (2020)
N3 derivative 11b		0.040 μM	0.72 μM	Dai et al. (2020)
Calpeptin		10.69 μM	72 nM	Ma et al. (2020b); Günther et al. (2021)
Carmofur		1.82 μM	24.30 μM	Jin et al. (2020b)

(Continued on following page)

TABLE 4 | (Continued) Mpro inhibitors.

Compound Name	Chemical Structure	IC ₅₀	EC ₅₀	References
Pelitinib			1.25 μM	Günther et al. (2021)
ML188 derivative 23R		0.2 ± 0.01 μM	3.03 μM	Kitamura et al. (2021)
Perampanel derivative 26		0.170 μM	0.98 μM	Zhang et al. (2021)

monomer is inactive (Goyal and Goyal, 2020). Compounds that can interfere with the dimeric interface may act as potent inhibitors.

INHIBITORS AGAINST MAIN PROTEASE

Although there is currently a good clinical candidate for COVID-19, focus should not be taken away from the study of other potential Mpro inhibitors. The inhibitor studies this past year and half could further help design new treatments for COVID-19 in addition to preparing for future coronavirus outbreaks. These studies have included drugs developed as treatment for other viruses and new compounds specific for coronaviruses. Because of their success in the treatment, the repurposing of FDA-approved drugs allows speeding up the experimental phases of a new therapy, since safety studies have already been validated. Several inhibitors have been developed against SARS-CoV-2 Mpro, and these are typically peptidomimetics that mimic natural peptide substrates (Jacobs et al., 2013; Tian et al., 2021; Jacobs et al., 2013; Tian et al., 2021). The warheads mainly contain Michael receptors, aldehydes, and different types of ketones, which covalently bind to the C145 residue in Mpro to exert an inhibitory effect. The α -ketoamide warhead is sterically more versatile than other warheads because it features two acceptors for H bonds from the protein, whereas the other warheads have only one such acceptor. Here, we focus on key interactions of some of the most promising results, which have become the basis for further derivatization (Table 4).

PF-07321332

To date, PF-07321332 is one of two orally available COVID-19 antiviral clinical candidates (along with Molnupiravir). The

structure of this inhibitor was revealed by Pfizer at the American Chemical Society Spring 2021 meeting (Halford, 2021). Ritonavir is commonly used in conjunction with other protease inhibitors to inhibit cytochrome P450-3A4. Co-administration with a low dose of ritonavir is expected to help slow the metabolism, or breakdown, of PF-07321332, allowing it to remain active in the body for longer periods of time at the higher concentrations needed to help combat the virus (Zeldin and Petruschke, 2004). In September 2021, they announced the start of the phase 2/3 trial to evaluate the prevention of illness in adults living in the same household as someone with COVID-19 (Pitts, 2021). Recently, Pfizer disclosed that PAXLOVID™ (a PF-07321,332/ritonavir combination) can reduce risk of hospitalization or death by 89% in non-hospitalized adult patients with COVID-19, who are at high risk of progressing to severe illness when administered within 3 days of symptom onset (Pfizer, 2021).

The prodrug PF-07321332 was specifically developed to be administered orally to block SARS-CoV-2 Mpro activity. It was derived from PF-00835231, a phase I clinical candidate (prodrug PF-07304814) originally developed by Pfizer in 2002–2003 against SARS-CoV-1 (Hoffman et al., 2020). Owen et al. reported improved antiviral activity (EC_{50} = 74.5 nM) compared to the parent compound (EC_{50} = 231 nM). PF-07321332 shares the dimethylcyclopropylproline and tert-leucine features of Boceprevir, an inhibitor developed for the Hepatitis C Virus (HCV) NS3 protease (described further below). Molecular simulations proposed that the new inhibitor PF-07321332 interacts similarly as Boceprevir (Figure 11A) with the additional feature of an H bond between the pyrrolidone group and H163, similar to the PF-00835231 interaction (Hoffman et al., 2020; Pavan et al., 2021). The co-crystal structure of PF-07321332 is set to be released soon (PDB:

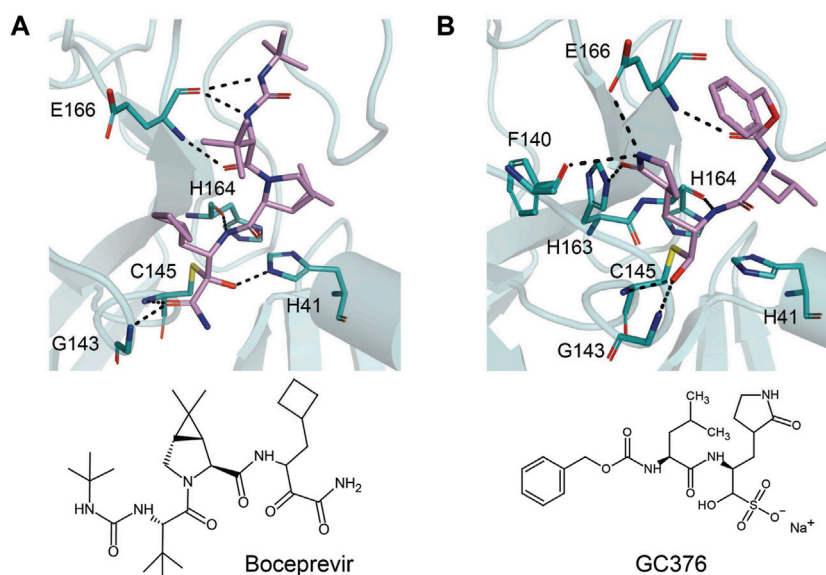


FIGURE 11 | Close-up view of the interactions between SARS-CoV-2 Mpro with Boceprevir and GC376. Close-up view of interaction between SARS-CoV-2 Mpro and inhibitors in crystal structures. Mpro is shown as cartoon representation, with residues involved in the interaction shown as sticks. Inhibitors are shown as violet sticks. Hydrogen bonds were labeled with dashed lines. **(A)** Boceprevir (PDB: 7C6S). **(B)** GC376 (PDB: 7C6U).

7RFW) (Owen et al., 2021). The preprint reveals that the inhibitor forms H bonding interactions with Q189, E166, and H163. The P1' nitrile forms a covalent thioimide adduct with the catalytic C145, which was confirmed to be reversible by recovery of Mpro activity after dilution of the complex (Owen et al., 2021).

Ebselen

Ebselen is an organoselenium molecule that can function as a glutathione peroxidase and peroxiredoxin mimic (Nakamura et al., 2002). It has been shown to form a seleno-sulfide bond with thiol groups of cysteine on several proteins, which results in anti-inflammatory, anti-microbial, and neuroprotective effects (Ampornadani et al., 2021). Ebselen was identified in a high-throughput screen as a potential hit of SARS-CoV-2 Mpro inhibitor with an IC_{50} between 0.67 and 2.1 μ M (Jin et al., 2020a; Ma et al., 2020a). Ampornadani et al. assessed derivatives for their inhibition of SARS-CoV-2 Mpro and anti-coronaviral activity (Ampornadani et al., 2021). Two of these ebselen-based selenium compounds exhibit greater inhibitory effectiveness against Mpro enzyme and SARS-CoV-2 replication. It is proposed that the ebselen-enzyme drug protein adduct is hydrolyzed by the conserved water in the catalytic pocket. Co-crystallographic structure of Mpro grown with ebselen and its derivative MR6-31-2 showed an electron density coordinating to C145, which is likely to be selenium due to its size and its absence in compound-free Mpro crystals. MR6-31-2 is nearly three times more effective with an EC_{50} value of 1.8 μ M (ebselen EC_{50} = 4.67 μ M) (Banerjee et al., 2021). As mentioned in the previous sections, ebselen and its derivatives have been shown to bind and inhibit PLpro, and this dual action inhibition may be the source of the potent antiviral activity.

Boceprevir

Boceprevir is an FDA-approved serine protease inhibitor to treat HCV infection. Similar to the coronavirus Mpro proteases, cleavage of the HCV polyprotein by the viral NS3 protease releases functional viral proteins essential for viral replication (Tomei et al., 1993). It was reported that the ketoamide group of Boceprevir can bind covalently to the catalytic S139 of HCV NS3 protease (Malcolm et al., 2006).

This drug was screened alongside other viral protease inhibitors and has been shown to inhibit the enzymatic activity of Mpro with an IC_{50} value of 4.13 μ M and has an EC_{50} value of 1.90 μ M against the SARS-CoV-2 virus (Ma et al., 2020b). In the Mpro–Boceprevir complex structure (PDB: 6ZRU and 7C6S) (Oerlemans et al., 2021; Fu et al., 2020), the nucleophilic C145 in Mpro forms a C–S covalent bond with the keto carbon of Boceprevir, and the resulting hydroxyl group forms an H bond with the side chain of H41 and stabilizes this conformation (Figure 11A). Boceprevir also interacts with the oxyanion hole, with the oxygen of the α -ketoamide forming H bonds with the main chain amides of C145 and G143. The tert-butyl urea group orients into the S4 pocket and is stabilized by several H bonds with the main chain oxygen of E166 and hydrophobic interactions with the side chains of M165, Q192, L167, and P168. The cyclobutylalanine P1 residue has no interaction with the S1 subsite (Fu et al., 2020).

GC376

GC376 is a bisulfite adduct prodrug of the corresponding aldehyde, GC373, which strongly inhibits the Mpro of several coronaviruses, including SARS-CoV-2 (IC_{50} value of 0.03–0.19 μ M and EC_{50} value of 0.92 μ M) (Ma et al., 2020b; Vuong et al., 2020). These drugs are able to block virus replication

in cell culture and are well tolerated by various cell lines in cellular cytotoxicity tests (Ma et al., 2020b), indicating that they are good candidates as antivirals for the treatment of COVID-19. An NMR study supports the proposal that, in aqueous solutions, diastereomers of GC373 and GC376 exist in a dynamic stereochemical equilibrium, with only the correct aldehyde isomer binding as a single hemithioacetal in the active site of Mpro (**Figure 11B**) (Vuong et al., 2021). The crystal structure of SARS-CoV-2 Mpro with GC376 indicates the bisulfite group is readily removed and the aldehyde form (GC373) covalently bonds to catalytic C145 (PDB: 7C6U). The ring at the P1 position of GC376/GC373 fits into the S1 pocket and has H bonding interactions with the carboxyl group of E166, the carbonyl group of F140, and the imidazole of H163. Inhibitor binding is further stabilized by the leucine of GC376 interacting with the hydrophobic S2 subsite and the carbonyl in P3 forming an H bond with the backbone amide of E166. In the SARS-CoV-2 dimer, the thioacetal hydroxide H bonds to “oxyanion hole” formed by the backbone amides of G143, S144, and C145, resulting in the (S)-configuration seen with other aldehydes (11a and 11b) (Vuong et al., 2020), but in the instance of three protomers per asymmetric unit, the third copy of GC376 was able to bind in the (R)-configuration with the hydroxide H bonding to H41 (Ma et al., 2020b).

GC376 has been shown to be more potent than Boceprevir; however, possible side effects in animal use could limit its use for less than 2 weeks (Fu et al., 2021). Improvements by modification of the chemical structure of GC376 resulted in a number of compounds with improved binding characteristics and nanomolar inhibition of SARS-CoV-2 Mpro. The optimal modification for the P2 site of the inhibitor was a cyclopropyl moiety. Inhibitors 2c and 2d emerged as key compounds for Mpro enzyme inhibition with better IC_{50} and

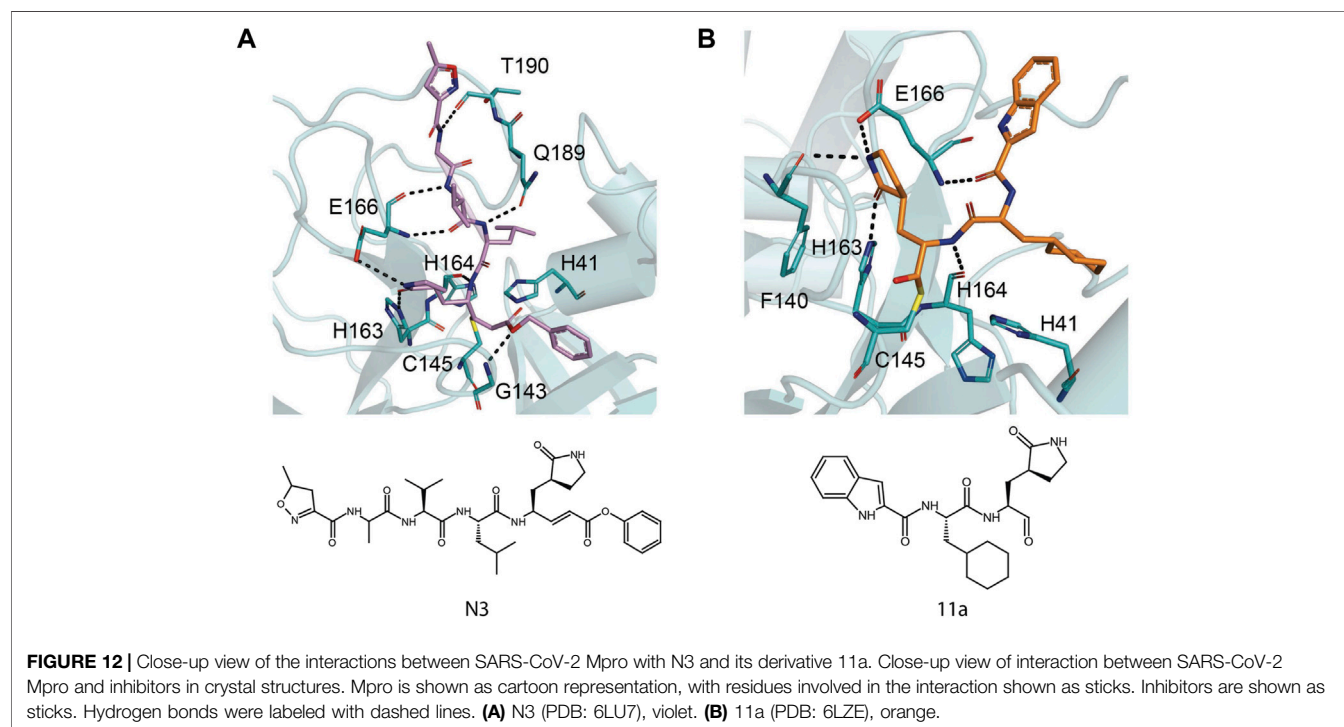
cellular EC_{50} values compared to the parent inhibitor GC376 (2c: $IC_{50} = 0.07 \mu M$, $EC_{50} = 0.57 \mu M$; 2d: $IC_{50} = 0.08 \mu M$, $EC_{50} = 0.7 \mu M$) (Vuong et al., 2021).

N3

A mechanism-based inhibitor, N3, which was identified by a structure assisted optimization program, can specifically inhibit Mpro from multiple coronaviruses, including SARS-CoV-1 and MERS-CoV (Yang et al., 2005; Jin et al., 2020a). N3 is an irreversible inhibitor that forms adduct with the catalytic cysteine by Michael addition of the $C\beta$ atom of the vinyl group. The crystal structure with SARS-CoV-2 Mpro shows that N3 binds to the active site in an extended conformation (PDB: 6LU7) (Jin et al., 2020a). The peptidyl backbone of the inhibitor forms an antiparallel sheet with residues 164–168 and residues 189–191 on the other. The P1' benzyl ester forms van der Waals interactions with T24 and T25. The γ -lactam ring at P1 inserts into S1 subsite and H bonds with H163. The side chain of leucine at P2 inserts deeply into the hydrophobic S2 subsite formed by H41, M49, Y54, M165, and D187. The side chain of valine at P3 is solvent exposed. The side chain of alanine at P4 occupies the hydrophobic pocket formed by the side chains of M165, L167, F185, and Q192 and the main chain of Q189. P5 makes van der Waals contacts with P168 and residues 190–191 (**Figure 12A**). N3 displayed inhibition against SARS-CoV-2 with an EC_{50} value $16.77 \mu M$ (Jin et al., 2020a).

11a and 11b

The co-crystal structure of N3 with SARS-CoV-2 has been the model for many structure-guided designs. Among those is the study by Dai et al. (2020). The aldehyde compounds 11a and 11b



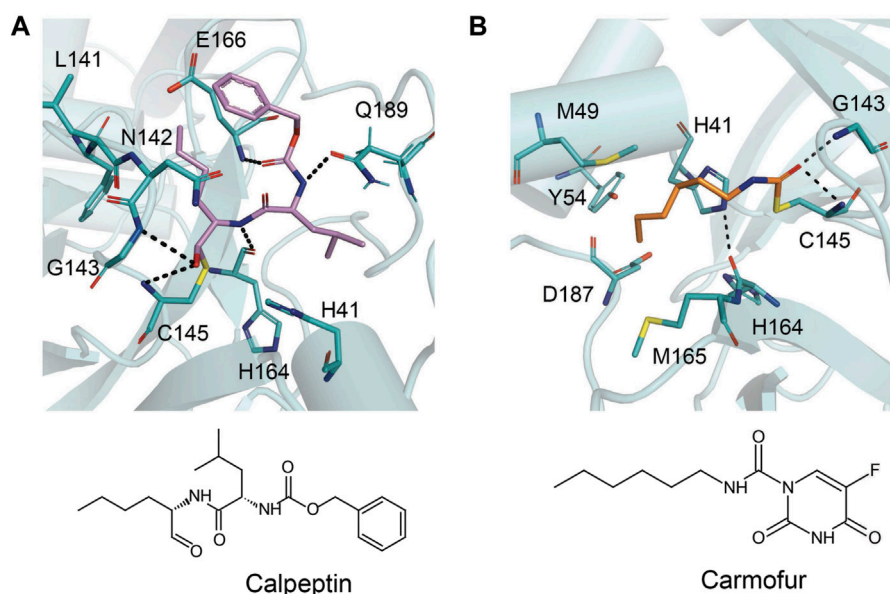


FIGURE 13 | Close-up view of the interactions between SARS-CoV-2 Mpro with calpeptin and carmofur. Close-up view of interaction between SARS-CoV-2 Mpro and inhibitors in crystal structures. Mpro is shown as cartoon representation, with residues involved in the interaction shown as sticks. Inhibitors are shown as sticks. Hydrogen bonds were labeled with dashed lines. **(A)** Calpeptin (PDB: 7AKU), violet. **(B)** Carmofur (PDB: 7BUY), orange.

showed good inhibitory activity against SARS-CoV-2 Mpro (11a: $IC_{50} = 0.053 \pm 0.005 \mu M$, 11b: $IC_{50} = 0.040 \pm 0.002 \mu M$) and good anti-SARS-CoV-2 infection activity in cell culture, with EC_{50} values of $0.53 \pm 0.01 \mu M$ and $0.72 \pm 0.09 \mu M$, respectively, by plaque assay. The crystal structure of SARS-CoV-2 Mpro with 11a and 11b shows that the carbon of the aldehyde group and the catalytic site C145 of SARS-CoV-2 Mpro form a standard 1.8 \AA C-S covalent bond (PDB: 6LZE and 6M0K) (**Figure 12B**). The oxygen atom of the aldehyde group also plays a crucial role in stabilizing the conformations of the inhibitor by forming an H bond with the backbone of residue C145 in the S1' site. The amide group on the lactam ring forms H bonds with F140 and H163. The cyclohexyl moiety of 11a at P2 deeply inserts into the S2 site and stacks with the imidazole ring of H41. The fluorine of the 3-fluorophenyl group of 11b is further stabilized by an H bond to Gln189. Relative to 11a administrated intravenously in CD-1 mice, 11b displayed a shorter $T_{1/2}$ (1.65 h) and a faster clearance rate (clearance = $20.6 \text{ ml min}^{-1} \text{ kg}^{-1}$), indicating that 11a is a better candidate for further clinical study (Dai et al., 2020; Liu et al., 2020).

Calpeptin

Calpeptin was the most potent inhibitor discovered in the large-scale X-ray crystallographic screen by Günther et al. ($EC_{50} = 72 \text{ nM}$) (Günther et al., 2021). Calpeptin structure binds covalently *via* its aldehyde group to C145, forming a thiohemiacetal (**Figure 13A**). This peptidomimetic inhibitor occupies substrate pockets S1 to S3, similar to the peptidomimetic inhibitors GC-376 and N3. The peptidomimetic backbone forms H bonds to the main chain of H143, C145, H164, and E166 and the side chain of Q189 (PDB: 7AKU) (**Figure 13A**). The norleucine side chain of calpeptin maintains van der Waals contacts with the backbone of F140, L141, and N142 of the oxyanion hole (Günther et al., 2021).

Carmofur

The antineoplastic drug carmofur is a derivative of 5-fluorouracil (5-FU) and has been used to treat colorectal cancer by inhibiting human acid ceramidase (Sakamoto et al., 2005). Human acid ceramidase cleaves carmofur, and the fatty acid moiety forms a covalent bond to the active site C143 (Dementiev et al., 2019). Jin et al. found carmofur as an inhibitor for SARS-CoV-2 Mpro when screening a library of about 10,000 compounds (Jin et al., 2020a). Carmofur inhibits the activity of SARS-CoV-2 Mpro *in vitro* with an IC_{50} value of $1.82 \mu M$ and inhibits viral replication with an EC_{50} value of $24.30 \mu M$ (Ma et al., 2020a). Mass spectrometry data showed that carmofur covalently binds to C145 (Jin et al., 2020a). The crystal structure of SARS-CoV-2 Mpro in complex with carmofur verifies that the compound directly modifies the catalytic cysteine and releases the 5-FU head (PDB: 7BUY) (Jin et al., 2020b). The fatty acid moiety points toward the hydrophobic S2 subsite composed of the side chains of H41, M49, Y54, M165, and D187. The inhibitor is involved in extensive hydrophilic and hydrophobic interactions with Mpro. The carbonyl oxygen of carmofur occupies the oxyanion hole and forms H bonds with the backbone amides of G143 and C145 (**Figure 13B**) (Jin et al., 2020b). In a study by Ma et al., the inhibition of SARS-CoV-2 Mpro by several compounds was tested for dependence on the reducing agent DTT. Carmofur could still bind in the absence of DTT but with lower potency (Ma et al., 2020a). Although carmofur is not an ideal candidate for SARS-CoV-2 Mpro, it could be further derivatized and optimized against this and future coronaviruses.

Pelitinib

Pelitinib was developed as an anticancer agent to bind to a cysteine in the active site of the tyrosine kinase epidermal

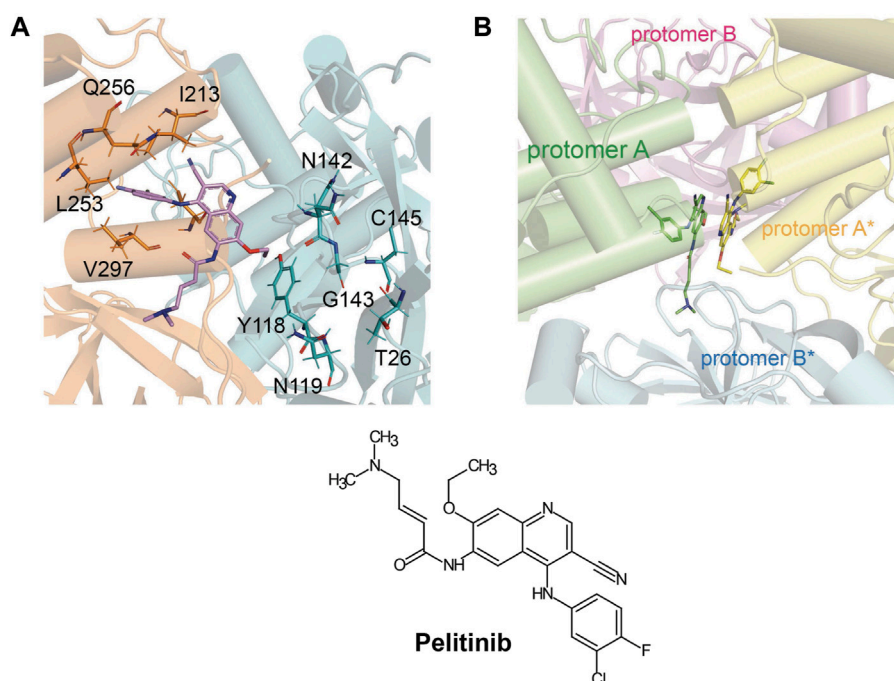


FIGURE 14 | Close-up view of the interactions between SARS-CoV-2 Mpro with pelitinib. Close-up view of interaction between SARS-CoV-2 Mpro and inhibitors in crystal structures. Mpro is shown as cartoon representation, with residues involved in the interaction shown as sticks. Inhibitors are shown as sticks. Hydrogen bonds were labeled with dashed lines. **(A)** Binding site of pelitinib (PDB: 7AXM), violet, in the Mpro dimer, orange and teal. **(B)** Crystal packing of pelitinib, green and yellow sticks. One Mpro dimer is shown in green and magenta. A second dimer (*) is shown in yellow and light blue.

growth factor receptor inhibitor (Wissner et al., 2003). It shows high antiviral activity in the screen performed by Günther et al. ($EC_{50} = 1.25 \mu\text{M}$) (Günther et al., 2021). Because pelitinib is an amine-catalyzed Michael acceptor, it was predicted to target the catalytic cysteine; however, electron density map of co-crystal structure of Mpro with pelitinib shows that it binds between the two Mpro protomers (PDB: 7AXM) (Günther et al., 2021). The ethyl ether of pelitinib makes contacts with T26, N119, N142, and G143 of one protomer, which perturbs the oxyanion hole necessary for Mpro activity (**Figure 14A**). The aromatic moieties of pelitinib form more extensive contacts within the helical domains of the second protomer. The substituted benzyl group inserts into a hydrophobic pocket formed by residues I213, L253, Q256, V297, and C300 from domain III. The 3-cyanoquinoline moiety interacts with S301 from the end of the C-terminal helix (Günther et al., 2021). Evaluation of the crystal packing indicates that two dimers of Mpro can interact *via* π -stacking of two pelitinib molecules (**Figure 14B**). It remains to be seen if this oligomeric interaction occurs in solution and is therefore another mode of inhibition of this compound.

Noncovalent Inhibitors

Drugs acting through covalent modifications of the target may likely be associated to off-target liability and consequent potentially toxic effects (Ghosh et al., 2020). Research efforts are also devoted to the search on novel noncovalent inhibitors

for 3CLpro inhibitors in order to circumvent these issues. ML188(R) is a noncovalent Mpro inhibitor derived in a high-throughput screen against SARS-CoV-1 Mpro (Jacobs et al., 2013). The pyridinyl from ML188(R) fits in the S1 pocket and forms an H bond with the H163 side chain. The furyl oxygen and its amide oxygen both form an H bond with G143. ML188(R) was reported to inhibit the SARS-CoV-1 Mpro with an IC_{50} value of $1.5 \pm 0.3 \mu\text{M}$ and the SARS-CoV viral replication in Vero E6 cells with an EC_{50} value of $12.9 \mu\text{M}$. Kitamura et al. (2021) designed and tested several noncovalent inhibitors based on ML188(R) (Kitamura et al., 2021). Compound 23 had improved enzymatic inhibition, and it was found that 23R is the active diastereomer with an IC_{50} value of $0.20 \pm 0.01 \mu\text{M}$. The antiviral activity was tested in cells expressing TMPRSS2 with an $EC_{50} = 3.03 \mu\text{M}$. The X-ray crystal structure of SARS-CoV-2 Mpro in complex with 23R reveals a ligand-induced binding pocket in between S2 and S4 sites that can be explored for drug design (PDB: 7KX5) (**Figure 15A**). Similarly, Zhang et al. chose a weak screen hit, perampanel, to redesign due to its simple structure (Zhang et al., 2021). Free-energy calculations provided guidance for favorable modifications. Compound 26 showed effective inhibition and antiviral activity ($IC_{50} = 0.170 \mu\text{M}$ and $EC_{50} = 0.98 \mu\text{M}$). The crystal structure of the compound 26 bound to Mpro shows H bonding to C145, G163, and E166, as well as halogen bonding between chlorine and Y54 (PDB: 7L14) (**Figure 15B**).

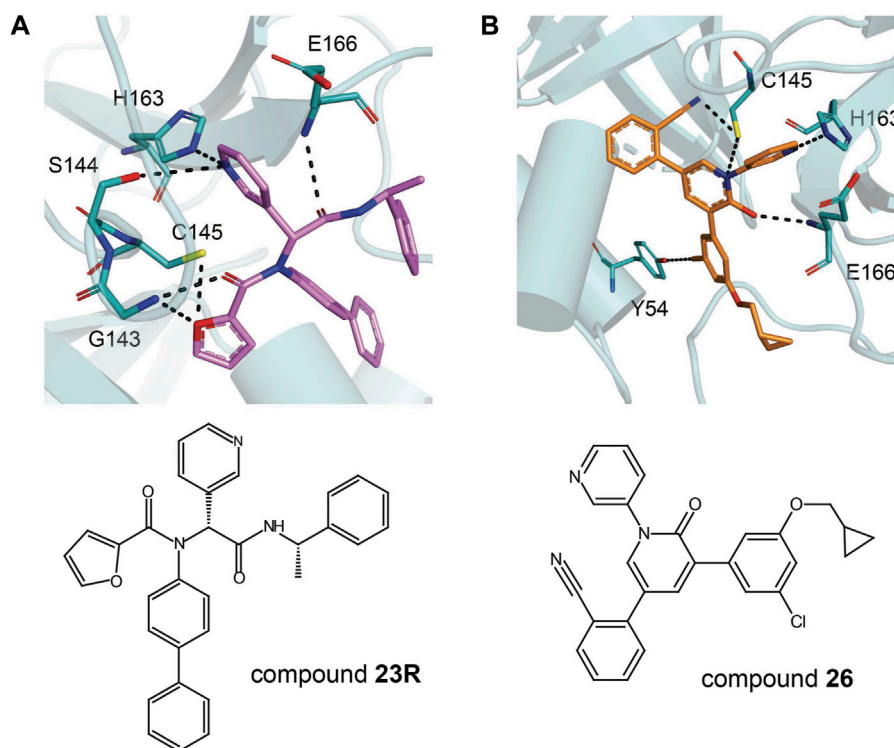


FIGURE 15 | Close-up view of the interactions between SARS-CoV-2 Mpro with ML188 derivative 23R and perampanel derivative 26. Close-up view of the interactions between SARS-CoV-2 Mpro and inhibitors in crystal structures. Mpro is shown as cartoon representation, with residues involved in the interaction shown as sticks. Inhibitors are shown as violet sticks. Hydrogen bonds were labeled with dashed lines. **(A)** Compound 23R (PDB: 7KX5), violet. **(B)** Compound 26 (PDB: 7L14), orange.

MUTATIONS IN SARS-COV-2 PAPAIN-LIKE PROTEASE AND MAIN PROTEASE

Mutation is a common phenomenon in viral systems and delays the identification of successful drug candidates. Constant monitoring of new variants and genetic variability within SARS-CoV-2 is extremely important for drug development and screening in order to eliminate those inhibitors with target binding sites with mutation prone residues. Genotyping of SARS-CoV-2 virus strains circulating worldwide have identified multiple recurrent non-synonymous mutations in proteases in variants of concerns (VOCs) (Table 5) (Amamuddy et al., 2020; Amin et al., 2021).

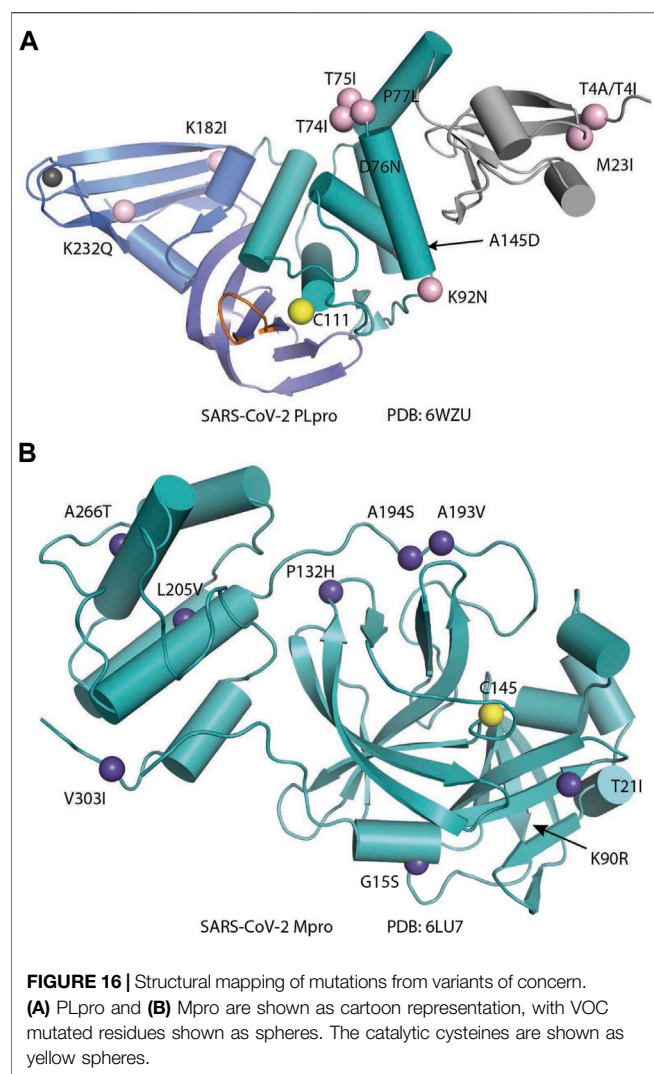
For PLpro, the mutations include A145D, M23I, and T4A from Alpha; K92N from Beta; K232Q from Gamma; P77L from Delta; T4A from Kappa; and T74I, T75I, D76N, and P77L from other stains (Figure 16A). These residues are away from catalytic site and will not disrupt the binding of inhibitors adjacent to the catalytic site; therefore, the development of PLpro inhibitors targeting P1–P4 sites is not negatively affected by the emergence of new variants. Still, the location of the mutation is related to the binding of Ubl. For example, mutation of T75 was shown to partially recover the activity of SARS-CoV-2 PLpro in cleaving K48-linked poly-Ub (Shin et al., 2020). It is interesting that multiple mutations were observed in VOCs in this region including T74, T75, N76, and P77. These mutations may potentially improve the poor reactivity of SARS-CoV-2 PLpro

toward K48-linked Ub as substrate. This hypothesis and underlying mechanism are being investigated.

In SARS-CoV-2 Mpro, G15 and K90 are the most common mutations to date in VOCs (Figure 16B) (Tzou et al., 2020; Krishnamoorthy and Fakhro, 2021). The mutation K90R is expected to provide stability to the domain I and improve the dimerization, which is required for enzymatic activity, and could possibly hinder compounds that target the dimer interface, such as pelitinib. Mpro appears to be relatively tolerant of mutations near the active site, and key residues in the active site (H41, F140, C145, and E166) so far show low mutation frequencies (Cross

TABLE 5 | Mutations identified in variant of concern genomes.

Variant	PLpro mutations	Mpro mutations
Alpha	A145D, M23I, T4A	—
Beta	K92N	K90R, A193V
Gamma	K232Q	—
Delta	P77L	—
Omicron	—	P132H
Eta	—	—
Iota	—	—
Kappa	T4I	—
Lambda	—	G15S
Mu	—	—
Others	P77L, T74I, T75I, D76N, K182I	G15S, A194S, L205V



et al., 2020; Portelli et al., 2020). Mutations in key residues, such as the catalytic dyad, would produce an inactive enzyme; therefore, these mutants are not expected to evolve. However, other mutations (the C44-P52 loop, T45, S46, E47, and L50) that contribute to access to the active site have been modeled and are anticipated to be energetically favorable (Bzówka et al., 2020). Bzówka et al. recommend including P39, R40, P52, G143, G146, and/or L167 in the binding mode of Mpro inhibitors, as these are energetically unfavorable to mutate.

CHALLENGES IN THE DEVELOPMENT OF DRUGS TARGETING PAPAIN-LIKE PROTEASE AND MAIN PROTEASE

Oxidation of Catalytic Cysteine

In an effort to obtain complex structure of SARS-CoV-1 PLpro with disulfiram, Lin et al. only observed electron density that fits beta-mercaptoethanol (PDB: 5Y3Q) (Lin et al., 2018). It seems that the catalytic cysteine of PLpro is sensitive to oxidation, and,

indeed, PLpro is often purified in the presence of high concentrations of reducing reagents (Klemm et al., 2020; Shin et al., 2020; Patchett et al., 2021). Considering the WT apo structure of PLpro is scarce, whereas the structure of C111S mutant is much more abundant, high reactivity of the catalytic cysteine exhibits both an advantage for targeting it with peptide suicide inhibitors, disulfide-based inhibitors, or selenium-containing inhibitors, and it posts as a challenge that the viral protease may use an oxidation–reduction cycle to evade inhibition or simply rely on reducing reagent to remove disulfide or selenium-based inhibitors. Although WT Mpro seems to have great crystallization properties, oxidation of catalytic cysteine was also observed (Kneller et al., 2020c).

Discrepancy in Biochemical Assay and Viral Replication Assay

Although GRL0617 is a potent inhibitor in both biochemical assays and cell-based viral replication assays, inconsistencies in some of the derivatives were reported. For example, Jerzy et al. (Osipiuk et al., 2021a) found that compounds 2 and 3 were promising PLpro inhibitors (IC_{50} values of 5.1 and 6.4 μ M, respectively) but failed in the viral replication assay. Compound 5 was the weakest inhibitor *in vitro* (IC_{50} values of 32.8 μ M) but performed well in the live viral replication assay (EC_{50} = 2.5 μ M). Shen et al. showed XR8-89 has highest potency for PLpro inhibition (IC_{50} = 113 nM), yet it has lower EC_{50} value than XR8-23 and XR8-24 (Shen et al., 2021). It was argued that differences in cell permeability and solubility could account for the differences between the *in vitro* biochemical assay data and viral replication data. Ma et al. developed a FlipGFP assay for quantifying the intracellular PLpro inhibition, which was achievable in the biosafety level 2 (BSL-2) setting and found a positive correlation between the results from the FlipGFP-PLpro assay and the antiviral assay (Ma et al., 2021a). Whether the FlipGFP-PLpro faithfully predicts the cellular antiviral activity of PLpro inhibitors awaits further verification by others.

Metabolic Processing

Another challenge is that some inhibitors may be easily metabolized. Báez-Santos et al. found Compound 15g being very unstable (Ghosh et al., 2010; Báez-Santos et al., 2014c). 15g has 3,4-methylenedioxy moiety, which is a known target of cytochrome P450s (Hodgson and Philpot 1974; Anders et al., 1984), whereas 3e and methoxypyridine 5c were significantly more stable (Ghosh et al., 2010; Báez-Santos et al., 2014c). Shen et al. argued that replacement of the naphthalene ring is also anticipated to improve metabolic stability (Shen et al., 2021) and found that ZN3-80 has superior stability than GRL0617 in human liver microsome stability assays (Shen et al., 2021). Cytotoxicity is also a consideration when refining these inhibitors. GRL0617, derivatives, and many other inhibitors did not show much cytotoxicity. Several inhibitors showed high selectivity toward SARS PLpro instead of DUBs, like GRL0617 (Ratia et al., 2008), compound 19 (Shan et al., 2021), and VIR250 and VIR251 (Patchett et al., 2021) (Rut et al., 2020a).

Cell System Bias and Off-Target Inhibition

A concern for screening Mpro inhibitors is the potential for hits to have cross-reactivity with other cysteine proteases. The most likely family of off-target host proteases are the cysteine cathepsins, which are broadly expressed in many cell types and are accessible to small-molecule and peptide-based inhibitors. SARS-CoV-2 can utilize multiple pathways to enter the host cell that depend on a variety of cellular proteases among which are cathepsins B and L, TMPRSS2, and furin (Bestle et al., 2020; Hoffmann et al., 2020; Shang et al., 2020). Lead Mpro inhibitors were tested A549 + ACE2 cells with and without expression of TMPRSS2, and all inhibitors showed a loss in potency with TMPRSS2 expression suggesting that many Mpro inhibitors have some level of antiviral activity due to inhibition of cathepsin-mediated host cell entry (Steuten et al., 2021). In this case, off-target effect can potentially be studied in the scope of polypharmacology. Off-target effects may also account for the discrepancy between biochemical assay and cell-based assay for inhibitors targeting PLpro. As with any drug discovery efforts, many other aspects like membrane permeability, drug efflux, and metabolism also play a critical role in the drug development pipeline.

COMBINATORIAL THERAPEUTIC APPROACHES

Drug Cocktails

Another strategy to consider with protease inhibition design is the combination of strong PLpro and/or Mpro inhibitors with drugs that inhibit other viral functions or patient clearance of treatment. By inhibiting Mpro and PLpro viral proteolysis, disulfiram/ebesen can prevent efficient cleavage of the replicase polyproteins into component NSPs. In case the virus

produces resistance against these proteases, disulfiram/ebesen can also inhibit the RTC core that is crucial for viral RNA synthesis, proofreading, and capping, thus restoring Remdesivir's ability to function as a delayed chain terminator (Chen et al., 2021). In addition, the combination of GC376 and Remdesivir was shown to completely inhibit viral replication in virus plaque assay, showing an additive effect of the joint application of RdRp inhibitors and protease inhibitors targeting different viral proteins (Fu et al., 2020).

AUTHOR CONTRIBUTIONS

ZL and KC: manuscript and figure and table preparation. LJ: figure preparation. SKO: manuscript preparation, editing, and revision. MD and TTH: manuscript editing and revision.

FUNDING

This work was supported by NIH R01 GM115568, R01 GM128731, and CPRIT RR200030 (SKO), and R01 ES025166 and R35 GM139610 (TTH). This work was also supported by National Science Center grant UMO-2020/01/0/NZ1/00063 and the "TEAM/2017-4/32" project (MD), which is carried out within the TEAM program of the Foundation for Polish Science, co-financed by the European Union under the European Regional Development Fund.

ACKNOWLEDGMENTS

The authors thank Lingmin Yuan, Digant Nayak, and Anindita Nayak for critically reading the manuscript.

REFERENCES

- Ahmad, B., Batool, M., Ain, Q. U., Kim, M. S., and Choi, S. (2021). Exploring the Binding Mechanism of PF-07321332 SARS-CoV-2 Protease Inhibitor through Molecular Dynamics and Binding Free Energy Simulations. *Int. J. Mol. Sci.* 22 (17). doi:10.3390/ijms22179124
- Amamuddy, O. S., Verkhrivker, G. M., and Bishop, Ö. T. (2020). Impact of Early Pandemic Stage Mutations on Molecular Dynamics of SARS-CoV-2 Mpro. *J. Chem. Inf. Model.* 60 (10), 5080–5102. doi:10.1021/acs.jcim.0c00634
- Amin, S. A., Banerjee, S., Ghosh, K., Gayen, S., and Jha, T. (2021). Protease Targeted COVID-19 Drug Discovery and its Challenges: Insight into Viral Main Protease (Mpro) and Papain-like Protease (PLpro) Inhibitors. *Bioorg. Med. Chem.* 29, 115860. doi:10.1016/j.bmc.2020.115860
- Ampornpanai, K., Meng, X., Shang, W., Jin, Z., Rogers, M., Zhao, Y., et al. (2021). Inhibition Mechanism of SARS-CoV-2 Main Protease by Ebselen and its Derivatives. *Nat. Commun.* 12 (1), 3061. doi:10.1038/s41467-021-23313-7
- Anand, K., Ziebuhr, J., Wadhwani, P., Mesters, J. R., and Hilgenfeld, R. (2003). Coronavirus Main Proteinase (3CL Pro) Structure: Basis for Design of Anti-SARS Drugs. *Science* 300 (5626), 1763–1767. doi:10.1126/science.1085658
- Anders, M. W., Sunram, J. M., and Wilkinson, C. F. (1984). Mechanism of the Metabolism of 1,3-benzodioxoles to Carbon Monoxide. *Biochem. Pharmacol.* 33 (4), 577–580. doi:10.1016/0006-2952(84)90310-1
- Azad, G. K., and Tomar, R. S. (2014). Ebselen, a Promising Antioxidant Drug: Mechanisms of Action and Targets of Biological Pathways. *Mol. Biol. Rep.* 41 (8), 4865–4879. doi:10.1007/s11033-014-3417-x
- Báez-Santos, Y. M., Barraza, S. J., Wilson, M. W., Agius, M. P., Mielech, A. M., Davis, N. M., et al. (2014). X-ray Structural and Biological Evaluation of a Series of Potent and Highly Selective Inhibitors of Human Coronavirus Papain-like Proteases. *J. Med. Chem.* 57 (6), 2393–2412. doi:10.1021/jm401712t
- Báez-Santos, Y. M., Barraza, S. J., Wilson, M. W., Agius, M. P., Mielech, A. M., Davis, N. M., et al. (2014). X-ray Structural and Biological Evaluation of a Series of Potent and Highly Selective Inhibitors of Human Coronavirus Papain-like Proteases. *J. Med. Chem.* 57 (6), 2393–2412. doi:10.1021/jm401712t
- Báez-Santos, Y. M., Mielech, A. M., Deng, X., Baker, S., and Mesecar, A. D. (2014). Catalytic Function and Substrate Specificity of the Papain-like Protease Domain of Nsp3 from the Middle East Respiratory Syndrome Coronavirus. *J. Virol.* 88 (21), 12511–12527. doi:10.1128/jvi.01294-14
- Báez-Santos, Y. M., St. John, S. E., and Mesecar, A. D. (2015). The SARS-Coronavirus Papain-like Protease: Structure, Function and Inhibition by Designed Antiviral Compounds. *Antiviral Res.* 115, 21–38. doi:10.1016/j.antiviral.2014.12.015
- Banerjee, R., Perera, L., and Tillekeratne, L. M. V. (2021). Potential SARS-CoV-2 Main Protease Inhibitors. *Drug Discov. Today* 26 (3), 804–816. doi:10.1016/j.drudis.2020.12.005
- Barretto, N., Jukneliene, D., Ratia, K., Chen, Z., Mesecar, A. D., and Baker, S. C. (2005). The Papain-like Protease of Severe Acute Respiratory Syndrome

- Coronavirus Has Deubiquitinating Activity. *J. Virol.* 79 (24), 15189–15198. doi:10.1128/jvi.79.24.15189-15198.2005
- Baum, A., Ajithdoss, D., Copin, R., Zhou, A., Lanza, K., Negron, N., et al. (2020). REGN-COV2 Antibodies Prevent and Treat SARS-CoV-2 Infection in Rhesus Macaques and Hamsters. *Science* 370 (6520), 1110–1115. doi:10.1126/science.abe2402
- Bayoumy, A. B., Simsek, M., Seinen, M. L., Mulder, C. J. J., Ansari, A., Peters, G. J., et al. (2020). The Continuous Rediscovery and the Benefit-Risk Ratio of Thioguanine, a Comprehensive Review. *Expert Opin. Drug Metab. Toxicol.* 16 (2), 111–123. doi:10.1080/17425255.2020.1719996
- Beigel, J. H., Tomashek, K. M., Dodd, L. E., Mehta, A. K., Zingman, B. S., Kalil, A. C., et al. (2020). Remdesivir for the Treatment of Covid-19 - Final Report. *N. Engl. J. Med.* 383 (19), 1813–1826. doi:10.1056/nejmoa2007764
- Békés, M., van der Heden van Noort, G. J., Ekkebus, R., Ovaa, H., Huang, T. T., and Lima, C. D. (2016). Recognition of Lys48-Linked Di-ubiquitin and Deubiquitinating Activities of the SARS Coronavirus Papain-like Protease. *Mol. Cell* 62 (4), 572–585. doi:10.1016/j.molcel.2016.04.016
- Bestle, D., Heindl, M. R., Limburg, H., Van Lam van, T., Pilgram, O., Moulton, H., et al. (2020). TMPRSS2 and Furin Are Both Essential for Proteolytic Activation of SARS-CoV-2 in Human Airway Cells. *Life Sci. Alliance* 3 (9), e202000786. doi:10.26508/lsa.202000786
- Bzówka, M., Mitusińska, K., Raczynska, A., Samol, A., Tuszyński, J. A., and Góra, A. (2020). Structural and Evolutionary Analysis Indicate that the SARS-CoV-2 Mpro Is a Challenging Target for Small-Molecule Inhibitor Design. *Int. J. Mol. Sci.* 21 (9). doi:10.3390/ijms21093099
- Chen, H., Wei, P., Huang, C., Tan, L., Liu, Y., and Lai, L. (2006). Only One Protomer Is Active in the Dimer of SARS 3C-like Proteinase. *J. Biol. Chem.* 281 (20), 13894–13898. doi:10.1074/jbc.m510745200
- Chen, T., Fei, C.-Y., Chen, Y.-P., Sargsyan, K., Chang, C.-P., Yuan, H. S., et al. (2021). Synergistic Inhibition of SARS-CoV-2 Replication Using Disulfiram/Ebselen and Remdesivir. *ACS Pharmacol. Transl. Sci.* 4 (2), 898–907. doi:10.1021/acspstsci.1c00022
- Cheng, K.-W., Cheng, S.-C., Chen, W.-Y., Lin, M.-H., Chuang, S.-J., Cheng, I.-H., et al. (2015). Thiopurine Analogs and Mycophenolic Acid Synergistically Inhibit the Papain-like Protease of Middle East Respiratory Syndrome Coronavirus. *Antiviral Res.* 115, 9–16. doi:10.1016/j.antiviral.2014.12.011
- Chou, C.-Y., Chien, C.-H., Han, Y.-S., Prebanda, M. T., Hsieh, H.-P., Turk, B., et al. (2008). Thiopurine Analogues Inhibit Papain-like Protease of Severe Acute Respiratory Syndrome Coronavirus. *Biochem. Pharmacol.* 75 (8), 1601–1609. doi:10.1016/j.bcp.2008.01.005
- Chou, C. Y., Lai, H. Y., Chen, H. Y., Cheng, S. C., Cheng, K. W., and Chou, Y. W. (2014). Structural Basis for Catalysis and Ubiquitin Recognition by the Severe Acute Respiratory Syndrome Coronavirus Papain-like Protease. *Acta Crystallogr. D Biol. Crystallogr.* 70 (Pt 2), 572–581. doi:10.1107/S1399004713031040
- Citarella, A., Scala, A., Piperno, A., and Micale, N. (2021). SARS-CoV-2 Mpro: A Potential Target for Peptidomimetics and Small-Molecule Inhibitors. *Biomolecules* 11 (4). doi:10.3390/biom11040607
- Clasman, J. R., Everett, R. K., Srinivasan, K., and Mesecar, A. D. (2020). Decoupling deISGylating and Deubiquitinating Activities of the MERS Virus Papain-like Protease. *Antiviral Res.* 174, 104661. doi:10.1016/j.antiviral.2019.104661
- Cook, W. J., Jeffrey, L. C., Carson, M., Chen, Z., and Pickart, C. M. (1992). Structure of a Diubiquitin Conjugate and a Model for Interaction with Ubiquitin Conjugating Enzyme (E2). *J. Biol. Chem.* 267 (23), 16467–16471. doi:10.1016/s0021-9258(18)42026-1
- Cross, T. J., Takahashi, G. R., Diessner, E. M., Crosby, M. G., Farahmand, V., Zhuang, S., et al. (2020). Sequence Characterization and Molecular Modeling of Clinically Relevant Variants of the SARS-CoV-2 Main Protease. *Biochemistry* 59 (39), 3741–3756. doi:10.1021/acs.biochem.0c00462
- Daczkowski, C. M., Dzimianski, J. V., Clasman, J. R., Goodwin, O., Mesecar, A. D., and Pegan, S. D. (2017). Structural Insights into the Interaction of Coronavirus Papain-like Proteases and Interferon-Stimulated Gene Product 15 from Different Species. *J. Mol. Biol.* 429 (11), 1661–1683. doi:10.1016/j.jmb.2017.04.011
- Dai, W., Zhang, B., Jiang, X. M., Su, H., Li, J., Zhao, Y., et al. (2020). Structure-based Design of Antiviral Drug Candidates Targeting the SARS-CoV-2 Main Protease. *Science* 368 (6497), 1331–1335. doi:10.1126/science.abb4489
- Dementiev, A., Joachimiak, A., Nguyen, H., Gorelik, A., Illes, K., Shabani, S., et al. (2019). Molecular Mechanism of Inhibition of Acid Ceramidase by Carmofur. *J. Med. Chem.* 62 (2), 987–992. doi:10.1021/acs.jmedchem.8b01723
- Deng, L., Wang, C., Spencer, E., Yang, L., Braun, A., You, J., et al. (2000). Activation of the I κ B Kinase Complex by TRAF6 Requires a Dimeric Ubiquitin-Conjugating Enzyme Complex and a Unique Polyubiquitin Chain. *Cell* 103 (2), 351–361. doi:10.1016/s0092-8674(00)00126-4
- Drag, M., Mikolajczyk, J., Bekes, M., Reyes-Turcu, F. E., Ellman, J. A., Wilkinson, K. D., et al. (2008). Positional-scanning Fluorogenic Substrate Libraries Reveal Unexpected Specificity Determinants of DUBs (Deubiquitinating Enzymes). *Biochem. J.* 415 (3), 367–375. doi:10.1042/bj20080779
- Freitas, B. T., Durie, I. A., Murray, J., Longo, J. E., Miller, H. C., Crich, D., et al. (2020). Characterization and Noncovalent Inhibition of the Deubiquitinase and deISGylase Activity of SARS-CoV-2 Papain-like Protease. *ACS Infect. Dis.* 6 (8), 2099–2109. doi:10.1021/acsinfectdis.0c00168
- Fu, L., Ye, F., Feng, Y., Yu, F., Wang, Q., Wu, Y., et al. (2020). Both Boceprevir and GC376 Efficaciously Inhibit SARS-CoV-2 by Targeting its Main Protease. *Nat. Commun.* 11 (1), 4417. doi:10.1038/s41467-020-18233-x
- Fu, Z., Huang, B., Tang, J., Liu, S., Liu, M., Ye, Y., et al. (2021). The Complex Structure of GRL0617 and SARS-CoV-2 PLpro Reveals a Hot Spot for Antiviral Drug Discovery. *Nat. Commun.* 12 (1), 488. doi:10.1038/s41467-020-20718-8
- Gao, X., Qin, B., Chen, P., Zhu, K., Hou, P., Wojdyla, J. A., et al. (2021). Crystal Structure of SARS-CoV-2 Papain-like Protease. *Acta Pharmaceutica Sinica B* 11 (1), 237–245. doi:10.1016/j.apsb.2020.08.014
- Ghosh, A. K., Brindisi, M., Shahabi, D., Chapman, M. E., and Mesecar, A. D. (2020). Drug Development and Medicinal Chemistry Efforts toward SARS-Coronavirus and Covid-19 Therapeutics. *ChemMedChem* 15 (11), 907–932. doi:10.1002/cmdc.202000223
- Ghosh, A. K., Takayama, J., Aubin, Y., Ratia, K., Chaudhuri, R., Baez, Y., et al. (2009). Structure-Based Design, Synthesis, and Biological Evaluation of a Series of Novel and Reversible Inhibitors for the Severe Acute Respiratory Syndrome-Coronavirus Papain-like Protease. *J. Med. Chem.* 52 (16), 5228–5240. doi:10.1021/jm900611t
- Ghosh, A. K., Takayama, J., Rao, K. V., Ratia, K., Chaudhuri, R., Mulhearn, D. C., et al. (2010). Severe Acute Respiratory Syndrome Coronavirus Papain-like Novel Protease Inhibitors: Design, Synthesis, Protein-Ligand X-ray Structure and Biological Evaluation. *J. Med. Chem.* 53 (13), 4968–4979. doi:10.1021/jm1004489
- Giri, R., Bhardwaj, T., Shegane, M., Gehi, B. R., Kumar, P., Gadhave, K., et al. (2021). Understanding COVID-19 via Comparative Analysis of Dark Proteomes of SARS-CoV-2, Human SARS and Bat SARS-like Coronaviruses. *Cell. Mol. Life Sci.* 78 (4), 1655–1688. doi:10.1007/s00018-020-03603-x
- Goyal, B., and Goyal, D. (2020). Targeting the Dimerization of the Main Protease of Coronaviruses: A Potential Broad-Spectrum Therapeutic Strategy. *ACS Comb. Sci.* 22 (6), 297–305. doi:10.1021/acscmbosci.0c00058
- Günther, S., Reinke, P. Y. A., Fernández-García, Y., Lieske, J., Lane, T. J., Ginn, H. M., et al. (2021). X-ray Screening Identifies Active Site and Allosteric Inhibitors of SARS-CoV-2 Main Protease. *Science* 372 (6542), 642–646. doi:10.1126/science.abf7945
- Gupta, P., Goyal, K., Kanta, P., Ghosh, A., and Singh, M. P. (2019). Novel 2019-coronavirus on New Year's Eve. *Indian J. Med. Microbiol.* 37 (4), 459–477. doi:10.4103/ijmm.ijmm_20_54
- Halford, B. (2021). Pfizer Unveils its Oral SARS-CoV-2 Inhibitor. *Chem. Eng. News*. 07-Apr-2021.
- Harcourt, B. H., Jukneliene, D., Kanjanahaluethai, A., Bechill, J., Severson, K. M., Smith, C. M., et al. (2004). Identification of Severe Acute Respiratory Syndrome Coronavirus Replicase Products and Characterization of Papain-like Protease Activity. *J. Virol.* 78 (24), 13600–13612. doi:10.1128/jvi.78.24.13600-13612.2004
- Hayden, M. S., and Ghosh, S. (2008). Shared Principles in NF- κ B Signaling. *Cell* 132 (3), 344–362. doi:10.1016/j.cell.2008.01.020
- Herold, J., Siddell, S. G., and Gorbalenya, A. E. (1999). A Human RNA Viral Cysteine Proteinase that Depends upon a Unique Zn²⁺-Binding finger Connecting the Two Domains of a Papain-like Fold. *J. Biol. Chem.* 274 (21), 14918–14925. doi:10.1074/jbc.274.21.14918

- Hilgenfeld, R. (2014). From SARS to MERS: Crystallographic Studies on Coronavirus Proteases Enable Antiviral Drug Design. *Febs j* 281 (18), 4085–4096. doi:10.1111/febs.12936
- Ho, W. (2003). Guideline on Management of Severe Acute Respiratory Syndrome (SARS). *The Lancet* 361 (9366), 1313–1315. doi:10.1016/s0140-6736(03)13085-1
- Hodgson, E., and Philpot, R. M. (1974). Interaction of Methylenedioxypheyl (1,3-benzodioxole) Compounds with Enzymes and Their Effects on Mammals. *Drug Metab. Rev.* 3 (2), 231–301. doi:10.3109/03602537408993744
- Hoffman, R. L., Kania, R. S., Brothers, M. A., Davies, J. F., Ferre, R. A., Gajiwala, K. S., et al. (2020). Discovery of Ketone-Based Covalent Inhibitors of Coronavirus 3CL Proteases for the Potential Therapeutic Treatment of COVID-19. *J. Med. Chem.* 63 (21), 12725–12747. doi:10.1021/acs.jmedchem.0c01063
- Hoffmann, M., Kleine-Weber, H., Schroeder, S., Krüger, N., Herrler, T., Erichsen, S., et al. (2020). SARS-CoV-2 Cell Entry Depends on ACE2 and TMPRSS2 and Is Blocked by a Clinically Proven Protease Inhibitor. *Cell* 181 (2), 271–280. doi:10.1016/j.cell.2020.02.052
- Hu, M., Li, P., Song, L., Jeffrey, P. D., Chenova, T. A., Wilkinson, K. D., et al. (2005). Structure and Mechanisms of the Proteasome-Associated Deubiquitinating Enzyme USP14. *Embo j* 24 (21), 3747–3756. doi:10.1038/sj.emboj.7600832
- Jacobs, J., Grum-Tokars, V., Zhou, Y., Turlington, M., Saldanha, S. A., Chase, P., et al. (2013). Discovery, Synthesis, and Structure-Based Optimization of a Series of N-(tert-butyl)-2-(N-arylamido)-2-(pyridin-3-yl) Acetamides (ML188) as Potent Noncovalent Small Molecule Inhibitors of the Severe Acute Respiratory Syndrome Coronavirus (SARS-CoV) 3CL Protease. *J. Med. Chem.* 56 (2), 534–546. doi:10.1021/jm301580n
- Jin, Z., Du, X., Xu, Y., Deng, Y., Liu, M., Zhao, Y., et al. (2020). Structure of Mpro from SARS-CoV-2 and Discovery of its Inhibitors. *Nature* 582 (7811), 289–293. doi:10.1038/s41586-020-2223-y
- Jin, Z., Zhao, Y., Sun, Y., Zhang, B., Wang, H., Wu, Y., et al. (2020). Structural Basis for the Inhibition of SARS-CoV-2 Main Protease by Antineoplastic Drug Carmofur. *Nat. Struct. Mol. Biol.* 27 (6), 529–532. doi:10.1038/s41594-020-0440-6
- J. Pitts (Editor) (2021). *Pfizer Starts Global Phase2/3 EPIC-PEP Study of Novel COVID-19 Oral Antiviral Candidate for post-exposure Prophylaxis in Adults* (New York, United States: Pfizer). Available at: <https://www.pfizer.com/news/press-release/>.
- Karin, M. (1999). How NF-Kb Is Activated: the Role of the Ikb Kinase (IKK) Complex. *Oncogene* 18 (49), 6867–6874. doi:10.1038/sj.onc.1203219
- Kelly, J. A., Olson, A. N., Neupane, K., Munshi, S., San Emeterio, J., Pollack, L., et al. (2020). Structural and Functional Conservation of the Programmed -1 Ribosomal Frameshift Signal of SARS Coronavirus 2 (SARS-CoV-2). *J. Biol. Chem.* 295 (31), 10741–10748. doi:10.1074/jbc.ac120.013449
- Kim, D., Lee, J.-Y., Yang, J.-S., Kim, J. W., Kim, V. N., and Chang, H. (2020). The Architecture of SARS-CoV-2 Transcriptome. *Cell* 181 (4), 914–921. doi:10.1016/j.cell.2020.04.011
- Kitamura, N., Sacco, M. D., Ma, C., Hu, Y., Townsend, J. A., Meng, X., et al. (2021). Expedited Approach toward the Rational Design of Noncovalent SARS-CoV-2 Main Protease Inhibitors. *J. Med. Chem.* doi:10.1021/acs.jmedchem.1c00509
- Klemm, T., Ebert, G., Calleja, D. J., Allison, C. C., Richardson, L. W., Bernardini, J. P., et al. (2020). Mechanism and Inhibition of the Papain-like Protease, PLpro, of SARS-CoV-2. *Embo j* 39 (18), e106275. doi:10.15252/embj.2020106275
- Kneller, D. W., Phillips, G., O'Neill, H. M., Tan, K., Joachimiak, A., Coates, L., et al. (2020). Room-temperature X-ray Crystallography Reveals the Oxidation and Reactivity of Cysteine Residues in SARS-CoV-2 3CL Mpro: Insights into Enzyme Mechanism and Drug Design. *IUCr* 7 (Pt 6), 1028–1035. doi:10.1107/S2052252520012634
- Kneller, D. W., Phillips, G., O'Neill, H. M., Jedrzejczak, R., Stols, L., Langan, P., et al. (2020). Structural Plasticity of SARS-CoV-2 3CL Mpro Active Site Cavity Revealed by Room Temperature X-ray Crystallography. *Nat. Commun.* 11 (1), 3202. doi:10.1038/s41467-020-16954-7
- Kneller, D. W., Phillips, G., Weiss, K. L., Pant, S., Zhang, Q., O'Neill, H. M., et al. (2020). Unusual Zwitterionic Catalytic Site of SARS-CoV-2 Main Protease Revealed by Neutron Crystallography. *J. Biol. Chem.* 295 (50), 17365–17373. doi:10.1074/jbc.ac120.016154
- Komander, D., and Rape, M. (2012). The Ubiquitin Code. *Annu. Rev. Biochem.* 81, 203–229. doi:10.1146/annurev-biochem-060310-170328
- Krishnamoorthy, N., and Fakhro, K. (2021). Identification of Mutation Resistance Coldspots for Targeting the SARS-CoV2 Main Protease. *IUBMB Life* 73 (4), 670–675. doi:10.1002/iub.2465
- Lapinsky, S. E., and Hawryluck, L. (2003). ICU Management of Severe Acute Respiratory Syndrome. *Intensive Care Med.* 29 (6), 870–875. doi:10.1007/s00134-003-1821-0
- Lei, J., Kusov, Y., and Hilgenfeld, R. (2018). Nsp3 of Coronaviruses: Structures and Functions of a Large Multi-Domain Protein. *Antiviral Res.* 149, 58–74. doi:10.1016/j.antiviral.2017.11.001
- Li, S. W., Wang, C. Y., Jou, Y. J., Huang, S. H., Hsiao, L. H., Wan, L., et al. (2016). SARS Coronavirus Papain-like Protease Inhibits the TLR7 Signaling Pathway through Removing Lys63-Linked Polyubiquitination of TRAF3 and TRAF6. *Int. J. Mol. Sci.* 17 (5). doi:10.3390/ijms17050678
- Li, Z., Wang, X., Cao, D., Sun, R., Li, C., and Li, G. (2020). Rapid Review for the Anti-coronavirus Effect of Remdesivir. *DD&T* 14 (2), 73–76. doi:10.5582/ddt.2020.01015
- Lim, C. T., Tan, K. W., Wu, M., Ulferts, R., Armstrong, L. A., Ozono, E., et al. (2021). Identifying SARS-CoV-2 Antiviral Compounds by Screening for Small Molecule Inhibitors of Nsp3 Papain-like Protease. *Biochem. J.* 478 (13), 2517–2531. doi:10.1042/bcj20210244
- Lin, M.-H., Moses, D. C., Hsieh, C.-H., Cheng, S.-C., Chen, Y.-H., Sun, C.-Y., et al. (2018). Disulfiram Can Inhibit MERS and SARS Coronavirus Papain-like Proteases via Different Modes. *Antiviral Res.* 150, 155–163. doi:10.1016/j.antiviral.2017.12.015
- Liu, Y., Liang, C., Xin, L., Ren, X., Tian, L., Ju, X., et al. (2020). The Development of Coronavirus 3C-like Protease (3CLpro) Inhibitors from 2010 to 2020. *Eur. J. Med. Chem.* 206, 112711. doi:10.1016/j.ejmech.2020.112711
- Lv, Z., Rickman, K. A., Yuan, L., Williams, K., Selvam, S. P., Woosley, A. N., et al. (2017). S. pombe Uba1-Ubc15 Structure Reveals a Novel Regulatory Mechanism of Ubiquitin E2 Activity. *Mol. Cell* 65 (4), 699–714. doi:10.1016/j.molcel.2017.01.008
- Lv, Z., Williams, K. M., Yuan, L., Atkinson, J. H., and Olsen, S. K. (2018). Crystal Structure of a Human Ubiquitin E1-Ubiquitin Complex Reveals Conserved Functional Elements Essential for Activity. *J. Biol. Chem.* 293 (47), 18337–18352. doi:10.1074/jbc.ra118.003975
- Ma, C., Hu, Y., Townsend, J. A., Lagarias, P. I., Marty, M. T., Kolocouris, A., et al. (2020). Ebselen, Disulfiram, Carmofur, PX-12, Tideglusib, and Shikonin Are Nonspecific Promiscuous SARS-CoV-2 Main Protease Inhibitors. *ACS Pharmacol. Transl. Sci.* 3 (6), 1265–1277. doi:10.1021/acspstci.0c00130
- Ma, C., Sacco, M. D., Hurst, B., Townsend, J. A., Hu, Y., Szeto, T., et al. (2020). Boceprevir, GC-376, and Calpain Inhibitors II, XII Inhibit SARS-CoV-2 Viral Replication by Targeting the Viral Main Protease. *Cell Res* 30 (8), 678–692. doi:10.1038/s41422-020-0356-z
- Ma, C., Sacco, M. D., Xia, Z., Lambrinidis, G., Townsend, J. A., Hu, Y., et al. (2021). Discovery of SARS-CoV-2 Papain-like Protease Inhibitors through a Combination of High-Throughput Screening and a FlipGFP-Based Reporter Assay. *ACS Cent. Sci.* 7 (7), 1245–1260. doi:10.1021/acscentsci.1c00519
- Ma, C., Tan, H., Choza, J., Wang, Y., and Wang, J. (2021). Validation and Invalidation of SARS-CoV-2 Main Protease Inhibitors Using the Flip-GFP and Protease-Glo Luciferase Assays. *Acta Pharmaceutica Sinica B*. doi:10.1016/j.apsb.2021.10.026
- Malcolm, B. A., Liu, R., Lahser, F., Agrawal, S., Belanger, B., Butkiewicz, N., et al. (2006). SCH 503034, a Mechanism-Based Inhibitor of Hepatitis C Virus NS3 Protease, Suppresses Polyprotein Maturation and Enhances the Antiviral Activity of Alpha Interferon in Replicon Cells. *Antimicrob. Agents Chemother.* 50 (3), 1013–1020. doi:10.1128/aac.50.3.1013-1020.2006
- Mielech, A. M., Chen, Y., Mesecar, A. D., and Baker, S. C. (2014). Nidovirus Papain-like Proteases: Multifunctional Enzymes with Protease, Deubiquitinating and deISGylating Activities. *Virus. Res.* 194, 184–190. doi:10.1016/j.virusres.2014.01.025
- Nakamura, Y., Feng, Q., Kumagai, T., Torikai, K., Ohigashi, H., Osawa, T., et al. (2002). Ebselen, a Glutathione Peroxidase Mimetic Seleno-Organic Compound, as a Multifunctional Antioxidant. *J. Biol. Chem.* 277 (4), 2687–2694. doi:10.1074/jbc.m109641200
- Oerlemans, R., Ruiz-Moreno, A. J., Cong, Y., Dinesh Kumar, N., Velasco-Velazquez, M. A., Neochoritis, C. G., et al. (2021). Repurposing the HCV NS3-4A Protease Drug Boceprevir as COVID-19 Therapeutics. *RSC Med. Chem.* 12 (3), 370–379. doi:10.1039/d0md00367k

- Osiupik, J., Azizi, S.-A., Dvorkin, S., Endres, M., Jedrzejczak, R., Jones, K. A., et al. (2021). Structure of Papain-like Protease from SARS-CoV-2 and its Complexes with Non-covalent Inhibitors. *Nat. Commun.* 12 (1), 743. doi:10.1038/s41467-021-21060-3
- Osiupik, J., Wydorski, P. M., Lanham, B. T., Tesar, C., Endres, M., Engle, E., et al. (2021). Dual Domain Recognition Determines SARS-CoV-2 PLpro Selectivity for Human ISG15 and K48-Linked Di-ubiquitin. *bioRxiv*. doi:10.1101/2021.09.15.460543
- Owen, D. R., Allerton, C. M. N., Anderson, A. S., Aschenbrenner, L., Avery, M., Bertritt, S., et al. (2021). An Oral SARS-CoV-2 Mpro Inhibitor Clinical Candidate for the Treatment of COVID-19. *Science* 354 (6575), 1586–1593. doi:10.1126/science.abl4784
- Park, J.-Y., Kim, J. H., Kim, Y. M., Jeong, H. J., Kim, D. W., Park, K. H., et al. (2012). Tanshinones as Selective and Slow-Binding Inhibitors for SARS-CoV Cysteine Proteases. *Bioorg. Med. Chem.* 20 (19), 5928–5935. doi:10.1016/j.bmc.2012.07.038
- Patchett, S., Lv, Z., Rut, W., Békés, M., Drag, M., Olsen, S. K., et al. (2021). A Molecular Sensor Determines the Ubiquitin Substrate Specificity of SARS-CoV-2 Papain-like Protease. *Cel Rep.* 36, 109754. doi:10.1016/j.celrep.2021.109754
- Pavan, M., Bolcato, G., Bassani, D., Sturlese, M., and Moro, S. (2021). Supervised Molecular Dynamics (SuMD) Insights into the Mechanism of Action of SARS-CoV-2 Main Protease Inhibitor PF-07321332. *J. Enzyme Inhib. Med. Chem.* 36 (1), 1646–1650. doi:10.1080/14756366.2021.1954919
- Perng, Y.-C., and Lenschow, D. J. (2018). ISG15 in Antiviral Immunity and beyond. *Nat. Rev. Microbiol.* 16 (7), 423–439. doi:10.1038/s41579-018-0020-5
- Pfizer (2021). Pfizer's Novel COVID-19 Oral Antiviral Treatment Candidate Reduced Risk of Hospitalization or Death by 89% in Interim Analysis or Phase 2/3 EPIC-HR Study. Available at: <https://www.pfizer.com/news/press-release/press-release-detail/pfizers-novel-covid-19-oral-antiviral-treatment-candidate>.
- Pillaiyar, T., Manickam, M., Namasivayam, V., Hayashi, Y., and Jung, S.-H. (2016). An Overview of Severe Acute Respiratory Syndrome-Coronavirus (SARS-CoV) 3CL Protease Inhibitors: Peptidomimetics and Small Molecule Chemotherapy. *J. Med. Chem.* 59 (14), 6595–6628. doi:10.1021/acs.jmedchem.5b01461
- Poreba, M., Salvesen, G. S., and Drag, M. (2017). Synthesis of a HyCoSuL Peptide Substrate Library to Dissect Protease Substrate Specificity. *Nat. Protoc.* 12 (10), 2189–2214. doi:10.1038/nprot.2017.091
- Portelli, S., Olshansky, M., Rodrigues, C. H. M., D'Souza, E. N., Myung, Y., Silk, M., et al. (2020). Exploring the Structural Distribution of Genetic Variation in SARS-CoV-2 with the COVID-3D Online Resource. *Nat. Genet.* 52 (10), 999–1001. doi:10.1038/s41588-020-0693-3
- Ratia, K., Kilianski, A., Baez-Santos, Y. M., Baker, S. C., and Mesecar, A. (2014). Structural Basis for the Ubiquitin-Linkage Specificity and deISGylating Activity of SARS-CoV Papain-like Protease. *Plos Pathog.* 10 (5), e1004113. doi:10.1371/journal.ppat.1004113
- Ratia, K., Pegan, S., Takayama, J., Sleeman, K., Coughlin, M., Baliji, S., et al. (2008). A Noncovalent Class of Papain-like Protease/deubiquitinase Inhibitors Blocks SARS Virus Replication. *Proc. Natl. Acad. Sci.* 105 (42), 16119–16124. doi:10.1073/pnas.0805240105
- Ratia, K., Saikatendu, K. S., Santarsiero, B. D., Barretto, N., Baker, S. C., Stevens, R. C., et al. (2006). Severe Acute Respiratory Syndrome Coronavirus Papain-like Protease: Structure of a Viral Deubiquitinating Enzyme. *Proc. Natl. Acad. Sci.* 103 (15), 5717–5722. doi:10.1073/pnas.0510851103
- Rut, W., Lv, Z., Zmudzinski, M., Patchett, S., Nayak, D., Snipas, S. J., et al. (2020). Activity Profiling and crystal Structures of Inhibitor-Bound SARS-CoV-2 Papain-like Protease: A Framework for Anti-COVID-19 Drug Design. *Sci. Adv.* 6 (42). doi:10.1126/sciadv.abd4596
- Rut, W., Groborz, K., Zhang, L., Sun, X., Zmudzinski, M., Pawlik, B., et al. (2021). SARS-CoV-2 Mpro Inhibitors and Activity-Based Probes for Patient-Sample Imaging. *Nat. Chem. Biol.* 17 (2), 222–228. doi:10.1038/s41589-020-00689-z
- Rut, W., Zmudzinski, M., Snipas, S. J., Bekes, M., Huang, T. T., and Drag, M. (2020). Engineered Unnatural Ubiquitin for Optimal Detection of Deubiquitinating Enzymes. *Chem. Sci.* 11 (23), 6058–6069. doi:10.1039/d0sc01347a
- Sakamoto, J., Hamada, C., Rahman, M., Kodaira, S., Ito, K., Nakazato, H., et al. (2005). An Individual Patient Data Meta-Analysis of Adjuvant Therapy with Carmofur in Patients with Curatively Resected Colon Cancer. *Jpn. J. Clin. Oncol.* 35 (9), 536–544. doi:10.1093/jjco/hyi147
- Sargsyan, K., Lin, C.-C., Chen, T., Grauffel, C., Chen, Y.-P., Yang, W.-Z., et al. (2020). Multi-targeting of Functional Cysteines in Multiple Conserved SARS-CoV-2 Domains by Clinically Safe Zn-Ejectors. *Chem. Sci.* 11 (36), 9904–9909. doi:10.1039/d0sc02646h
- Shan, H., Liu, J., Shen, J., Dai, J., Xu, G., Lu, K., et al. (2021). Development of Potent and Selective Inhibitors Targeting the Papain-like Protease of SARS-CoV-2. *Cel Chem. Biol.* 28 (6), 855–865. e9. doi:10.1016/j.chembiol.2021.04.020
- Shang, J., Wan, Y., Luo, C., Ye, G., Geng, Q., Auerbach, A., et al. (2020). Cell Entry Mechanisms of SARS-CoV-2. *Proc. Natl. Acad. Sci. USA* 117 (21), 11727–11734. doi:10.1073/pnas.2003138117
- Sheahan, T. P., Sims, A. C., Zhou, S., Graham, R. L., Pruijssers, A. J., Agostini, M. L., et al. (2020). An Orally Bioavailable Broad-Spectrum Antiviral Inhibits SARS-CoV-2 in Human Airway Epithelial Cell Cultures and Multiple Coronaviruses in Mice. *Sci. Transl. Med.* 12 (541), eabb5883. doi:10.1126/scitranslmed.abb5883
- Shen, Z., Ratia, K., Cooper, L., Kong, D., Lee, H., Kwon, Y., et al. (2021). Potent, Novel SARS-CoV-2 PLpro Inhibitors Block Viral Replication in Monkey and Human Cell Cultures. *bioRxiv*. doi:10.1101/2021.02.13.431008
- Shin, D., Mukherjee, R., Grewe, D., Bojkova, D., Baek, K., Bhattacharya, A., et al. (2020). Papain-like Protease Regulates SARS-CoV-2 Viral Spread and Innate Immunity. *Nature* 587 (7835), 657–662. doi:10.1038/s41586-020-2601-5
- Siegel, D., Hui, H. C., Doerfler, E., Clarke, M. O., Chun, K., Zhang, L., et al. (2017). Discovery and Synthesis of a Phosphoramidate Prodrug of a Pyrrolo[2,1-F] [triazin-4-Amino] Adenine C-Nucleoside (GS-5734) for the Treatment of Ebola and Emerging Viruses. *J. Med. Chem.* 60 (5), 1648–1661. doi:10.1021/acs.jmedchem.6b01594
- Simón, L., and Goodman, J. M. (2010). Enzyme Catalysis by Hydrogen Bonds: the Balance between Transition State Binding and Substrate Binding in Oxyanion Holes. *J. Org. Chem.* 75 (6), 1831–1840. doi:10.1021/jo901503d
- Smith, E., Davis-Gardner, M. E., Garcia-Ordóñez, R. D., Nguyen, T.-T., Hull, M., Chen, E., et al. (2020). High-Throughput Screening for Drugs that Inhibit Papain-like Protease in SARS-CoV-2. *SLAS DISCOVERY: Advancing Sci. Drug Discov.* 25 (10), 1152–1161. doi:10.1177/2472555220963667
- Steuten, K., Kim, H., Widen, J. C., Babin, B. M., Onguka, O., Lovell, S., et al. (2021). Challenges for Targeting SARS-CoV-2 Proteases as a Therapeutic Strategy for COVID-19. *ACS Infect. Dis.* 7 (6), 1457–1468. doi:10.1021/acsinfectdis.0c00815
- Swaim, C. D., Perng, Y.-C., Zhao, X., Canadeo, L. A., Harastani, H. H., Darling, T. L., et al. (2021). 6-Thioguanine Blocks SARS-CoV-2 Replication by Inhibition of PLpro Protease Activities. *iScience* 24 (10), 103213. doi:10.1016/j.isci.2021.103213
- Świderek, K., and Moliner, V. (2020). Revealing the Molecular Mechanisms of Proteolysis of SARS-CoV-2 Mpro by QM/MM Computational Methods. *Chem. Sci.* 11 (39), 10626–10630. doi:10.1039/d0sc02823a
- Tian, D., Liu, Y., Liang, C., Xin, L., Xie, X., Zhang, D., et al. (2021). An Update Review of Emerging Small-Molecule Therapeutic Options for COVID-19. *Biomed. Pharmacother.* 137, 111313. doi:10.1016/j.bioph.2021.111313
- Tomei, L., Failla, C., Santolini, E., De Francesco, R., and La Monica, N. (1993). NS3 Is a Serine Protease Required for Processing of Hepatitis C Virus Polyprotein. *J. Virol.* 67 (7), 4017–4026. doi:10.1128/jvi.67.7.4017-4026.1993
- Tzou, P. L., Tao, K., Nouhin, J., Rhee, S. Y., Hu, B. D., Pai, S., et al. (2020). Coronavirus Antiviral Research Database (CoV-RDB): An Online Database Designed to Facilitate Comparisons between Candidate Anti-coronavirus Compounds. *Viruses* 12 (9), 1006. doi:10.3390/v12091006
- Vuong, W., Fischer, C., Khan, M. B., van Belkum, M. J., Lamer, T., Willoughby, K. D., et al. (2021). Improved SARS-CoV-2 Mpro Inhibitors Based on Feline Antiviral Drug GC376: Structural Enhancements, Increased Solubility, and Micellar Studies. *Eur. J. Med. Chem.* 222, 113584. doi:10.1016/j.ejmech.2021.113584
- Vuong, W., Khan, M. B., Fischer, C., Arutyunova, E., Lamer, T., Shields, J., et al. (2020). Feline Coronavirus Drug Inhibits the Main Protease of SARS-CoV-2 and Blocks Virus Replication. *Nat. Commun.* 11 (1), 4282. doi:10.1038/s41467-020-18096-2
- Wang, C., Deng, L., Hong, M., Akkaraju, G. R., Inoue, J.-i., and Chen, Z. J. (2001). TAK1 Is a Ubiquitin-dependent Kinase of MKK and IKK. *Nature* 412 (6844), 346–351. doi:10.1038/35085597
- Warren, T. K., Jordan, R., Lo, M. K., Ray, A. S., Mackman, R. L., Soloveva, V., et al. (2016). Therapeutic Efficacy of the Small Molecule GS-5734 against Ebola Virus in Rhesus Monkeys. *Nature* 531 (7594), 381–385. doi:10.1038/nature17180
- Weglarz-Tomczak, E., Tomczak, J. M., Talma, M., Burda-Grabowska, M., Giurg, M., and Brul, S. (2021). Identification of Ebelen and its Analogues as Potent

- Covalent Inhibitors of Papain-like Protease from SARS-CoV-2. *Sci. Rep.* 11 (1), 3640. doi:10.1038/s41598-021-83229-6
- Wissner, A., Overbeek, E., Reich, M. F., Floyd, M. B., Johnson, B. D., Mamuya, N., et al. (2003). Synthesis and Structure–Activity Relationships of 6,7-Disubstituted 4-Anilinoquinoline-3-Carbonitriles. The Design of an Orally Active, Irreversible Inhibitor of the Tyrosine Kinase Activity of the Epidermal Growth Factor Receptor (EGFR) and the Human Epidermal Growth Factor Receptor-2 (HER-2). *J. Med. Chem.* 46 (1), 49–63. doi:10.1021/jm020241c
- Woo, P. C. Y., Huang, Y., Lau, S. K. P., and Yuen, K.-Y. (2010). Coronavirus Genomics and Bioinformatics Analysis. *Viruses* 2 (8), 1804–1820. doi:10.3390/v2081803
- Xu, Y., Chen, K., Pan, J., Lei, Y., Zhang, D., Fang, L., et al. (2021). Repurposing Clinically Approved Drugs for COVID-19 Treatment Targeting SARS-CoV-2 Papain-like Protease. *Int. J. Biol. Macromolecules* 188, 137–146. doi:10.1016/j.ijbiomac.2021.07.184
- Yang, H., Xie, W., Xue, X., Yang, K., Ma, J., Liang, W., et al. (2005). Design of Wide-Spectrum Inhibitors Targeting Coronavirus Main Proteases. *Plos Biol.* 3 (10), e324. doi:10.1371/journal.pbio.0030324
- Yuan, L., Lv, Z., Atkison, J. H., and Olsen, S. K. (2017). Structural Insights into the Mechanism and E2 Specificity of the RBR E3 Ubiquitin Ligase HHARI. *Nat. Commun.* 8 (1), 211. doi:10.1038/s41467-017-00272-6
- Zeldin, R. K., and Petruschke, R. A. (2004). Pharmacological and Therapeutic Properties of Ritonavir-Boosted Protease Inhibitor Therapy in HIV-Infected Patients. *J. Antimicrob. Chemother.* 53 (1), 4–9. doi:10.1093/jac/dkh029
- Zhang, C.-H., Stone, E. A., Deshmukh, M., Ippolito, J. A., Ghahremanpour, M. M., Tirado-Rives, J., et al. (2021). Potent Noncovalent Inhibitors of the Main Protease of SARS-CoV-2 from Molecular Sculpting of the Drug Perampanel Guided by Free Energy Perturbation Calculations. *ACS Cent. Sci.* 7 (3), 467–475. doi:10.1021/acscentsci.1c00039
- Zhang, L., Lin, D., Kusov, Y., Nian, Y., Ma, Q., Wang, J., et al. (2020). α -Ketoamides as Broad-Spectrum Inhibitors of Coronavirus and Enterovirus Replication: Structure-Based Design, Synthesis, and Activity Assessment. *J. Med. Chem.* 63 (9), 4562–4578. doi:10.1021/acs.jmedchem.9b01828
- Zhang, L., Lin, D., Sun, X., Curth, U., Drosten, C., Sauerhering, L., et al. (2020). Crystal Structure of SARS-CoV-2 Main Protease Provides a Basis for Design of Improved α -ketoamide Inhibitors. *Science* 368 (6489), 409–412. doi:10.1126/science.abb3405
- Zhao, Y., Du, X., Duan, Y., Pan, X., Sun, Y., You, T., et al. (2021). High-throughput Screening Identifies Established Drugs as SARS-CoV-2 PLpro Inhibitors. *Protein & Cell* 12, 877–888. doi:10.1007/s13238-021-00836-9
- Zhou, L., Zuo, Z., and Chow, M. S. S. (2005). Danshen: an Overview of its Chemistry, Pharmacology, Pharmacokinetics, and Clinical Use. *J. Clin. Pharmacol.* 45 (12), 1345–1359. doi:10.1177/0091270005282630
- Zmudzinski, M., Rut, W., Olech, K., Granda, J., Giurg, M., Burda-Grabowska, M., et al. (2020). Ebselen Derivatives Are Very Potent Dual Inhibitors of SARS-CoV-2 Proteases - PLpro and Mpro in *In Vitro* Studies. *bioRxiv*. doi:10.1101/2020.08.30.273979

Conflict of Interest: The authors declare that the research was conducted in the absence of any commercial or financial relationships that could be construed as a potential conflict of interest.

Publisher's Note: All claims expressed in this article are solely those of the authors and do not necessarily represent those of their affiliated organizations or those of the publisher, the editors, and the reviewers. Any product that may be evaluated in this article, or claim that may be made by its manufacturer, is not guaranteed or endorsed by the publisher.

Copyright © 2022 Lv, Cano, Jia, Drag, Huang and Olsen. This is an open-access article distributed under the terms of the Creative Commons Attribution License (CC BY). The use, distribution or reproduction in other forums is permitted, provided the original author(s) and the copyright owner(s) are credited and that the original publication in this journal is cited, in accordance with accepted academic practice. No use, distribution or reproduction is permitted which does not comply with these terms.



An Enhanced Hybrid Screening Approach to Identify Potent Inhibitors for the SARS-CoV-2 Main Protease From the NCI Compound Library

Shuhua G. Li^{1†}, Kai S. Yang^{1†}, Lauren R. Blankenship¹, Chia-Chuan D. Cho¹, Shiqing Xu^{1*}, Hongbin Wang^{2*} and Wenshe Ray Liu^{1,3,4,5*}

¹Texas A&M Drug Discovery Laboratory, Department of Chemistry, Texas A&M University, College Station, TX, United States, ²Center for Biomedical Informatics, College of Medicine, Texas A&M University, Houston, TX, United States, ³Institute of Biosciences and Technology and Department of Translational Medical Sciences, College of Medicine, Texas A&M University, Houston, TX, United States, ⁴Department of Biochemistry and Biophysics, Texas A&M University, College Station, TX, United States, ⁵Department of Molecular and Cellular Medicine, College of Medicine, Texas A&M University, College Station, TX, United States

OPEN ACCESS

Edited by:

Zhenjun Yang,
Peking University, China

Reviewed by:

Jesus Simal-Gandara,
University of Vigo, Spain
Jun Wang,
Rutgers, The State University of New
Jersey, United States

*Correspondence:

Shiqing Xu
shiqing.xu@tamu.edu
Hongbin Wang
hongbinwang@tamu.edu
Wenshe Ray Liu
wsliu2007@tamu.edu

[†]These authors have contributed
equally to this work

Specialty section:

This article was submitted to
Medicinal and Pharmaceutical
Chemistry,
a section of the journal
Frontiers in Chemistry

Received: 16 November 2021

Accepted: 28 January 2022

Published: 17 February 2022

Citation:

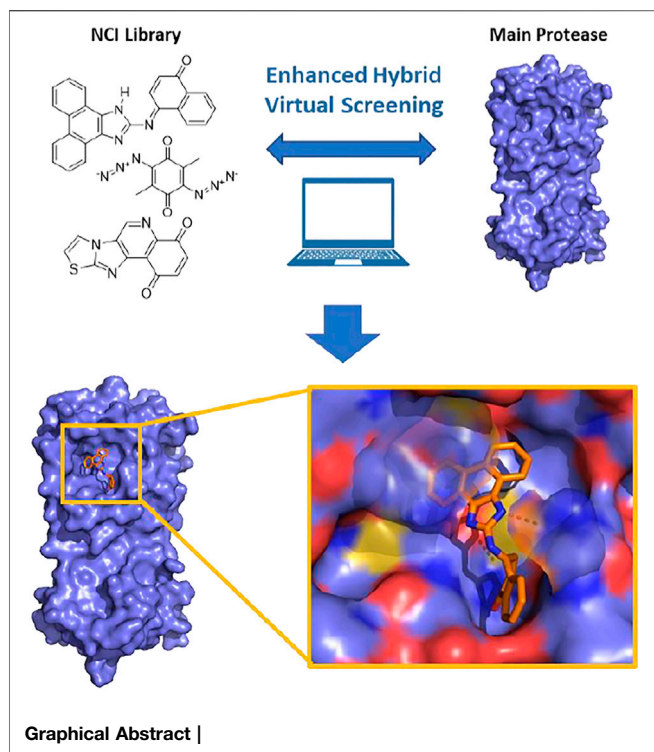
Li SG, Yang KS, Blankenship LR,
Cho C-CD, Xu S, Wang H and Liu WR
(2022) An Enhanced Hybrid Screening
Approach to Identify Potent Inhibitors
for the SARS-CoV-2 Main Protease
From the NCI Compound Library.
Front. Chem. 10:816576.
doi: 10.3389/fchem.2022.816576

The emergence and rapid spread of SARS-CoV-2, the pathogen of COVID-19, have caused a worldwide public health crisis. The SARS-CoV-2 main protease (Mpro) is an essential enzyme for the virus and therefore an appealing target for the development of antivirals to treat COVID-19 patients. Recently, many *in silico* screenings have been performed against the main protease to discover novel hits. However, the actual hit rate of virtual screening is often low, and most of the predicted compounds are false positive hits. In this study, we developed a refined virtual screening strategy that incorporated molecular docking and post-docking filtering based on parameters including molecular weight and surface area, aiming to achieve predictions with fewer false positive hits. We applied this strategy to the NCI library containing 284,176 compounds against Mpro. *In vitro* potency analyses validated several potent inhibitors and thus confirmed the feasibility of our virtual screening strategy. Overall, The study resulted in several potent hit Mpro inhibitors, in which two inhibitors have IC₅₀ values below 1 μ M, that are worth being further optimized and explored. Meanwhile, the refined virtual screen strategy is also applicable to improve general *in silico* screening hit rates and is useful to accelerate drug discovery for treating COVID-19 and other viral infections.

Keywords: COVID-19, SAR-CoV-2, main protease, virtual screening, statistical analysis

INTRODUCTION

In the past 2 decades, coronaviruses (CoV) have caused three major worldwide infectious disease outbreaks including the severe acute respiratory syndrome (SARS) in 2003 (Lee et al., 2003; Cheng et al., 2007), the Middle East respiratory syndrome (MERS) in 2012 (Zaki et al., 2012; de Groot et al., 2013) and the coronavirus disease 2019 (COVID-19) (Gates, 2020). Their CoV pathogens are namely SARS-CoV, MERS-CoV and SARS-CoV-2, respectively. Compared to the previous two CoV outbreaks, COVID-19 has a worldwide impact that has been so severe that it is often compared to the 1918 influenza pandemic (Gates, 2020; Morens et al., 2020). According to the statistics that was released from the World Health Organization (WHO) on 12 Jan 2021, the confirmed worldwide



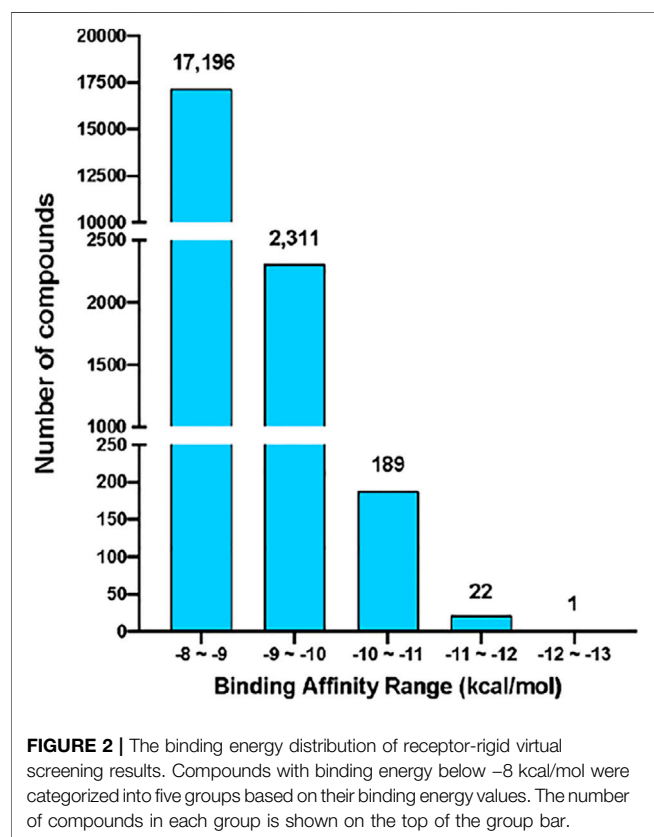
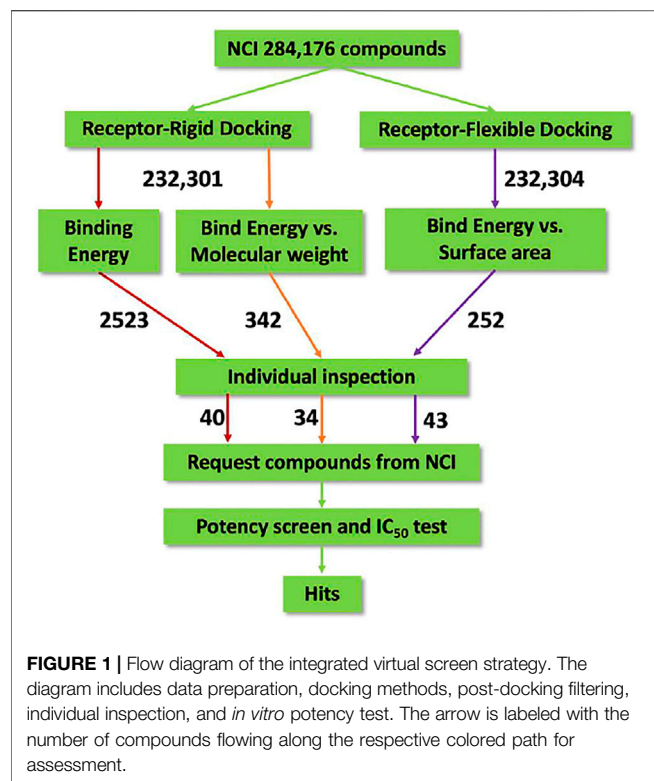
COVID-19 cases have exceeded 312 million, of which more than 5 million patients have succumbed to death (WHO (2022) COVID-19 Dashboard). The typical COVID-19 symptoms include shortness of breath, cough and fever. In advanced cases, the infection could lead to dyspnea, pneumonia, kidney failure and even death (Huang et al., 2020). Institutions and companies around the world have been exerting much effort in rapidly developing vaccines and drugs to fight COVID-19. Three COVID-19 vaccines developed by Pfizer/BioNTech, Moderna and Johnson and Johnson have been approved or authorized by U.S. Food and Drug Administration (FDA) for human immunization in the United States. Although vaccines are promising in containing the pandemic, their availability does not diminish the urgent need for other effective antiviral drugs. Existing COVID-19 vaccines target the membrane Spike protein of SARS-CoV-2, which is highly mutable (Morse et al., 2020). New viral strains with critical mutations in Spike have emerged in various countries such as the United Kingdom, South Africa and Indian (Vilar and Isom, 2021). The efficacy of vaccines against these strains (as well as newer yet-to-emerge ones) is uncertain. Vaccines are also preventative, making them not an option for the treatment of COVID-19 patients. Hence, in addition to vaccines, it is necessary to develop therapeutic drugs for both prevention and treatment as we are now observing new waves of the COVID-19 pandemic from Delta and Omicron strains. As a quick access to effective antivirals, drug repurposing has been broadly conducted (Vatansever et al., 2021a). Although the FDA has approved some repurposed drugs including remdesivir to treatment COVID-19, most current evidence have shown that these repurposed drugs provide mild benefits to patients (Wang et al., 2020). In the context of the disastrous damage of COVID-

19 to public health, civil society and the global economy, the search for effective drugs against SARS-CoV-2 is in urgent demand.

SARS-CoV-2 is a positive RNA virus that belongs to the *betacoronavirus* genus of the *coronaviridae* family under the order *Nidovirales* (Helmy et al., 2020). The genome of SARS-CoV-2 is composed of 14 open reading frames that encode 4 structural proteins, 16 nonstructural proteins (Nsps) and several accessory proteins (Astuti and Ysrafil, 2020). SARS-CoV-2's entry into a host cell is initiated by binding the viral Spike protein to the cellular receptor angiotensin-converting enzyme 2. Viral fusion to the host cell endosome is promoted by the cellular surface serine protease. After entry and release of viral genomic RNA, two large open reading frames ORF1a and ORF1ab are translated, producing viral polyproteins pp1a and pp1ab. Both pp1a and pp1ab need to undergo proteolytic cleavage to form 16 Nsps that are essential for the virus in its reproduction and pathogenesis. The proteolytic cleavage of pp1a and pp1ab is an autocatalytic process. Two internal polypeptide regions, Nsp3 and Nsp5, possess cysteine protease activities that cleave themselves and all other Nsps from the two polypeptides. Nsp3 is commonly referred to as papain-like protease (PLpro) and Nsp5 as 3C-like protease (3CLpro) or, more recently, main protease (Mpro) (V'Kovski et al., 2021). Although we have yet to fully understand the SARS-CoV-2 biology and COVID-19 pathogenesis, current research results have established that activities of both PLpro and Mpro are essential for the viral replication and pathogenesis. Of the two proteases, Mpro processes 13 out of the total 16 Nsps. Therefore, small-molecule medicines that can potently inhibit SARS-CoV-2 Mpro are potentially effective treatment options for COVID-19 (Yang et al., 2021).

Recently, *in silico* screening has been used to identify potential drugs against SARS-CoV-2 and results from these investigations have been reported (Rakib et al., 2020; Mahmud et al., 2021a; Mahmud et al., 2021b; Jang et al., 2021; Khan et al., 2021; Rakib et al., 2021). Natural product studies have been done recently using computational approaches to study different inhibitors for SARS-CoV-2 Mpro (Rakib et al., 2020; Khan et al., 2021). The results of the computational approaches can then be verified further by using *in vitro* and *in vivo* experiments on the compounds identified with the highest potential binding affinities to SARS-CoV-2 Mpro. This approach was recently used to identify ethaselen, a selenium containing heterocycle, that is on its way to becoming a potential drug to combat SARS-CoV-2 infections (Rakib et al., 2021). This combined approach can be expanded past the current pandemic into other infections, such as was recently done to investigate drug candidates against MERS-CoV by targeting S1-NTD (Bouback et al., 2021). Computational biological techniques allow for increased efficiency and lowers the total compounds that need to be further tested to those most likely to succeed.

However, the actual hit rate of most virtual screening is low. Many predicted drug candidates are false positives (Vatansever et al., 2021b). This is partially due to the difficulties in accurately modeling and predicting protein-ligand binding free energy. This body of research suggests that it is difficult to identify false

**TABLE 1 |** Binding energy vs. molecular weight of virtual screening results.

Binding Affinity(kcal/mol)	-8 to -9	-9 to -10	-10 to -11	-11 to -12	-12 to -13
Molecular Weight(Da)					
0 to 100	—	—	—	—	—
100 to 200	—	—	—	—	—
200 to 300	539	6	—	—	—
300 to 400	5457	331	5	—	—
400 to 500	6502	786	40	2	—
500 to 600	2811	648	37	6	—
600 to 700	1038	294	40	3	—
700 to 800	339	113	34	8	—
800 to 900	194	56	16	1	—
900 to 1000	110	20	7	1	—
1000 to 1200	49	14	5	1	1
1200 to 1300	37	10	1	—	—
1300 to 1400	30	14	—	—	—
1400 to 1500	16	7	—	—	—
1500 to 1600	5	4	—	—	—
1600 to 1700	2	1	1	—	—
1700 to 1800	5	—	—	—	—
1800 to 1900	4	1	—	—	—
1900 to 2000	1	—	—	—	—
2000 to 2100	2	—	—	—	—

positives based on docking and simulation results alone. Therefore, better strategies are required to increase the hit rates. In this work, we incorporated effective filtering methods after molecular docking to improve the hit rate. Rigid and flexible docking were conducted parallelly. The raw docking results were then submitted to an analysis based on their molecular weights and surface area. Compounds that deviated far from their average binding score levels were identified as candidates and retained for further individual inspection. This virtual drug screening strategy, comprising the rigid/flexible docking, post-docking filtering and individual inspection, was applied to identify hit candidates targeting SARS-CoV-2 Mpro, using a recently determined crystal structure (Jin et al., 2020). A collection of 284,176 NCI compounds was screened. After identifying hit candidates through virtual screening, *in vitro* potency evaluation of hit candidates was performed to identify potent hits. The *in vitro* potency evaluation revealed 19 compounds with IC_{50} values in inhibiting Mpro below $100 \mu M$, among them 2 compounds with very high potency with IC_{50} values below $1 \mu M$.

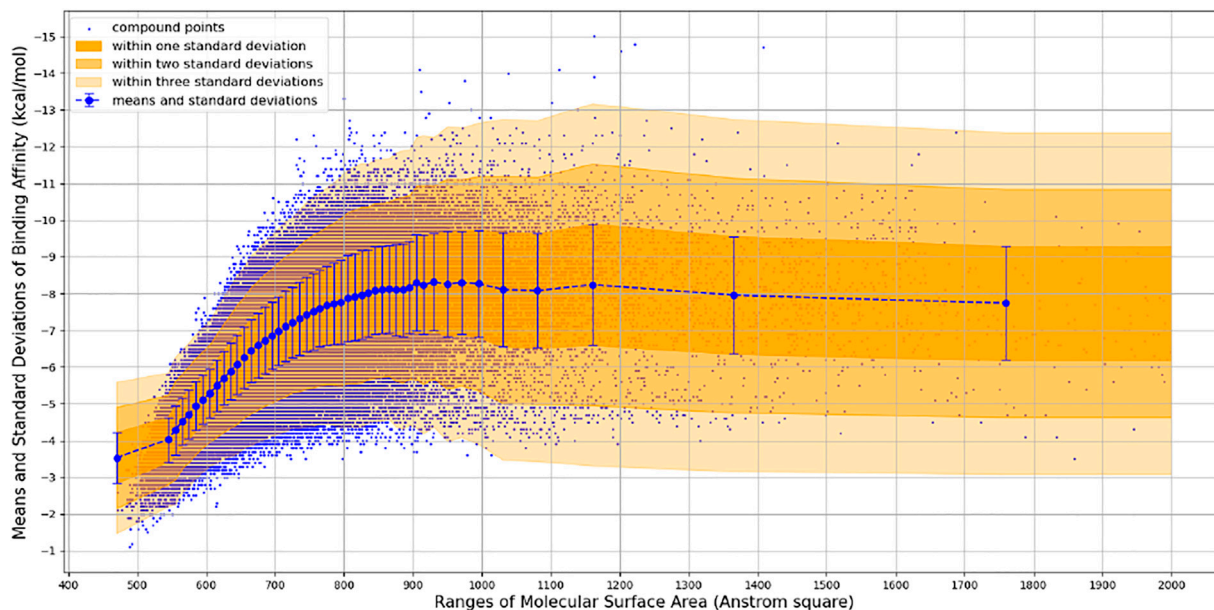
RESULTS AND DISCUSSION

Receptor-Rigid Docking on the NCI Library

The virtual screening process and strategy in this study are described in Figure 1. 284,176 NCI compounds in the SDF format were downloaded and converted to the PDBQT format using the program OpenBabel. All prepared compounds were submitted to virtual screening against the active site of Mpro based on the PDB entry 6LU7 using the program Autodock Vina. Mpro has P1, P2 and P4 binding pockets for its substrates. These

TABLE 2 | Comparison of two binding energy distributions (receptor-flex vs. receptor-rigid) for compounds with molecular weight lower than 400 Da.

REceptor/Energy Ranges	-8 to -9	-9 to -10	-10 to -11	-11 to -12	-12 to -13	Total
Receptor-Flexible	16,383	2,607	229	14	2	19,235
Receptor-Rigid	5996	337	5	—	—	6,338

**FIGURE 3** | Binding Energy vs. Molecular Surface Area of Receptor-Flexible Docking Results. The surface areas are binned with 10 Å², and then the mean and standard deviation of binding energy within each surface area bin is calculated. In order to get more reliable statistical results, we use a simple adaptive strategy to merge surface area bins so that each surface area bin contains at least 1,000 compound data points.

pockets were included during the docking process. After the receptor-rigid docking study, docking structures for 232,301 compounds were obtained. Each compound has at most 20 binding modes that were ranked based on their binding energy. Only the binding mode with the best binding energy of each compound was subsequently assessed. These docking structures were ranked based on their top binding energy, which led to 19,719 docking structures with top binding energy below -8 kcal/mol. The binding energy distribution of 19,719 compounds was calculated (Figure 2). The majority of compounds had binding energy between -8 kcal/mol to -9 kcal/mol. Only 2,523 compounds had binding energy lower than -9 kcal/mol. Compounds with binding energy lower than -9 kcal/mol were considered as promising hit candidates and further submitted for individual inspection. The individual inspection of compounds is based on three criteria: chemical correctness that assesses the 3D molecular conformations, pocket fitting that verifies that there are at least two fragments from a ligand fitted into two active site pockets of Mpro, and hydrophobicity that removes molecules that lead to favorable calculated binding energy apparently due to strong hydrophobicity of the compounds. Based on these criteria, we manually inspected the 2,523 receptor-rigid docking results with

binding energy below -9.0 kcal/mol. 40 compounds were selected and requested from NCI for further *in vitro* potency testing.

Since binding energy correlates partially with the molecular weight, to further increase the accuracy of hit prediction, we also took the molecular weight of compounds into account. The distribution of binding energy vs. molecular weight was calculated (Table 1). 342 compounds with molecular weight between 200 and 400 Da and binding energy below -9 kcal/mol were considered as promising hit candidates and inspected individually. As a result of the inspection process, 34 out of 342 compounds were also requested from NCI for further *in vitro* potency testing. Please keep in mind that these 34 compounds were identified on the top of 40 compounds that were selected already by considering the contribution of the molecular size to the binding energy.

Receptor-Flexible Docking on the NCI Library

The virtual screening process in the receptor-flexible docking path was similar to that of the receptor-rigid situation, except that four residues were allowed to be flexible during docking. By inspecting potential interactions in the active site of Mpro involved in the binding of ligands, we defined H41, M49, N142 and Q189 as the four flexible

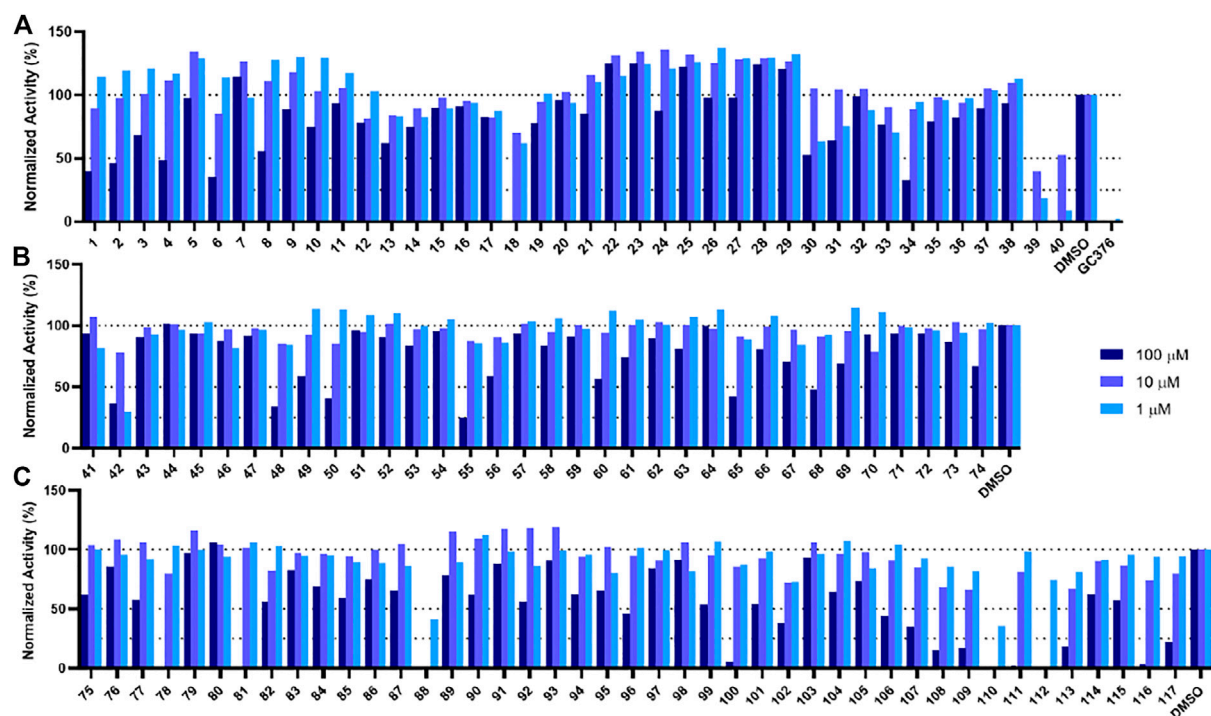


FIGURE 4 | Initial screening of Mpro inhibition by selected compounds from docking. Tested compounds are selected from (A) the batch selected with affinity from receptor-rigid docking, (B) the batch selected with binding energy vs. molecular weight from receptor-rigid docking, and (C) the batch selected from receptor-flexible docking. 100, 10 and 1 μM were used for each inhibitor to perform the inhibition assay. Fluorescence intensity was monitored with respect to the control that had no inhibitor provided.

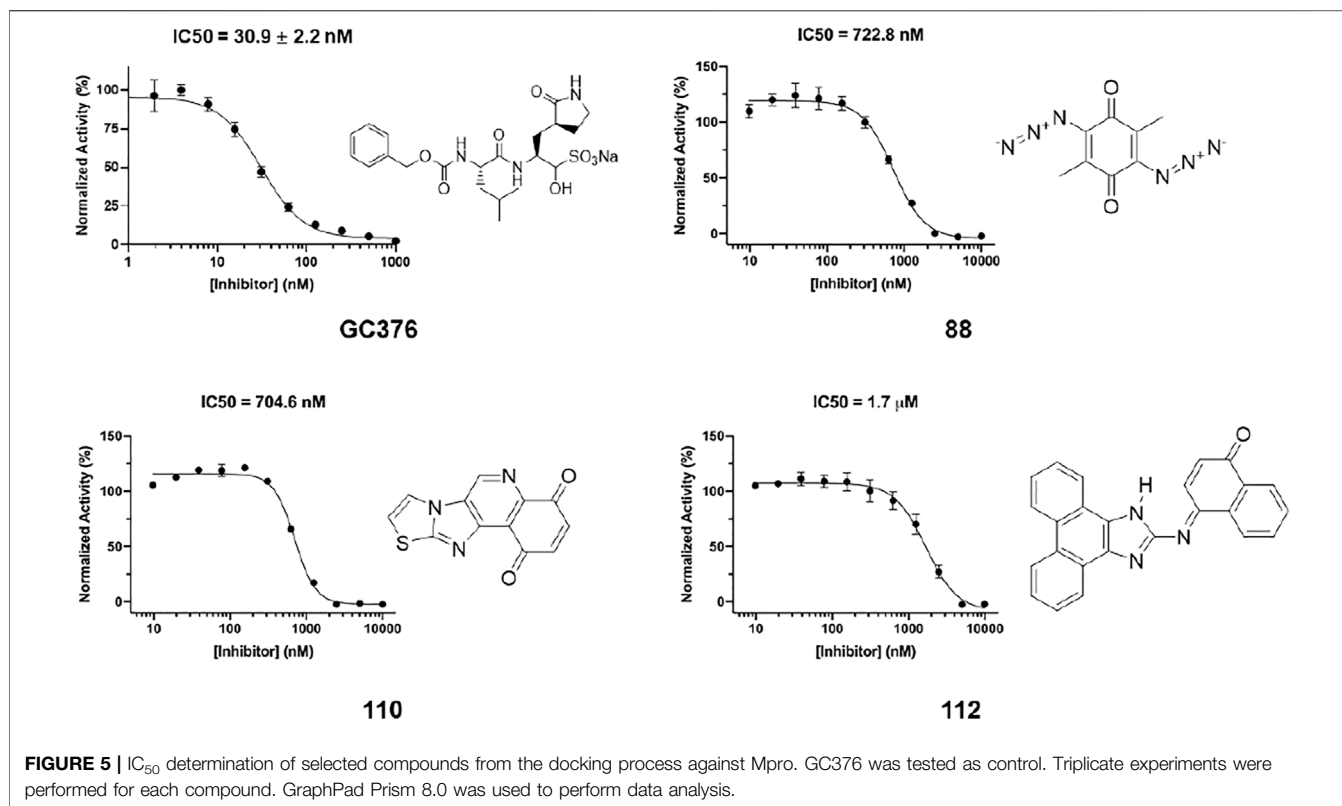
residues. We obtained docking structures for 232,304 compounds and then ranked them based on their top binding energy. We analyzed 19,235 receptor-flexible docking results with molecular weights smaller than 400 Da and binding energy below -8 kcal/mol (Table 2). When compared to Receptor-Rigid docking, Receptor-Flexible docking resulted in more compounds with binding energy below -9 kcal/mol. This indicates that Receptor-Flexible docking may increase the chance to identify potential potent compounds for mimicking the solvent state of Mpro.

We observed that the number of promising hit candidates for further manual screening (2,852) is far more than that of receptor-rigid docking (342). In order to further narrow down the range of compound candidates, we further analyzed the distribution of binding energy vs. the molecular surface area (Figure 3). Here, we regard the molecular surface area as a more reliable metric than the molecular weight to measure the compound size. Most virtual screening programs calculate binding energy between a target and a ligand based on their potential van der Waals and other interactions that are heavily influenced by the compound size. The NCI library has a large compound library size that can be potentially statistically analyzed to reduce artificial influence on the binding energy by the compound size. By statistically analyzing binding energy vs. the molecular size, it can potentially allow us to obtain compounds with binding energy below the average level of each surface area group, and thus minimize potential artificial effects of the compound size in contributing to calculated binding energy. 252 compounds with molecular surface area smaller than

800 \AA^2 were selected with binding energy outside $+3$ standard deviations of the distribution of their corresponding surface area groups. We use 800 \AA^2 as a surface area cutting line since molecules with surface area bigger than 800 \AA^2 will be difficult for structure-activity relationship studies. Manual screening was also applied based on the chemical correctness, pocket fitting, and hydrophobic criteria outlined above. 43 compounds were selected and requested from NCI for further *in vitro* potency testing.

Potency Screening and IC_{50} Determination for Selected Compounds From Receptor-Rigid Docking

In order to test the potency of selected compounds from the rigid model-based molecular docking, two batches of a total of 74 compounds were requested from NCI. The first batch contained 40 compounds which were selected based on just binding energy (below -9 kcal/mol), and the second batch contained 34 compounds which were selected based on the relationship between binding energy and molecular weight. These compounds were dissolved in DMSO to a concentration of 10 mM and stored at -20°C for further usage. The potency of selected compounds was screened at a concentration of 100 μM , 10 and 1 μM . First, the inhibitors were incubated with 50 nM Mpro at 37°C for 30 min. Then the reaction was initiated by adding 100 μM of a fluorescent substrate Sub3 (Vatansever et al., 2021a). The assay was monitored by a plate reader with Ex336/Em455 for 30 min. The first 10 min was fitted with



linear regression by GraphPad Prism. The initial slope value was used as normalized activity. GC376 was tested as a control (Yang et al., 2021). As shown in **Figure 4A**, at 100 μM, 8 out of 40 compounds displayed more than 50% inhibition of the activity of Mpro (Compounds 1, 2, 4, 6, 18, 34, 39, and 40). These 8 compounds were subjected to a more thorough IC₅₀ assay (**Supplementary Figure S2**). Five compounds had a determined IC₅₀ value below 100 μM. Notably, compounds 39 and 40 show potent inhibition with IC₅₀ values as 17.9 and 19.4 μM, respectively (**Supplementary Figure S5, Supplementary Table S1**). In the batch with the molecular weight considered (**Figure 4B**), 6 out of 34 compounds exhibited more than 50% inhibition of Mpro activity (Compounds 42, 48, 50, 55, 65, 68). 4 out of these 6 compounds had an IC₅₀ value below 100 μM. If we consider the hits rate as IC₅₀ less than 50 μM, the average hit rate for rigid-docking is about 2.7%. All the tested compound structures can be found in **Supplementary Figure S1**, and docking poses of potent compounds are shown in **Supplementary Figure S3**. Our results clearly showed that by taking the contribution of the molecular size to the calculated binding energy into account, additional compounds with high potency can be identified.

Potency Screening and IC₅₀ Determination for Selected Compounds From Receptor-Flexible Docking

In order to test the potency of selected compounds from flexible model-based molecular docking, 43 selected compounds were

requested from NCI. The same protocol as the rigid-model docking batch was applied. The initial 100 μM screening shows 16 compounds out of 43 suppressed the activity of Mpro by more than 50% (**Figure 4C**). Those compounds which inhibited activity more than 75% were subjected to an IC₅₀ test (**Supplementary Figure S2**). Eleven compounds out of 12 had an IC₅₀ of less than 100 μM, 7 compounds had an IC₅₀ value less than 50 μM. The hit rate for this batch is 16% (7/43), which is dramatically higher than the rigid-model docking result. This result indicates that the flexible docking method significantly increases the hit candidate rate and lowers the percentage of false positives. Compounds 78, 88, 109, 110, 111 and 112 showed potent IC₅₀ values of 13.3, 0.723, 12.8, 0.705, 10.3 and 1.69 μM respectively (**Figure 5, Supplementary Figure S2, Supplementary Table S1**). These 6 compounds exhibit critical and competitive potency *in vitro* when compared to current non-covalent Mpro inhibitors. Among them, compounds 88, 110 and 112 could covalently react with the active site C145 of Mpro. Considering these three compounds are all quinones that could oxidize the catalytic cysteine of Mpro instead of binding, we test all of them on another cysteine protease of SARS-CoV-2, PLpro. The results should show that these three compounds are more selective on Mpro than PLpro, and confirm that at least compound 88 and 110 specifically inhibit the activity of Mpro (**Supplementary Figure S4**). All the tested compound structures can be found in **Supplementary Figure S1**, and docking poses of potent compounds are shown in **Supplementary Figure S3**. Our results clearly demonstrated that the combination of flexible model-based docking and the statistical analysis of binding energy vs. molecular size to identify molecules with high binding energy deviation from the

average binding energy of its belonged group is an optimal approach to narrow down compound candidates with high potency.

CONCLUSION

Since 2003, there have been three coronavirus disease outbreaks. Researchers have predicted that additional coronavirus diseases will emerge with higher frequency. For both combating the current pandemic and preparing to contain future coronavirus disease outbreaks, it is imperative to develop small molecule antivirals that can be applied generally to inhibit coronaviruses. Due to its conserveness among coronaviruses, Mpro is an attractive drug target for broad-spectrum antivirals. In this study, we performed both Receptor-Rigid docking and Receptor-Flexible docking on the NCI compound collection that contains 284,176 compounds. The docking results were further processed using a refined strategy. The binding energy *vs.* molecular weight filter was applied to the receptor-rigid docking results, and the binding affinity *vs.* surface area filter was applied to the receptor-flexible docking results. After docking, individual inspection was conducted based on the chemical correctness, pocket fitting and hydrophobic criteria. We show that this strategy has significantly increased the accuracy rate compared to the standard virtual screening method, which only ranks by binding energy. The feasibility of our approach has been validated by the *in vitro* potency testing results, which led to the identification of several potent inhibitors. Two inhibitors have IC₅₀ values below 1 μ M, making them among most potent Mpro inhibitors that have been discovered so far. Almost all inhibitors that have been discovered in this study are reported for the first time. Their mechanisms of action need to be explored for aiding structure-activity relationship studies to identify more potent inhibitors with drug-like features as preclinical candidates for COVID-19.

Although the enhanced hybrid screening approach has been successfully developed and applied in searching for potent drug candidates, there are still some challenges that need to be conquered as well as improvement that could be explored in the following research. First, the outcome of receptor-flexible docking relies on the residues chosen. The four residues we choose in this paper are based on our previous crystallographic structure study of Mpro (Yang et al., 2021). Better understanding of the interactions between target and inhibitors will be critical in making the choices of residues for flexible docking. Second, the individual inspection dramatically relied on personal experience and knowledge. Finding a method to precisely evaluate the potential potency of inhibitors instead of using manual inspection will be a good future exploration. Third, *in vitro* screens and IC₅₀ tests for large amounts of potential compounds are a time- and labor-consuming step. A more efficient way, such as incorporation of high throughput screening, would significantly accelerate the *in vitro* potency test.

MATERIALS AND METHODS

Chemicals

All compounds used in this study were requested from The Developmental Therapeutics Program (DTP) of National

Cancer Institute (NCI) without further purification and characterization (Monga and Sausville, 2002).

Protein Preparation of SARS-CoV-2 Mpro

The crystal structure of the SARS-CoV-2 Mpro in complex with an N3 inhibitor (PDB ID: 6LU7) was obtained from the RCSB Protein Data Bank (<https://www.rcsb.org/>). Only chain A of the structure was used in our docking-based virtual screening studies. The cognate ligand was extracted from the structure. In AutoDockTools-1.5.7 (Sanner, 1999; Morris et al., 2009), water molecules were deleted, and polar hydrogens were added to the structure. Finally, the prepared protein structure was converted into a PDBQT file for further receptor-rigid docking studies.

In addition to receptor-rigid docking, we also conducted receptor-flexible docking, which was motivated by our two observations. One is that residues Met49 and Asn142 were observed to cause significant conformation changes at the active site. The other one is that residues His41 and Gln189 were observed to form important interactions with inhibitors (Yang et al., 2021). Considering these structural characteristics, we made side chains of residues Met49, Asn142, His41 and Gln189 flexible. Similarly, we used AutoDockTools-1.5.7 (Sanner, 1999; Morris et al., 2009) to delete water molecules, add polar hydrogens, and then split the receptor into a rigid part and a flexible part. Both of the prepared rigid part and the flexible part of the protein structure were converted into PDBQT files for further receptor-flexible docking studies.

Ligand Preparation of NCI Open Chemicals Repository

The DTP of NCI maintains a repository with synthetic compounds and pure natural products that are available at no cost to investigators for non-clinical research purposes (Monga and Sausville, 2002). The repository collection is a uniquely diverse set of more than 200,000 compounds. A collection of 284,176 2D compound structures in SDF format are also provided. We converted these 2D SDF files into 3D PDBQT files using OpenBabel-3.1.1 (O'Boyle et al., 2011) with the "--gen3d dg" option. A total of 279,442 compounds were successfully converted.

Docking Parameters and Method

In addition to receptor and ligand preparations, AutoDockTools-1.5.7 (Sanner, 1999; Morris et al., 2009) was also used for grid parameter setting. The cognate ligand of crystal structure 6LU7 suggested the inhibitor binding site. A grid box with dimensions 30 \times 30 \times 30 centered at the coordinates X = -10.0, Y = 13.0, and Z = 70.0 was used to represent the search space. Then we applied AutoDock Vina (Trott et al., 2010) docking protocol with options of 8 CPUs to use and maximum 20 binding modes to generate. Only the top binding energy and binding modes were shown in this paper. In order to speed up the virtual screening process, the commands for both compound format conversion and molecular docking of 279,442 compounds were distributed among more than 6,000 requested CPUs from Texas A&M High Performance Research Computing Clusters.

Recombinant Mpro Protein Expression and Purification

The pET28a-His-SUMO-Mpro construct was made based on a pET28a plasmid modified with an N-terminal His-SUMO tag. The gene encoding Mpro was amplified from a previous plasmid pBAD-sfGFP-Mpro using the forward primer 5'-CGCGGATCCGGGTTTCGCAAG-3' and the reverse primer 5'-CCGCTCGAGTTACTGAAAAGTTACGCC-3'. The amplified PCR product was digested by *Bam*HI and *Xho*I and ligated into the vector pET28a-His-SUMO plasmid that was digested with the same restriction enzymes. The gene sequence of His-SUMO-Mpro was verified by sequencing at Eton Bioscience Inc.

The pET28a-His-SUMO-Mpro construct was transformed into *E. coli* BL21 (DE3) cells. Transformed cells were cultured at 37°C in 6 L 2xYT medium with kanamycin (50 g/ml) for 3 h and induced with isopropyl-D-1-thiogalactoside (IPTG) at final concentration of 1 mM when the OD₆₀₀ reached 0.8. After 3 h, cells were harvested by centrifugation at 12,000 rpm, 4°C for 30 min. Cell pellets were resuspended in 150 ml buffer A (20 mM Tris, 100 mM NaCl, 10 mM imidazole, pH 8.0) and then lysed by sonication on ice. The lysate was clarified by centrifugation at 16,000 rpm, 4°C for 30 min. The supernatant was loaded onto a nickel-chelating column with high affinity Ni-charged resin from GenScript and washed with 10 column volumes of buffer A to remove unspecifically bound proteins, which was followed by elution using buffer B (20 mM Tris, 100 mM NaCl, 250 mM imidazole, pH 8.0). The protein eluates were subjected to buffer exchange with buffer C (20 mM Tris, 10 mM NaCl, 1 mM dithiothreitol (DTT), pH 8.0) by using a HiPrep 26/10 desalting column (GE Healthcare). The His-SUMO-Mpro proteins were digested with SUMO protease overnight at 4°C. The digested protein was applied to a nickel-chelating column again to remove the His-tagged SUMO protease, the His-SUMO tag, and the expressed protein with uncleaved His-SUMO tag. The tag-free Mpro protein was loaded onto an anion-exchange column with Q Sepharose, Fast Flow (GE Healthcare) equilibrated with buffer C for further purification. The column was eluted by buffer D (20 mM Tris, 1 M NaCl, 1 mM DTT, pH 8.0) with a linear gradient ranging from 0 to 500 mM NaCl. Fractions eluted from the anion exchange column were condensed and loaded to a size exclusion column with HiPrep 16/60 Sephacryl S-100 HR (GE Healthcare) pre-equilibrated with buffer E (20 mM Tris, 100 mM NaCl, 1 mM DTT, 1 mM EDTA, pH 7.8). The eluted Mpro protein in buffer E was concentrated to 20 mg/ml and stored in -80°C for further use.

IC₅₀ Analysis

The assays were carried out with 50 nM enzyme and 10 μM substrate at 37°C with continuous shaking. The Sub3 substrate (DABCYL-Lys-Thr-Ser-Ala-Val-Leu-Gln-Ser-Gly-Phe-Arg-Lys-Met-Glu-EDANS) was purchased from BACHEM and stored as 1 mM solution in 100% DMSO. Enzyme activity was monitored by detecting fluorescence with excitation at 336 nm and emission at 455 nm wavelength. The dilution buffer (used for enzyme and substrate dilution) is 10 mM Na_xH_yPO₄, 10 mM NaCl, 0.5 mM EDTA, pH 7.6. Final composition of the assay buffer is 10 mM

Na_xH_yPO₄, 10 mM NaCl, 0.5 mM EDTA, 2 μM DTT (coming from enzyme stock solution), pH 7.6 with 1.25% DMSO. All inhibitors were stored as 10 mM in 100% DMSO solutions in a -20°C freezer.

For the IC₅₀ analysis, the inhibitor was diluted to 400-fold times higher than the highest working concentration to make the secondary stock solution (i.e., if the highest working concentration of inhibitor is 2 μM, then the inhibitor was diluted from its 10 mM stock solution to 800 μM in DMSO). 10 μL from this secondary stock solution was added to 990 μL of the dilution buffer. Serial dilutions were carried out in the dilution buffer containing 1% DMSO to ensure all the inhibitor serial dilutions contained 1% DMSO. 25 μL of each inhibitor solution were added to a 96-well plate with a multichannel pipettor. Next, 25 μL of a 200 nM enzyme solution (diluted from 10 μM enzyme storage solution in 10 mM Na_xH_yPO₄, 10 mM NaCl, 0.5 mM EDTA, pH 7.6, 1 mM DTT in the dilution buffer) was added by a multichannel pipettor and mixed by pipetting up and down three times. Then, the enzyme-inhibitor solution was incubated at 37°C for 30 min. During the incubation period, 20 μM of the substrate solution was prepared by diluting from 1 mM stock solution in the dilution buffer. When the incubation period was over, 50 μL of the 20 μM substrate solution was added to each well using a multichannel pipettor and the assay started. Data recording was stopped after 30 min. Data treatment was done with GraphPad Prism 8.0. The first 0–300 s were analyzed by linear regression for initial slope analyses. Then, the initial slopes were normalized and IC₅₀ values were determined by inhibitor vs response - Variable slope (four parameters).

DATA AVAILABILITY STATEMENT

The raw data supporting the conclusions of this article will be made available by the authors, without undue reservation.

AUTHOR CONTRIBUTIONS

SX, HW, and WL designed the project and drafted the manuscript. SL did the virtual screening. KY, LB, and CC characterized identified compounds.

FUNDING

This work was supported in part by the Welch Foundation grant A-1715 and the Texas A&M X-Grants mechanism. Portions of this research were conducted with the advanced computing resources provided by Texas A&M High Performance Research Computing.

SUPPLEMENTARY MATERIAL

The Supplementary Material for this article can be found online at: <https://www.frontiersin.org/articles/10.3389/fchem.2022.816576/full#supplementary-material>

REFERENCES

- Astuti, I., and Ysrafil, Y. (2020). Severe Acute Respiratory Syndrome Coronavirus 2 (SARS-CoV-2): An Overview of Viral Structure and Host Response. *Diabetes Metab. Syndr. Clin. Res. Rev.* 14, 407–412. doi:10.1016/j.dsx.2020.04.020
- Bouback, T. A., Pokhrel, S., Albeshri, A., Aljohani, A. M., Samad, A., Alam, R., et al. (2021). Pharmacophore-Based Virtual Screening, Quantum Mechanics Calculations, and Molecular Dynamics Simulation Approaches Identified Potential Natural Antiviral Drug Candidates against MERS-CoV S1-NTD. *Molecules* 26. doi:10.3390/molecules26164961
- Cheng, V. C. C., Lau, S. K. P., Woo, P. C. Y., and Yuen, K. Y. (2007). Severe Acute Respiratory Syndrome Coronavirus as an Agent of Emerging and Reemerging Infection. *Clin. Microbiol. Rev.* 20, 660–694. doi:10.1128/cmr.00023-07
- de Groot, R. J., Baker, S. C., Baric, R. S., Brown, C. S., Drosten, C., Enjuanes, L., et al. (2013). Middle East Respiratory Syndrome Coronavirus (MERS-CoV): Announcement of the Coronavirus Study Group. *J. Virol.* 87, 7790–7792. doi:10.1128/jvi.01244-13
- Gates, B. (2020). Responding to Covid-19 - A Once-In-A-Century Pandemic. *N. Engl. J. Med.* 382, 1677–1679. doi:10.1056/nejmp2003762
- Helmy, Y. A., Fawzy, M., Elswad, A., Sobieh, A., Kenney, S. P., and Shehata, A. A. (2020). The COVID-19 Pandemic: A Comprehensive Review of Taxonomy, Genetics, Epidemiology, Diagnosis, Treatment, and Control. *J. Clin. Med.* 9. doi:10.3390/jcm9041225
- Huang, C., Wang, Y., Li, X., Ren, L., Zhao, J., Hu, Y., et al. (2020). Clinical Features of Patients Infected with 2019 Novel Coronavirus in Wuhan, China. *The Lancet* 395, 497–506. doi:10.1016/s0140-6736(20)30183-5
- Jang, W. D., Jeon, S., Kim, S., and Lee, S. Y. (2021). Drugs Repurposed for COVID-19 by Virtual Screening of 6,218 Drugs and Cell-Based Assay. *Proc. Natl. Acad. Sci. U S A.* 118. doi:10.1073/pnas.2024302118
- Jin, Z., Du, X., Xu, Y., Deng, Y., Liu, M., Zhao, Y., et al. (2020). Structure of Mpro from SARS-CoV-2 and Discovery of its Inhibitors. *Nature* 582, 289–293. doi:10.1038/s41586-020-2223-y
- Khan, J., Sakib, S. A., Mahmud, S., Khan, Z., Islam, M. N., Sakib, M. A., et al. (2021). Identification of Potential Phytochemicals from Citrus Limon against Main Protease of SARS-CoV-2: Molecular Docking, Molecular Dynamic Simulations and Quantum Computations. *J. Biomol. Struct. Dyn.*, 1–12. doi:10.1080/07391102.2021.1947893
- Lee, N., Hui, D., Wu, A., Chan, P., Cameron, P., Joynt, G. M., et al. (2003). A Major Outbreak of Severe Acute Respiratory Syndrome in Hong Kong. *N. Engl. J. Med.* 348, 1986–1994. doi:10.1056/nejmoa030685
- Mahmud, S., Biswas, S., Paul, G. K., Mita, M. A., Promi, M. M., Afrose, S., et al. (2021). Plant-Based Phytochemical Screening by Targeting Main Protease of SARS-CoV-2 to Design Effective Potent Inhibitors. *Biology (Basel)* 10. doi:10.3390/biology10070589
- Mahmud, S., Paul, G. K., Afrose, M., Islam, S., Gupta, S. B. R., Razu, M. H., et al. (2021). Efficacy of Phytochemicals Derived from *Avicennia officinalis* for the Management of COVID-19: A Combined In Silico and Biochemical Study. *Molecules* 26. doi:10.3390/molecules26082210
- Monga, M., and Sausville, E. (2002). Developmental Therapeutics Program at the NCI: Molecular Target and Drug Discovery Process. *Leukemia* 16, 520–526. doi:10.1038/sj.leu.2402464
- Morens, D. M., Daszak, P., and Taubenberger, J. K. (2020). Escaping Pandora's Box - Another Novel Coronavirus. *N. Engl. J. Med.* 382, 1293–1295. doi:10.1056/nejmp2002106
- Morris, G. M., Huey, R., Lindstrom, W., Sanner, M. F., Belew, R. K., Goodsell, D. S., et al. (2009). AutoDock4 and AutoDockTools4: Automated Docking with Selective Receptor Flexibility. *J. Comput. Chem.* 30, 2785–2791. doi:10.1002/jcc.21256
- Morse, J. S., Lalonde, T., Xu, S., and Liu, W. R. (2020). Learning from the Past: Possible Urgent Prevention and Treatment Options for Severe Acute Respiratory Infections Caused by 2019-nCoV. *Chembiochem* 21, 730–738. doi:10.1002/cbic.202000047
- O'Boyle, N. M., Banck, M., James, C. A., Morley, C., Vandermeersch, T., and Hutchison, G. R. (2011). Open Babel: An Open Chemical Toolbox. *J. Cheminform* 3, 33. doi:10.1186/1758-2946-3-33
- Rakib, A., Paul, A., Chy, M. N. U., Sami, S. A., Baral, S. K., Majumder, M., et al. (2020). Biochemical and Computational Approach of Selected Phytocompounds from *Tinospora Crispa* in the Management of COVID-19. *Molecules* 25. doi:10.3390/molecules25173936
- Rakib, A., Nain, Z., Sami, S. A., Mahmud, S., Islam, A., Ahmed, S., et al. (2021). A Molecular Modelling Approach for Identifying Antiviral Selenium-Containing Heterocyclic Compounds that Inhibit the Main Protease of SARS-CoV-2: an In Silico Investigation. *Brief. Bioinform.* 22, 1476–1498. doi:10.1093/bib/bbab045
- Sanner, M. F. (1999). Python: a Programming Language for Software Integration and Development. *J. Mol. Graph Model.* 17, 57–61.
- Trott, O., Olson, A. J., and Vina, A. D. (2010). AutoDock Vina: Improving the Speed and Accuracy of Docking with a New Scoring Function, Efficient Optimization, and Multithreading. *J. Comput. Chem.* 31, 455–461. doi:10.1002/jcc.21334
- V'Kovski, P., Kratzel, A., Steiner, S., Stalder, H., and Thiel, V. (2021). Coronavirus Biology and Replication: Implications for SARS-CoV-2. *Nat. Rev. Microbiol.* 19, 155–170.
- Vatansever, E. C., Yang, K. S., Drelich, A. K., Kratch, K. C., Cho, C.-C., Kempaiah, K. R., et al. (2021). Bepridil Is Potent against SARS-CoV-2 In Vitro. *Proc. Natl. Acad. Sci. USA* 118, e2012201118. doi:10.1073/pnas.2012201118
- Vatansever, E. C., Yang, K. S., Drelich, A. K., Kratch, K. C., Cho, C. C., Kempaiah, K. R., et al. (2021). Bepridil Is Potent against SARS-CoV-2 In Vitro. *Proc. Natl. Acad. Sci. U S A.* 118. doi:10.1073/pnas.2012201118
- Vilar, S., and Isom, D. G. (2021). One Year of SARS-CoV-2: How Much Has the Virus Changed. *Biology (Basel)* 10. doi:10.3390/biology10020091
- Wang, Y., Zhang, D., Du, G., Du, R., Zhao, J., Jin, Y., et al. (2020). Remdesivir in Adults with Severe COVID-19: a Randomised, Double-Blind, Placebo-Controlled, Multicentre Trial. *The Lancet* 395, 1569–1578. doi:10.1016/s0140-6736(20)31022-9
- WHO (2022). *WHO Coronavirus (COVID-19) Dashboard*.
- Yang, K. S., Ma, X. R., Ma, Y., Alugubelli, Y. R., Scott, D. A., Vatansever, E. C., et al. (2021). A Quick Route to Multiple Highly Potent SARS-CoV-2 Main Protease Inhibitors. *ChemMedChem* 16, 942–948. doi:10.1002/cmdc.202000924
- Zaki, A. M., van Boheemen, S., Bestebroer, T. M., Osterhaus, A. D. M. E., and Fouchier, R. A. M. (2012). Isolation of a Novel Coronavirus from a Man with Pneumonia in Saudi Arabia. *N. Engl. J. Med.* 367, 1814–1820. doi:10.1056/nejmoa1211721

Conflict of Interest: The authors declare that the research was conducted in the absence of any commercial or financial relationships that could be construed as a potential conflict of interest.

Publisher's Note: All claims expressed in this article are solely those of the authors and do not necessarily represent those of their affiliated organizations, or those of the publisher, the editors and the reviewers. Any product that may be evaluated in this article, or claim that may be made by its manufacturer, is not guaranteed or endorsed by the publisher.

Copyright © 2022 Li, Yang, Blankenship, Cho, Xu, Wang and Liu. This is an open-access article distributed under the terms of the Creative Commons Attribution License (CC BY). The use, distribution or reproduction in other forums is permitted, provided the original author(s) and the copyright owner(s) are credited and that the original publication in this journal is cited, in accordance with accepted academic practice. No use, distribution or reproduction is permitted which does not comply with these terms.



Potential Inhibitors Targeting Papain-Like Protease of SARS-CoV-2: Two Birds With One Stone

Haihai Jiang^{1*†}, Peiyao Yang^{2†} and Jin Zhang^{1*}

¹School of Basic Medical Sciences, Nanchang University, Nanchang, China, ²Queen Mary School, Nanchang University, Nanchang, China

OPEN ACCESS

Edited by:

Jun Wang,
The State University of New Jersey,
United States

Reviewed by:

Jerry M. Parks,
Oak Ridge National Laboratory (DOE),
United States
M. Joanne Lemieux,
University of Alberta, Canada

*Correspondence:

Haihai Jiang
haihaijiang2020@ncu.edu.cn
Jin Zhang
zhangxiaokong@hotmail.com

[†]These authors contribute equally to
this work

Specialty section:

This article was submitted to
Medicinal and Pharmaceutical
Chemistry,
a section of the journal
Frontiers in Chemistry

Received: 26 November 2021

Accepted: 28 January 2022

Published: 23 February 2022

Citation:

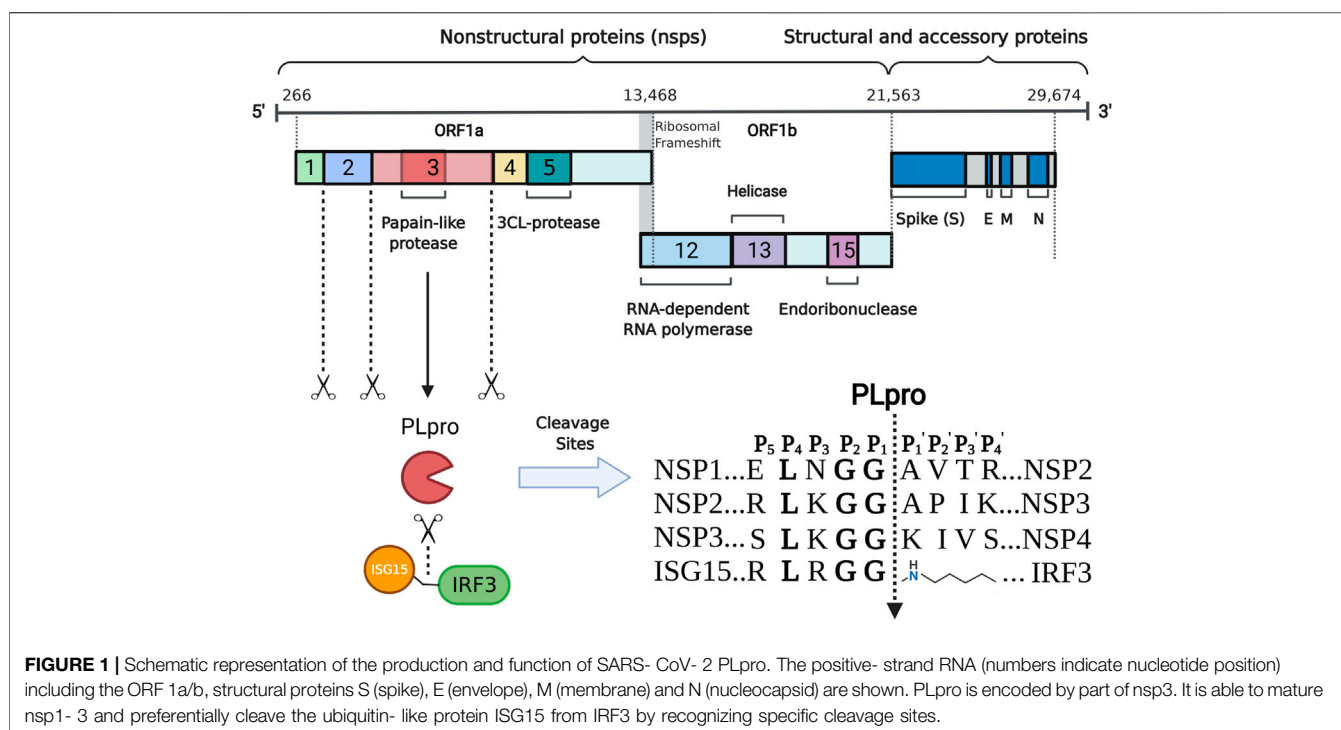
Jiang H, Yang P and Zhang J (2022)
Potential Inhibitors Targeting Papain-
Like Protease of SARS-CoV-2: Two
Birds With One Stone.
Front. Chem. 10:822785.
doi: 10.3389/fchem.2022.822785

Severe acute respiratory syndrome Coronavirus-2 (SARS-CoV-2), the pathogen of the Coronavirus disease-19 (COVID-19), is still devastating the world causing significant chaos to the international community and posing a significant threat to global health. Since the first outbreak in late 2019, several lines of intervention have been developed to prevent the spread of this virus. Nowadays, some vaccines have been approved and extensively administered. However, the fact that SARS-CoV-2 rapidly mutates makes the efficacy and safety of this approach constantly under debate. Therefore, antivirals are still needed to combat the infection of SARS-CoV-2. Papain-like protease (PLpro) of SARS-CoV-2 supports viral reproduction and suppresses the innate immune response of the host, which makes PLpro an attractive pharmaceutical target. Inhibition of PLpro could not only prevent viral replication but also restore the antiviral immunity of the host, resulting in the speedy recovery of the patient. In this review, we describe structural and functional features on PLpro of SARS-CoV-2 and the latest development in searching for PLpro inhibitors. Currently available inhibitors targeting PLpro as well as their structural basis are also summarized.

Keywords: COVID-19, SARS-CoV-2, papain-like protease, inhibitor, crystal structure

INTRODUCTION

Severe acute respiratory syndrome coronavirus 2 (SARS-CoV-2), causing the coronavirus disease 2019 (COVID-19) (Wu F. et al., 2020; Zhu et al., 2020), is the third highly pathogenic human coronavirus in this century after the SARS-CoV emerged in 2003 (Stadler et al., 2003) and the Middle East Respiratory Syndrome Coronavirus (MERS-CoV) emerged in 2012 (Chafekar and Fielding, 2018). Although it has a relatively lower mortality rate, SARS-CoV-2 exhibits a higher transmission efficiency compared to SARS-CoV and MERS-CoV (Madewell et al., 2020; Patel et al., 2020). The rapid spread of SARS-CoV-2 has continued to cause a worldwide pandemic and posed a serious threat to global public health since the beginning of 2020. The SARS-CoV-2 infection mostly affects the lungs and causes symptoms of varying degrees of morbidity, ranging from asymptomatic infection to mild infection with flu-like illness or severe infection with lung injury (Chen et al., 2020; Huang et al., 2020; Wang et al., 2020). COVID-19 outbreak has resulted in over 320 million confirmed cases as of 16 January 2022, including nearly 5.5 million deaths (<https://www.who.int/publications/m/item/weekly-epidemiological-update-on-covid-19-18-january-2022>). Though vaccines have been administered on a large scale, this viral disease is far from being controlled, in particular, due to the occurrence of cumulative mutations. Given the ongoing pandemic and disruptive



impact, there is still an urgent need to develop new antiviral strategies for the prompt and effective therapy of SARS-CoV-2 infection.

SARS-CoV-2 is an enveloped, single-stranded, and positive-sense RNA virus (+ssRNA) which belongs to the *Coronaviridae* family (Khailany et al., 2020; Zhou et al., 2020). Coronaviruses can be divided into four groups indicated with the Greek letters α , β , γ , and δ , respectively (Su et al., 2016). Along with the newly emerged SARS-CoV-2, seven coronaviruses are currently able to infect humans, among which HCoV-NL63 and HCoV-229E belong to α coronavirus, while the others (HCoV-HKU1, HCoV-OC43, SARS-CoV, MERS-CoV, and SARS-CoV-2) belong to β coronavirus (Ye et al., 2020). Similar to other human coronaviruses, the genome of SARS-CoV-2 has two open reading frames that encode two replicase polyproteins, namely pp1a and pp1ab. The polyproteins are digested into sixteen mature non-structural proteins (nsp1-16) by two cysteine proteases, chymotrypsin-like protease (3CLpro or Mpro) encoded by nsp5 and papain-like protease (PLpro) encoded by nsp3. Mpro cleavage results in the releasing of the functional nsp4-16, while PLpro cleavage results in the maturation of nsp1-3 (Fehr and Perlman, 2015).

Importantly, SARS-CoV-2 PLpro possesses additional function of inhibiting interferon related antiviral responses of the host (Klemm et al., 2020; Shin et al., 2020). Given that SARS-CoV-2 causes a substantially higher mortality rate in elderly patients with compromised immune systems (Ruan 2020; Wu and McGoogan 2020), viral factors that mitigate or evade from immune responses are desirable drug targets. Thus, therapy by targeting SARS-CoV-2 PLpro can not only suppress viral infection but also promote antiviral immunity, which is

similar to killing two birds with one stone. Herein, this review updates the recent research progress in the structure and function of SARS-CoV-2 PLpro and the discovery of PLpro inhibitors against COVID-19.

STRUCTURAL AND FUNCTIONAL FEATURES OF SARS-COV-2 PLPRO

The genome of SARS-CoV-2 is approximately 30 kb in size and contains at least 12 open reading frames (ORF) that flanked by 5'-cap and 3'-poly(A) tail (Wu A. et al., 2020; Zhang RH. et al., 2020). The 3'-terminal one-thirds of the SARS-CoV-2 genome encodes four structural proteins (spike protein, envelope protein, membrane protein, and nucleocapsid protein) and several accessory proteins, while two-thirds of the SARS-CoV-2 genome at the 5'-terminal encodes two replicase polyproteins, namely pp1a (about 450 KD) and pp1ab (about 750 KD) (Figure 1). These two polyproteins can be cleaved by virus-encoded PLpro and 3C-like protease into 16 non-structural proteins. Many of them are localized to the double membrane like vesicles and assemble into a replication complex on the cytoplasmic face of the endoplasmic reticulum (Knoops et al., 2008; Klein et al., 2020). PLpro is part of the largest non-structural protein nsp3 and is highly conserved (Lei et al., 2018). Often two copies, referred to as PL1pro and PL2pro, are found in coronaviruses and the two PLpros show distinct substrate specificity in different coronaviruses (Woo et al., 2010; Mielech et al., 2014). For example, PL1pro of mouse hepatitis virus processes between nsp1/2 and between nsp2/3, while PL2pro processes between nsp3/4 (Bonilla et al., 1997;

Kanjanahaluethai and Baker, 2000). In the case of HCoV-NL63, PL1pro cleaves between nsp1/2, while PL2pro cleaves between nsp2/3 and between nsp3/4 (Chen et al., 2007). However, like SARS-CoV and MERS-CoV, only one functional PLpro is encoded in SARS-CoV-2. After being released from nsp3 through autocleavage, SARS-CoV-2 PLpro recognizes the common motif LXGG(A/K)X between nsp1/2, nsp2/3, and nsp3/4 (X represents any type of amino acid) and cleaves between glycine and alanine/lysine residues (Anirudhan et al., 2021), which is essential for coronavirus RNA synthesis and viral survival (Shamsi et al., 2021; Yadav et al., 2021). Enzyme activity analysis revealed that the S2 site of PLpro strictly recognizes glycine and the S4 site preferentially recognizes amino acids with hydrophobic side chains, while the S3 site has broader substrate specificity and can recognize any type of amino acid (Rut et al., 2020).

Beyond the role in cleaving the viral polypeptide, PLpro also participates in regulating host antiviral innate immunity through antagonising ubiquitin and ubiquitin-like modifications (Shin et al., 2020; Klemm et al., 2020). The host elicits various defense strategies to thwart viral infection. During viral invasion, the host could recognize the specific viral components through pattern recognition receptors and subsequently produce type I interferon and proinflammatory cytokines to establish the first line of host defense against viral infection. Ubiquitins and ubiquitin-like protein ISG15, an interferon-induced protein, are important post-translation modifying processes and have emerged as crucial players at this stage (Zheng and Gao, 2019; Zheng and Gao, 2020; Perng and Lenschow, 2018; McClain and Vabret, 2020). In response, virus often repurposes its protease to evade host antiviral immunity through deubiquitinating and deISGylating activities (James et al., 2011; Swatek et al., 2018). In the case of SARS-CoV-2, PLpro can remove ubiquitin and ISG15 modifications from host proteins by cleaving the consensus site (LXGG) (Figure 1) (Swaim et al., 2020). Similar to SARS-CoV PLpro, SARS-CoV-2 PLpro shows detectable activity for K48-linked ubiquitin chains but not K63, even though at a substantially slower rate (Freitas et al., 2020; Rut et al., 2020; Shin et al., 2020). Unlike SARS-CoV PLpro that predominantly cleaves K48 ubiquitin chains, PLpro of SARS-CoV-2 shows an enhanced deISGylation activity (Freitas et al., 2020; Rut et al., 2020; Shin et al., 2020). However, the deISGylation activity is sensitive to species-species differences (Freitas et al., 2020). SARS-CoV-2 PLpro appears to prefer ISG15s from sheep and the vesper bat, but shows no protease activity for the ISG15 substrate from fish. The deISGylase activities are moderate for ISG15s from human, pig, camel, and mouse, while weak for ISG15s from Egyptian fruit bat, hedgehog, and northern tree shrew. The preference of PLpro in processing ISG15 substrates may indicate the species that SARS-CoV-2 can productively infect.

Recently, the crystal structure of the 315-residue SARS-CoV-2 PLpro has been solved (Osipiuk et al., 2021). Similar to PLpros of SARS-CoV and MERS-CoV, SARS-CoV-2 PLpro contains a ubiquitin-like domain at N-terminal and a catalytic domain at C-terminal, which can be divided into three subdomains, namely thumb, palm and finger subdomains (Figure 2A). The catalytic site of SARS-CoV-2 PLpro contains a classical catalytic triad, consisting

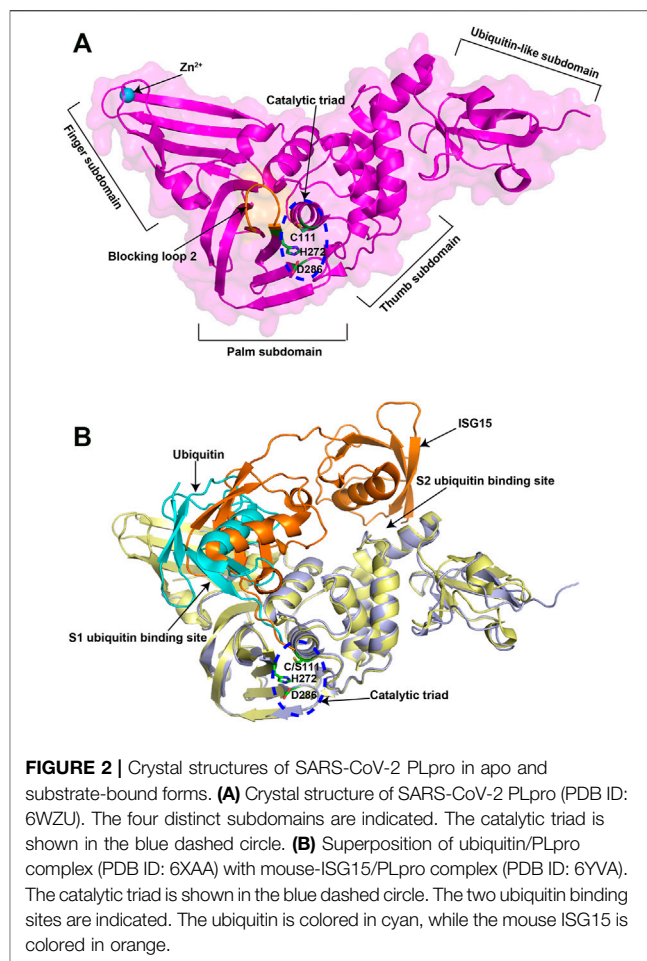


FIGURE 2 | Crystal structures of SARS-CoV-2 PLpro in apo and substrate-bound forms. **(A)** Crystal structure of SARS-CoV-2 PLpro (PDB ID: 6WZU). The four distinct subdomains are indicated. The catalytic triad is shown in the blue dashed circle. **(B)** Superposition of ubiquitin/PLpro complex (PDB ID: 6XAA) with mouse-ISG15/PLpro complex (PDB ID: 6YVA). The catalytic triad is shown in the blue dashed circle. The two ubiquitin binding sites are indicated. The ubiquitin is colored in cyan, while the mouse ISG15 is colored in orange.

of Cys111, His273, and Asp287, and is situated at the interface between thumb and palm subdomains. A 6-amino-acid (267–272 residues) flexible loop named blocking loop 2 (BL2) near the catalytic site plays an important role in controlling the access to the active site (Ratia et al., 2008). The finger subdomain contains a zinc-ribbon region and zinc ion binding is necessary for enzyme catalysis and structural integrity of PLpro (Tian et al., 2021; Zhao et al., 2021).

PLpro possesses two ubiquitin binding sites (S1 and S2) for the recognition of its substrates, ubiquitin and ISG15, with the structural basis of which has also been elucidated (Klemm et al., 2020; Shin et al., 2020). S1 ubiquitin binding site recognizes the C-terminal domain of ISG15 through a different binding orientation compared with ubiquitin (Figure 2B). S2 ubiquitin binding site not only recognizes the N-terminal domain of ISG15, but also provides exquisite specificity for the distal ubiquitin of K48-linked diubiquitin chains. Residue Phe69 and Thr75 in the S2 ubiquitin-binding site are key amino acids for PLpro to interact with Ile44 in ISG15, which may contribute to the enhanced affinity for ISG15. However, these observations are based on the available structures of SARS-CoV-2 PLpro in complex with ubiquitin or mouse full-length ISG15. It would be of interest in future to determine the structure of human full-length ISG15 or K48-diubiquitin in complex with SARS-CoV-2 PLpro.

Nevertheless, these data reveal the 3D structures of PLpro at both apo state and substrate-binding state, which facilitates the PLpro based drug design. Molecules that mimic the hydrophobic interaction with SARS-CoV-2 PLpro observed in its substrates or alter the conformation of BL2 in the active site will affect the protease activity.

STRATEGIES IN PLPRO INHIBITOR DEVELOPMENT

Drug Repurposing

Drug repurposing refers to the discovery of new therapeutic uses of clinically available drugs. It is a prompt strategy in searching of medications for COVID-19 therapy since the traditional drug discovery process can be costly and takes decades to complete (Aherfi et al., 2021; Hijikata et al., 2021; Mslati et al., 2021; Shende et al., 2021). As repurposed drugs have gone through clinical trial, important parameters of these drugs, such as inhibitory potential, cell permeability, bio-availability, and safety, have been well characterized and can be available in a short time in face of pandemics (Pushpakom et al., 2019). Since the outbreak of COVID-19 in late December, 2019, drug repurposing has been employed to deal with this worldwide health emergency by targeting PLpro, even though such efforts were not as successful as hoped at the beginning of the pandemic.

The disclosure of high resolution crystal structures of SARS-CoV-2 PLpro has made virtual screening a useful strategy in drug repurposing (Gao et al., 2021; Ma et al., 2021; Osipiuk et al., 2021). In several studies, the crystal structure of SARS-CoV-2 PLpro was included in a molecular docking analysis to identify PLpro inhibitors (Choudhury et al., 2021; Hosseini et al., 2021). In addition, pharmacophore based screen is an alternative method to obtain potential inhibitors (Kouznetsova et al., 2020). Although virtual screening is a useful strategy for drug repurposing, further *in vitro* and *in vivo* tests are necessary to confirm its activities against SARS-CoV-2 PLpro.

High-throughput screening (HTS) is another useful strategy in drug repurposing. It selects the most promising candidates from a large number of molecules via experimental approaches. Smith et al. developed a cell-based luciferase complementation assay to evaluate the inhibition of known drugs against SARS-CoV-2 viral PLpro (Smith et al., 2020). Based on the fluorescence-based enzymatic inhibition assay, several groups have identified potential inhibitors of SARS-CoV-2 PLpro with the IC₅₀ value under 10 μ M (Cho et al., 2021; Xu et al., 2021; Zhao et al., 2021). Although not all the identified compounds exhibited good performance in a cell-based assay, they could serve as a starting point for further chemical modification.

Discovery of New Drug Leads

Discovery of new drug leads is an important step to develop a novel drug. It involves the employment of a wide range of technologies including virtual screening, high-throughput screening and structure-based drug design (Guido et al., 2011). These interdisciplinary expertises are complementary and comprehensive application of a variety of techniques in

identification of new lead compounds is feasible. The general process of leads identification includes two essential steps, namely hits generation and subsequent hits validation. Compared with drug repurposing, screenings for hit compounds, either *in vitro* or *in silico*, incorporate a much larger scale of molecules including microbial metabolites, natural products and marine-derived bio-active compounds (Cragg and Newman, 2013; Kumar et al., 2021; Quimque et al., 2021). Since the outbreak of COVID-19, the widespread use of combinatorial screening has revealed a large amount of hit compounds that specifically target SARS-CoV-2 PLpro (Amin et al., 2021; Gogoi et al., 2021; Goyzueta-Mamani et al., 2021; Hajbabaie et al., 2021; Jade et al., 2021; Jamal et al., 2021; Kumar et al., 2021; Li et al., 2021; Quimque et al., 2021; Rahul and Sarkar, 2021; Rudrapal et al., 2021; Stasiulewicz et al., 2021). Hits generated through the initial screens are further validated with an aim to choose the best ones to serve as leads for drug developments. As not all the identified lead compounds exhibited desired activities, co-crystallization of these effective inhibitors with PLpro is often adopted to investigate how the two molecules interact (Wang et al., 2021), which can inform further lead optimization and future drug design.

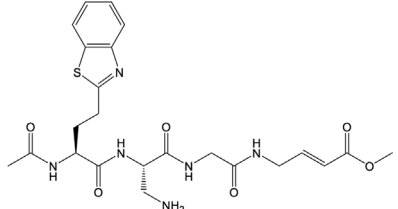
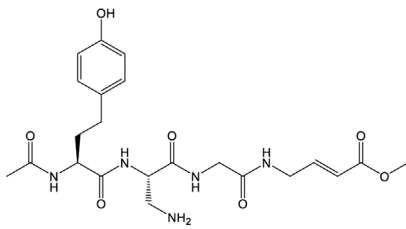
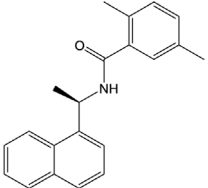
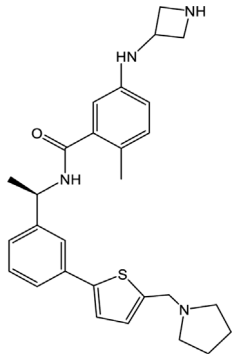
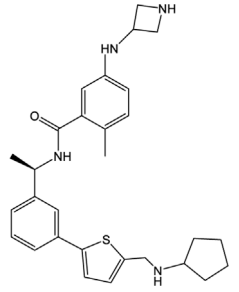
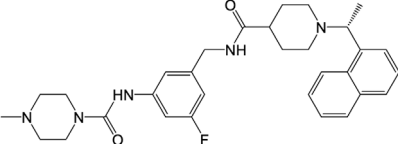
Optimization of Lead Compounds

Once a potential lead is identified, lead optimization is pressing as the potency, selectivity, or pharmacokinetic parameters of leads identified may not be satisfactory. Thus, optimization of lead compounds is a crucial step in the development of new drugs. As an example of success, Shan et al. optimized GRL0617 based on the GRL0617/PLpro complex structure and found analogue **19** has favorable potency and selectivity against SARS-CoV-2 PLpro (Shan et al., 2021). Also, Ma et al. optimized the Jun9-13-7 and Jun9-13-9 (Ma et al., 2021), while Weglarz-Tomczak et al. modified ebselen (Weglarz-Tomczak et al., 2021). Both optimized inhibitors are more potent than parent compounds. It is worth noting that all these optimized inhibitors suppress the PLpro activity at nanomolar level, representing the most potent inhibitors at the time of this manuscript submission.

POTENTIAL SARS-COV-2 PLPRO INHIBITORS

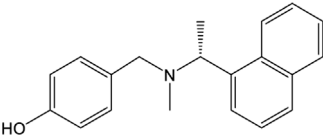
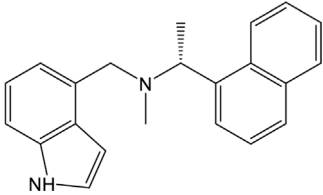
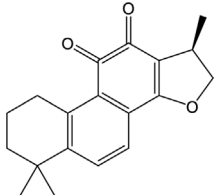
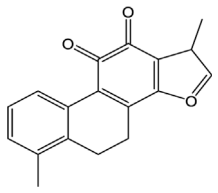
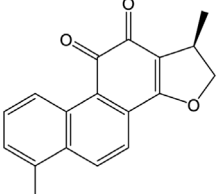
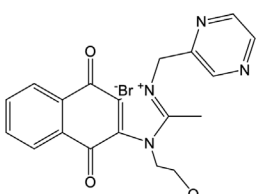
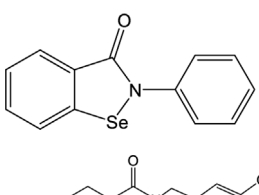
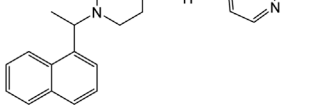
Many inhibitors have been identified against SARS-CoV-2 PLpro by using the strategies as stated above, even though no PLpro inhibitor has been approved by the US Food and Drug Administration (FDA) for marketing. Cysteine protease inhibitors can be divided into two categories, namely, covalent and non-covalent inhibitors. Covalent inhibitors form a C-S thioether linkage with the catalytic residue cysteine, while the non-covalent inhibitors interact with the protease through non-covalent binding which is always a reversible process (Aljoudi et al., 2020). SARS-CoV-2 PLpro inhibitors identified to date are mostly non-covalent, including naphthalene-based inhibitors, FDA approved drugs and natural products. As follows, we review the promising inhibitors currently known that target SARS-CoV-2 PLpro with the representative ones summarized in **Table 1**.

TABLE 1 | Representative potential inhibitors of SARS-CoV-2 PLpro.

Inhibitor	Enzyme inhibition activity (IC ₅₀)	Antiviral potency (EC ₅₀)	Crystal structure in complex with PLpro (PDB ID)	Molecular structure	References
VIR250	NA	NA	6WUU		Rut et al. (2020)
VIR251	NA	NA	6WX4		Rut et al. (2020)
GRL0617	2.05 ± 0.12 μM	Vero E6: 23.64 ± 4.72 μM; Caco2-hACE2: 19.96 ± 8.82 μM	7CMD		Ma et al. (2021); Gao et al. (2021)
XR8-24	0.56 ± 0.03 μM	A549: 1.4 ± 0.1 μM	7LBS		Shen et al. (2021)
XR8-23	0.39 ± 0.05 μM	A549: 1.2 ± 0.2 μM	NA		Shen et al. (2021)
19	0.44 ± 0.05 μM	hACE2-HeLa: 0.18 ± 0.10 μM	NA		Shan et al. (2021)

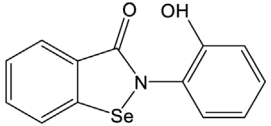
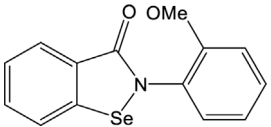
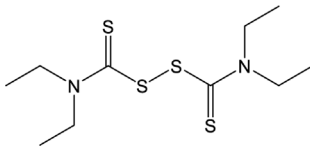
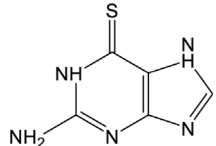
(Continued on following page)

TABLE 1 | (Continued) Representative potential inhibitors of SARS-CoV-2 PLpro.

Inhibitor	Enzyme inhibition activity (IC ₅₀)	Antiviral potency (EC ₅₀)	Crystal structure in complex with PLpro (PDB ID)	Molecular structure	References
Jun9-72-2	0.67 ± 0.08 μM	Vero E6: 6.62 ± 0.31 μM; Caco2-hACE2: 7.90 ± 2.40 μM	7SDR		Ma et al. (2021)
Jun9-75-4	0.62 ± 0.06 μM	Vero E6: 7.88 ± 1.44 μM; Caco2-hACE2: 12.48 ± 3.43 μM	NA		Ma et al. (2021)
Cryptotanshinone	5.63 ± 1.45 μM	Vero E6: 0.70 ± 0.09 μM	NA		Zhao et al. (2021)
Tanshinone I	2.21 ± 0.10 μM	Vero E6: 2.26 ± 0.11 μM	NA		Zhao et al. (2021)
Dihydrotanshinone I	0.5861 μM	Vero E6: 8.148 μM	NA		Lim et al. (2021)
YM155	2.47 ± 0.46 μM	Vero E6: 0.17 ± 0.02 μM	7D7L		Zhao et al. (2021)
Ebselen	2.02 ± 1.02 μM	Vero E6: 4.67 ± 0.80 μM	NA		Jin et al. (2020); Ma et al. (2020)
Rac5c	0.81 μM	NA	NA		Klemm et al. (2020)

(Continued on following page)

TABLE 1 | (Continued) Representative potential inhibitors of SARS-CoV-2 PLpro.

Inhibitor	Enzyme inhibition activity (IC ₅₀)	Antiviral potency (EC ₅₀)	Crystal structure in complex with PLpro (PDB ID)	Molecular structure	References
1d	0.236 μ M	NA	NA		Weglarczy-Tomczak et al. (2021)
1e	0.256 μ M	NA	NA		Weglarczy-Tomczak et al. (2021)
Disulfiram	7.52 \pm 2.13 μ M	NA	NA		Sargsyan et al. (2020)
6-TG	NA	Vero E6: 2.13 \pm 1.16 μ M	NA		Bayoumy et al. (2020)

NA: Not available.

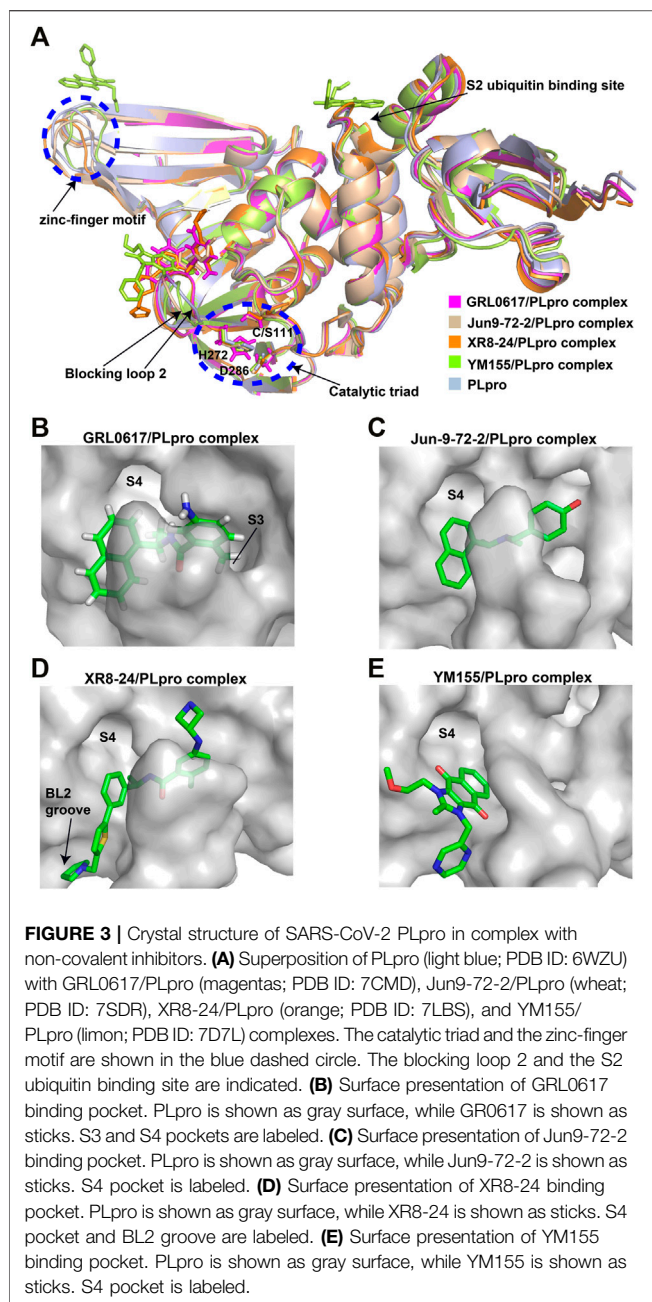
Naphthalene-Based Inhibitors

GRL0617, a naphthalene-based drug, was previously developed as a non-covalent inhibitor of SARS-CoV PLpro (Ratia et al., 2008). In various high-throughput screen studies for SARS-CoV-2 PLpro inhibitors, it has stood out for its potent protease inhibition and antiviral activities, with the IC₅₀ being around 2.0 μ M and EC₅₀ being around 20 μ M, respectively (Table 1) (Gao et al., 2021; Fu et al., 2021; Osipiuk et al., 2021; Klemm et al., 2020; Freitas et al., 2020). Several groups then resolved the crystal structure of SARS-CoV-2 PLpro in complex with GRL0617 and revealed its inhibitory mechanism (Gao et al., 2021; Fu et al., 2021; Osipiuk et al., 2021; Ma et al., 2021). According to the structural information, GRL0617 fits well with the substrate cleft with its aromatic ring and naphthalene group inserted into S3 and S4 pockets, respectively (Figures 3A,B). Unlike other inhibitors such as VIR251 (described below), which stabilizes the BL2 in an open conformation, GRL0617 keeps this loop in a close conformation (Figure 3A) (Rut et al., 2020; Gao et al., 2021). Thus, GRL0617 prevents the substrate from entering the active site and is therefore a competitive inhibitor. These findings inspire the discovery of new generation of naphthalene based PLpro inhibitors.

Osipiuk et al. reported several GRL0617 analogues that also show good inhibition of SARS-CoV-2 PLpro (Osipiuk et al., 2021). However, none of them show more potent inhibition of SARS-CoV-2 PLpro compared with GRL0617. Later, Ma et al. reported two lead compounds, Jun9-13-7 and Jun9-13-9, that

exhibits similar potency compared with GRL0617 (Ma et al., 2021). Encouragingly, two of the optimized forms, Jun9-72-2 and Jun9-75-4, show more potent enzymatic inhibition and antiviral activity compared to GRL0617. The IC₅₀ and EC₅₀ values of Jun9-72-2 and Jun9-54-7 are several-fold lower than those of GRL0617 (Table 1), thus making them very effective PLpro inhibitors. Jun9-72-2 adopts a similar binding model with GRL0617 (Figures 3A,C). Shan et al. focused on the structure-based optimization of GRL0617 for searching for improved GRL0617 analogues (Shan et al., 2021), as GRL0617 lacks sufficient potency for development as an antiviral agent. Finally, 9 GRL0617 analogues carrying a shared naphthyl subunit were found to be more potent than GRL0617. Among these, analogue 19 exhibits an inhibitory activity against SARS-CoV-2 PLpro with the IC₅₀ value of 0.44 μ M and an antiviral activity against SARS-CoV-2 with the IC₅₀ value of 0.18 μ M (Table 1). Moreover, analogue 19 shows no significant cross-inhibition against another 10 deubiquitinating enzymes (DUB) or DUB-like proteases even at the concentration of 10 μ M (Shan et al., 2021). Collectively, analogue 19 is a promising SARS-CoV-2 PLpro inhibitor in virtue of its high degree of potency and selectivity.

In addition to GRL0617, another three previously identified naphthalene-based inhibitors, namely, rac3j, rac3k, and rac5c (the racemic version of 3j, 3k, and 5c, respectively), also show a promising inhibitory activity against SARS-CoV-2 PLpro. Rac5c is the best one with an *in vitro* IC₅₀ value of 0.81 μ M (Table 1)



(Klemm et al., 2020). In the antiviral assay, rac5c could protect SARS-CoV-2 infected Vero cells from cytopathic effect without causing cell toxicity at a concentration of 11 μM , indicating the striking antiviral effects.

XR8-23/XR8-24

Shen et al. attached more attention in optimizing the potency of GRL0617 by exploring the engagement of additional binding sites beyond those utilized by GRL0617 (Shen et al., 2021). ZN-2-184, a derivative of GRL0617 with an azetidine substitution on the phenyl ring, yielded a 2-fold improved affinity through extending interaction with Glu167 of PLpro. ZN-3-80, a derivative of ZN-2-

184 with the naphthyl group replaced by a biaryl group, showed improved metabolic stability compared with GRL0617. Further attempt explored the derivatization of the 2-phenylthiophene scaffold (ZN-3-80) to exploit additional interactions with the BL2 groove, a promising site that has not yet been recognized by other PLpro inhibitors. Among the newly synthesized 2-phenylthiophene inhibitors, two well-designed robust ones, XR8-23 and XR8-24, display low nanomolar potency against SARS-CoV-2 PLpro (IC_{50} values of 0.39 and 0.56 μM , respectively) and low micromolar potency against viral infection in human lung epithelial A549 cells (EC_{50} values of 1.4 and 1.2 μM , respectively) (Table 1) (Shen et al., 2021), which improved greatly over GRL0617. Furthermore, XR8-23 and XR8-24 shows satisfactory bioavailability after intraperitoneal injection in a mouse model, even though their *in vivo* antiviral activities remain to be investigated.

XR8-23 has a basic amine side chain extending from the thiophene group, which leads to dissociation rates slower and potency stronger than those of ZN-3-80 and GRL0617. XR8-24 contains a pyrrolidine ring extending from the thiophene group, which results in the formation of a putative hydrogen bond with Tyr264 and accordingly accounts for its superior potency. XR8-24 do not access the active site, but engage the BL2 groove to enforce the sealing of the active site, as proved by the crystal structure of XR8-24 in complex with SARS-CoV-2 PLpro (Figures 3A,D) (Shen et al., 2021).

YM155

A high-throughput screen also identified a new lead YM155, a phase I clinical trial antineoplastic drug. It inhibits SARS-CoV-2 PLpro with an IC_{50} value of 2.47 μM and shows robust antiviral activity with an EC_{50} value of 0.17 μM (Table 1) (Zhao et al., 2021). The crystal structure of SARS-CoV-2 PLpro (with a C111S mutation) in complex with YM155 unravels a unique interaction mechanism, which may explain the strong inhibition achieved by YM155 against PLpro. In addition to targeting the substrate-binding pocket like GRL0617, YM155 also targets the thumb domain and the zinc finger motif (Figures 3A,E). Thus, YM155 not only blocks the entrance of substrate into the active site, but also hampers the molecular interactions between PLpro and ISG15 and affects the stability of the zinc-finger motif and enzyme activity.

Natural Products

A wide range of natural products provide an ideal library for the screen and identification of new drug candidates targeting SARS-CoV-2 PLpro. Flavonoids are a kind of widely distributed plant secondary metabolites with more than 9,000 structures currently identified (Wang et al., 2018). As the largest group of polyphenolic compounds in higher plants, flavonoids have shown PLpro inhibitory effects and antiviral activities against SARS-CoV and MERS-CoV *in vitro* (Jo et al., 2020; Solnier and Fladerer, 2020). In the setting of SARS-CoV-2, several members of flavonoids, including coumaroyltyramine, cryptotanshinone, kaempferol, moupinamide, N-cis-feruloyltyramine, quercetin, and tanshinone IIa, were identified as SARS-CoV-2 PLpro ligands using an *in silico* docking analysis (Zhang D.-h. et al.,

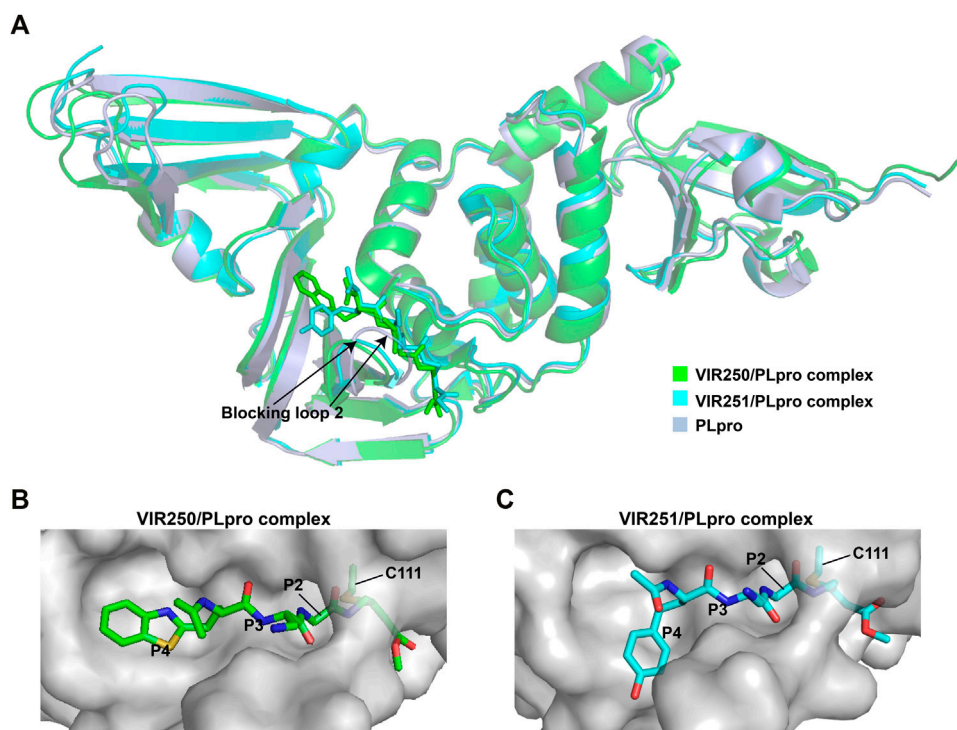


FIGURE 4 | Crystal structures of SARS-CoV-2 PLpro in complex with covalent inhibitors. **(A)** Superposition of SARS-CoV-2 PLpro (light blue; PDB ID: 6WZU) with VIR250/PLpro (green; PDB ID: 6WUJ) and VIR251/PLpro (cyan; PDB ID: 6WX4) complexes. The blocking loop 2 is indicated. **(B)** Surface presentation of VIR250 binding pocket. PLpro is shown as gray surface, while VIR250 is shown as sticks. The catalytic cysteine of PLpro forms a covalent bond with VIR250. The P2-P4 positions are labeled. **(C)** Surface presentation of VIR251 binding pocket. PLpro is shown as gray surface, while VIR251 is shown as sticks. The catalytic cysteine of PLpro forms a covalent bond with VIR251. The P2-P4 positions are labeled.

2020), despite the lack of *in vitro* evidence for their efficacy. These compounds might interfere with substrate entering the active sites through interacting with the region between the thumb and palm domains (Zhang D.-h. et al., 2020). Cryptotanshinone, one of the active ingredient from the Chinese herbal medicine, *Salvia miltiorrhiza*, was emphasized for its potential in inhibiting SARS-CoV-2 PLpro in another study (Zhao et al., 2021). *In vitro*, cryptotanshinone inhibits PLpro with an IC_{50} value of $5.63 \mu M$ and display antiviral activity with an EC_{50} value of $0.70 \mu M$ (Table 1), which is comparable to that of remdesivir ($0.77 \mu M$). Structurally similar with cryptotanshinone, tanshinone I possesses similar inhibition against SARS-CoV-2 PLpro (Diniz et al., 2021; Zhao et al., 2021). In addition, dihydrotanshinone I, another tanshinone derivative, could effectively inhibit the SARS-CoV-2 proliferation at an EC_{50} of $8 \mu M$ and is not cytotoxic even at high concentrations (Lim et al., 2021). Thus, tanshinones and its analogues have the potential to treat SARS-CoV-2 infection. Actually, “Xuebijing”, a complex traditional Chinese preparation consisting of *Salvia miltiorrhiza*, has been included in the Chinese clinical treatment strategy for COVID-19 and reduces multiple organ damage through anti-inflammation and improving immune function (Tong et al., 2020). Other natural compounds, such as EGCG (a Green Tea Catechin) (Chourasia et al., 2021), cyanovirin-N (Naidoo et al., 2021), several Terpene compounds (Diniz et al., 2021), and

propolis derivatives (Yosri et al., 2021), were also extensively studied in molecular simulations and exhibited high binding affinities with SARS-CoV-2 PLpro. But further *in vitro* and *in vivo* studies are needed to verify their potential. Collectively, it indicates that these herbal compounds can be potential antivirals against SARS-CoV-2. Further studies on the mode of interaction between PLpro and these compounds may shed light on future drug discovery.

Approved Drugs

Repurposing approved drugs is a potential alternative strategy to restrict SARS-CoV-2 infection. 6-Thioguanine (6-TG) is an orally-delivered anti-leukemia and immunosuppressant agent (Bayoumy et al., 2020). A recent study showed that 6-TG could inhibit viral replication of SARS-CoV-2 with an EC_{50} of $2.13 \mu M$, which is similar to that of remdesivir and approximately 15-fold lower than that of GRL0617 (Swaim et al., 2021). Four clinically approved hepatitis C protease inhibitors (simeprevir, vaniprevir, paritaprevir, and grazoprevir) have also recently been shown to inhibit SARS-CoV-2 PLpro *in vitro* and viral replication in Vero-E6 cells (Bafna et al., 2021). The blockade of viral infection for these drugs display synergistic effects to the antiviral activity of remdesivir with the EC_{50} values ranging from 4.25 to $10.8 \mu M$. In addition, simeprevir, vaniprevir, and grazoprevir exert dual inhibition of both Mpro and PLpro, while

paritaprevir only targets PLpro (Bafna et al., 2021). Losartan is a clinically available drug used to treat several diseases including diabetic nephropathy and primary hypertension (Mulla and Siddiqui, 2021). Despite of a weak inhibitory effect on deubiquitinase or deISGylase activity of the SARS-CoV-2 PLpro, Losartan is effective to decrease viral replication and the EC_{50} value is $13.7 \mu\text{M}$ in the pre-infection treatment experiment (Nejat et al., 2021), suggesting that its anti-SARS-CoV-2 activity not purely depend on PLpro inhibition. Another approved drug, disulfiram, is an thiol reagent designed for alcohol aversion therapy by targeting hepatic aldehyde dehydrogenase (Lipsky et al., 2001; Krampe and Ehrenreich, 2010). It has been recently repurposed as an inhibitor of other cysteine-containing enzymes such as methyltransferase, urease, and cysteine protease of coronaviruses (Paranjpe et al., 2014; Diaz-Sanchez et al., 2016; Lin et al., 2018; Ma et al., 2020; Sargsyan et al., 2020), indicating broad-spectrum characteristics. According to pieces of evidences, disulfiram could doubly inhibit Mpro and PLpro of SARS-CoV-2 with the IC_{50} values of 9.35 and $7.52 \mu\text{M}$, respectively (Sargsyan et al., 2020; Weglarz-Tomczak et al., 2021). The mechanism of action by disulfiram may involve the covalent interaction with Zn^{2+} -bound or catalytic cysteine.

VIR250/VIR251

The peptidomimetic inhibitors VIR250 and VIR251 are the covalent inhibitors of SARS-CoV-2 PLpro identified from a combinatorial substrate library (Rut et al., 2020). These two covalent inhibitors show good inhibition against both SARS-CoV and SARS-CoV-2 PLpros with little cross-reactive to human deubiquitinating enzymes. Crystal structures of VIR250 and VIR251 in complex with PLpro were resolved to 2.79 \AA and 1.65 \AA , respectively (Rut et al., 2020). They have very similar molecular structures and accordingly adopt similar binding modes with PLpro (Figure 4A). Specifically, β -carbon of the glycine vinyl methyl ester (GlyVME) at the P1 position covalently links to the sulfur atom of Cys111 of SARS-CoV-2 PLpro (Figures 4B,C). In addition, P1-P3 moieties of both inhibitors engage SARS-CoV-2 PLpro mainly through polar interactions and hydrogen bonds, while P4 moiety engages PLpro through hydrophobic interactions. However, the extension of these two inhibitors at the P4 position adopts opposite orientations. Thus, additional binding space in this pocket remains to be exploited, which may inspire further drug optimization. Based on the structure of VIR251 in complex with SARS-CoV-2 PLpro, several potential inhibitors were screened against PLpro with a similar interaction mode (Delre et al., 2020; Pang et al., 2020), suggesting that VIR251, as well as VIR250, can be a good starting point for the discovery of new drugs.

Ebselen

Ebselen is a low-molecular-weight selenoorganic drug with excellent properties in antioxidation, anti-inflammation, antiatherosclerosis, and cytoprotective effects (Azad and Tomar, 2014; Belvisi et al., 2000; Singh et al., 2017). This compound shows inhibition against Mpro and PLpro of SARS-CoV-2 with the IC_{50} values of 0.67 and $2.36 \mu\text{M}$, respectively (Sargsyan et al., 2020; Ma et al., 2020; Jin et al., 2020; Weglarz-Tomczak et al., 2021), which are slightly more

potent than disulfiram. In a cell-based assay, ebselen exhibits promising antiviral activity with the EC_{50} of $4.67 \mu\text{M}$ (Ma et al., 2020; Jin et al., 2020). The inhibition of ebselen against PLpro is an irreversible process that seems to associate with the covalent interaction between selenium atom from ebselen and sulphur atom from catalytic cysteine (Sargsyan et al., 2020; Weglarz-Tomczak et al., 2021). Subsequent modification of ebselen results in significantly increased inhibitory potency against PLpro from SARS-CoV-2. Four ebselen derivatives, namely **1d**, **1e**, **2d**, and **2e**, have IC_{50} constants in the nanomolar range, which is one order of magnitude lower than that of ebselen. Among these, **1d** and **1e** appear to be the most potent derivatives with the IC_{50} values of 236 and 256 nM, respectively (Table 1). The hydroxy (**1d**) or methoxy group (**1e**) substitution in the ortho position of the phenyl ring of ebselen may adopt additional interactions with the conserved residues in the active site, thus contributing to the increased potency (Weglarz-Tomczak et al., 2021). As ebselen has inhibitory activity against numerous targets, it is unlikely to be a viable candidate for further development as a clinical PLpro inhibitor.

DISCUSSION

The outbreak of COVID-19 has caused a global concern and seriously affects the living styles of most people. PLpro, a multi-functional protease of SARS-CoV-2, can not only digest the polyprotein precursor to generate non-structural proteins but also mitigate the RIG-I-mediated innate immunity triggered by viral infection (Klemm et al., 2020; Shin et al., 2020). Its immunomodulatory effects play an important role in disease progression. Moreover, PLpro is a highly conserved protein among coronaviruses, thus is an ideal target to develop broad-spectrum inhibitors against SARS-CoV, SARS-CoV-2 and future emerged coronavirus strains. This review updates the research progress in developing novel and potent inhibitors of SARS-CoV-2 PLpro, which may reveal some insights into future drug discovery and new strategies for the COVID-19 combat.

Generally, PLpro seems to be a greatly overlooked drug target that lacks research. Numerous research efforts have focused on developing inhibitors of Mpro, another cysteine protease of SARS-CoV-2, but relatively few have focused on PLpro inhibition. Part of the reason can be that PLpro is relatively more challenging to target in the comparison of Mpro. One of the challenges is the presence of homologous host DUBs. Thus, the specificity of the PLpro inhibitor is an important parameter that deserves more attention in the PLpro inhibitor discovery.

Even though a variety of inhibitors against SARS-CoV-2 PLpro have been found as mentioned above, a large portion of hits compounds identified in high-throughput screening and virtual screening have not been further evaluated. For those newly identified inhibitors, *in vitro* studies in a SARS-CoV-2 setting are required to determine its potency. Many studies only evaluated the inhibition of PLpro protease activity by the inhibitor, but ignored the evaluation of its antiviral activities which significantly contribute to the ultimate drug efficacy. As far as the antiviral activity is concerned, most studies conducted this

cell-based assay in *vero* E6 cells which is responsible for the limitation. It is better to perform the antiviral assay in human cells, such as Calu3 cells or normal human airway epithelial cells, the result of which would give different but more clinically relevant EC₅₀ values. Moreover, little has been done to test the absorption, distribution, metabolism, and excretion (ADME) and toxicity of these inhibitors. It is necessary to establish a suitable animal model for more rigorous *in vivo* effect evaluation. Then subsequent clinical candidate selection can be possible.

As for mechanistic studies, few structures of inhibitors in complex with PLpro have been resolved. Co-crystallization combined with computational methods can accelerate the disclosure of interaction modes between the inhibitors and PLpro, which can inform future structure-based drug design. Some achievements have been made in the optimization of lead compounds such as GRL0617 and ebselen. Also, additional *in vitro* and *in vivo* evaluations of these potent derivatives are needed in the future.

Drug repurposing is an important strategy in drug discovery. Several existing broad-spectrum antiviral drugs such as dual inhibitors, disulfiram and ebselen, have shown robust inhibition of viral protease and are undergoing clinical trials. These drugs may favour the first line of defence for rapid response. As the high infectivity of SARS-CoV-2 has provoked continuous outbreaks all over the world, the comprehensive applications of drug repurposing, new leads identification, and

structure-based leads optimization are expected to further accelerate the discovery process and develop specific inhibitors that are safe, effective and well-tolerated for COVID-19 therapy.

In conclusion, though some encouraging results are available, the drug discovery of SARS-CoV-2 PLpro is still far from meeting the needs. Future researches need to fill the above-mentioned vacancies for developing a promising clinical candidate and an effective PLpro inhibitor with both potency and selectivity eventually.

AUTHOR CONTRIBUTIONS

HJ: conceived the topic and wrote the original draft. PY: assisted in writing and organizing the draft. JZ: conceived the topic, supervised the work and approved the final draft. All authors read and approved the final draft.

FUNDING

JZ was supported by the Thousand Young Talents Program of China, the National Natural Science Foundation of China (Grant No. 31770795; Grant No. 81974514), and the Jiangxi Province Natural Science Foundation (Grant No. 20181ACB20014).

REFERENCES

- Aherfi, S., Pradines, B., Devaux, C., Honore, S., Colson, P., Scola, B. L., et al. (2021). Drug Repurposing against SARS-CoV-1, SARS-CoV-2 and MERS-CoV. *Future Microbiol.* 16, 1341–1370. doi:10.2217/fmb-2021-0019
- Aljoudi, A., Biji, I., El Rashedy, A., and Soliman, M. E. S. (2020). Covalent versus Non-covalent Enzyme Inhibition: Which Route Should We Take? A Justification of the Good and Bad from Molecular Modelling Perspective. *Protein J.* 39 (2), 97–105. doi:10.1007/s10930-020-09884-2
- Amin, S. A., Ghosh, K., Gayen, S., and Jha, T. (2021). Chemical-informatics Approach to COVID-19 Drug Discovery: Monte Carlo Based QSAR, Virtual Screening and Molecular Docking Study of Some In-House Molecules as Papain-like Protease (PLpro) Inhibitors. *J. Biomol. Struct. Dyn.* 39 (13), 4764–4773. doi:10.1080/07391102.2020.1780946
- Anirudhan, V., Lee, H., Cheng, H., Cooper, L., and Rong, L. (2021). Targeting SARS-CoV-2 Viral Proteases as a Therapeutic Strategy to Treat COVID-19. *J. Med. Virol.* 93 (5), 2722–2734. doi:10.1002/jmv.26814
- Azad, G. K., and Tomar, R. S. (2014). Ebselen, a Promising Antioxidant Drug: Mechanisms of Action and Targets of Biological Pathways. *Mol. Biol. Rep.* 41 (8), 4865–4879. doi:10.1007/s11033-014-3417-x
- Bafna, K., White, K., Harish, B., Rosales, R., Ramelot, T. A., Acton, T. B., et al. (2021). Hepatitis C Virus Drugs that Inhibit SARS-CoV-2 Papain-like Protease Synergize with Remdesivir to Suppress Viral Replication in Cell Culture. *Cel Rep.* 35 (7), 109133. doi:10.1016/j.celrep.2021.109133
- Bayoumy, A. B., Simsek, M., Seinen, M. L., Mulder, C. J. J., Ansari, A., Peters, G. J., et al. (2020). The Continuous Rediscovery and the Benefit-Risk Ratio of Thioguanine, a Comprehensive Review. *Expert Opin. Drug Metab. Toxicol.* 16 (2), 111–123. doi:10.1080/17425255.2020.1719996
- Belvisi, M. G., Haddad, E. B., Battaram, C., Birrell, M., Foster, M., and Webber, S. (2000). Anti-inflammatory Properties of Ebselen in a Model of Sephadex-Induced Lung Inflammation. *Eur. Respir. J.* 15 (3), 579–581. doi:10.1034/j.1399-3003.2000.15.25.x
- Bonilla, P. J., Hughes, S. A., and Weiss, S. R. (1997). Characterization of a Second Cleavage Site and Demonstration of Activity in Trans by the Papain-like
- Proteinase of the Murine Coronavirus Mouse Hepatitis Virus Strain A59. *J. Virol.* 71 (2), 900–909. doi:10.1128/jvi.71.2.900-909.1997
- Chafekar, A., and Fielding, B. (2018). MERS-CoV: Understanding the Latest Human Coronavirus Threat. *Viruses* 10 (2), 93. doi:10.3390/v10020093
- Chen, N., Zhou, M., Dong, X., Qu, J., Gong, F., Han, Y., et al. (2020). Epidemiological and Clinical Characteristics of 99 Cases of 2019 Novel Coronavirus Pneumonia in Wuhan, China: a Descriptive Study. *The Lancet* 395 (10223), 507–513. doi:10.1016/s0140-6736(20)30211-7
- Chen, Z., Wang, Y., Ratia, K., Mesecar, A. D., Wilkinson, K. D., and Baker, S. C. (2007). Proteolytic Processing and Deubiquitinating Activity of Papain-like Proteases of Human Coronavirus NL63. *J. Virol.* 81 (11), 6007–6018. doi:10.1128/jvi.02747-06
- Cho, C. C., Li, S. G., Lalonde, T. J., Yang, K. S., Yu, G., Qiao, Y., et al. (2021). Drug Repurposing for the SARS-CoV-2 Papain-like Protease. *ChemMedChem* 17, e202100455. doi:10.1002/cmdc.202100455
- Choudhury, S., Moullick, D., Borah, A., Saikia, P., and Mazumder, M. K. (2021). In Search of Drugs to Alleviate Suppression of the Host's Innate Immune Responses against SARS-CoV-2 Using a Molecular Modeling Approach. *Silico Pharmacol.* 9 (1), 26. doi:10.1007/s40203-021-00085-y
- Chourasia, M., Koppula, P., Battu, A., Ouseph, M., and Singh, A. (2021). EGCG, a Green Tea Catechin, as a Potential Therapeutic Agent for Symptomatic and Asymptomatic SARS-CoV-2 Infection. *Molecules* 26 (5), 1200. doi:10.3390/molecules26051200
- Cragg, G. M., and Newman, D. J. (2013). Natural Products: a Continuing Source of Novel Drug Leads. *Biochim. Biophys. Acta (Bba) - Gen. Subjects* 1830 (6), 3670–3695. doi:10.1016/j.bbagen.2013.02.008
- Delre, P., Caporuscio, F., Saviano, M., and Mangiatordi, G. F. (2020). Repurposing Known Drugs as Covalent and Non-covalent Inhibitors of the SARS-CoV-2 Papain-like Protease. *Front. Chem.* 8, 594009. doi:10.3389/fchem.2020.594009
- Díaz-Sánchez, Á., Alvarez-Parrilla, E., Martínez-Martínez, A., Aguirre-Reyes, L., Orozpe-Olvera, J., Ramos-Soto, M., et al. (2016). Inhibition of Urease by Disulfiram, an FDA-Approved Thiol Reagent Used in Humans. *Molecules* 21 (12), 1628. doi:10.3390/molecules21121628
- Diniz, L. R. L., Perez-Castillo, Y., Elshabrawy, H. A., Filho, C. d. S. M. B., and de Sousa, D. P. (2021). Bioactive Terpenes and Their Derivatives as Potential SARS-CoV-2 Proteases Inhibitors from Molecular Modeling Studies. *Biomolecules* 11 (1), 74. doi:10.3390/biom11010074

- Fehr, A. R., and Perlman, S. (2015). Coronaviruses: an Overview of Their Replication and Pathogenesis. *Methods Mol. Biol.* 1282, 1–23. doi:10.1007/978-1-4939-2438-7_1
- Freitas, B. T., Durie, I. A., Murray, J., Longo, J. E., Miller, H. C., Crich, D., et al. (2020). Characterization and Noncovalent Inhibition of the Deubiquitinase and deISGylase Activity of SARS-CoV-2 Papain-like Protease. *ACS Infect. Dis.* 6 (8), 2099–2109. doi:10.1021/acinfeddis.0c00168
- Fu, Z., Huang, B., Tang, J., Liu, S., Liu, M., Ye, Y., et al. (2021). The Complex Structure of GRL0617 and SARS-CoV-2 PLpro Reveals a Hot Spot for Antiviral Drug Discovery. *Nat. Commun.* 12 (1), 488. doi:10.1038/s41467-020-20718-8
- Gao, X., Qin, B., Chen, P., Zhu, K., Hou, P., Wojdyla, J. A., et al. (2021). Crystal Structure of SARS-CoV-2 Papain-like Protease. *Acta Pharmaceutica Sinica B* 11 (1), 237–245. doi:10.1016/j.apsb.2020.08.014
- Gogoi, M., Borkotoky, M., Borchetia, S., Chowdhury, P., Mahanta, S., and Barooah, A. K. (2021). Black tea Bioactives as Inhibitors of Multiple Targets of SARS-CoV-2 (3CLpro, PLpro and RdRp): a Virtual Screening and Molecular Dynamic Simulation Study. *J. Biomol. Struct. Dyn.* 1–24. doi:10.1080/07391102.2021.1897679
- Goyzueta-Mamani, L. D., Barazorda-Ccahuana, H. L., Mena-Ulecia, K., and Chávez-Fumagalli, M. A. (2021). Antiviral Activity of Metabolites from Peruvian Plants against SARS-CoV-2: An In Silico Approach. *Molecules* 26 (13), 3882. doi:10.3390/molecules26133882
- Hajbabaie, R., Harper, M. T., and Rahman, T. (2021). Establishing an Analogue Based In Silico Pipeline in the Pursuit of Novel Inhibitory Scaffolds against the SARS Coronavirus 2 Papain-like Protease. *Molecules* 26 (4), 1134. doi:10.3390/molecules26041134
- Hijikata, A., Shionyu, C., Nakae, S., Shionyu, M., Ota, M., Kanaya, S., et al. (2021). Current Status of Structure-Based Drug Repurposing against COVID-19 by Targeting SARS-CoV-2 Proteins. *Biophysics* 18, 226–240. doi:10.2142/biophysico.bppb-v18.025
- Hosseini, M., Chen, W., Xiao, D., and Wang, C. (2021). Computational Molecular Docking and Virtual Screening Revealed Promising SARS-CoV-2 Drugs. *Precis Clin. Med.* 4 (1), 1–16. doi:10.1093/pcmedi/pbab001
- Huang, C., Wang, Y., Li, X., Ren, L., Zhao, J., Hu, Y., et al. (2020). Clinical Features of Patients Infected with 2019 Novel Coronavirus in Wuhan, China. *The Lancet* 395 (10223), 497–506. doi:10.1016/s0140-6736(20)30183-5
- Jade, D., Ayyamperumal, S., Tallapaneni, V., Joghee Nanjan, C. M., Barge, S., Mohan, S., et al. (2021). Virtual High Throughput Screening: Potential Inhibitors for SARS-CoV-2 PLPRO and 3CLPRO Proteases. *Eur. J. Pharmacol.* 901, 174082. doi:10.1016/j.ejphar.2021.174082
- Jamalan, M., Barzegari, E., and Gholami-Borujeni, F. (2021). Structure-Based Screening to Discover New Inhibitors for Papain-like Proteinase of SARS-CoV-2: An In Silico Study. *J. Proteome Res.* 20 (1), 1015–1026. doi:10.1021/acs.jproteome.0c00836
- James, T. W., Frias-Staheli, N., Bacik, J.-P., Livingston Macleod, J. M., Khajepour, M., Garcia-Sastre, A., et al. (2011). Structural Basis for the Removal of Ubiquitin and Interferon-Stimulated Gene 15 by a Viral Ovarian Tumor Domain-Containing Protease. *Proc. Natl. Acad. Sci.* 108 (6), 2222–2227. doi:10.1073/pnas.1013388108
- Jin, Z., Du, X., Xu, Y., Deng, Y., Liu, M., Zhao, Y., et al. (2020). Structure of Mpro from SARS-CoV-2 and Discovery of its Inhibitors. *Nature* 582 (7811), 289–293. doi:10.1038/s41586-020-2223-y
- Jo, S., Kim, S., Shin, D. H., and Kim, M.-S. (2020). Inhibition of SARS-CoV 3CL Protease by Flavonoids. *J. Enzyme Inhib. Med. Chem.* 35 (1), 145–151. doi:10.1080/14756366.2019.1690480
- Kanjanahaluethai, A., and Baker, S. C. (2000). Identification of Mouse Hepatitis Virus Papain-like Proteinase 2 Activity. *J. Virol.* 74 (17), 7911–7921. doi:10.1128/jvi.74.17.7911-7921.2000
- Khailany, R. A., Safdar, M., and Ozaslan, M. (2020). Genomic Characterization of a Novel SARS-CoV-2. *Gene Rep.* 19, 100682. doi:10.1016/j.genrep.2020.100682
- Klein, S., Cortese, M., Winter, S. L., Wachsmuth-Melm, M., Neufeldt, C. J., Cerikan, B., et al. (2020). SARS-CoV-2 Structure and Replication Characterized by In Situ Cryo-Electron Tomography. *Nat. Commun.* 11 (1), 5885. doi:10.1038/s41467-020-19619-7
- Klemm, T., Ebert, G., Calleja, D. J., Allison, C. C., Richardson, L. W., Bernardini, J. P., et al. (2020). Mechanism and Inhibition of the Papain-like Protease, PLpro, of SARS-CoV-2. *EMBO J.* 39 (18), e106275. doi:10.15252/embj.2020106275
- Knoops, K., Kikkert, M., Worm, S. H. E. v. d., Zevenhoven-Dobbe, J. C., van der Meer, Y., Koster, A. J., et al. (2008). SARS-coronavirus Replication Is Supported by a Reticulovesicular Network of Modified Endoplasmic Reticulum. *Plos Biol.* 6 (9), e226. doi:10.1371/journal.pbio.0060226
- Kouznetsova, V. L., Zhang, A., Tatineni, M., Miller, M. A., and Tsigelny, I. F. (2020). Potential COVID-19 Papain-like Protease PLpro Inhibitors: Repurposing FDA-Approved Drugs. *PeerJ* 8, e9965. doi:10.7717/peerj.9965
- Krampe, H., and Ehrenreich, H. (2010). Supervised Disulfiram as Adjunct to Psychotherapy in Alcoholism Treatment. *Curr. Pharm. Des.* 16 (19), 2076–2090. doi:10.2174/138161210791516431
- Kumar, V., Parate, S., Yoon, S., Lee, G., and Lee, K. W. (2021). Computational Simulations Identified Marine-Derived Natural Bioactive Compounds as Replication Inhibitors of SARS-CoV-2. *Front. Microbiol.* 12, 647295. doi:10.3389/fmicb.2021.647295
- Lei, J., Kusov, Y., and Hilgenfeld, R. (2018). Nsp3 of Coronaviruses: Structures and Functions of a Large Multi-Domain Protein. *Antiviral Res.* 149, 58–74. doi:10.1016/j.antiviral.2017.11.001
- Li, L., Ma, L., Hu, Y., Li, X., Yu, M., Shang, H., et al. (2022). Natural Biflavones Are Potent Inhibitors against SARS-CoV-2 Papain-like Protease. *Phytochemistry* 193, 112984. doi:10.1016/j.phytochem.2021.112984
- Lim, C. T., Tan, K. W., Wu, M., Ulferts, R., Armstrong, L. A., Ozono, E., et al. (2021). Identifying SARS-CoV-2 Antiviral Compounds by Screening for Small Molecule Inhibitors of Nsp3 Papain-like Protease. *Biochem. J.* 478 (13), 2517–2531. doi:10.1042/bcj20210244
- Lin, M.-H., Moses, D. C., Hsieh, C.-H., Cheng, S.-C., Chen, Y.-H., Sun, C.-Y., et al. (2018). Disulfiram Can Inhibit MERS and SARS Coronavirus Papain-like Proteases via Different Modes. *Antiviral Res.* 150, 155–163. doi:10.1016/j.antiviral.2017.12.015
- Lipsky, J. J., Shen, M. L., and Naylor, S. (2001). In Vivo inhibition of Aldehyde Dehydrogenase by Disulfiram. *Chemico-Biological Interactions* 130–132 (1–3), 93–102. doi:10.1016/s0009-2797(00)00225-8
- Ma, C., Hu, Y., Townsend, J. A., Lagarias, P. I., Marty, M. T., Kolocouris, A., et al. (2020). Ebselen, Disulfiram, Carmofur, PX-12, Tideglusib, and Shikonin Are Nonspecific Promiscuous SARS-CoV-2 Main Protease Inhibitors. *ACS Pharmacol. Transl. Sci.* 3 (6), 1265–1277. doi:10.1021/acspstci.0c00130
- Ma, C., Sacco, M. D., Xia, Z., Lambrinidis, G., Townsend, J. A., Hu, Y., et al. (2021). Discovery of SARS-CoV-2 Papain-like Protease Inhibitors through a Combination of High-Throughput Screening and a FlipGFP-Based Reporter Assay. *ACS Cent. Sci.* 7 (7), 1245–1260. doi:10.1021/acscentsci.1c00519
- Madewell, Z. J., Yang, Y., Longini, I. M., Jr., Halloran, M. E., and Dean, N. E. (2020). Household Transmission of SARS-CoV-2. *JAMA Netw. Open* 3 (12), e2031756. doi:10.1001/jamanetworkopen.2020.31756
- McClain, C. B., and Vabret, N. (2020). SARS-CoV-2: the many Pros of Targeting PLpro. *Sig Transduct. Target. Ther.* 5 (1), 223. doi:10.1038/s41392-020-00335-z
- Mielech, A. M., Chen, Y., Mesecar, A. D., and Baker, S. C. (2014). Nidovirus Papain-like Proteases: Multifunctional Enzymes with Protease, Deubiquitinating and deISGylating Activities. *Virus. Res.* 194, 184–190. doi:10.1016/j.virusres.2014.01.025
- Mslati, H., Gentile, F., Perez, C., and Cherkasov, A. (2021). Comprehensive Consensus Analysis of SARS-CoV-2 Drug Repurposing Campaigns. *J. Chem. Inf. Model.* 61 (8), 3771–3788. doi:10.1021/acs.jcim.1c00384
- Mulla, S., and Siddiqui, W. J. (2021). *Losartan*. Treasure Island (FL): StatPearls.
- Naidoo, D., Kar, P., Roy, A., Mutanda, T., Bwapwa, J., Sen, A., et al. (2021). Structural Insight into the Binding of Cyanovirin-N with the Spike Glycoprotein, Mpro and PLpro of SARS-CoV-2: Protein-Protein Interactions, Dynamics Simulations and Free Energy Calculations. *Molecules* 26 (17), 5114. doi:10.3390/molecules26175114
- Nejat, R., Sadr, A. S., Freitas, B., Crabtree, J., Pegan, S. D., Tripp, R. A., et al. (2021). Losartan Inhibits SARS-CoV-2 Replication In Vitro. *J. Pharm. Pharm. Sci.* 24, 390–399. doi:10.18433/jpps31931
- Osiptuk, J., Azizi, S.-A., Dvorkin, S., Endres, M., Jedrzejczak, R., Jones, K. A., et al. (2021). Structure of Papain-like Protease from SARS-CoV-2 and its Complexes with Non-covalent Inhibitors. *Nat. Commun.* 12 (1), 743. doi:10.1038/s41467-021-21060-3
- Pang, J., Gao, S., Sun, Z., and Yang, G. (2020). Discovery of Small Molecule PLpro Inhibitor against COVID-19 Using Structure-Based Virtual Screening, Molecular Dynamics Simulation, and Molecular mechanics/Generalized

- Born Surface Area (MM/GBSA) Calculation. *Struct. Chem.* 1-8, 1-8. doi:10.1007/s11224-020-01665-y
- Paranjpe, A., Zhang, R., Ali-Osman, F., Bobustuc, G. C., and Srivenugopal, K. S. (2014). Disulfiram Is a Direct and Potent Inhibitor of Human O6-Methylguanine-DNA Methyltransferase (MGMT) in Brain Tumor Cells and Mouse Brain and Markedly Increases the Alkylating DNA Damage. *Carcinogenesis* 35 (3), 692-702. doi:10.1093/carcin/bgt366
- Patel, K. P., Vunnam, S. R., Patel, P. A., Krill, K. L., Korbitz, P. M., Gallagher, J. P., et al. (2020). Transmission of SARS-CoV-2: an Update of Current Literature. *Eur. J. Clin. Microbiol. Infect. Dis.* 39 (11), 2005-2011. doi:10.1007/s10096-020-03961-1
- Perng, Y.-C., and Lenschow, D. J. (2018). ISG15 in Antiviral Immunity and beyond. *Nat. Rev. Microbiol.* 16 (7), 423-439. doi:10.1038/s41579-018-0020-5
- Pushpakom, S., Iorio, F., Eyers, P. A., Escott, K. J., Hopper, S., Wells, A., et al. (2019). Drug Repurposing: Progress, Challenges and Recommendations. *Nat. Rev. Drug Discov.* 18 (1), 41-58. doi:10.1038/nrd.2018.168
- Quimque, M. T. J., Notarte, K. I. R., Fernandez, R. A. T., Mendoza, M. A. O., Liman, R. A. D., Lim, J. A. K., et al. (2021). Virtual Screening-Driven Drug Discovery of SARS-CoV2 Enzyme Inhibitors Targeting Viral Attachment, Replication, post-translational Modification and Host Immunity Evasion Infection Mechanisms. *J. Biomol. Struct. Dyn.* 39 (12), 4316-4333. doi:10.1080/07391102.2020.1776639
- Rahul, S., and Sarkar, A. (2021). Microbial Based Natural Compounds as Potential Inhibitors for SARS-CoV-2 Papain-like Protease (PLpro): a Molecular Docking and Dynamic Simulation Study. *J. Biomol. Struct. Dyn.* 1-11. doi:10.1080/07391102.2021.1997815
- Ratia, K., Pegan, S., Takayama, J., Sleeman, K., Coughlin, M., Baliji, S., et al. (2008). A Noncovalent Class of Papain-like Protease/deubiquitinase Inhibitors Blocks SARS Virus Replication. *Proc. Natl. Acad. Sci.* 105 (42), 16119-16124. doi:10.1073/pnas.0805240105
- Ruan, S. (2020). Likelihood of Survival of Coronavirus Disease 2019. *Lancet Infect. Dis.* 20 (6), 630-631. doi:10.1016/s1473-3099(20)30257-7
- Rudrapal, M., Issahaku, A. R., Agoni, C., Bendale, A. R., Nagar, A., Soliman, M. E. S., et al. (2021). In Silico screening of Phytopolyphenolics for the Identification of Bioactive Compounds as Novel Protease Inhibitors Effective against SARS-CoV-2. *J. Biomol. Struct. Dyn.* 1-17. doi:10.1080/07391102.2021.1944909
- Rut, W., Lv, Z., Zmudzinski, M., Patchett, S., Nayak, D., Snipas, S. J., et al. (2020). Activity Profiling and crystal Structures of Inhibitor-Bound SARS-CoV-2 Papain-like Protease: A Framework for Anti-COVID-19 Drug Design. *Sci. Adv.* 6 (42), eabd4596. doi:10.1126/sciadv.abd4596
- Sargsyan, K., Lin, C.-C., Chen, T., Grauffel, C., Chen, Y.-P., Yang, W.-Z., et al. (2020). Multi-targeting of Functional Cysteines in Multiple Conserved SARS-CoV-2 Domains by Clinically Safe Zn-Ejectors. *Chem. Sci.* 11 (36), 9904-9909. doi:10.1039/d0sc02646h
- Shamsi, A., Mohammad, T., Anwar, S., Amani, S., Khan, M. S., Husain, F. M., et al. (2021). Potential Drug Targets of SARS-CoV-2: From Genomics to Therapeutics. *Int. J. Biol. Macromolecules* 177, 1-9. doi:10.1016/j.ijbiomac.2021.02.071
- Shan, H., Liu, J., Shen, J., Dai, J., Xu, G., Lu, K., et al. (2021). Development of Potent and Selective Inhibitors Targeting the Papain-like Protease of SARS-CoV-2. *Cel Chem. Biol.* 28 (6), 855-865. doi:10.1016/j.chembiol.2021.04.020
- Shen, Z., Ratia, K., Cooper, L., Kong, D., Lee, H., Kwon, Y., et al. (2021). Design of SARS-CoV-2 PLpro Inhibitors for COVID-19 Antiviral Therapy Leveraging Binding Cooperativity. *J. Med. Chem.* doi:10.1021/acs.jmedchem.1c01307
- Shende, P., Khanolkar, B., and Gaud, R. S. (2021). Drug Repurposing: New Strategies for Addressing COVID-19 Outbreak. *Expert Rev. Anti-infective Ther.* 19 (6), 689-706. doi:10.1080/14787210.2021.1851195
- Shin, D., Mukherjee, R., Grewe, D., Bojkova, D., Baek, K., Bhattacharya, A., et al. (2020). Papain-like Protease Regulates SARS-CoV-2 Viral Spread and Innate Immunity. *Nature* 587 (7835), 657-662. doi:10.1038/s41586-020-2601-5
- Singh, V. P., Poon, J.-f., Yan, J., Lu, X., Ott, M. K., Butcher, R. J., et al. (2017). Nitro-, Azo-, and Amino Derivatives of Ebselen: Synthesis, Structure, and Cytoprotective Effects. *J. Org. Chem.* 82 (1), 313-321. doi:10.1021/acs.joc.6b02418
- Smith, E., Davis-Gardner, M. E., Garcia-Ordóñez, R. D., Nguyen, T.-T., Hull, M., Chen, E., et al. (2020). High-Throughput Screening for Drugs that Inhibit Papain-like Protease in SARS-CoV-2. *SLAS DISCOVERY: Advancing Sci. Drug Discov.* 25 (10), 1152-1161. doi:10.1177/2472555220963667
- Solnier, J., and Fladerer, J. P. (2020). Flavonoids: A Complementary Approach to Conventional Therapy of COVID-19? *Phytochem. Rev.*, 1-23. doi:10.1007/s11101-020-09720-6
- Stadler, K., Masignani, V., Eickmann, M., Becker, S., Abrignani, S., Klenk, H.-D., et al. (2003). SARS - Beginning to Understand a New Virus. *Nat. Rev. Microbiol.* 1 (3), 209-218. doi:10.1038/nrmicro775
- Stasiulewicz, A., Maksymiuk, A. W., Nguyen, M. L., Belza, B., and Sulkowska, J. I. (2021). SARS-CoV-2 Papain-like Protease Potential Inhibitors-In Silico Quantitative Assessment. *Ijms* 22 (8), 3957. doi:10.3390/ijms22083957
- Su, S., Wong, G., Shi, W., Liu, J., Lai, A. C. K., Zhou, J., et al. (2016). Epidemiology, Genetic Recombination, and Pathogenesis of Coronaviruses. *Trends Microbiol.* 24 (6), 490-502. doi:10.1016/j.tim.2016.03.003
- Swaim, C. D., Canadeo, L. A., Monte, K. J., Khanna, S., Lenschow, D. J., and Huibregtse, J. M. (2020). Modulation of Extracellular ISG15 Signaling by Pathogens and Viral Effector Proteins. *Cel Rep.* 31 (11), 107772. doi:10.1016/j.celrep.2020.107772
- Swaim, C. D., Dwivedi, V., Perng, Y.-C., Zhao, X., Canadeo, L. A., Harastani, H. H., et al. (2021). 6-Thioguanine Blocks SARS-CoV-2 Replication by Inhibition of PLpro. *iScience* 24 (10), 103213. doi:10.1016/j.isci.2021.103213
- Swatek, K. N., Aumayr, M., Pruneda, J. N., Visser, L. J., Berryman, S., Kueck, A. F., et al. (2018). Irreversible Inactivation of ISG15 by a Viral Leader Protease Enables Alternative Infection Detection Strategies. *Proc. Natl. Acad. Sci. USA* 115 (10), 2371-2376. doi:10.1073/pnas.1710617115
- Tian, D., Liu, Y., Liang, C., Xin, L., Xie, X., Zhang, D., et al. (2021). An Update Review of Emerging Small-Molecule Therapeutic Options for COVID-19. *Biomed. Pharmacother.* 137, 111313. doi:10.1016/j.biopha.2021.111313
- Tong, T., Wu, Y.-Q., Ni, W.-J., Shen, A.-Z., and Liu, S. (2020). The Potential Insights of Traditional Chinese Medicine on Treatment of COVID-19. *Chin. Med.* 15, 51. doi:10.1186/s13020-020-00326-w
- V. C. Guido, R., Oliva, G., and D. Andricopulo, A. (2011). Modern Drug Discovery Technologies: Opportunities and Challenges in lead Discovery. *Cchts* 14 (10), 830-839. doi:10.2174/138620711797537067
- Wang, C., Horby, P. W., Hayden, F. G., and Gao, G. F. (2020). A Novel Coronavirus Outbreak of Global Health Concern. *The Lancet* 395 (10223), 470-473. doi:10.1016/s0140-6736(20)30185-9
- Wang, T.-y., Li, Q., and Bi, K.-s. (2018). Bioactive Flavonoids in Medicinal Plants: Structure, Activity and Biological Fate. *Asian J. Pharm. Sci.* 13 (1), 12-23. doi:10.1016/j.ajps.2017.08.004
- Wang, Z., Yang, L., and Zhao, X.-E. (2021). Co-crystallization and Structure Determination: An Effective Direction for Anti-SARS-CoV-2 Drug Discovery. *Comput. Struct. Biotechnol. J.* 19, 4684-4701. doi:10.1016/j.csbj.2021.08.029
- Weglarz-Tomczak, E., Tomczak, J. M., Talma, M., Burda-Grabowska, M., Giurg, M., and Brul, S. (2021). Identification of Ebselen and its Analogues as Potent Covalent Inhibitors of Papain-like Protease from SARS-CoV-2. *Sci. Rep.* 11 (1), 3640. doi:10.1038/s41598-021-83229-6
- Woo, P. C. Y., Huang, Y., Lau, S. K. P., and Yuen, K.-Y. (2010). Coronavirus Genomics and Bioinformatics Analysis. *Viruses* 2 (8), 1804-1820. doi:10.3390/v2081803
- Wu, A., Peng, Y., Huang, B., Ding, X., Wang, X., Niu, P., et al. (2020b). Genome Composition and Divergence of the Novel Coronavirus (2019-nCoV) Originating in China. *Cell Host & Microbe* 27 (3), 325-328. doi:10.1016/j.chom.2020.02.001
- Wu, F., Zhao, S., Yu, B., Chen, Y.-M., Wang, W., Song, Z.-G., et al. (2020a). A New Coronavirus Associated with Human Respiratory Disease in China. *Nature* 579 (7798), 265-269. doi:10.1038/s41586-020-2008-3
- Wu, Z., and McGoogan, J. M. (2020). Characteristics of and Important Lessons from the Coronavirus Disease 2019 (COVID-19) Outbreak in China. *JAMA* 323 (13), 1239-1242. doi:10.1001/jama.2020.2648
- Xu, Y., Chen, K., Pan, J., Lei, Y., Zhang, D., Fang, L., et al. (2021). Repurposing Clinically Approved Drugs for COVID-19 Treatment Targeting SARS-CoV-2 Papain-like Protease. *Int. J. Biol. Macromolecules* 188, 137-146. doi:10.1016/j.ijbiomac.2021.07.184
- Yadav, R., Chaudhary, J. K., Jain, N., Chaudhary, P. K., Khanra, S., Dhamija, P., et al. (2021). Role of Structural and Non-structural Proteins and Therapeutic Targets of SARS-CoV-2 for COVID-19. *Cells* 10 (4), 821. doi:10.3390/cells10040821

- Ye, Z.-W., Yuan, S., Yuen, K.-S., Fung, S.-Y., Chan, C.-P., and Jin, D.-Y. (2020). Zoonotic Origins of Human Coronaviruses. *Int. J. Biol. Sci.* 16 (10), 1686–1697. doi:10.7150/ijbs.45472
- Yosri, N., Abd El-Wahed, A. A., Ghonaim, R., Khattab, O. M., Sabry, A., Ibrahim, M. A. A., et al. (2021). Anti-Viral and Immunomodulatory Properties of Propolis: Chemical Diversity, Pharmacological Properties, Preclinical and Clinical Applications, and In Silico Potential against SARS-CoV-2. *Foods* 10 (8), 1776. doi:10.3390/foods10081776
- Zhang, D.-h., Wu, K.-l., Zhang, X., Deng, S.-q., and Peng, B. (2020b). *In Silico* screening of Chinese Herbal Medicines with the Potential to Directly Inhibit 2019 Novel Coronavirus. *J. Integr. Med.* 18 (2), 152–158. doi:10.1016/j.joim.2020.02.005
- Zhang, R. H., Ai, X., Liu, Y., Li, C. H., and Zhang, H. L. (2020a). Genomic Characterization and Phylogenetic Evolution of the SARS-CoV-2. *Acta Virol.* 64 (4), 496–500. doi:10.4149/av_2020_403
- Zhao, Y., Du, X., Duan, Y., Pan, X., Sun, Y., You, T., et al. (2021). High-throughput Screening Identifies Established Drugs as SARS-CoV-2 PLpro Inhibitors. *Protein Cell* 12 (11), 877–888. doi:10.1007/s13238-021-00836-9
- Zheng, Y., and Gao, C. (2019). E3 Ubiquitin Ligases, the Powerful Modulator of Innate Antiviral Immunity. *Cell Immunol.* 340, 103915. doi:10.1016/j.cellimm.2019.04.003
- Zheng, Y., and Gao, C. (2020). Fine-tuning of Antiviral Innate Immunity by Ubiquitination. *Adv. Immunol.* 145, 95–128. doi:10.1016/bs.ai.2019.11.004
- Zhou, P., Yang, X.-L., Wang, X.-G., Hu, B., Zhang, L., Zhang, W., et al. (2020). A Pneumonia Outbreak Associated with a New Coronavirus of Probable Bat Origin. *Nature* 579 (7798), 270–273. doi:10.1038/s41586-020-2012-7
- Zhu, N., Zhang, D., Wang, W., Li, X., Yang, B., Song, J., et al. (2020). A Novel Coronavirus from Patients with Pneumonia in China, 2019. *N. Engl. J. Med.* 382 (8), 727–733. doi:10.1056/nejmoa2001017

Conflict of Interest: The authors declare that the research was conducted in the absence of any commercial or financial relationships that could be construed as a potential conflict of interest.

Publisher's Note: All claims expressed in this article are solely those of the authors and do not necessarily represent those of their affiliated organizations, or those of the publisher, the editors, and the reviewers. Any product that may be evaluated in this article, or claim that may be made by its manufacturer, is not guaranteed or endorsed by the publisher.

Copyright © 2022 Jiang, Yang and Zhang. This is an open-access article distributed under the terms of the Creative Commons Attribution License (CC BY). The use, distribution or reproduction in other forums is permitted, provided the original author(s) and the copyright owner(s) are credited and that the original publication in this journal is cited, in accordance with accepted academic practice. No use, distribution or reproduction is permitted which does not comply with these terms.



Crystallization of Feline Coronavirus M^{pro} With GC376 Reveals Mechanism of Inhibition

Jimmy Lu^{1,2}, Sizhu Amelia Chen^{1,2}, Muhammad Bashir Khan¹, Raelynn Brassard^{1,2}, Elena Arutyunova^{1,2}, Tess Lamer³, Wayne Vuong³, Conrad Fischer^{3†}, Howard S. Young¹, John C. Vederas³ and M. Joanne Lemieux^{1,2*}

¹Department of Biochemistry, University of Alberta, Edmonton, AB, Canada, ²Li Ka Shing Institute of Virology, University of Alberta, Edmonton, AB, Canada, ³Department of Chemistry, University of Alberta, Edmonton, AB, Canada

OPEN ACCESS

Edited by:

Matthew Bogyo,
Stanford University, United States

Reviewed by:

Nir London,
Weizmann Institute of Science, Israel
Jun Wang,
Rutgers, The State University of New
Jersey, United States

*Correspondence:

M. Joanne Lemieux
joanne.lemieux@ualberta.ca

†Present Address:

Conrad Fischer,
Department of Physical Sciences,
Barry University, Miami Shores, FL,
United States

Specialty section:

This article was submitted to
Medicinal and Pharmaceutical
Chemistry,
a section of the journal
Frontiers in Chemistry

Received: 11 January 2022

Accepted: 01 February 2022

Published: 24 February 2022

Citation:

Lu J, Chen SA, Khan MB, Brassard R, Arutyunova E, Lamer T, Vuong W, Fischer C, Young HS, Vederas JC and Lemieux MJ (2022) Crystallization of Feline Coronavirus M^{pro} With GC376 Reveals Mechanism of Inhibition. *Front. Chem.* 10:852210. doi: 10.3389/fchem.2022.852210

Coronaviruses infect a variety of hosts in the animal kingdom, and while each virus is taxonomically different, they all infect their host *via* the same mechanism. The coronavirus main protease (M^{pro}, also called 3CL^{pro}), is an attractive target for drug development due to its essential role in mediating viral replication and transcription. An M^{pro} inhibitor, GC376, has been shown to treat feline infectious peritonitis (FIP), a fatal infection in cats caused by internal mutations in the feline enteric coronavirus (FECV). Recently, our lab demonstrated that the feline drug, GC373, and prodrug, GC376, are potent inhibitors of SARS-CoV-2 M^{pro} and solved the structures in complex with the drugs; however, no crystal structures of the FIP virus (FIPV) M^{pro} with the feline drugs have been published so far. Here, we present crystal structures of FIPV M^{pro}-GC373/GC376 complexes, revealing the inhibitors covalently bound to Cys144 in the active site, similar to SARS-CoV-2 M^{pro}. Additionally, GC376 has a higher affinity for FIPV M^{pro} with lower nanomolar K_i values compared to SARS-CoV and SARS-CoV-2 M^{pro}. We also show that improved derivatives of GC376 have higher potency for FIPV M^{pro}. Since GC373 and GC376 represent strong starting points for structure-guided drug design, determining the crystal structures of FIPV M^{pro} with these inhibitors are important steps in drug optimization and structure-based broad-spectrum antiviral drug discovery.

Keywords: 3CL^{pro}, coronavirus, feline infectious peritonitis (FIP), FCoV, protease, GC376, antiviral, COVID-19

INTRODUCTION

Coronaviruses are single-stranded, positive-sense RNA viruses that affect mammals and birds, causing a variety of diseases (Anand et al., 2003). Containing one of the largest genomes among RNA viruses (~27–31 kb), the family Coronaviridae makes up four genera: Alpha-, Beta-, Gamma-, and Deltacoronavirus (Báez-Santos et al., 2015). Coronaviruses take over the host's transcriptional machinery by encoding two overlapping polyproteins, pp1a and pp1ab, which are cleaved by coronavirus-encoded proteases—papain-like protease (PL^{pro}) and main protease (M^{pro}, also called 3CL^{pro}) (Thiel et al., 2003)—forming 16 nonstructural proteins (nsps) that are essential for viral replication (de Wit et al., 2016). M^{pro}, a cysteine protease, cleaves the polyproteins at 11 conserved sites containing the Leu-Gln↓(Ser, Ala, Gly) sequence, releasing the nsps required for the viral replicase complex (Hegyi and Ziebuhr, 2002). Since M^{pro} cleavage is required for subsequent viral replication and transcription, M^{pro} is an attractive target for drug development against coronaviruses (Yin et al., 2007).

Due to their rapid transmission and lethality, coronaviruses pose a major threat to public health (Chen et al., 2020). This was seen in previous global coronavirus outbreaks such as the severe acute respiratory syndrome coronavirus (SARS-CoV) outbreak in 2002/3, the Middle East respiratory syndrome coronavirus (MERS-CoV) outbreak of 2012, and more recently, the COVID-19 pandemic caused by SARS-CoV-2 in 2019 and onward (de Wit et al., 2016; Hu et al., 2021). Aside from humans, coronaviruses infect other mammals including felines, ferrets, mink, and pigs (Perera et al., 2018; Stout et al., 2020; Ye et al., 2020). Feline enteric coronavirus (FECV), an Alphacoronavirus, is commonly found among domestic cats; however, infected cats are usually asymptomatic or experience mild enteritis (Felten and Hartmann, 2019). Feline infectious peritonitis (FIP) derives from internal mutations in FECV shifting tropism from enterocytes to macrophages resulting in a 100% fatality rate in cats, thus FIP virus (FIPV) is vertically transmitted (Dye & Siddell, 2005; Felten and Hartmann, 2019). It is worth noting that mutations in FECV M^{Pro} have not been associated with increased virulence in FIPV (Pedersen, 2014). M^{Pro} inhibitors which block viral replication have, therefore, been extensively studied against different coronaviruses as a means to develop broad-spectrum antivirals (Hegyi and Ziebuhr, 2002; Kim et al., 2012; Bai et al., 2021).

Various peptidomimetic inhibitors have been developed against viral M^{Pro} (Yin et al., 2007; St. John et al., 2015; Wang et al., 2016). In 2011, a peptide-based inhibitor of M^{Pro} was reported as a promising antiviral drug to combat norovirus infection (Tiew et al., 2011). That inhibitor has since been modified and the new derivative, GC376, was shown to inhibit FIPV M^{Pro} with sub-micromolar IC₅₀ values (Kim et al., 2012). GC376, a dipeptidyl aldehyde bisulfite adduct, is a prodrug that converts into the active-form aldehyde, GC373, upon administration, effectively binding the active site of M^{Pro} and stopping viral replication (Kim et al., 2013; Kim et al., 2015). Other studies have demonstrated that GC376 was successful in reversing the progression of experimentally induced FIP as well as naturally occurring FIP in cats, demonstrating that peptide-based inhibitors are effective against coronavirus infections *in vivo* (Kim et al., 2016; Pedersen et al., 2018).

With the success GC376 has had in treating FIP in cats, it was then postulated to be an effective inhibitor to treat SARS-CoV-2 infections (Vuong et al., 2020). We have previously reported that the prodrug GC376 and drug GC373 are potent inhibitors of SARS-CoV and SARS-CoV-2 M^{Pro} with K_i values in the nanomolar range (Arutyunova et al., 2021). The crystal structures of SARS-CoV and SARS-CoV-2 M^{Pro} in complex with the feline drugs revealed the inhibitor forming a covalent bond with Cys145 as a hemithioacetal in the active site (Vuong et al., 2020). The varied effectiveness of GC376 against M^{Pro} of different coronaviruses suggests structural differences in drug binding (Kim et al., 2012; Arutyunova et al., 2021). Despite the research invested in the feline drugs with regard to FIP, no crystal structure of FIPV M^{Pro} with GC376 or GC373 has been solved to date.

In this study, we solved the crystal structure of FIPV M^{Pro} (FIPV WSU-79/1146) in complex with the drug, GC373, and prodrug, GC376, to reveal the architecture of the active site with bound inhibitors. Furthermore, we examined the improved

derivatives of GC376 and demonstrated their higher potency toward FIPV M^{Pro}. As GC376 and GC373 were successfully used to treat FIP in cats, they are considered strong starting points in drug design to treat COVID-19 in humans. Here, we compare the structural similarities and differences between SARS-CoV-2 M^{Pro} and FIPV M^{Pro} with the feline drugs for antiviral drug optimization against SARS-CoV-2 and the development of future broad-spectrum antivirals.

MATERIALS AND METHODS

Inhibitor and Fluorescence Resonance Energy Transfer Substrate Synthesis

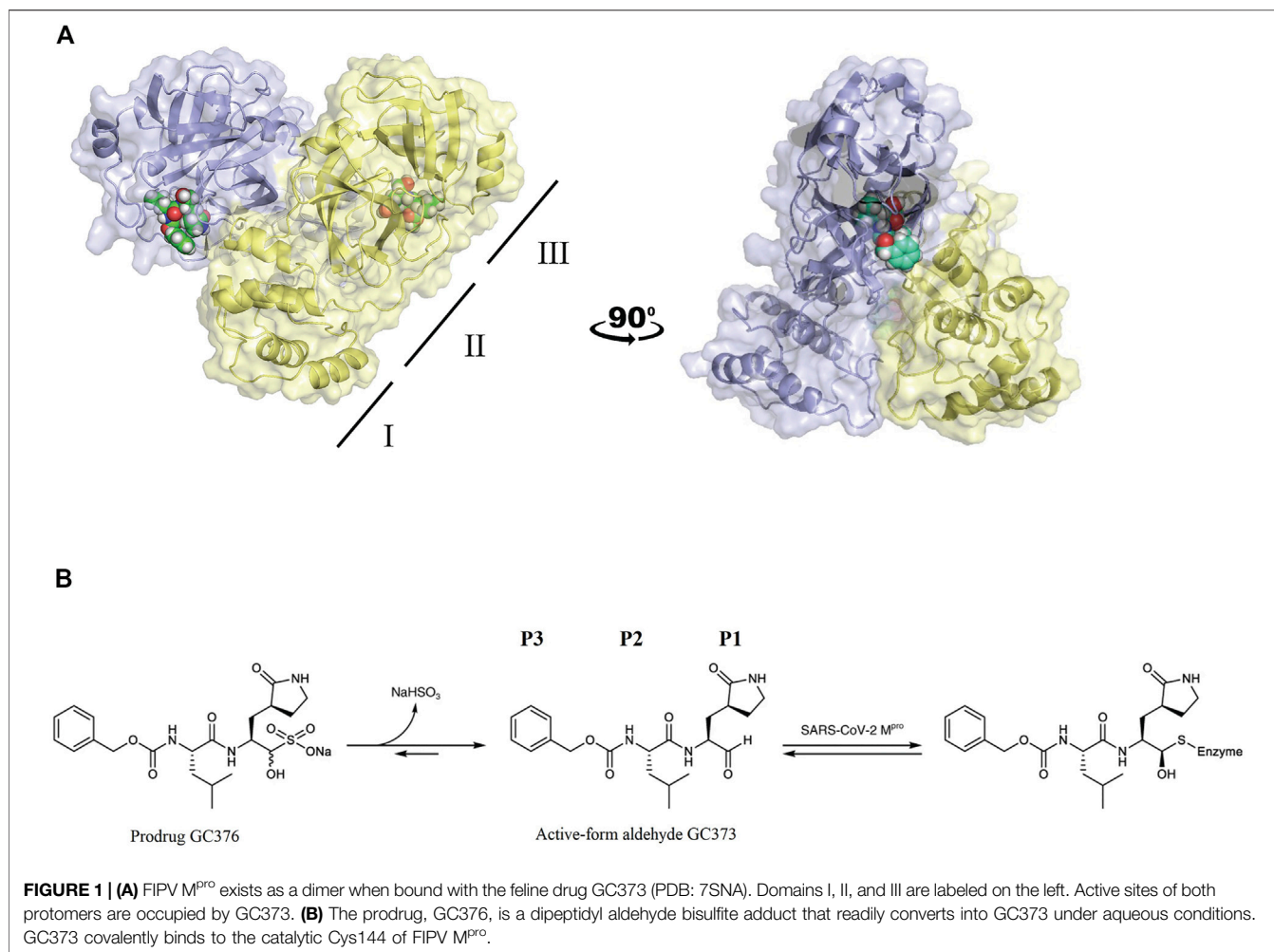
Inhibitors GC373, GC376, and their derivatives, as well as the FRET assay peptide substrate, Abz-SVTLQSG-Y(NO₂)-R, were synthesized according to methods previously described (Vuong et al., 2020; Vuong et al., 2021).

Cloning, Expression, and Purification of Feline Infectious Peritonitis Virus M^{Pro}

The FIPV WSU-79/1146 M^{Pro} gene was synthesized (Bio Basic, Canada) and cloned into pET SUMO expression vector (Invitrogen, United States), generating a fusion protein with a His-tagged SUMO domain at the N-terminus. The construct was transformed into BL21 (DE3) *Escherichia coli*, where protein expression was induced with 0.5 mM isopropyl β-D-1-thiogalactopyranoside (IPTG) once OD₆₀₀ reached 0.5–0.6 and then grown for an additional 5 h at 32°C. The cells were harvested by centrifugation (5,000 ×g for 20 min at 4°C), suspended in lysis buffer (20 mM Tris-HCl, 150 mM NaCl, 5 mM imidazole, pH 7.8), and lysed using the Emulsiflex C3 High Pressure Homogenizer. Cellular debris was removed by centrifugation at 20,000 ×g for 45 min at 4°C. The isolated supernatant was applied onto a Ni-NTA column (Qiagen, Canada), the resin was washed with 10 column volumes of lysis buffer containing 20 mM imidazole, and the protein was eluted with a step gradient of 100–1000 mM imidazole in lysis buffer. The eluted fractions were analyzed by sodium dodecyl sulfate–polyacrylamide gel electrophoresis, pooled based on purity and dialyzed against 20 mM Tris-HCl, 150 mM NaCl, 1 mM TCEP, pH 7.8, for 2 h at 4°C. The SUMO tag was cleaved off using His-tagged SUMO protease (McLab, United States) and both the N-terminal SUMO tag and SUMO protease were removed by passing the protein sample through a Ni-NTA column. The flow-through containing FIPV M^{Pro} was further purified using size exclusion chromatography (Superdex increase 10/300 GL, GE Healthcare), with buffer containing 20 mM Tris-HCl, 150 mM NaCl, 1 mM TCEP, pH 7.8. The fractions containing FIPV M^{Pro} were pooled and concentrated using an Amicon Ultra-15 filter with a MWCO of 10 kDa.

Crystallization of Feline Infectious Peritonitis Virus M^{Pro} With GC373 and GC376

Purified FIPV M^{Pro} was dialyzed against 5 mM Tris-HCl, 5 mM NaCl, 1 mM TCEP, pH 7.8 buffer at 4°C overnight and concentrated



to 10 mg/ml using an Amicon Ultra-15 filter with a MWCO of 10 kDa. FIPV M^{Pro} was incubated with GC373 or GC376 (5× molar excess) at 4°C for 2 h prior to crystallization. The protein was subjected to the PACT and JCSG crystallization screens (Molecular Dimensions, United States). Crystals were observed with sitting drop trays at room temperature. The crystals of FIPV M^{Pro} with GC376 were obtained using a protein:buffer ratio of 1:1 with 2.0 M ammonium sulfate, 0.1 M Bis-Tris, pH 5.5. The crystals of FIPV M^{Pro} with GC373 were obtained using a 2:1, protein:buffer ratio with 0.2 M calcium chloride dihydrate, 0.1 M MES, 20% (w/v) PEG 6000, pH 6.0. The crystals were frozen in liquid nitrogen using 19% glycerol as a cryoprotectant.

Diffraction Data Collection, Model Building, and Structural Refinement

The diffraction data were collected at Canadian Light Source using beamline CMCF-BM (08B1) and PILATUS3 S 6M detector, Saskatchewan, Canada. Several data sets were collected from different crystals and were processed using SCALA and XDS. The diffraction data set of the GC373 was processed to 2.05 Å, in a monoclinic C2 space group, while the GC376 were processed to

1.93 Å, in an orthorhombic P2₁2₁2₁ space group. The structures were determined by molecular replacement using the crystal structure of the apo-FIPV M^{Pro} (PDB entry: 5EU8) as the search model. GC376 and GC373 were manually fit in the density using Coot. The structures were then refined by using the Phenix software. Data statistics, processing, and model refinement are given in **Supplementary Table S1**.

Enzyme Kinetics of Feline Infectious Peritonitis Virus M^{Pro}

A fluorescence resonance energy transfer (FRET)-based cleavage assay was performed using a synthetic peptide fluorescent substrate containing the cleavage site of FIPV M^{Pro} [Abz-SVTLQ↓SG-Tyr (NO₂)-R] as described previously (Vuong et al., 2020; Vuong et al., 2021). For K_i determination, 50 nM FIPV M^{Pro} was preincubated with GC376 in the concentration range of 0.01–0.4 μM for 10 min at 37°C. The enzymatic reactions using 1–500 μM of FRET substrate in activity buffer (25 mM Bis-Tris, 1 mM DTT, pH 7.0) were started with the addition of protease. For IC₅₀ determination, 100 nM of FIPV M^{Pro} was incubated with an inhibitor concentration range of 0.25 nM–100 μM in activity buffer. The reaction was started with

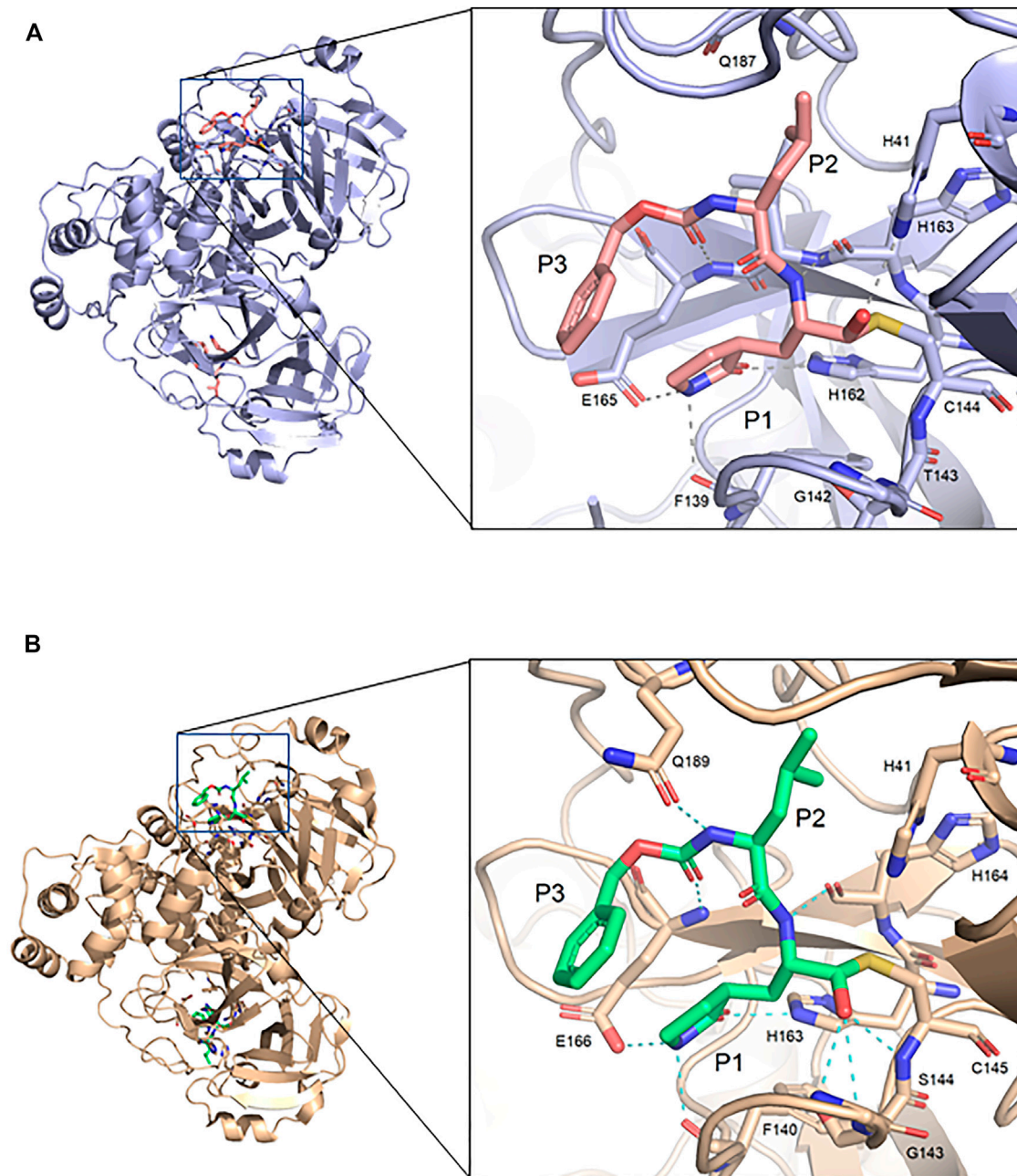


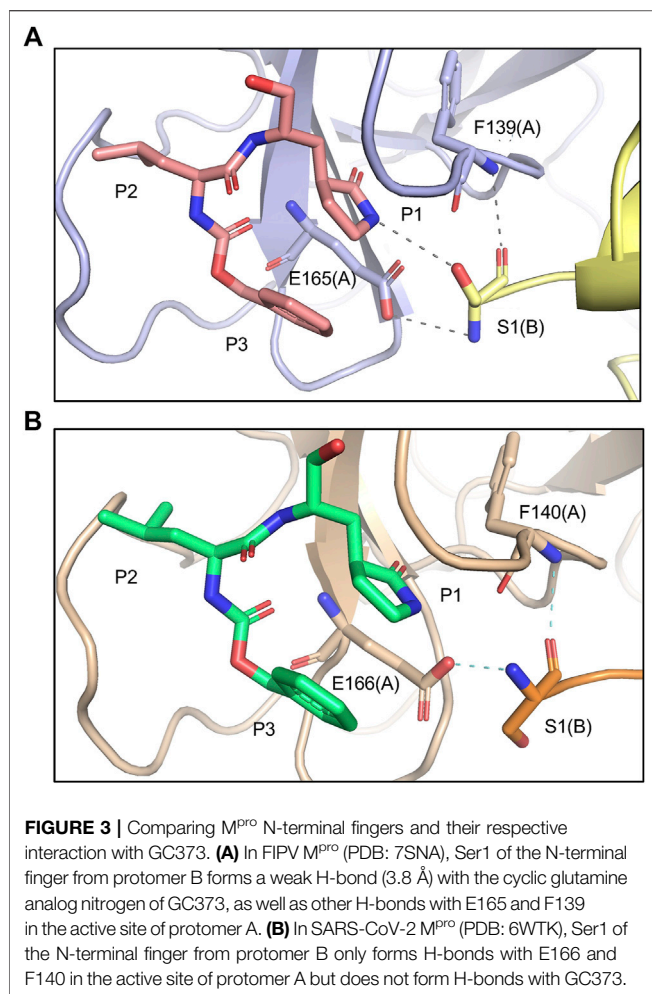
FIGURE 2 | Comparison of FIPV M^{pro} and SARS-CoV-2 M^{pro} bound to GC373. **(A)** Crystal structure of FIPV M^{pro} with GC373 in lavender (PDB: 7SNA) and **(B)** SARS-CoV-2 M^{pro} with GC373 in tan (PDB: 6WTK).

40 μ M of FRET substrate. The fluorescence signal of the FRET peptide cleavage product was monitored at an emission wavelength of 420 nm with excitation at 320 nm, using a Cytation 5 Imaging Multi-Mode Reader (BioTek) for 7 min at 37°C. The kinetic data were analyzed using computer-fit calculation (Prism 9.0, GraphPad Software). The slopes of the Lineweaver–Burk plots were plotted versus the concentration of GC376, and the K_i was determined from the x-axis intercept as $-K_i$. The experiments were performed in triplicate.

RESULTS

The Overview of Feline Infectious Peritonitis Virus M^{pro}-GC373/376 Complex Structure

Crystal structures of FIPV M^{pro} in complex with the drug GC373 (PDB: 7SNA) and prodrug GC376 (PDB: 7SMV) were solved to 2.05 Å and 1.93 Å, respectively (Supplementary Table S1). GC376 being the dipeptidyl aldehyde bisulfite adduct form of the drug converts into the active-form aldehyde GC373, thus



making both structures identical. In both structures, FIPV M^{pro} crystallized as a dimer, with each protomer being comprised of three domains (**Figure 1A**), similar to other viral M^{pro}. Domains I and II have a six-stranded antiparallel β -barrel structure, and domain III is a globular cluster of five antiparallel α -helices, connected to domain II by a long loop. The active site of FIPV M^{pro} contains a Cys144–His41 catalytic dyad located in a cleft between domain I and domain II. Domain III regulates the dimerization of the M^{pro} which is required for its catalytic activity. The N-terminal residues (N-finger) of protomer A fits between domains II and III of the protomer A and interacts with residues in domain II of protomer B helping shape the S1 substrate-binding subsite in the active site.

GC373 Is Stabilized by H-Bond Network in the Active Site of Feline Infectious Peritonitis Virus M^{pro}

The GC373 inhibitor covalently binds FIPV M^{pro} and is stabilized by hydrogen bonding and hydrophobic interactions in a similar manner to SARS-CoV and SARS-CoV-2 M^{pro}. In both structures, a covalent bond between Cys144 and the aldehyde of the feline drug reveals that the bisulfite leaving group indeed was removed upon

TABLE 1 | Comparison of K_i values of GC376 between FIPV M^{pro}, SARS-CoV M^{pro}, and SARS-CoV-2 M^{pro}. Data are presented as mean \pm SEM, $n = 3$.

Protease	Calculated K _i (nM)
FIPV M ^{pro}	2.1
SARS-CoV M ^{pro}	20
SARS-CoV-2 M ^{pro}	40

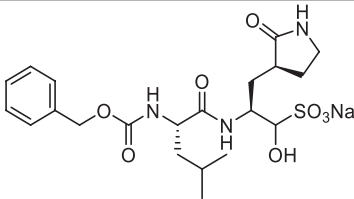
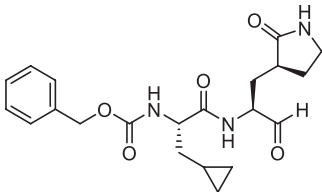
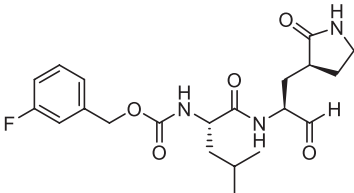
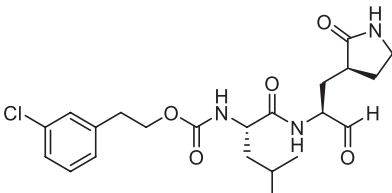
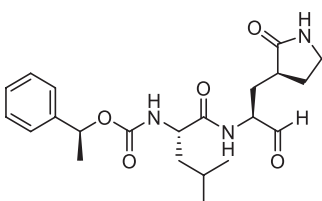
^aData from Arutyunova et al. (2021).

binding (**Figure 1B**). Weak H-bonding was observed between the oxyanion of the inhibitor and His41, the general base in the catalytic dyad, which is distinct from SARS-CoV-2 (**Figure 2A**) (Vuong et al., 2020). For the P1 position of the inhibitor, the N γ of the lactam ring sits in the S1 pocket and forms a H-bond with the carbonyl oxygen of Phe139 (**Supplementary Figure S1A**), a conserved feature in other M^{pro} structures with GC373 (Arutyunova et al., 2021). The S2 pocket that supports hydrophobic interactions of a Leu moiety is formed with His41, Ile51, and Leu164 (**Supplementary Figure S2A**). This differs from the stabilization network found in SARS-CoV-2 M^{pro} for the same feline drug. Meanwhile, the P3 benzyl moiety interacts with the P1 lactam ring by pi stacking, similar to that observed in the SARS-CoV-2 M^{pro} structure (Vuong et al., 2020).

Feline Infectious Peritonitis Virus M^{pro} and SARS-CoV-2 M^{pro} Have Similar Overall Structure

FIPV and SARS-CoV-2 M^{pro} share 60% sequence similarity, however, the active-site region exhibits even greater conservation (**Supplementary Figure S3**). Comparing the overall structures, both bound to GC373, the RMSD was calculated to be 1.16 Å. While the active site cavity of both FIPV and SARS-CoV-2 M^{pro} are composed of identical residues, the structures of M^{pro} in complex with GC373 or GC376, reveal some differences in inhibitor binding. In FIPV M^{pro}, GC373 is stabilized in the active site by H-bonding with His41 (**Figure 2A**, **Supplementary Figure S1B**). By contrast, SARS-CoV (not shown) and SARS-CoV-2 M^{pro} form a stable acyl-intermediate with the drug through a H-bonding network with the backbones of Cys145, Ser144, and Gly143 residues (**Figure 2B**, **Supplementary Figure S6**). Furthermore, the S2 pocket that supports hydrophobic interactions of the drug's Leu moiety is formed with His41, Ile51, and Leu164 in FIPV M^{pro}, but with His41, Met49, and Met165 in SARS-CoV-2 M^{pro} (**Supplementary Figure S2B**). In SARS-CoV-2 M^{pro}, Gln189 plays an integral role in stabilizing the dipeptide backbone of the inhibitor (Bai et al., 2021), however in FIPV M^{pro}, we observe an unstructured loop fit between the S3 and S4 pocket to form hydrophobic interactions, thus further supporting binding of the inhibitor (**Supplementary Figures S4, S5**). In FIPV M^{pro}, Ser1 of the N-terminal finger from protomer B forms a weak H-bond (3.8 Å) with the cyclic glutamine analog nitrogen of GC373 in the active site of protomer A, however, this is not seen in SARS-CoV-2 M^{pro} (**Figure 3A**). Furthermore, the side chain hydroxyl group and backbone amide of Ser1 in protomer B form H-bonds with Glu165 and Phe139 in the active site of protomer A. This is comparable to SARS-CoV and SARS-CoV-2 M^{pro} structures where Ser1 of the N-terminal finger (protomer B) forms H-bonds

TABLE 2 | Singly modified derivatives of GC373 at the P2 or P3 positions and their corresponding IC₅₀ values. Data are presented as mean ± SEM, *n* = 3.

Entry	Structure	FIPV M ^{Pro} IC ₅₀ (μM)	SARS-CoV-2 M ^{Pro} IC ₅₀ (μM) ^a
GC376		0.13 ± 0.02	0.19 ± 0.04
1a		0.10 ± 0.07	0.05 ± 0.01
1d		0.07 ± 0.01	0.13 ± 0.04
1e		0.13 ± 0.02	0.15 ± 0.05
1g		0.43 ± 0.09	0.27 ± 0.09

^aData from Vuong et al. (2021).

with Glu166 and Phe140 (protomer A) to shape the P1 position (**Figure 3B**). These structural changes led us to examine the inhibitory parameters of GC376 with FIPV M^{Pro} for comparison with SARS-CoV and SARS-CoV-2 M^{Pro}.

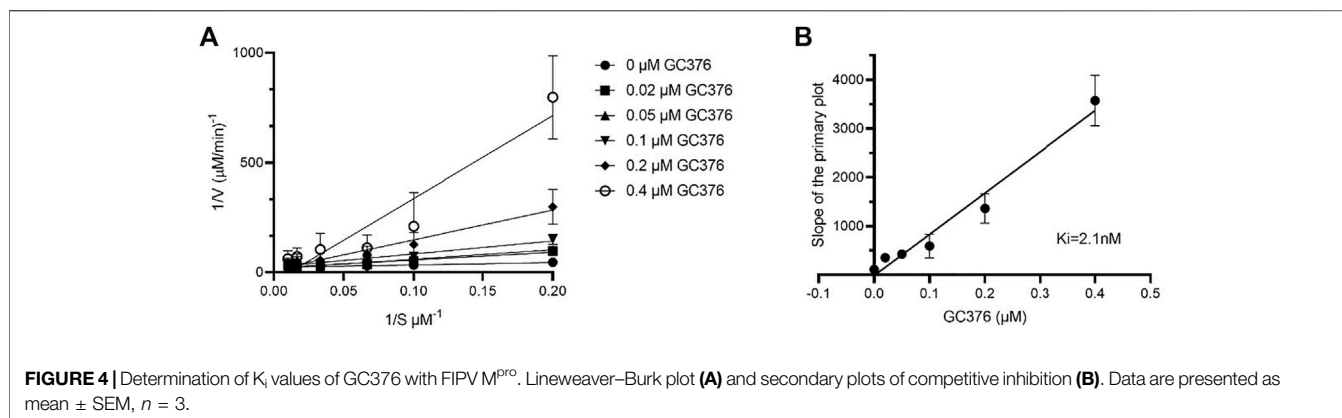
GC376 Has Higher Affinity to Feline Infectious Peritonitis Virus M^{Pro} Compared to SARS-CoV-2

IC₅₀ and K_i values quantitatively reflect the potency and affinity of a drug and are therefore important parameters to consider when undergoing inhibitor design. First, we determined the catalytic parameters of FIPV M^{Pro} using our synthetic peptide FRET-substrate (**Supplementary Table S2**) (Arutyunova et al., 2021).

Interestingly, feline coronavirus protease exhibited 24 times slower catalytic turnover rate than M^{Pro} of SARS-CoV-2 with the same substrate, and a lower K_m value. The K_i values for GC376 inhibition were determined to be 2.1 nM for FIPV M^{Pro} (**Figure 4**), lower in comparison to previously determined K_i values of SARS-CoV and SARS-CoV-2 M^{Pro}, which were 20 and 40 nM, respectively (**Table 1**) (Vuong et al., 2020; Arutyunova et al., 2021).

Improved Derivatives of GC376 Are Also Potent Toward Feline Infectious Peritonitis Virus M^{Pro}

We recently demonstrated that derivatives of GC376 with singly or doubly modified constituents resulted in improved potency



with SARS-CoV-2 M^{Pro}, having lower IC₅₀ and EC₅₀ values (Vuong et al., 2021). The singly modified compounds contain derivatives that include a cyclopropyl group (1a) in the P2 position where the S2 pocket typically recognizes a Leu residues side chain, and a 3-fluorobenzyl (2c) or 3-chlorophenylethyl group (2d) in the P3 position recognized by the S4 pocket (Table 2). The doubly modified compounds all included a cyclopropyl group in the P2 position, as well as a 3-fluorobenzyl (2c), 3-chlorophenylethyl (2d), or 4-methoxyindole (2e) group at the P3 position (Table 3). In order to assess if these inhibitor derivatives also have improved potency with FIPV M^{Pro} as they did with SARS-CoV-2 M^{Pro}, IC₅₀ values were calculated and compared. *In vitro* analysis with purified FIPV M^{Pro} revealed that the doubly modified inhibitor had stronger effects on IC₅₀ values than a singly modified inhibitor, bringing the IC₅₀ to the double-digit nanomolar range. This is a similar trend as seen with SARS-CoV-2 M^{Pro} using the same doubly modified inhibitors. Overall, this suggests that inhibitors targeting FIPV M^{Pro} can be improved and warrant further assessment in cellular and animal studies.

DISCUSSION

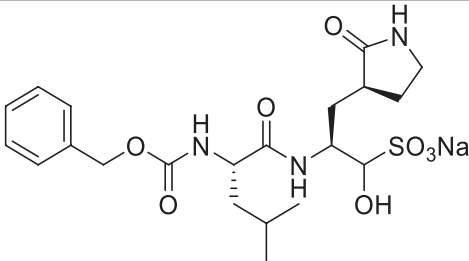
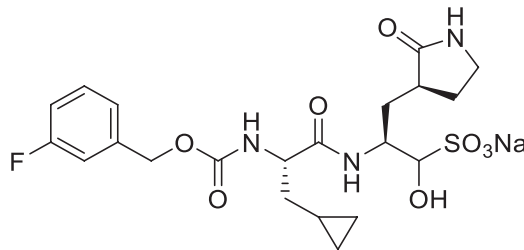
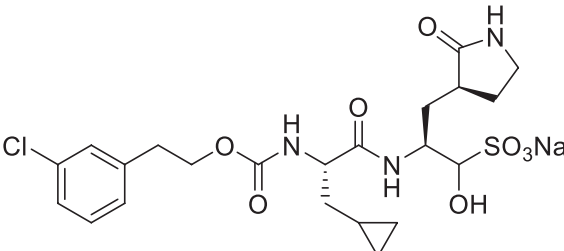
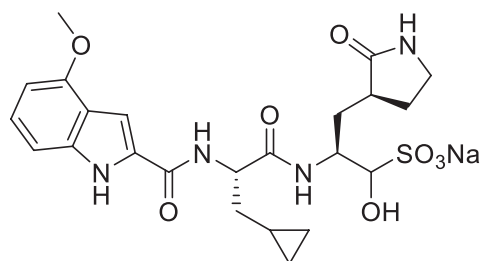
The FECV is commonly detected among domestic house cats and causes mild to no symptoms; however, mutations in FECV lead to FIP, a lethal systemic infection in cats. The M^{Pro} inhibitor GC373 and its bisulfide aldehyde GC376 have been shown to treat the otherwise fatal infection in experimentally infected FIP cats, as well as naturally acquired FIP cats. Furthermore, GC376 has also been shown to be an effective inhibitor of other viral M^{Pro} such as norovirus (PDB: 3UR9), transmissible gastric epidemic virus (PDB: 4F49), MERS-CoV (PDB: 5WTJ), porcine epidemic diarrhea virus (PDB: 6L70), SARS-CoV (PDB: 7LCQ), and more recently, SARS-CoV-2 (PDB: 6WTJ) (Tiew et al., 2011; Kim et al., 2015; Galasiti Kankanamalage et al., 2018; Vuong et al., 2020; Ye et al., 2020; Arutyunova et al., 2021). Our work here reports the crystal structure of GC376 and GC373 with FIPV M^{Pro}, allowing for its comparison with recent structures of viral proteases with these inhibitors and complementing the work done by others in developing the drug for treating FIP in cats.

The overall architecture of GC373 bound to FIPV M^{Pro} is similar to other structures where the drug forms a C-shaped structure with pi stacking between the lactam ring and benzyl group in the P1 and P3 positions, respectively. While structures of SARS-CoV-2 M^{Pro} co-crystallized with GC376 solved by other groups have shown the drug binding in both R and S hemithioacetal isomer conformations (Ma et al., 2020), here we only see the R conformation of the drug bound to FIPV M^{Pro}. We observe hydrogen binding of the oxyanion of GC373 to the general base His41 in FIPV M^{Pro}, similar to MERS-CoV and norovirus M^{Pro} (Kim et al., 2012; Galasiti Kankanamalage et al., 2018). Nonetheless, this binding is in contrast to SARS-CoV, SARS-CoV-2, and PEDV M^{Pro}, where the oxyanion is bound by traditional backbone residues of the oxyanion hole (Kim et al., 2012; Lee et al., 2020; Arutyunova et al., 2021). Overall, this suggests flexibility in the binding between the active site residues and inhibitor, and further highlights the feline drugs' broad specificity.

We have previously shown that the N-terminal tail of M^{Pro} plays a role in dimerization and drug stabilization (Arutyunova et al., 2021). The FIPV M^{Pro}-GC373 complex reveals weak hydrogen bonding of the hydroxyl group of Ser1 (protomer B) with the cyclic glutamine analog in GC373, bound to the active site of protomer A, providing additional coordination for the inhibitor. By contrast, no interaction is observed between Ser1 and GC373 in SARS-CoV-2 M^{Pro}. This led us to compare the inhibitory parameters of GC376 between the two M^{Pro} to determine if these structural differences lead to improved drug binding. We recently showed that GC376 was an effective inhibitor of SARS-CoV M^{Pro} and SARS-CoV-2 M^{Pro} with K_i values of 20 and 40 nM, respectively (Table 1). In comparison, GC376 inhibited the FIPV M^{Pro} with a K_i of 2.1 nM, 20 times higher in affinity than SARS-CoV-2 M^{Pro}. Together, the difference in K_i values further reflects structural plasticity among various M^{Pro} that results in differences in how the drug binds the active site and thus affecting drug potency.

In order to increase the potency of GC376, our team has recently developed modified derivatives which showed lower IC₅₀ values for SARS-CoV-2 M^{Pro} compared to the parent compound (Vuong et al., 2021). The modification of P2 was

TABLE 3 | Doubly modified derivatives of GC376 at the P2 and P3 positions and their corresponding IC₅₀ values. Data are presented as mean ± SEM, *n* = 3.

Entry	Structure	FIPV M ^{Pro} IC ₅₀ (μM)	SARS-CoV-2 M ^{Pro} IC ₅₀ (μM) ^a
GC376		0.13 ± 0.02	0.19 ± 0.04
2c		0.03 ± 0.01	0.07 ± 0.01
2d		0.05 ± 0.02	0.08 ± 0.02
2e		0.06 ± 0.02	0.04 ± 0.01

^aData from Vuong et al. (2021).

chosen to be lipophilic since our previous crystal structures demonstrate that the S2 pocket responsible for binding the leucine moiety was mostly hydrophobic. The modification of the P3 position allowed for enhanced dipole interactions with the S4 pocket of the enzyme, potentially contributing to the higher affinity (Wang et al., 2016). Importantly, these derivatives, in particular the ones with double modifications, exhibit lower IC₅₀ values with FIPV M^{Pro} compared to SARS-CoV-2 M^{Pro}. Moving forward, enhanced drugs are needed for both FIPV infections as well as other coronavirus-related outbreaks. This crystal structure of FIPV M^{Pro} in complex with GC376 will assist us in accelerating development of new derivatives to be used in clinical trials as broad-spectrum antivirals.

DATA AVAILABILITY STATEMENT

The original contributions presented in the study are included in the article/**Supplementary Material**, and further inquiries can be directed to the corresponding author.

AUTHOR CONTRIBUTIONS

JL and SAC contributed to protein purification. JL, SAC, MK, HY, and MJL contributed to crystallization and structure determination. TL contributed to FRET-substrate synthesis. WV, CF, and JV contributed to inhibitor design. WV and CF contributed to inhibitor synthesis. RB, JL, SAC, and EA contributed to enzyme

kinetics. SAC wrote the initial draft. All authors read and approved the manuscript.

FUNDING

Funding for the project were provided by Canadian Institutes of Health Research (CIHR) COVID Rapid Response grants: NSERC SOF-549297-2019, CIHR VR3-172655, and Canada Foundation for Innovation.

ACKNOWLEDGMENTS

We thank the staff at CLS beamline CMCF-BM (08B1), in particular Michel Fodje. Part or all of the research described

in this article was performed using beamline CMCF-BM at the Canadian Light Source, a national research facility of the University of Saskatchewan, which is supported by the Canada Foundation for Innovation (CFI), the Natural Sciences and Engineering Research Council (NSERC), the National Research Council (NRC), the Canadian Institutes of Health Research (CIHR), the Government of Saskatchewan, and the University of Saskatchewan.

SUPPLEMENTARY MATERIAL

The Supplementary Material for this article can be found online at: <https://www.frontiersin.org/articles/10.3389/fchem.2022.852210/full#supplementary-material>

REFERENCES

- Anand, K., Ziebuhr, J., Wadhwani, P., Mesters, J. R., and Hilgenfeld, R. (2003). Coronavirus Main Proteinase (3CL Pro) Structure: Basis for Design of Anti-SARS Drugs. *Science* 300, 1763–1767. doi:10.1126/science.1085658
- Arutyunova, E., Khan, M. B., Fischer, C., Lu, J., Lamer, T., Vuong, W., et al. (2021). N-terminal Finger Stabilizes the S1 Pocket for the Reversible Feline Drug GC376 in the SARS-CoV-2 Mpro Dimer. *J. Mol. Biol.* 433 (13), 167003. doi:10.1016/j.jmb.2021.167003
- Báez-Santos, Y. M., St. John, S. E., and Mesecar, A. D. (2015). The SARS-Coronavirus Papain-like Protease: Structure, Function and Inhibition by Designed Antiviral Compounds. *Antiviral Res.* 115, 21–38. doi:10.1016/j.antiviral.2014.12.015
- Bai, B., Belovodskiy, A., Hena, M., Kandadai, A. S., Joyce, M. A., Saffran, H. A., et al. (2021). Peptidomimetic α -Acetyloxymethylketone Warheads with Six-Membered Lactam P1 Glutamine Mimic: SARS-CoV-2 3CL Protease Inhibition, Coronavirus Antiviral Activity, and *In Vitro* Biological Stability. *J. Med. Chem.* Online ahead of print. doi:10.1021/acs.jmedchem.1c00616
- Chen, Y., Liu, Q., and Guo, D. (2020). Emerging Coronaviruses: Genome Structure, Replication, and Pathogenesis. *J. Med. Virol.* 92 (4), 418–423. doi:10.1002/jmv.25681
- de Wit, E., van Doremalen, N., Falzarano, D., and Munster, V. J. (2016). SARS and MERS: Recent Insights into Emerging Coronaviruses. *Nat. Rev. Microbiol.* 14 (8), 523–534. doi:10.1038/nrmicro.2016.81
- Dye, C., and Siddell, S. G. (2005). Genomic RNA Sequence of Feline Coronavirus Strain FIPV WSU-79/1146. *J. Gen. Virol.* 86 (8), 2249–2253. doi:10.1099/vir.0.80985-0
- Felten, S., and Hartmann, K. (2019). Diagnosis of Feline Infectious Peritonitis: A Review of the Current Literature. *Viruses* 11 (11), 1068. doi:10.3390/v11111068
- Galasiti Kankanamalage, A. C., Kim, Y., Damalanka, V. C., Rathnayake, A. D., Fehr, A. R., Mehzabeen, N., et al. (2018). Structure-guided Design of Potent and Permeable Inhibitors of MERS Coronavirus 3CL Protease that Utilize a Piperidine Moiety as a Novel Design Element. *Eur. J. Med. Chem.* 150, 334–346. doi:10.1016/j.ejmech.2018.03.004
- Hegyi, A., and Ziebuhr, J. (2002). Conservation of Substrate Specificities Among Coronavirus Main Proteinases. *J. Gen. Virol.* 83 (3), 595–599. doi:10.1099/0022-1317-83-3-595
- Hu, B., Guo, H., Zhou, P., and Shi, Z.-L. (2021). Characteristics of SARS-CoV-2 and COVID-19. *Nat. Rev. Microbiol.* 19 (3), 141–154. doi:10.1038/s41579-020-00459-7
- Kim, Y., Liu, H., Kankanamalage, A. C. G., Weerasekara, S., Hua, D. H., Groutas, W. C., et al. (2016). Correction: Reversal of the Progression of Fatal Coronavirus Infection in Cats by a Broad-Spectrum Coronavirus Protease Inhibitor. *Plos Pathog.* 12 (5), e1005650. doi:10.1371/journal.ppat.1005650
- Kim, Y., Lovell, S., Tiew, K.-C., Mandadapu, S. R., Alliston, K. R., Battaile, K. P., et al. (2012). Broad-Spectrum Antivirals against 3C or 3C-like Proteinases of Picornaviruses, Noroviruses, and Coronaviruses. *J. Virol.* 86 (21), 11754–11762. doi:10.1128/jvi.01348-12
- Kim, Y., Mandadapu, S. R., Groutas, W. C., and Chang, K.-O. (2013). Potent Inhibition of Feline Coronaviruses with Peptidyl Compounds Targeting Coronavirus 3C-like Protease. *Antiviral Res.* 97 (2), 161–168. doi:10.1016/j.antiviral.2012.11.005
- Kim, Y., Shivanna, V., Narayanan, S., Prior, A. M., Weerasekara, S., Hua, D. H., et al. (2015). Broad-Spectrum Inhibitors against 3C-like Proteinases of Feline Coronaviruses and Feline Caliciviruses. *J. Virol.* 89 (9), 4942–4950. doi:10.1128/jvi.03688-14
- Lee, J., Worrall, L. J., Vuckovic, M., Rosell, F. I., Gentile, F., Ton, A.-T., et al. (2020). Crystallographic Structure of Wild-type SARS-CoV-2 Main Proteinase Acyl-Enzyme Intermediate with Physiological C-Terminal Autoproteolysis Site. *Nat. Commun.* 11 (1). doi:10.1038/s41467-020-19662-4
- Ma, C., Sacco, M. D., Hurst, B., Townsend, J. A., Hu, Y., Szeto, T., et al. (2020). Boceprevir, GC-376, and Calpain Inhibitors II, XII Inhibit SARS-CoV-2 Viral Replication by Targeting the Viral Main Proteinase. *Cell Res.* 30 (8), 678–692. doi:10.1038/s41422-020-0356-z
- Pedersen, N. C. (2014). An Update on Feline Infectious Peritonitis: Diagnostics and Therapeutics. *Vet. J.* 201 (2), 133–141. doi:10.1016/j.tvjl.2014.04.016
- Pedersen, N. C., Kim, Y., Liu, H., Galasiti Kankanamalage, A. C., Eckstrand, C., Groutas, W. C., et al. (2018). Efficacy of a 3C-like Protease Inhibitor in Treating Various Forms of Acquired Feline Infectious Peritonitis. *J. Feline Med. Surg.* 20 (4), 378–392. doi:10.1177/1098612x17729626
- Perera, K. D., Galasiti Kankanamalage, A. C., Rathnayake, A. D., Honeyfield, A., Groutas, W., Chang, K.-O., et al. (2018). Protease Inhibitors Broadly Effective against Feline, Ferret and Mink Coronaviruses. *Antiviral Res.* 160, 79–86. doi:10.1016/j.antiviral.2018.10.015
- St. John, S. E., Therkelsen, M. D., Nyalapatla, P. R., Osswald, H. L., Ghosh, A. K., and Mesecar, A. D. (2015). X-ray Structure and Inhibition of the Feline Infectious Peritonitis Virus 3C-like Protease: Structural Implications for Drug Design. *Bioorg. Med. Chem. Lett.* 25 (22), 5072–5077. doi:10.1016/j.bmcl.2015.10.023
- Stout, A. E., André, N. M., Jaimes, J. A., Millet, J. K., and Whittaker, G. R. (2020). Coronaviruses in Cats and Other Companion Animals: Where Does SARS-CoV-2/covid-19 Fit? *Vet. Microbiol.* 247, 108777. doi:10.1016/j.vetmic.2020.108777
- Thiel, V., Ivanov, K. A., Putics, Á., Hertzog, T., Schelle, B., Bayer, S., et al. (2003). Mechanisms and Enzymes Involved in SARS Coronavirus Genome Expression. *J. Gen. Virol.* 84 (9), 2305–2315. doi:10.1099/vir.0.19424-0
- Tiew, K.-C., He, G., Aravapalli, S., Mandadapu, S. R., Gunnam, M. R., Alliston, K. R., et al. (2011). Design, Synthesis, and Evaluation of Inhibitors of Norwalk Virus 3C Protease. *Bioorg. Med. Chem. Lett.* 21 (18), 5315–5319. doi:10.1016/j.bmcl.2011.07.016
- Vuong, W., Fischer, C., Khan, M. B., Van Belkum, M. J., Lamer, T., Willoughby, K. D., et al. (2021). Improved SARS-CoV-2 Mpro Inhibitors Based on Feline Antiviral

- Drug GC376: Structural Enhancements, Increased Solubility, and Micellar Studies. *Eur. J. Med. Chem.* 222, 113584. doi:10.1016/j.ejmech.2021.113584
- Vuong, W., Khan, M. B., Fischer, C., Arutyunova, E., Lamer, T., Shields, J., et al. (2020). Feline Coronavirus Drug Inhibits the Main Protease of SARS-CoV-2 and Blocks Virus Replication. *Nat. Commun.* 11 (1), 4282. doi:10.1038/s41467-020-18096-2
- Wang, F., Chen, C., Liu, X., Yang, K., Xu, X., and Yang, H. (2016). Crystal Structure of Feline Infectious Peritonitis Virus Main Protease in Complex with Synergetic Dual Inhibitors. *J. Virol.* 90 (4), 1910–1917. doi:10.1128/jvi.02685-15
- Ye, G., Wang, X., Tong, X., Shi, Y., Fu, Z. F., and Peng, G. (2020). Structural Basis for Inhibiting Porcine Epidemic Diarrhea Virus Replication with the 3C-like Protease Inhibitor GC376. *Viruses* 12 (2), 240. doi:10.3390/v12020240
- Yin, J., Niu, C., Cherney, M. M., Zhang, J., Huitema, C., Eltis, L. D., et al. (2007). A Mechanistic View of Enzyme Inhibition and Peptide Hydrolysis in the Active Site of the SARS-CoV 3C-like Peptidase. *J. Mol. Biol.* 371 (4), 1060–1074. doi:10.1016/j.jmb.2007.06.001

Conflict of Interest: The authors declare that the research was conducted in the absence of any commercial or financial relationships that could be construed as a potential conflict of interest.

Publisher's Note: All claims expressed in this article are solely those of the authors and do not necessarily represent those of their affiliated organizations, or those of the publisher, the editors, and the reviewers. Any product that may be evaluated in this article, or claim that may be made by its manufacturer, is not guaranteed or endorsed by the publisher.

Copyright © 2022 Lu, Chen, Khan, Brassard, Arutyunova, Lamer, Vuong, Fischer, Young, Vederas and Lemieux. This is an open-access article distributed under the terms of the Creative Commons Attribution License (CC BY). The use, distribution or reproduction in other forums is permitted, provided the original author(s) and the copyright owner(s) are credited and that the original publication in this journal is cited, in accordance with accepted academic practice. No use, distribution or reproduction is permitted which does not comply with these terms.



The Molecular Basis of the Effect of Temperature on the Structure and Function of SARS-CoV-2 Spike Protein

Faez Iqbal Khan^{1,2}, Kevin A. Lobb^{3*} and Dakun Lai^{2*}

¹Department of Biological Sciences, School of Science, Xi'an Jiaotong-Liverpool University, Suzhou, Jiangsu, China, ²School of Electronic Science and Engineering, University of Electronic Science and Technology of China, Chengdu, China, ³Department of Chemistry, Rhodes University, Grahamstown, South Africa

OPEN ACCESS

Edited by:

Matthew Boggy,
Stanford University, United States

Reviewed by:

Shashikant Ray,
Mahatma Gandhi Central University,
Motihari, India
Mohammad Hassan Baig,
Yonsei University Health System,
South Korea

*Correspondence:

Dakun Lai
dklai@uestc.edu.cn
Kevin A. Lobb
K.Lobb@ru.ac.za

Specialty section:

This article was submitted to
Biological Modeling and Simulation,
a section of the journal
Frontiers in Molecular Biosciences

Received: 03 November 2021

Accepted: 27 January 2022

Published: 25 March 2022

Citation:

Khan FI, Lobb KA and Lai D (2022) The
Molecular Basis of the Effect of
Temperature on the Structure and
Function of SARS-CoV-2
Spike Protein.
Front. Mol. Biosci. 9:794960.
doi: 10.3389/fmolb.2022.794960

The remarkable rise of the current COVID-19 pandemic to every part of the globe has raised key concerns for the current public healthcare system. The spike (S) protein of SARS-CoV-2 shows an important part in the cell membrane fusion and receptor recognition. It is a key target for vaccine production. Several researchers studied the nature of this protein under various environmental conditions. In this work, we applied molecular modeling and extensive molecular dynamics simulation approaches at 0°C (273.15 K), 20°C (293.15 K), 40°C (313.15 K), and 60°C (333.15 K) to study the detailed conformational alterations in the SARS-CoV-2 S protein. Our aim is to understand the influence of temperatures on the structure, function, and dynamics of the S protein of SARS-CoV-2. The structural deviations, and atomic and residual fluctuations were least at low (0°C) and high (60°C) temperature. Even the internal residues of the SARS-CoV-2 S protein are not accessible to solvent at high temperature. Furthermore, there was no unfolding of SARS-CoV-2 spike S reported at higher temperature. The most stable conformations of the SARS-CoV-2 S protein were reported at 20°C, but the free energy minimum region of the SARS-CoV-2 S protein was sharper at 40°C than other temperatures. Our findings revealed that higher temperatures have little or no influence on the stability and folding of the SARS-CoV-2 S protein.

Keywords: SARS-CoV-2, COVID-19, spike protein, MD simulations, Gibbs free energy

INTRODUCTION

The outbreaks of Severe Acute Respiratory Syndrome CoV 1 (SARS-CoV-1), Middle-East Respiratory Syndrome CoV (MERS-CoV), and Severe Acute Respiratory Syndrome CoV 2 (SARS-CoV-2) were caused by zoonotic viruses in 2003, 2012, and 2019–2020 with a fatality ratio of 10%, 35%, and 5%, respectively (Lee et al., 2003; Cheng et al., 2007; Zaki et al., 2012; de Groot et al., 2013; Reusken et al., 2013; Rothan and Byraredy, 2020). The International Virus Classification Commission (ICTV) termed this 2019 novel CoV as SARS-CoV-2 (Chen et al., 2020; Zhu et al., 2020). SARS-CoV-2 virus spread from humans to humans, and animals to humans (Khan et al., 2020a; Khan et al., 2021a). The COVID-19-infected patient develops mild to moderate symptoms and recovers. Some patients have serious symptoms such as atypical pneumonia and chest pain (Huang et al., 2020a; Cheung et al., 2020; Lu et al., 2020; Rothan and Byraredy, 2020). The phenomenal spread of the current COVID-19 pandemic to every part of the sphere has raised key concerns for the healthcare system. To combat this pandemic, the researchers are using all possible

approaches and practices to inhibit the synthesis of crucial non-structural viral proteins, inhibit the viral replicase enzyme, inhibit the formation of viral RNA, prevent the self-assembly of viruses, or boost the human immune response against the virus.

The Spike (S) protein of SARS-CoV-2 performs a vital part in the cell membrane fusion and receptor recognition. It has two subunits such as S1 and S2. A receptor-binding domain (RBD) is present on the S1 subunit. The RBD recognizes and attaches to the host receptor angiotensin-converting enzyme 2 (ACE-2). The membrane fusion (MF) is facilitated by the S2 subunit by making 6 helical bundles through two heptad repeat (HR) domains (Huang et al., 2020b). The S protein has a size of 180–200 kDa. It has an extracellular N-terminal, a transmembrane (TM) attached to the membrane, and small intracellular C-terminal domains.

The S proteins are covered with polysaccharide for camouflage and escaping the host immune system in the course of entry (Huang et al., 2020b). The S protein of SARS-CoV-2 contains 1,273 amino acid residues. It contains a signal peptide (1–13 amino acids), an S1 subunit (14–685 residues), and an S2 subunit (686–1,273 residues). The S1 subunit has 14–305 N-terminal domain amino acids and 319–541 RBD amino acids. The S2 subunit has 788–806 fusion peptide (FP) amino acids, 912–984 HR1 amino acids, 1,163–1,213 HR2 amino acids, 1,213–1,237 TM domain amino acids, and 1,237–1,273 cytoplasm domain amino acids (Xia et al., 2020). The SARS-CoV-2 S protein lives as a sedentary precursor in native state. During the viral contagion, the proteases from target cells trigger the S protein by slicing it into two different subunits (Bertram et al., 2013), which is needed for triggering the MF domain after entry of virus into the target cells.

The SARS-CoV-2 S protein is an important target for vaccine production. In this work, we applied molecular modeling and molecular dynamics simulations approaches at 0°C (273.15 K), 20°C (293.15 K), 40°C (313.15 K), and 60°C (333.15 K) to study the detailed conformational variations in the SARS-CoV-2 S protein. It is worth noting that, experimentally, in terms of information on inactivation of viruses, data in the range 40–60°C are essential (Bertrand et al., 2012). Our findings revealed that higher temperatures have little or no influence on the SARS-CoV-2 S protein. We found that the structural deviations, atomic, and residual fluctuations were least at low (0°C) and high (60°C) temperature. The solvent accessible area plot indicated that the internal residues of SARS-CoV-2 spike protein are not exposed to solvent at high temperature. The secondary structure scheme indicated that there was no such denaturation of the SARS-CoV-2 S protein at higher temperature. The most stable conformations of the SARS-CoV-2 S protein was found at 20°C, but the free energy state region of SARS-CoV-2 spike protein was sharper at 40°C than other temperatures.

MATERIALS AND METHODS

Structure Modeling of the SARS-CoV-2 S Protein

The structures of S protein of SARS-CoV-2 (PDB: 6vsb) were taken from PDB (Wrapp et al., 2020). The missing atoms in the

structure of S protein were modeled using MODELLER (Webb and Sali, 2016). The complete protocols are stated in preceding publications (Khan et al., 2015; Khan et al., 2016c; Khan et al., 2017a; Khan et al., 2017b; Khan et al., 2021d). Structure analysis was performed using PDBsum (Laskowski et al., 2018) and numerous modules of MD simulations. PyMOL was used for visualization and drawing structure.

MD Simulations

MD simulations were achieved on SARS-CoV-2 spike protein at 0°C (273.15 K), 20°C (293.15 K), 40°C (313.15 K), and 60°C (333.15 K) via GROMACS 2018.2 (Van Der Spoel et al., 2005) using a standard protocol (Khan et al., 2020b; Khan et al., 2020c; Khan et al., 2021b). Na⁺ and Cl[−] ions were supplemented to neutralize the system. Absolute production phase of 100 ns was attained at 0°C (273.15 K), 20°C (293.15 K), 40°C (313.15 K), and 60°C (333.15 K). The complete MD simulation procedure is cited in prior publications (Khan et al., 2016a; Khan et al., 2016b; Durrani et al., 2020; Hassan et al., 2020; Qausain et al., 2020).

Essential Dynamics

ED was obtained for the SARS-CoV-2 S protein at 0°C (273.15 K), 20°C (293.15 K), 40°C (313.15 K), and 60°C (333.15 K). It is estimated as:

$$C_{ij} = \langle (r_i - \langle r_i \rangle) \times (r_j - \langle r_j \rangle) \rangle (i, j = 1, 2, 3, \dots, 3N). \quad (1)$$

r_i denotes the coordinate, i th Ca atom, N signifies the Ca atoms, and $\langle r_i \rangle$ indicates time average over all configurations (Khan et al., 2020d).

Gibbs Free Energy Landscape

GFE landscape can suggest conformational variations in the SARS-CoV-2 S protein at 0°C (273.15 K), 20°C (293.15 K), 40°C (313.15 K), and 60°C (333.15 K) (Khan et al., 2016c). The GFE landscape was projected on PC1 and PC2.

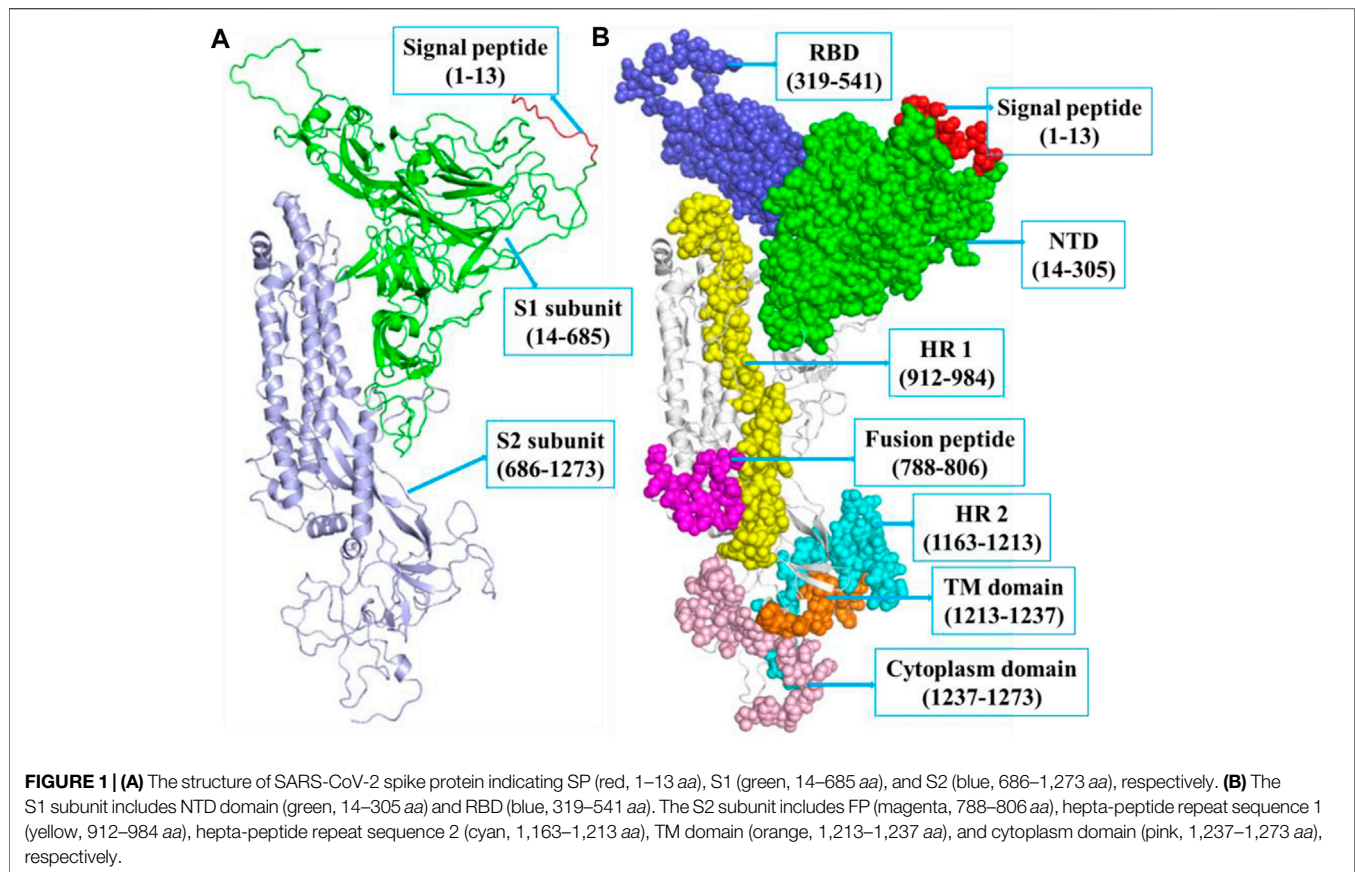
$$G_{(PC1, PC2)} = -k_B T \ln P_{(PC1, PC2)}. \quad (2)$$

k_B , T , and $P_{(PC1, PC2)}$ denote Boltzmann constant, temperature, and normalized joint probability distribution for SARS-CoV-2 spike protein at 0°C (273.15 K), 20°C (293.15 K), 40°C (313.15 K), and 60°C (333.15 K) respectively.

RESULTS AND DISCUSSION

Structure Analysis of Spike Protein

The SARS-CoV-2 spike protein comprises N-terminal, TM, and C-terminal segments (Bosch et al., 2003). It consists of a signal peptide (1–13 residues at the N-terminal), an S1 subunit (14–685 amino acid residues), and an S2 subunit (686–1,273 amino acid residues). The S1 is accountable for receptor attachment, and S2 is accountable for membrane fusion. The S1 subunit contains 14–305 NTD residues and 319–541 RBD residues. The S2 contains 788–806 FP amino acid residues, 912–984 HR1 residues, 1,163–1,213 HR2 residues, 1,213–1,237 TM domain residues, and 1,237–1,273 cytoplasm domain residues (Huang



et al., 2020b). The residues that participated in strand, α -helix, and 3–10 helix formations are 271 (28.3%), 190 (19.8%), and 23 (2.4%), respectively. The structure of spike protein includes 18 β -hairpins, 13 β -sheets, 52 β -strands, 18 β -bulges, 29 helix-helix interactions, 22 helices, 16 γ -turns, 76 β -turns, and 12 disulfides (Figure 1).

Structural Deviations

To investigate the structural dynamics of the SARS-CoV-2 S protein, the RMSD, RMSF, and the R_g were considered throughout 100-ns MD simulations at 0°C (273.15 K), 20°C (293.15 K), 40°C (313.15 K), and 60°C (333.15 K), respectively (Kuzmanic and Zagrovic, 2010). The mean RMSD values of the SARS-CoV-2 S protein at 0, 20, 40, and 60°C were estimated to be 1.53, 2.51, 3.26, and 2.23 nm, respectively (Figure 2). It has been estimated that RMSD values, and residual and atomic fluctuations increase from 0 to 40°C. It attained a low structural deviation equilibrium at 60°C. The SARS-CoV-2 S protein is least deviated at low (0°C) and high (60°C) temperature. The average radius of gyration (R_g) values for the SARS-CoV-2 S protein at 0, 20, 40, and 60°C was found to be 4.09, 4.37, 4.32, and 3.48 nm, respectively. The R_g is described as the allotment of atoms of a molecule around its axis. The calculation of R_g is a significant indicator that is broadly used in calculating the structural activity. At different temperatures, there is a conformational change in the SARS-CoV-2 S protein that

changes the radius of gyration. It was estimated that the SARS-CoV-2 S protein is tightly packed at 60°C. At 20°C–40°C, it shows high fluctuations throughout the time scale.

Solvent Accessible Surface Area

It has been assumed as a significant element in molecular stability and folding analysis. The average solvent accessible surface area values for the SARS-CoV-2 S protein at 0, 20, 40, and 60°C were found to be 437.71, 439.92, 418.90, and 384.66 nm², respectively (Figure 3). The solvation energy for the SARS-CoV-2 S protein at 0, 20, 40, and 60°C was found to be 752.14, 730.93, 668.86, and 657.95 kJ/mol/nm², respectively. An increase in temperature from 0 to 20°C has not much effect on SASA of the SARS-CoV-2 S protein. At 40°C–60°C, the solvent accessible surface area of the SARS-CoV-2 S protein continuously decreases. This specifies that the internal residues of the SARS-CoV-2 S protein are not exposed to solvent at high temperature. This might be due to stability and compactness of the SARS-CoV-2 S protein at higher temperature. The solvation energy refers to the free-energy change during the simulations. The solvation free energy is also less at higher temperature. The solvent accessible surface area was further divided into hydrophobic and hydrophilic regions. The hydrophobic regions for the SARS-CoV-2 S protein at 0, 20, 40, and 60°C were found to be 224.22, 224.34, 221.61, and 218.62 nm², respectively. The

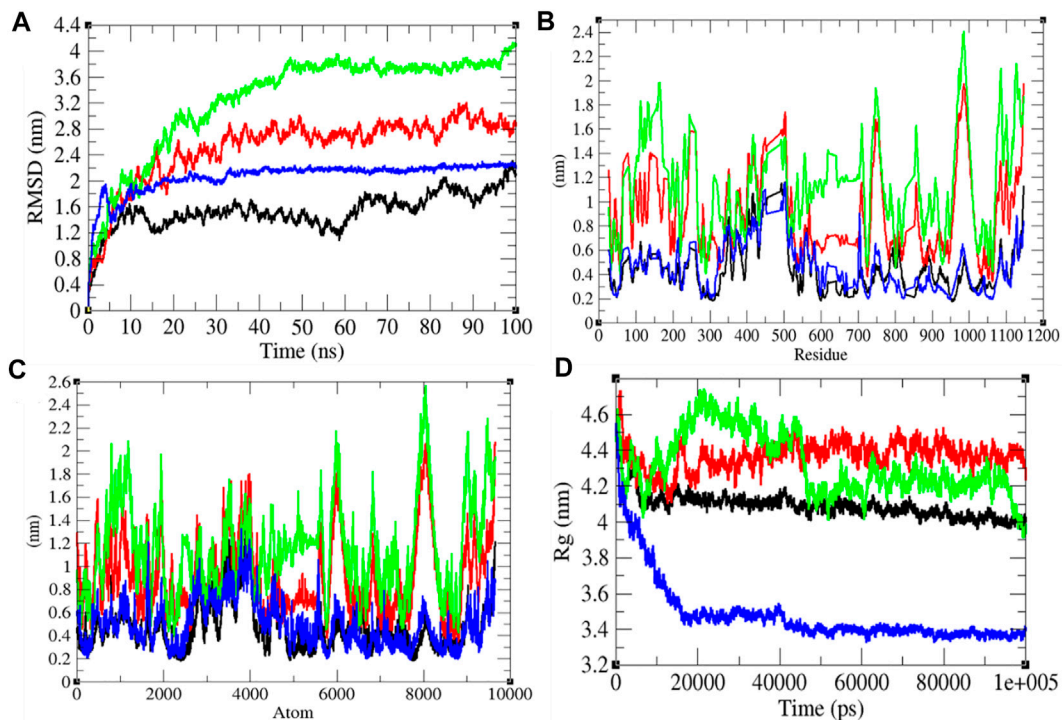


FIGURE 2 | Structural dynamics. **(A)** RMSD plot for the SARS-CoV-2 S protein vs. time. **(B)** RMSF vs. residues. **(C)** RMSF vs. residues. **(D)** R_g plot vs. time. The values calculated at 0°C (black), 20°C (red), 40°C (green), and 60°C (blue), respectively.

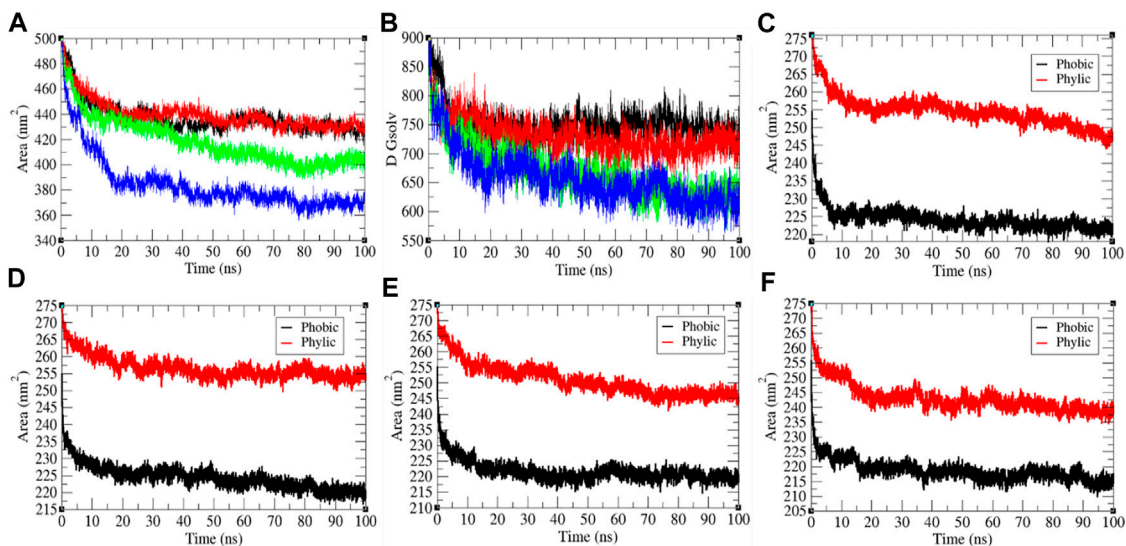


FIGURE 3 | The solvent accessible surface area of the SARS-CoV-2 S protein. **(A)** SASA vs. time. **(B)** Free energy of solvation vs. time. The color codes have the same meaning as described in **Figure 2**. It was resolved into hydrophobic and hydrophilic regions for the SARS-CoV-2 S protein at **(C)** 0°C, **(D)** 20°C, **(E)** 40°C, and **(F)** 60°C, respectively.

hydrophilic regions for the SARS-CoV-2 S protein at 0, 20, 40, and 60°C were 254.52, 256.53, 250.9, and 243.08 nm², respectively. Both hydrophobic and hydrophilic regions are sparingly accessible to solvent at higher temperatures.

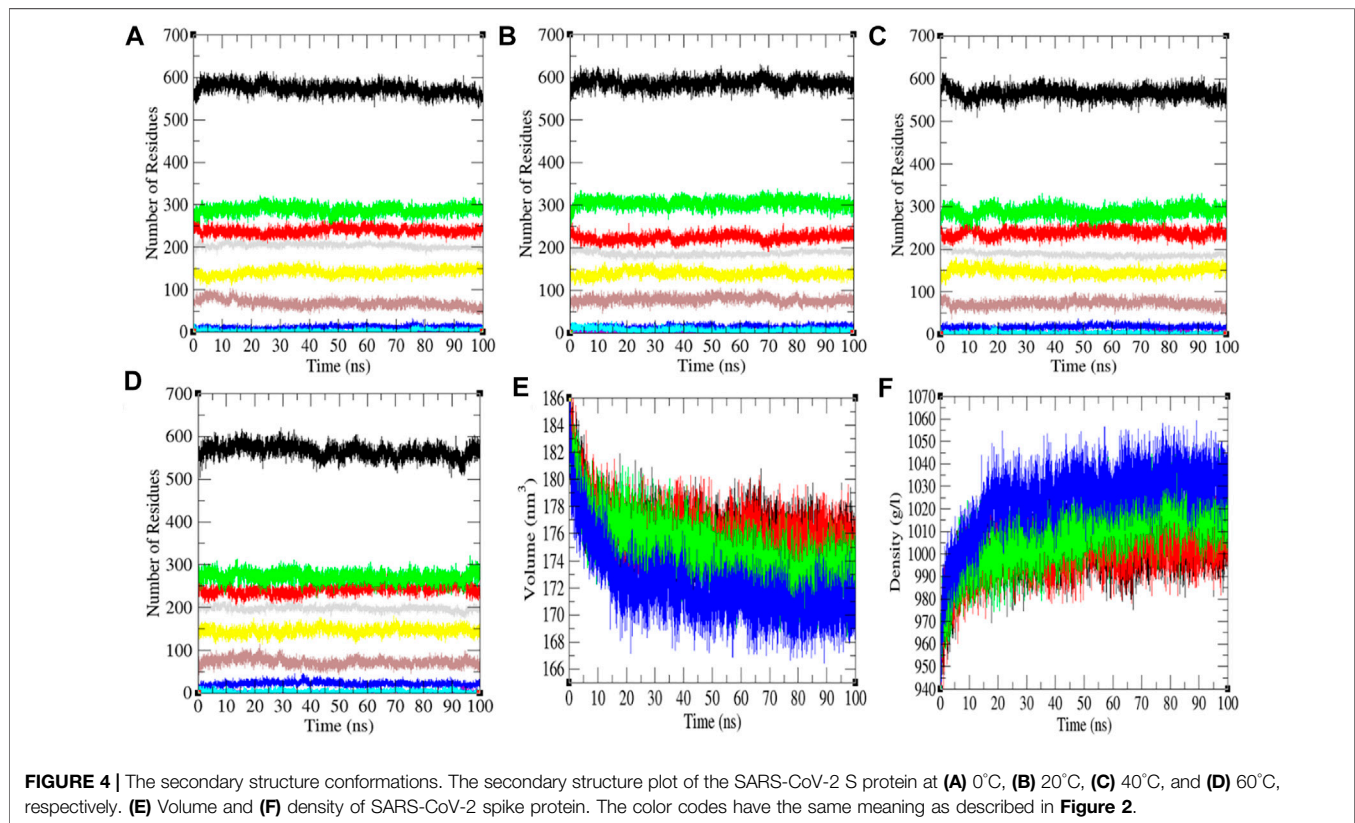
Secondary Structure Analysis

The secondary structure in the SARS-CoV-2 S protein was analyzed at each period at 0, 20, 40, and 60°C (**Table 1**). The mean residues involved in the assembly of the SARS-CoV-2 S protein at 0, 20, 40,

TABLE 1 | Percentage of residues in SARS-CoV-2 spike protein at 0, 20, 40, and 60°C contributed in mean structure development.

Temperature (°C)	Secondary structure (SS %)							
	Structure ^a	Coil	β -sheet	β -bridge	Bend	Turn	α -helix	3_{10} -helix
0	60	25	30	1	15	7	21	0
20	61	23	32	2	15	8	20	1
40	59	25	30	2	15	8	20	0
60	59	25	28	2	15	8	21	0

^aStructure = α -helix + β -sheet + β -bridge + Turn.



and 60°C were found to be 60%, 61%, 59%, and 59%, respectively (Figure 4). There was no such unfolding of the SARS-CoV-2 S protein reported at higher temperature from this analysis. The β -sheet of the SARS-CoV-2 S protein slightly unfolds from 30 to 28% at 60°C, while the α -helix (21%) remained unchanged at 60°C. The most stable conformation of the SARS-CoV-2 S protein was found at 20°C. Furthermore, we calculated the volume and density of the SARS-CoV-2 S protein at 0, 20, 40, and 60°C, respectively. Moreover, the volume of the SARS-CoV-2 S protein was found to be 176.02, 176.04, 174.71, and 172.03 nm³ at 0, 20, 40, and 60°C, respectively, while the density of the SARS-CoV-2 S protein was calculated to be 1,001.84 g/L, 1,001.72 g/L, 1,009.39 g/L, and 1,025.18 g/L at 0, 20, 40, and 60°C, respectively. The volume of the SARS-CoV-2 S protein slightly decreases and density increases at higher temperature. This might be due to different structure conformations at higher temperatures.

Hydrogen Bonding and the Mean Square Displacement

The H-bond is a noteworthy element in stabilizing the molecule. It was estimated between the main chain and side chains (M-S) of the SARS-CoV-2 S protein at 0, 20, 40, and 60°C, respectively. The mean H-bonds between M-S chains of the SARS-CoV-2 S protein were found to be 413.43, 407.89, 417.99, and 417.51 at 0, 20, 40, and 60°C, respectively (Figure 5). The strength of hydrogen bonds becomes stronger at 40–60°C. There is no sign of denaturation at higher temperatures. Furthermore, the mean square displacement (MSD) of atoms from a set of original positions of the SARS-CoV-2 S protein at 0, 20, 40, and 60°C was computed. The displacement of atoms from a set of initial positions of the SARS-CoV-2 S protein was estimated to be higher at 40°C only. In short, higher temperature has not much impact on unfolding and denaturation of the SARS-CoV-2 S protein.

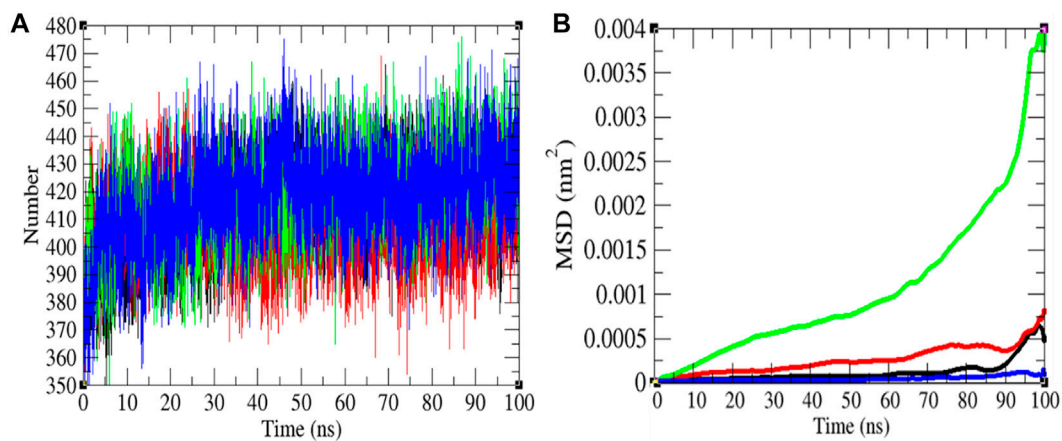


FIGURE 5 | Hydrogen bonds and MSD. **(A)** The H-bond estimation between M-S chains of the SARS-CoV-2 S protein was calculated. The color codes have the same meaning as described in **Figure 2**. **(B)** The MSD of the SARS-CoV-2 S protein at 0°C (black), 20°C (red), 40°C (green), and 60°C (blue), respectively.

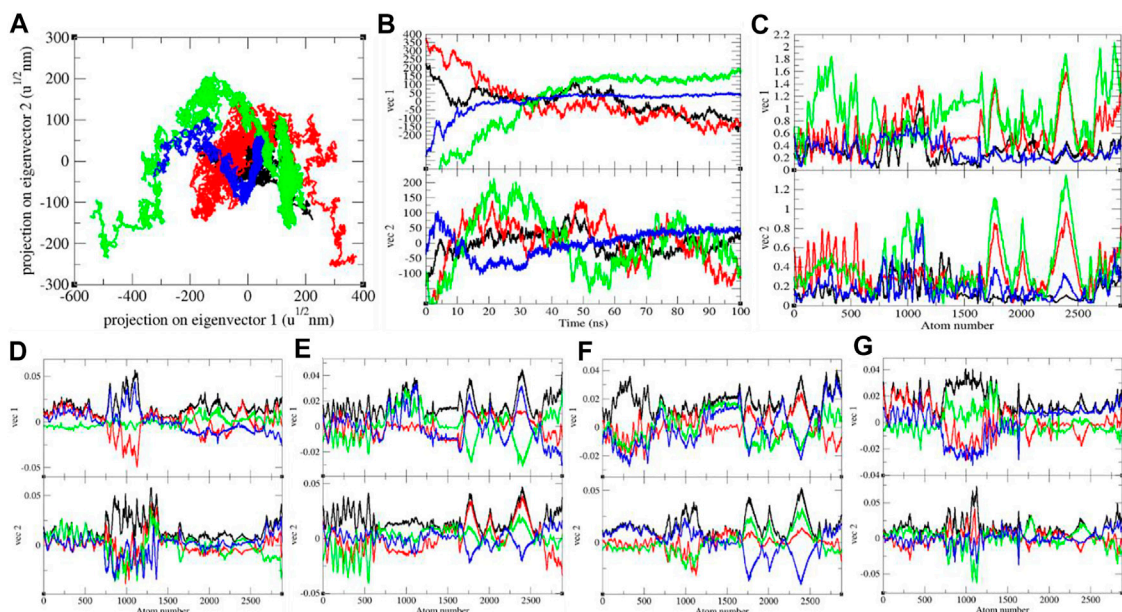


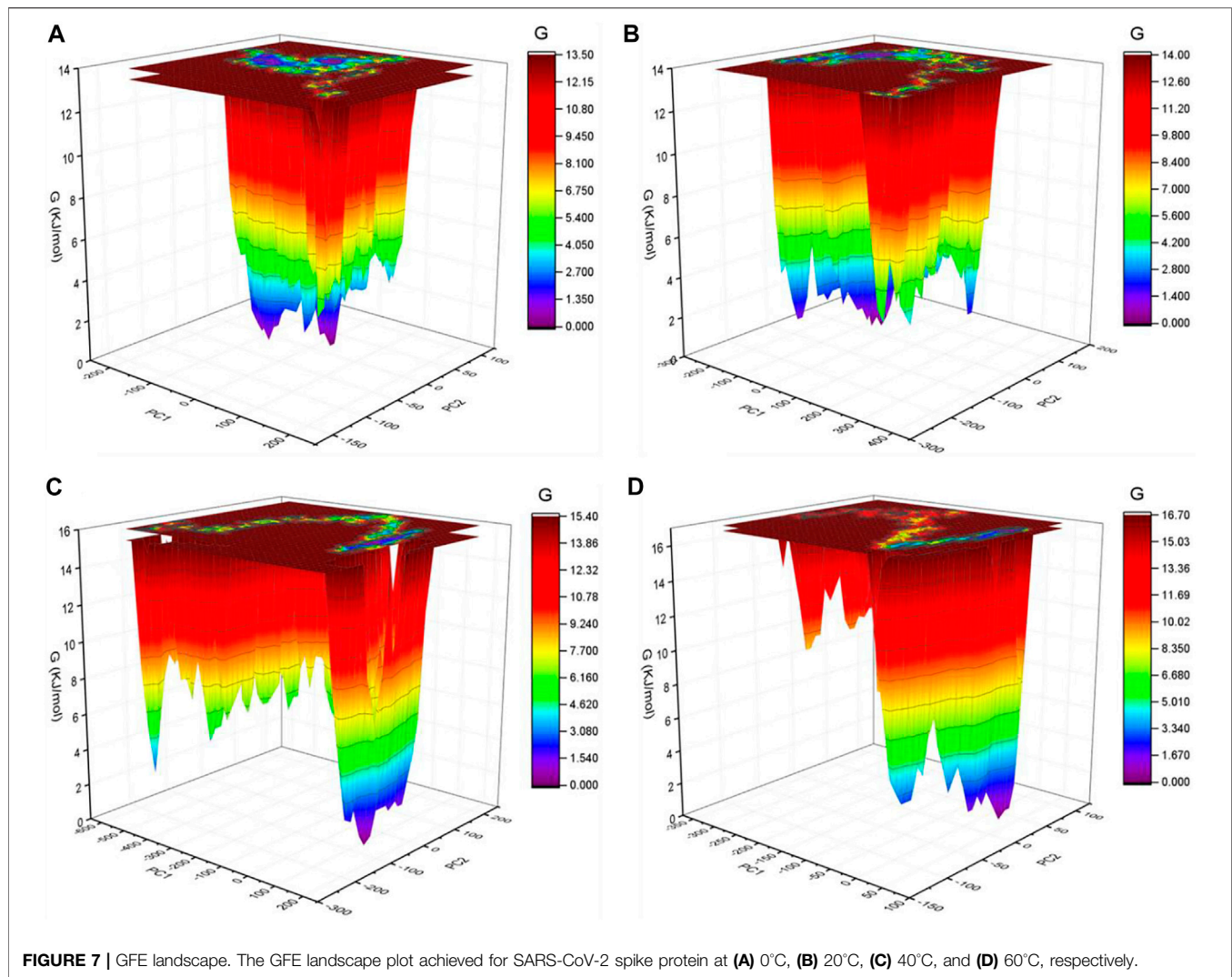
FIGURE 6 | **(A)** The 2D projection and **(B)** projections of trajectories of SARS-CoV-2 spike protein. **(C)** Eigen RMSF. The color codes have the same meaning as described in **Figure 2**. The Eigen components were calculated for SARS-CoV-2 spike protein at **(D)** 0°C, **(E)** 20°C, **(F)** 40°C, and **(G)** 60°C, respectively.

Principal Component Analysis

It shows global expansion of the SARS-CoV-2 S protein at 0, 20, 40, and 60°C. It estimates mean atomic motions of the SARS-CoV-2 S protein at 0, 20, 40, and 60°C. The eigenvalues were 8,360.61, 33,665.60, 53,083.50, and 8,911.24 nm² for the SARS-CoV-2 S protein at 0, 20, 40, and 60°C, respectively. It was higher at 20–40°C (**Figure 6**). The average atomic motions in the SARS-CoV-2 S protein was highest at 40°C. The atomic motions are also related to activity in case of protein molecules. It can be assumed that at low and high environmental temperatures, the atomic motions and activity of the SARS-CoV-2 S protein are low.

GFE Landscape

The GFE landscape exhibited diverse forms for the SARS-CoV-2 S protein at 0, 20, 40, and 60°C (**Figure 7**). Every atomic pair covariance displays diverse frameworks in respective events. The GFE patterns are relatively similar with minor changes at 0–20°C and 40–60°C. The following GFE curve with reflective blue shade implies lower energy state. Extra blue regions describe shifts in the molecular conformation lagged by the thermodynamically new favorable areas. The GFE state in the global energy minimum section of the SARS-CoV-2 S protein at 40°C is sharper than other temperatures. This indicates that temperature slightly affects the GFE patterns in the case of the SARS-CoV-2 spike protein. The GFE landscape suggests that the



temperature slightly affects the atomic motions of SARS-CoV-2 spike protein. The denaturation was not reported from the secondary structure analysis. The potential energy and the enthalpy were also calculated during the course of simulations. The potential energy was found to be $-10,713,734.28$ kJ/mol, $-10,434,949.84$ kJ/mol, $-10,161,602.16$ kJ/mol, and $-9,893,572.08$ kJ/mol at 0, 20, 40, and 60°C, respectively. The enthalpy was found to be $-9,100,901.71$ kJ/mol, $-8,704,052.14$ kJ/mol, $-8,312,630.26$ kJ/mol, and $-7,926,537.36$ kJ/mol at 0, 20, 40, and 60°C, respectively.

Recently, several inhibitors and their mode of action have been demonstrated (Khan et al., 2021c; Rani et al., 2021). Edwards et al. found that the spike protein samples kept at diverse temperatures did not show any considerable denaturation, while they observed an increase in upper molecular weight bands in a sample that was kept at 37°C (Edwards et al., 2021). Kumar et al. imitated SARS-CoV-2 by polymer beads covered with the S protein of SARS-CoV-2 to investigate the effect of different temperatures on attachment of virus-imitating nano-spheres to lung tissues incubated at 33 and 37°C. They found that the existence of the RBD of S protein controlled the binding by Calu-3 airway epithelial tissues. They

also found that there was no temperature correlation to binding of BSA-coated nano-spheres. Additionally, the 4–40°C temperature had no influence on S-RBD-ACE-2 ligand–receptor, and the negligible effect on the S-RBD protein structure (up to 40°C) was reported. The protein denaturation occurred at 51°C. Their outcomes suggested that 4–40°C temperature has a slight influence on SARS-CoV-2 and ACE-2 contact (Kumar et al., 2021). Zhou et al. performed MD simulations at 36–40°C to prove SARS-CoV-2 and ACE2 binding. They found that it was less stable under 40°C than under 37°C, and reduced infection rate at higher temperature (Zhou et al., 2021). Martí et al. also performed MD simulations at 298 K (24.85°C), 310 K (36.85°C), 324 K (50.85°C), 338 K (64.85°C), 358 K (84.85°C), and 373 K (99.85°C), respectively. They suggested that temperature brings structural and conformational variations in the S1 subunit and affects the RBD. Nevertheless, the influence of temperature up to 373 K was not adequate to cause a noteworthy alteration of the S protein of SARS-CoV-2 (Martí et al., 2021). Our results also suggested that the temperature has the least effect on the structure conformations of S protein of SARS-CoV-2.

CONCLUSION

Previously, we published several articles based on finding potential inhibitors of SARS-CoV-2. In the present work, we focused on the SARS-CoV-2 S protein as it performs a vital part in the cell membrane fusion and receptor recognition. Researchers have demonstrated the nature of the S protein of SARS-CoV-2 on diverse environmental conditions. We applied molecular modeling and extensive molecular dynamics simulations approaches at different temperatures to investigate the structural conformational of SARS-CoV-2 spike protein. There are several hypotheses proposed regarding the temperature dependence of the COVID-19 transmission. We concluded that temperature has no effect or has the least effect on the structure conformations of S protein of SARS-CoV-2. Minor changes were reported in the structure and thermodynamic properties that are mentioned in this paper.

DATA AVAILABILITY STATEMENT

The datasets presented in this study can be found in online repositories. The names of the repository/repositories and accession number(s) can be found in the article/Supplementary Material.

REFERENCES

- Bertram, S., Dijkman, R., Habjan, M., Heurich, A., Gierer, S., Glowacka, I., et al. (2013). TMPRSS2 Activates the Human Coronavirus 229E for Cathepsin-independent Host Cell Entry and Is Expressed in Viral Target Cells in the Respiratory Epithelium. *J. Virol.* 87, 6150–6160. doi:10.1128/jvi.03372-12
- Bertrand, I., Schijven, J. F., Sánchez, G., Wyn-Jones, P., Ottoson, J., Morin, T., et al. (2012). The Impact of Temperature on the Inactivation of Enteric Viruses in Food and Water: A Review. *J. Appl. Microbiol.* 112, 1059–1074. doi:10.1111/j.1365-2672.2012.05267.x
- Bosch, B. J., Van Der Zee, R., De Haan, C. A. M., and Rottier, P. J. M. (2003). The Coronavirus Spike Protein Is a Class I Virus Fusion Protein: Structural and Functional Characterization of the Fusion Core Complex. *J. Virol.* 77, 8801–8811. doi:10.1128/jvi.77.16.8801-8811.2003
- Chen, Y., Liu, Q., and Guo, D. (2020). Emerging Coronaviruses: Genome Structure, Replication, and Pathogenesis. *J. Med. Virol.* 92, 418–423. doi:10.1002/jmv.25681
- Cheng, V. C. C., Lau, S. K. P., Woo, P. C. Y., and Yuen, K. Y. (2007). Severe Acute Respiratory Syndrome Coronavirus as an Agent of Emerging and Reemerging Infection. *Clin. Microbiol. Rev.* 20, 660–694. doi:10.1128/cmr.00023-07
- Cheung, K. S., Hung, I. F. N., Chan, P. P. Y., Lung, K. C., Tso, E., Liu, R., et al. (2020). Gastrointestinal Manifestations of SARS-CoV-2 Infection and Virus Load in Fecal Samples from a Hong Kong Cohort: Systematic Review and Meta-Analysis. *Gastroenterology* 159, 81–95. doi:10.1053/j.gastro.2020.03.065
- de Groot, R. J., Baker, S. C., Baric, R. S., Brown, C. S., Drosten, C., Enjuanes, L., et al. (2013). Middle East Respiratory Syndrome Coronavirus (MERS-CoV): Announcement of the Coronavirus Study Group. *J. Virol.* 87, 7790–7792. doi:10.1128/jvi.01244-13
- Durrani, R., Khan, F. I., Ali, S., Wang, Y., and Yang, B. (2020). A Thermolabile Phospholipase B from *Talaromyces marneffe* GD-0079: Biochemical Characterization and Structure Dynamics Study. *Biomolecules* 10, 231. doi:10.3390/biom10020231
- Edwards, R. J., Mansouri, K., Stalls, V., Manne, K., Watts, B., Parks, R., et al. (2021). Cold Sensitivity of the SARS-CoV-2 Spike Ectodomain. *Nat. Struct. Mol. Biol.* 28, 128–131. doi:10.1038/s41594-020-00547-5
- Hassan, F., Khan, F. I., Song, H., Lai, D., and Juan, F. (2020). Effects of Reverse Genetic Mutations on the Spectral and Photochemical Behavior of a

AUTHOR CONTRIBUTIONS

Conceptualization, FK and DL. Methodology, FK. Software, FK and KL. Validation, FK and DL. Formal analysis, FK and DL. Investigation, FK and DL. Resources, FK and DL. Data curation, FK and DL. Writing—original draft preparation, FK, KL, and DL. Writing—review and editing, FK. Visualization, FK; supervision, DL. Project administration, DL. Funding acquisition, FK and DL. All authors have read and agreed to the published version of the manuscript.

FUNDING

This work was supported by the Sichuan Science and Technology Program (No. 2021YFH0093), and the China Postdoctoral Science Foundation (No. 2020M673187).

ACKNOWLEDGMENTS

We would like to acknowledge The Centre for High Performance Computing (CHPC), South Africa.

- Photoactivatable Fluorescent Protein PAiRFP1. *Spectrochimica Acta A: Mol. Biomol. Spectrosc.* 228, 117807. doi:10.1016/j.saa.2019.117807
- Huang, C., Wang, Y., Li, X., Ren, L., Zhao, J., Hu, Y., et al. (2020a). Clinical Features of Patients Infected with 2019 Novel Coronavirus in Wuhan, China. *The Lancet* 395, 497–506. doi:10.1016/s0140-6736(20)30183-5
- Huang, Y., Yang, C., Xu, X.-F., Xu, W., and Liu, S.-W. (2020b). Structural and Functional Properties of SARS-CoV-2 Spike Protein: Potential Antivirus Drug Development for COVID-19. *Acta Pharmacol. Sin* 41, 1141–1149. doi:10.1038/s41401-020-0485-4
- Khan, A., Khan, M., Saleem, S., Babar, Z., Ali, A., Khan, A. A., et al. (2020a). Phylogenetic Analysis and Structural Perspectives of RNA-dependent RNA-Polymerase Inhibition from SARs-CoV-2 with Natural Products. *Interdiscip. Sci. Comput. Life Sci.* 12, 335–348. doi:10.1007/s12539-020-00381-9
- Khan, A., Umbreen, S., Hameed, A., Fatima, R., Zahoor, U., Babar, Z., et al. (2021a). In Silico Mutagenesis-Based Remodelling of SARS-CoV-1 Peptide (ATLQAIAS) to Inhibit SARS-CoV-2: Structural-Dynamics and Free Energy Calculations. *Interdiscip. Sci. Comput. Life Sci.* 13, 521–534. doi:10.1007/s12539-021-00447-2
- Khan, F. I., Bisetty, K., Wei, D.-Q., and Hassan, M. I. (2016a). A pH Based Molecular Dynamics Simulations of Chitinase II Isolated from *Thermomyces lanuginosus* SSBP. *Cogent Biol.* 2, 1168336. doi:10.1080/23312025.2016.1168336
- Khan, F. I., Govender, A., Permaul, K., Singh, S., and Bisetty, K. (2015). Thermostable Chitinase II from *Thermomyces lanuginosus* SSBP: Cloning, Structure Prediction and Molecular Dynamics Simulations. *J. Theor. Biol.* 374, 107–114. doi:10.1016/j.jtbi.2015.03.035
- Khan, F. I., Gupta, P., Roy, S., Azum, N., Alamry, K. A., Asiri, A. M., et al. (2020b). Mechanistic Insights into the Urea-Induced Denaturation of Human Sphingosine Kinase 1. *Int. J. Biol. Macromolecules* 161, 1496–1505. doi:10.1016/j.ijbiomac.2020.07.280
- Khan, F. I., Hassan, F., Ali, H., and Lai, D. (2021b). Mechanism of pH-Induced Conformational Changes in MurE Ligase Obtained from *Salmonella enterica* Serovar Typhi. *J. Biomol. Struct. Dyn.* 39, 1898–1905. doi:10.1080/07391102.2020.1739560
- Khan, F. I., Hassan, F., Anwer, R., Juan, F., and Lai, D. (2020c). Comparative Analysis of Bacteriophytochrome Agp2 and its Engineered Photoactivatable NIR Fluorescent Proteins PAiRFP1 and PAiRFP2. *Biomolecules* 10, 1286. doi:10.3390/biom10091286

- Khan, F. I., Kang, T., Ali, H., and Lai, D. (2021c). Remdesivir Strongly Binds to RNA-dependent RNA Polymerase, Membrane Protein, and Main Protease of SARS-CoV-2: Indication from Molecular Modeling and Simulations. *Front. Pharmacol.* 12, 710778. doi:10.3389/fphar.2021.710778
- Khan, F. I., Lai, D., Anwer, R., Azim, I., and Khan, M. K. A. (2020d). Identifying Novel Sphingosine Kinase 1 Inhibitors as Therapeutics against Breast Cancer. *J. Enzyme Inhib. Med. Chem.* 35, 172–186. doi:10.1080/14756366.2019.1692828
- Khan, F. I., Lan, D., Durrani, R., Huan, W., Zhao, Z., and Wang, Y. (2017a). The Lid Domain in Lipases: Structural and Functional Determinant of Enzymatic Properties. *Front. Bioeng. Biotechnol.* 5, 16. doi:10.3389/fbioe.2017.00016
- Khan, F. I., Nizami, B., Anwer, R., Gu, K.-R., Bisetty, K., Hassan, M. I., et al. (2017b). Structure Prediction and Functional Analyses of a Thermostable Lipase Obtained from *Shewanella Putrefaciens*. *J. Biomol. Struct. Dyn.* 35, 2123–2135. doi:10.1080/07391102.2016.1206837
- Khan, F. I., Shahbaaz, M., Bisetty, K., Waheed, A., Sly, W. S., Ahmad, F., et al. (2016b). Large Scale Analysis of the Mutational Landscape in β -glucuronidase: A Major Player of Mucopolysaccharidosis Type VII. *Gene* 576, 36–44. doi:10.1016/j.gene.2015.09.062
- Khan, F. I., Song, H., Hassan, F., Tian, J., Tang, L., Lai, D., et al. (2021d). Impact of Amino Acid Substitutions on the Behavior of a Photoactivatable Near Infrared Fluorescent Protein PAiRFP1. *Spectrochimica Acta Part A: Mol. Biomol. Spectrosc.* 253, 119572. doi:10.1016/j.saa.2021.119572
- Khan, F. I., Wei, D.-Q., Gu, K.-R., Hassan, M. I., and Tabrez, S. (2016c). Current Updates on Computer Aided Protein Modeling and Designing. *Int. J. Biol. Macromolecules* 85, 48–62. doi:10.1016/j.ijbiomac.2015.12.072
- Kumar, S., Paul, A., Chatterjee, S., Pütz, S., Nehra, N., Wang, D. S., et al. (2021). Effect of Ambient Temperature on Respiratory Tract Cells Exposed to SARS-CoV-2 Viral Mimicking Nanospheres-An Experimental Study. *Biointerphases* 16, 011006. doi:10.1116/6.0000743
- Kuzmanic, A., and Zagrovic, B. (2010). Determination of Ensemble-Average Pairwise Root Mean-Square Deviation from Experimental B-Factors. *Biophysical J.* 98, 861–871. doi:10.1016/j.bpj.2009.11.011
- Laskowski, R. A., Jabłońska, J., Pravda, L., Vařeková, R. S., and Thornton, J. M. (2018). PDBsum: Structural Summaries of PDB Entries. *Protein Sci.* 27, 129–134. doi:10.1002/pro.3289
- Lee, N., Hui, D., Wu, A., Chan, P., Cameron, P., Joynt, G. M., et al. (2003). A Major Outbreak of Severe Acute Respiratory Syndrome in Hong Kong. *N. Engl. J. Med.* 348, 1986–1994. doi:10.1056/nejmoa030685
- Lu, R., Zhao, X., Li, J., Niu, P., Yang, B., Wu, H., et al. (2020). Genomic Characterisation and Epidemiology of 2019 Novel Coronavirus: Implications for Virus Origins and Receptor Binding. *The Lancet* 395, 565–574. doi:10.1016/s0140-6736(20)30251-8
- Martí, D., Torras, J., Bertran, O., Turon, P., and Alemán, C. (2021). Temperature Effect on the SARS-CoV-2: A Molecular Dynamics Study of the Spike Homotrimeric Glycoprotein. *Comput. Struct. Biotechnol. J.* 19, 1848–1862. doi:10.1016/j.csbj.2021.03.037
- Qausain, S., Khan, F. I., Lai, D., Hassan, M. I., Basheeruddin, M., Ahmed, N., et al. (2020). Mechanistic Insights into the Urea-Induced Denaturation of a Non-seleno Thiol Specific Antioxidant Human Peroxiredoxin 6. *Int. J. Biol. Macromolecules* 161, 1171–1180. doi:10.1016/j.ijbiomac.2020.05.168
- Rani, J., Bhargav, A., Khan, F. I., Ramachandran, S., Lai, D., and Bajpai, U. (2021). In Silico prediction of Natural Compounds as Potential Multi-Target Inhibitors of Structural Proteins of SARS-CoV-2. *J. Biomol. Struct. Dyn.*, 1–17. doi:10.1080/07391102.2021.1968497
- Reusken, C. B., Haagmans, B. L., Müller, M. A., Gutierrez, C., Godeke, G.-J., Meyer, B., et al. (2013). Middle East Respiratory Syndrome Coronavirus Neutralising Serum Antibodies in Dromedary Camels: a Comparative Serological Study. *Lancet Infect. Dis.* 13, 859–866. doi:10.1016/s1473-3099(13)70164-6
- Rothan, H. A., and Byraredy, S. N. (2020). The Epidemiology and Pathogenesis of Coronavirus Disease (COVID-19) Outbreak. *J. Autoimmun.* 109, 102433. doi:10.1016/j.jaut.2020.102433
- Van Der Spoel, D., Lindahl, E., Hess, B., Groenhof, G., Mark, A. E., and Berendsen, H. J. C. (2005). GROMACS: Fast, Flexible, and Free. *J. Comput. Chem.* 26, 1701–1718. doi:10.1002/jcc.20291
- Webb, B., and Sali, A. (2016). Comparative Protein Structure Modeling Using MODELLER. *Curr. Protoc. Protein Sci.* 86, 5.6.1–5.6.37. doi:10.1002/cpps.20
- Wrapp, D., Wang, N., Corbett, K. S., Goldsmith, J. A., Hsieh, C.-L., Abiona, O., et al. (2020). Cryo-EM Structure of the 2019-nCoV Spike in the Prefusion Conformation. *Science* 367, 1260–1263. doi:10.1126/science.abb2507
- Xia, S., Zhu, Y., Liu, M., Lan, Q., Xu, W., Wu, Y., et al. (2020). Fusion Mechanism of 2019-nCoV and Fusion Inhibitors Targeting HR1 Domain in Spike Protein. *Cell Mol Immunol* 17, 765–767. doi:10.1038/s41423-020-0374-2
- Zaki, A. M., Van Boheemen, S., Bestebroer, T. M., Osterhaus, A. D. M. E., and Fouchier, R. A. M. (2012). Isolation of a Novel Coronavirus from a Man with Pneumonia in Saudi Arabia. *N. Engl. J. Med.* 367, 1814–1820. doi:10.1056/nejmoa1211721
- Zhou, Z., Yang, Z., Ou, J., Zhang, H., Zhang, Q., Dong, M., et al. (2021). Temperature Dependence of the SARS-CoV-2 Affinity to Human ACE2 Determines COVID-19 Progression and Clinical Outcome. *Comput. Struct. Biotechnol. J.* 19, 161–167. doi:10.1016/j.csbj.2020.12.005
- Zhu, N., Zhang, D., Wang, W., Li, X., Yang, B., Song, J., et al. (2020). A Novel Coronavirus from Patients with Pneumonia in China, 2019. *N. Engl. J. Med.* 382, 727–733. doi:10.1056/nejmoa2001017

Conflict of Interest: The authors declare that the research was conducted in the absence of any commercial or financial relationships that could be construed as a potential conflict of interest.

Publisher's Note: All claims expressed in this article are solely those of the authors and do not necessarily represent those of their affiliated organizations, or those of the publisher, the editors, and the reviewers. Any product that may be evaluated in this article, or claim that may be made by its manufacturer, is not guaranteed or endorsed by the publisher.

Copyright © 2022 Khan, Lobb and Lai. This is an open-access article distributed under the terms of the Creative Commons Attribution License (CC BY). The use, distribution or reproduction in other forums is permitted, provided the original author(s) and the copyright owner(s) are credited and that the original publication in this journal is cited, in accordance with accepted academic practice. No use, distribution or reproduction is permitted which does not comply with these terms.



Hydrazones and Thiosemicarbazones Targeting Protein-Protein-Interactions of SARS-CoV-2 Papain-like Protease

Wiebke Ewert^{1*}, Sebastian Günther^{1*}, Francesca Miglioli², Sven Falke¹, Patrick Y. A. Reinke¹, Stephan Niebling³, Christian Günther³, Huijiong Han⁴, Vasundara Srinivasan⁵, Hévila Brognaro⁵, Julia Lieske¹, Kristina Lorenzen⁴, Maria M. Garcia-Alai³, Christian Betzel⁵, Mauro Carcelli², Winfried Hinrichs⁶, Dominga Rogolino² and Alke Meents¹

OPEN ACCESS

Edited by:

Matthew Bogyo,
Stanford University, United States

Reviewed by:

Paolo A. Calligari,
University of Rome Tor Vergata, Italy
Sagar Chittori,
St. Jude Children's Research Hospital,
United States

*Correspondence:

Wiebke Ewert
wiebke.ewert@desy.de
Sebastian Günther
sebastian.guenther@desy.de

Specialty section:

This article was submitted to
Medicinal and Pharmaceutical
Chemistry,
a section of the journal
Frontiers in Chemistry

Received: 09 December 2021

Accepted: 28 February 2022

Published: 11 April 2022

Citation:

Ewert W, Günther S, Miglioli F, Falke S,
Reinke PYA, Niebling S, Günther C,
Han H, Srinivasan V, Brognaro H,
Lieske J, Lorenzen K, Garcia-Alai MM,
Betzel C, Carcelli M, Hinrichs W,
Rogolino D and Meents A (2022)
Hydrazones and Thiosemicarbazones
Targeting Protein-Protein-Interactions
of SARS-CoV-2 Papain-like Protease.
Front. Chem. 10:832431.
doi: 10.3389/fchem.2022.832431

¹Center for Free-Electron Laser Science CFEL, Deutsches Elektronen-Synchrotron DESY, Hamburg, Germany, ²Department of Chemistry, Life Sciences and Environmental Sustainability, University of Parma, Parma, Italy, ³European Molecular Biology Laboratory Hamburg, DESY, Hamburg, Germany, ⁴European XFEL GmbH, Schenefeld, Germany, ⁵Institute of Biochemistry and Molecular Biology, Laboratory for Structural Biology of Infection and Inflammation, Department of Chemistry, University Hamburg, Hamburg, Germany, ⁶Institute of Biochemistry, University Greifswald, Greifswald, Germany

The papain-like protease (PLpro) of SARS-CoV-2 is essential for viral propagation and, additionally, dysregulation of the host innate immune system. Using a library of 40 potential metal-chelating compounds we performed an X-ray crystallographic screening against PLpro. As outcome we identified six compounds binding to the target protein. Here we describe the interaction of one hydrazone (H1) and five thiosemicarbazone (T1-T5) compounds with the two distinct natural substrate binding sites of PLpro for ubiquitin and ISG15. H1 binds to a polar groove at the S1 binding site by forming several hydrogen bonds with PLpro. T1-T5 bind into a deep pocket close to the polyubiquitin and ISG15 binding site S2. Their interactions are mainly mediated by multiple hydrogen bonds and further hydrophobic interactions. In particular compound H1 interferes with natural substrate binding by sterical hindrance and induces conformational changes in protein residues involved in substrate binding, while compounds T1-T5 could have a more indirect effect. Fluorescence based enzyme activity assay and complementary thermal stability analysis reveal only weak inhibition properties in the high micromolar range thereby indicating the need for compound optimization. Nevertheless, the unique binding properties involving strong hydrogen bonding and the various options for structural optimization make the compounds ideal lead structures. In combination with the inexpensive and undemanding synthesis, the reported hydrazone and thiosemicarbazones represent an attractive scaffold for further structure-based development of novel PLpro inhibitors by interrupting protein-protein interactions at the S1 and S2 site.

Keywords: drug discovery, COVID-19, papain-like protease, x-ray crystallography, deubiquitination, SARS-CoV-2, lead compounds

INTRODUCTION

Within the last 20 years, the world has been confronted with three emerging zoonotic coronaviruses, namely severe acute respiratory syndrome coronavirus (SARS-CoV-1), middle east respiratory syndrome coronavirus (MERS-CoV) and SARS-CoV-2, which collectively have claimed more than five million victims so far (de Wit et al., 2016; WHO, 2021). Previous research on coronaviruses together with recent advances in biotechnology enabled the rapid development of novel vaccines in the current COVID-19 pandemic caused by SARS-CoV-2 (V'kovski et al., 2020; Tregoning et al., 2021). Although current vaccines offer good protection against most virus variants, there is still an urgent demand for complementary antiviral drugs that are suitable for patients who are already infected, cannot be vaccinated, are immune compromised or do not have access to any vaccination. The occurrence of immune escape variants further highlights the need for alternative treatments.

The high similarity to SARS-CoV-1 in genome sequence and viral replication helped to rapidly understand the biology of the newly emerged coronavirus SARS-CoV-2 (Lu et al., 2020; Zhou et al., 2020). Both genomes encode 16 non-structural proteins (nsps) including two cysteine proteases, which are essential for viral replication. These proteases are named main protease (Mpro, alternatively 3C-like protease) and papain-like protease (PLpro) and are responsible for the sequential proteolytic cleavage of the two polyproteins 1a and 1ab, which are the primary translation products of the viral genome (Chan et al., 2020). While Mpro releases 11 nsps from the polyprotein chains including itself (Zhang et al., 2020), PLpro is a component of the largest multidomain replicase subunit (nsp3) and recognizes the sequence LXGG (residues P4-P1) in between nsps 1–4 (Barretto et al., 2006). Both proteases, but in particular Mpro, have been the target of several extensive drug development projects (Citarella et al., 2021; Günther et al., 2021). As druggable target, PLpro has the advantage that its catalytic activity is not only essential for viral propagation but also interferes with the host innate immune system (Vabret et al., 2020). Post-translational modifications (PTM) like the conjugation with ubiquitin and ubiquitin-like proteins, including interferon-stimulating gene 15 (ISG15), regulate the cellular location of proteins, their stability and, by this, their antiviral effect (Mevisen and Komander, 2017). PLpro can revoke these PTMs by hydrolysing the isopeptide bond at the C-terminus of cellular ubiquitin (Ub) and ISG15, which results in a dysregulation in the production of cytokines and chemokines and type I interferon response (Liu et al., 2021; Munnur et al., 2021). Together with other dysregulations this leads to an excessive immune response (“cytokine storm”) that causes additional collateral damage and is widely responsible for the substantial morbidity and mortality in COVID-19 patients. Targeting PLpro with newly designed drugs can therefore not only inhibit the viral replication but presumably also promote the host immune function, rendering PLpro as a highly attractive and prioritised drug target.

PLpro is a monomer in solution and has a right-handed ubiquitin specific protease (USP) fold which consists of four domains—the N-terminal ubiquitin-like (Ubl) domain, the

thumb, palm and fingers domain (Ratia et al., 2006) (Figure 1). At the tip of the fingers a zinc ion is coordinated, which is essential for protease activity (Barretto et al., 2005). The peptide bond cleavage in the active site is catalyzed by a conserved catalytic triad (C111-H272-D286) that is located at the interface of the thumb and palm domain. Identification of specific active site inhibitors for PLpro, including approaches to analyse peptidic, non-peptidic and “dual target” inhibitors (Rut et al., 2020; Zmudzinski et al., 2020; Shen et al., 2021), is particularly challenging due to a rather “featureless” active site and a high similarity to host deubiquitinases compared to proteases like Mpro. Access to the PLpro active site is regulated by a flexible blocking loop 2 (BL2) which is involved in substrate binding (Báez-Santos et al., 2015). PLpro binds ubiquitin and ubiquitin-like proteins at two distinct sites, S1 and S2, thereby providing specificity for K48-polyubiquitin (K48-Ub₂) and ISG15 (Figures 1, 2) (Békés et al., 2016; Klemm et al., 2020). These sites do not refer to the commonly used notation of peptide substrate-binding sites of proteases according to Schechter and Berger (Schechter and Berger, 1967).

While current research focuses primarily on inhibitors that bind to the S1 site and interfere with the deubiquitinase activity of PLpro, the aim of our work was to find inhibitors, as for example disulfiram (Sargsyan et al., 2020), that interact with the ion in the zinc finger but not with the active site of the protease. Although the zinc finger and the catalytic site are about 40 Å apart, the correct zinc coordination is mandatory for structural stability and protease activity of SARS-CoV-2 PLpro (Barretto et al., 2005). Inhibition of a viral enzyme by coordinating one or more metal cofactors represents a successful strategy in the development of novel therapeutic agents (Chen et al., 2019); in particular, chelation of Zinc (II) ions by N-acylhydrazones seems related to interesting biological effects (Hsu et al., 2012; Huan et al., 2020). Some data indicating that this approach is applicable to SARS-CoV-2 viral proteins have already been disclosed (te Velthuis et al., 2010; Panchariya et al., 2021). Thus, we defined a small in-house library of 40 previously synthesized quinolone, hydroxyquinoline, thiosemicarbazone and hydrazone compounds (Supplementary Table S1), that have been proved to be protein inhibitors in other relevant viral metalloenzymes (Rogolino et al., 2015; Carcelli et al., 2016; Carcelli et al., 2017) and investigated their interaction with PLpro by high-resolution X-ray crystallography and additional *in vitro* and *in silico* analyses.

MATERIALS AND METHODS

Cloning, Expression and Purification

The PLpro polypeptide corresponding to amino acid residues 746–1,060 of SARS-CoV-2 nsp3 (YP_009742610.1) was cloned into pETM11 with an additional N-terminal His6-tag and TEV-cleavage site. The construct was overexpressed in *E. coli* Rosetta (DE3) according to a previously published protocol (Studier, 2005) and purified for subsequent crystallization. Lysis was carried out in 50 mM NaH₂PO₄ buffer supplemented with 150 mM NaCl and 10 mM imidazole at pH 7.2 using

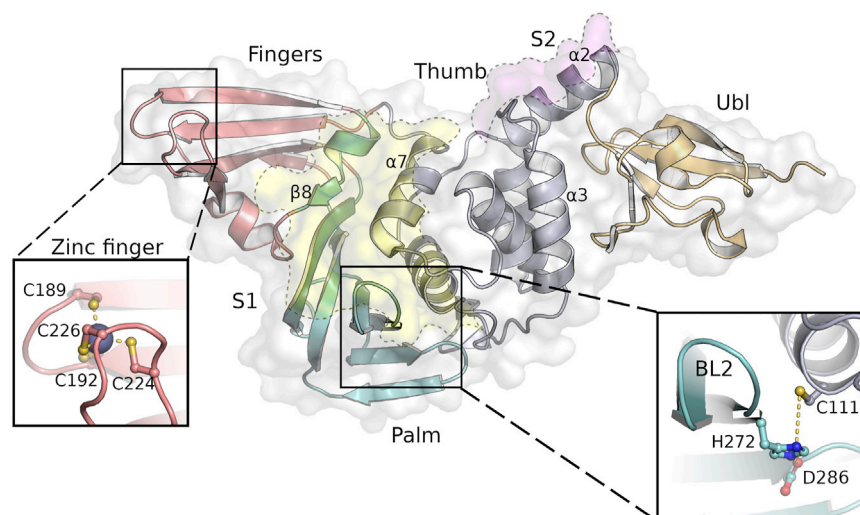


FIGURE 1 | SARS-CoV-2 PLpro structure with the four domains and important features of this protein indicated as follows: fingers (salmon), palm (cyan), thumb (purple) and Ubl domain (orange). The substrate binding sites S1 and S2 are highlighted as yellow and pink areas, while the close-ups show the tetrahedral coordinated zinc-ion at the finger tips and the highly conserved catalytic triad next to the flexible BL2. Secondary structure motifs further discussed are labeled accordingly.

ultrasound for cell disruption. After separation of cell fragments and dissolved protein, a subsequent Ni-NTA chromatography step was used to extract the fusion protein. The cleavage of the histidine tag was achieved by TEV protease during an overnight dialysis step at 8°C. After removing the TEV protease and His₆-tag *via* Ni-NTA resin, a final size exclusion chromatography was performed using a HiLoad 16/600 Superdex 75 column attached to an ÄKTA purifier (GE Healthcare) to purify the protein to homogeneity in 50 mM Tris-HCl, 150 mM NaCl and 1 mM TCEP at pH 7.8.

Protein Crystallization

Crystallization of PLpro was achieved by mixing 0.2 µL protein (20 mg/ml) with 0.1 µL of reservoir solution consisting of 100 mM Tris-HCl buffer pH 8.0, 10% (w/w) glycerol and 0.8 M NaH₂PO₄/1.2 M K₂HPO₄. The crystallization drops were prepared using an Oryx6 pipetting robot (Douglas Instruments) and equilibrated by sitting drop vapor diffusion against 40 µL reservoir solution. Bipyramidal crystals appeared within a few days at 4°C and reached a final size of approximately 100 µm. Crystals were soaked with reservoir solution containing up to 5 mM of the respective compound with a final DMSO concentration of 5%. After 24 h the soaked crystals were harvested and cryo-cooled in liquid nitrogen for subsequent X-ray diffraction data collection.

Data Collection, Processing, Hit Finding and Refinement

Data collection was performed at beamline P11 at the PETRA III storage ring at DESY in Hamburg (Germany). The obtained data sets were processed with DIALS (Winter et al., 2018). The results for each data set were subjected to automated structure refinement using phenix (Liebschner et al., 2019) followed by pan data set density analysis (PanDDA) (Pearce et al., 2017) using

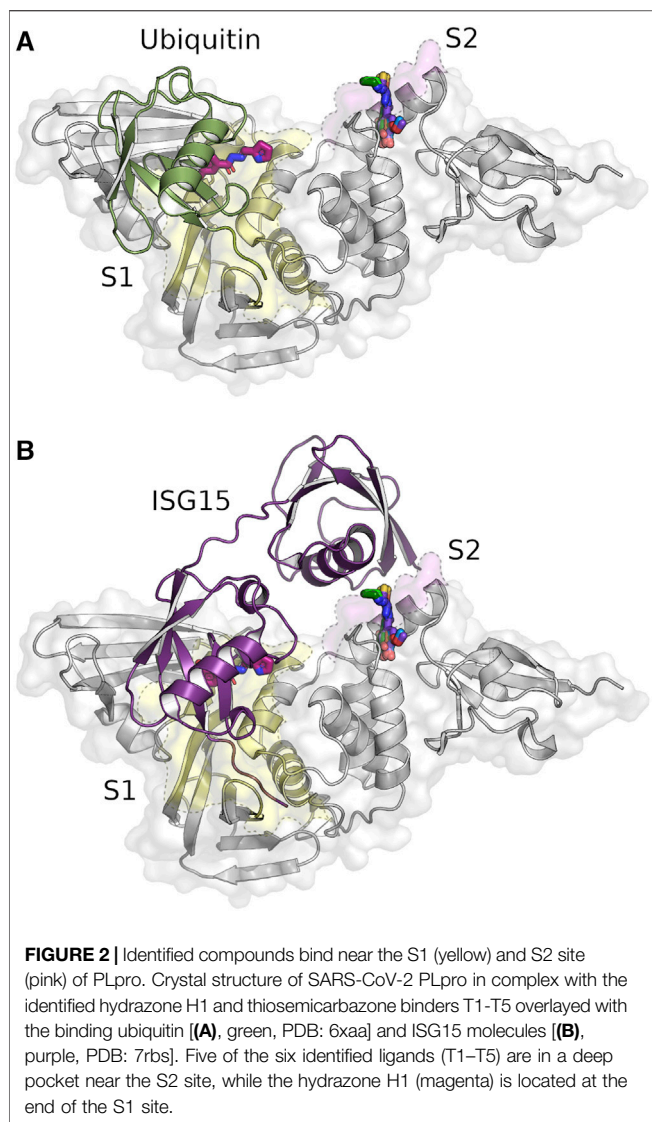
default parameters. The results were manually inspected for hits. Identified hits were further refined by alternating rounds of refinement using phenix.refine (Afonine et al., 2018) and manual model building in COOT (Emsley and Cowtan, 2004). Diffraction data quality indicators and refinement statistics for all data sets are summarized in **Supplementary Table S2**.

Fluorescence Polarization-Based Activity Assay

Assays were performed using Ub-KG-TAMRA (UbiQ-012, UbiQ bio) and human ISG15-KG-TAMRA (UbiQ-287, UbiQ bio) to determine the inhibitory potential of the selected compounds on PLpro activity following the protocol described by Klemm et al. (2020). With substrate concentration kept at 150 nM, PLpro concentration was set to 500 nM for Ub-TAMRA- and to 5 nM for ISG15-TAMRA-cleavage. The protein was preincubated with 500 µM or 5 µM of the selected compounds for 20 min at RT before addition of substrate. Reactions were monitored using a Spark 20 M plate reader (Tecan) with optical settings for the TAMRA fluorophore (excitation: 540 nm, emission: 590 nm). Data was plotted and analyzed using the software Origin (OriginLab).

Nano Differential Scanning Fluorimetry

Nano Differential Scanning Fluorimetry (nDSF) measurements were performed with a Nanotemper Prometheus NT.48 fluorimeter (Nanotemper) controlled by PR. ThermControl using Prometheus Premium grade capillaries (Nanotemper). The excitation power was adjusted to obtain fluorescence counts above 2,000 RFU for 330 and 350 nm. For all measurements a PLpro concentration of around 2 mg/ml in 50 mM Tris-HCl, 150 mM NaCl, 1 mM TCEP, pH 7.8 containing 5% DMSO was used with varying ligand



concentrations. For the initial melting temperature screening, we have used a ligand concentration of 500 μM (468 μM for T3). For the fluorescence titrations 1:1 dilution series with 15 points (19 points for T5) of ligands was created and then the protein solution was added. Ligand concentrations range from 500 μM to 28 nM (5 mM–19 nM for T5). After incubation of 30 min, the solutions were transferred to capillaries and transferred to the Prometheus fluorimeter for the measurement.

Data were analyzed and visualized with self-written python scripts using the Python modules Numpy (Oliphant, 2006; van der Walt et al., 2011), Matplotlib (Hunter, 2007), Scipy (Virtanen et al., 2020) and Pandas (McKinney, 2010) and the publicly available eSPC data analysis platform (Burastero et al., 2021). The fluorescence titration of T5 was fitted with a simple 1:1 binding model.

$$F_{350\text{nm}}([L]_0) = F_{\text{upper}} + (F_{\text{upper}} - F_{\text{lower}}) * (1 - \alpha([L]_0)) \quad (1)$$

$$\alpha([L]_0) = \left([P]_0 - K_D - [L]_0 + \sqrt{([P]_0 + [L]_0 + K_D)^2 - 4*[P]_0*[L]_0} \right) / (2*[P]_0) \quad (2)$$

Molecular Docking

Molecular docking was performed using AutoDock4.2.6 (Morris et al., 2009). Protein coordinates were obtained from the corresponding PDB-files (7qcg, 7qch, 7qci, 7qcj, 7qck, and 7qcm) and processed with AutoDockTools. The covalently connected ligand structures were chosen depending on the structural overlay visible when aligning the corresponding PLpro structures with PDB-files 7ofs, 7oft or 7ofu (**Supplementary Table S3**) and prepared using eLBOW (Moriarty et al., 2009) and AutoDockTools. Grid maps with a box of $45 \times 35 \times 35$ grid points (T1–T5) or with a box of $45 \times 35 \times 45$ grid points (H1) with 0.375 Å spacing were set around the corresponding binding sites. The docking calculations were performed using the Lamarckian genetic algorithm (GA) combining a global search with a local search (Morris et al., 1998). The most favorable structure with the highest binding energy in the maximum cluster of the docked conformations was chosen as the representative structure in Autodock. To calculate reliable binding energies the representatives structures were further processed with Haddock (van Zundert et al., 2016; Honorato et al., 2021) and Prodigy webserver (Kurkcuoglu et al., 2018; Vangone et al., 2019).

Synthesis of Compounds

Compounds 1–40 were synthesized following literature methods according to references reported in **Supplementary Table S1**. Characterization of compounds T1–T5 and H1 is reported in the Supplementary Information Paragraph.

RESULTS

Compounds Bind at Two Different Substrate Binding Sites in SARS-CoV-2 PLpro

In total 71 diffraction data sets from crystals with 40 different compounds were collected with high resolution limits ranging from 1.6–3.0 Å. In the subsequent analysis of the X-ray diffraction data nine compounds were identified binding to PLpro in PanDDA difference electron density maps (Pearce et al., 2017). Out of these nine hits the binding modes of six different compounds could be unambiguously determined in data sets with a diffraction limit of 1.75–1.92 Å (**Figure 2**).

Interestingly, none of the anticipated zinc binders was found near the zinc binding site but instead at a previously undescribed groove within the S1 site (**Figure 2A**) and a pocket between the S2 binding site and Ubl domain (**Figure 2B**). The S1 site is targeted by hydrazone H1, whereas five thiosemicarbazones (T1–T5) bind to the S2 site (**Supplementary Table S1**, highlighted ligands). For

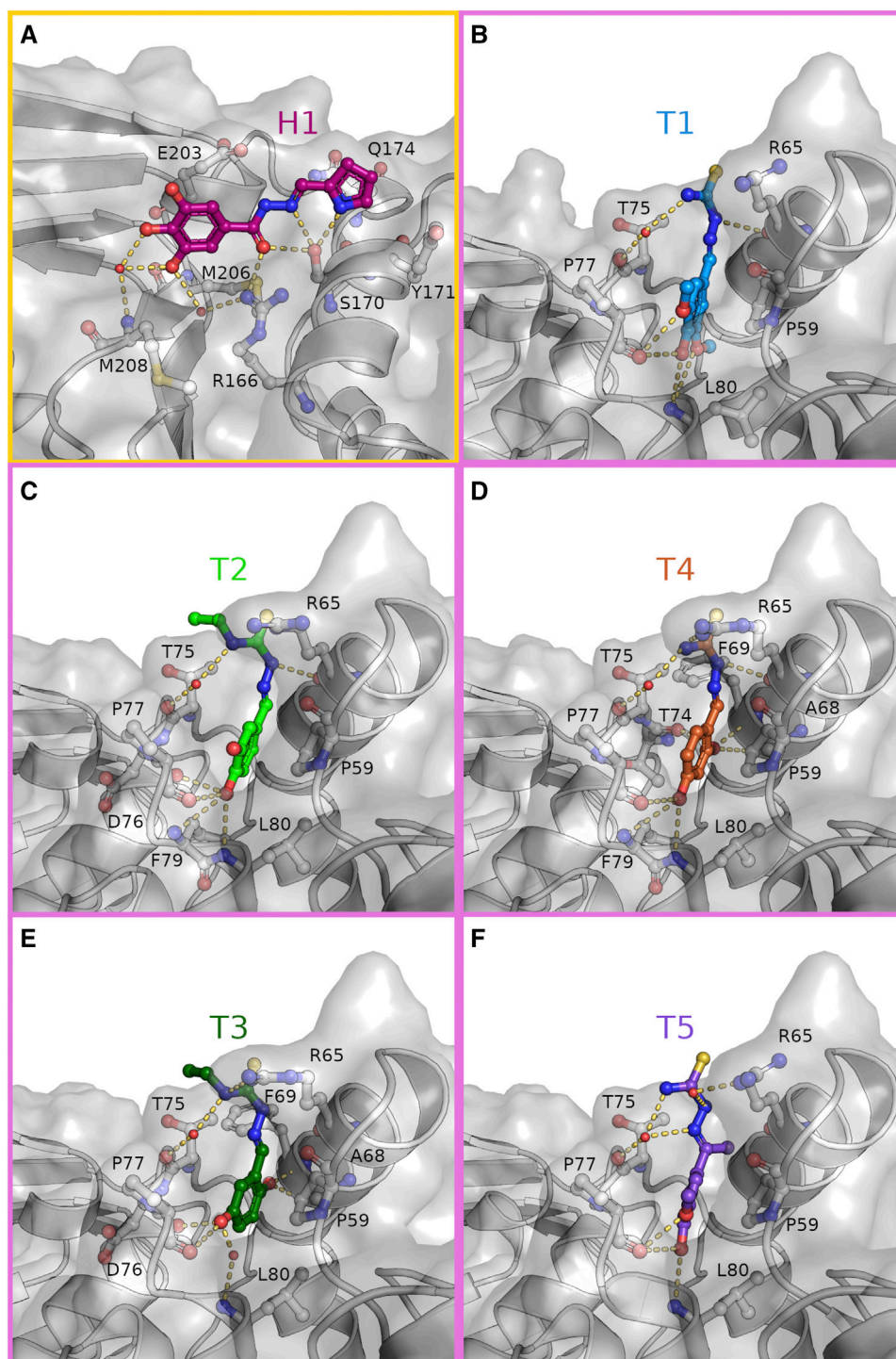


FIGURE 3 | Hydrazone and thiosemicarbazones are stabilized in their binding positions by an extensive hydrogen bonding network. Close-up view on the binding of H1 [(A), magenta] to the S1 site (yellow frame) and T1-T5 (B-F) to the S2 site (pink frames). Compounds and interacting residues are shown as sticks with compounds highlighted by individual colouring. Possible interactions within hydrogen bonding distance with the surrounding residues are shown as dashes.

both binding sites, one compound each showed superior electron density maps, where the compound could be refined with full occupancy (**Supplementary Figure S1**). In all six structures compound binding induced only local rearrangements at the

binding sites with an overall r.m.s.d. of 0.15–0.25 Å compared to the ligand-free structure (PDB: 7nfv). All compounds bind non-covalently, primarily through hydrogen bonds and π -alkyl interactions (**Figure 3**).

The hydrazone compound H1 binds in a polar groove at the S1 site of PLpro between β -strand $\beta 8$ (M206—M208) of the palm and helix $\alpha 7$ (V165—H175) of the thumb domain. In this groove H1 is stabilized by eight hydrogen bonds (**Figure 3A** and **Supplementary Figure S2A**). Here, the hydroxyl side chain of S170 acts as a hydrogen bond acceptor and donor to the nitrogen atoms of the pyrrole and imino moiety, respectively. The central carbonyl oxygen of H1 is the hydrogen bond acceptor for side chain of R166 and again S170, while two phenolic hydroxyl groups of the terminal benzene substituent are hydrogen bonded *via* one water molecule to the amide nitrogen of M208. One of these hydroxyl groups forms a second hydrogen bond to the main chain carbonyl of M206, whereas the third hydroxyl is solvent exposed. When compared with the ligand-free structure (PDB: 7nfv) S170 is observed in an alternative rotameric state, which is moved 1.7 Å by the attractive interaction towards H1 (**Supplementary Figure S3A**). An additional side chain rearrangement in the surrounding residues is observed for residue Q174, which adopts two side chain conformations in the ligand-free structure but prefers only one conformation in the H1 bound structure. In this position the carboxamide side chain has moved by 3.9 Å (conformation A) and 0.9 Å (conformation B), respectively, to complement the compound binding by a hydrogen bond to the π -system of the hydrazone. Further stabilization is achieved by C-H $\cdots\pi$ interactions between the phenyl ring of the compound with the side chain of E203 and the pyrrole ring with the aromatic side chain of Y171.

The thiosemicarbazone derivatives T1–T5 all bind in a deep pocket close to the S2 site with a volume of about 70 Å³ (**Figures 3B–F** and **Supplementary Figures S2B–F**). This cavity is enclosed by helices $\alpha 2$ (D62—Y72) and $\alpha 3$ (residues P77—K92) of the thumb domain and loop 7 connecting the Ubl with the thumb domain. Here the phenolic system of the compounds points into the N-terminal turn (residues P77–L80) of the thumb helix $\alpha 3$ suitable to interact with the helical dipole. In this position the aromatic plane becomes a part of the hydrophobic interface between T75, P77 and the adjacent Ubl domain residue P59 through C-H $\cdots\pi$ interactions (**Figures 2, 3B**). The substitutions on the phenolic system in T1–T5 form a hydrogen bonding pattern exclusive with main chain atoms of the N-terminal helical turn of $\alpha 3$. The different arrangements of hydroxyl- and methoxy substituents at the benzene ring determine the final orientations of the phenolic system, displacing the ring system in plane. While the overall position of the thiosemicarbazide moiety of T1–T5 are almost identical with polar interactions to the side chain and main chain carbonyl of R65 ($\alpha 2$), minor differences are observed due to the variation of the hydroxylation pattern. The specific binding modes for each compound are explained in more detail in the following.

Within the group of thiosemicarbazones, compound T1 showed the best difference electron density map and was refined with full occupancy. Compounds T2–T5 could only be refined with lower occupancy, but highly resemble the T1 binding position (**Supplementary Figure S1**). The more defined electron density of T1 is probably caused by the advantageous pattern of hydroxyl and methoxy substituents at the benzene ring (**Figure 3B**). Especially the *para*-hydroxyl group, present in

four of the thiosemicarbazones, plays a key role in anchoring the molecule at the bottom of the binding pocket, as this substitution acts as a hydrogen bond donor and acceptor to the backbone carbonyl of P77 and the amide N-H of L80, respectively. Only in T3 this interaction is guided by a phenolic hydroxyl group in *meta*-position (**Figure 3E**). Due to the attractive hydrogen bonding pattern to the N-terminal turn of helix $\alpha 3$ the plane of the benzene ring of T3 is shifted to place its *meta*-hydroxyl substituent similar to the *para*-hydroxyl groups of T1, T2, T4, and T5. While the direct hydrogen bond to L80 is substituted by the main chain carbonyl of D76, T3 still interacts with L80 through a water mediated hydrogen bond.

For all five thiosemicarbazones, the thiosemicarbazide fragment is sandwiched by side chains R65 ($\alpha 2$) and T75 (loop $\alpha 2$, $\alpha 3$) and its terminal thiourea points towards the solvent. This fragment forms polar interactions with the side chain of R65. In case of T1, T2 and T4 this moiety is held in position by a hydrogen bond of the hydrazine N-H to the backbone carbonyl of residues R65 (**Figures 3B–D**).

Thiosemicarbazones T2 and T3 both feature an ethyl chain at N3 of the thiourea moiety, which extends in the direction of T75 and thereby reduces the solvent accessible area of this residue (**Figures 3C,E**). T5 is the only compound with a methyl substituent at the C=N bond of the thiosemicarbazone. This methyl group points towards the backbone atoms of the C-terminal turn of $\alpha 2$ (F69) displacing the T5 benzene axis slightly, while the phenolic *para*-hydroxyl still determines the overall position inside the binding pocket (**Figure 3F**).

In comparison to the ligand-free structure again two conformational rearrangements in the surrounding residues are observable (**Supplementary Figure S3B**). As a result of the T1 binding the guanidyl group of R65 is displaced by 3.0 Å to open the binding pocket for the thiourea moiety of this compound. To fully accommodate this ligand further opening of the pocket is induced by the sterical requirements of the methoxy groups of T1, which enable the side chain movement of L80 by 1.7 Å compared to the ligand-free structure.

Compound Binding Indicates Sterical Hindrance for Substrate Binding

All six compounds bind in close proximity to the S1 and S2 sites that are responsible for binding the native PLpro substrates ubiquitin and ISG15. Superposition of these PLpro complex structures (PDB: 6xaa, 7rbs, respectively) with our structures suggests that in particular compound H1 is partially overlapping with the natural substrate binding site. In addition, we observed altered interactions of key PLpro residues involved in substrate binding (**Figure 4**).

Ubiquitin binds to the S1 site of PLpro by sitting on the palm domain and is additionally held in position by the fingers domain (**Figure 2A**). In addition to numerous nonpolar interactions, multiple intermolecular hydrogen bonds within the active site and the adjacent S1 site support this binding. At the core of the ubiquitin binding interface around residue I44_{Ub} are four non-covalent bonds between ubiquitin and PLpro (one hydrogen

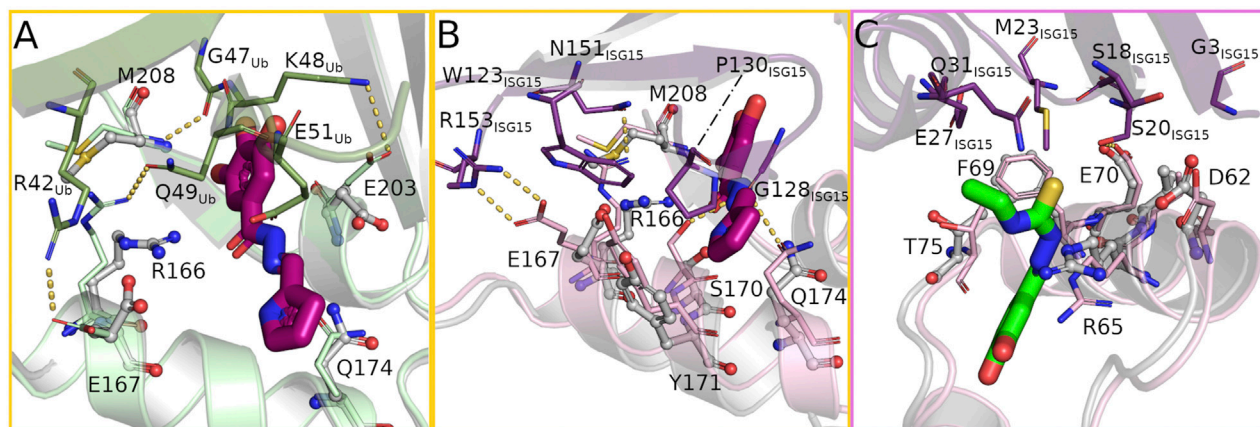


FIGURE 4 | The bound compounds interfere with key residues for substrate binding at the S1 (yellow frame) and S2 (pink frame) site. **(A)** Overlay of ubiquitin bound to PLpro (PDB: 6xaa, PLpro light green, ubiquitin green) and the hydrazone bound structure (PLpro grey, H1 magenta) showing the rearrangement of several PLpro-ubiquitin interacting side chains to form hydrogen bonds with the compound. **(B,C)** Overlay of PLpro complexed with human ISG15 (PDB: 7rbs, PLpro light pink, ISG15 purple) and PLpro bound with hydrazone H1 and thiosemicarbazone T2 (PLpro grey, H1 magenta, T2 green) at the S1 and S2 sites respectively highlighting the structural differences in binding the compound or substrate.

bond, three salt bridges), all of which are likely disrupted by binding of H1 (**Figure 4A**). Interestingly only the hydrogen bond is lost due to direct sterical hindrance (M208/G47_{Ub}), whereas the three salt bridges (R166/Q49_{Ub}, E167/R42_{Ub}, and E203/K48_{Ub}) are disrupted due to side chain reorientations towards the bound ligand. While E203 alters its conformation without direct interaction with the ligand, residues R166 and E167 are not only attracted by H1 but even form alternative hydrogen bonds with each other and H1 to support a highly polar ligand environment. In addition to these changes the ligand further interferes sterically with residue E51_{Ub}.

The C-terminal domain of human ISG15 binds mainly to the thumb domain at the S1 site of PLpro and interacts with a different set of residues compared to the PLpro/ubiquitin complex (**Figure 2B**). The key interaction sites mediating the contacts between PLpro and ISG15 can be found around ISG15 residues W123_{ISG15} and P130_{ISG15} (Fu et al., 2021; Osipiuk et al., 2021) (**Figure 4B**). Within PLpro an overall upward shift of 1.7 Å in the interacting helix α7 becomes visible that strengthens ISG15 binding. Five hydrogen bonds between G128_{ISG15} and S170/Q174, N151_{ISG15} and R166 and R153_{ISG15} and E167 thereby stabilize the interface. Especially the latter one contributes to the interaction of the proteins, as the side chain not only forms two hydrogen bonds but further has an aliphatic interaction with W123_{ISG15}. Y171 further stabilizes ISG15 binding by π-stacking interactions with P130_{ISG15}. Superposition of the H1 complex with the PLpro/ISG15 structure reveals a variety of side chain rearrangements which show that ISG15 binding could not only be affected by direct overlap with the compound but also by multiple lost interactions. While the hydrogen bonds with G128_{ISG15} are likely disrupted by the sterical clash of H1 and the ISG15 loop comprising residues F126_{ISG15} to P130_{ISG15}, the interaction between N151_{ISG15} and R166 is impaired due to the movement of the arginine side chain by 4.0 Å that forms a

hydrogen bond with H1 in the complex structure. This rearrangement is accompanied by two additional side chain movements of residues E167 and M208. As a result, residues W123_{ISG15} and R166 show a significant overlap with these residues, which likely further destabilizes ISG15 binding at the S1 site.

The binding of the N-terminal domain of human ISG15 to the S2 site is mediated mainly by interactions between helix α2 of PLpro and two β-strands of ISG15 (**Figure 4C**). While residues G3_{ISG15}, S20_{ISG15} and M23_{ISG15} form a hydrophobic patch that interacts with V66, additional stabilization is formed by a hydrogen bond between S20_{ISG15} and E70 and a C-H...π interaction between M23_{ISG15} and F69. For the ISG15 helix interacting with the PLpro loop containing T75 also residues E27_{ISG15} and Q31_{ISG15} contribute to the binding. As the thiosemicarbazone compounds bind in close proximity to the S2 site, but not prominently at the interface of the N-terminal domain of ISG15 and PLpro, the potential for direct sterical interference by these ligands is rather small compared to H1. However, a closer look at the surrounding residues suggests that the thiosemicarbazones may alter the polarity and flexibility of the S2 binding site. T1–T5 are located at the interface of the Ubl and thumb domain and could interfere with the mobility of the Ubl domain by disturbing the interaction network between residues P59, P77 and T75. T75 is highly relevant for ISG15 binding, as it can directly alter the conformation of F69 (Bosken et al., 2020). T2 and T3 may further affect the interaction of PLpro T75 with E27_{ISG15}, as the ethyl N3 substituent is positioned close to T75 (**Figure 4C**).

To test the inhibitory potential of the six compounds on substrate turnover, T1–T5 and H1 were examined in a fluorescence polarization assay (**Figure 5**) using ubiquitin and human ISG15 as substrates. The results show the highly divergent turnover rates for both substrates and the preference of SARS-

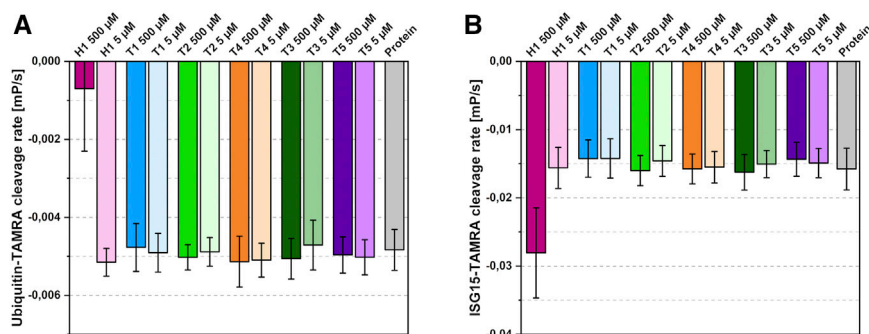


FIGURE 5 | Effects of the identified binders on substrate cleavage rates. **(A)** Ubiquitin-cleavage rate of PLpro in the presence of 500 μ M or 5 μ M compound. **(B)** ISG15-cleavage rate of PLpro in the presence of 500 μ M or 5 μ M compound. Compounds coloured according to **Figure 3**; protein shown in grey. Average of four independent experiments with standard deviation shown.

CoV-2 PLpro for ISG15 (Freitas et al., 2020). While the thiosemicarbazones show no inhibitory effect on substrate turnover at the tested concentrations, a significant inhibition of the ubiquitin cleavage can be detected for 500 μ M of hydrazone H1. The fivefold decrease in substrate turnover is consistent with the expected sterical interference at the S1 site as mentioned above. Surprisingly, ISG15 turnover in the presence of 500 μ M of H1 is not reduced but rather increased twofold compared to ligand-free PLpro. For the other compounds, no inhibitory effect was detected at the tested concentrations.

As missing inhibition can be caused by low binding affinities of the compounds, additional nano DSF measurements were performed (**Supplementary Figure S4**). The thermal shift assay showed a considerable stabilization for all compounds (**Supplementary Figure S4A**) in combination with a strong quenching of the intrinsic protein fluorescence caused by the ligands. This strong fluorescence quenching renders the thermal unfolding curve almost featureless for some of the ligands. The signal at 350 nm shows the clearest transitions and was therefore selected to calculate the melting temperature shifts. To estimate the binding affinity of the compounds we performed nDSF/fluorescence titrations, which are shown in **Supplementary Figures S4B, S4C**. These titrations indicate dissociation constants in the high micromolar range for all tested compounds. However, due to the low solubility of the ligands, high enough concentrations for a reliable K_D determination by isothermal analysis (Bai et al., 2019; Niebling et al., 2021) or the initial fluorescence fit are missing. One exception is T5, for which higher concentration data are available. A fit of the initial fluorescence at 330 nm yields an apparent K_D of approximately 200 μ M. The fluorescence titration of T5 is very similar to the other tested ligands, therefore we expect dissociation constants in the same range.

Docking Studies Reveal Lead Compound Potential

While most of the compounds do not show a clear inhibitory effect in our assays, their binding positions make them highly valuable candidates in the development of new lead compounds

targeting PLpro. To explore the possibilities of compound extension, *in silico* experiments were performed. Here we considered additional PLpro binders from the protein data bank. Among these, three recently described phenolic fragments were further analyzed and included in the compound extensions (Srinivasan et al., 2021), as they were found in adjacent binding positions of the S2 site of SARS-CoV-2 PLpro and show partial overlap with our ligands (**Supplementary Figure S5**). 4-(2-hydroxyethyl)-phenol (YRL; PDB: 7ofs) and 4-hydroxybenzaldehyde (HBA; PDB: 7oft) bind in a pocket next to the phenol moiety of the thiosemicarbazones T1-T5 (**Supplementary Figures S5B, S5C**). The *para*-substituent of both phenol derivatives is observed in a position, which is almost identical to a *meta*-methoxy substituent of T1. A similar situation is observed for a *meta*-hydroxyl of H1 related to a symmetry mate of methyl 3,4-dihydroxybenzoate (HE9; PDB: 7ofu) in close proximity to H1 (**Supplementary Figure S5A**). Molecular docking with either YRL or HBA covalently linked to the specific thiosemicarbazone structures was performed based on the best overlap of these structures, while H1 was elongated with HE9. The resulting docked compounds thereby largely resemble the two experimentally determined binding positions, highlighting the specific interactions of these compounds within their binding pockets, and show an increase of predicted binding energies of 0.8–1.8 kcal/mol relative to the also docked non-extended initial binders (**Figure 6A**).

For H1 the docking visualizes the high number of possible polar interaction partners within binding distance to the original crystallographic compound position (**Figure 6B**). In addition to the previously described interactions, the extended compound can further form two hydrogen bonds to the side chain of E167 and main chain carbonyl of E203 due to a 40° rotation around the central carbonyl oxygen relative to the parental compound. In this orientation the newly added phenolic fragment is bound tightly to the protein via two hydrogen bonds between its *meta*- and *para*-hydroxyl group and the main chain carbonyl and amide nitrogen of M208. This suggests that even shallow binding grooves can be useful targets for drug development and opens up possibilities for a variety of polar fragments to be added to the phenol and pyrrole moieties of H1.

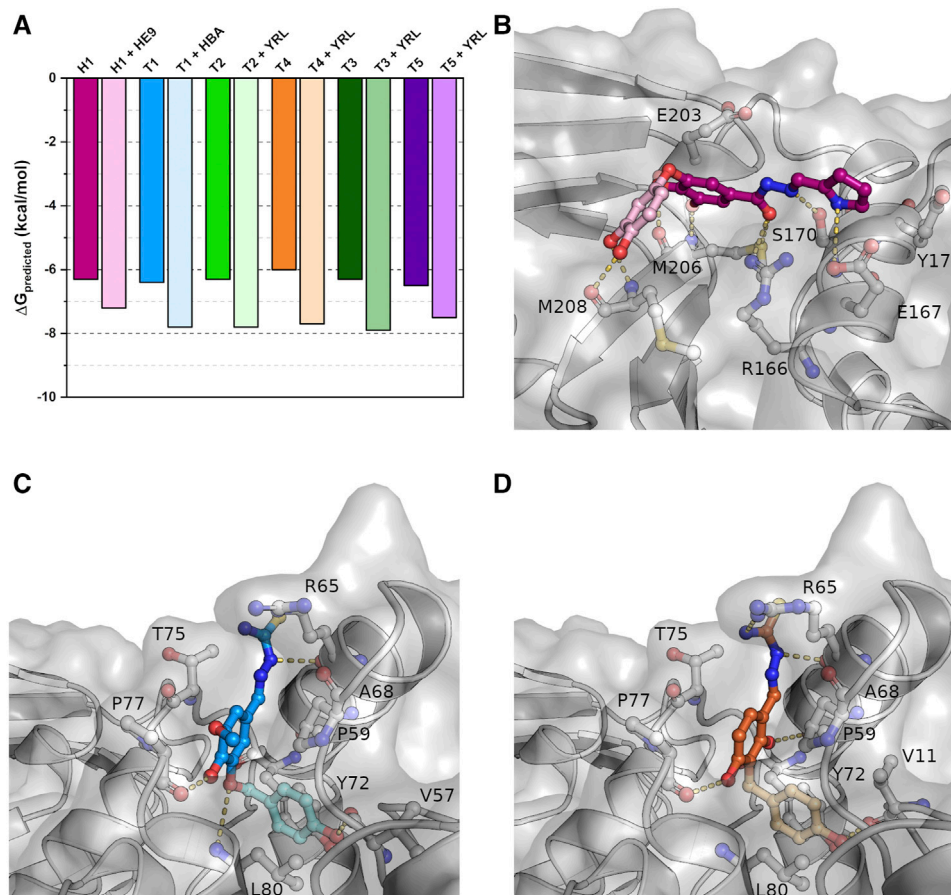


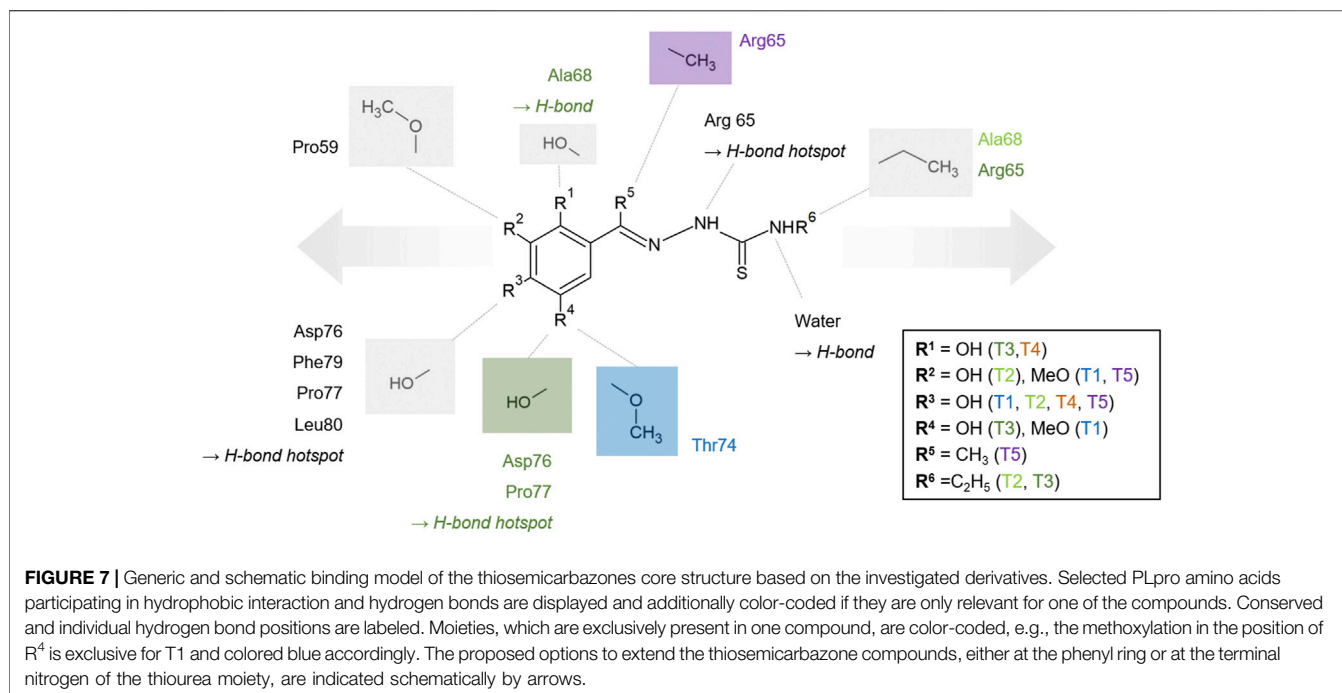
FIGURE 6 | Docking studies of extended compounds highlight potential of binders as lead compounds. **(A)** Results of the docking studies of crystallized and elongated binders. **(B)** The docked compound combining H1 (magenta) with HE9 (PDB: 7ofu, light pink) binding to the S1 site. **(C)** T1 (blue) combined with HBA (PDB: 7oft, light blue) binding to the S2 site. **(D)** T4 (orange) combined with YRL (PDB: 7ofs, light orange) binding to the S2 site. Shown are representative structures of the maximum cluster of the docked conformations.

Similar to H1, also the thiosemicarbazones in conjunction with the phenolic fragments are predicted to bind tighter inside their binding pocket indicated by lower predicted binding energies. In contrast to hydrazone H1, the compounds are not stabilized by additional hydrogen bonds but mainly by hydrophobic interactions within the binding pocket that is enlarged due to the rotation of side chain L80 (**Figures 6C,D**). As a result of this movement the extended compounds form new π -stacking and π -alkyl interactions with the side chains of P59, Y72 and L80. The *para*-hydroxyl group of the added phenolic fragments is further stabilized by a hydrogen bond to the main chain carbonyl of V11 or V57. Differences in binding energies between the thiosemicarbazones, caused by the individual phenolic substitution patterns, were reduced for the compound extension by the addition of the second phenol ring. As a result, the extended compounds will most likely not only possess an increased binding affinity but also an increased inhibitory potential as the separate phenolic fragments alone were already shown to inhibit deubiquitination by PLpro (Srinivasan et al., 2021).

DISCUSSION

In the search for inhibitors of SARS-CoV-2 PLpro, we performed an X-ray crystallography-based screening. Surprisingly, none of the compounds of our small library of 40 putative zinc coordinating ligands were found to bind at the zinc binding site. Instead we identified six compounds binding to the S1 site (hydrazone H1) or S2 site (thiosemicarbazones T1-T5) of PLpro. These sites function as binding sites for ubiquitin and ISG15 as substrates.

The hydrazone H1 is binding directly at the center of the S1 substrate binding interface, interfering with residues R166/E167 which are highly important for substrate recognition. Mutations at E167, which forms mandatory interactions with both substrates, strongly reduce PLpro activity (Fu et al., 2021; Osipiuk et al., 2021). Binding of H1 has likely a similar effect on E167 as these mutations. Indeed, our biochemical characterization confirms an inhibitory effect of H1 on ubiquitin cleavage by PLpro. At the same time H1 binding to the S1 site does not reduce ISG15 cleavage by PLpro, which might be explained by the reported important interaction of ISG15 with



the S2 site of PLpro (Klemm et al., 2020; Osipiuk et al., 2021). As the central role of E167 is not only reported for SARS-CoV-2 but also for SARS-CoV-1 at this site (Békés et al., 2016), the structural features of H1 have the potential to inhibit the deubiquitinase activity of different betacoronaviruses. With differing substrate preferences between the different PLpros (Freitas et al., 2020) it remains to be investigated if H1 can interfere with their specific activity.

The thiosemicarbazones T1-T5 target the S2 binding site. In the binding pocket, the substituents at the phenolic ring of the compounds form a distinct hydrogen bonding pattern exclusively with main chain atoms of the N-terminal helical turn of $\alpha 3$. In contrast to H1 binding at the S1 site, compound binding of T1-T5 to the S2 site of PLpro shows no inhibitory effect. Based on the structural data this might be explained by the smaller overlap of our compounds with natural substrates binding to the S2 site. In addition, with binding affinities of the compounds in the high micromolar range, competitive inhibition will be difficult to detect in our experiments, as the affinity for ISG15 is reported in the lower micromolar range and ubiquitin affinity is approximately 120 μM (Fu et al., 2021; Osipiuk et al., 2021).

Nevertheless the S2 site is highly important for substrate recognition and PLpro activity in general. As T1-T5 are binding to the S2 site at the interface of the Ubl and thumb domain, their thiosemicarbazide moieties interact with residues P77 and T75, which together with V66 are critical for the substrate preferences of SARS-CoV-2 (Shin et al., 2020; Osipiuk et al., 2021). Any mutations of these residues vary the surface properties. In particular size and hydrophobicity of residue 75 alters the second ubiquitin binding site and influences the binding affinity for ISG15 and K48-Ub₂ (Shin et al., 2020). While SARS-CoV-2 PLpro normally shows a higher

efficacy for ISG15 cleavage (Freitas et al., 2020; Klemm et al., 2020; Rut et al., 2020), SARS-CoV-1 with a leucine at this position prefers K48-Ub₂. Even though showing no inhibition in the present form, binding positions and extensive interactions of the tested compounds represent valuable lead structures for the development of effective inhibitors of PLpro with higher affinity and specificity. Altering the S2 site properties with ligands based on our compounds offers the potential to efficiently slow down the main deubiquitinase activity not only for SARS-CoV-2 but also for other PLpros, as the compounds bind mainly sequence independently to the protein back bone. Therefore, it is reasonable to assume that this type of compound potentially tolerates mutations of the protein, which for example already occurred in the SARS-CoV-2 delta variant (P77L) (Patchett et al., 2021).

Our *in silico* approach of extending the initial binders is a first step in structure-based development of novel inhibitors. Combination of such a fragment extension with the multiple options for substitutions at the phenolic rings highlights the potential of developing hydrazones and thiosemicarbazones into potent PLpro inhibitors (Figure 7 and Supplementary Figure S6). The compounds T1-T5 already underline the significance of hydroxylation in *para* position combined with hydroxylation or methoxylation in *meta* position to form multiple hydrogen bonds especially with residues P77 and L80. In addition to the thiosemicarbazide core moiety, which is already involved in hydrogen bonds with R65, further compound optimization can potentially enhance the steric interference with ISG15. T2 and T3, which are ethyl substituted at this position, represent the first example for extensions at this site and already demonstrated that such a modification does not decrease the binding ability. This position could be further

explored by a bulkier substitution to maximize the sterical hindrance of ISG15 binding, which should consistently abolish protein-protein interactions and reduce the deubiquitinase activity of PLpro due to a highly altered binding surface at the S2 site.

The compound interaction hotspots, including the interactions of the polar thiocarbonyl moiety, resemble the modular composition of other previously described thiocarbazonate lead compounds (Osmaniye et al., 2021). While thiosemicarbazones currently attract significant interest as anticancer agents (Baruffini et al., 2020), they also show antiviral activity against smallpox and other viruses (Kune, 1964; Rogolino et al., 2015). Hydrazones have shown biological activity for treatment of Alzheimer's disease, cancer and inflammation with properties rendering them beneficial for medicinal applications (Wahbeh and Milkowski, 2019; de Oliveira Carneiro Brum et al., 2020). These reports can help to increase the pharmacokinetic properties of new designed derivatives based on our lead structures.

Although multiple inhibitors have already been reported for PLpro in different *in vitro* and *in silico* studies, the importance of searching for new inhibitors remains high. Targeting the coronaviral proteases essentially involved in processing the building blocks of the viral transcriptase/replicase complex, continues to be highly attractive (Hilgenfeld, 2014; Dai et al., 2020). Nonetheless, recently published results indicate that some of the previously suggested PLpro inhibitors may lack specificity or optimal pharmaceutical properties (Ma and Wang, 2022). Furthermore, the active site of PLpro does not provide a variety of individual structural features or scaffolds that are in favor for active site drug development. Thus, the identified lead compounds at two different binding sites along with a defined modification strategy are a good starting point to specifically target PLpro deubiquitinase activity and thereby viral replication.

Overall, on the basis of our structural studies, *in vitro* evaluation and *in silico* analysis the described hydrazone and thiosemicarbazone derivatives represent valuable lead compounds targeting the protein-protein interaction of SARS-CoV-2 PLpro. Further investigation of the molecular mechanisms and antiviral properties of improved compounds based on these leads are in progress as the urgent demand for antiviral drugs in the current COVID-19 pandemic remains.

DATA AVAILABILITY STATEMENT

The crystal structures presented in this study can be found in online repositories. The names of the repository/repositories and accession number(s) can be found below: <https://www.rcsb.org/>, 7qcg, 7qch, 7qci, 7qcj, 7qck, and 7qcm. Further original contributions presented in the study are included in the

article/**Supplementary Material**, further inquiries can be directed to the corresponding authors.

AUTHOR CONTRIBUTIONS

DR and AM designed the research. WE, SG, SF, PR, WH, and AM wrote the manuscript. HH, SF and HB participated in sample preparation. VS and PR participated in crystallization. PR, SG, JL, and WE performed crystallographic data collection and analysis. WE performed the FP assay and docking studies. CG and SN performed the nDSF measurements. FM, MC and DR designed and synthesized the compounds. CB, KL, MG-A, DR, and AM supervised the project. All authors contributed to the discussion of results and proofreading and approved the submitted version.

FUNDING

This work was supported by the Helmholtz society through the projects FISCOV and SFragX. We acknowledge financial support from the Federal Ministry of Education and Research (BMBF) via projects 16GW0277 and 031B0405D. DR was supported by Progetti di ricerca di Rilevante Interesse Nazionale (PRIN, Grant N. 2017BMK8JR). This work has benefited from the equipment and framework of the COMP-HUB Initiative, funded by the "Departments of Excellence" program of the Italian Ministry for Education, University and Research (No. MIUR, 2018–2022).

ACKNOWLEDGMENTS

We acknowledge Deutsches Elektronen-Synchrotron (DESY, Hamburg, Germany), a member of the Helmholtz Association HGF, for the provision of experimental facilities. Parts of this research were carried out at PETRA III at beamline P11. This research was supported in part through the Maxwell computational resources operated at Deutsches Elektronen-Synchrotron DESY, Hamburg, Germany. We acknowledge the use of the XBI biological sample preparation laboratory at European XFEL, enabled by the XBI User Consortium, and the use of the Protein Production Core Facility at CSSB, DESY. We thank "Centro Interfacoltà Misure Giuseppe Casnati" of the University of Parma for use of their facilities. We acknowledge technical support by the SPC facility at EMBL Hamburg.

SUPPLEMENTARY MATERIAL

The Supplementary Material for this article can be found online at: <https://www.frontiersin.org/articles/10.3389/fchem.2022.832431/full#supplementary-material>

REFERENCES

- Afonine, P. V., Poon, B. K., Read, R. J., Sobolev, O. V., Terwilliger, T. C., Urzhumtsev, A., et al. (2018). Real-space Refinement in PHENIX for Cryo-EM and Crystallography. *Acta Cryst. Sect D Struct. Biol.* 74, 531–544. doi:10.1107/S2059798318006551
- Báez-Santos, Y. M., St. John, S. E., and Mesecar, A. D. (2015). The SARS-Coronavirus Papain-like Protease: Structure, Function and Inhibition by Designed Antiviral Compounds. *Antiviral Res.* 115, 21–38. doi:10.1016/j.antiviral.2014.12.015
- Bai, N., Roder, H., Dickson, A., and Karanicolas, J. (2019). Isothermal Analysis of ThermoFluor Data Can Readily Provide Quantitative Binding Affinities. *Sci. Rep.* 9, 2650. doi:10.1038/s41598-018-37072-x
- Barretto, N., Jukneliene, D., Ratia, K., Chen, Z., Mesecar, A. D., and Baker, S. C. (2005). The Papain-like Protease of Severe Acute Respiratory Syndrome Coronavirus Has Deubiquitinating Activity. *J. Virol.* 79, 15189–15198. doi:10.1128/JVI.79.24.15189-15198.2005
- Barretto, N., Jukneliene, D., Ratia, K., Chen, Z., Mesecar, A. D., and Baker, S. C. (2006). Deubiquitinating Activity of the SARS-CoV Papain-like Protease. *Adv. Exp. Med. Biol.* 581, 37–41. doi:10.1007/978-0-387-33012-9_5
- Baruffini, E., Ruotolo, R., Bisceglie, F., Montalbano, S., Ottonello, S., Pelosi, G., et al. (2020). Mechanistic Insights on the Mode of Action of an Antiproliferative Thiosemicarbazone-Nickel Complex Revealed by an Integrated Chemogenomic Profiling Study. *Sci. Rep.* 10, 10524. doi:10.1038/s41598-020-67439-y
- Békés, M., van der Heden van Noort, G. J., Ekkebus, R., Ova, H., Huang, T. T., and Lima, C. D. (2016). Recognition of Lys48-Linked Di-ubiquitin and Deubiquitinating Activities of the SARS Coronavirus Papain-like Protease. *Mol. Cell* 62, 572–585. doi:10.1016/j.molcel.2016.04.016
- Bosken, Y. K., Cholko, T., Lou, Y.-C., Wu, K.-P., and Chang, C.-e. A. (2020). Insights into Dynamics of Inhibitor and Ubiquitin-like Protein Binding in SARS-CoV-2 Papain-like Protease. *Front. Mol. Biosci.* 7, 174. doi:10.3389/fmolb.2020.00174
- Burastero, O., Niebling, S., Defelipe, L. A., Günther, C., Struve, A., and Garcia Alai, M. M. (2021). eSPC: an Online Data-Analysis Platform for Molecular Biophysics. *Acta Cryst. Sect D Struct. Biol.* 77, 1241–1250. doi:10.1107/S2059798321008998
- Carcelli, M., Rogolino, D., Gatti, A., De Luca, L., Sechi, M., Kumar, G., et al. (2016). N-acylhydrazone Inhibitors of Influenza Virus PA Endonuclease with Versatile Metal Binding Modes. *Sci. Rep.* 6, 31500. doi:10.1038/srep31500
- Carcelli, M., Rogolino, D., Gatti, A., Pala, N., Corona, A., Caredda, A., et al. (2017). Chelation Motifs Affecting Metal-dependent Viral Enzymes: N'-acylhydrazone Ligands as Dual Target Inhibitors of HIV-1 Integrase and Reverse Transcriptase Ribonuclease H Domain. *Front. Microbiol.* 8, 440. doi:10.3389/fmicb.2017.00440
- Chan, J. F.-W., Kok, K.-H., Zhu, Z., Chu, H., To, K. K.-W., Yuan, S., et al. (2020). Genomic Characterization of the 2019 Novel Human-Pathogenic Coronavirus Isolated from a Patient with Atypical Pneumonia after Visiting Wuhan. *Emerging Microbes Infections* 9, 221–236. doi:10.1080/22221751.2020.1719902
- Chen, A. Y., Adamek, R. N., Dick, B. L., Credille, C. V., Morrison, C. N., and Cohen, S. M. (2019). Targeting Metalloenzymes for Therapeutic Intervention. *Chem. Rev.* 119, 1323–1455. doi:10.1021/acs.chemrev.8b00201
- Citarella, A., Scala, A., Piperno, A., and Micale, N. (2021). SARS-CoV-2 Mpro: A Potential Target for Peptidomimetics and Small-Molecule Inhibitors. *Biomolecules* 11, 607. doi:10.3390/biom11040607
- Dai, W., Zhang, B., Jiang, X.-M., Su, H., Li, J., Zhao, Y., et al. (2020). Structure-based Design of Antiviral Drug Candidates Targeting the SARS-CoV-2 Main Protease. *Science* 368, 1331–1335. doi:10.1126/science.abb4489
- de Oliveira Carneiro Brum, J., França, T. C. C., LaPlante, S. R., and Villar, J. D. F. (2020). Synthesis and Biological Activity of Hydrazones and Derivatives: A Review. *Mini. Rev. Med. Chem.* 20, 342–368. doi:10.2174/138557519666191014142448
- de Wit, E., van Doremalen, N., Falzarano, D., and Munster, V. J. (2016). SARS and MERS: Recent Insights into Emerging Coronaviruses. *Nat. Rev. Microbiol.* 14, 523–534. doi:10.1038/nrmicro.2016.81
- Emsley, P., and Cowtan, K. (2004). Coot: Model-Building Tools for Molecular Graphics. *Acta Crystallogr. D Biol. Cryst.* 60, 2126–2132. doi:10.1107/S0907444904019158
- Freitas, B. T., Durie, I. A., Murray, J., Longo, J. E., Miller, H. C., Crich, D., et al. (2020). Characterization and Noncovalent Inhibition of the Deubiquitinase and deISGylase Activity of SARS-CoV-2 Papain-like Protease. *ACS Infect. Dis.* 6, 2099–2109. doi:10.1021/acinfecdis.0c00168
- Fu, Z., Huang, B., Tang, J., Liu, S., Liu, M., Ye, Y., et al. (2021). The Complex Structure of GRL0617 and SARS-CoV-2 PLpro Reveals a Hot Spot for Antiviral Drug Discovery. *Nat. Commun.* 12, 488. doi:10.1038/s41467-020-20718-8
- Günther, S., Reinke, P. Y. A., Fernández-García, Y., Lieske, J., Lane, T. J., Ginn, H. M., et al. (2021). X-ray Screening Identifies Active Site and Allosteric Inhibitors of SARS-CoV-2 Main Protease. *Science* 372, 642–646. doi:10.1126/science.abf7945
- Hilgenfeld, R. (2014). From SARS to MERS: Crystallographic Studies on Coronaviral Proteases Enable Antiviral Drug Design. *FEBS J.* 281, 4085–4096. doi:10.1111/febs.12936
- Honorato, R. V., Koukos, P. I., Jiménez-García, B., Tsaregorodtsev, A., Verlati, M., Giachetti, A., et al. (2021). Structural Biology in the Clouds: The WeNMR-EOSC Ecosystem. *Front. Mol. Biosci.* 8, 708. doi:10.3389/fmolb.2021.729513
- Hsu, D. C., Roth, H. S., West, D. C., Botham, R. C., Novotny, C. J., Schmid, S. C., et al. (2012). Parallel Synthesis and Biological Evaluation of 837 Analogues of Procaspase-Activating Compound 1 (PAC-1). *ACS Comb. Sci.* 14, 44–50. doi:10.1021/co2001372
- Huan, L. C., Anh, D. T., Hai, P.-T., Anh, L. D., Park, E. J., Ji, A. Y., et al. (2020). Design, Synthesis, and Evaluation of Novel N'-substituted-1-(4-chlorobenzyl)-1H-indol-3-carbohydrazides as Antitumor Agents. *J. Enzyme Inhib. Med. Chem.* 35, 1854–1865. doi:10.1080/14756366.2020.1816997
- Hunter, J. D. (2007). Matplotlib: A 2D Graphics Environment. *Comput. Sci. Eng.* 9, 90–95. doi:10.1109/MCSE.2007.55
- Klemm, T., Ebert, G., Calleja, D. J., Allison, C. C., Richardson, L. W., Bernardini, J. P., et al. (2020). Mechanism and Inhibition of the Papain-like Protease, PLpro, of SARS-CoV-2. *EMBO J.* 39, e106275. doi:10.15252/emboj.2020106275
- Kune, G. A. (1964). To-Day's Drugs: Methisazone. *Br. Med. J.* 2, 621.
- Kurkcuoglu, Z., Koukos, P. I., Citro, N., Trellet, M. E., Rodrigues, J. P. G. L. M., Moreira, I. S., et al. (2018). Performance of HADDOCK and a Simple Contact-Based Protein-Ligand Binding Affinity Predictor in the D3R Grand Challenge 2. *J. Comput. Aided Mol. Des.* 32, 175–185. doi:10.1007/s10822-017-0049-y
- Liebschner, D., Afonine, P. V., Baker, M. L., Bunkóczi, G., Chen, V. B., Croll, T. I., et al. (2019). Macromolecular Structure Determination Using X-Rays, Neutrons and Electrons: Recent Developments in Phenix. *Acta Cryst. Sect D Struct. Biol.* 75, 861–877. doi:10.1107/S2059798319011471
- Liu, G., Lee, J.-H., Parker, Z. M., Acharya, D., Chiang, J. J., van Gent, M., et al. (2021). ISG15-dependent Activation of the Sensor MDA5 Is Antagonized by the SARS-CoV-2 Papain-like Protease to Evade Host Innate Immunity. *Nat. Microbiol.* 6, 467–478. doi:10.1038/s41564-021-00884-1
- Lu, R., Zhao, X., Li, J., Niu, P., Yang, B., Wu, H., et al. (2020). Genomic Characterisation and Epidemiology of 2019 Novel Coronavirus: Implications for Virus Origins and Receptor Binding. *Lancet* 395, 565–574. doi:10.1016/S0140-6736(20)30251-8
- Ma, C., and Wang, J. (2022). Validation and Invalidation of SARS-CoV-2 Papain-like Protease Inhibitors. *ACS Pharmacol. Transl. Sci.* 5, 102–109. doi:10.1021/acspstci.1c00240
- McKinney, W. (2010). "Data Structures for Statistical Computing in Python," in Proceedings of the 9th Python in Science Conference, Austin, Texas, 28.06–03.07, 56–61. doi:10.25080/Majora-92bf1922-00a
- Mevissen, T. E. T., and Komander, D. (2017). Mechanisms of Deubiquitinase Specificity and Regulation. *Annu. Rev. Biochem.* 86, 159–192. doi:10.1146/annurev-biochem-061516-044916
- Moriarty, N. W., Grosse-Kunstleve, R. W., and Adams, P. D. (2009). Electronic Ligand Builder and Optimization Workbench (eLBOW): a Tool for Ligand Coordinate and Restraint Generation. *Acta Crystallogr. D Biol. Cryst.* 65, 1074–1080. doi:10.1107/S0907444909029436
- Morris, G. M., Goodsell, D. S., Halliday, R. S., Huey, R., Hart, W. E., Belew, R. K., et al. (1998). Automated Docking Using a Lamarckian Genetic Algorithm and an Empirical Binding Free Energy Function. *J. Comput. Chem.* 19, 1639–1662. doi:10.1002/(SICI)1096-987X(19981115)19:14<1639::AID-JCC10>3.0.CO;2-B

- Morris, G. M., Huey, R., Lindstrom, W., Sanner, M. F., Belew, R. K., Goodsell, D. S., et al. (2009). AutoDock4 and AutoDockTools4: Automated Docking with Selective Receptor Flexibility. *J. Comput. Chem.* 30, 2785–2791. doi:10.1002/jcc.21256
- Munnur, D., Teo, Q., Eggermont, D., Lee, H. H. Y., Thery, F., Ho, J., et al. (2021). Altered ISGylation Drives Aberrant Macrophage-dependent Immune Responses during SARS-CoV-2 Infection. *Nat. Immunol.* 22, 1416–1427. doi:10.1038/s41590-021-01035-8
- Niebling, S., Burastero, O., Bürgi, J., Günther, C., Defelipe, L. A., Sander, S., et al. (2021). FoldAffinity: Binding Affinities from nDSF Experiments. *Sci. Rep.* 11, 9572. doi:10.1038/s41598-021-88985-z
- Oliphant, T. (2006). *Guide to NumPy*. USA: Tregol Publishing.
- Osiupik, J., Wydorski, P. M., Lanham, B. T., Tesar, C., Endres, M., Engle, E., et al. (2021). Dual Domain Recognition Determines SARS-CoV-2 PLpro Selectivity for Human ISG15 and K48-Linked Di-ubiquitin. *bioRxiv*. [Preprint]. doi:10.1101/2021.09.15.460543
- Osmaniye, D., Kurban, B., Sağlık, B. N., Levent, S., Özkay, Y., and Kaplançıklı, Z. A. (2021). Novel Thiosemicarbazone Derivatives: *In Vitro* and *In Silico* Evaluation as Potential MAO-B Inhibitors. *Molecules* 26, 6640. doi:10.3390/molecules26216640
- Panchariya, L., Khan, W. A., Kuila, S., Sonkar, K., Sahoo, S., Ghoshal, A., et al. (2021). Zinc2+ Ion Inhibits SARS-CoV-2 Main Protease and Viral Replication. *In Vitro. Chem. Commun.* 57, 10083–10086. doi:10.1039/D1CC03563K
- Patchett, S., Lv, Z., Rut, W., Békés, M., Drag, M., Olsen, S. K., et al. (2021). A Molecular Sensor Determines the Ubiquitin Substrate Specificity of SARS-CoV-2 Papain-like Protease. *Cel Rep.* 36, 109754. doi:10.1016/j.celrep.2021.109754
- Pearce, N. M., Krojer, T., Bradley, A. R., Collins, P., Nowak, R. P., Talon, R., et al. (2017). A Multi-crystal Method for Extracting Obscured Crystallographic States from Conventionally Uninterpretable Electron Density. *Nat. Commun.* 8, 15123. doi:10.1038/ncomms15123
- Ratia, K., Saikatendu, K. S., Santarsiero, B. D., Barretto, N., Baker, S. C., Stevens, R. C., et al. (2006). Severe Acute Respiratory Syndrome Coronavirus Papain-like Protease: Structure of a Viral Deubiquitinating Enzyme. *Proc. Natl. Acad. Sci.* 103, 5717–5722. doi:10.1073/pnas.0510851103
- Rogolino, D., Bacchi, A., De Luca, L., Rispoli, G., Sechi, M., Stevaert, A., et al. (2015). Investigation of the Salicylaldehyde Thiosemicarbazone Scaffold for Inhibition of Influenza Virus PA Endonuclease. *J. Biol. Inorg. Chem.* 20, 1109–1121. doi:10.1007/s00775-015-1292-0
- Rut, W., Lv, Z., Zmudzinski, M., Patchett, S., Nayak, D., Snipas, S. J., et al. (2020). Activity Profiling and crystal Structures of Inhibitor-Bound SARS-CoV-2 Papain-like Protease: A Framework for Anti-COVID-19 Drug Design. *Sci. Adv.* 6, eabd4596. doi:10.1126/sciadv.abd4596
- Sargsyan, K., Lin, C.-C., Chen, T., Grauffel, C., Chen, Y.-P., Yang, W.-Z., et al. (2020). Multi-targeting of Functional Cysteines in Multiple Conserved SARS-CoV-2 Domains by Clinically Safe Zn-Ejectors. *Chem. Sci.* 11, 9904–9909. doi:10.1039/D0SC02646H
- Schechter, I., and Berger, A. (1967). On the Size of the Active Site in Proteases. I. Papain. *Biochem. Biophys. Res. Commun.* 27, 157–162. doi:10.1016/s0006-291x(67)80055-x
- Shen, Z., Ratia, K., Cooper, L., Kong, D., Lee, H., Kwon, Y., et al. (2021). Design of SARS-CoV-2 PLpro Inhibitors for COVID-19 Antiviral Therapy Leveraging Binding Cooperativity. *J. Med. Chem.* 65, 2940–2955. doi:10.1021/acs.jmedchem.1c01307
- Shin, D., Mukherjee, R., Grewe, D., Bojkova, D., Baek, K., Bhattacharya, A., et al. (2020). Papain-like Protease Regulates SARS-CoV-2 Viral Spread and Innate Immunity. *Nature* 587, 657–662. doi:10.1038/s41586-020-2601-5
- Srinivasan, V., Brognaro, H., Prabhu, P. R., Souza, E. E. D., Günther, S., Reinke, P. Y. A., et al. (2021). SARS-CoV-2 Papain-like Protease PLpro in Complex with Natural Compounds Reveal Allosteric Sites for Antiviral Drug Design. *bioRxiv*. [Preprint]. doi:10.1101/2021.11.17.468943
- Studier, F. W. (2005). Protein Production by Auto-Induction in High-Density Shaking Cultures. *Protein Expr. Purif.* 41, 207–234. doi:10.1016/j.pep.2005.01.016
- te Velthuis, A. J. W., van den Worm, S. H. E., Sims, A. C., Baric, R. S., Snijder, E. J., and van Hemert, M. J. (2010). Zn²⁺ Inhibits Coronavirus and Arterivirus RNA Polymerase Activity *In Vitro* and Zinc Ionophores Block the Replication of These Viruses in Cell Culture. *Plos Pathog.* 6, e1001176. doi:10.1371/journal.ppat.1001176
- Tregoning, J. S., Flight, K. E., Higham, S. L., Wang, Z., and Pierce, B. F. (2021). Progress of the COVID-19 Vaccine Effort: Viruses, Vaccines and Variants versus Efficacy, Effectiveness and Escape. *Nat. Rev. Immunol.* 21, 626–636. doi:10.1038/s41577-021-00592-1
- V'kovski, P., Kratzel, A., Steiner, S., Stalder, H., and Thiel, V. (2020). Coronavirus Biology and Replication: Implications for SARS-CoV-2. *Nat. Rev. Microbiol.* 19, 155–170. doi:10.1038/s41579-020-00468-6
- Vabret, N., Britton, G. J., Gruber, C., Hegde, S., Kim, J., Kuksin, M., et al. (2020). Immunology of COVID-19: Current State of the Science. *Immunity* 52, 910–941. doi:10.1016/j.immuni.2020.05.002
- van der Walt, S., Colbert, S. C., and Varoquaux, G. (2011). The NumPy Array: A Structure for Efficient Numerical Computation. *Comput. Sci. Eng.* 13, 22–30. doi:10.1109/MCSE.2011.37
- van Zundert, G. C. P., Rodrigues, J. P. G. L. M., Trellet, M., Schmitz, C., Kastiris, P. L., Karaca, E., et al. (2016). The HADDOCK2.2 Web Server: User-Friendly Integrative Modeling of Biomolecular Complexes. *J. Mol. Biol.* 428, 720–725. doi:10.1016/j.jmb.2015.09.014
- Vangone, A., Schaarschmidt, J., Koukos, P., Geng, C., Citro, N., Trellet, M. E., et al. (2019). Large-scale Prediction of Binding Affinity in Protein-Small Ligand Complexes: the PRODIGY-LIG Web Server. *Bioinformatics* 35, 1585–1587. doi:10.1093/bioinformatics/bty816
- Virtanen, P., Gommers, R., Oliphant, T. E., Haberland, M., Reddy, T., Cournapeau, D., et al. (2020). SciPy 1.0: Fundamental Algorithms for Scientific Computing in Python. *Nat. Methods* 17, 261–272. doi:10.1038/s41592-019-0686-2
- Wahbeh, J., and Milkowski, S. (2019). The Use of Hydrazones for Biomedical Applications. *SLAS Techn.* 24, 161–168. doi:10.1177/2472630318822713
- WHO (2021). WHO Coronavirus (COVID-19) Dashboard. Available at: <https://covid19.who.int> (Accessed November 27, 2021).
- Winter, G., Waterman, D. G., Parkhurst, J. M., Brewster, A. S., Gildea, R. J., Gerstel, M., et al. (2018). DIALS: Implementation and Evaluation of a New Integration Package. *Acta Cryst. Sect D Struct. Biol.* 74, 85–97. doi:10.1107/S2059798317017235
- Zhang, L., Lin, D., Sun, X., Curth, U., Drosten, C., Sauerhering, L., et al. (2020). Crystal Structure of SARS-CoV-2 Main Protease Provides a Basis for Design of Improved α -ketoamide Inhibitors. *Science* 368, 409–412. doi:10.1126/science.abb3405
- Zhou, P., Yang, X.-L., Wang, X.-G., Hu, B., Zhang, L., Zhang, W., et al. (2020). A Pneumonia Outbreak Associated with a New Coronavirus of Probable Bat Origin. *Nature* 579, 270–273. doi:10.1038/s41586-020-2012-7
- Zmudzinski, M., Rut, W., Olech, K., Granda, J., Giurg, M., Burda-Grabowska, M., et al. (2020). Ebselen Derivatives Are Very Potent Dual Inhibitors of SARS-CoV-2 Proteases - PLpro and Mpro in *In Vitro* Studies. *bioRxiv*. [Preprint]. doi:10.1101/2020.08.30.273979

Conflict of Interest: The authors declare that the research was conducted in the absence of any commercial or financial relationships that could be construed as a potential conflict of interest.

Publisher's Note: All claims expressed in this article are solely those of the authors and do not necessarily represent those of their affiliated organizations, or those of the publisher, the editors and the reviewers. Any product that may be evaluated in this article, or claim that may be made by its manufacturer, is not guaranteed or endorsed by the publisher.

Copyright © 2022 Ewert, Günther, Miglioli, Falke, Reinke, Niebling, Günther, Han, Srinivasan, Brognaro, Lieske, Lorenzen, Garcia-Alai, Betzel, Carcelli, Hinrichs, Rogolino and Meents. This is an open-access article distributed under the terms of the Creative Commons Attribution License (CC BY). The use, distribution or reproduction in other forums is permitted, provided the original author(s) and the copyright owner(s) are credited and that the original publication in this journal is cited, in accordance with accepted academic practice. No use, distribution or reproduction is permitted which does not comply with these terms.



OPEN ACCESS

Edited by:

Wenshe Ray Liu,
Texas A&M University, United States

Reviewed by:

Jun Wang,
Rutgers, The State University of New
Jersey, United States
Shiqing Xu,
Texas A&M University, United States

*Correspondence:

Guillaume Lessene
glessene@wehi.edu.au
David Komander
dk@wehi.edu.au

[†]These authors have contributed
equally to this work

Specialty section:

This article was submitted to
Medicinal and Pharmaceutical
Chemistry,
a section of the journal
Frontiers in Chemistry

Received: 24 January 2022

Accepted: 15 March 2022

Published: 12 April 2022

Citation:

Calleja DJ, Kuchel N, Lu BGC,
Birkinshaw RW, Klemm T,
Doerflinger M, Cooney JP,
Mackiewicz L, Au AE, Yap YQ,
Blackmore TR, Katneni K, Crighton E,
Newman J, Jarman KE, Call MJ,
Lechtenberg BC, Czabotar PE,
Pellegrini M, Charman SA, Lowes KN,
Mitchell JP, Nachbur U, Lessene G
and Komander D (2022) Insights Into
Drug Repurposing, as Well as
Specificity and Compound Properties
of Piperidine-Based SARS-CoV-2
PLpro Inhibitors.
Front. Chem. 10:861209.
doi: 10.3389/fchem.2022.861209

Insights Into Drug Repurposing, as Well as Specificity and Compound Properties of Piperidine-Based SARS-CoV-2 PLpro Inhibitors

Dale J. Calleja^{1†}, Nathan Kuchel^{1†}, Bernadine G. C. Lu¹, Richard W. Birkinshaw¹, Theresa Klemm¹, Marcel Doerflinger¹, James P. Cooney¹, Liana Mackiewicz¹, Amanda E. Au¹, Yu Q. Yap¹, Timothy R Blackmore¹, Kasiram Katneni², Elly Crighton², Janet Newman³, Kate E. Jarman¹, Melissa J. Call¹, Bernhard C. Lechtenberg¹, Peter E. Czabotar¹, Marc Pellegrini¹, Susan A. Charman², Kym N. Lowes¹, Jeffrey P. Mitchell¹, Ueli Nachbur¹, Guillaume Lessene^{1,4*} and David Komander^{1*}

¹Department of Medical Biology, Walter and Eliza Hall Institute, University of Melbourne, Melbourne, VIC, Australia, ²Centre for Drug Candidate Optimisation, Monash Institute of Pharmaceutical Sciences, Monash University, Parkville, VIC, Australia,

³Commonwealth Scientific and Industrial Research Organisation (CSIRO), Biomedical Program, Parkville, VIC, Australia,

⁴Department of Pharmacology and Therapeutics, The University of Melbourne, Melbourne, VIC, Australia

The COVID-19 pandemic continues unabated, emphasizing the need for additional antiviral treatment options to prevent hospitalization and death of patients infected with SARS-CoV-2. The papain-like protease (PLpro) domain is part of the SARS-CoV-2 non-structural protein (nsp)-3, and represents an essential protease and validated drug target for preventing viral replication. PLpro moonlights as a deubiquitinating (DUB) and deISGylating enzyme, enabling adaptation of a DUB high throughput (HTS) screen to identify PLpro inhibitors. Drug repurposing has been a major focus through the COVID-19 pandemic as it may provide a fast and efficient route for identifying clinic-ready, safe-in-human antivirals. We here report our effort to identify PLpro inhibitors by screening the ReFRAME library of 11,804 compounds, showing that none inhibit PLpro with any reasonable activity or specificity to justify further progression towards the clinic. We also report our latest efforts to improve piperidine-scaffold inhibitors, 5c and 3k, originally developed for SARS-CoV PLpro. We report molecular details of binding and selectivity, as well as *in vitro* absorption, distribution, metabolism and excretion (ADME) studies of this scaffold. A co-crystal structure of SARS-CoV-2 PLpro bound to inhibitor 3k guides medicinal chemistry efforts to improve binding and ADME characteristics. We arrive at compounds with improved and favorable solubility and stability characteristics that are tested for inhibiting viral replication. Whilst still requiring significant improvement, our optimized small molecule inhibitors of PLpro display decent antiviral activity in an *in vitro* SARS-CoV-2 infection model, justifying further optimization.

Keywords: Nsp3, PLpro, inhibitor, SARS-CoV-2, repurposing, structure, ADME, COVID-19

INTRODUCTION

The COVID-19 pandemic continues unabated in many countries, and while large-scale vaccination efforts are underway, the management of population health, economic impact and as-of-yet unknown long-term effects on physical and mental health will be a key challenge for the next decade. To truly overcome the threat posed by the causative coronavirus (CoV), SARS-CoV-2, and its emerging variants of concern, it is paramount to generate and clinically validate additional, orthogonally acting antiviral drugs (Dolgin, 2021). We envisage that small molecule drugs that target the viral proteins themselves, acting in concert with vaccination, will stop viral replication in cells and hence impact on virus fitness and transmission (Dolgin, 2021). Such drugs will act to treat established disease but, perhaps more importantly, also work as a prophylaxis to prevent disease in high-risk populations. The targets required for such small molecule drugs are well established: the CoV genome comprises non-structural proteins (nsps) that each fulfills (an) essential function(s), and therefore offer a host of putative targets (Hartenian et al., 2020). Several stand out based upon essentiality, druggability and proof-of-concept work performed (Gao et al., 2020; Hillen et al., 2020; Hoffmann et al., 2020; Klemm et al., 2020; Shin et al., 2020; Zhang et al., 2020; Zhou et al., 2020). These include the viral replicase, comprised of several nsps that recombine after production to assemble the viral machinery responsible for carbon-copying viral genetic material (Subissi et al., 2014; Malone et al., 2022), as well as two essential proteases, nsp3/PLpro and nsp5/Mpro responsible for releasing individual nsps from the viral polyprotein (Hartenian et al., 2020). Whereas nsp3/PLpro is responsible for releasing the first four nsps, Mpro generates nsp5 to nsp16 (Fan et al., 2004; Harcourt et al., 2004).

PLpro refers to the protease domain within the 1945 amino acid (aa) multi-domain protein nsp3. As a conserved papain-like Cys protease from the C16 family (Rawlings et al., 2012), PLpro hydrolyses amino acid sequences with a specific Leu-Xaa-Gly-Gly motif, found at the junctions between nsp1/2, nsp2/3 and nsp3/4 (where Xaa is Asn, Lys or Lys, respectively) (Rut et al., 2020). Importantly, the same motif is present within a subset of human proteins that are also targeted by PLpro/nsp3; most notable are the C-terminus of human ubiquitin and the ubiquitin-like modifier, Interferon Stimulated Gene 15 (ISG15) that comprise a Leu-Arg-Gly-Gly motif. Indeed, ubiquitin and ISG15 are intricately involved in the human anti-viral response (Heaton et al., 2016; Perng and Lenschow, 2018), enabling the virus to directly interfere with host signalling processes. Moreover, the fact that PLpro also acts as a deubiquitinase (DUB) and deISGylase, enables the exploitation of many tools and assays to measure PLpro activity (Hassiepen et al., 2007; Hospenthal et al., 2015; Gui et al., 2020).

The PLpro enzyme of previous CoVs, in particular SARS-CoV and MERS-CoV have been studied in great detail by the teams of Andrew Mesecar, Scott Pegan, Chris Lima and others (Harcourt et al., 2004; Barretto et al., 2005; Lindner et al., 2005; Ratia et al.,

2006; Ratia et al., 2008; Ghosh et al., 2009; Ghosh et al., 2010; Báez-Santos et al., 2014; Lee et al., 2015; Békés et al., 2016). We and others identified many of the previously described features also in SARS-CoV-2 PLpro, including its essentiality in viral replication (Freitas et al., 2020; Klemm et al., 2020; Rut et al., 2020; Shin et al., 2020). Indeed, SARS-CoV and SARS-CoV-2 PLpro share 82% sequence identity (Freitas et al., 2020; Klemm et al., 2020; Rut et al., 2020; Shin et al., 2020).

Inhibitor development campaigns against SARS-CoV PLpro have resulted in two main chemical scaffolds (Ratia et al., 2008; Ghosh et al., 2009; Ghosh et al., 2010; Báez-Santos et al., 2014) the benzamide ring (“**GRL-0617**” family of compounds) and the piperidine carboxamide (“**5c**” family of compounds) series. Both have undergone considerable medicinal chemistry efforts to arrive at compounds with sub-micromolar *in vitro* inhibitory activity (Ghosh et al., 2009; Ghosh et al., 2010; Báez-Santos et al., 2014). As the SARS-CoV and MERS-CoV epidemics subsided, unfortunately so did the development of inhibitors identified in early drug discovery campaigns.

The SARS-CoV-2 pandemic reignited PLpro drug discovery in two areas. Many efforts focused on drug repurposing, aiming to identify a PLpro inhibitor within the already approved drugs and drug candidates available. The benefits of this approach are often mistakenly considered as to provide an immediate starting point for clinical studies, and it is important to recognise that it does not alleviate the need for pre-clinical development (Pushpakom et al., 2019; Begley et al., 2021). The urgency of the COVID-19 pandemic nonetheless justified this avenue of exploration on the exceedingly small chance that potent drugs optimized for one target may be equally potent against new targets. We critically discuss the reported results from putative PLpro inhibitors identified from repurposing approaches in our associated Review (Calleja et al., this issue).

Secondly, we and others showed that **GRL-0617** and **5c** compounds could efficiently block SARS-CoV-2 PLpro both *in vitro* and in cells and stop viral replication in cell culture (Klemm et al., 2020; Shin et al., 2020). Efficacy of these early lead compounds was promising but required improvements. Several papers have by now described iterations of the **GRL-0617** series compounds (Ma et al., 2021; Osipiuk et al., 2021; Shen et al., 2021), for details, see our associated Review on these drug discovery efforts (Calleja et al., this issue).

Here, we present our efforts to identify PLpro inhibitors within the ReFRAME compound library (Janes et al., 2018), showing that none are suitable for further development. Secondly, we update on our efforts to characterize the **5c** scaffold of PLpro inhibitors we first described in Klemm et al. (2020). A co-crystal structure of PLpro bound to the related compound, **3k**, and additional analyses explain compound specificity, however, compound stability profiling on **5c** identified numerous metabolic liabilities. A medicinal chemistry campaign with the aim to improve compound properties (efficacy and stability) resulted in compounds with the same potency as **5c**, but with improved ADME properties. These preliminary studies indicate that significant improvements are still required to arrive at a lead candidate.

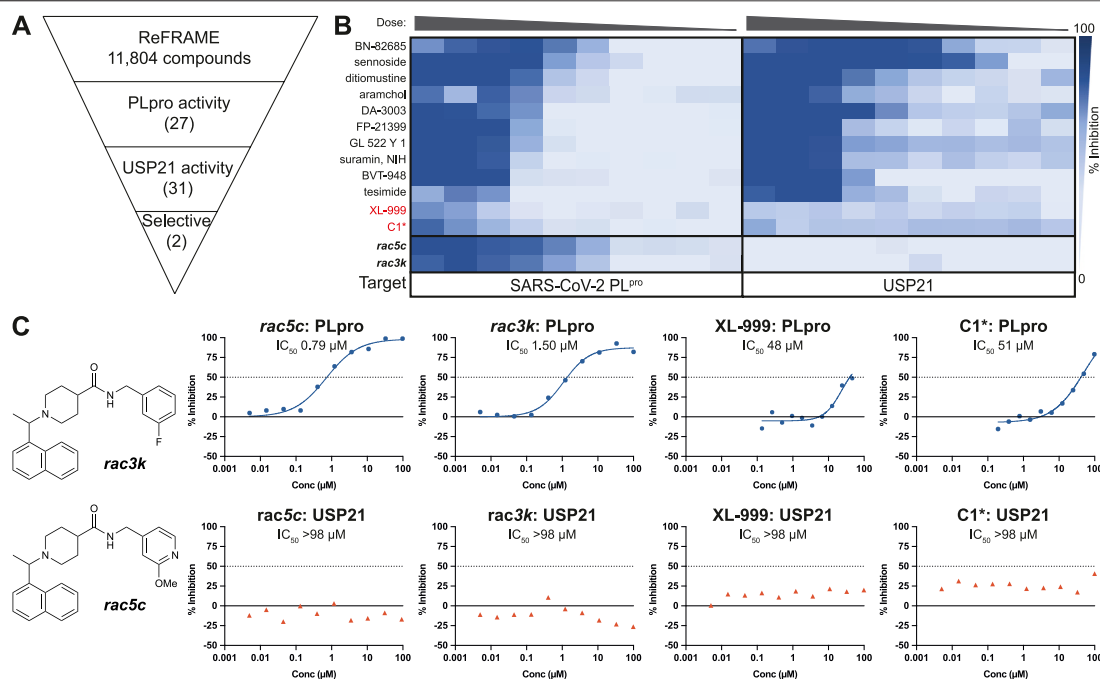


FIGURE 1 | High Throughput Screen (HTS) of the ReFRAME library for inhibitors of SARS-CoV-2 PLpro. **(A)** Schematic showing the screening cascade for the identification of selective PLpro inhibitors. 11,804 compounds were screened at 8.33, 4.17 or 0.83 μM through a primary screen against PLpro. Hits showing a median absolute deviation >2.5 (over the DMSO negative control) were selected for a 10-point titration assays against PLpro and a counter screen against USP21 (5 nM). Of the 53 total hits from the screen, 27 compounds retested showing activity against PLpro in the 10-point titration, and 31 showed activity against USP21. Two compounds, XL-999 and C1*, were found to be selective for PLpro over USP21. **(B)** 10-point titration for the top 12 compounds showing activity against SARS-CoV-2 PLpro. Compounds were assayed at a top concentration of 100 μM and titrated using 1:2 (PLpro) or 1:3 (USP21) serial dilutions. 100 μM *rac5c* was used as a positive control for the HTS. 10-point titration curves of *rac5c* and *rac3k* were performed in a separate control assay and are shown for comparison. **(C)** Two selective hits from the screening of the ReFRAME library were XL-999 and C1*, with an IC_{50} of 48 and 51 μM , respectively. Both were found to be weak inhibitors of PLpro and were not further investigated. 10-point titration curves of *rac5c* and *rac3k* were performed in a separate control assay and are shown for comparison. IC_{50} values were derived from one set of independent experiments ($n = 1$).

RESULTS

Testing ReFRAME Compounds Against PLpro

Most published activity-based PLpro assays measure cleavage of a FRET-labelled peptide substrate based on a native cleavage sequence such as the C-terminus of ubiquitin or ISG15 (LRLRGG). An alternative assay for PLpro assesses hydrolysis of ubiquitin-Rhodamine110; Rhodamine110 is cleaved not off a peptide but off the 8.5 kDa ubiquitin moiety. PLpro binds to ubiquitin-Rhodamine110 more tightly when compared to peptides as it interacts with a significant portion of the 8,000 \AA^2 ubiquitin surface (see our associated Review for a discussion on assay design). In our previous work (Klemm et al., 2020), we adapted a ubiquitin-Rhodamine110-based high throughput screening (HTS) assay to identify small molecule PLpro inhibitors as previously developed for human DUBs (Turnbull et al., 2017). A first drug repurposing campaign was performed, in the hope to uncover human-safe medications that could be progressed towards the clinic. We ideally required nanomolar inhibitory activity, a “clean” specificity profile against human DUBs (Turnbull et al., 2017) and sensible chemistry

lacking reactive groups or PAINS (Baell and Holloway, 2010). However, screening 5,576 molecules including 3,727 unique FDA approved small molecule drugs, we failed to identify suitable compounds that would enable progression to the clinic (Klemm et al., 2020).

We now extended these studies to include the ReFRAME library (Janes et al., 2018), which is a collection of 11,804 compounds, mostly approved drugs and drug candidates that had progressed to late-stage clinical trials, and hence had in-human safety data associated (Janes et al., 2018). As before, our PLpro HTS yielded excellent and highly robust, reproducible data (Figure 1, Supplementary Figure S1). 53 compounds passed the primary screen, and 27 showed inhibitory potential in 10-point titration studies (Figures 1A,B, Supplementary Figure S1D). The latter were also tested against USP21 as a selectivity counter screen. All but two compounds showed identical inhibition towards USP21, indicating off-target issues, compound reactivity, and/or assay interference (Figure 1B, Supplementary Figure S1D). The two remaining compounds were XL-999, a receptor tyrosine kinase and FLT3 kinase inhibitor (DrugBank (Wishart et al., 2008) ID: DB05014), and a derivative of codeine, an opioid receptor agonist (Figure 1C).

Both compounds displayed only weak *in vitro* inhibitory activity against PLpro (IC₅₀ 48 and 51 μ M, respectively) (**Figure 1C**) and had been optimized for their human targets. Weak activity against PLpro (necessitating extreme dosing regimes) rendered both compounds unsuitable for progression towards the clinic. Compounds were also considered unsuitable as starting points for medicinal chemistry due to inferior potency and ligand efficiency when compared to other scaffolds (see below).

While we performed these studies, a second group also reported screening of SARS-CoV-2 PLpro against the ReFRAME library (Redhead et al., 2021). The best compound in their assays, Tarloxotinib, demonstrated inhibitory activity against PLpro, and strikingly, in a separate set of experiments also inhibited Mpro. In our PLpro assay, Tarloxotinib did not show any inhibitory activity (**Supplementary Figure S1**). Both proteases hold very different active sites such that appropriate orthogonal assays must be performed when identifying potential Mpro/PLpro dual-inhibitors. In the mentioned study, Tarloxotinib identification as a hit was not followed up with any counter screens against other human DUBs, nor direct binding assays against PLpro.

Together, based on our own results and published studies (Klemm et al., 2020; Redhead et al., 2021), we conclude that drug repurposing against PLpro is not feasible. Moreover, the premise to arrive at immediate treatments appears somewhat flawed since any compound repurposing would still require extensive pre-clinical development for a new indication. Our assessment (further elaborated in our associated Review in this Issue of *Frontiers in Chemistry*) is in line with work in other therapeutic areas, as highlighted recently (Begley et al., 2021).

Further Characterization of Piperidine Scaffold PLpro Inhibitors, **3k** and **5c**

Drug repurposing by us and others failed to uncover compounds that could progress to the clinic, and while some of the structurally characterized hits reported by others may serve as potential starting points, we chose to focus on and further characterize the more amenable sub- μ M piperidine based inhibitors previously reported for SARS-CoV and SARS-CoV-2 PLpro, namely the **5c** family of compounds. In our earlier work (Klemm et al., 2020), we described the effects of compounds **rac5c** and **rac3k** (**Figure 1C**, **Supplementary Figure S2**), which inhibited PLpro with an IC₅₀ of 600–800 nM, and which decreased SARS-CoV-2 viral titers (TCID₅₀) by 2–3 orders of magnitude when tested at 11 μ M concentration in a cellular infection model, which is comparable to Remdesivir at 12.5 μ M (Klemm et al., 2020).

Reported compounds **5c** and **3k** contain a stereocenter between the naphthalene and piperidine rings. In our earlier study, we used racemic mixtures, **rac5c** and **rac3k**. Previous work on SARS-CoV PLpro described the (R)-enantiomer as having improved activity when compared to the (S)-enantiomer (Báez-Santos et al., 2014). We synthesized and tested the (R)-enantiomers of both **5c** and **3k** *in vitro* and the results showed no loss in inhibitory activity over their racemic counterparts (**Supplementary Figure S2A**). For the remainder of the study, we used the (R)-enantiomers of the compound series and refer to

TABLE 1 | Data collection and refinement statistics. Values in parentheses are for highest-resolution shell.

	SARS-CoV-2 PLpro bound to inhibitor 3k
Data collection	
Space group	<i>P</i> 2 ₁ 2 ₁ 2
Cell dimensions	
<i>a</i> , <i>b</i> , <i>c</i> (Å)	72.951, 90.632, 99.766
α , β , γ (°)	90.00, 90.00, 90.00
Resolution (Å)	38.49 – 2.66 (2.76 – 2.66)
<i>R</i> _{merge} (within I+/I-)	0.062 (0.608)
< <i>I</i> / <i>σ</i> >	7.0 (0.9)
Completeness (%)	99.8 (98.9)
Redundancy	2.0 (2.0)
Refinement	
Resolution (Å)	38.49 – 2.66
No. reflections	19521
<i>R</i> _{work} / <i>R</i> _{free}	0.200/0.257
No. atoms	
Protein	4792
Ligand/ion	141
Water	31
<i>B</i> -factors	
Protein	57.4
Ligand/ion	69.8
Water	46.0
R.m.s deviations	
Bond lengths (Å)	0.005
Bond angles (°)	0.81

them as **3k** and **5c**. As most studies for SARS-CoV-2 PLpro focused on optimizing the inhibitor **GRL-0617** (discussed in our associated Review) we compared PLpro inhibition by **GRL-0617** to the **5c** family of compounds. We observed similar IC₅₀ values (**Supplementary Figure S2B**) to those reported in other studies (Fu et al., 2021; Ma et al., 2021; Osipiuk et al., 2021; Shen et al., 2021) and confirmed observations from the original SARS-CoV work that **5c** remains a more potent inhibitor of SARS-CoV-2 PLpro when compared to **GRL-0617** (**Supplementary Figure S2**).

The structure of **3k** bound to SARS-CoV PLpro is published (PDB 4OW0) (Báez-Santos et al., 2014). We co-crystallized **3k** with a mutant form of SARS-CoV-2 PLpro in which the catalytic Cys111 was changed to Ser (PLpro^{C111S}), which we and others found to yield a more stable enzyme (Osipiuk et al., 2021). The best crystal diffracted to 2.66 Å, and structure determination by molecular replacement revealed the structure of the PLpro bound to **3k** (**Table 1**; **Figures 2, 3**, **Supplementary Figure S3**). The new crystal form (space group *P*2₁2₁2, see a list of all SARS-CoV-2 crystal forms in our associated Review) has two molecules in the asymmetric unit; both molecules are superimposable with an RMSD of 0.51 Å, and show excellent electron density for the ligand in identical ligand binding sites (**Figure 2C**, **Supplementary Figures S3B,C**).

The new crystal structure contributes to the understanding of how **3k** and **5c** inhibit SARS-CoV-2 PLpro and confirm many of the aspects previously illuminated in the SARS-CoV PLpro complex structures of the same series (Báez-Santos et al., 2014). Firstly, compound binding does not invoke gross

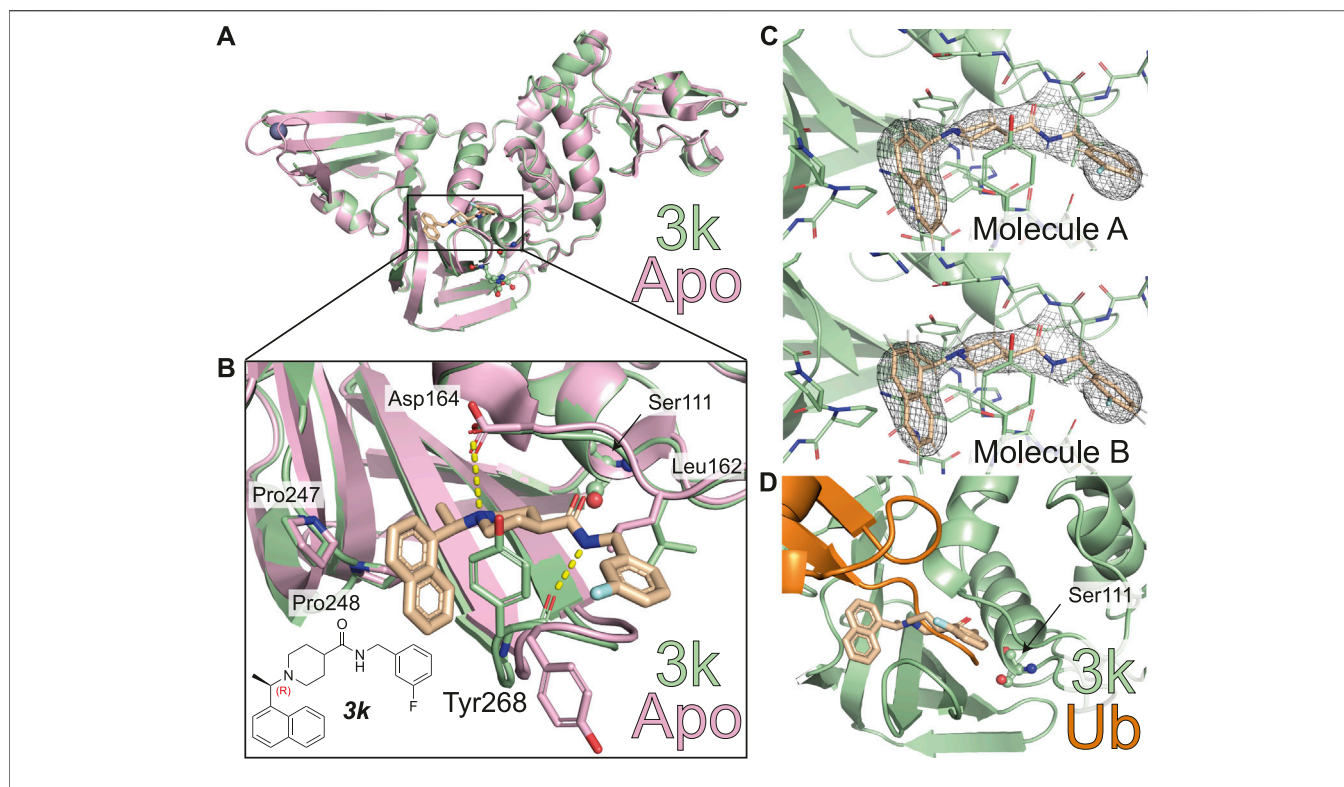


FIGURE 2 | Molecular basis for inhibition of SARS-CoV-2 PLpro by **3k**. **(A)** Structure of SARS-CoV-2 PLpro bound to **3k** in green, with inhibitor in wheat colour in ball-and stick representation representing the (R)-enantiomer. A superimposed structure of apo PLpro [pink, PDB 6WZU (Osipiuk et al., 2021)] shows that the inhibitor does not induce global conformational changes. Catalytic residues are shown in ball and stick representation, and a bound zinc ion in apo PLpro is shown as a grey sphere. **(B)** Close-up view of the ligand binding site for **3k** with key residues indicated. The chemical structure of **3k** is also shown, with the stereocenter labelled in red. Hydrogen bonds are indicated by yellow dotted lines. **(C)** $2|F_o| - |F_c|$ electron density map contoured at 1σ for **3k** of molecule A (top) and molecule B (bottom) in the asymmetric unit. Also see **Supplementary Figure S3**. **(D)** Close-up view of the ligand binding site for inhibitor **3k** overlaid with ubiquitin-bound PLpro in orange [PLpro ~ Ub, PDB 6XAA (Klemm et al., 2020)]. The catalytic Cys111 of PLpro was mutated to a Ser (C111S) in the compound complex. **3k** binding inhibits PLpro catalytic activity by blocking the C-terminus of Ub or ISG15 entering the catalytic cleft.

conformational perturbation of the PLpro fold when compared to apo or ubiquitin-bound PLpro (RMSD 0.44 Å compared to apo PLpro, PDB 6WRH (Osipiuk et al., 2021) and 0.48 Å compared to ubiquitin-bound PLpro PDB 6XAA (Klemm et al., 2020) (Figure 2A). The (R)-enantiomer of the compound was used for co-crystallisation and lies in the binding site (Figure 2B). **3k** occupies the channel required by the enzyme to hold to the C-terminal tail of ubiquitin and ISG15, which is on two sides lined by the static core of the PLpro Thumb domain and held in place by the more flexible blocking loop (aa 267–272), termed BL2, an extended β -hairpin that folds over the compound binding site (Figures 2B,D). Tyr268 at the turn of BL2 restrains the central piperidine ring, almost entirely burying it in the enzyme; the piperidine amino group further forms a hydrogen bond with the side chain of Asp164 of the Thumb domain. The naphthyl ring extends into a hydrophobic pocket towards the ubiquitin binding bowl in PLpro, packing against Pro247 and Pro248 (Figure 2B). On the other side of the molecule extending towards the catalytic Cys, a substituted phenyl group is connected to the *para*-position of the piperidine ring by an amide-linker that forms interactions with both the domain and BL2, including through a key hydrogen bond between the

compound amide and the backbone carbonyl of BL2 Tyr268. The substituted phenyl ring extends outwards from the domain core, due to side-chain rotation of Leu162, which blocks the path to the catalytic Cys111 (Figures 2B,D). As a result, **3k** and related compounds appear to wrap around BL2, remotely from the catalytic Cys111 (closest compound distance 9.7 Å), yet directly competing with ubiquitin/Ubl-tail binding to the protease channel. There are no sequence differences in residues lining the compound binding site between SARS-CoV and SARS-CoV-2 PLpro, and all interactions described here for SARS-CoV-2 PLpro with **3k** were seen in the previous structures of SARS-CoV PLpro with **3k** (Báez-Santos et al., 2014) (Figure 3A).

Molecular Basis for Compound Specificity Towards SARS-CoV and SARS-CoV-2 PLpro

To better understand cross-CoV PLpro specificity, and ideally identify or engineer a cross-specific inhibitor, we expanded our assay platform and routinely included SARS-CoV and MERS-CoV PLpro. The BL2 sequence is a poorly conserved region of CoV PLpro, and explains the inability of MERS-CoV PLpro to bind to and be inhibited by SARS-CoV PLpro inhibitors

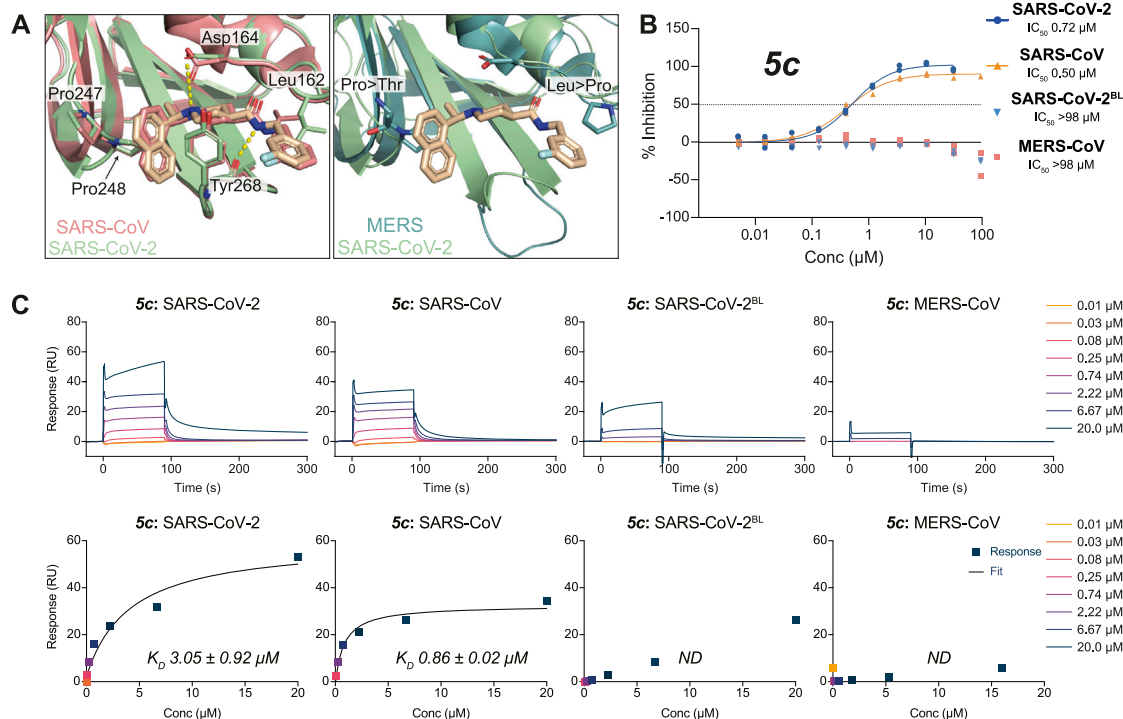


FIGURE 3 | Molecular basis for the inhibitor specificity towards PLpro variants. **(A)** Close-up view of the overlay between the ligand binding sites of **3k** in complex with SARS-CoV-2 PLpro (green) and SARS-CoV PLpro in salmon (PDB 4OW0 (Báez-Santos et al., 2014)) or MERS-CoV PLpro in teal (PDB 4RNA (Lee et al., 2015)). Cross reactivity by **3k** between species is a consequence from the conservation of key interacting residues as indicated. Crucial differences in interacting residues underpin compound specificity. **(B)** **5c** was tested for specificity to inhibit SARS-CoV PLpro, MERS-CoV PLpro, SARS-CoV-2 PLpro, or SARS-CoV-2 PLpro with residues 267–272 of blocking loop 2 (BL2) substituted for those in MERS-CoV (SARS-CoV-2^{BL}) in a UbRh assay. Inhibitor **5c** is cross-reactive with SARS-CoV PLpro and SARS-CoV-2 PLpro but not with MERS-CoV PLpro. These data indicate that engaging the conserved BL2 is crucial for the inhibition of PLpro by **5c**. Experiments were performed using the HTS assay as two independent experiments ($n = 2$) each containing two technical replicates. Individual data points represent the mean replicate value for each experiment. **(C)** SPR assays for compound **5c** against PLpro variants from **(B)**. The top panels show double referenced sensorgram data as a function of time and the bottom show steady-state dose response curves. Absence of inhibitor **5c** cross-reactivity with MERS-CoV PLpro can be explained by a loss in direct binding. Minor binding can be detected when assayed against SARS-CoV-2^{BL} PLpro compared with MERS-CoV PLpro and confirms most free energy loss during binding is resulting from interactions with the conserved BL2. SPR data for **3k** can be found in **Supplementary Figure S5**. All SPR experiments were performed in triplicate; a representative example is shown. See **Supplementary Table S1** for all data and **Supplementary Figure S9** for the response curves of the remaining experiments.

TABLE 2 | Inhibitory activity based on HTS screen (IC_{50}) and binding constants based on SPR (K_D) for **3k**, **5c** and **9**. SPR data for **3k** and **9** can be found in **Supplementary Figures S5, S8, Supplementary Table S1**.

	3k		5c		9	
	IC_{50} (μ M)	K_D (μ M)	IC_{50} (μ M)	K_D (μ M)	IC_{50} (μ M)	K_D (μ M)
SARS-CoV-2	1.02	2.40 ± 0.43	0.72	3.05 ± 0.92	0.76	1.86 ± 0.46
SARS-CoV	0.86	0.71 ± 0.07	0.50	0.86 ± 0.02	0.70	0.82 ± 0.02
MERS-CoV	>98	ND	>98	ND	>98	ND
SARS-CoV-2 ^{BL}	>98	ND	>98	ND	>98	ND

NT, not tested; ND, not detected.

including **5c** and **3k** (Lee et al., 2015) (**Figures 3A,B**). To investigate these observations in the context of SARS-CoV-2 PLpro we also engineered a SARS-CoV-2 variant in which the BL2 loop was changed to the equivalent sequence of MERS-CoV. In this variant termed SARS-CoV-2 PLpro^{BL}, the 4-amino acid (aa) BL2 loop of SARS-CoV-2 PLpro (G-NYQC-G) was replaced

with the 5-aa sequence of MERS-CoV PLpro (G-IETAV-G) that lacks Tyr268. SARS-CoV-2 PLpro^{BL} shows lower activity compared to wild-type PLpro in ISG15 and tri-ubiquitin-cleavage assays (**Supplementary Figure S4**), yet all enzymes performed similarly in the ubiquitin-Rhodamine110 assay used in our HTS platform (data not shown). As anticipated, **5c** and **3k**

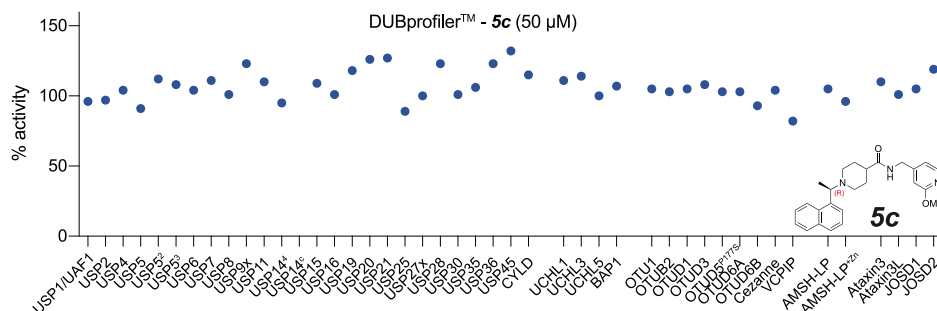


FIGURE 4 | Inhibitor **5c** does not cross react with human DUBs. **5c** was screened at 50 μM against a commercial DUB specificity panel (Ubiquigent) that included several human USP family enzymes that are structurally the most similar DUB enzymes to PLpro. **5c** does not notably inhibit any of the tested human DUBs at 50 μM concentration. USP5², USP5 assay performed with addition of ubiquitin at K_D; USP5³, USP5 assay performed with addition of ubiquitin at B_{max}. USP14⁴ indicates assay performed in the presence of proteasome-vinyl sulfone at K_D. USP14^c indicates the proteasome-vinyl sulfone control only without USP14. See Methods.

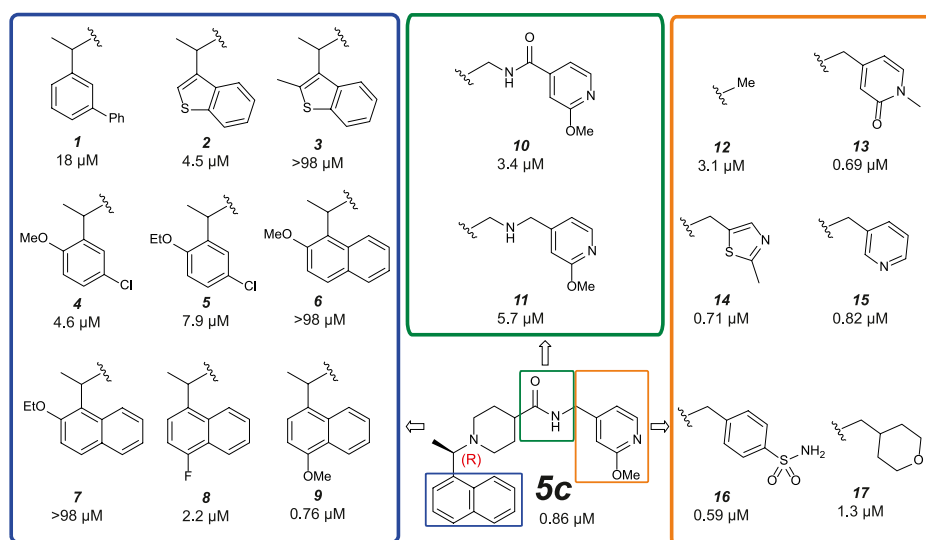


FIGURE 5 | Medicinal Chemistry elaborations to improve piperidine based PLpro inhibitors. Subset of tested piperidine based PLpro inhibitors molecules indicating how the **5c** scaffold was altered. The blue box shows alterations to the naphthyl ring, the green box shows modifications of the amide linkage and the orange box shows a subset of the most potent alterations to the benzylic group. These data exposed key insights for improving inhibitor **5c** (i) tight SAR is evident around the naphthyl position, with only minor modifications able to achieve <1 μM activity; (ii) the amide and its positioning is important to compound activity; (iii) modifications at the benzylic group gave the most potent compounds. This position appears the most malleable to achieve improved potency against SARS-CoV-2 PLpro. The calculated IC₅₀ (μM) is noted below each compound and is the average of two or four (**9** only) independent experiments ($n = 2$) each containing two technical replicates. Dose response curves can be found in **Supplementary Figures S6, S8**.

inhibited SARS-CoV and SARS-CoV-2 PLpro similarly but failed to act on MERS-CoV PLpro or the SARS-CoV-2 PLpro^{BL} variant (**Figure 3C**, **Supplementary Figure S5A**, **Table 2**).

To confirm direct binding and learn about binding characteristics of our inhibitory compounds to PLpro, we established a surface plasmon resonance (SPR) platform using PLpro of SARS-CoV, SARS-CoV-2 and MERS-CoV, as well as the SARS-CoV-2 PLpro^{BL} mutant in parallel. For **5c** and **3k**, results confirmed those obtained in the biochemical screening assays, also confirming that **5c** and **3k** lost binding to SARS-CoV-2 PLpro^{BL} (**Figure 3C**, **Supplementary Figure S5B**, **Table 2**).

Finally, we assessed the activity of the compounds against a panel of human DUBs, since specificity for PLpro over related human DUBs is essential to avoid toxicity issues. While PLpro is dissimilar at the sequence and structural level to any human DUB family, all known DUBs bind ubiquitin *via* the extended C-terminus. The selectivity of **3k** had been studied to a limited extent against a small panel of representative DUBs (Báez-Santos et al., 2014). We extended these studies by testing **5c** with a commercial DUB panel comprising 41 enzymes from all DUB families, assessed with a ubiquitin-Rhodamine110 assay (**Figure 4**). The results showed that **5c**, at 50 μM , did not

inhibit any of the human DUBs tested (**Figure 4**). The clean specificity profile of **5c** alleviates some concerns regarding off-target toxicity in human cells and tissues.

Elaboration and Improvement of Piperidine-Based PLpro Inhibitors

To improve compound properties, a medicinal chemistry campaign was initiated, focusing on key aspects of the compound. We learned from previous published works that attempted to improve the piperidine scaffold for SARS-CoV PLpro (Báez-Santos et al., 2014; Báez-Santos et al., 2015; Ghosh et al., 2020), enabling us to explore novel chemical space. We also knew that **3k** and **5c** were metabolically labile (discussed below) and our designs also aimed to improve the ADME properties of compounds.

In our attempts to improve both potency against SARS-CoV-2 PLpro and metabolic stability, we generated more than 250 derivatives of the **5c** series of compounds (a selection of which is shown in **Figure 5**). All generated compounds were tested in our HTS platform against SARS-CoV-2 PLpro and counter screened against USP21 (**Supplementary Figure S6**). Selected compounds were also screened against other PLpro enzymes and underwent SPR characterization.

Naphthyl rings are often considered an undesirable functional group as they hold numerous metabolic liabilities including increased lipophilicity, and are considered possible toxicophores. Thus, we hypothesized the naphthyl ring was a significant contributor to the overall metabolic liability of these compounds and hence the primary target for optimization. Given that the π -stack arrangement with Pro247, Pro248 and Tyr268 of the blocking loop is known to be a significant contributor in **5c** binding to the SARS-CoV PLpro (Ratia et al., 2008; Báez-Santos et al., 2014) we sought to replicate this interaction with isosteric replacements. Based on the observation that **5c** and *rac5c* are equipotent in the primary assay (**Supplementary Figure S2A**) (Klemm et al., 2020) and for ease of synthesis, modifications to the naphthyl were initially prepared and tested as racemates (blue in **Figure 5**). Previously reported isosteric quinoline modifications (Báez-Santos et al., 2014) which maintained modest activity towards SARS-CoV PLpro were not comparable to the potency afforded by the naphthyl ring and were thus avoided. Replacement with a biphenyl (**1**, for compound numbering, refer to **Figure 5**), decreased potency 20-fold. Likewise, isosteric replacement with a benzothiophene moiety in **2** negatively impacted the potency whilst the substituted benzothiophene **3** was completely inactive. Surprisingly, simpler di-substituted phenyl rings (compounds **4** and **5**) maintained modest activity. However, the similar methoxy and ethoxy ortho substitutions on the naphthyl ring were not tolerated (e.g., **6** and **7**). The fluorine substitution in **8** resulted in 3-fold activity loss while the methoxy derivative **9** showed comparative activity to the parent **5c**; together, this data suggests that the interaction pocket for the naphthyl doesn't tolerate electron deficient substituents but may tolerate electron-donating ones.

Next, we turned our attention to the amide bond (green box in **Figure 5**). Structural information suggests the amide carbonyl

forms no key interaction with the protein. However, reversal of the amide bond **10** proved 4-fold less potent than the parent **5c**. The amino analogue **11** led to an 7-fold drop in potency. Finally, we looked at optimizing the terminal benzyl group (orange box in **Figure 5**). Deletion analogue **12** resulted in only a 4-fold loss of potency suggesting that the existing substituents at this position contribute only moderately to the overall binding affinity of the small molecule. A variety of novel substituents were introduced at this position (data not shown), most of which were reasonably well tolerated. However, only groups that improved on the simple compound **12** were considered as advanceable. A subset of the more potent analogues exploring this position are shown in **Figure 5**. Heterocycles appear to be the most advantageous substitution at this position with several examples such as **13–15** reaching parity with the parent **5c** on potency. Of note, benzenesulfonamide and tetrahydropyran derivatives **16** and **17**, were also amongst the most potent analogues. These results indicate that this position can be further optimised to enhance the ligand efficiency of this series. Parallel work (Shan et al., 2021) reported a significant improvement in activity through modification of the benzylic group (**18** in **Supplementary Figure S7**). We attempted to replicate these results (**Supplementary Figure S7A**) (Shan et al., 2021) and in our hands, this compound is on par with **5c**, and does not show vastly improved potency (**Supplementary Figures S7A,B**).

Compound **9** (**Figure 5**) retained high activity (760 nM, comparable to **5c**) and thus was selected for further orthogonal SPR assays against our panel of DUBs (see above, **Table 2**, **Supplementary Figure S8**). The key difference in **9** is a substitution on the naphthyl ring, a methoxy group in the 4 position, which does not impact compound potency or binding affinity. This substituent may however modulate positively the properties of the naphthyl ring, which prompted us to perform initial *in vitro* ADME studies on compound **9**, and compare this with **3k** and **5c**.

Preliminary ADME Assessment With Selected PLpro Inhibitors

To obtain an initial assessment of the ADME properties, selected compounds were characterized for their metabolic stability when incubated with human or mouse liver microsomes (HLM or MLM, respectively), mouse plasma stability, kinetic solubility, Caco-2 permeability, and mouse plasma protein binding. As shown in **Table 3**, both **3k** and **5c** were metabolically labile in both HLM and MLM. Compound **9** was slightly more stable in comparison to **3k** and **5c**. Preliminary metabolite identification studies suggested that common primary metabolites (**Figure 6A**) included a dihydrodiol on the naphthalene (confirmed by analysis of the CID spectrum, data not shown), N-dealkylation at the piperidine nitrogen, amide hydrolysis (**3k** and **5c**), and O-demethylation (**5c** and **9**). Multiple mono- and di-oxygenation products were also detected for each compound, but the sites of oxygenation were not determined.

Compound **3k** was also highly susceptible to hydrolysis in mouse plasma and degradation was prevented by the addition of bis-*para*-nitrophenylphosphate (BNPP), a known inhibitor of carboxylesterases that are present in plasma and various

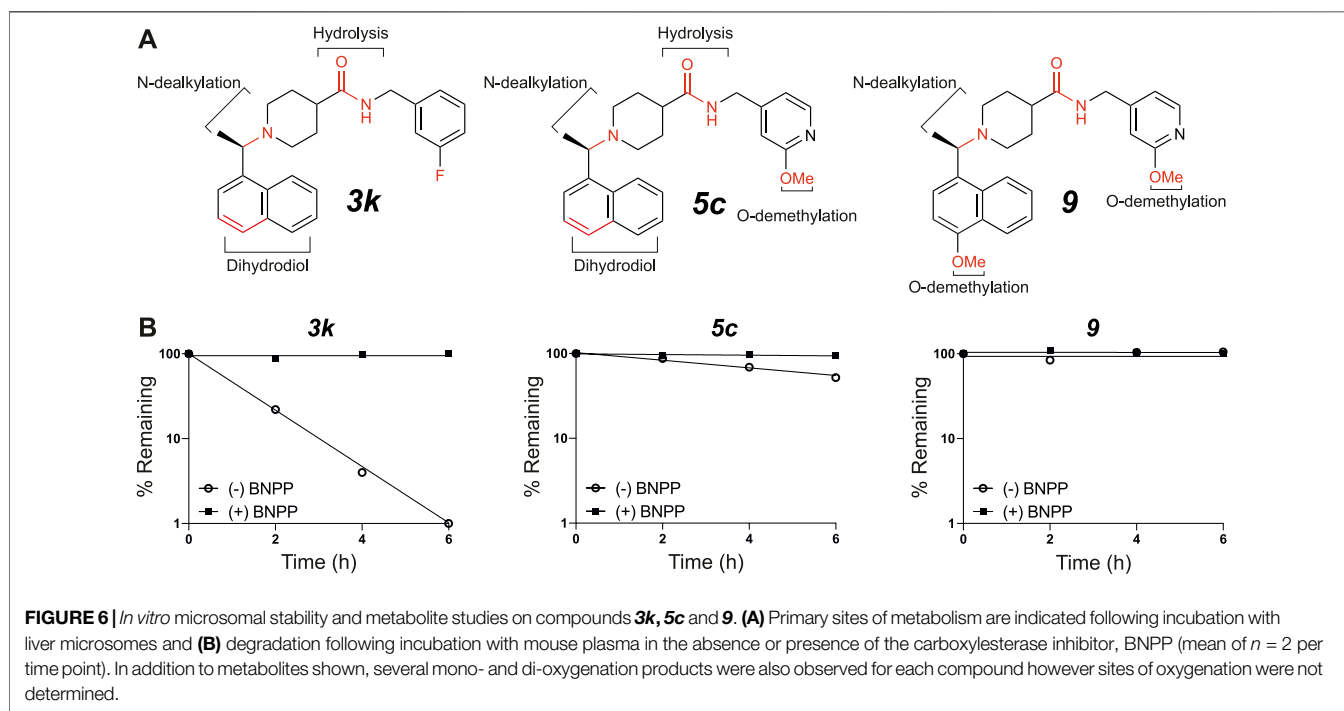
TABLE 3 | ADME properties for selected compounds. Microsomal stability.

Compound	cLogD _{7.4}	HLM		MLM	
		CL _{int} (μL/min/mg)	T _{1/2} (min)	CL _{int} (μL/min/mg)	T _{1/2} (min)
3k	2.5	247 ^a	7	337 ^a	5
5c	1.6	110 ^a	16	86 ^a	20
9	1.7	45	39	50	35

cLog D_{7.4} determined using Jchem for Excel (ChemAxon, ver 21.2.0).

CL_{int}, intrinsic clearance.

^aDegradation also detected in controls in the absence of cofactor.

**TABLE 4 |** Kinetic solubility, Caco-2 permeability and mouse plasma protein binding.

Compound	Kinetic solubility (μg/ml)		Caco-2 A-B/B-A P _{app} (10 ⁻⁶ cm/s)	Mouse plasma protein binding (% bound) ^a
	pH 2.0	pH 6.5		
3k	>100	12.5 – 25	35/36	95.3
5c	>100	50 – 100	53/55	86.3
9	>140	70 – 140	46/46	90.1

NT, not tested.

^aMeasured in the presence of BNPP, to prevent hydrolysis.

tissues (Eng et al., 2010). Plasma-mediated hydrolysis was also evident for **5c**, although the rate of degradation was much less pronounced than for **3k** (Figure 6B). For both **3k** and **5c**, the amide hydrolysis product was detected at the end of the incubation. Interestingly, hydrolysis of **9** was not detected in either microsomes or plasma. Collectively, these results suggest that the *O*-methoxy pyridine (**5c**) in place of the fluorophenyl (**3k**) reduces the rate of hydrolysis (possibly due to a reduction in

Log D), and that the combination of the *O*-methoxy pyridine (in both **5c** and **9**) and the methoxy on the naphthalene in **9** greatly reduces the rate of hydrolysis of the central amide (Figure 6B).

Kinetic solubility was good (>100 μg/ml) under conditions representative of the fasted gastric environment (pH 2) but was reduced under conditions that reflect the fasted upper small intestine (pH 6.5) where most drug absorption occurs (Table 4). For **5c**, **3k** and **9**, Caco-2 permeability was high and

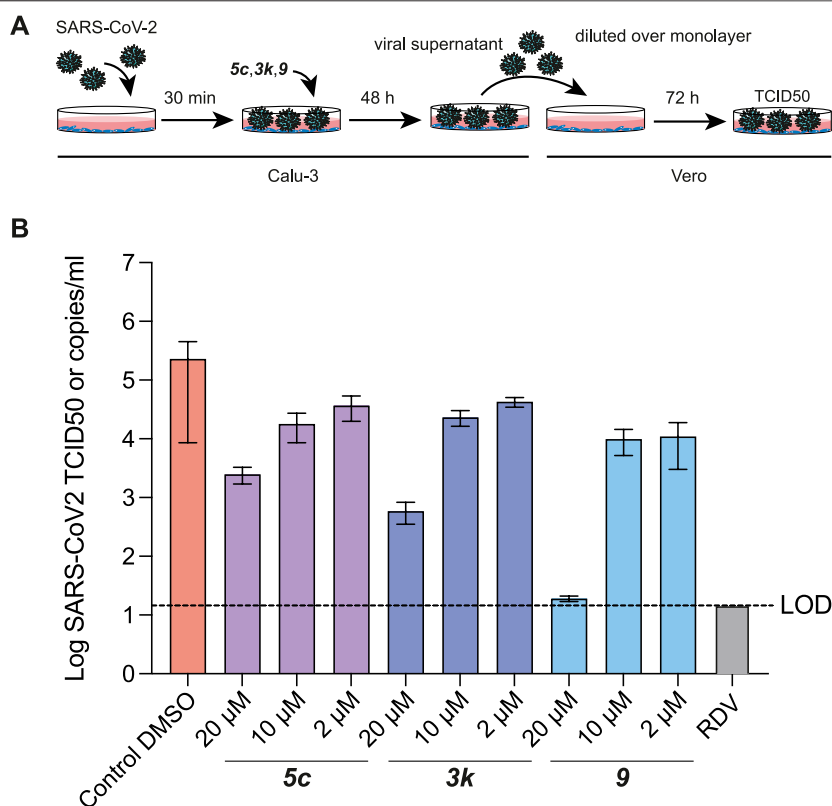


FIGURE 7 | TCID50 Assays for compound **5c**, **3k** and **9**. **(A)** Schematic and time-course of TCID50 determination. Vero cells were infected with SARS-CoV-2 containing supernatant obtained from infected Calu-3 cells, and treated as shown in the cartoon (see Methods). **(B)** TCID50 data, mean and standard deviation for one of two representative experiments with six technical replicates each. Compound **9** retained antiviral activity in preventing viral replication, and in stabilising the naphthyl ring appears to correlate with a modest increase in antiviral activity. Remdesivir (RDV) was used for comparison and assayed at 12.5 μM. Experiments were performed as three independent experiments ($n = 3$) each containing six technical replicates. Values shown are the mean of the three independent experiments, error bars indicate the standard error of the mean. LOD = limit of detection.

there was no evidence of efflux suggesting that permeability would not limit oral absorption (Table 4). Mouse plasma protein binding was moderate (**5c** and **9**) to high (**3k**) (Table 4).

These preliminary ADME results suggest that the major limiting factor for this series to achieve high and prolonged *in vivo* exposure is likely to be hepatic metabolism, accompanied by plasma-mediated hydrolysis for some compounds. Such liabilities are common for early-stage inhibitors and may be addressed by future rounds of medicinal chemistry.

5c Derivatives Inhibitors are Potent Inhibitors of SARS-CoV-2 Infection in Cells

Our previous work had already indicated that **rac5c** was a potent inhibitor of SARS-CoV-2 replication, in a live-infection model using Calu-3 cells, with no evidence of cytotoxicity up to 33 μM (Klemm et al., 2020). We performed similar assays measuring the median tissue culture infection dose (TCID50), of SARS-CoV-2 infection in presence of increasing amounts of **5c**, **3k** and **9** (Figure 7). Our results again indicated a 1-log reduction of viral titer at 10 μM compound concentration, while 20 μM of compound **9** reduced viral titer below the limit of detection (Figure 7B). Overall, these results show again that specific inhibition of SARS-CoV-2 PLpro invokes a

potent antiviral response, and that small molecule inhibitors of PLpro may prove to be efficacious as novel COVID-19 treatments.

DISCUSSION AND CONCLUSION

We here confirm that PLpro is a promising drug target for COVID-19 that requires *de novo* drug discovery. There is currently little evidence that drug repurposing, a method hoped to be a silver bullet to tackle the COVID-19 pandemic, will be of any benefit, and we show in this work and our associated Review that drug repurposing has failed in the context of PLpro as it has in other settings.

Nonetheless, we also provide promising new insights into how piperidine-based PLpro inhibitors, including the well-studied SARS-CoV PLpro inhibitor **5c**, may be derivatized to generate potent and importantly, more drug-like inhibitors. Indeed, we show that commonly used PLpro inhibitors suffer from a multitude of liabilities, mostly due to the presence of a naphthyl moiety that is present in both **5c** but also **GRL-0617** compounds (see associated Review). In the context of the **GRL-0617** series, we note that recent reports have shown that this moiety can be successfully replaced using a substituted

2-phenylthiophene scaffold with no loss in potency (Shen et al., 2021). Our work shows small changes can also ameliorate the properties of the naphthyl-based inhibitors though it is likely that the path towards *in vivo*- or even clinically suitable compounds is likely to be long.

The druggability of PLpro has so far proven challenging, and high affinity (below 100 nM) compounds have not been reported. Despite this, the considerable efforts applied to inhibiting PLpro and full structural enablement have significantly advanced our understanding such that it remains a viable drug target for treating COVID-19.

Once successful, we anticipate that a PLpro inhibitor will have similarly or even more potent anti-CoV activity, as observed for Mpro inhibitors that have recently been approved. Indeed, in addition to blocking the essential protein processing steps in the viral replication cycle, inhibiting PLpro may also serve additional purposes: as a DUB and deISGylase, PLpro prevents virus-induced derailing of the cellular inflammatory and antiviral cascades affected by PLpro mediated cleavage of ubiquitin and ISG15, and may at least in part be responsible for the observed inflammatory flares reported in COVID-19 patients. We therefore consider PLpro as the ultimate drug target in Coronaviruses, that, although challenging, will likely provide significant safeguarding against future pandemics.

METHODS

Protein Biochemistry, Structural Biology and Compound Screening Molecular Biology

Bacterial pOPIN-B expression vectors (Berrow et al., 2007) for SARS-CoV-2 PLpro amino acids (aa) 1563-1878 of polyprotein 1 ab, GenBank: QHD43415, with aa E1564 designated as residue 1, were reported previously (Klemm et al., 2020). SARS-CoV PLpro^{WT} (aa 1541-1855 of polyprotein 1 ab, RefSeq: NP_828849.7) and MERS-CoV PLpro^{WT} (aa 1482-1803 of polyprotein 1 ab, RefSeq: YP_009047202) were codon optimised for bacterial expression, synthesized (Integrated DNA Technologies) and cloned into pOPIN-B digested with KpnI and HindIII using In-Fusion[®] HD cloning (Takara Clontech). The SARS-CoV-2 PLpro BL2 mutant (SARS-CoV-2 PLpro^{BL}) was generated by NEB Q5[®] Site-Directed Mutagenesis of the SARS-CoV-2 PLpro^{WT} plasmid (fwd 5'-GAGTATACG GGCATCGAGACTGCAGTCGGTCACTACAAA C-3', rev 5'-CGATGCGCAGGTGAACGTTTC-3').

For crystallography, we matched a construct used previously (Osipiuk et al., 2021), which has a 1-aa shorter SARS-CoV-2 PLpro sequence (aa 1564-1878) preceded by a Ser-Asn-Ala sequence and includes a catalytic Cys111 mutation to Ser (SARS-CoV-2 PLpro^{C111S}). The coding sequence was cloned into pOPIN-S which features a His-SUMO-tag. SUMO protease (SEN1) was produced according to (Pruneda et al., 2016).

Protein Purification

SARS-CoV-2 PLpro^{WT}, SARS-CoV-2 PLpro^{BL}, SARS-CoV PLpro^{WT}, MERS-CoV PLpro^{WT} and SARS-CoV-2 PLpro^{C111S}

expression vectors were transformed into *E. coli* Rosetta[®] 2 (DE3) competent cells (Novagen) and bacterial cells were grown in 2xYT medium at 37°C. At OD₆₀₀ = 0.8 the temperature was reduced to 18°C and expression was induced with 0.3 mM IPTG. Cells were harvested 16 h post induction and stored at -80°C until purification.

For purification, cells were resuspended in lysis buffer/Buffer A (50 mM Tris pH 7.5, 500 mM NaCl, 5 mM β-ME, 10 mM Imidazole) supplemented with lysozyme (2 mg/ml), DNaseI (100 μg/ml), MgCl₂ (5 mM) and cOmplete EDTA-free protease inhibitor cocktail tablets (Roche) and lysed by sonication. Lysates were cleared by centrifugation at 40,000 g for 30 min at 4°C. The clarified lysate was filtered through a 0.45 μm syringe filter and His-tagged proteins were captured using a HisTrap HP column (5 ml, Cytiva). The captured protein was washed with 10 CV of 30 mM imidazole wash buffer (Buffer A+ 10% Buffer B) and eluted using five column volumes of 100% Buffer B (Buffer A+ 300 mM Imidazole). Pooled fractions were desalted into 100% Buffer A using a HiPrep 26/10 Desalting column (Cytiva) and then supplemented with His-3C or His-SEN1 protease for His-tag and His-SUMO tag cleavage respectively. Following overnight incubation at 4°C, the cleaved His-tag, His-SUMO tag and His-tagged proteases were captured using a HisTrap HP column (5 ml, Cytiva). The extracted PLpro found in the flow through was further purified by size exclusion chromatography using a HiLoad 16/600 Superdex 75 pg column (Cytiva) equilibrated with storage buffer (20 mM Tris pH 7.5, 150 mM NaCl, 1 mM TCEP).

For HTS, SARS-CoV-2 PLpro^{WT} was purified as above. For SPR storage buffer, 20 mM Tris pH 7.5 was replaced with 10 mM HEPES pH 7.5, for crystallisation, 150 mM NaCl was replaced with 50 mM NaCl. Protein samples were concentrated, flash frozen in liquid nitrogen and stored at -80°C.

SARS-2-CoV-PLpro Activity Assay

Assays were essentially performed as described previously (Klemm et al., 2020). In short, SARS-CoV-2 PLpro activity was monitored in a fluorescence intensity assay using the substrate ubiquitin-Rhodamine110, that only becomes fluorescent on cleavage. For HTS, the assay buffer contained 20 mM Tris (pH 8), 1 mM TCEP, 0.03% BSA and 0.01% Triton-X, for all other assays, 1 mM TCEP was replaced with 1 mM GSH. Experiments were performed in 1536-well black non-binding plates (Greiner 782900) with a final reaction volume of 6 μL.

SARS-2-CoV PLpro enzyme (final concentration 50 nM) was added to the plates and incubated at room temperature for 10 min. ubiquitin-Rhodamine110 (final concentration 100 nM) was added to start the reaction and incubated for 12 min at room temperature. For endpoint assays the reaction was stopped by addition of citric acid (1 μL) at a final concentration of 10 mM. All additions were performed using the CERTUS FLEX (v2.0.1, Gyger). The reaction was monitored by an increase in fluorescence (excitation 485 nm and emission 520 nm) on a PHERAstar[®] (v5.41, BMG Labtech) using the FI 485 520 optic module.

Data was normalised to 1% DMSO (negative control, 0% inhibition) and 100 μM Compound 5c (positive control, 100% inhibition).

SARS-2-CoV-PLpro^{WT} Gel Based Activity Assay

Assays were essentially performed as described previously (Klemm et al., 2020). In short, SARS-2-CoV PLpro activity was monitored using SDS-PAGE and tracking the cleavage of K48 Ub₃ or hISG15 by SARS-CoV-2 PLpro^{WT} or SARS-CoV-2 PLpro^{BL}, over time. Each respective enzyme was incubated at 0.25 μM with 2 μM substrate and the reaction was stopped at indicated time points by mixing with NuPAGE® loading dye supplemented with β-mercaptoethanol. The assay buffer contained 20 mM Tris (pH 7.5), 100 mM NaCl and 10 mM DTT. Experiments were performed at 21°C.

SARS-2-CoV-PLpro^{WT} Specificity Assay (Ubiquigent)

SARS-CoV-2 PLpro^{WT} protein and compound **5c** were supplied to Ubiquigent (Dundee, United Kingdom). **5c** was assayed using the commercial Ubiquigent Ub-Rh based DUBprofiler® drug discovery screening platform and results were analysed and provided by Ubiquigent.

High Throughput Screen of the ReFRAME Library

A total of 11,804 compounds from the ReFrame (Repurposing, Focused Rescue and Accelerated Medchem) library were screened. Assay-ready plates were prepared at the Global Health Drug Discovery Institute (GHDDI), China. 5 nL of compounds were dry spotted onto 1536-well plates. Stock concentrations of compounds were 10, 5 and 1 mM and final test concentrations were 8.33, 4.17 and 0.83 μM respectively in final 1% DMSO.

Reagents were dispensed using the CERTUS FLEX (v2.0.1, Gyger). Microplates were centrifuged using the Microplate Centrifuge (Agilent) and read on the PHERAstar® (v5.41, BMG Labtech) using the FI 485 520 optic module.

Data was normalised to 1% DMSO (negative control, 0% inhibition) and 100 μM Compound **5c** (positive control, 100% inhibition). Screen assay quality was monitored by calculation of robust Z' by the following formula where (+) denotes the positive controls (low signal), (-) denotes the negative controls (high signal) and MAD is the median absolute deviation:

$$\text{robust } Z' = 1 - \frac{3 * (\text{MAD}_{-} + \text{MAD}_{+})}{\text{abs}(\text{median}_{-} - \text{median}_{+})}$$

where $\text{MAD} = 1.4826 * \text{median}(\text{abs}(x - \text{median}(x)))$

Plates were excluded from analysis if robust Z' < 0.5. Hits were selected as >2.5 * MAD over the median of the negative control.

To determine the potency of the inhibitors, a series of 10-pt, 1:2 serial dilutions was performed from a highest starting concentration of 100 μM. The 10-point titration curves were fitted with a 4-parameter logistic nonlinear regression model and the IC₅₀ reported is the inflection point of the curve. Data was analysed in TIBCO Spotfire® 7.11.2.

Counter Screen

To confirm that the compounds were specifically inhibiting SARS-CoV-2 PLpro rather than interfering with the fluorescence readout, human USP21 was used as the counter screen assay as previously (Klemm et al., 2020). The same buffer,

reagent dispenser and plate reader as in the PLpro assay was used. USP21 enzyme (final concentration 5 nM) was added to the plates and incubated at room temperature for 10 min. ubiquitin-Rhodamine110 (final concentration 100 nM) was added to start the reaction and incubated for 2 min at room temperature. Reaction was stopped by addition of citric acid (1 μL) at a final concentration of 10 mM. A series of 10-pt, 1:3 serial dilutions was performed from a highest starting concentration of 100 μM. The 10-point titration curves were fitted with a 4-parameter logistic nonlinear regression model and the IC₅₀ reported is the inflection point of the curve. Data was analysed in TIBCO Spotfire® 7.11.2.

Crystallisation

Crystallisation screening was performed at the CSIRO's Collaborative Crystallisation Centre (C3) in Melbourne, Australia. The SARS-CoV-2 PLpro complex with **3k** was generated by incubation of SARS-CoV-2 PLpro^{C111S} (13 mg/ml) with 2 mM inhibitor, overnight at 4°C and precipitate removed by centrifugation. Crystals grew in 0.1 M bis-tris chloride pH 5.46, 0.117 M Zinc Acetate, 21.6% PEG 8000 in a 96-well sitting drop vapour diffusion plate (150 nL protein to 150 nL reservoir solution) at 8°C. Crystals were cryoprotected with reservoir solution supplemented with 15% glycerol and 1 mM inhibitor before vitrification in liquid nitrogen.

Data Collection, Phasing and Refinement

Diffraction data were collected at the Australian Synchrotron (Australian Nuclear Science and Technology Organisation, ANSTO) beamline MX2 (Aragão et al., 2018) (wavelength: 0.953725 Å, temperature: 100 K). An auto-processed dataset was generated at the synchrotron using XDS, Aimless and Pointless (Evans, 2006, 2011; Kabsch, 2010). The dataset was solved by molecular replacement in Phaser (McCoy et al., 2007) using the apo structure of SARS-CoV-2 PLpro [PDB 6WRH (Osipiuk et al., 2021)] as a search model.

Refinement and model building was performed in PHENIX (Adams et al., 2011) and Coot (Emsley et al., 2010). TLS parameters were set to one TLS group per chain. Additional NCS refinement was utilised in each refinement cycle. Geometric restraints for **3k** were generated by the GRADE web server (<http://grade.globalphasing.org>). Models were validated using MolProbity (Williams et al., 2018). Final Ramachandran statistics were 0.00% outliers, 1.63% allowed and 98.64% favoured. Structural figures were generated using PyMol. Further data collection and refinement statistics can be found in **Table 1**.

Surface Plasmon Resonance

Experiments were performed on a BIAcore 8K + instrument (Cytiva, United States) PLpro proteins were diluted into 10 mM sodium acetate pH 5 prior to immobilisation on a CM5 sensor chip (Cytiva, United States) by amine coupling. Compounds were diluted to desired concentrations between 20 and 0.01 μM in a running buffer consisting of 20 mM HEPES pH 7.4, 150 mM sodium chloride, 0.05% P20 detergent, 1 mM TCEP and 2% DMSO. Multi cycle kinetics were performed with 90 s

associations and 300 s dissociations with no further regeneration. Binding constants were determined in BIAcore insight evaluation (version 3.0.12) at steady-state, averaging response over 5 s with a midpoint 5 s before the end of the association phase. Final K_D values were determined by averaging the values from three independent experiments, reporting mean and standard deviation.

Medicinal Chemistry

Experimental

All reagents were used as received from commercial suppliers unless otherwise stated. NMR spectra were recorded at ambient temperature either on Bruker Avance IITM 300 MHz, Bruker Avance IIITM 400 MHz or Bruker Avance IIITM HD 400 MHz instruments in the specified deuterated solvents. Observed proton absorptions were reported as units of parts per million (ppm) relative to respective residual solvent peaks, CDCl₃ (d 7.26), DMSO-d₆ (d 2.50). Multiplicities were reported: s (singlet), d (doublet), t (triplet), q (quartet), dd (doublet of doublets), dt (doublet of triplets) and m (multiplet). Coupling constants were reported as a J value in Hertz (Hz). HPLC/UPLC and LC-MS data was obtained on either an Agilent 6120 series with a Phenomenex Poroshell 120 EC-C18, (2.1 mm × 30 mm, 2.7 mm) column[#] or Waters Acquity H-Class UPLC/MS with Acquity HSS-T3 (2.1 mm × 100 mm, 1.8 mm) column* or Prontosil-EP1 (4.6 × 250 mm) 5 μm column using a gradient elution of 5–100% acetonitrile in water containing 0.1% formic acid. Preparative HPLC was performed on a Waters X-Bridge TM prep C18 OBD column (19 mm × 100 mm, 5 mM) using various gradients based on analytical retentions using water and acetonitrile containing 0.1% formic acid over 10 min at a flow rate of 20 ml/min. Abbreviations: DCM (dichloromethane), EDCI[N-(3-Dimethylaminopropyl)-N'-ethylcarbodiimide hydrochloride], DIEA (N,N-diisopropylamine), THF (tetrahydrofuran), MeOH (methanol), EtOAc (ethyl acetate), EtOH (ethanol), DMF (N,N'-dimethylformamide), HATU {1-[Bis(dimethylamino)methylene]-1H-1,2,3-triazolo [4,5-b]pyridinium 3-oxid hexafluorophosphate}.

Literature compounds **3k** (Báez-Santos et al., 2014), **5c** (Báez-Santos et al., 2014) and **18** (Shan et al., 2021) were synthesised as previously described in their respective references.

3k

¹H NMR (300 MHz, CDCl₃) δ 8.48–8.38 (m, 1H), 7.90–7.80 (m, 1H), 7.74 (d, J = 8.0 Hz, 1H), 7.57 (d, J = 7.3 Hz, 1H), 7.53–7.38 (m, 3H), 7.32–7.22 (m, 1H), 7.01 (d, J = 7.5 Hz, 1H), 6.99–6.90 (m, 2H), 5.76 (s, 1H), 4.43 (d, J = 5.8 Hz, 2H), 4.11 (q, J = 6.3 Hz, 1H), 3.24 (d, J = 11.0 Hz, 1H), 2.90 (d, J = 11.6 Hz, 1H), 2.22–1.64 (m, 7H), 1.47 (d, J = 6.7 Hz, 3H). ES + MS: (M + H) 391.2. HPLC[#] t_g = 1.59 min.

5c

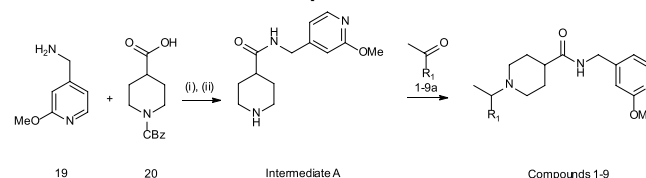
¹H NMR (300 MHz, CDCl₃) δ 8.48–8.39 (m, 1H), 8.08 (dd, J = 5.3, 0.6 Hz, 1H), 7.89–7.80 (m, 1H), 7.74 (d, J = 8.1 Hz, 1H), 7.57 (d, J = 6.5 Hz, 1H), 7.52–7.38 (m, 3H), 6.73 (dd, J = 5.3, 1.4 Hz, 1H), 6.58 (dd, J = 1.4, 0.7 Hz, 1H), 5.79 (t, J = 5.7 Hz, 1H), 4.39 (d, J = 6.0 Hz, 2H), 4.11 (q, J = 6.6 Hz, 1H), 3.91 (s, J = 2.8 Hz, 3H), 3.24 (d, J = 11.7 Hz, 1H), 2.91 (d, J = 11.3 Hz, 1H), 2.24–1.68 (m,

7H), 1.47 (d, J = 6.7 Hz, 3H). ES + MS: (M + H) 404.2. HPLC[#] t_g = 1.23 min.

18

¹H NMR (300 MHz, DMSO) δ 8.70 (s, 1H), 8.50–8.40 (m, 1H), 8.27 (t, J = 5.6 Hz, 1H), 7.98–7.86 (m, 1H), 7.80 (d, J = 7.9 Hz, 1H), 7.63–7.40 (m, 4H), 7.28 (dt, J = 12.0, 2.3 Hz, 1H), 7.11 (s, 1H), 6.63–6.49 (m, 1H), 4.27–4.03 (m, 3H), 3.48–3.38 (m, 4H), 3.07 (s, 1H), 2.78 (s, 1H), 2.33 (s, 4H), 2.25–2.08 (m, 4H), 2.01 (s, 2H), 1.73 (d, J = 12.0 Hz, 1H), 1.67–1.47 (m, 3H), 1.41 (d, J = 6.0 Hz, 3H). ES + MS: (M + H) 532.0 HPLC[#] t_g = 0.99 min.

General Methods – Compounds 1–9



Step (i): To a stirred solution of 1-[(benzyloxy)carbonyl]piperidine-4-carboxylic acid (3.00 g, 11.4 mmol) in DCM (60 ml) was added EDCI (5.46 g, 28.5 mmol), 1H-1,2,3-benzotriazol-1-ol hydrate (4.36 g, 28.5 mmol) and DIEA (9.95 ml, 57.0 mmol). After stirring for 10 min, (2-methoxy-4-yl)methanamine (1.89 g, 13.7 mmol) was added under N₂ atmosphere. The reaction mixture was stirred at ambient temperature until completion of the reaction (TLC monitoring), the reaction was quenched with saturated NH₄Cl (50 ml) and extracted with DCM (2 × 50 ml). The combined organic layer was dried over anhydrous Na₂SO₄ and evaporated under reduced pressure. The compound was purified by CombiFlash (SiO₂, 100% EtOAc) to give benzyl 4-[(2-methoxy-4-yl)methyl]carbamoylpiperidine-1-carboxylate (2.80 g, 64% yield) as an off-white solid. ¹H NMR (400 MHz, DMSO) δ 8.43 (t, J = 5.7 Hz, 1H), 8.07 (d, J = 5.2 Hz, 1H), 7.44–7.26 (m, 5H), 6.82 (d, J = 5.0 Hz, 1H), 6.61 (s, 1H), 5.07 (s, 2H), 4.23 (d, J = 5.9 Hz, 2H), 4.02 (d, J = 13.2 Hz, 2H), 3.82 (s, 3H), 2.84 (br s, 2H), 2.47–2.36 (m, 1H), 1.74 (d, J = 11.5 Hz, 2H), 1.47 (qd, J = 12.5, 4.2 Hz, 2H). ES + MS: (M + H) 384.15 HPLC* t_g = 2.08 min.

Step (ii): To a stirred solution of benzyl 4-[(2-methoxy-4-yl)methyl]carbamoylpiperidine-1-carboxylate (2.80 g, 7.30 mmol) in THF (20 ml) and MeOH (20 ml) was added 20% Pd(OH)₂ on carbon (2.80 g, 100% w/w) at ambient temperature. The resulting mixture was stirred for 3 h under H₂ pressure (atm). After completion of reaction (by TLC monitoring) the reaction mixture was filtered through Celite® and the filter cake washed with MeOH. The filtrate was collected and concentrated *in vacuo* to give **Intermediate A** as a yellow oil. The product was used without purification for further reaction. ¹H NMR (400 MHz, DMSO) δ 8.35 (s, 1H), 8.07 (d, J = 5.3 Hz, 1H), 6.82 (d, J = 5.2 Hz, 1H), 6.59 (s, 1H), 4.22 (d, J = 6.0 Hz, 2H), 3.82 (s, 3H), 2.99 (d, J = 12.3 Hz, 2H), 2.76 (d, J = 11.7 Hz, 1H), 2.37–2.24 (m, 1H), 2.20–2.04 (m, 1H), 1.92–1.76 (m, 1H), 1.74–1.38 (m, 4H). ES + MS: (M + H) 250.15 HPLC* t_g = 0.58 min.

General Reductive Alkylation

1-[1-[(1,1'-biphenyl)-3-yl]ethyl]-N-[(2-methoxy-pyridin-4-yl)methyl]piperidine-4-carboxamide, (**1**). To a stirred solution of 1-[(1,1'-biphenyl)-3-yl]ethanone (133 mg, 0.68 mmol) and Intermediate A (170 mg, 0.68 mmol) in THF (10 ml) at 0°C was added Ti(OⁱPr)₄ (621 μL, 2.05 mmol) under nitrogen and the temperature raised to 80°C for 16 h. The reaction mixture was cooled to 0°C, diluted with MeOH (5 ml) and then sodium borohydride (61.0 mg, 1.70 mmol) was added under N₂. The reaction mixture was allowed to achieve ambient temperature and stirred until complete by LCMS & TLC. The reaction mixture was concentrated in vacuo and diluted with saturated NaHCO₃ (10 ml) and extracted with EtOAc (3 × 10 ml). The combined organics were dried over anhydrous Na₂SO₄ and concentrated *in vacuo*. The crude residue was purified by preparative HPLC to give the title compound (138 mg, 47% yield). ¹H NMR (300 MHz, DMSO) δ 8.30 (t, *J* = 6.0 Hz, 1H), 8.15 (s, 1H), 8.05 (d, *J* = 5.7 Hz, 1H), 7.69 – 7.61 (m, 2H), 7.59 – 7.27 (m, 7H), 6.80 (dd, *J* = 5.3, 1.3 Hz, 1H), 6.58 (s, 1H), 4.21 (d, *J* = 5.9 Hz, 2H), 3.81 (s, 3H), 3.57 (q, *J* = 6.7 Hz, 1H), 3.04 (d, *J* = 11.1 Hz, 1H), 2.85 (d, *J* = 11.5 Hz, 1H), 2.21 – 2.06 (m, 1H), 2.05 – 1.84 (m, 2H), 1.81 – 1.48 (m, 4H), 1.35 (d, *J* = 6.8 Hz, 3H). ES + MS: (M + H) 430.2 HPLC[#] *t*_g = 1.36 min.

1-[1-[benzo(b)thiophen-3-yl]ethyl]-N-[(2-methoxy-pyridin-4-yl)methyl]piperidine-4-carboxamide formate (**2**). The title compound was prepared as described for compound **1** from 1-[benzo(b)thiophen-3-yl]ethanone in 20% yield. ¹H NMR (400 MHz, DMSO) δ 8.30 (t, *J* = 6.0 Hz, 1H), 8.13 (dd, *J* = 9.4, 8.0 Hz, 2H), 8.05 (d, *J* = 5.2 Hz, 1H), 7.98 – 7.92 (m, 1H), 7.52 (s, 1H), 7.36 (pd, *J* = 7.0, 1.2 Hz, 2H), 6.79 (d, *J* = 4.2 Hz, 1H), 6.57 (s, 1H), 4.20 (d, *J* = 5.9 Hz, 2H), 4.04 (q, *J* = 6.5 Hz, 1H), 3.80 (s, 3H), 2.95 – 2.81 (m, 2H), 2.18 – 2.05 (m, 2H), 1.97 (t, *J* = 10.4 Hz, 1H), 1.73 – 1.54 (m, 3H), 1.53 – 1.36 (m, 4H). ES + MS: (M + H) 410.17 HPLC^{*} *t*_g = 4.59 min.

N-[(2-methoxy-pyridin-4-yl)methyl]-1-[1-[2-methylbenzo(b)thiophen-3-yl]ethyl]piperidine-4-carboxamide (**3**). The title compound was prepared as described for compound **1** from 1-[2-methylbenzo(b)thiophen-3-yl]ethanone in 2% yield. ¹H NMR (400 MHz, DMSO) δ 8.34 (t, *J* = 6.0 Hz, 1H), 8.22 (d, *J* = 8.0 Hz, 1H), 8.05 (d, *J* = 5.2 Hz, 1H), 7.82 (d, *J* = 7.7 Hz, 1H), 7.33 – 7.23 (m, 2H), 6.81 (d, *J* = 5.0 Hz, 1H), 6.59 (s, 1H), 4.21 (d, *J* = 6.0 Hz, 2H), 3.81 (s, 3H), 3.65 (q, *J* = 6.7 Hz, 1H), 3.34 (d, *J* = 8.0 Hz, 1H), 3.29 (s, 3H), 2.60 (d, *J* = 11.3 Hz, 1H), 2.22 – 2.14 (m, 1H), 1.95 – 1.64 (m, 4H), 1.55 (d, *J* = 11.7 Hz, 1H), 1.50 – 1.33 (m, 4H). ES + MS: (M + H) 424.03 HPLC^{*} *t*_g = 6.31 min.

1-[1-(5-chloro-2-methoxyphenyl)ethyl]-N-[(2-methoxy-pyridin-4-yl)methyl]piperidine-4-carboxamide (**4**). The title compound was prepared as described for compound **1** from 1-(5-chloro-2-methoxyphenyl)ethanone in 82% yield. ¹H NMR (300 MHz, Chloroform-*d*) δ 8.08 (dd, *J* = 5.3, 0.7 Hz, 1H), 7.41 (d, *J* = 2.7 Hz, 1H), 7.14 (dd, *J* = 8.7, 2.7 Hz, 1H), 6.82 – 6.70 (m, 2H), 6.58 (h, *J* = 1.5, 0.8 Hz, 1H), 5.85 (s, 1H), 4.40 (d, *J* = 6.1 Hz, 2H), 3.91 (s, 4H), 3.79 (s, 3H), 3.21 (d, *J* = 11.2 Hz, 1H), 2.87 (d, *J* = 9.3 Hz, 1H), 2.22 – 1.65 (m, 7H), 1.26 (d, *J* = 6.7 Hz, 3H). ES + MS: (M + H) 418.0 HPLC[#] *t*_g = 1.09 min.

1-[1-(5-chloro-2-ethoxyphenyl)ethyl]-N-[(2-methoxy-pyridin-4-yl)methyl]piperidine-4-carboxamide (**5**). The title compound

was prepared as described for compound **1** from 1-(5-chloro-2-ethoxyphenyl)ethanone in 65% yield. ¹H NMR (300 MHz, Chloroform-*d*) δ 8.08 (dd, *J* = 5.3, 0.7 Hz, 1H), 7.39 (d, *J* = 2.7 Hz, 1H), 7.12 (dd, *J* = 8.7, 2.7 Hz, 1H), 6.80 – 6.70 (m, 2H), 6.62 – 6.55 (m, 1H), 5.84 (s, 1H), 4.40 (d, *J* = 6.0 Hz, 2H), 4.05 – 3.88 (m, 6H), 3.20 (d, *J* = 11.0 Hz, 1H), 2.89 (d, *J* = 11.1 Hz, 1H), 2.23 – 1.67 (m, 7H), 1.40 (t, *J* = 7.0 Hz, 3H), 1.27 (d, *J* = 6.8 Hz, 3H). ES + MS: (M + H) 432.2 HPLC[#] *t*_g = 1.28 min.

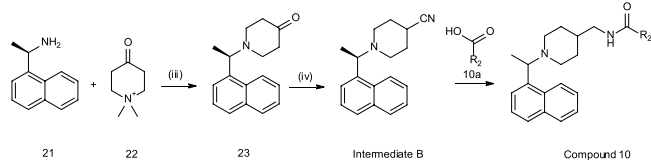
1-[1-(2-methoxynaphthalen-1-yl)ethyl]-N-[(2-methoxy-pyridin-4-yl)methyl]piperidine-4-carboxamide formate (**6**). The title compound was prepared as described for compound **1** from 1-(2-methoxynaphthalen-1-yl)ethanone in 15% yield. ¹H NMR (400 MHz, DMSO) δ 9.01 (d, *J* = 7.3 Hz, 1H), 8.34 (t, *J* = 5.6 Hz, 1H), 8.15 (s, 1H), 8.05 (d, *J* = 5.2 Hz, 1H), 7.82 (d, *J* = 8.7 Hz, 2H), 7.43 – 7.39 (m, 2H), 7.32 (t, *J* = 7.5 Hz, 1H), 6.80 (d, *J* = 5.2 Hz, 1H), 6.58 (s, 1H), 4.35 (d, *J* = 4.9 Hz, 1H), 4.20 (d, *J* = 5.8 Hz, 2H), 3.89 (s, 3H), 3.80 (s, 3H), 3.44 (d, *J* = 10.7 Hz, 1H), 2.55 (d, *J* = 10.9 Hz, 1H), 2.24 – 2.13 (m, 1H), 1.93 (s, br, 1H), 1.88 – 1.70 (m, 3H), 1.50 (d, *J* = 13.7 Hz, 1H), 1.46 – 1.34 (m, 4H). ES + MS: (M + H) 434.25 HPLC^{*} *t*_g = 4.62 min.

1-[1-(2-ethoxynaphthalen-1-yl)ethyl]-N-[(2-methoxy-pyridin-4-yl)methyl]piperidine-4-carboxamide (**7**). The title compound was prepared as described for compound **1** from 1-(2-ethoxynaphthalen-1-yl)ethanone in 4% yield. ¹H NMR (400 MHz, DMSO) δ 9.03 (d, *J* = 8.6 Hz, 1H), 8.33 (t, *J* = 5.9 Hz, 1H), 8.05 (d, *J* = 5.2 Hz, 1H), 7.79 (t, *J* = 9.6, 2H), 7.46 – 7.28 (m, 3H), 6.80 (d, *J* = 5.1 Hz, 1H), 6.58 (s, 1H), 4.36 (q, *J* = 6.5 Hz, 1H), 4.25 – 4.09 (m, 4H), 3.80 (s, 3H), 3.42 (d, *J* = 11.2 Hz, 1H), 2.55 (d, *J* = 12.3 Hz, 1H), 2.24 – 2.12 (m, 1H), 1.89 (t, *J* = 10.7 Hz, 1H), 1.85 – 1.67 (m, 3H), 1.49 (d, *J* = 12.4 Hz, 1H), 1.45 – 1.32 (m, 7H). ES + MS: (M + H) 448.22 HPLC^{*} *t*_g = 4.87 min.

1-[1-(4-fluoronaphthalen-1-yl)ethyl]-N-[(2-methoxy-pyridin-4-yl)methyl]piperidine-4-carboxamide (**8**). The title compound was prepared as described for compound **1** from 1-(4-fluoronaphthalen-1-yl)ethanone in 48% yield. ¹H NMR (400 MHz, DMSO) δ 8.51 (d, *J* = 7.7 Hz, 1H), 8.32 (t, *J* = 5.8 Hz, 1H), 8.06 (t, *J* = 5.6 Hz, 2H), 7.67 – 7.58 (m, 2H), 7.51 (dd, *J* = 7.6, 6.0 Hz, 1H), 7.27 (dd, *J* = 10.4, 8.2 Hz, 1H), 6.80 (d, *J* = 5.1 Hz, 1H), 6.57 (s, 1H), 4.20 (d, *J* = 5.9 Hz, 2H), 4.15 (q, *J* = 6.5 Hz, 1H), 3.80 (s, 3H), 3.02 (d, *J* = 10.8 Hz, 1H), 2.80 (d, *J* = 11.2 Hz, 1H), 2.22 – 2.10 (m, 1H), 2.09 – 1.96 (m, 2H), 1.71 (d, *J* = 12.4 Hz, 1H), 1.67 – 1.44 (m, 3H), 1.39 (d, *J* = 6.6 Hz, 3H). ES + MS: (M + H) 422.21 HPLC^{*} *t*_g = 5.88 min.

1-[1-(4-methoxynaphthalen-1-yl)ethyl]-N-[(2-methoxy-pyridin-4-yl)methyl]piperidine-4-carboxamide (**9**). The title compound was prepared as described for compound **1** from 1-(4-methoxynaphthalen-1-yl)ethanone in 17% yield. ¹H NMR (400 MHz, DMSO) δ 8.41 (d, *J* = 8.3 Hz, 1H), 8.32 (t, *J* = 5.8 Hz, 1H), 8.17 (d, *J* = 8.0 Hz, 1H), 8.05 (d, *J* = 5.3 Hz, 1H), 7.50 (dt, *J* = 14.8, 7.1 Hz, 2H), 7.42 (d, *J* = 8.0 Hz, 1H), 6.91 (d, *J* = 8.1 Hz, 1H), 6.80 (d, *J* = 5.3 Hz, 1H), 6.57 (s, 1H), 4.20 (d, *J* = 5.8 Hz, 2H), 4.12 – 4.01 (m, 1H), 3.95 (s, 3H), 3.80 (s, 3H), 3.02 (d, *J* = 10.2 Hz, 1H), 2.82 (d, *J* = 11.2 Hz, 1H), 2.23 – 2.08 (m, 2H), 2.01 (q, *J* = 10.0 Hz, 2H), 1.70 (d, *J* = 13.3 Hz, 1H), 1.66 – 1.45 (m, 2H), 1.38 (d, *J* = 6.5 Hz, 3H). ES + MS: (M + H) 434.21 HPLC^{*} *t*_g = 4.72 min.

General Methods – Compound 10



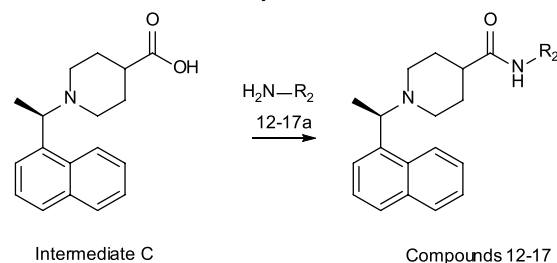
Step (iii): (1R)-1-(1-(1-naphthyl)ethanamine (1.41 g, 8.24 mmol) and potassium carbonate (2.56 g, 18.3 mmol) were taken up in EtOH (20 ml) and Water (5 ml) and warmed to 60°C. Concurrently, 1,1-dimethylpiperidin-4-one iodide (2.31 g, 9.06 mmol) was dissolved in EtOH:water (1:2, 5 ml) and added drop-wise to the previous mixture. The resulting mixture was heated to reflux for 4 h. After this time the EtOH was removed *in vacuo* and the remaining aqueous extracted with EtOAc. The extracts were combined, dried over anhydrous MgSO₄, filtered, and concentrated in *vacuo*. The crude material was purified by combi-flash (SiO₂, 0–15%EtOAc/DCM) to give 1-[(1R)-1-(1-naphthyl)ethyl]piperidin-4-one (1.44 mg, 69% yield) as a yellow oil. ¹H NMR (300 MHz, CDCl₃) δ 8.50 – 8.41 (m, 1H), 7.92 – 7.83 (m, 1H), 7.77 (d, *J* = 8.2 Hz, 1H), 7.62 (d, *J* = 7.1 Hz, 1H), 7.56 – 7.41 (m, 3H), 4.34 (q, *J* = 6.7 Hz, 1H), 2.98 – 2.73 (m, 4H), 2.52 – 2.32 (m, 4H), 1.54 (d, *J* = 6.7 Hz, 3H). ES + MS: (M + H) 272.1. HPLC[#] *t*_g = 0.89 min.

Step (iv): To a solution of 1-[(1R)-1-(1-naphthyl)ethyl]piperidin-4-one (1.43 g, 5.65 mmol) in THF (40 ml) was added 1-(isocyanomethylsulfonyl)-4-methyl-benzene (1.21 g, 6.17 mmol) followed by potassium *tert*-butoxide (760 mg, 6.77 mmol) and dry MeOH (5 ml). The reaction was stirred at ambient temperature over 18 h. After this time the reaction was concentrated in *vacuo* and the crude residue partitioned between saturated NaHCO₃ and EtOAc. The layers were separated and the aqueous further extracted with EtOAc. The extracts were combined, dried over anhydrous MgSO₄, filtered, and concentrated in *vacuo*. The crude residue was purified by combi-flash (SiO₂, 0–5%EtOAc/DCM) to give 1-[(1R)-1-(1-naphthyl)ethyl]piperidine-4-carbonitrile (417 mg, 28% yield) **INTERMEDIATE B** as a yellow oil. ¹H NMR (300 MHz, CDCl₃) δ 8.44 – 8.35 (m, 1H), 7.91 – 7.81 (m, 1H), 7.75 (d, *J* = 8.1 Hz, 1H), 7.57 – 7.39 (m, 5H), 4.16 (q, *J* = 6.7 Hz, 1H), 2.97 – 2.76 (m, 1H), 2.76 – 2.55 (m, 2H), 2.52 – 2.27 (m, 2H), 2.00 – 1.74 (m, 4H), 1.47 (d, *J* = 6.7 Hz, 3H). ES + MS: (M + H) 265.2. HPLC[#] *t*_g = 1.11 min.

(R)-2-methoxy-N-[(1-(1-(naphthalen-1-yl)ethyl)piperidin-4-yl)methyl]isonicotinamide (**10**). To a 0°C solution of INTERMEDIATE B (88.4 mg, 0.334 mmol) in dry THF (3 ml) under N₂ was added lithium aluminium hydride (14.2 mg, 0.374 mmol) in one portion. The reaction was allowed to achieve ambient temperature and stirred over 18 h. The reaction was quenched by minimal drop-wise addition of 1M Rochelle's salt. The reaction mixture was then filtered through Celite®, the filter cake washed with EtOAc and the filtrate concentrated in *vacuo*. The crude material was used directly in the subsequent coupling step without further purification. To a solution of crude amine (45.0 mg, 0.168 mmol), 2-methoxypyridine-4-carboxylic acid (25.7 mg, 0.168 mmol) and DIEA (35.0 μL, 0.201 mmol) in

DMF (3 ml) was added HATU (64.0 mg, 0.168 mmol). The reaction was stirred at ambient temperature over 18 h. The reaction was diluted with saturated NaHCO₃ and extracted with EtOAc. The extracts were combined, washed with water (x3) and brine, dried over anhydrous MgSO₄, filtered, and concentrated in *vacuo*. The crude material was purified by preparative HPLC to give 2-methoxy-N-[[1-[(1R)-1-(1-naphthyl)ethyl]-4-piperidyl]methyl]pyridine-4-carboxamide (23.3 mg, 34% yield) as a pale yellow oil. ¹H NMR (300 MHz, CDCl₃) δ 8.26 – 8.17 (m, 2H), 8.04 (d, *J* = 8.3 Hz, 1H), 7.98 – 7.88 (m, 2H), 7.83 (s, 1H), 7.66 – 7.50 (m, 3H), 7.39 (dd, *J* = 5.4, 1.5 Hz, 1H), 5.16 – 5.07 (m, 1H), 3.97 (d, *J* = 12.0 Hz, 1H), 3.92 (s, 3H), 3.32 (td, *J* = 13.5, 6.7 Hz, 3H), 2.70 – 2.33 (m, 3H), 2.09 – 1.89 (m, 6H), 1.80 (d, *J* = 11.7 Hz, 1H). ES + MS: (M + H) 404.2. HPLC[#] *t*_g = 1.39 min.

General Methods – Compounds 12–17



Intermediate C was prepared as previously described (Báez-Santos et al., 2014).

¹H NMR (300 MHz, MeOD) δ 8.30 (d, *J* = 8.5 Hz, 1H), 8.02 (t, *J* = 8.5 Hz, 2H), 7.87 (d, *J* = 7.4 Hz, 1H), 7.74 – 7.56 (m, 3H), 5.45 (dd, *J* = 13.3, 6.6 Hz, 1H), 4.04 (d, *J* = 10.6 Hz, 1H), 3.29 – 3.08 (m, 2H), 2.98 (t, *J* = 13.4 Hz, 1H), 2.59 (t, *J* = 12.5 Hz, 1H), 2.29 (d, *J* = 12.7 Hz, 1H), 2.21 – 1.95 (m, 2H), 1.88 (d, *J* = 6.8 Hz, 3H), 1.83 – 1.65 (m, 1H). ES + MS: (M + H) 284.1. HPLC* *t*_g = 1.04 min.

General Amide Coupling – Compounds 12–17

(R)-N-methyl-1-(1-(naphthalen-1-yl)ethyl)piperidine-4-carboxamide (**12**). To a solution of Intermediate C (50 mg, 0.18 mmol) and methylamine hydrochloride (13 mg, 0.19 mmol) in DMF (3 ml) under N₂ was added DIEA (70 μL, 0.40 mmol) followed by HATU (75 mg, 0.20 mmol). The reaction stirred at ambient temperature until complete by LCMS. The reaction was diluted with water and extracted with EtOAc. The extracts were combined, washed with water (x3) and brine, dried over anhydrous MgSO₄, filtered and concentrated in *vacuo*. The crude residue was purified by preparative HPLC to give the title compound in 32% yield. ¹H NMR (400 MHz, DMSO) δ 8.45 (d, *J* = 7.7 Hz, 1H), 7.91 (d, *J* = 7.8 Hz, 1H), 7.80 (d, *J* = 6.8 Hz, 1H), 7.63 (s, 1H), 7.58 – 7.41 (m, 3H), 4.13 (s, 1H), 3.04 (d, *J* = 10.1 Hz, 1H), 2.76 (d, *J* = 10.1 Hz, 1H), 2.12 – 1.89 (m, 3H), 1.65 (d, *J* = 10.8 Hz, 1H), 1.52 (s, *J* = 15.4 Hz, 3H), 1.39 (d, *J* = 4.7 Hz, 3H). ES + MS: (M + H) 297.17. HPLC* *t*_g = 4.57 min.

(R)-N-[(1-(1-methyl-2-oxo-1,2-dihydropyridin-4-yl)methyl)-1-(1-(naphthalen-1-yl)ethyl)piperidine-4-carboxamide (**13**). The title compound was prepared as described for compound **12** from 4-(aminomethyl)-1-methylpyridin-2(1H)-one hydrochloride in

57% yield. ^1H NMR (300 MHz, CDCl_3) δ 8.42 (d, J = 7.1 Hz, 1H), 7.89 – 7.79 (m, 1H), 7.74 (d, J = 8.3 Hz, 1H), 7.57 (d, J = 5.7 Hz, 1H), 7.53 – 7.38 (m, 3H), 7.18 (d, J = 7.0 Hz, 1H), 6.36 (d, J = 1.1 Hz, 1H), 6.07 – 5.98 (m, 2H), 4.25 (d, J = 6.1 Hz, 2H), 4.17 – 4.05 (m, 1H), 3.48 (s, 3H), 3.23 (d, J = 12.6 Hz, 1H), 2.90 (d, J = 9.4 Hz, 1H), 2.27 – 1.66 (m, 7H), 1.46 (t, J = 7.5 Hz, 3H). ES + MS: (M + H) 404.2. HPLC $^{\#}$ t_g = 0.98 min.

(*R*)-*N*-[(2-methylthiazol-5-yl)methyl]-1-(1-(naphthalen-1-yl)ethyl)piperidine-4-carboxamide (**14**). The title compound was prepared as described for compound **12** from (2-methylthiazol-5-yl)methanamine in 25% yield. ^1H NMR (400 MHz, DMSO) δ 8.44 (d, J = 8.0 Hz, 1H), 8.37 (t, J = 5.2 Hz, 1H), 7.91 (d, J = 7.3 Hz, 1H), 7.79 (d, J = 7.6 Hz, 1H), 7.58 – 7.42 (m, 4H), 7.39 (s, 1H), 4.33 (d, J = 5.7 Hz, 2H), 4.13 (q, J = 5.4 Hz, 1H), 3.04 (d, J = 8.8 Hz, 1H), 2.77 (d, J = 10.8 Hz, 1H), 2.56 (s, 3H), 2.14 – 1.91 (m, 3H), 1.66 (d, J = 12.0 Hz, 1H), 1.60 – 1.44 (m, 3H), 1.39 (d, J = 6.1 Hz, 3H). ES + MS: (M + H) 394.18. HPLC $^{\#}$ t_g = 5.20 min.

(*R*)-1-(1-(naphthalen-1-yl)ethyl)-*N*-(pyridin-3-ylmethyl)piperidine-4-carboxamide (**15**). The title compound was prepared as described for compound **12** from pyridin-3-ylmethanamine in 11% yield. ^1H NMR (400 MHz, DMSO) δ 8.46 – 8.42 (m, 3H), 8.32 (t, J = 5.4 Hz, 1H), 7.91 (d, J = 7.4 Hz, 1H), 7.80 (d, J = 7.7 Hz, 1H), 7.62 – 7.42 (m, 5H), 7.32 (dd, J = 7.8, 4.8 Hz, 1H), 4.25 (d, J = 5.9 Hz, 2H), 4.15 (s, br, 1H), 3.06 (d, J = 10.1 Hz, 1H), 2.79 (d, J = 10.0 Hz, 1H), 2.21 – 2.08 (m, 1H), 2.01 (s, br, 2H), 1.71 (d, J = 13.1 Hz, 1H), 1.67 – 1.46 (m, 3H), 1.40 (d, J = 5.9 Hz, 3H). ES + MS: (M + H) 374.21. HPLC $^{\#}$ t_g = 4.93 min.

(*R*)-1-(1-(naphthalen-1-yl)ethyl)-*N*-(4-sulfamoylbenzyl)piperidine-4-carboxamide formate (**16**). The title compound was prepared as described for compound **12** from 4-(aminomethyl)benzenesulfonamide hydrochloride in 46% yield. ^1H NMR (300 MHz, DMSO) δ 8.45 (d, J = 7.1 Hz, 1H), 8.35 (t, J = 5.7 Hz, 1H), 8.14 (s, 1H), 7.95 – 7.87 (m, 1H), 7.80 (d, J = 8.0 Hz, 1H), 7.74 (d, J = 8.4 Hz, 2H), 7.58 – 7.42 (m, 4H), 7.36 (d, J = 8.4 Hz, 2H), 7.28 (s, 2H), 4.28 (d, J = 5.9 Hz, 2H), 4.16 (q, J = 6.9 Hz, 1H), 3.08 (d, J = 10.6 Hz, 1H), 2.79 (d, J = 11.2 Hz, 1H), 2.23 – 1.94 (m, 3H), 1.73 (d, J = 13.5 Hz, 1H), 1.67 – 1.46 (m, 3H), 1.40 (d, J = 6.6 Hz, 3H). ES + MS: (M + H) 452.2. HPLC $^{\#}$ t_g = 1.08 min.

(*R*)-1-(1-(naphthalen-1-yl)ethyl)-*N*-((tetrahydro-2H-pyran-4-yl)methyl)piperidine-4-carboxamide (**17**). The title compound was prepared as described for compound **12** from (tetrahydro-2H-pyran-4-yl)methanamine in 78% yield. ^1H NMR (300 MHz, CDCl_3) δ 8.42 (d, J = 7.5 Hz, 1H), 7.89 – 7.80 (m, 1H), 7.74 (d, J = 8.1 Hz, 1H), 7.57 (d, J = 7.1 Hz, 1H), 7.53 – 7.38 (m, 3H), 5.53 (s, 1H), 4.15 – 4.07 (m, 1H), 4.01 – 3.89 (m, 2H), 3.34 (td, J = 11.8, 2.2 Hz, 2H), 3.23 (d, J = 11.0 Hz, 1H), 3.14 (t, J = 6.4 Hz, 2H), 2.90 (d, J = 11.3 Hz, 1H), 2.18 – 1.94 (m, 3H), 1.94 – 1.62 (m, 6H), 1.62 – 1.51 (m, 2H), 1.47 (d, J = 6.6 Hz, 3H), 1.28 (qd, J = 12.1, 4.5 Hz, 2H). ES + MS: (M + H) 381.2. HPLC $^{\#}$ t_g = 1.07 min.

General Synthesis Compound 11

(*R*)-1-(2-methoxypyridin-4-yl)-*N*-((1-(1-(naphthalen-1-yl)ethyl)piperidin-4-yl)methyl)methanamine formate (**11**). To a stirred solution of **5c** (200 mg, 0.50 mmol) in THF (10 ml) was added 2.5M lithium aluminium hydride in THF (595 μL , 1.49 mmol) at 0°C under N_2 . Then the reaction mixture was heated to 90°C and stirred for 5 h. After completion of the reaction (TLC

Monitoring), the reaction mixture was quenched with 0.1 ml water, 0.1 ml 15% aq. NaOH and 0.2 ml water respectively at 0°C. The reaction mixture was filtered through Celite $^{\text{®}}$ and the filter cake washed with THF. The combined organics were dried over anhydrous Na_2SO_4 and concentrated in vacuo. The crude residue was purified by preparative HPLC to give the title compound in 14% yield. ^1H NMR (400 MHz, DMSO) δ 8.43 (d, J = 7.2 Hz, 1H), 8.17 (s, 1H), 8.05 (d, J = 5.2 Hz, 1H), 7.94 – 7.87 (m, 1H), 7.79 (d, J = 8.0 Hz, 1H), 7.57 – 7.42 (m, 4H), 6.92 (d, J = 5.2 Hz, 1H), 6.75 (s, 1H), 4.15 (q, J = 6.5 Hz, 1H), 3.81 (s, 3H), 3.67 (s, 2H), 3.04 (d, J = 10.2 Hz, 1H), 2.74 (d, J = 11.1 Hz, 1H), 2.33 (d, J = 6.5 Hz, 2H), 2.05 – 1.93 (m, 2H), 1.72 (d, J = 12.6 Hz, 1H), 1.60 (d, J = 12.4 Hz, 1H), 1.45 – 1.33 (m, 4H), 1.15 – 0.99 (m, 2H). ES + MS: (M + H) 390.24. HPLC t_g = 4.78 min.

Absorption, Distribution, Metabolism and Excretion Studies

Microsomal Stability and Metabolite Identification

The microsomal stability assay was performed by incubating compounds (1 μM) with human or mouse liver microsomes (0.4 mg/ml, Sekisui XenoTech, Kansas City, KS) suspended in 0.1 M phosphate buffer (pH 7.4) containing 1 U/mL glucose-6-phosphate dehydrogenase at 37°C. The metabolic reaction was initiated by the addition of an NADPH-regenerating system (final concentrations of 1.3 mM NADP, 3.5 mM glucose-6-phosphate, and 3.3 mM MgCl_2). Control samples that did not include cofactor were also included. Samples were mixed and maintained at 37°C using a microplate incubator (THERMOstar $^{\text{®}}$, BMG Labtech GmbH, Offenburg, Germany) and quenched at various time points over 60 min by the addition of acetonitrile containing metolazone as an internal standard. Quenched samples were centrifuged, and the supernatant removed and analyzed by LC/MS (Waters Xevo G2 QToF MS coupled to an Acquity UPLC) using a Supelco Ascentis Express RP C8 column (5 cm \times 2.1 mm, 2.7 μm) and a mobile phase consisting of 0.05% formic acid in water and 0.05% formic acid in acetonitrile and mixed under gradient conditions. The flow rate was 0.4 ml/min and injection volume was 5 μL . The *in vitro* intrinsic clearance was calculated from the first order degradation rate constant for substrate depletion.

Metabolite identification was conducted with the assistance of Waters UNIFI software and candidate masses were filtered based on retention time, mass error and the response relative to that of the parent. The identity of an M+34 metabolite as the dihydrodiol on the naphthalene was confirmed by analysis of the CID spectrum. For other metabolites, identification was based on accurate mass only.

Kinetic Solubility

Kinetic solubility was determined based on a method described previously (Bevan and Lloyd, 2000). Test compounds prepared at 10 mg/ml in DMSO were diluted into buffer (pH 2.0 or pH 6.5) to give a 1% v/v final DMSO concentration. After standing for 30 min at ambient temperature, samples were analyzed via nephelometry to determine a solubility range. The maximum

value of the assay is 100 µg/ml and the minimum value is 1.6 µg/ml.

Caco-2 Permeability

The apparent permeability coefficient was assessed using Caco-2 cell monolayers as described previously (Charman et al., 2020). Briefly, experiments were conducted over 120 min using an aqueous transport buffer (pH 7.4 Hanks balanced salt solution containing 20 mM HEPES) in both the apical and basolateral chambers. Propranolol (high permeability control), lucifer yellow (low permeability control) and rhodamine 123 (P-gp substrate) were used as controls. Donor solutions were prepared by spiking compound into transport buffer, equilibrating at 37°C for approximately 4 h, and centrifuging to remove any precipitated material. The supernatant was used as the donor solution and flux was assessed over 120 min. Samples were taken from the donor chamber at the start and end of the transport experiment, and from the acceptor chamber at 5–6 time points. The volume of acceptor solution removed was replaced with blank transport buffer and concentrations corrected for the dilution. Samples were stored frozen at -80°C until analysis by LC/MS as described below. The apparent permeability coefficient (P_{app}) was calculated as $P_{app} = (dQ/dt)/(C_o \times A)$, where dQ/dt is the rate of permeation across the cell monolayer, C_o is the initial donor concentration and A is the monolayer surface area. P_{app} was measured in both the apical to basolateral (A-B) and basolateral to apical (B-A) directions and the efflux ratio was calculated as $B-A P_{app}/A-B P_{app}$. Mass balance was also confirmed.

Plasma Stability

Compound stability in mouse plasma was assessed in the absence and presence of 500 µM bis-*para*-nitrophenyl phosphate (BNPP), a known carboxylesterase inhibitor (Eng et al., 2010). Compound was spiked into blank mouse plasma (that had been pre-equilibrated with blank solvent or 500 µM BNPP at 37°C for 1 h) and maintained at 37°C under a humidified CO₂-enriched (2%) atmosphere for pH control. Samples were collected at 0, 2, 4 and 6 h ($n = 2$ aliquots per time point) and snap frozen on dry ice and stored at -80°C until analysis by LC/MS.

Plasma Protein Binding

Mouse protein binding was determined via rapid equilibrium dialysis (RED) using a method modified from that reported previously (Curran et al., 2011). Mouse plasma (with 500 µM BNPP as a carboxylesterase inhibitor) was spiked with compound, mixed, and aliquots taken to determine the compound concentration in pre-dialysis matrix. The remaining spiked matrix was equilibrated at 37°C (~10 min) prior to adding to the RED inserts (300 µL per insert). Inserts ($n = 4$ per compound) were placed in a Teflon holding plate and dialysed against protein-free 0.1 M phosphate buffered saline (pH 7.4; 500 µL per insert) at 37°C on an orbital plate shaker (ThermoMixer C, Eppendorf; 800 rpm). At the end of the 6 h dialysis period, aliquots were taken from the donor and dialysate chambers to obtain measures of the total and free concentrations, respectively. To control solution pH, the dialysis was performed

in an incubator under a humidified CO₂-enriched (2%) atmosphere and the pH of the post-dialysis matrix and dialysate were confirmed to be within pH 7.4 ± 0.1. The donor and dialysate samples were matrix matched (to a common composition of 50/50 plasma and buffer) and stored frozen at -80°C until analysis by LC/MS. The fraction unbound was determined as the ratio of the dialysate to donor concentration with the assumption that the system had reached steady state equilibrium at the end of the dialysis period.

LC/MS Analysis

Plasma protein binding and Caco-2 samples were assayed by LC/MS using a Waters Xevo TQ MS coupled to a Waters Acquity UPLC. The column was a Supelco Ascentis Express RP C8 column (5 cm × 2.1 mm, 2.7 µm) and the mobile phase consisted of 0.05% formic acid in water and 0.05% formic acid in acetonitrile mixed under gradient elution conditions with a 4 min cycle time, 0.4 ml/min flow rate and a 4 µL injection volume. Detection was conducted by electrospray ionization under positive and negative mode with multiple reaction monitoring. Diazepam was included as an internal standard and MS transitions included (m/z) 391.3 > 154.91 (3k), 404.23 > 250.18 (5c), 434.16 > 185.06 (9), and 285.04 > 193.07 (diazepam). The calibration standards were prepared in blank 50/50 plasma and buffer mixture (same matrix as the samples). Proteins were precipitated with acetonitrile (2:1 acetonitrile:matrix) and sample concentrations quantified by comparison to the calibration standards. Accuracy (% bias) and precision (%RSD) were within ±12% and <10%, respectively, for all compounds.

Cell-Based Studies and Infection Assays

Cell Lines Used

Calu-3 and Vero (CCL-81) cells displayed expected cell morphologies and were sent for validation to Garvan Molecular Genetics facility (on 15 June 2020). Cell lines were screened on a monthly basis for *mycoplasma* contamination using the Plasmotest kit (Invivogen) as per manufacturer's instructions. All used cells were *mycoplasma* free.

Cell Culture

Calu-3 cells were cultured in Dulbecco's Modified Eagle Medium F12 supplemented with 10% (v/v) heat-inactivated foetal bovine serum (FBS; Sigma-Aldrich), 100 U/ml penicillin and 100 mg/ml streptomycin at 37°C and 5% CO₂.

For infection studies, Vero (CCL-81) cells were cultured in Dulbecco's Modified Eagle Medium (DMEM + 1 g/L D-Glucose, L-Glutamine and 110 mg/L Sodium Pyruvate; Gibco) supplemented with 10% (v/v) heat-inactivated fetal bovine serum (FBS; Sigma-Aldrich), 100 U/mL penicillin and 100 mg/ml streptomycin at 37°C and 5% CO₂.

SARS-CoV-2 Infection and Inhibitor Treatment

SARS-CoV-2 was obtained from The Peter Doherty Institute for Infection and Immunity (Melbourne, Australia), where the virus was isolated from a traveller from Wuhan arriving in

Melbourne and admitted to hospital in early 2020. Viral material was used to inoculate Vero/hSLAM cells for culture, characterisation and rapid sharing of the isolate (Caly et al., 2020).

For infection assays Calu-3 cells were seeded in a volume of 100 μ L DMEM F12 into tissue culture-treated flat-bottom 96-well plates (Falcon) at a density of 3.5×10^4 cells/well and incubated overnight before infection and/or treatment at confluency. On day of infection and/or treatment cells were washed twice with serum free DMEM medium and infected with SARS-CoV-2 and MOI of 0.1 in 25 μ L of serum-free medium containing TPCK trypsin (0.5 μ g/ml working concentration, ThermoFisher). Cells were cultured at 37°C and 5% CO₂ for 30 min. Cells were topped up with 150 μ L of medium containing PLpro inhibitor compounds at indicated concentrations in 6 replicates per concentration. At 48 h post infection/treatment, 100 μ L of supernatant was harvested from each well and kept frozen at -80°C.

Median Tissue Culture Infectious Dose (TCID₅₀) Assay

For TCID₅₀ assays, Vero cells were seeded in a volume of 100 μ L DMEM medium into tissue culture treated flat-bottom 96-well plates (Falcon) at a density of 1×10^4 cells/well and incubated overnight. The next day, Vero plates were washed twice with PBS and 125 μ L of DMEM +100 U/mL penicillin and 100 mg/ml streptomycin (serum free) + TPCK trypsin (0.5 μ g/ml working conc) was added and kept at 37°C, 5% CO₂. Calu-3 cell supernatants were thawed and serial 1:7 dilutions prepared in 96-well round bottom plates at 6 replicates per dilution. 25 μ L of serially diluted calu-3 supernatant were added onto Vero cells and plates incubated for 4 days at 37°C, 5% CO₂ before measuring cytopathic effect under a light microscope. The TCID₅₀ calculation was performed using the Spearman and Kärber method.

DATA AVAILABILITY STATEMENT

The datasets presented in this study can be found in online repositories. The names of the repository/repositories and accession number(s) can be found below: Protein Data Bank, ID: 7TZJ.

AUTHOR CONTRIBUTIONS

DK, GL and UN coordinated the study. DC performed crystallography, with help from TK, BCL, JN, MC and DK. NK and YY performed medicinal chemistry guided by GL and JM. BGCL ran high throughput screening under guidance from KL, KJ and JM, and with assistance of AA and TB. RB performed surface plasmon resonance. MD, JC and LM performed PC3 studies with input from MP. KK and EC performed ADME studies guided by SC. NK, GL, JM, DC, BCL, DK, PC, RB, TK and UN contributed to compound designs.

FUNDING

This work was funded by The Walter and Eliza Hall Institute of Medical Research, an NHMRC/MRFF “VirDUB” grant MRF2002119 (to DK, GL, MP, and PC), NHMRC Investigator Grants and Fellowships (GNT1178122 to DK, GNT0637350 to MP, and GNT1117089 to GL), a Wellcome Trust Grant (WT222698/Z/21/Z to DK, GL, and MP), NHMRC Independent Research Institutes Infrastructure Support Scheme grant (361646) and Victorian State Government Operational Infrastructure Support grant, and a generous donation by Hengyi Pacific Pty Ltd to support COVID-19 research. Compound screening was conducted at the Walter and Eliza Hall Institute’s National Drug Discovery Centre (NDDC). The NDDC received grant funding from the Australian Government and the Victorian State Government, with additional support from generous philanthropic donors including Mike Fitzpatrick, Helen Sykes and AWM Electrical. WEHI’s screening facilities and the Centre for Drug Candidate Optimisation (CDCO, Monash University) are also supported by Therapeutic Innovation Australia (TIA). TIA is supported by the Australian Government through the National Collaborative Research Infrastructure Strategy (NCRIS) program. The CDCO is also supported by the Monash Technology Research Platform network.

ACKNOWLEDGMENTS

We would like to thank Kanta Subbarao (Peter Doherty Institute, Melbourne) for live SARS-CoV-2 virus. The Australian Drug Discovery Library (ADDL) was compiled with the financial assistance of MTPConnect. We acknowledge Compounds Australia (www.compoundsaustralia.com) for their provision of specialised compound management and logistics services to the project. We would like to thank the Global Health Drug Discovery Institute (GHDDI, China) for providing the ReFRAME library. Crystallographic data collection was undertaken using the MX2 beamline at the Australian Synchrotron, part of ANSTO, and made use of the Australian Cancer Research Foundation (ACRF) detector. We would like to thank our CRO, Jubilant Biosys Ltd. (India) for their work in synthesizing some of the compounds described in this work.

SUPPLEMENTARY MATERIAL

The Supplementary Material for this article can be found online at: <https://www.frontiersin.org/articles/10.3389/fchem.2022.861209/full#supplementary-material>

Supplementary Figure S1 | (A) The screening data quality for the ReFRAME library screen was monitored by the robust Z', calculated on 128 negative and 128 positive control wells for each assay plate. All plates had a robust Z' > 0.5 with an average value of 0.65 across 9 plates. **(B)** Signal to background (S/B) ratio for each of the plates screen. S/B was consistent with an average of 3 across all plates screened. **(C)** Summary of screen data expressed at % inhibition. The hit selection criteria was defined as compounds where % inhibition was >2.5* MAD above the average of the negative control. There were 789 compounds identified using these criteria. 53

compounds were selected and the potency was determined in 10-point titrations. **(D)** 10-point titration for 53 compounds identified from a HTS of the ReFRAME library. Compounds were assayed at a top concentration of 100 μ M and titrated using 1:2 (PLpro) or 1:3 (USP21) serial dilutions. 100 μ M *rac5c* was used as a positive control for the HTS. The top 12 most potent compounds are also shown in **Figure 1B**.

Supplementary Figure S2 | (A) Dose response curves for *rac5c*, *5c*, *rac3k* and *3k*. The (R)-enantiomers of both *5c* and *3k* were synthesized and their activity was compared against their racemic counterparts. The inhibitory activity was tested in two independent experiments ($n = 2$) each containing two technical replicates using the HTS assay. Individual data points represent the mean replicate value for each experiment. **(B)** Chemical structure and dose response curve for the literature compound *GRL-0617*. The inhibitory activity was tested in two independent experiments ($n = 2$) each containing two technical replicates using the HTS assay. We observed a similar IC_{50} to reports in other studies (Fu et al., 2021; Ma et al., 2021; Osipiuk et al., 2021; Shen et al., 2021). This confirms observations seen with SARS-CoV that *5c* remains a more potent inhibitor PLpro. Individual data points represent the mean replicate value for each experiment.

Supplementary Figure S3 | (A) Electron density map $2|F_o| - |F_c|$ at 1 σ for the asymmetric unit. SARS-CoV-2 PLpro is shown as a ribbon and *3k* is shown in stick representation. **(B, C)** Electron density map $2|F_o| - |F_c|$ at 1 σ of the ligand binding site for *3k* in molecule A (chain A) or for molecule B (chain B), with key interacting/changed residues indicated. In both chains, clear electron density can also be seen atop the ligand that was modelled as a single molecule of DMSO. The DMSO is held in place by interacting with the carbonyl in *3k*.

Supplementary Figure S4 | To ensure the SARS-CoV-2 PLpro BL (PLpro^{BL}) mutant was active prior to calculating dose response curves, triubiquitin (top) and pro-ISG15 (bottom) cleavage was followed over time and visualised on Coomassie-stained SDS-PAGE gels [see Methods and (Klemm et al., 2020)]. PLpro^{BL} retained activity, though was less active compared to wild-type PLpro. A catalytically dead PLpro (PLpro^{C111S}) was used as a negative control for the assay.

Supplementary Figure S5 | (A) *3k* was tested for specificity to inhibit SARS-CoV PLpro, MERS-CoV PLpro, SARS-CoV-2 PLpro, or SARS-CoV-2 PLpro with residues 267-272 of blocking loop 2 (BL2) substituted for those in MERS-CoV (SARS-CoV-2^{BL}) in a UbRh assay. Inhibitor *3k* is cross-reactive with SARS-CoV PLpro and SARS-CoV-2 PLpro but not with MERS-CoV PLpro. These data indicate that engaging the conserved BL2 is crucial for the inhibition of PLpro by *3k*. Experiments were performed using the HTS assay as two independent experiments ($n = 2$) each containing two technical replicates. Individual data points represent the mean replicate value for each experiment. **(B)** SPR assays for compound *3k* against PLpro variants from **Figure 3B**. The top panels show double referenced sensorgram data as a function of time and the bottom show steady-state dose response curves. As for *5c*, absence of inhibitor reactivity with MERS-CoV PLpro can be explained by a loss in direct binding. Binding was measured by detecting changes in response units (RU) of the sensor chip. All SPR experiments were performed in triplicate; a representative example is shown. See **Supplementary Table S1** for all data and **Supplementary Figure S9** for the response curves of the remaining experiments.

REFERENCES

- Adams, P. D., Afonine, P. V., Bunkóczi, G., Chen, V. B., Echols, N., Headd, J. J., et al. (2011). The Phenix Software for Automated Determination of Macromolecular Structures. *Methods* 55, 94–106. doi:10.1016/j.ymeth.2011.07.005
- Aragão, D., Aishima, J., Cherukuvada, H., Clarken, R., Clift, M., Cowieson, N. P., et al. (2018). MX2: a High-Flux Undulator Microfocus Beamline Serving Both the Chemical and Macromolecular Crystallography Communities at the Australian Synchrotron. *J. Synchrotron Radiat.* 25, 885–891. doi:10.1107/s1600577518003120
- Baell, J. B., and Holloway, G. A. (2010). New Substructure Filters for Removal of Pan Assay Interference Compounds (PAIS) from Screening Libraries and for Their Exclusion in Bioassays. *J. Med. Chem.* 53, 2719–2740. doi:10.1021/jm901137j

Supplementary Figure S6 | Dose response curves used to calculate the inhibitory activity of the selected compounds shown in **Figure 5**. Experiments were performed using the HTS assay as two independent experiments ($n = 2$) each containing two technical replicates. Individual data points represent the mean replicate value for each experiment.

Supplementary Figure S7 | (A) Chemical structure and dose response curve for the literature compound *18* identified as compound *19* in the corresponding publication (Shan et al., 2021). The inhibitory activity was tested in four independent experiments ($n = 4$) each containing two technical replicates using the HTS assay and does not appear to improve on that seen for *5c* in our hands. Individual data points represent the mean replicate value for each experiment. **(B)** SPR assay for literature compound *18* against SARS-CoV-2 PLpro. The top panels show double referenced sensorgram data as a function of time and the bottom show steady-state dose response curves. No direct binding assays were performed in (Shan et al., 2021) and here we show the affinity for compound *18* lies within the range of *5c* and does not appear to improve on the binding affinity with PLpro. Binding was measured by detecting changes in response units (RU) of the sensor chip. All SPR experiments were performed in triplicate; a representative example is shown. See **Supplementary Table S1** for all data and **Supplementary Figure S9** for the response curves of the remaining experiments.

Supplementary Figure S8 | (A) *9* was tested for specificity to inhibit SARS-CoV PLpro, MERS-CoV PLpro, SARS-CoV-2 PLpro, or SARS-CoV-2 PLpro with residues 267-272 of blocking loop 2 (BL2) substituted for those in MERS-CoV (SARS-CoV-2^{BL}) in a UbRh assay. Inhibitor *9* is cross-reactive with SARS-CoV PLpro and SARS-CoV-2 PLpro but not with MERS-CoV PLpro. The presence of a methoxy on the naphthalene appears to favour improved metabolic stability rather than affecting direct binding with PLpro. Experiments were performed using the HTS assay as four independent experiments ($n = 4$) each containing two technical replicates. Individual data points represent the mean replicate value for each experiment. **(B)** SPR assays for compound *9* against PLpro variants from **Figure 3B**. The top panels show double referenced sensorgram data as a function of time and the bottom show steady-state dose response curves. The presence of a methoxy on the naphthalene appears to favour improved metabolic stability rather than affecting direct binding with PLpro. Binding was measured at steady-state by detecting changes in response units (RU) of the sensor chip averaging over 5 s prior to the end of the analyte injection. All SPR experiments were performed in triplicate; a representative example is shown. See **Supplementary Table S1** for all data and **Supplementary Figure S9** for the response curves of the remaining experiments.

Supplementary Figure S9 | All compounds tested by SPR were performed in triplicate as independent experiments. This Panel shows the remaining two dose response curves for the SPR assays noted throughout the main text and in **Supplementary Table S1**. The mean value of all three experiments \pm SD is reported throughout the text.

Supplementary Table S1 | SPR affinities determined at steady state for three independent experiments (Exp1, Exp2 and Exp3) reporting mean and 1 SD for each experiment group. Dose response curves are shown in **Figure 3C**, **Supplementary Figures S5, S7–S9**.

- Báez-Santos, Y. M., Barraza, S. J., Wilson, M. W., Agius, M. P., Mielech, A. M., Davis, N. M., et al. (2014). X-ray Structural and Biological Evaluation of a Series of Potent and Highly Selective Inhibitors of Human Coronavirus Papain-like Proteases. *J. Med. Chem.* 57, 2393–2412. doi:10.1021/jm401712t
- Báez-Santos, Y. M., St. John, S. E., and Mesecar, A. D. (2015). The SARS-Coronavirus Papain-like Protease: Structure, Function and Inhibition by Designed Antiviral Compounds. *Antiviral Res.* 115, 21–38. doi:10.1016/j.antiviral.2014.12.015
- Barretto, N., Jukneliene, D., Ratia, K., Chen, Z., Mesecar, A. D., and Baker, S. C. (2005). The Papain-like Protease of Severe Acute Respiratory Syndrome Coronavirus Has Deubiquitinating Activity. *J. Virol.* 79, 15189–15198. doi:10.1128/jvi.79.24.15189-15198.2005
- Begley, C. G., Ashton, M., Baell, J., Bettess, M., Brown, M. P., Carter, B., et al. (2021). Drug Repurposing: Misconceptions, Challenges, and Opportunities for Academic Researchers. *Sci. Transl. Med.* 13, eabd5524. doi:10.1126/scitranslmed.abd5524

- Békés, M., van der Heden van Noort, G. J., Ekkebus, R., Ovaa, H., Huang, T. T., and Lima, C. D. (2016). Recognition of Lys48-Linked Di-ubiquitin and Deubiquitinating Activities of the SARS Coronavirus Papain-like Protease. *Mol. Cell* 62, 572–585. doi:10.1016/j.molcel.2016.04.016
- Berrow, N. S., Alderton, D., Sainsbury, S., Nettleship, J., Assenberg, R., Rahman, N., et al. (2007). A Versatile Ligation-independent Cloning Method Suitable for High-Throughput Expression Screening Applications. *Nucleic Acids Res.* 35, e45. doi:10.1093/nar/gkm047
- Bevan, C. D., and Lloyd, R. S. (2000). A High-Throughput Screening Method for the Determination of Aqueous Drug Solubility Using Laser Nephelometry in Microtiter Plates. *Anal. Chem.* 72, 1781–1787. doi:10.1021/ac9912247
- Caly, L., Druce, J., Roberts, J., Bond, K., Tran, T., Kosteci, R., et al. (2020). Isolation and Rapid Sharing of the 2019 Novel Coronavirus (SARS-CoV-2) from the First Patient Diagnosed with COVID-19 in Australia. *Med. J. Aust.* 212, 459–462. doi:10.5694/mja2.50569
- Charman, S. A., Andreu, A., Barker, H., Blundell, S., Campbell, A., Campbell, M., et al. (2020). An *In Vitro* Toolbox to Accelerate Anti-malarial Drug Discovery and Development. *Malar. J.* 19, 1. doi:10.1186/s12936-019-3075-5
- Curran, R. E., Claxton, C. R. J., Hutchison, L., Harradine, P. J., Martin, I. J., and Littlewood, P. (2011). Control and Measurement of Plasma pH in Equilibrium Dialysis: Influence on Drug Plasma Protein Binding. *Drug Metab. Dispos.* 39, 551–557. doi:10.1124/dmd.110.036988
- Dolgin, E. (2021). The Race for Antiviral Drugs to Beat COVID - and the Next Pandemic. *Nature* 592, 340–343. doi:10.1038/d41586-021-00958-4
- Emsley, P., Lohkamp, B., Scott, W. G., and Cowtan, K. (2010). Features and Development of Coot. *Acta Crystallogr. D Biol. Cryst.* 66, 486–501. doi:10.1107/s0907444910007493
- Eng, H., Niosi, M., McDonald, T. S., Wolford, A., Chen, Y., Simila, S. T. M., et al. (2010). Utility of the Carboxylesterase Inhibitorbis-Para-Nitrophenylphosphate (BNPP) in the Plasma Unbound Fraction Determination for a Hydrolytically Unstable Amide Derivative and Agonist of the TGR5 Receptor. *Xenobiotica* 40, 369–380. doi:10.3109/00498251003706598
- Evans, P. R. (2011). An Introduction to Data Reduction: Space-Group Determination, Scaling and Intensity Statistics. *Acta Crystallogr. D Biol. Cryst.* 67, 282–292. doi:10.1107/s090744491003982x
- Evans, P. (2006). Scaling and Assessment of Data Quality. *Acta Crystallogr. D Biol. Cryst.* 62, 72–82. doi:10.1107/s0907444905036693
- Fan, K., Wei, P., Feng, Q., Chen, S., Huang, C., Ma, L., et al. (2004). Biosynthesis, Purification, and Substrate Specificity of Severe Acute Respiratory Syndrome Coronavirus 3C-like Proteinase. *J. Biol. Chem.* 279, 1637–1642. doi:10.1074/jbc.m310875200
- Freitas, B. T., Durie, I. A., Murray, J., Longo, J. E., Miller, H. C., Crich, D., et al. (2020). Characterization and Noncovalent Inhibition of the Deubiquitinase and deISGylase Activity of SARS-CoV-2 Papain-like Protease. *ACS Infect. Dis.* 6, 2099–2109. doi:10.1021/acsinfectdis.0c00168
- Fu, Z., Huang, B., Tang, J., Liu, S., Liu, M., Ye, Y., et al. (2021). The Complex Structure of GRL0617 and SARS-CoV-2 PLpro Reveals a Hot Spot for Antiviral Drug Discovery. *Nat. Commun.* 12, 488. doi:10.1038/s41467-020-20718-8
- Gao, Y., Yan, L., Huang, Y., Liu, F., Zhao, Y., Cao, L., et al. (2020). Structure of the RNA-dependent RNA Polymerase from COVID-19 Virus. *Science* 368, 779–782. doi:10.1126/science.abb7498
- Ghosh, A. K., Brindisi, M., Shahabi, D., Chapman, M. E., and Mesecar, A. D. (2020). Drug Development and Medicinal Chemistry Efforts toward SARS-Coronavirus and Covid-19 Therapeutics. *Chemmedchem* 15, 907–932. doi:10.1002/cmdc.202000223
- Ghosh, A. K., Takayama, J., Aubin, Y., Ratia, K., Chaudhuri, R., Baez, Y., et al. (2009). Structure-Based Design, Synthesis, and Biological Evaluation of a Series of Novel and Reversible Inhibitors for the Severe Acute Respiratory Syndrome-Coronavirus Papain-like Protease. *J. Med. Chem.* 52, 5228–5240. doi:10.1021/jm900611t
- Ghosh, A. K., Takayama, J., Rao, K. V., Ratia, K., Chaudhuri, R., Mulhearn, D. C., et al. (2010). Severe Acute Respiratory Syndrome Coronavirus Papain-Like Novel Protease Inhibitors: Design, Synthesis, Protein-Ligand X-Ray Structure and Biological Evaluation. *J. Med. Chem.* 53, 4968–4979. doi:10.1021/jm1004489
- Gui, W., Paudel, P., and Zhuang, Z. (2020). Activity-Based Ubiquitin Probes for Investigation of Deubiquitinases. *Compr. Nat. Prod. Iii* 2020, 589–602. doi:10.1016/b978-0-12-409547-2.14672-4
- Harcourt, B. H., Jukneliene, D., Kanjanahaluethai, A., Bechill, J., Severson, K. M., Smith, C. M., et al. (2004). Identification of Severe Acute Respiratory Syndrome Coronavirus Replicase Products and Characterization of Papain-like Protease Activity. *J. Virol.* 78, 13600–13612. doi:10.1128/jvi.78.24.13600-13612.2004
- Hartenian, E., Nandakumar, D., Lari, A., Ly, M., Tucker, J. M., and Glaunsinger, B. A. (2020). The Molecular Virology of Coronaviruses. *J. Biol. Chem.* 295, 12910–12934. doi:10.1074/jbc.rev120.013930
- Hassiepen, U., Eidhoff, U., Meder, G., Bulber, J.-F., Hein, A., Bodendorf, U., et al. (2007). A Sensitive Fluorescence Intensity Assay for Deubiquitinating Proteases Using Ubiquitin-Rhodamine110-glycine as Substrate. *Anal. Biochem.* 371, 201–207. doi:10.1016/j.ab.2007.07.034
- Heaton, S. M., Borg, N. A., and Dixit, V. M. (2016). Ubiquitin in the Activation and Attenuation of Innate Antiviral Immunity. *J. Exp. Med.* 213, 1–13. doi:10.1084/jem.20151531
- Hillen, H. S., Kocic, G., Farnung, L., Dienemann, C., Tegunov, D., and Cramer, P. (2020). Structure of Replicating SARS-CoV-2 Polymerase. *Nature* 584, 154–156. doi:10.1038/s41586-020-2368-8
- Hoffmann, M., Kleine-Weber, H., Schroeder, S., Krüger, N., Herrler, T., Erichsen, S., et al. (2020). SARS-CoV-2 Cell Entry Depends on ACE2 and TMPRSS2 and Is Blocked by a Clinically Proven Protease Inhibitor. *Cell* 181, 271–280. e8. doi:10.1016/j.cell.2020.02.052
- Hospenthal, M. K., Mevissen, T. E. T., and Komander, D. (2015). Deubiquitinase-based Analysis of Ubiquitin Chain Architecture Using Ubiquitin Chain Restriction (UbiCRest). *Nat. Protoc.* 10, 349–361. doi:10.1038/nprot.2015.018
- Janes, J., Young, M. E., Chen, E., Rogers, N. H., Burgstaller-Muehlbacher, S., Hughes, L. D., et al. (2018). The ReFRAME Library as a Comprehensive Drug Repurposing Library and its Application to the Treatment of Cryptosporidiosis. *Proc. Natl. Acad. Sci. U.S.A.* 115, 10750–10755. doi:10.1073/pnas.1810137115
- Kabsch, W. (2010). XDS. *Acta Crystallogr. D Biol. Cryst.* 66, 125–132. doi:10.1107/s09074449090047337
- Klemm, T., Ebert, G., Calleja, D. J., Allison, C. C., Richardson, L. W., Bernardini, J. P., et al. (2020). Mechanism and Inhibition of the Papain-like Protease, PLpro, of SARS-CoV-2. *Embo J.* 39. doi:10.15252/embj.2020106275
- Lee, H., Lei, H., Santarsiero, B. D., Gatz, J. L., Cao, S., Rice, A. J., et al. (2015). Inhibitor Recognition Specificity of MERS-CoV Papain-like Protease May Differ from that of SARS-CoV. *ACS Chem. Biol.* 10, 1456–1465. doi:10.1021/cb500917m
- Lindner, H. A., Fotouhi-Ardakani, N., Lytvyn, V., Lachance, P., Sulea, T., and Me'nard, R. (2005). The Papain-like Protease from the Severe Acute Respiratory Syndrome Coronavirus Is a Deubiquitinating Enzyme. *J. Virol.* 79, 15199–15208. doi:10.1128/jvi.79.24.15199-15208.2005
- Ma, C., Sacco, M. D., Xia, Z., Lambrinidis, G., Townsend, J. A., Hu, Y., et al. (2021). Discovery of SARS-CoV-2 Papain-like Protease Inhibitors through a Combination of High-Throughput Screening and a FlipGFP-Based Reporter Assay. *ACS Cent. Sci.* 7, 1245–1260. doi:10.1021/acscentsci.1c00519
- Malone, B., Urakova, N., Snijder, E. J., and Campbell, E. A. (2022). Structures and Functions of Coronavirus Replication-Transcription Complexes and Their Relevance for SARS-CoV-2 Drug Design. *Nat. Rev. Mol. Cell Biol.* 23, 21–39. doi:10.1038/s41580-021-00432-z
- McCoy, A. J., Grosse-Kunstleve, R. W., Adams, P. D., Winn, M. D., Storoni, L. C., and Read, R. J. (2007). Phasercrystallographic Software. *J. Appl. Cryst.* 40, 658–674. doi:10.1107/s0021889807021206
- Osipiuk, J., Azizi, S.-A., Dvorkin, S., Endres, M., Jedrzejczak, R., Jones, K. A., et al. (2021). Structure of Papain-like Protease from SARS-CoV-2 and its Complexes with Non-covalent Inhibitors. *Nat. Commun.* 12, 743. doi:10.1038/s41467-021-21060-3
- Perng, Y.-C., and Lenschow, D. J. (2018). ISG15 in Antiviral Immunity and beyond. *Nat. Rev. Microbiol.* 16, 423–439. doi:10.1038/s41579-018-0020-5
- Pruneda, J. N., Durkin, C. H., Geurink, P. P., Ovaa, H., Santhanam, B., Holden, D. W., et al. (2016). The Molecular Basis for Ubiquitin and Ubiquitin-like Specificities in Bacterial Effector Proteases. *Mol. Cell* 63, 261–276. doi:10.1016/j.molcel.2016.06.015
- Pushpakom, S., Iorio, F., Eyers, P. A., Escott, K. J., Hopper, S., Wells, A., et al. (2019). Drug Repurposing: Progress, Challenges and Recommendations. *Nat. Rev. Drug Discov.* 18, 41–58. doi:10.1038/nrd.2018.168
- Ratia, K., Pegan, S., Takayama, J., Sleeman, K., Coughlin, M., Baliji, S., et al. (2008). A Noncovalent Class of Papain-like Protease/deubiquitinase Inhibitors Blocks SARS Virus Replication. *Proc. Natl. Acad. Sci. U.S.A.* 105, 16119–16124. doi:10.1073/pnas.0805240105

- Ratia, K., Saikatendu, K. S., Santarsiero, B. D., Barretto, N., Baker, S. C., Stevens, R. C., et al. (2006). Severe Acute Respiratory Syndrome Coronavirus Papain-like Protease: Structure of a Viral Deubiquitinating Enzyme. *Proc. Natl. Acad. Sci. U.S.A.* 103, 5717–5722. doi:10.1073/pnas.0510851103
- Rawlings, N. D., Barrett, A. J., and Bateman, A. (2012). MEROPS: the Database of Proteolytic Enzymes, Their Substrates and Inhibitors. *Nucleic Acids Res.* 40, D343–D350. doi:10.1093/nar/gkr987
- Redhead, M. A., Owen, C. D., Brewitz, L., Collette, A. H., Lukacik, P., Strain-Damerell, C., et al. (2021). Bispecific Repurposed Medicines Targeting the Viral and Immunological Arms of COVID-19. *Sci. Rep.* 11, 13208. doi:10.1038/s41598-021-92416-4
- Rut, W., Lv, Z., Zmudzinski, M., Patchett, S., Nayak, D., Snipas, S. J., et al. (2020). Activity Profiling and crystal Structures of Inhibitor-Bound SARS-CoV-2 Papain-like Protease: A Framework for Anti-COVID-19 Drug Design. *Sci. Adv.* 6. doi:10.1126/sciadv.abd4596
- Shan, H., Liu, J., Shen, J., Dai, J., Xu, G., Lu, K., et al. (2021). Development of Potent and Selective Inhibitors Targeting the Papain-like Protease of SARS-CoV-2. *Cell Chem. Biol.* 28, 855–865. doi:10.1016/j.chembiol.2021.04.020
- Shen, Z., Ratia, K., Cooper, L., Kong, D., Lee, H., Kwon, Y., et al. (2021). Design of SARS-CoV-2 PLpro Inhibitors for COVID-19 Antiviral Therapy Leveraging Binding Cooperativity. *J. Med. Chem.* 65, 2940–2955. doi:10.1021/acs.jmedchem.1c01307
- Shin, D., Mukherjee, R., Grewe, D., Bojkova, D., Baek, K., Bhattacharya, A., et al. (2020). Papain-like Protease Regulates SARS-CoV-2 Viral Spread and Innate Immunity. *Nature* 587, 657–662. doi:10.1038/s41586-020-2601-5
- Subissi, L., Imbert, I., Ferron, F., Collet, A., Coutard, B., Decroly, E., et al. (2014). SARS-CoV ORF1b-Encoded Nonstructural Proteins 12–16: Replicative Enzymes as Antiviral Targets. *Antiviral Res.* 101, 122–130. doi:10.1016/j.antiviral.2013.11.006
- Turnbull, A. P., Ioannidis, S., Krajewski, W. W., Pinto-Fernandez, A., Heride, C., Martin, A. C. L., et al. (2017). Molecular Basis of USP7 Inhibition by Selective Small-Molecule Inhibitors. *Nature* 550, 481–486. doi:10.1038/nature24451
- Williams, C. J., Headd, J. J., Moriarty, N. W., Prisant, M. G., Videau, L. L., Deis, L. N., et al. (2018). MolProbity: More and Better Reference Data for Improved All-Atom Structure Validation. *Protein Sci.* 27, 293–315. doi:10.1002/pro.3330
- Wishart, D. S., Knox, C., Guo, A. C., Cheng, D., Shrivastava, S., Tzur, D., et al. (2008). DrugBank: a Knowledgebase for Drugs, Drug Actions and Drug Targets. *Nucleic Acids Res.* 36, D901–D906. doi:10.1093/nar/gkm958
- Zhang, L., Lin, D., Sun, X., Curth, U., Drosten, C., Sauerhering, L., et al. (2020). Crystal Structure of SARS-CoV-2 Main Protease Provides a Basis for Design of Improved α -ketoamide Inhibitors. *Science* 368, 409–412. doi:10.1126/science.abb3405
- Zhou, P., Yang, X.-L., Wang, X.-G., Hu, B., Zhang, L., Zhang, W., et al. (2020). A Pneumonia Outbreak Associated with a New Coronavirus of Probable Bat Origin. *Nature* 579, 270–273. doi:10.1038/s41586-020-2012-7

Conflict of Interest: DK serves on the Scientific Advisory Board of BioTherX Inc.

The remaining authors declare that the research was conducted in the absence of any commercial or financial relationships that could be construed as a potential conflict of interest.

Publisher's Note: All claims expressed in this article are solely those of the authors and do not necessarily represent those of their affiliated organizations, or those of the publisher, the editors, and the reviewers. Any product that may be evaluated in this article, or claim that may be made by its manufacturer, is not guaranteed or endorsed by the publisher.

Copyright © 2022 Calleja, Kuchel, Lu, Birkinshaw, Klemm, Doerflinger, Cooney, Mackiewicz, Au, Yap, Blackmore, Katneni, Crighton, Newman, Jarman, Call, Lechtenberg, Czabotar, Pellegrini, Charman, Lowes, Mitchell, Nachbur, Lessene and Komander. This is an open-access article distributed under the terms of the Creative Commons Attribution License (CC BY). The use, distribution or reproduction in other forums is permitted, provided the original author(s) and the copyright owner(s) are credited and that the original publication in this journal is cited, in accordance with accepted academic practice. No use, distribution or reproduction is permitted which does not comply with these terms.



Inhibitors of SARS-CoV-2 PLpro

Dale J. Calleja^{1,2}, Guillaume Lessene^{1,2,3*} and David Komander^{1,2*}

¹Walter and Eliza Hall Institute, Parkville, VIC, Australia, ²Department of Medical Biology, University of Melbourne, Melbourne, VIC, Australia, ³Department of Pharmacology and Therapeutics, The University of Melbourne, Melbourne, VIC, Australia

OPEN ACCESS

Edited by:

Wenshe Ray Liu,
Texas A&M University, United States

Reviewed by:

Rui Xiong,
University of Illinois at Chicago,
United States
Shiqing Xu,
Texas A&M University, United States

*Correspondence:

Guillaume Lessene
glessene@wehi.edu.au
David Komander
dk@wehi.edu.au

Specialty section:

This article was submitted to
Medicinal and Pharmaceutical
Chemistry,
a section of the journal
Frontiers in Chemistry

Received: 15 February 2022

Accepted: 28 March 2022

Published: 26 April 2022

Citation:

Calleja DJ, Lessene G and
Komander D (2022) Inhibitors of
SARS-CoV-2 PLpro.
Front. Chem. 10:876212.
doi: 10.3389/fchem.2022.876212

The emergence of SARS-CoV-2 causing the COVID-19 pandemic, has highlighted how a combination of urgency, collaboration and building on existing research can enable rapid vaccine development to fight disease outbreaks. However, even countries with high vaccination rates still see surges in case numbers and high numbers of hospitalized patients. The development of antiviral treatments hence remains a top priority in preventing hospitalization and death of COVID-19 patients, and eventually bringing an end to the SARS-CoV-2 pandemic. The SARS-CoV-2 proteome contains several essential enzymatic activities embedded within its non-structural proteins (nsps). We here focus on nsp3, that harbours an essential papain-like protease (PLpro) domain responsible for cleaving the viral polyprotein as part of viral processing. Moreover, nsp3/PLpro also cleaves ubiquitin and ISG15 modifications within the host cell, derailing innate immune responses. Small molecule inhibition of the PLpro protease domain significantly reduces viral loads in SARS-CoV-2 infection models, suggesting that PLpro is an excellent drug target for next generation antivirals. In this review we discuss the conserved structure and function of PLpro and the ongoing efforts to design small molecule PLpro inhibitors that exploit this knowledge. We first discuss the many drug repurposing attempts, concluding that it is unlikely that PLpro-targeting drugs already exist. We next discuss the wealth of structural information on SARS-CoV-2 PLpro inhibition, for which there are now ~30 distinct crystal structures with small molecule inhibitors bound in a surprising number of distinct crystallographic settings. We focus on optimisation of an existing compound class, based on SARS-CoV PLpro inhibitor GRL-0617, and recapitulate how new GRL-0617 derivatives exploit different features of PLpro, to overcome some compound liabilities.

Keywords: antiviral drug discovery, SARS-CoV-2, COVID-19, papain like protease (PLpro), Nsp3, GRL-0617, structure-activity relationship (SAR), medicinal chemistry

INTRODUCTION

The COVID-19 pandemic and its causative coronavirus (CoV), SARS-CoV-2 continues to wreak havoc in many countries. The rate at which global disruption took place and the continual challenges presented to countries globally, and to people individually, lack comparisons to any other events in past generations. Science stepped up to the challenge, and provided a remarkable response, and solutions, saving lives within a very short timeframe, through implementation of public health measures and even more strikingly, through rapid development of vaccines. Considering that global or local measures on how to deal with a pandemic were by-and-large non-existent prior to 2020, this has been an extraordinary feat. At the same time, the latest emergence of the SARS-CoV-2 Omicron variants (B.1.1.529) serves as a reminder that the pandemic is far from over and COVID-19 continues to kill people daily. It is now widely accepted that it is essential to not only provide

protection but also improve treatment options for individuals in which SARS-CoV-2 infection may lead to severe illness, hospitalisation, and death.

One form of such treatments emerges from exploiting the accumulated knowledge around the viral pathogens, in particular Coronaviruses (Almeida et al., 1968; Hartenian et al., 2020; V'kovski et al., 2020). The first Coronaviruses, B814 (Tyrrell and Bynoe, 1965), 229E (Hamre and Procknow, 1966) and OC43 (McIntosh et al., 1967) were identified in the late 1960s and CoV infections in humans are quite common, mostly leading to mild symptoms, and were therefore largely neglected in the wider population and in the scientific community (Paules et al., 2020). The first widely noted, deadly-to-human, CoV was SARS-CoV (Drosten et al., 2003; Ksiazek et al., 2003; Peiris et al., 2003), that caused an epidemic in 2003. Since then, new CoVs were identified frequently, to include NL63-CoV (Hoek et al., 2004), HKU1-CoV (Woo et al., 2005), MERS-CoV (Drosten et al., 2003; Boheemen et al., 2012), and then in December 2019, SARS-CoV-2 (Wu F. et al., 2020; Lu et al., 2020; Zhou et al., 2020; Zhu et al., 2020). Deadly (but not exceedingly infectious) viruses such as SARS-CoV and MERS-CoV clearly showed their pathological potential (Paules et al., 2020). Predicting the origin for SARS-CoV-2 or that of the next CoV remains difficult (Andersen et al., 2020; Zhang and Holmes, 2020; Holmes et al., 2021; Koopmans et al., 2021) largely because their use of discontinuous transcription for viral replication, which allows for a high rate of recombination between different species (Sola et al., 2015), a feature also noted in SARS-CoV-2 (Kim et al., 2020).

Despite this considerable sequence diversity within CoVs, the overall makeup of the CoV genome is identical and offers numerous functional access points for interference. The main steps in a viral life cycle include entry into the host cell, followed by release of the viral genome that is then translated by the host cells' ribosomes (Hartenian et al., 2020; V'kovski et al., 2020). The translation products are polypeptides that require processing, self-cleavage, into individual functional proteins that either have structural roles in forming viral particles, or non-structural roles such as facilitating replication of the viral genome. Assembly of new viral particles and exocytosis of the mature virions through the formation of double membraned vesicles (DMVs) completes the viral life cycle (Hartenian et al., 2020; V'kovski et al., 2020). The roles of each of the viral structural/accessory protein and non-structural proteins (nsps) have been studied extensively (Hartenian et al., 2020; V'kovski et al., 2020; Chazal, 2021). Targeting essential steps early in the process of viral replication has been the most successful strategy to stop CoV infection.

Creation of 16 individual nsps and (re)assembly of a subset to generate a functional viral replicase responsible for carbon-copying viral genetic material (Subissi et al., 2014; Malone et al., 2022) are the key upstream steps conserved in all CoVs, and have been the focus of antiviral drug discovery (Malone et al., 2022). The drug Remdesivir, first developed against the replicase of the Hepatitis C virus and later found to also target the Ebola virus (*Zaire Ebolavirus* of the *Filoviridae* family unrelated to CoVs) (Warren et al., 2016; Tchesnokov et al., 2019) and zoonotic CoVs (Sheahan et al., 2017; Agostini et al., 2018; Brown et al., 2019; Eastman et al., 2020), had been the first and for some time only

FDA approved small molecule treatment of COVID-19 (Beigel et al., 2020; FDA, 2020; Goldman et al., 2020; Spinner et al., 2020). Its utility has since been refuted by the World Health Organisation (WHO) (Consortium et al., 2020), and Remdesivir is no longer recommended for use in the clinic (WHO, Therapeutics and COVID-19 Living Guideline, 03 March 2022 Update). Ridgeback Therapeutics and Merck developed and clinically tested Molnupiravir, an oral SARS-CoV-2 replicase inhibitor, which was approved by the FDA in December 2021, and which was initially reported to show 50% efficacy against hospitalisation or death in COVID-19 patients (Bernal et al., 2021; Fischer et al., 2021). Molnupiravir benefitted from earlier work on the Venezuelan equine encephalitis virus (an *Alphavirus* of the *Togoviridae* family unrelated to CoVs) before its focus was shifted towards testing against CoVs. Molnupiravir inhibits viral replication in mouse models of SARS-CoV and MERS-CoV (Sheahan et al., 2020) and of SARS-CoV-2 in ferrets (Cox et al., 2021). Unlike Remdesivir which acts to terminate chain elongation during viral replication (Tchesnokov et al., 2019; Gordon C. J. et al., 2020), Molnupiravir induces countless mutations in the nascent RNA strand, effectively causing the virus to mutate itself to death (Gordon et al., 2021; Willyard, 2021). The efficacy of Molnupiravir has since been revised to 30% (Kozlov, 2021) and concerns were raised that Molnupiravir may induce mutations in patient DNA (Zhou et al., 2021). Despite these issues, Molnupiravir was FDA-approved in December 2021 for emergency use in at-risk adults (FDA, 2021).

The steps prior to assembly of the viral replicase present a further, exploitable viral Achilles Heel. Cleavage of the viral polyprotein is facilitated by two viral proteases that perform specific cleavage events to release individual nsps (Hartenian et al., 2020; V'kovski et al., 2020). The first protease is a papain-like protease domain, PLpro, within the large nsp3 protein, which is responsible for cleaving sequences between nsp1 and nsp2, nsp2 and nsp3, and nsp3 and nsp4 (Harcourt et al., 2004). The second protease is the main protease or Mpro encoded by nsp5, which is responsible for cleaving the polypeptides at 11 further sites to release the remaining 12 nsps (Fan et al., 2004). Both activities are essential for viral replication and therefore, both PLpro and Mpro are prime drug targets in CoVs, including SARS-CoV-2 (Hilgenfeld, 2014; Báez-Santos et al., 2015; Lei et al., 2018). Indeed, in late 2021, an oral Mpro inhibitor termed Nirmatrelvir successfully completed clinical trials (clinical trial identifier NCT04960202, NCT05011513) (Owen et al., 2021), and became the third FDA approved small molecule drug against SARS-CoV-2, reaching 89% efficacy in clinical settings against severely ill patients (NCT04960202). The development of Nirmatrelvir benefitted from corporate memory available within Pfizer, who restarted earlier drug discovery efforts targeting SARS-CoV Mpro, leading to a record-breaking timeline for the development of a first-in-human approved small molecule drug (Owen et al., 2021). Mpro inhibitors are further reviewed in (Cui et al., 2020) and (Mengist et al., 2021).

In this Review, we focus on inhibiting PLpro, the remaining highly attractive and druggable target in CoVs (also recently

reviewed in (Jiang et al., 2022)). Like Mpro, PLpro is a Cysteine protease, however both enzymes are structurally unrelated and cleave distinct sequences. Moreover, while Mpro appears to have only a small number of non-viral host substrates (Gordon DE. et al., 2020), PLpro moonlights as a potent regulator of host cell signalling processes for its ability to cleave ubiquitin and ubiquitin-like interferon-stimulated gene (ISG)15 posttranslational modifications. The latter deubiquitinase/DUB and deISGylase activities enable use of methodologies, tools and assays developed for current drug discovery efforts that target human DUBs, which have emerged as drug targets for a variety of conditions from cancer (Fraile et al., 2012) to neurodegenerative diseases (Schmidt et al., 2021); however to date only few DUB inhibitors have entered into clinical trials and none have been approved for use in humans (Schauer et al., 2020).

Despite cleaving ubiquitin and ISG15, PLpro is structurally dissimilar to human DUBs. Nevertheless, some parallels to human ubiquitin specific proteases (USPs) can be drawn (Mevisen and Komander, 2016). These similarities became apparent through the initial structural studies on SARS-CoV and MERS-CoV PLpro, reported over the last 15 years in a host of comprehensive studies by the Mesecar, Pegan, Lima and other labs (Harcourt et al., 2004; Barretto et al., 2005; Lindner et al., 2005; Ratia et al., 2006; Lee et al., 2015; Békés et al., 2016). The works explained biochemistry and substrate binding for DUB and ISG15 cleavage in molecular detail, and highlighted variations on the theme of PLpro activities present between CoVs. A further highly significant insight into SARS-CoV in particular, was the drugability of PLpro by small molecule inhibitors. Influential studies in 2008 and 2010 (Ratia et al., 2008; Ghosh et al., 2009, 2010) reported on two distinct chemical series, disclosed some of the first co-crystal structures of a DUB inhibited by small molecules, and presented considerable SAR data on each series of sub- μM inhibitors. A follow up study in 2014 then improved on the metabolic stability of these compounds, as well as presenting a co-crystal structure of SARS-CoV PLpro in complex with compound **3k** (Báez-Santos et al., 2014) (also see our associated manuscript, Calleja et al., in this issue).

In 2020, many research groups including ours quickly appreciated the high similarity at the sequence and structural level between SARS-CoV and SARS-CoV-2 PLpro, and excitingly, it was found that SARS-CoV PLpro inhibitors were able to also inhibit SARS-CoV-2 PLpro with almost identical activity profiles (Freitas et al., 2020; Klemm et al., 2020; Shin et al., 2020). We focussed our efforts on a series of compounds based on a central piperidine chemical scaffold, the most developed and potent SARS-CoV PLpro inhibitors available, and we showed that **5c**, a compound targeting SARS-CoV PLpro (Báez-Santos et al., 2014), was a potent *in vitro* inhibitor with antiviral activity in a cell-based SARS-CoV-2 infection model (Klemm et al., 2020). Our latest data on this series of compounds is discussed in Calleja et al. elsewhere in this issue. Many other groups focussed on a second chemical scaffold, exemplified by a compound named **GRL-0617** (Ratia et al., 2008; Ghosh et al., 2009). A wealth of data reported within the last 2 years, has since provided structural data to the Protein Data Bank (PDB) on numerous co-crystal structures for this scaffold. We here review the ideas and

progress revealed in recent publications, starting by a discussion of the manifold efforts to inhibit PLpro *via* available medicines, in drug repurposing campaigns.

DRUG REPURPOSING

Successful drug discovery efforts beginning from hit discovery can take decades and billions of dollars of investment. For PLpro and Mpro, earlier campaigns may (and in case of Mpro, did) accelerate such timelines considerably. However, when the pandemic hit, drug repurposing (or repositioning) was heralded as a way to fast track translation, with the assumption that within the available, but somewhat limited, collection of drugs approved for use in humans, some may have off-label uses for COVID-19. This initially offered high hopes of success, perhaps for the wrong reasons (Begley et al., 2021). In fact, there are only very few examples of successful drug repurposing (Begley et al., 2021).

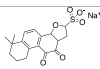
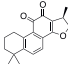
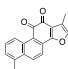
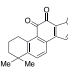
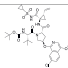
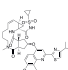
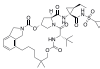
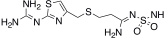
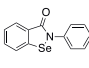
Nonetheless, many drug repurposing libraries exist that include FDA-approved small molecules, but also compounds that have undergone late-stage preclinical development or entered clinical trials. Such commonly used libraries include the ReFRAME (Repurposing, Focused Rescue and Accelerate MedChem) (Janes et al., 2018), the Sigma Aldrich LOPAC[®] 1,280 (List Of Pharmacologically Active Compounds) and other designer libraries, hand-selected by researchers. Many High Throughput Screening (HTS) campaigns for drug repurposing involved either target-based assays or phenotypic screening to identify drugs for treating COVID-19.

BIOCHEMICAL ASSAY DESIGN FOR PLPRO HTS—TECHNICAL CONSIDERATIONS

High throughput screens for viral proteases are typically activity based *in vitro* screens exploiting knowledge of protease target sequence(s). Most screens are based on fluorescence spectroscopy, where a fluorophore is conjugated to a peptide substrate based on its natural cleavage sequence. For PLpro, an additional route exploited its DUB activity. Activity-based DUB assays measure cleavage of a folded protein, ubiquitin, at its C-terminus, and enzymes such as PLpro not only comprise binding elements for the C-terminal sequence (LRLRGG) of ubiquitin or ISG15, but also contain a binding surface that covers a significant portion of the 8,000 Å² ubiquitin surface. Indeed, it has been shown that cleavage of a fluorophore conjugated to ubiquitin is >10,000-fold more efficient than cleavage of a peptide-only substrate. The presence of ubiquitin likely orients and stabilises the target peptide in the catalytic cleft, contributing to catalytic efficiency of the cleavage reaction (Dang et al., 1998).

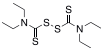
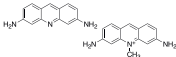
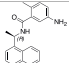
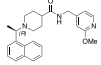
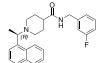
For both types of assays, hydrolysis of the substrate peptide or ubiquitin releases the fluorophore and generates a fluorescent signal indicative of enzyme activity that can be measured. 7-Amido-4-Methylcoumarin (AMC) (Dang et al., 1998) or a

TABLE 1 | Summary of reported drug repurposing attempts against SARS-CoV-2 PLpro.

Name	Chemical Structure(s)	Current Clinical Use(s)	Primary assay	Orthogonal Assay(s)	Counter Screen(s)	Comments	References(s)
Tanshinone and derivatives							
Sodium Tanshinone IIA Sulfonate		Hypertension, Myocardial infarction, coronary artery disease	Z-ALKGG-AMC	SPR (K_D of 61 μ M)	No	- Dosage used substantially higher than the clinic - K_D measured of 61 μ M	Xu et al. (2021)
Cryptotanshinone		Immunosuppressant, anticancer treatment, vasodilator	ISG15-FITC (FP assay) Plaque reduction assay	No	No	- Not tested against full Ub substrate - No assay to measure direct binding - More potent in cells than in biochemical assay, suggests cytotoxicity	Lim et al. (2021); Zhao et al. (2021)
Tanshinone I		Oncolytic treatment, chemopreventative agent	Abz-FTLKGGAPTKVT-DNP (FRET)	No	No	- Not tested against full Ub substrate	Lim et al. (2021)
Tanshinone IIA		Oncolytic drug, vasodilator, treatment of stroke				- No conclusive follow up assays - Known inducer of apoptosis Fang et al. (2021)	
HCV Drugs							
Asunaprevir		Hepatitis C Virus (HCV), NS3/4 serine protease inhibitor	Z-RLRGG-AMC	No	No	- Extremely low starting IC_{50} (54 μ M) - Optimised for a very different protease	Anson et al. (2020)
Simeprevir			Phenotypic screen	No	No	- Entirely phenotypic screen - Often a sharp decline in cell viability, indicating just lagging in dying of virus	Anson et al., (2020); Gammeltoft et al. (2021)
Vaniprevir/ Simeprevir			Z-RLRGG-AMC	No	No	- Follow up assays solely synergistic phenotypic screens	
Others							
Famotidine		H2AR agonist – stomach and intestinal ulcers	Z-ALKGG-AMC ISG15-FITC (FP assay)	No	No	- Dosing used far exceeds its intended indication - Refuted in a recent <i>in vitro</i> study Loffredo et al. (2021)	Wu et al., 2020a; Kandeel et al., 2020)
Ebselen		Meniere's disease and hearing loss	Ub-AMC	No	No	- Se is highly reactive against cysteines - Only showed inhibitory activity after a prolonged incubation	Sargsyan et al. (2020); Weglarz-Tomczak et al. (2021)
(Continued on following page)							

(Continued on following page)

TABLE 1 | (Continued) Summary of reported drug repurposing attempts against SARS-CoV-2 PLpro.

Name	Chemical Structure(s)	Current Clinical Use(s)	Primary assay	Orthogonal Assay(s)	Counter Screen(s)	Comments	References(s)
Disulfiram		Anti-cancer agent	Abz-FTLKGGAFTKVT-DNP (FRET)	No	No	- Likely nonspecific to all zinc finger containing proteins (including other DUBs)	Sargsyan et al. (2020)
Acriflavine		Nil	Z-RLRGG-AMC	No	No	- DNA intercalating agent - Biological targets are unclear	Napolitano et al. (2022)
Repurposed “lead” compounds							
GRL-0617		Nil	Varies (see Table 2)	Yes	Yes	- Repurposed early stage compound optimised for SARS-CoV	Shin et al. (2020) and see Table 2
5c		Nil	Ub-Rh110	Yes	Yes		Klemm et al. (2020); Shan et al. (2021)
3k		Nil	Ub-Rh110	Yes	Yes		Calleja et al. in this issue

disubstituted Rhodamine moiety (Rh110) (Hassiepen et al., 2007) are well established fluorophores for measuring enzymatic cleavage of ubiquitin substrates. AMC however, holds a significant disadvantage as its excitation wavelength is in the UV range (341 nm). While most HTS screens will use substrate concentrations of around or below the K_m to identify competitive inhibitors, in the situation of highly active enzymes (such as in the case of most viral proteases), the K_m for the enzyme is low and the concentration of compound required to detect inhibition is high enough such that compounds may absorb UV light, and thus run the risk of being potentially identified as false positives. The Rh110 moiety is advantageous in assaying for potential PLpro inhibitors, as it alleviates many of the AMC limiting factors, as well as provides a broader dynamic range. Pan Assay Interfering Compounds (PAINS) (Baell and Holloway, 2010) are a key challenge in any HTS campaign and may have been overlooked in some studies reported during the pandemic. Their identification can be difficult and can distract from bona fide hits. A key consideration in the identification of viral protease inhibitors is the design of suitable and ideally meaningful secondary assays and counter screens, to test for direct binding of compounds to target, and to assess specificity by testing compounds on other protease(s) (structurally similar or dissimilar). Indeed, from our experience, many small molecule “hits” from an enzymatic assay fail to confirm in orthogonal assays such as SPR and ITC, and therefore stringent criteria for activity and binding in orthogonal assays are essential for DUB drug discovery programs. Notably, the results reported over the last 2 years discussed below, have often failed to include careful evaluation and validation of the hits arising from HTS campaigns,

and most repurposing campaigns did not provide orthogonal analysis of their “hit” compounds (summarised in **Table 1**). Moreover, while *in vitro* assays are often performed against the PLpro domain in isolation, a further, important orthogonal assay expands on this work to test the activity of PLpro inhibitors towards full-length nsp3 as expressed by the virus. A nice advance for testing compounds against full-length nsp3, are cell-based activity assays based on the FlipGFP reporter (Zhang et al., 2019), an assay shown to be successful in detecting the inhibition of both Mpro (Froggatt et al., 2020) and PLpro (Ma et al., 2021).

CRITICAL ASSESSMENT OF EXAMPLES OF DRUG REPURPOSING “HITS”

Numerous drug repurposing studies reported putative PLpro inhibitors. We do not discuss a large set of *in silico* studies based on compound docking as they lack binding or inhibition data, but focus on those studies where biochemical data was obtained. For repurposing using a PLpro directed assay, distinct HTS libraries were used, including the ReFRAME library (Smith et al., 2020; Redhead et al., 2021) and Calleja et al. in this issue of *Frontiers In Chemistry*, LOPAC1280 (Klemm et al., 2020), ApexBio FDA approved drug library (Xu et al., 2021), the Pathogens Box Library from Medicines for Malaria Venture (Smith et al., 2020), and libraries of FDA approved drugs and natural products from Selleck Chem (Zhao et al., 2021). In addition, some reports used custom, hand-selected compound libraries (Anson et al., 2020; Lim et al., 2021). Each effort yielded

putative PLpro inhibitors, summarised in **Table 1** and discussed below.

Tanshinone and Derivatives

Multiple studies have reported Tanshinone derivatives as inhibitors of SARS-CoV-2 viral replication with PLpro as the proposed target (Lim et al., 2021; Xu et al., 2021; Zhao et al., 2021). Tanshinones are compounds found naturally in the plant *Salvia miltiorrhiza* commonly used in Chinese medicine. It is thought that many naturally bioactive molecules are inhibitors of the CoV proteases (Benarba and Pandiella, 2020; Khare et al., 2020; Chen W. et al., 2021) and the fact that Tanshinones have appeared in multiple independent studies, including that for SARS-CoV, could indicate it is a true inhibitor of PLpro. A follow-up study (Ma and Wang, 2022) thoroughly tested the reported Tanshinone based compounds in a cellular assay, and invalidated earlier findings by showing that compound activity was much lower than reported. Moreover, many of the aforementioned studies lack effective orthogonal assays demonstrating a direct interaction between these compounds and PLpro. Tanshinone derivatives feature many chemical liabilities; two reactive ketone groups and an orthoquinone moiety are known to be redox substrates. Redox cycling compounds have been shown to generate hydrogen peroxide (H_2O_2) in the presence of reducing agents found in most protein buffers (Johnston, 2011). The presence of a strong oxidant such as H_2O_2 in biochemical screening assays could interfere with assay readouts and/or would likely irreversibly oxidise the catalytic cysteine of PLpro and render the protein inactive—with the causative compounds appearing as false positives. On the other hand, it is interesting that only Tanshinone derivatives with a naphthalene group (Tanshinone I) were able to inhibit DUB activity (Park et al., 2012), as this chemical group features strongly in known PLpro inhibitors (see below). Lack of evidence for direct binding, but more concerningly, no assessment of off-target effects and/or cellular toxicity, make this inhibitor class an unlikely contender for a useful PLpro-based drug.

Hepatitis C Drugs Asunaprevir, Simeprevir and Grazoprevir

Another set of known drugs gaining traction for use as COVID treatment came from a boutique library of FDA approved Hepatitis C virus (HCV) drugs. Asunaprevir, Simeprevir and Grazoprevir (Anson et al., 2020) are nanomolar HCV NS3/NS4 serine protease inhibitors and were suggested to also target SARS-CoV-2 PLpro. One report (Gammeltoft et al., 2021) showed that combination treatment of Remdesivir with either Simeprevir, Grazoprevir or Paritaprevir was able to reduce viral titers in an *in vitro* viral replication assay. However, it was not clear whether these effects were synergistic nor did the work specify a putative target for the drugs. As for many identified treatments of viral replication, there was also a delicate balance between effectiveness and

cytotoxicity at the concentrations required. The resulting poor Selectivity Index of the compounds suggests that use in humans would be challenging. Another study (Bafna et al., 2021) showed promising synergistic data for Paritaprevir and Grazoprevir in combination with Remdesivir. The hypothesis that PLpro is the target of the drugs was undermined by data showing only a weak inhibitory activity (20–25%) against PLpro in an AMC assay (Bafna et al., 2021). Again, this suggested that compound efficacy is most likely due to off-target effects. As before, incomplete reports lacking thorough biochemical investigation combined with the need for high, likely toxic, dosages of these compounds raises questions about their use as effective treatments for COVID-19 and for their specificity towards PLpro. Moreover, with a starting IC_{50} of $54\mu M$ (Anson et al., 2020) for Asunaprevir, medicinal chemistry to improve these already complex compounds would prove challenging.

Famotidine

Famotidine entered the repurposing stage after reports of a retrospective study in China highlighted patients taking the drug exhibited improved clinical outcomes—the data associated with these reports remain unpublished. Famotidine, marketed as Pepcid®, is an FDA approved histamine H2 receptor antagonist prescribed to treat heartburn. Two retrospective studies later conducted in the US also confirmed similar findings (Freedberg et al., 2020; Mather et al., 2020), however, like most reports for repurposed drugs, the mechanism of action underlying the observed beneficial effects remain ill-defined (Mura et al., 2021). One computational study suggested Mpro (Wu C. et al., 2020) as the target, while another suggested PLpro (Kandeel et al., 2020). Experimental data found no evidence for Famotidine to bind or inhibit PLpro *in vitro*, and the compound was unable to inhibit SARS-CoV-2 replication in a cellular infection model (Loffredo et al., 2021). It is possible that the observed clinical benefits of Famotidine resulted from its primary function as a histamine H2A receptor antagonist (Malone et al., 2021). Nevertheless, the DrugBank (Wishart et al., 2006, 2017) database indicates that Famotidine has entered a number of clinical trials for the treatment of COVID-19 (DrugBank Accession Number DB00927); the results of the studies are yet to be released.

Cysteine Modifying Compounds, Ebselen and Disulfiram

Ebselen and Disulfiram are two cysteine reactive compounds, which were previously identified as inhibitors of SARS-CoV and MERS-CoV PLpro (Lin et al., 2018) and more recently of SARS-CoV-2 PLpro and Mpro (Jin et al., 2020; Ampornnanai et al., 2021). For PLpro, it was proposed that enzyme inhibition occurs by inducing oxidation of the catalytic cysteine, or one of the cysteines found in the zinc finger domain, thereby reducing PLpro stability (Sargsyan et al., 2020; Weglarz-Tomczak et al., 2021). Interestingly, similar

reactivity with the catalytic cysteine of Mpro was recently observed, sparking optimistic hopes of a multitarget drug. However, Ebselen is a Selenium containing promiscuous cysteine protease inhibitor (Ma et al., 2020). A recent structure of Ebselen in complex with PLpro C111S mutant (PDB 7M1Y) showed that Ebselen binds distally from both the active site and the zinc binding “Fingers” domain (unpublished). Indeed, the lack of specificity (Ma et al., 2020), common occurrence as a false-positive hit in HTS campaigns, and promiscuous and likely toxic nature of the compounds make such broad oxidants questionable for clinical development towards a viral protease.

Acriflavine

Acriflavine (ACF), published as a low μM (IC_{50}) PLpro inhibitor, was another drug identified with potential for repurposing. ACF showed promising antiviral activity in a number of different cell lines though it was unable to rival Remdesivir in blocking viral replication in the lungs of K18-ACE2 mice (Napolitano et al., 2022). The published structure of PLpro in complex with a component of ACF, Proflavine (PDB 7NT4), indicates Proflavine is the active component inhibiting PLpro. Proflavine exists as a low level DNA intercalating agent (and hence a possible carcinogen) (Gatasheh et al., 2017), which likely elicits an antiviral response *via* premature activation of the cGAS-STING pathway (Pépin et al., 2017). Confounding its on-target specificity, ACF has been shown to reduce tumour growth by directly inhibiting HIF-1 α dimerization (Lee et al., 2009). ACF appears to be under investigation for its use in treating diseases such as cancer (Cheloni et al., 2017; Mangraviti et al., 2017; Nehme et al., 2020) and malaria (Dana et al., 2014); or as a topical ointment for treating chronic urinary tract infections (Gama et al., 2020). The myriad of indications points towards the polypharmacology of Acriflavine and it is important to note that this compound is not currently approved by the FDA for any of these indications.

PHENOTYPIC SCREENS

In addition to PLpro targeted *in vitro* screens, numerous phenotypic screens, measuring the impact of available drugs on SARS-CoV-2 replication in cells, have been performed and reported. While simple conceptually, phenotypic screens can be more complex than biochemical assays and require careful target identification and validation studies to fully elucidate the mechanism underpinning the cellular effect. Phenotypic screen also do not alleviate the need for extensive medicinal chemistry (Moffat et al., 2017). As a result, many compounds dubbed as having potential for repurposing (Riva et al., 2020) have not been further explored. Several detailed reviews recently covered the various drug repurposing attempts for SARS-CoV-2 (Guy et al., 2020; Santos et al., 2020; Ng et al., 2021).

Most prominently, phenotypic screens were performed using a number of known libraries such as the ReFRAME library (Riva et al., 2020), or those from the National Centre for Advancing Translational Sciences (NCATS) (Chen C. Z. et al., 2021), and

some of these studies suggested some candidate drugs that inhibited SARS-CoV-2. However, the target of these drugs in a phenotypic screen could either be a viral protein, or a host protein essential for the virus. Importantly, from a PLpro targeting perspective, there was no overlap between putative PLpro inhibitors from *in vitro* studies, and compounds derived from phenotypic screens. This suggested that identified PLpro targeting compounds were not active in phenotypic screens and that compounds derived from phenotypic screens were unlikely to act through PLpro.

Conclusion for Part I: Drug Repurposing Remains a Complex and Challenging Approach

At the start of the pandemic, without vaccination or active antiviral drugs, drug repurposing was heralded as a silver bullet, and repurposing campaigns were deemed quick-and-easy ways to produce clinic-ready anti-virals. This was ill-considered as outlined recently (Begley et al., 2021), since the development process for any drug remains complex with many ethical and financial considerations such as intellectual property, clinical equipoise and understanding of the drug in a new disease context. In the rare cases where a drug has been repurposed, considerable pre-clinical work is still needed prior to clinical studies. Another concept that seems underappreciated is that drugs are often designed to be very specific modulators of their target proteins. It is therefore highly unlikely that the same compound will have a similar level of potency against an unrelated target. As a consequence, it is likely that significant medicinal chemistry efforts would still be required.

Still, in the DrugBank database, there are currently over 3,000 clinical trials directed towards repurposing efforts for the treatment of COVID-19. Following three separate clinical trials, Remdesivir is currently the only repurposed drug to receive FDA approval for treating COVID-19 (Beigel et al., 2020; FDA, 2020; Goldman et al., 2020; Spinner et al., 2020). This is not surprising, as the mechanism behind viral RNA-dependent-RNA polymerases (RdRp) are inherently conserved. Remdesivir is a nucleoside analogue, required by all viruses to replicate, and initially it held promise as a broad-spectrum antiviral medication. However, despite the apparent theoretical similarities, even Remdesivir failed to be an efficacious drug against COVID-19 and would likely require re-development to optimise it for the SARS-CoV-2 Replicase.

“Lead repurposing” however, has nicely worked for SARS-CoV-2 PLpro. We and others showed that early-stage inhibitors developed for SARS-CoV PLpro are also efficacious against SARS-CoV-2 PLpro. The two most potent of these, **5c** and **GRL-0617**, originated from earlier high throughput screening campaigns followed up by substantial structure guided medicinal chemistry efforts (Ratia et al., 2008; Ghosh et al., 2009; Báez-Santos et al., 2014). While development of SARS-CoV PLpro inhibitors stopped well short of clinical studies, both series have been further advanced against SARS-CoV-2. The efforts toward repurposing outlined above are summarised in **Table 1** and we further discuss our own data on **5c** series of compounds in the associated research paper (Calleja et al., this issue). Here, we focus on latest reported developments for **GRL-0617** series compounds.

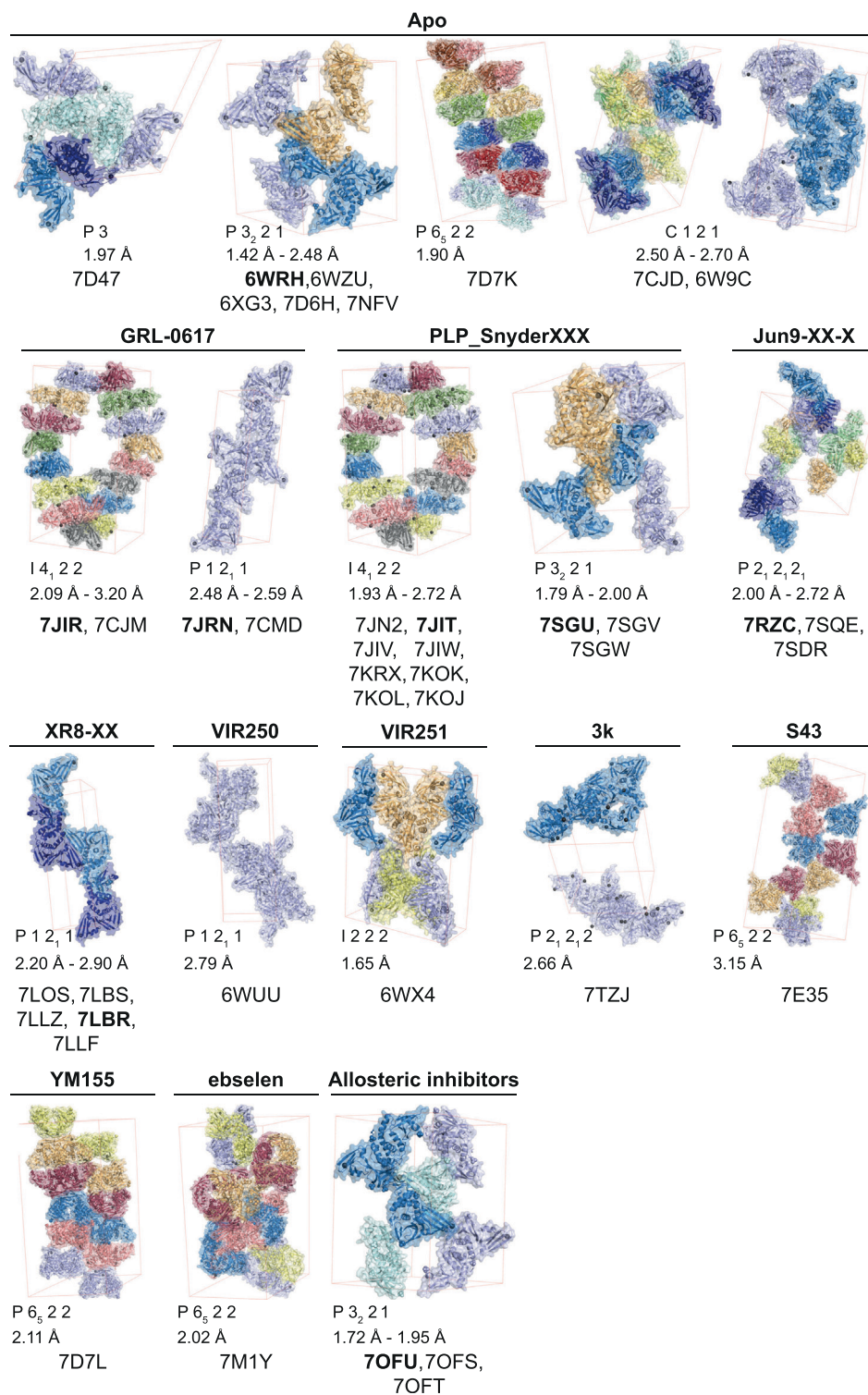


FIGURE 1 | Reported apo and compound structures of SARS-CoV-2 PLpro. Shown are unliganded and compound bound structures publicly released in the Protein Data Bank (PDB) since the beginning of the COVID-19 pandemic. The unit cell for each space group is shown (thin red lines) and the corresponding symmetry mates from the asymmetric unit are depicted with matching colours. The structures are grouped according to their bound ligands, the ligand is labelled above each unit cell, and the corresponding PDB accession numbers shown below. The obtained resolution or resolution range for each crystallographic setting is indicated.

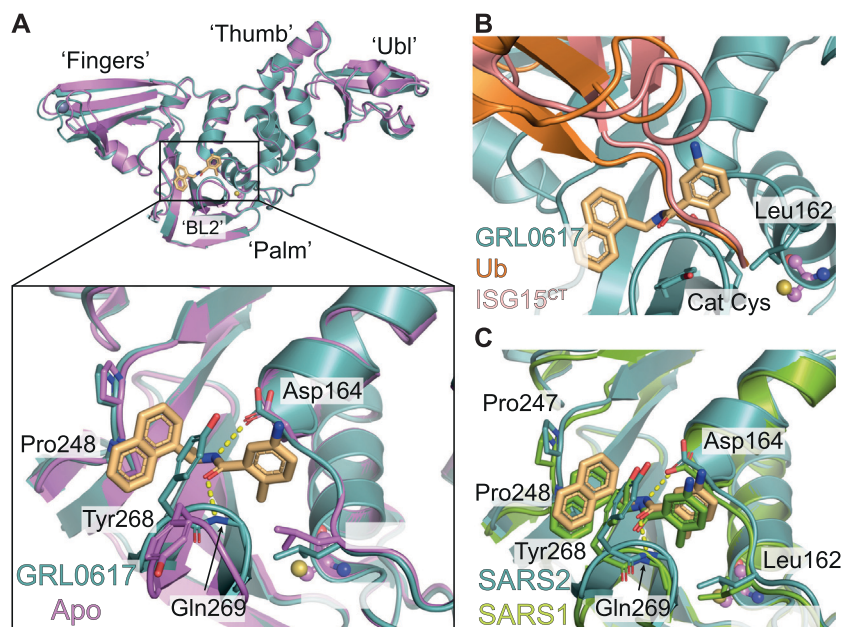


FIGURE 2 | Molecular basis for inhibition of SARS-CoV-2 PLpro by **GRL-0617**. **(A)** Structure of SARS-CoV-2 PLpro bound to **GRL-0617** in teal (PDB 7JRN (Ma et al., 2021)), with inhibitor in wheat colour in ball-and stick representation representing the (R)-enantiomer. A close-up view of the ligand binding site for **GRL-0617** with key residues indicated is also shown and hydrogen bonds are displayed as a dashed yellow line. A superimposed structure of apo PLpro [purple, PDB 6WZU (Osipiuk et al., 2021)] shows that the inhibitor does not induce global conformational changes. The catalytic Cys is shown in ball and stick representation, and a bound zinc ion in apo PLpro is shown as a grey sphere. **(B)** Close-up view of the **GRL-0617** binding site overlaid with ubiquitin from the ubiquitin-PLpro complex in orange [PLpro ~ Ub, PDB 6XAA (Klemm et al., 2020)] and with ISG15 from PLpro bound to the C-terminal ISG15 Ubl fold in pink [PLpro ~ ISG15^{CT}, PDB 6XA9 (Klemm et al., 2020)]. The orthomethyl residues in a pocket formed by Leu162, Tyr264, and Tyr273 occupying the position of the Arg74 in Ub or Arg155 in ISG15. Upon ligand binding, Leu162 rotates its side chain to block the channel and the path of the Ubl tail to the catalytic Cys111. The catalytic Cys111 is shown in ball and stick representation. **(C)** Close up view of the ligand binding site for **GRL-0617** in SARS-CoV-2 PLpro in teal overlaid with SARS-CoV PLpro in green [PDB 3E9S (Ratia et al., 2008)]. Key residues are fully conserved between SARS-CoV and SARS-CoV-2 which explains cross specificity of compounds. Hydrogen bonds are displayed as a dashed yellow line.

Structural Biology Enables SARS-CoV-2 PLpro Drug Discovery

The start of the pandemic triggered by a previously unknown pathogen, has led to an unprecedented response of the structural biology community that focused on the proteins of SARS-CoV-2 with all available tools and techniques. As a result, structures of the SARS-CoV-2 proteome have flooded the PDB. The first crystal structures of PLpro were those bound to monoubiquitin (PDB 6XAA) (Klemm et al., 2020), the C-terminal domain of human ISG15 (ISG15^{CTD}, PDB 6XA9) (Klemm et al., 2020), full length mouse ISG15 (PDB 6YVA) (Shin et al., 2020), as well as high resolution apo structures [PDB IDs 7D47, 7NFV, 6W9C—unpublished, 6WRH, 6WZU, 6XG3 (Osipiuk et al., 2021), 7D6H (Shan et al., 2021), 7D7K (Zhao et al., 2021) and 7CJD (Gao et al., 2020)]. The first inhibitor bound structures utilised peptide-based inhibitors, VIR250 (PDB 6WUU) (Rut et al., 2020) and VIR251 (PDB 6WX4) (Rut et al., 2020). Collectively, these apo- and substrate-bound structures were instrumental to provide comprehensive insight into PLpro function and mechanism, but also highlighted the rather high similarity between SARS-CoV and SARS-CoV-2 PLpro. Notably, SARS-CoV-2 PLpro appears to be highly amenable to crystallisation, and there are to date 14 distinct crystal settings (different space

groups and/or unit cell dimensions) for PLpro and its complexes (Figure 1). Indeed, the majority of by-now available structures of SARS-CoV-2 PLpro, are complex structures with bound inhibitors, especially from the **GRL-0617** class (Figures 1, 2). Elsewhere in this issue, we report a structure of SARS-CoV-2 PLpro bound to inhibitor **3k** explaining intricacies of the piperidine carboxamide based inhibitors, **5c** and **3k**. This series of compounds were reviewed early in the pandemic (Ghosh et al., 2020) and we discuss our medicinal chemistry efforts geared towards addressing metabolic liabilities of these compounds.

Definition and exploitation of the **GRL-0617** binding pocket or ‘hot spot’ (Fu et al., 2021), which is shared with **3k/5c**-class compounds, has substantially benefited from structure-guided drug design. New reports focussing on optimising **GRL-0617** for its binding site are published frequently, and the current state-of-play is reviewed in the next sections.

Origin of **GRL-0617**

HTS campaigns performed by the team of Andrew Mesecar against SARS-CoV PLpro, followed by extensive medicinal chemistry led to the development of **GRL-0617** (Ratia et al., 2008; Ghosh et al., 2009), a SARS-CoV inhibitor with sub-μM

TABLE 2 | Currently reported potencies (IC_{50} , μM) of *GRL-0617* against SARS-CoV-2 PLpro.

IC_{50} (μM)	Primary assay	References
1.15	Ub-Rh110	Calleja et al. this issue
0.74	Ub-AMC	Shin et al. (2020)
1.50	ISG15-AMC	
0.88	Ub-AMC	Ma et al. (2021)
1.68	ISG15-AMC	
1.39	Z-RLRGG-AMC	Zhao et al. (2021)
1.61	Z-RLRGG-AMC	Shen et al. (2021)
2.1	Z-RLRGG-AMC	Fu et al. (2021)
2.2	(DabcyI)-FTLRGGAPTKV-(Edans)	Gao et al. (2020)
2.3	LKGG-(CV-2)	Osipiuk et al. (2021)
2.4	Z-RLRGG-AMC	Freitas et al. (2020)

activity *in vitro* that inhibited SARS-CoV viral replication in cell-based infection studies. The mechanism of inhibition was explained *via* a co-crystal structure (PDB 3E9S) (Ratia et al., 2008), highlighting how the compound targeted the binding channel required to interact with the cleavage motif. Researchers quickly realised that identical residues line the

ligand binding sites in SARS-CoV-2 PLpro, and it was no surprise that *GRL-0617* also inhibited viral replication of SARS-CoV-2 (Freitas et al., 2020; Shin et al., 2020). These results further cemented PLpro as an excellent drug target for COVID-19 antiviral treatments. Subsequent structures of SARS-CoV-2 PLpro in complex with *GRL-0617* (Gao et al., 2020; Fu et al., 2021; Osipiuk et al., 2021) confirmed that the binding site and mode of inhibition, as a reversible competitive inhibitor, was virtually identical to that for SARS-CoV PLpro.

OVERVIEW OF THE PLPRO INHIBITOR BINDING SITE

GRL-0617 binds to a groove within the ‘Palm’ domain of PLpro (for nomenclature **Figure 2A**), used to hold the cleavage motif of PLpro. However, the most prominent aspect of its binding mechanism relies on a flexible segment, termed blocking loop 2 (BL2) (Lee et al., 2015), a β -hairpin that folds over the core of the compound and shields it from solvent. Tyr268 at the tip of the β -hairpin restrains the substituted benzamide, almost entirely

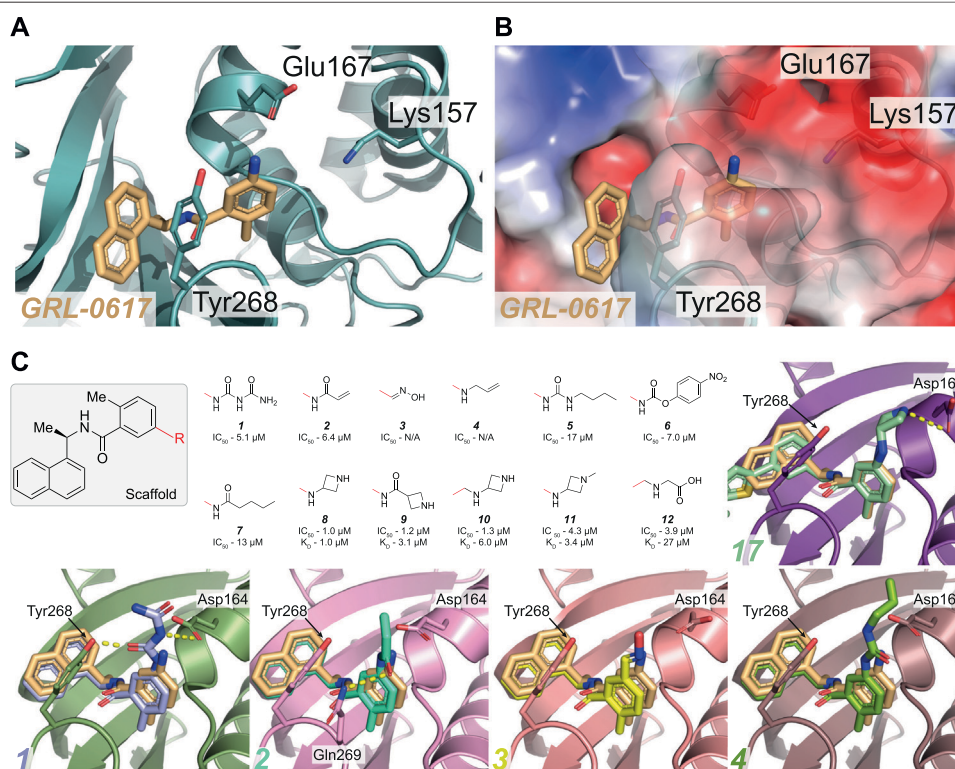


FIGURE 3 | Overview of the reported attempts to target Glu167 in PLpro. **(A,B)** Close up view of the *GRL-0617* binding pocket with PLpro in teal in cartoon representation **(A)** or as with the calculated surface charge overlaid **(B)**. The inhibitor is shown in wheat colour in ball and stick representation. Residues Lys157 to Glu167 in the PLpro Thumb domain form a shallow negatively charged pocket. Several compounds target the side chain of Glu167 to improve potency of *GRL-0617*. **(C)** The *GRL-0617* scaffold (boxed) was extended at the para-position of the benzene ring (at the R position). The red line indicates the handle used for the respective substituents - in *GRL-0617* an amino group is present at this position. Given compound data refer to, IC_{50} from *in vitro* activity assays, and K_D values from SPR where available (See **Table 3** for the compound identifiers from their respective publications). Basic amines appear to be most tolerated at this position while replacement with alkyl groups are detrimental to activity of the compound. Co-crystal structures for **1–4** and **17** (**Figure 4**) are shown [PDB IDs **1** (7JIT), **2** (7JIW), **3** (7KOL), **4** (7KOJ), **17** (7LBS)]. Compounds **3** and **4** were published in the PDB but excluded from the final publication, so no IC_{50} data is available (Osipiuk et al., 2021).

TABLE 3 | Compound IDs from their respective studies for those reported in **Figures 2–5**.

Review ID	Reference ID	IC ₅₀ (μM)	Primary assay	References	Review ID	Reference ID	IC ₅₀ (μM)	Primary assay	References
1	Snyder_495 (2)	5.1	LKGG-(CV-2)	Osipiuk et al. (2021)	20	XR8-89 (94)	0.11	Z-RLRGG-AMC	Shen et al. (2021)
2	Snyder_530 (3)	6.4			21	XR8-69 (89)	0.37		
3 ^a	Snyder_496	—			22	XR8-23 (72)	0.39		
4 ^a	Snyder_494	—			23	XR8-32-1 (75)	0.97		
5	5	17			24	XR8-30 (74)	0.75		
6	6	7			25	DY-3-63 (18)	>100		
7	7	13			26	ZN-2-193 (21)	>10		
8	ZN-2-184 (5)	1.01	Z-RLRGG-AMC	Shen et al. (2021)	27	ZN-2-192 (20)	4.8	(DabcyI)-FTLRGGAPTKV-(Edans)	Ma et al. (2021)
9	ZN-2-186 (7)	1.2			28	Jun9-13-7	7.3		
10	DY2-144 (14)	1.3			29	Jun9-13-9	6.7		
11	ZN-2-188-2 (11)	4.3			30	Jun9-53-2	0.89		
12	ZN-3-56 (13)	3.9			31	Jun9-72-2	0.67		
13	ZN-3-80 (65)	0.59			32	Jun9-87-3	0.80		
14	XR8-8 (66)	1.3			33	Jun9-87-2	0.90		
15	ZN-3-79 (59)	1.9			34	Jun9-87-1	0.87		
16	DY-2-153 (60)	1.8			35	Jun9-75-5	0.56		
17	XR8-24 (73)	0.56			36	Jun9-84-3	0.67		
18	XR8-65 (86)	0.33			37	Jun9-75-4	0.62		
19	XR8-83 (92)	0.21			38	Jun9-85-1	0.66		

^a**3** and **4** structures were published in the PDB, prior to publication of (Osipiuk et al., 2021), but excluded from the final publication. The two compounds were presented in this Review to illustrate their structural features.

burying it in the enzyme (**Figure 2A**). On one side of the compound, the naphthyl ring extends into a hydrophobic groove between BL2 and the Palm domain, packing against Pro247 and Pro248. Two hydrogen bonds further stabilise the compound in its binding site; the amide nitrogen of the compound with the side chain of Asp164 of the “Thumb” domain; and the amide carbonyl of the compound with the backbone of Gln269 on BL2 (**Figure 2A**). Towards the catalytic Cys111, some 7 Å away, an orthomethyl group on the substituted phenyl ring fits into a hydrophobic pocket lined by Leu162, Tyr264 and Tyr273 (**Figures 2A,B**), occupying the position of the usually positively charged residue (Lys or Arg) preceding the Gly-Gly motif (including Arg74 in ubiquitin or Arg155 in ISG15; hereafter, we refer to the ubiquitin residue numbers). Leu162 that lines the channel in apo and substrate bound structures, rotates its side chain to block the channel and the path to catalytic Cys111, and now interacts with the substituted phenyl of the compound (**Figures 2A,B**) (see peptide inhibitors below for an example of where Leu162 indeed rotates again to open the congested channel). This conformational change is seen in all **GRL-0617** or **5c** compound structures to date and is a good indicator of compound binding.

As discussed above, the binding mode for **GRL-0617** to SARS-CoV-2 PLpro could be anticipated due to high structural and sequence identity with SARS-CoV PLpro. Indeed, the interacting residues and all compound interactions are conserved between SARS-CoV and SARS-CoV-2 PLpro (**Figure 2C**). The work in the last 2 years elaborated the vicinity of the GRL scaffold, mainly in order to improve on the observed IC₅₀ of ~1–2 μM *in vitro* (**Table 2** for a list of

current studies, their HTS assay(s) and observed IC₅₀ of **GRL-0617**). Since **GRL-0617** was already the result of extensive medicinal chemistry, most researchers attempted to achieve potency increase by expanding the **GRL-0617** core.

Targeting Glutamate 167 (Glu167)

The first crystal structures of **GRL-0617** bound to SARS-CoV-2 PLpro reveal that the orientation of the steric clash between the orthomethyl group on the benzene ring and the amide group forces the methyl into an orientation that mimics the substrate backbone of ubiquitin Arg74 (**Figures 2B, 3A**). In this orientation, the charged Glu167 side chain is solvent exposed and within reach by expanding from the 5-amino group towards (**Figures 3A,B**). Prior SAR on SARS-CoV PLpro indicated that changes to this site were tolerated (Ghosh et al., 2009; Welker et al., 2021) and hence several groups have since attempted to expand from this handle.

One of the earliest groups to design compounds targeting Glu167 (**1–7**, **Figure 3C** and **Table 3**) was at the Centre for Structural Genomics of Infectious Diseases (CSIG), and reported co-crystal structures for four compounds (**1–4**, **Figure 3C**) (Osipiuk et al., 2021). In **1**, a carbonyl group creates additional hydrogen bonds with Glu167 (3.0 Å bond distance) and Tyr268 hydroxyl from the BL2 loop (2.4 Å), whereas an acrylamide moiety in **2** adopts a different conformation, forming a H-bond interaction with the side chain of Gln269 (3.2 Å). The remaining compounds (**3–4**) make no new interactions (**Figure 3C**). Although **1** and **2** both have additional contacts with PLpro, they incur a > 2-fold loss in potency observed in comparison with **GRL-0617**

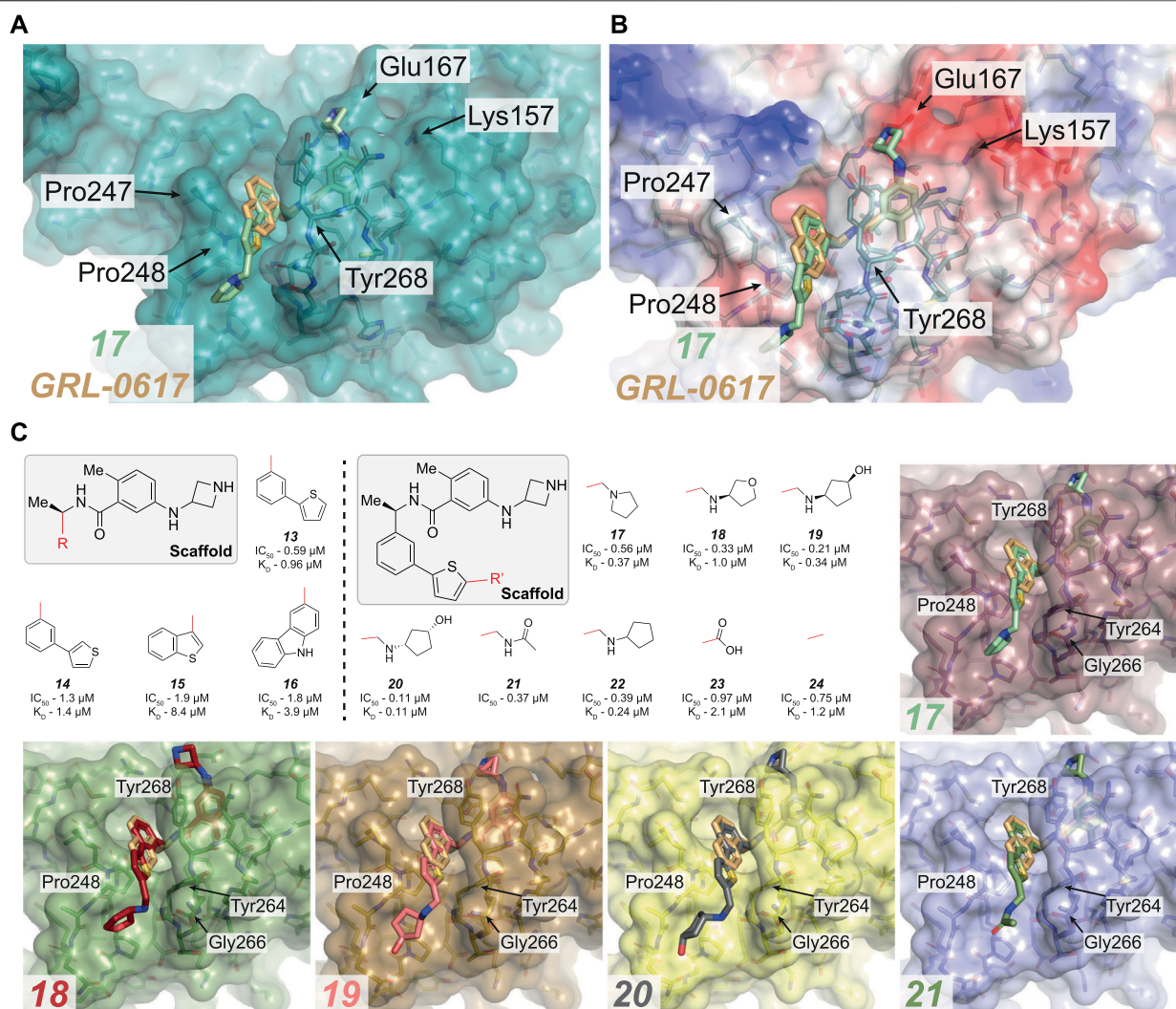


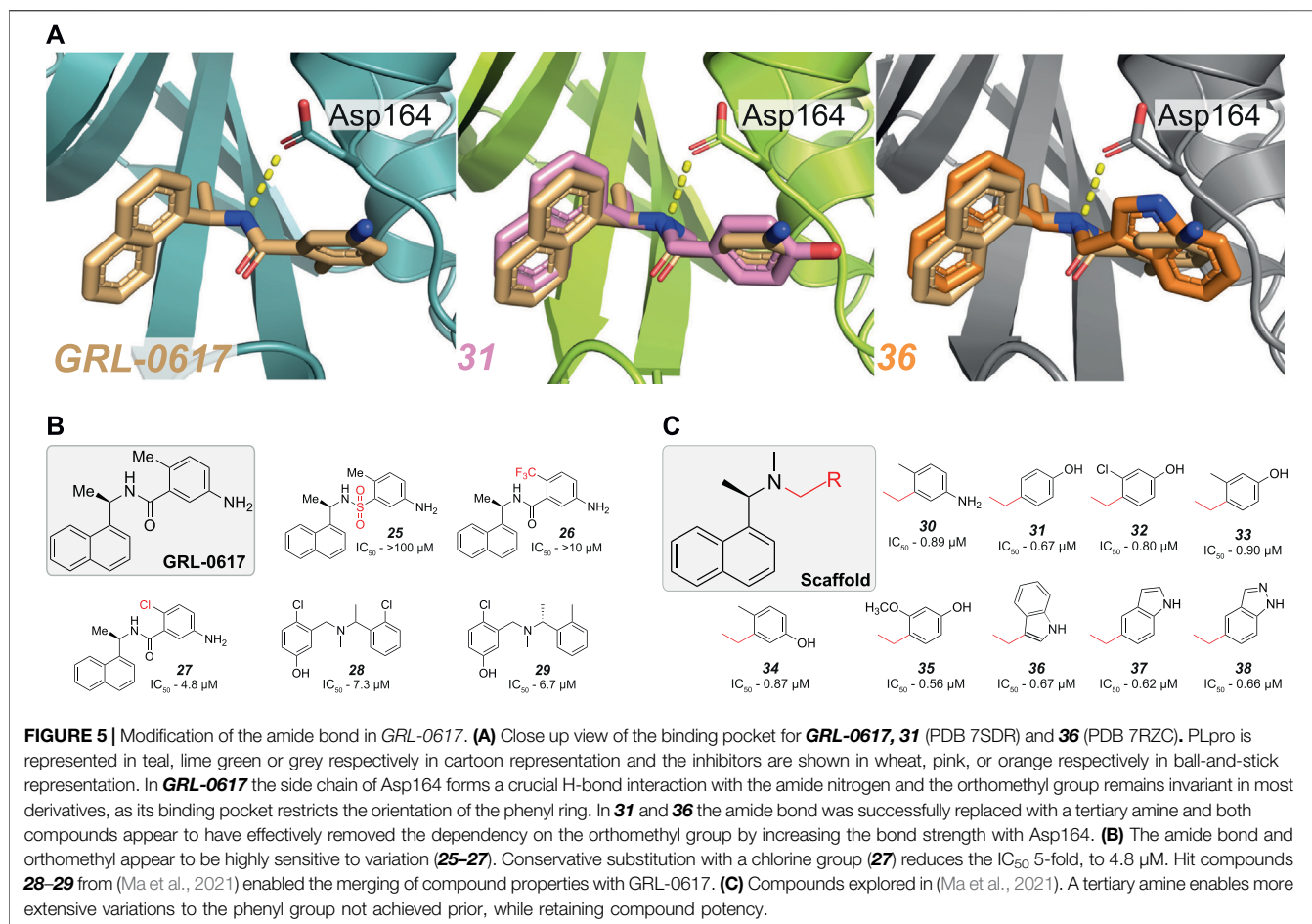
FIGURE 4 | Overview of compounds which successfully replaced the naphthyl ring in **GRL-0617**. **(A,B)** Close up view of the **GRL-0617** binding pocket with PLpro represented in teal in cartoon representation overlaid with the surface representation **(A)** or calculated surface charge of the protein **(B)**. **GRL-0617** in wheat colour and compound **17** in green are depicted in ball and stick representation. In **(A)** the key residues are noted to highlight the BL2 groove formed by closure of the blocking loop and induced upon ligand binding. **17** shows that the replacement of the naphthalene ring with a 2-phenylthiophene appears to effectively replace the dependency of the naphthyl group. The BL2 groove is then engaged by a basic amine tail to improve potency. **(C)** Boxed (left), the parent scaffold for modifying the naphthyl group. Boxed (right) Second iteration of compound designs, starting at the 2-phenyl thiophene scaffold (**13**). The red line indicates the handle used for the respective substitution. Compound data refer to IC₅₀ from *in vitro* activity assays, and K_D values from SPR where available (see **Table 3** for the compound identifiers from their respective publications). **13–16**, the 2-phenyl thiophene appears to successfully replace the naphthyl ring while still maintaining potency. **17–24**, Aromatics containing basic amines appear to be the most potent at this position. Co-crystal structures for **17–21** are shown [PDB IDs, **17** (7LBS), **18** (7LOS), **19** (7LLF), **20** (7LBR), **21** (7LLZ)]. In the case of **17**, the basic nitrogen interacts with residues lining the BL2 groove.

(**Table 2**) suggesting that the new interactions do not enhance the stability of the complex. Similarly, all other compounds reported in (Osipiuk et al., 2021) (**5–7**, **Figure 3C**), did not improve on **GRL-0617**.

Another series of compounds (Shen et al., 2021) observed the variable activity of extensions towards Glu167 (**8–12**, **Figure 3C**). The direct addition of an azetidine ring to the 5-amino group of **GRL-0617** in **8** provided the most potent and successfully increased the potency of **GRL-0617** from 1.6 to 1.0 μM (**Table 2**; **Figure 3C**). A modelled structure of **8**

highlighted a potential interaction between Glu167 and the azetidine nitrogen, a prediction then confirmed by a crystal structure of a related compound, from the same study (**17**, **Figure 3C**) (Shen et al., 2021). In **17**, the naphthyl ring is replaced with a 2-phenylthiophene scaffold (**Figure 4**), the effects of which are described in the next section.

Alternative analogues prepared by Osipiuk et al. (2021) also engaged Glu167, but none of them were as potent as the azetidine containing compounds reported by Shen et al. (2021). Azetidine nitrogens are more basic than amides,



ureas, anilines, or carbamates used by Osipiuk et al., which may explain the marked difference in efficacy. Compounds **8**, **9**, and **10** display a narrow IC_{50} range of 1.0, 1.2 and 1.3 μ M (Figure 3C), respectively, but differing only in their positioning of the H-bond acceptor. Removing the H-bond acceptor entirely in this position resulted in a 4-fold loss of potency (compounds **11–12**). It is interesting to note that these subtle changes in protein-ligand interactions appear more pronounced when comparing the K_D values of these compounds obtained by SPR (1.0, 3.1 and 6.0 μ M respectively, Figure 3C).

It is clear from Osipiuk et al. (2021) and Shen et al. (2021), that targeting Glu167 in isolation is unlikely to provide significant improvement in activity required to justify *in vivo* studies. Nevertheless, both studies provided valuable structural information about PLpro compound binding.

Targeting the BL2 Groove and the Naphthyl Ring

The naphthyl ring in *GRL-0617*, a moiety crucial for its activity, packs in a tight hydrophobic pocket of PLpro (Figures 4A,B). The original SAR for naphthyl ring

substitutions was performed for SARS-CoV PLpro: both empirical and computational methods confirmed its replacements obliterate compound activity (with the 1-naphthyl being preferred over the 2-naphthyl) (Ghosh et al., 2009; Amin et al., 2021; Welker et al., 2021). Notwithstanding its contribution to the binding affinity of *GRL-0617* to PLpro, naphthyl groups come with many liabilities (outlined below), so it is not surprising that many groups have attempted to find more suitable and druglike isosteres.

Naphthyl moieties exist in clinically used drugs in a broad range of diseases, but their presence must be carefully considered as they can add significant metabolic liabilities and are often viewed as toxicophores (Makar et al., 2019). In addition, they significantly increase lipophilicity of a compound. Shen et al. (2021) combined their designs targeting Glu167 with additional changes to the naphthyl ring (**13–16**, Figure 4C and Table 3), achieving sub- μ M efficacy *in vitro* (**17–24**, Figure 4C and Table 3). Their most successful replacement was a 2-phenylthiophene scaffold, which notably leveraged binding cooperativity when combined with the azetidine ring targeting Glu167 (compare **8** in Figure 3C and **13** in Figure 4C). Interestingly, further substitutions to this scaffold were tolerated (**17–24**, Figure 4C) and those with a basic amine “tail” were favoured (**17–22**, Figure 4C).

Several structures were reported (17–21), and each highlighted that the novel scaffold targeted a previously unexplored hydrophobic “BL2 groove” found adjacent to the blocking loop; (Shen et al., 2021). Intriguingly, all but compound 17 showed disordered ‘tail’ regions in BL2 groove, suggesting that it remains highly flexible. It might be possible that each of the “tail” regions are trapped by a network of transient interactions with residues lining the BL2 groove (Gly266, Pro248 and Tyr264) that together contribute to an overall lower free energy state, possibly explaining the observed mobility and disorder within the crystal structures. In the case of 17, the basic nitrogen interacts with residues lining the BL2 groove - including the amide backbones of Tyr264 and Tyr268 (Figure 4C), and explains the observed improvement in potency when compared to the thiophene scaffold alone (compare 13). 17 also exhibited a ~5-fold lower dissociation rate (K_D) and improved antiviral efficacy over **GRL-0617**. It was exciting to see the improved antiviral efficacy accompanied by the replacement of the naphthyl group. Replacing this compound moiety is a promising development on this class of inhibitors as it likely represents a metabolic liability along the path to the clinic.

A Tertiary Amine Connects GRL-0617 Based Compounds to Asp164

Another delicate interaction formed between PLpro and **GRL-0617** is a network of hydrogen bonds between the central carboxamide, the side chain of Asp164 and the backbone nitrogen of Gln269 (Figures 2A, 5A). Various attempts have failed to replace the central amide in **GRL-0617** (Shen et al., 2021; Welker et al., 2021) where the isosteric change to a sulphonamide group also dramatically reduced activity (25, Figure 5B and Table 3) (Shen et al., 2021). In **GRL-0617**, the amide is juxtaposed by the orthomethyl substituent found on the phenyl ring amide (Figure 5A) mimicking the backbone of ubiquitin Arg74. The orthomethyl is invariant in all iterations of **GRL-0617** mentioned thus far, and compound activity is extremely sensitive to changes at this site (Ghosh et al., 2009; Shen et al., 2021). For example, changing the methyl for a trifluoro-methyl (26, Figure 5B and Table 3), a larger group with different electronegativity, ablated compound activity, whereas exchanging the methyl with a chlorine group (27, Figure 5B and Table 3) decreases potency by ~5-fold (Shen et al., 2021).

Another recent HTS campaign (Ma et al., 2021), identified two hit compounds (28–29, Figure 5B and Table 3) which differed from **GRL-0617** in that the hits were lacking the naphthyl ring and the central amide was replaced with a tertiary amine. Furthering their efforts, the team were able to merge the properties of all three compounds to achieve sub μ M efficacy in many of their optimised compounds (30–38, Figure 5C). In **GRL-0617**, the carboxamide carbonyl forms a connection with the backbone nitrogen of Gln269 (Figure 2A), a connection presumably lost when replaced with a tertiary amine. In their new compounds, the tertiary amine would likely be protonated in physiological conditions - exposing a positively charged

nitrogen instead of the neutral NH of the amide. Interestingly, the protonated tertiary amine appeared to substitute for the loss of the carboxamide connection, as 30 still retained equipotent activity to **GRL-0617**. Structures from two of their optimised compounds, were later released by the CSIG (31, 36, Figure 5A, PDB 7SDR and 7RZC, respectively) confirming that the amine indeed formed a more prominent H-bond with the side chain of Asp164—the carboxyl group of which rotates slightly to optimise the interaction (Figure 5A, compare **GRL-0617**).

Another important insight from this new scaffold was that it allowed for a greater diversity of substitutions on the phenyl group, alleviating the need for an orthomethyl group. Similar potency was achieved with compounds where the *ortho*-position was either unsubstituted (31, Figure 5C), substituted with chlorine (32, Figure 5C) or larger groups (33–35, Figure 5C) and further, the entire phenyl could be replaced with an indole group (36–38, Figure 5C). Hence, the idea to replace the amide bond with a tertiary amine appears to have unlocked a useful new scaffold for SAR exploration.

The above examples highlight the progress of the scientific community in elaborating a decade-old PLpro inhibitor, **GRL-0617**, through iterative medicinal chemistry. While not discussed here, many of the applied design principles may also guide improvements for other PLpro inhibitor series, in particular the piperidine scaffolds exemplified by compounds 5c and 3k (see Table 1). Whilst not achieved to date, we are confident that low nM inhibitors for PLpro, likely required for meaningful clinical translation, are within reach.

An Alternative Strategy: Covalent Peptide Inhibitors

A common strategy to target Cys proteases is to identify and then permute peptide-based inhibitors that directly target the catalytic Cys. While peptide inhibitors are challenging as drugs due to metabolic liabilities, susceptibility towards amide bond hydrolysis and poor cell penetration, they are a mainstay for medicines mimicking protein-protein interactions (PPIs) (Lau and Dunn, 2018). This strategy has worked recently for Mpro, and is the basis for the now-FDA approved covalent Mpro peptidomimetic inhibitor from Pfizer, Nirmatrelvir (Owen et al., 2021). An important aspect was that Mpro is exquisitely specific for hydrolysing substrates directly after a glutamine residue, a property not seen in any human cysteine protease, alleviating cross-specificity and toxicity concerns. This is somewhat more of a problem for PLpro, since the existing PLpro target preference for the LXGG (Rut et al., 2020) motif is present in ~100 DUBs and other ubiquitin-like proteases in the human genome.

Yet, the Olsen group generated competitive, covalent peptide inhibitors for PLpro from a combination of natural and unnatural amino acids (Rut et al., 2020). The peptides, dubbed VIR250 and VIR251, were effective inhibitors across multiple CoV species however, their specificity against human Ubl proteases were not reported. Peptide inhibitors may prove

useful in deciphering the required residues that dictate specificity through the protease active site, and the co-crystal structures obtained (PDB 6WUU, 6WX4) contributed early-on to the detailed characterisation of SARS-CoV-2 PLpro.

To improve on the efficacy of such inhibitors for PLpro, there have been recent attempts at combining the specificity of small molecules (such as **GRL-0617**) with the potency of covalent peptides or war heads (Liu et al., 2021a; Parks et al., 2021). In particular the latter manuscript, currently available as a preprint, discusses how **GRL-0617** is derivatised to reach the catalytic Cys111, and a crystal structure shows that Leu162 indeed rotates again to open the congested channel typically observed in liganded PLpro structures. It is interesting to note that PLpro retains this plasticity, though it appears that other compounds (2 in **Figure 3C**) are unable to invoke this conformational change despite incorporating potential covalent war heads.

This approach to synthesize peptide-drug conjugates (PDCs) targeting SARS-CoV-2 PLpro appeared to improve on specificity toward the catalytic cysteine. Yet, these PDCs were still found to be nonselective for the other ten cysteines found in PLpro (Liu et al., 2021a). While peptide-based inhibitors remain an interesting avenue for development, the issues of their specificity for PLpro, and typically low oral bioavailability indicate that, as for Nirmatrelvir (Owen et al., 2021), significant medicinal chemistry will be required to convert the peptidic features into more favourable drug-like properties.

Other Identified Small Molecule Inhibitors of PLpro

There are several other studies that identified small molecule inhibitors of PLpro that are here mentioned for completeness. One study identified the Survivin inhibitor YM155 (Zhao et al., 2021), and while a structure bound to PLpro was released (PDB 7D7L), it appears that no direct interactions are taking place to indicate this is a true PLpro inhibitor. Further, the side chain from the crucial Tyr268 residue, claimed to embrace the compound in a similar fashion to **GRL-0617**, remains unresolved in the submitted structure. In addition, YM155 was also found to be cytotoxic in a recent follow up study (Ma and Wang, 2022).

Another study identified a well-known pan DUB inhibitor, PR-619 (Liu et al., 2021b) and the USP1 inhibitor SJB2-043 as direct inhibitors of PLpro. Both highlight the similarity of PLpro to human DUBs, and may be interesting tools for *in vitro* experiments, though **GRL-0617** seems a superior tool at this point. Others also identified 6-thioguanine and 6-mercaptopurine (Sivakumar and Stein, 2021; Swaim et al., 2021), which were later invalidated as either inactive or toxic in follow-up cellular assays (Ma and Wang, 2022). Finally, a number of naturally occurring compounds were also highlighted (Srinivasan et al., 2021) for their activity as allosteric inhibitors of PLpro (preprint at the time of

writing this Review). Structures of these (**Figure 1**) highlighted that they inhibit substrate binding at the S2 site of PLpro, a feature not yet seen for any PLpro inhibitors. Allosteric inhibitors are a largely unexplored avenue for targeting PLpro and it remains unclear how effective such inhibitors would be in the context of inhibiting full length Nsp3. While new insights may be gleaned from e.g., structural work with non-specific compounds in principle, all mentioned compounds seem very far away to warrant clinical development.

CONCLUSION AND OUTLOOK

We have witnessed the unprecedented rise of a global pandemic caused by the lethal coronavirus SARS-CoV-2. To date, it is estimated that COVID-19 has killed almost 6 million people worldwide. However, the response from the scientific community has also been unprecedented, in scale, speed and collaborative spirit. Many researchers have refocused their efforts to better understand, and eventually help defeat, SARS-CoV-2, and we have witnessed a striking number of incredible scientific achievements, first-and-foremost a global vaccination effort based on latest technological achievements. In addition, the pandemic has propelled to the forefront, and shown the immense value of, areas of basic research that were considered niche only a few years ago. Indeed, the achievements described here were building on a rich well of prior knowledge, provided by a small number of research labs that have studied earlier coronaviruses for decades, and whose work has identified cell biological and biochemical mechanisms, validated and de-risked viral targets, and provided essential starting points to make quick progress in drug discovery.

It is clear that antiviral drugs for COVID-19 remain one of the most pressing necessities to regain normality after the pandemic. The first antivirals have recently emerged and will quickly become key tools for clinicians treating COVID-19 patients. However, it can also be safely assumed that SARS-CoV-2 will find a way to alleviate this new attack, and the emergence of drug resistance mutants is just a matter of time. For this and other reasons, our efforts to develop new antivirals, for SARS-CoV-2 and ideally all CoVs, need to continue and require long-term support and funding.

In our minds, PLpro is the prime untapped target for the next CoV antiviral medicine. It is, by now, well-studied and understood, essential for CoV lifecycle, and its moonlighting functions as DUB and deISGylase derail our cellular inflammatory responses, a hallmark of the most marked pathologic outcomes of COVID-19. This latter function as a DUB, presents challenges and opportunities. On one hand, specific DUB inhibitors are notoriously challenging to develop, and have to date only been achieved for a handful of DUBs out of the pool of ~100 human enzymes. For example, the USP7 specific inhibitors, FT671 and FT827, each relied on pockets not found in the apo or substrate

bound forms of the enzyme, and which were induced upon ligand binding (Turnbull et al., 2017). This feature is also observed for the current PLpro inhibitors which target the BL2 “hot spot” and though the scaffolds targeting this site had been relatively limited prior to the pandemic, the studies mentioned in this Review have highlighted possibilities to generate novel chemical scaffolds. Only one DUB inhibitor has entered clinical trials to date. Surprisingly and despite high structural conservation of PLpro required to cleave specific sequences, to date the identified inhibitors seem all SARS-CoV and SARS-CoV-2 specific and do not target MERS-CoV (most other CoV PLpros have not been assessed). It needs to be seen whether a pan-CoV PLpro inhibitor is achievable.

Nonetheless, as we detail in this Review, armed with prior knowledge from SARS-CoV and in just 2 years we have seen rapid developments to advance a promising inhibitor scaffold, based on **GRL-0617**. Further increases in potency are paramount to enter lead optimisation, and then a detailed assessment and improvement of pharmacokinetics or pharmacodynamics is required. Such studies will be important contributions for the advancement of PLpro inhibitors to the clinic. Considering the speed of discovery and scale of the global effort, we expect to see breakthroughs on the **GRL-0617** series, the related piperidine-based **5c** series, and/or on as yet unreported compound series originating from fresh HTS campaigns, later in 2022.

REFERENCES

- Agostini, M. L., Andres, E. L., Sims, A. C., Graham, R. L., Sheahan, T. P., Lu, X., et al. (2018). Coronavirus Susceptibility to the Antiviral Remdesivir (GS-5734) Is Mediated by the Viral Polymerase and the Proofreading Exoribonuclease. *Mbio* 9, e00221–18. doi:10.1128/mbio.00221-18
- Almeida, J. D., Berry, D. M., Cunningham, C. H., Hamre, D., Hofstad, M. S., Mallucci, L., et al. (1968). Virology: Coronaviruses. *Nature* 220, 650. doi:10.1038/220650b0
- Amin, S. A., Ghosh, K., Singh, S., Qureshi, I. A., Jha, T., and Gayen, S. (2021). Exploring Naphthyl Derivatives as SARS-CoV Papain-like Protease (PLpro) Inhibitors and its Implications in COVID-19 Drug Discovery. *Mol. Divers.* 26, 215–228. doi:10.1007/s11030-021-10198-3
- Ampornadani, K., Meng, X., Shang, W., Jin, Z., Rogers, M., Zhao, Y., et al. (2021). Inhibition Mechanism of SARS-CoV-2 Main Protease by Ebselen and its Derivatives. *Nat. Commun.* 12, 3061. doi:10.1038/s41467-021-23313-7
- Andersen, K. G., Rambaut, A., Lipkin, W. I., Holmes, E. C., and Garry, R. F. (2020). The Proximal Origin of SARS-CoV-2. *Nat. Med.* 26, 450–452. doi:10.1038/s41591-020-0820-9
- Anson, B. J., Chapman, M. E., Lendy, E. K., Pshenychnyi, S., D'Aquila, R. T., Satchell, K. J. F., et al. (2020). Broad-spectrum Inhibition of Coronavirus Main and Papain-like Proteases by HCV Drugs. *Res. Square (Preprint)*. doi:10.21203/rs.3.rs-26344/v1
- Baell, J. B., and Holloway, G. A. (2010). New Substructure Filters for Removal of Pan Assay Interference Compounds (PAINS) from Screening Libraries and for Their Exclusion in Bioassays. *J. Med. Chem.* 53, 2719–2740. doi:10.1021/jm901137j
- Báez-Santos, Y. M., Barraza, S. J., Wilson, M. W., Agius, M. P., Mielech, A. M., Davis, N. M., et al. (2014). X-ray Structural and Biological Evaluation of a Series of Potent and Highly Selective Inhibitors of Human Coronavirus Papain-like Proteases. *J. Med. Chem.* 57, 2393–2412. doi:10.1021/jm401712t
- Báez-Santos, Y. M., St. John, S. E., and Mesecar, A. D. (2015). The SARS-Coronavirus Papain-like Protease: Structure, Function and Inhibition by Designed Antiviral Compounds. *Antiviral Res.* 115, 21–38. doi:10.1016/j.antiviral.2014.12.015
- Bafna, K., White, K., Harish, B., Rosales, R., Ramelot, T. A., Acton, T. B., et al. (2021). Hepatitis C Virus Drugs that Inhibit SARS-CoV-2 Papain-like Protease Synergize with Remdesivir to Suppress Viral Replication in Cell Culture. *Cel Rep.* 35, 109133. doi:10.1016/j.celrep.2021.109133
- Barretto, N., Jukneliene, D., Ratia, K., Chen, Z., Mesecar, A. D., and Baker, S. C. (2005). The Papain-like Protease of Severe Acute Respiratory Syndrome Coronavirus Has Deubiquitinating Activity. *J. Virol.* 79, 15189–15198. doi:10.1128/jvi.79.24.15189-15198.2005
- Begley, C. G., Ashton, M., Baell, J., Bettess, M., Brown, M. P., Carter, B., et al. (2021). Drug Repurposing: Misconceptions, Challenges, and Opportunities for Academic Researchers. *Sci. Transl. Med.* 13, eabd5524. doi:10.1126/scitranslmed.abd5524
- Beigel, J. H., Tomashek, K. M., Dodd, L. E., Mehta, A. K., Zingman, B. S., Kalil, A. C., et al. (2020). Remdesivir for the Treatment of Covid-19 - Final Report. *N. Engl. J. Med.* 383, 1813–1826. doi:10.1056/nejmoa2007764
- Békés, M., van der Heden van Noort, G. J., Ekkebus, R., Ovaa, H., Huang, T. T., and Lima, C. D. (2016). Recognition of Lys48-Linked Di-ubiquitin and Deubiquitinating Activities of the SARS Coronavirus Papain-like Protease. *Mol. Cell* 62, 572–585. doi:10.1016/j.molcel.2016.04.016
- Benarba, B., and Pandiella, A. (2020). Medicinal Plants as Sources of Active Molecules against COVID-19. *Front. Pharmacol.* 11, 1189. doi:10.3389/fphar.2020.01189
- Brown, A. J., Won, J. J., Graham, R. L., Dinnon, K. H., Sims, A. C., Feng, J. Y., et al. (2019). Broad Spectrum Antiviral Remdesivir Inhibits Human Endemic and Zoonotic Deltacoronaviruses with a Highly Divergent RNA Dependent RNA Polymerase. *Antiviral Res.* 169, 104541. doi:10.1016/j.antiviral.2019.104541
- Chazal, N. (2021). Coronavirus, the King Who Wanted More Than a Crown: From Common to the Highly Pathogenic SARS-CoV-2, Is the Key in the Accessory Genes? *Front. Microbiol.* 12, 682603. doi:10.3389/fmicb.2021.682603

AUTHOR CONTRIBUTIONS

DC, GL and DK designed the Review and DC wrote the first draft, which was refined by GL and DK.

FUNDING

PLpro work in the labs of DK and GL is funded by The Walter and Eliza Hall Institute of Medical Research, an NHMRC/MRFF “VirDUB” grant MRF2002119 (to DK, GL, Marc Pellegrini, and Peter Czabotar), NHMRC Investigator Grants and Fellowships (GNT1178122 to DK and GNT1117089 to GL), a Wellcome Trust Grant WT222698/Z/21/Z (to DK, GL, and Marc Pellegrini) and by a generous donation by Hengyi Pacific Pty Ltd. to support COVID-19 research.

ACKNOWLEDGMENTS

We thank the members of our labs, all contributors to the PLpro drug discovery programme, our consumer advocates, and the scientific colleagues working on PLpro for their enthusiasm and insights. We apologise to those researchers whose work could not be discussed or cited due to space considerations.

- Cheloni, G., Tanturli, M., Tusa, I., Ho DeSouza, N., Shan, Y., Gozzini, A., et al. (2017). Targeting Chronic Myeloid Leukemia Stem Cells with the Hypoxia-Inducible Factor Inhibitor Acriflavine. *Blood* 130, 655–665. doi:10.1182/blood-2016-10-745588
- Chen, C. Z., Shinn, P., Itkin, Z., Eastman, R. T., Bostwick, R., Rasmussen, L., et al. (2021a). Drug Repurposing Screen for Compounds Inhibiting the Cytopathic Effect of SARS-CoV-2. *Front. Pharmacol.* 11, 592737. doi:10.3389/fphar.2020.592737
- Chen, W., Wang, Z., Wang, Y., and Li, Y. (2021b). Natural Bioactive Molecules as Potential Agents against SARS-CoV-2. *Front. Pharmacol.* 12, 702472. doi:10.3389/fphar.2021.702472
- Cho, C. C., Li, S. G., Lalonde, T. J., Yang, K. S., Yu, G., Qiao, Y., et al. (2021b). Drug Repurposing for the SARS-CoV-2 Papain-Like Protease. *Chemmedchem* 17, 202100455. doi:10.1002/cmdc.202100455
- Consortium, W. S. T., Pan, H., Peto, R., Henao-Restrepo, A.-M., Preziosi, M.-P., Sathiyamoorthy, V., et al. (2021). Repurposed Antiviral Drugs for Covid-19 - Interim WHO Solidarity Trial Results. *N. Engl. J. Med.* 384, 497–511. doi:10.1056/nejmoa2023184
- Cox, R. M., Wolf, J. D., and Plemper, R. K. (2021). Therapeutically Administered Ribonucleoside Analogue MK-4482/EIDD-2801 Blocks SARS-CoV-2 Transmission in Ferrets. *Nat. Microbiol.* 6, 11–18. doi:10.1038/s41564-020-00835-2
- Cui, W., Yang, K., and Yang, H. (2020). Recent Progress in the Drug Development Targeting SARS-CoV-2 Main Protease as Treatment for COVID-19. *Front. Mol. Biosci.* 7, 616341. doi:10.3389/fmolb.2020.616341
- Dana, S., Prusty, D., Dhayal, D., Gupta, M. K., Dar, A., Sen, S., et al. (2014). Potent Antimalarial Activity of Acriflavine *In Vitro* and *In Vivo*. *ACS Chem. Biol.* 9, 2366–2373. doi:10.1021/cb500476q
- Dang, L. C., Melandri, F. D., and Stein, R. L. (1998). Kinetic and Mechanistic Studies on the Hydrolysis of Ubiquitin C-Terminal 7-Amido-4-Methylcoumarin by Deubiquitinating Enzymes. *Biochemistry* 37, 1868–1879. doi:10.1021/bi9723360
- Drosten, C., Günther, S., Preiser, W., van der Werf, S., Brodt, H.-R., Becker, S., et al. (2003). Identification of a Novel Coronavirus in Patients with Severe Acute Respiratory Syndrome. *N. Engl. J. Med.* 348, 1967–1976. doi:10.1056/nejmoa030747
- Eastman, R. T., Roth, J. S., Brimacombe, K. R., Simeonov, A., Shen, M., Patnaik, S., et al. (2020). Remdesivir: A Review of its Discovery and Development Leading to Emergency Use Authorization for Treatment of COVID-19. *ACS Cent. Sci.* 6, 672–683. doi:10.1021/acscentsci.0c00489
- Fan, K., Wei, P., Feng, Q., Chen, S., Huang, C., Ma, L., et al. (2004). Biosynthesis, Purification, and Substrate Specificity of Severe Acute Respiratory Syndrome Coronavirus 3C-like Proteinase. *J. Biol. Chem.* 279, 1637–1642. doi:10.1074/jbc.m310875200
- Fang, Z. y., Zhang, M., Liu, J.-n., Zhao, X., Zhang, Y.-q., and Fang, L. (2021). Tanshinone IIA: A Review of its Anticancer Effects. *Front. Pharmacol.* 11, 611087. doi:10.3389/fphar.2020.611087
- FDA (2021). Coronavirus (COVID-19) Update: FDA Authorizes Additional Oral Antiviral for Treatment of COVID-19 in Certain Adults. Available at: <https://www.fda.gov/news-events/press-announcements/coronavirus-covid-19-update-fda-authorizes-additional-oral-antiviral-treatment-covid-19-certain> (Accessed January 13, 2022).
- FDA (2020). FDA Approves First Treatment for COVID-19. Available at: <https://www.fda.gov/news-events/press-announcements/fda-approves-first-treatment-covid-19> (Accessed September 15, 2021).
- Fischer, W. A., Eron, J. J., Holman, W., Cohen, M. S., Fang, L., Szwedczyk, L. J., et al. (2022). A Phase 2a Clinical Trial of Molnupiravir in Patients with COVID-19 Shows Accelerated SARS-CoV-2 RNA Clearance and Elimination of Infectious Virus. *Sci. Transl. Med.* 14, eabl7430. doi:10.1126/scitranslmed.abl7430
- Fraile, J. M., Quesada, V., Rodríguez, D., Freije, J. M. P., and López-Otín, C. (2012). Deubiquitinases in Cancer: New Functions and Therapeutic Options. *Oncogene* 31, 2373–2388. doi:10.1038/onc.2011.443
- Freedberg, D. E., Conigliaro, J., Wang, T. C., Tracey, K. J., Callahan, M. V., Abrams, J. A., et al. (2020). Famotidine Use Is Associated with Improved Clinical Outcomes in Hospitalized COVID-19 Patients: A Propensity Score Matched Retrospective Cohort Study. *Gastroenterology* 159, 1129–1131.e3. doi:10.1053/j.gastro.2020.05.053
- Freitas, B. T., Durie, I. A., Murray, J., Longo, J. E., Miller, H. C., Crich, D., et al. (2020). Characterization and Noncovalent Inhibition of the Deubiquitinase and deISGylase Activity of SARS-CoV-2 Papain-like Protease. *ACS Infect. Dis.* 6, 2099–2109. doi:10.1021/acscinfecdis.0c00168
- Froggatt, H. M., Heaton, B. E., and Heaton, N. S. (2020). Development of a Fluorescence-Based, High-Throughput SARS-CoV-2 3CL Pro Reporter Assay. *J. Virol.* 94, e01265–20. doi:10.1128/jvi.01265-20
- Fu, Z., Huang, B., Tang, J., Liu, S., Liu, M., Ye, Y., et al. (2021). The Complex Structure of GRL0617 and SARS-CoV-2 PLpro Reveals a Hot Spot for Antiviral Drug Discovery. *Nat. Commun.* 12, 488. doi:10.1038/s41467-020-20718-8
- Gama, C. R. B., Pombo, M. A. G., Nunes, C. P., Gama, G. F., Mezitis, S. G., Suchmacher Neto, M., et al. (2020). Treatment of Recurrent Urinary Tract Infection Symptoms with Urinary Antiseptics Containing Methenamine and Methylene Blue: Analysis of Etiology and Treatment Outcomes. *Rru Vol.* 12, 639–649. doi:10.2147/rru.s279060
- Gammeltuft, K. A., Zhou, Y., Duarte Hernandez, C. R., Galli, A., Offersgaard, A., Costa, R., et al. (2021). Hepatitis C Virus Protease Inhibitors Show Differential Efficacy and Interactions with Remdesivir for Treatment of SARS-CoV-2 *In Vitro*. *Antimicrob. Agents Chemother.* 65, e02680–20. doi:10.1128/aac.02680-20
- Gao, X., Qin, B., Chen, P., Zhu, K., Hou, P., Wojdyła, J. A., et al. (2021). Crystal Structure of SARS-CoV-2 Papain-like Protease. *Acta Pharmaceutica Sinica B* 11, 237–245. doi:10.1016/j.apsb.2020.08.014
- Gatasheh, M. K., Kannan, S., Hemalatha, K., and Imrana, N. (2017). Proflavine an Acridine DNA Intercalating Agent and strong Antimicrobial Possessing Potential Properties of Carcinogen. *Karbala Int. J. Mod. Sci.* 3, 272–278. doi:10.1016/j.kijoms.2017.07.003
- Ghosh, A. K., Brindisi, M., Shahabi, D., Chapman, M. E., and Mesecar, A. D. (2020). Drug Development and Medicinal Chemistry Efforts toward SARS-Coronavirus and Covid-19 Therapeutics. *Chemmedchem* 15, 907–932. doi:10.1002/cmdc.202000223
- Ghosh, A. K., Takayama, J., Aubin, Y., Ratia, K., Chaudhuri, R., Baez, Y., et al. (2009). Structure-Based Design, Synthesis, and Biological Evaluation of a Series of Novel and Reversible Inhibitors for the Severe Acute Respiratory Syndrome-Coronavirus Papain-like Protease. *J. Med. Chem.* 52, 5228–5240. doi:10.1021/jm900611t
- Ghosh, A. K., Takayama, J., Rao, K. V., Ratia, K., Chaudhuri, R., Mulhearn, D. C., et al. (2010). Severe Acute Respiratory Syndrome Coronavirus Papain-like Novel Protease Inhibitors: Design, Synthesis, Protein–Ligand X-ray Structure and Biological Evaluation. *J. Med. Chem.* 53, 4968–4979. doi:10.1021/jm1004489
- Goldman, J. D., Lye, D. C. B., Hui, D. S., Marks, K. M., Bruno, R., Montejano, R., et al. (2020). Remdesivir for 5 or 10 Days in Patients with Severe Covid-19. *N. Engl. J. Med.* 383, 1827–1837. doi:10.1056/nejmoa2015301
- Gordon, C. J., Tchesnokov, E. P., Schinazi, R. F., and Götte, M. (2021). Molnupiravir Promotes SARS-CoV-2 Mutagenesis via the RNA Template. *J. Biol. Chem.* 297, 100770. doi:10.1016/j.jbc.2021.100770
- Gordon, C. J., Tchesnokov, E. P., Woolner, E., Perry, J. K., Feng, J. Y., Porter, D. P., et al. (2020a). Remdesivir Is a Direct-Acting Antiviral that Inhibits RNA-dependent RNA Polymerase from Severe Acute Respiratory Syndrome Coronavirus 2 with High Potency. *J. Biol. Chem.* 295, 6785–6797. doi:10.1074/jbc.ra120.013679
- Gordon, D. E., Jang, G. M., Bouhaddou, M., Xu, J., Obernier, K., White, K. M., et al. (2020b). A SARS-CoV-2 Protein Interaction Map Reveals Targets for Drug Repurposing. *Nature* 583, 459–468. doi:10.1038/s41586-020-2286-9
- Guy, R. K., DiPaola, R. S., Romanelli, F., and Dutch, R. E. (2020). Rapid Repurposing of Drugs for COVID-19. *Science* 368, 829–830. doi:10.1126/science.abb9332
- Hamre, D., and Procknow, J. J. (1966). A New Virus Isolated from the Human Respiratory Tract. *Exp. Biol. Med.* 121, 190–193. doi:10.3181/00379727-121-30734
- Harcourt, B. H., Jukneliene, D., Kanjanahaluethai, A., Bechill, J., Severson, K. M., Smith, C. M., et al. (2004). Identification of Severe Acute Respiratory Syndrome Coronavirus Replicase Products and Characterization of Papain-like Protease Activity. *J. Virol.* 78, 13600–13612. doi:10.1128/jvi.78.24.13600-13612.2004
- Hartenian, E., Nandakumar, D., Lari, A., Ly, M., Tucker, J. M., and Glaunsinger, B. A. (2020). The Molecular Virology of Coronaviruses. *J. Biol. Chem.* 295, 12910–12934. doi:10.1074/jbc.rev120.013930
- Hassiepen, U., Eidhoff, U., Meder, G., Bulber, J.-F., Hein, A., Bodendorf, U., et al. (2007). A Sensitive Fluorescence Intensity Assay for Deubiquitinating Proteases

- Using Ubiquitin-Rhodamine110-glycine as Substrate. *Anal. Biochem.* 371, 201–207. doi:10.1016/j.ab.2007.07.034
- Hilgenfeld, R. (2014). From SARS to MERS: Crystallographic Studies on Coronavirus Proteases Enable Antiviral Drug Design. *Febs J.* 281, 4085–4096. doi:10.1111/febs.12936
- Holmes, E. C., Goldstein, S. A., Rasmussen, A. L., Robertson, D. L., Crits-Christoph, A., Wertheim, J. O., et al. (2021). The Origins of SARS-CoV-2: A Critical Review. *Cell* 184, 4848–4856. doi:10.1016/j.cell.2021.08.017
- Janes, J., Young, M. E., Chen, E., Rogers, N. H., Burgstaller-Muehlbacher, S., Hughes, L. D., et al. (2018). The ReFRAME Library as a Comprehensive Drug Repurposing Library and its Application to the Treatment of Cryptosporidiosis. *Proc. Natl. Acad. Sci. U.S.A.* 115, 10750–10755. doi:10.1073/pnas.1810137115
- Jayk Bernal, A., Gomes da Silva, M. M., Musungaie, D. B., Kovalchuk, E., Gonzalez, A., Delos Reyes, V., et al. (2022). Molnupiravir for Oral Treatment of Covid-19 in Nonhospitalized Patients. *N. Engl. J. Med.* 386, 509–520. doi:10.1056/nejmoa2116044
- Jiang, H., Yang, P., and Zhang, J. (2022). Potential Inhibitors Targeting Papain-like Protease of SARS-CoV-2: Two Birds with One Stone. *Front. Chem.* 10, 822785. doi:10.3389/fchem.2022.822785
- Jin, Z., Du, X., Xu, Y., Deng, Y., Liu, M., Zhao, Y., et al. (2020). Structure of Mpro from SARS-CoV-2 and Discovery of its Inhibitors. *Nature* 582, 289–293. doi:10.1038/s41586-020-2223-y
- Johnston, P. A. (2011). Redox Cycling Compounds Generate H₂O₂ in HTS Buffers Containing strong Reducing Reagents-Real Hits or Promiscuous Artifacts? *Curr. Opin. Chem. Biol.* 15, 174–182. doi:10.1016/j.cbpa.2010.10.022
- Kandeel, M., Abdelrahman, A. H. M., Oh-Hashi, K., Ibrahim, A., Venugopala, K. N., Morsy, M. A., et al. (2020). Repurposing of FDA-Approved Antivirals, Antibiotics, Anthelmintics, Antioxidants, and Cell Protectives against SARS-CoV-2 Papain-like Protease. *J. Biomol. Struct. Dyn.* 39, 5129–5136. 8. doi:10.1080/07391102.2020.1784291
- Khare, P., Sahu, U., Pandey, S. C., and Samant, M. (2020). Current Approaches for Target-specific Drug Discovery Using Natural Compounds against SARS-CoV-2 Infection. *Virus. Res.* 290, 198169. doi:10.1016/j.virusres.2020.198169
- Kim, D., Lee, J.-Y., Yang, J.-S., Kim, J. W., Kim, V. N., and Chang, H. (2020). The Architecture of SARS-CoV-2 Transcriptome. *Cell* 181, 914–921.e10. doi:10.1016/j.cell.2020.04.011
- Klemm, T., Ebert, G., Calleja, D. J., Allison, C. C., Richardson, L. W., Bernardini, J. P., et al. (2020). Mechanism and Inhibition of the Papain-like Protease, PLpro, of SARS-CoV-2. *Embo J.* 39. doi:10.15252/embj.2020106275
- Koopmans, M., Daszak, P., Dedkov, V. G., Dwyer, D. E., Farag, E., Fischer, T. K., et al. (2021). Origins of SARS-CoV-2: Window Is Closing for Key Scientific Studies. *Nature* 596, 482–485. doi:10.1038/d41586-021-02263-6
- Kozlov, M. (2021). Merck's COVID Pill Loses its Lustre: what that Means for the Pandemic. *Nature*. doi:10.1038/d41586-021-03667-0
- Ksiazek, T. G., Erdman, D., Goldsmith, C. S., Zaki, S. R., Peret, T., Emery, S., et al. (2003). A Novel Coronavirus Associated with Severe Acute Respiratory Syndrome. *N. Engl. J. Med.* 348, 1953–1966. doi:10.1056/nejmoa030781
- Lau, J. L., and Dunn, M. K. (2018). Therapeutic Peptides: Historical Perspectives, Current Development Trends, and Future Directions. *Bioorg. Med. Chem.* 26, 2700–2707. doi:10.1016/j.bmc.2017.06.052
- Lee, H., Lei, H., Santarsiero, B. D., Gatz, J. L., Cao, S., Rice, A. J., et al. (2015). Inhibitor Recognition Specificity of MERS-CoV Papain-like Protease May Differ from that of SARS-CoV. *ACS Chem. Biol.* 10, 1456–1465. doi:10.1021/cb500917m
- Lee, K., Zhang, H., Qian, D. Z., Rey, S., Liu, J. O., and Semenza, G. L. (2009). Acriflavine Inhibits HIF-1 Dimerization, Tumor Growth, and Vascularization. *Proc. Natl. Acad. Sci. U.S.A.* 106, 17910–17915. doi:10.1073/pnas.0909353106
- Lei, J., Kusov, Y., and Hilgenfeld, R. (2018). Nsp3 of Coronaviruses: Structures and Functions of a Large Multi-Domain Protein. *Antiviral Res.* 149, 58–74. doi:10.1016/j.antiviral.2017.11.001
- Lim, C. T., Tan, K. W., Wu, M., Ulferts, R., Armstrong, L. A., Ozono, E., et al. (2021). Identifying SARS-CoV-2 Antiviral Compounds by Screening for Small Molecule Inhibitors of Nsp3 Papain-like Protease. *Biochem. J.* 478, 2517–2531. doi:10.1042/bcj20210244
- Lin, M.-H., Moses, D. C., Hsieh, C.-H., Cheng, S.-C., Chen, Y.-H., Sun, C.-Y., et al. (2018). Disulfiram Can Inhibit MERS and SARS Coronavirus Papain-like Proteases via Different Modes. *Antiviral Res.* 150, 155–163. doi:10.1016/j.antiviral.2017.12.015
- Lindner, H. A., Fotouhi-Ardakani, N., Lytvyn, V., Lachance, P., Sulea, T., and Me'nard, R. (2005). The Papain-like Protease from the Severe Acute Respiratory Syndrome Coronavirus Is a Deubiquitinating Enzyme. *J. Virol.* 79, 15199–15208. doi:10.1128/jvi.79.24.15199-15208.2005
- Liu, N., Zhang, Y., Lei, Y., Wang, R., Zhan, M., Liu, J., et al. (2022a). Design and Evaluation of a Novel Peptide-Drug Conjugate Covalently Targeting SARS-CoV-2 Papain-like Protease. *J. Med. Chem.* 65, 876–884. doi:10.1021/acs.jmedchem.1c02022
- Loffredo, M., Lucero, H., Chen, D.-Y., O'Connell, A., Bergqvist, S., Munawar, A., et al. (2021). The In-Vitro Effect of Famotidine on SARS-CoV-2 Proteases and Virus Replication. *Sci. Rep.* 11, 5433. doi:10.1038/s41598-021-84782-w
- Lu, R., Zhao, X., Li, J., Niu, P., Yang, B., Wu, H., et al. (2020). Genomic Characterisation and Epidemiology of 2019 Novel Coronavirus: Implications for Virus Origins and Receptor Binding. *The Lancet* 395, 565–574. doi:10.1016/s0140-6736(20)30251-8
- Ma, C., Hu, Y., Townsend, J. A., Lagarias, P. I., Marty, M. T., Kolocouris, A., et al. (2020). Ebselen, Disulfiram, Carmofur, PX-12, Tideglusib, and Shikonin Are Nonspecific Promiscuous SARS-CoV-2 Main Protease Inhibitors. *ACS Pharmacol. Transl. Sci.* 3, 1265–1277. doi:10.1021/acspstci.0c00130
- Ma, C., Sacco, M. D., Xia, Z., Lambrinidis, G., Townsend, J. A., Hu, Y., et al. (2021). Discovery of SARS-CoV-2 Papain-like Protease Inhibitors through a Combination of High-Throughput Screening and a FlipGFP-Based Reporter Assay. *ACS Cent. Sci.* 7, 1245–1260. doi:10.1021/acscentsci.1c00519
- Ma, C., and Wang, J. (2022). Validation and Invalidation of SARS-CoV-2 Papain-like Protease Inhibitors. *ACS Pharmacol. Transl. Sci.* 5, 102–109. doi:10.1021/acspstci.1c00240
- Makar, S., Saha, T., and Singh, S. K. (2019). Naphthalene, a Versatile Platform in Medicinal Chemistry: Sky-High Perspective. *Eur. J. Med. Chem.* 161, 252–276. doi:10.1016/j.ejmech.2018.10.018
- Malone, B., Urakova, N., Snijder, E. J., and Campbell, E. A. (2022). Structures and Functions of Coronavirus Replication-Transcription Complexes and Their Relevance for SARS-CoV-2 Drug Design. *Nat. Rev. Mol. Cell Biol.* 23, 21–39. doi:10.1038/s41580-021-00432-z
- Malone, R. W., Tisdall, P., Fremont-Smith, P., Liu, Y., Huang, X.-P., White, K. M., et al. (2021). COVID-19: Famotidine, Histamine, Mast Cells, and Mechanisms. *Front. Pharmacol.* 12, 633680. doi:10.3389/fphar.2021.633680
- Mangraviti, A., Raghavan, T., Volpin, F., Skuli, N., Gullotti, D., Zhou, J., et al. (2017). HIF-1 α -Targeting Acriflavine Provides Long Term Survival and Radiological Tumor Response in Brain Cancer Therapy. *Sci. Rep.* 7, 14978. doi:10.1038/s41598-017-14990-w
- Mather, J. F., Seip, R. L., and McKay, R. G. (2020). Impact of Famotidine Use on Clinical Outcomes of Hospitalized Patients with COVID-19. *Am. J. Gastroenterol.* 115, 1617–1623. doi:10.14309/ajg.000000000000083210.14309/ajg.0000000000000832
- McIntosh, K., Dees, J. H., Becker, W. B., Kapikian, A. Z., and Chanock, R. M. (1967). Recovery in Tracheal Organ Cultures of Novel Viruses from Patients with Respiratory Disease. *Proc. Natl. Acad. Sci. U.S.A.* 57, 933–940. doi:10.1073/pnas.57.4.933
- Mengist, H. M., Dilnessa, T., and Jin, T. (2021). Structural Basis of Potential Inhibitors Targeting SARS-CoV-2 Main Protease. *Front. Chem.* 9, 622898. doi:10.3389/fchem.2021.622898
- Mevisen, T. E. T., and Komander, D. (2017). Mechanisms of Deubiquitinase Specificity and Regulation. *Annu. Rev. Biochem.* 86, 159–192. doi:10.1146/annurev-biochem-061516-044916
- Moffat, J. G., Vincent, F., Lee, J. A., Eder, J., and Prunotto, M. (2017). Opportunities and Challenges in Phenotypic Drug Discovery: an Industry Perspective. *Nat. Rev. Drug Discov.* 16, 531–543. doi:10.1038/nrd.2017.111
- Mura, C., Preissner, S., Preissner, R., and Bourne, P. E. (2021). A Birds-Eye (Re) View of Acid-Suppression Drugs, COVID-19, and the Highly Variable Literature. *Front. Pharmacol.* 12, 700703. doi:10.3389/fphar.2021.700703
- Napolitano, V., Dabrowska, A., Schorpp, K., Mourão, A., Barreto-Duran, E., Benedyk, M., et al. (2022). Acriflavine, a Clinically Approved Drug, Inhibits SARS-CoV-2 and Other Betacoronaviruses. *Cell Chem. Biol.* doi:10.1016/j.chembiol.2021.11.006
- Nehme, R., Hallal, R., El Dor, M., Kobeissy, F., Gouilleux, F., Mazurier, F., et al. (2021). Repurposing of Acriflavine to Target Chronic Myeloid Leukemia Treatment. *Cmc* 28, 2218–2233. doi:10.2174/0929867327666200908114411

- Ng, Y. L., Salim, C. K., and Chu, J. J. H. (2021). Drug Repurposing for COVID-19: Approaches, Challenges and Promising Candidates. *Pharmacol. Ther.* 228, 107930. doi:10.1016/j.pharmthera.2021.107930
- Osiptuk, J., Azizi, S.-A., Dvorkin, S., Endres, M., Jedrzejczak, R., Jones, K. A., et al. (2021). Structure of Papain-like Protease from SARS-CoV-2 and its Complexes with Non-covalent Inhibitors. *Nat. Commun.* 12, 743. doi:10.1038/s41467-021-21060-3
- Owen, D. R., Allerton, C. M. N., Anderson, A. S., Aschenbrenner, L., Avery, M., Berritt, S., et al. (2021). An Oral SARS-CoV-2 M Pro Inhibitor Clinical Candidate for the Treatment of COVID-19. *Science* 374, 1586–1593. doi:10.1126/science.abc4784
- Park, J.-Y., Kim, J. H., Kim, Y. M., Jeong, H. J., Kim, D. W., Park, K. H., et al. (2012). Tanshinones as Selective and Slow-Binding Inhibitors for SARS-CoV Cysteine Proteases. *Bioorg. Med. Chem.* 20, 5928–5935. doi:10.1016/j.bmc.2012.07.038
- Paules, C. I., Marston, H. D., and Fauci, A. S. (2020). Coronavirus Infections—More Than Just the Common Cold. *Jama* 323, 707–708. doi:10.1001/jama.2020.0757
- Peiris, J., Lai, S., Poon, L., Guan, Y., Yam, L., Lim, W., et al. (2003). Coronavirus as a Possible Cause of Severe Acute Respiratory Syndrome. *The Lancet* 361, 1319–1325. doi:10.1016/s0140-6736(03)13077-2
- Pépin, G., Nejad, C., Thomas, B. J., Ferrand, J., McArthur, K., Bardin, P. G., et al. (2017). Activation of cGAS-dependent Antiviral Responses by DNA Intercalating Agents. *Nucleic Acids Res.* 45, 198–205. doi:10.1093/nar/gkw878
- Ratia, K., Pegan, S., Takayama, J., Sleeman, K., Coughlin, M., Balji, S., et al. (2008). A Noncovalent Class of Papain-like Protease/deubiquitinase Inhibitors Blocks SARS Virus Replication. *Proc. Natl. Acad. Sci. U.S.A.* 105, 16119–16124. doi:10.1073/pnas.0805240105
- Ratia, K., Saikatendu, K. S., Santarsiero, B. D., Barretto, N., Baker, S. C., Stevens, R. C., et al. (2006). Severe Acute Respiratory Syndrome Coronavirus Papain-like Protease: Structure of a Viral Deubiquitinating Enzyme. *Proc. Natl. Acad. Sci. U.S.A.* 103, 5717–5722. doi:10.1073/pnas.0510851103
- Redhead, M. A., Owen, C. D., Brewitz, L., Collette, A. H., Lukacik, P., Strain-Damerell, C., et al. (2021). Bispecific Repurposed Medicines Targeting the Viral and Immunological Arms of COVID-19. *Sci. Rep.* 11, 13208. doi:10.1038/s41598-021-92416-4
- Riva, L., Yuan, S., Yin, X., Martin-Sancho, L., Matsunaga, N., Pache, L., et al. (2020). Discovery of SARS-CoV-2 Antiviral Drugs through Large-Scale Compound Repurposing. *Nature* 586, 113–119. doi:10.1038/s41586-020-2577-1
- Rut, W., Lv, Z., Zmudzinski, M., Patchett, S., Nayak, D., Snipas, S. J., et al. (2020). Activity Profiling and crystal Structures of Inhibitor-Bound SARS-CoV-2 Papain-like Protease: A Framework for Anti-COVID-19 Drug Design. *Sci. Adv.* 6, eabd4596. doi:10.1126/sciadv.abd4596
- Sanders, B., Pohkrel, S., Labbe, A., Mathews, I., Cooper, C., Davidson, R., et al. (2021). Potent and Selective Covalent Inhibitors of the Papain-like Protease from SARS-CoV-2. *Res. Square*. doi:10.21203/rs.3.rs-906621/v1
- Santos, J., Brierley, S., Gandhi, M. J., Cohen, M. A., Moschella, P. C., and Declan, A. B. L. (2020). Repurposing Therapeutics for Potential Treatment of SARS-CoV-2: A Review. *Viruses* 12, 705. doi:10.3390/v12070705
- Sargsyan, K., Lin, C.-C., Chen, T., Grauffel, C., Chen, Y.-P., Yang, W.-Z., et al. (2020). Multi-targeting of Functional Cysteines in Multiple Conserved SARS-CoV-2 Domains by Clinically Safe Zn-Ejectors. *Chem. Sci.* 11, 9904–9909. doi:10.1039/d0sc02646h
- Schauer, N. J., Magin, R. S., Liu, X., Doherty, L. M., and Buhrlage, S. J. (2020). Advances in Discovering Deubiquitinating Enzyme (DUB) Inhibitors. *J. Med. Chem.* 63, 2731–2750. doi:10.1021/acs.jmedchem.9b01138
- Schmidt, M. F., Gan, Z. Y., Komander, D., and Dewson, G. (2021). Ubiquitin Signalling in Neurodegeneration: Mechanisms and Therapeutic Opportunities. *Cell Death Differ.* 28, 570–590. doi:10.1038/s41418-020-00706-7
- Shan, H., Liu, J., Shen, J., Dai, J., Xu, G., Lu, K., et al. (2021). Development of Potent and Selective Inhibitors Targeting the Papain-like Protease of SARS-CoV-2. *Cel. Chem. Biol.* 28, 855–865. e9. doi:10.1016/j.chembiol.2021.04.020
- Sheahan, T. P., Sims, A. C., Graham, R. L., Menachery, V. D., Gralinski, L. E., Case, J. B., et al. (2017). Broad-spectrum Antiviral GS-5734 Inhibits Both Epidemic and Zoonotic Coronaviruses. *Sci. Transl. Med.* 9, doi:10.1126/scitranslmed.aal3653
- Sheahan, T. P., Sims, A. C., Zhou, S., Graham, R. L., Pruijssers, A. J., Agostini, M. L., et al. (2020). An Orally Bioavailable Broad-Spectrum Antiviral Inhibits SARS-CoV-2 in Human Airway Epithelial Cell Cultures and Multiple Coronaviruses in Mice. *Sci. Transl. Med.* 12, eabb5883. doi:10.1126/scitranslmed.abb5883
- Shen, Z., Ratia, K., Cooper, L., Kong, D., Lee, H., Kwon, Y., et al. (2021). Design of SARS-CoV-2 PLpro Inhibitors for COVID-19 Antiviral Therapy Leveraging Binding Cooperativity. *J. Med. Chem.* 65, 2940–2955. doi:10.1021/acs.jmedchem.1c01307
- Shin, D., Mukherjee, R., Grewe, D., Bojkova, D., Baek, K., Bhattacharya, A., et al. (2020). Papain-like Protease Regulates SARS-CoV-2 Viral Spread and Innate Immunity. *Nature* 587, 657–662. doi:10.1038/s41586-020-2601-5
- Sivakumar, D., and Stein, M. (2021). Binding of SARS-CoV Covalent Non-covalent Inhibitors to the SARS-CoV-2 Papain-like Protease and Ovarian Tumor Domain Deubiquitinases. *Biomolecules* 11, 802. doi:10.3390/biom11060802
- Smith, E., Davis-Gardner, M. E., Garcia-Ordóñez, R. D., Nguyen, T.-T., Hull, M., Chen, E., et al. (2020). High-Throughput Screening for Drugs that Inhibit Papain-like Protease in SARS-CoV-2. *SLAS DISCOVERY: Advancing Sci. Drug Discov.* 25, 1152–1161. doi:10.1177/2472555220963667
- Sola, I., Almazán, F., Zúñiga, S., and Enjuanes, L. (2015). Continuous and Discontinuous RNA Synthesis in Coronaviruses. *Annu. Rev. Virol.* 2, 265–288. doi:10.1146/annurev-virology-100114-055218
- Spinner, C. D., Gottlieb, R. L., Criner, G. J., Arribas López, J. R., Cattelan, A. M., Soriano Viladomiu, A., et al. (2020). Effect of Remdesivir vs Standard Care on Clinical Status at 11 Days in Patients with Moderate COVID-19. *Jama* 324, 1048–1057. doi:10.1001/jama.2020.16349
- Srinivasan, V., Brognaro, H., Prabhu, P. R., de Souza, E. E., Günther, S., Reinke, P. Y. A., et al. (2021/2021). SARS-CoV-2 Papain-like Protease PLpro in Complex with Natural Compounds Reveal Allosteric Sites for Antiviral Drug Design. *Biorxiv* 1117, 468943. doi:10.1101/2021.11.17.468943
- Subissi, L., Imbert, I., Ferron, F., Collet, A., Coutard, B., Decroly, E., et al. (2014). SARS-CoV ORF1b-Encoded Nonstructural Proteins 12–16: Replicative Enzymes as Antiviral Targets. *Antiviral Res.* 101, 122–130. doi:10.1016/j.antiviral.2013.11.006
- Swaim, C. D., Dwivedi, V., Perng, Y.-C., Zhao, X., Canadeo, L. A., Harastani, H. H., et al. (2021). 6-Thioguanine Blocks SARS-CoV-2 Replication by Inhibition of PLpro. *Iscience* 24, 103213. doi:10.1016/j.isci.2021.103213
- Tchesnokov, E., Feng, J., Porter, D., and Götte, M. (2019). Mechanism of Inhibition of Ebola Virus RNA-dependent RNA Polymerase by Remdesivir. *Viruses* 11, 326. doi:10.3390/v11040326
- Turnbull, A. P., Ioannidis, S., Krajewski, W. W., Pinto-Fernandez, A., Heride, C., Martin, A. C. L., et al. (2017). Molecular Basis of USP7 Inhibition by Selective Small-Molecule Inhibitors. *Nature* 550, 481–486. doi:10.1038/nature24451
- Tyrrell, D. A. J., and Bynoe, M. L. (1965). Cultivation of a Novel Type of Common-Cold Virus in Organ Cultures. *Bmj* 1, 1467–1470. doi:10.1136/bmj.1.5448.1467
- van Boheemen, S., de Graaf, M., Lauber, C., Bestebroer, T. M., Raj, V. S., Zaki, A. M., et al. (2012). Genomic Characterization of a Newly Discovered Coronavirus Associated with Acute Respiratory Distress Syndrome in Humans. *Mbio* 3, e00473–12. doi:10.1128/mbio.00473-12
- van der Hoek, L., Pyrc, K., Jebbink, M. F., Vermeulen-Oost, W., Berkhout, R. J. M., Wolthers, K. C., et al. (2004). Identification of a New Human Coronavirus. *Nat. Med.* 10, 368–373. doi:10.1038/nm1024
- V'kovski, P., Kratzel, A., Steiner, S., Stalder, H., and Thiel, V. (2020). Coronavirus Biology and Replication: Implications for SARS-CoV-2. *Nat. Rev. Microbiol.* 19, 155–170. doi:10.1038/s41579-020-00468-6
- Warren, T. K., Jordan, R., Lo, M. K., Ray, A. S., Mackman, R. L., Soloveva, V., et al. (2016). Therapeutic Efficacy of the Small Molecule GS-5734 against Ebola Virus in Rhesus Monkeys. *Nature* 531, 381–385. doi:10.1038/nature17180
- Weglarz-Tomczak, E., Tomczak, J. M., Talma, M., Burda-Grabowska, M., Giurg, M., and Brul, S. (2021). Identification of Ebselen and its Analogues as Potent Covalent Inhibitors of Papain-like Protease from SARS-CoV-2. *Sci. Rep.* 11, 3640. doi:10.1038/s41598-021-83229-6
- Welker, A., Kersten, C., Müller, C., Madhugiri, R., Zimmer, C., Müller, P., et al. (2021). Structure-Activity Relationships of Benzamides and Isoindolines Designed as SARS-CoV Protease Inhibitors Effective against SARS-CoV-2. *Chemmedchem* 16, 340–354. doi:10.1002/cmdc.202000548
- Willyard, C. (2021). How Antiviral Pill Molnupiravir Shot Ahead in the COVID Drug hunt. *Nature*. doi:10.1038/d41586-021-02783-1
- Wishart, D. S., Feunang, Y. D., Guo, A. C., Lo, E. J., Marcu, A., Grant, J. R., et al. (2017). DrugBank 5.0: a Major Update to the DrugBank Database for 2018. *Nucleic Acids Res.* 46, D1074–D1082. doi:10.1093/nar/gkx1037
- Wishart, D. S., Knox, C., Guo, A. C., Shrivastava, S., Hassanali, M., Stothard, P., et al. (2006). DrugBank: a Comprehensive Resource for In Silico Drug Discovery and Exploration. *Nucleic Acids Res.* 34, D668–D672. doi:10.1093/nar/gkj067
- Woo, P. C. Y., Lau, S. K. P., Chu, C.-m., Chan, K.-h., Tsoi, H.-w., Huang, Y., et al. (2005). Characterization and Complete Genome Sequence of a Novel

- Coronavirus, Coronavirus HKU1, from Patients with Pneumonia. *J. Virol.* 79, 884–895. doi:10.1128/jvi.79.2.884-895.2005
- Wu, C., Liu, Y., Yang, Y., Zhang, P., Zhong, W., Wang, Y., et al. (2020a). Analysis of Therapeutic Targets for SARS-CoV-2 and Discovery of Potential Drugs by Computational Methods. *Acta Pharmaceutica Sinica B* 10, 766–788. doi:10.1016/j.apsb.2020.02.008
- Wu, F., Zhao, S., Yu, B., Chen, Y.-M., Wang, W., Song, Z.-G., et al. (2020b). A New Coronavirus Associated with Human Respiratory Disease in China. *Nature* 579, 265–269. doi:10.1038/s41586-020-2008-3
- Xu, Y., Chen, K., Pan, J., Lei, Y., Zhang, D., Fang, L., et al. (2021). Repurposing Clinically Approved Drugs for COVID-19 Treatment Targeting SARS-CoV-2 Papain-like Protease. *Int. J. Biol. Macromolecules* 188, 137–146. doi:10.1016/j.ijbiomac.2021.07.184
- Zhang, Q., Schepis, A., Huang, H., Yang, J., Ma, W., Torra, J., et al. (2019). Designing a Green Fluorogenic Protease Reporter by Flipping a Beta Strand of GFP for Imaging Apoptosis in Animals. *J. Am. Chem. Soc.* 141, 4526–4530. doi:10.1021/jacs.8b13042
- Zhang, Y.-Z., and Holmes, E. C. (2020). A Genomic Perspective on the Origin and Emergence of SARS-CoV-2. *Cell* 181, 223–227. doi:10.1016/j.cell.2020.03.035
- Zhao, Y., Du, X., Duan, Y., Pan, X., Sun, Y., You, T., et al. (2021). High-throughput Screening Identifies Established Drugs as SARS-CoV-2 PLpro Inhibitors. *Protein Cell* 12, 877–888. doi:10.1007/s13238-021-00836-9
- Zhou, P., Yang, X.-L., Wang, X.-G., Hu, B., Zhang, L., Zhang, W., et al. (2020). A Pneumonia Outbreak Associated with a New Coronavirus of Probable Bat Origin. *Nature* 579, 270–273. doi:10.1038/s41586-020-2012-7
- Zhou, S., Hill, C. S., Sarkar, S., Tse, L. V., Woodburn, B. M. D., Schinazi, R. F., et al. (2021). β -d-N4-hydroxycytidine Inhibits SARS-CoV-2 through Lethal Mutagenesis but Is Also Mutagenic to Mammalian Cells. *J. Infect. Dis.* 224, 415–419. doi:10.1093/infdis/jiab247
- Zhu, N., Zhang, D., Wang, W., Li, X., Yang, B., Song, J., et al. (2020). A Novel Coronavirus from Patients with Pneumonia in China, 2019. *N. Engl. J. Med.* 382, 727–733. doi:10.1056/nejmoa2001017

Conflict of Interest: DK serves on the SAB of BioTheryX Inc.

The remaining authors declare that the research was conducted in the absence of any commercial or financial relationships that could be construed as a potential conflict of interest.

Publisher's Note: All claims expressed in this article are solely those of the authors and do not necessarily represent those of their affiliated organizations, or those of the publisher, the editors and the reviewers. Any product that may be evaluated in this article, or claim that may be made by its manufacturer, is not guaranteed or endorsed by the publisher.

Copyright © 2022 Calleja, Lessene and Komander. This is an open-access article distributed under the terms of the Creative Commons Attribution License (CC BY). The use, distribution or reproduction in other forums is permitted, provided the original author(s) and the copyright owner(s) are credited and that the original publication in this journal is cited, in accordance with accepted academic practice. No use, distribution or reproduction is permitted which does not comply with these terms.



Self-Masked Aldehyde Inhibitors of Human Cathepsin L Are Potent Anti-CoV-2 Agents

Ji Yun Zhu¹, Linfeng Li^{1,2}, Aleksandra Drelich², Bala C. Chenna¹, Drake M. Mellott^{1,2}, Zane W. Taylor^{3,2}, Vivian Tat², Christopher Z. Garcia¹, Ardala Katzfuss¹, Chien-Te K. Tseng² and Thomas D. Meek^{1*}

OPEN ACCESS

Edited by:

Matthew Bogyo,
Stanford University, United States

Reviewed by:

Nicola Micale,
University of Messina, Italy
Reik Löser,
Helmholtz Association of German
Research Centres (HZ), Germany

*Correspondence:

Thomas D. Meek
Thomas.Meek@ag.tamu.edu

*Present Address:

Linfeng Li,
Center for Novel Target and
Therapeutic Intervention, Institute of
Life Sciences, Chongqing Medical
University, Chongqing, China
Drake M. Mellott, Agios Pharmaceuticals,
Cambridge, MA, United States
Zane W. Taylor, RD Platform Technology
and Science, GlaxoSmithKline
Pharmaceuticals, Collegeville, PA,
United States

Specialty section:

This article was submitted to
Chemical Biology,
a section of the journal
Frontiers in Chemistry

Received: 01 February 2022

Accepted: 12 April 2022

Published: 04 July 2022

Citation:

Zhu J, Li L, Drelich A, Chenna BC,
Mellott DM, Taylor ZW, Tat V,
Garcia CZ, Katzfuss A,
Tseng C-T and Meek TD (2022) Self-
Masked Aldehyde Inhibitors of Human
Cathepsin L Are Potent Anti-CoV-
2 Agents.
Front. Chem. 10:867928.
doi: 10.3389/fchem.2022.867928

¹Department of Biochemistry and Biophysics, College of Agriculture and Life Sciences, Texas A&M University College Station, College Station, TX, United States, ²Department of Microbiology and Immunology, John Sealy School of Medicine, University of Texas Medical Branch at Galveston, Galveston, TX, United States, ³Department of Chemistry, College of Science, Texas A&M University College Station, College Station, TX, United States

Cysteine proteases comprise an important class of drug targets, especially for infectious diseases such as Chagas disease (cruzain) and COVID-19 (3CL protease, cathepsin L). Peptide aldehydes have proven to be potent inhibitors for all of these proteases. However, the intrinsic, high electrophilicity of the aldehyde group is associated with safety concerns and metabolic instability, limiting the use of aldehyde inhibitors as drugs. We have developed a novel class of compounds, self-masked aldehyde inhibitors (SMAs) which are based on the dipeptide aldehyde inhibitor (Cbz-Phe-Phe-CHO, **1**), for which the P₁ Phe group contains a 1'-hydroxy group, effectively, an *o*-tyrosinyl aldehyde (Cbz-Phe-*o*-Tyr-CHO, **2**; (Li *et al.* (2021) *J. Med. Chem.* 64, 11,267–11,287)). Compound **2** and other SMAs exist in aqueous mixtures as stable δ -lactols, and apparent catalysis by the cysteine protease cruzain, the major cysteine protease of *Trypanosoma cruzi*, results in the opening of the lactol ring to afford the aldehydes which then form reversible thiohemiacetals with the enzyme. These SMAs are also potent, time-dependent inhibitors of human cathepsin L (K_i = 11–60 nM), an enzyme which shares 36% amino acid identity with cruzain. As inactivators of cathepsin L have recently been shown to be potent anti-SARS-CoV-2 agents in infected mammalian cells (Mellott *et al.* (2021) *ACS Chem. Biol.* 16, 642–650), we evaluated SMAs in VeroE6 and A549/ACE2 cells infected with SARS-CoV-2. These SMAs demonstrated potent anti-SARS-CoV-2 activity with values of EC_{50} = 2–8 μ M. We also synthesized pro-drug forms of the SMAs in which the hydroxyl groups of the lactols were O-acylated. Such pro-drug SMAs resulted in significantly enhanced anti-SARS-CoV-2 activity (EC_{50} = 0.3–0.6 μ M), demonstrating that the O-acylated-SMAs afforded a level of stability within infected cells, and are likely converted to SMAs by the action of cellular esterases. Lastly, we prepared and characterized an SMA in which the sidechain adjacent to the terminal aldehyde is a 2-pyridonyl-alanine group, a mimic of both phenylalanine and glutamine. This compound (**9**) inhibited both cathepsin L and 3CL

Abbreviations: AMC, 7-amino-4-methylcoumarin; CHAPS, 3-[3-(cholamidopropyl)dimethylammonio]-1-propanesulfonate; Cbz/Z, benzyloxycarbonyl; DMSO, dimethyl sulfoxide; DTT, dithiothreitol; EDTA, ethylenediaminetetraacetic acid; SMAI, self-masked aldehyde inhibitor; Z-FR-AMC, carboxybenzyl-L-phenylalanine-L-arginine-7-amino-4-methylcoumarin.

protease at low nanomolar concentrations, and also exerted anti-CoV-2 activity in an infected human cell line.

Keywords: SARS coronavirus-2, cathepsin L, self-masked aldehydes, reversible covalent inactivation, COVID-19, cysteine proteases

INTRODUCTION

The global COVID-19 pandemic, caused by the β -coronavirus SARS-CoV-2, has, as of the end of 2021, resulted in 289 million cases and 5.4 million deaths worldwide (Johns Hopkins University of Medicine, 2022). The socio-economic consequences of this pandemic are difficult to overstate. Despite the availability of effective vaccines since 2021, and the recent (emergency use) approval of a bespoke, small-molecule drug (Paxlovid (Pfizer, 2021); nirmatrelvir, combined with ritonavir) for the treatment of COVID-19, the emergence of new variant forms of the SARS-CoV-2 virus, such as the delta and omicron strains, will require further discovery of new therapeutic agents to counter the inevitable development of SARS-CoV-2 variants that are resistant to these first-generation drugs.

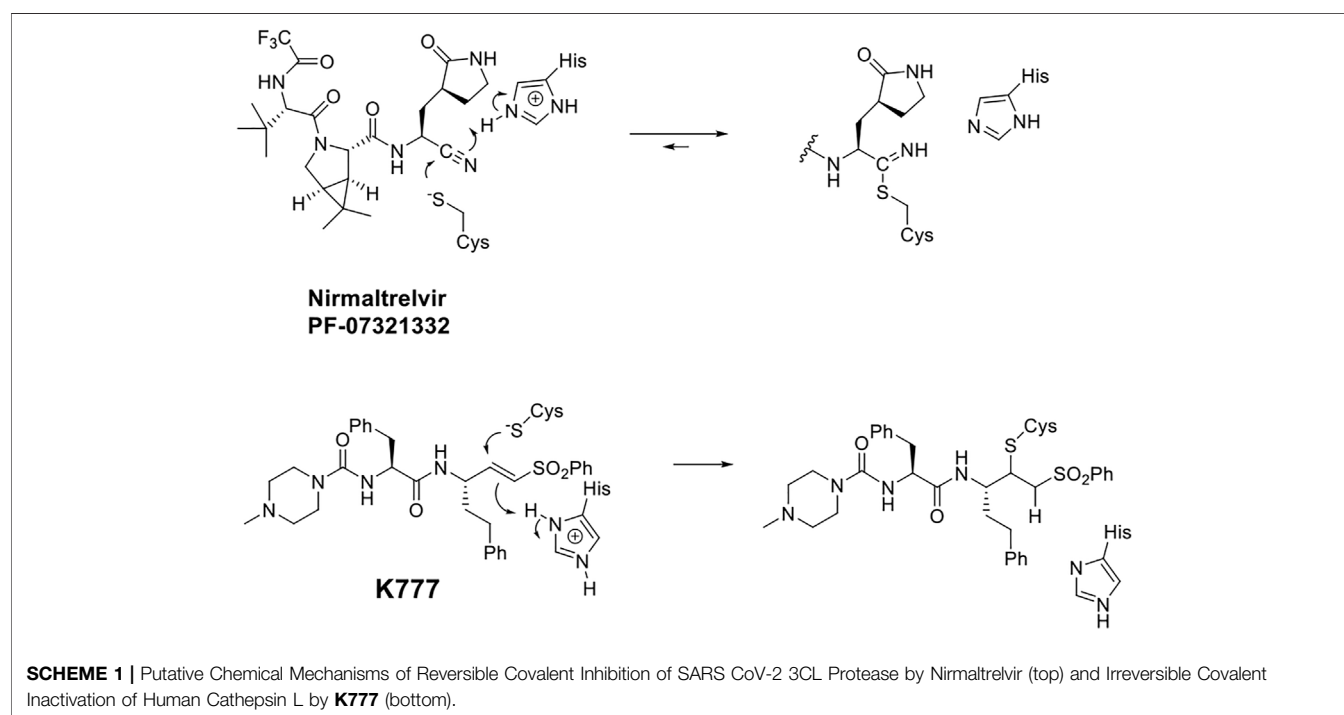
The virally-encoded cysteine protease known as the Main protease, or 3CL protease (Zhang et al., 2020; Dai et al., 2020; and Mellott et al., 2021), is the target of nirmatrelvir, also known as **PF-07321332** (Owen et al., 2021) (**Scheme 1**). **PF-07321332** exerts reversible covalent inhibition of the 3CL protease by a putative mechanism of action involving the formation of a thioimide adduct (**Scheme 1**) (Bai et al., 2021; Owen et al., 2021).

In general, the most effective inhibitors of cysteine proteases are peptide analogues bearing electrophilic warheads, which undergo reaction with the active-site cysteine (Puzer et al.,

2004; Cianni et al., 2019; and Cianni et al., 2021). The peptide or peptidomimetic moieties of such inhibitors are based on the substrate specificity of the target cysteine protease, and are therefore designed to selectively guide the appended warhead to the active-site of intent.

In this regard, the preferred peptide substrates of the cysteine protease cathepsin L (Brömme et al., 1994; Puzer et al., 2004) and cruzain (Zhai and Meek, 2018) contain leucine, phenylalanine, or a similar amino-acid sidechain at the P_2 (Schechter and Berger, 1967) of the peptide, while for the CoV-2 3CL protease, a virtually invariant glutamine is found at the P_1 position, and leucine and other hydrophobic amino-acid sidechains exist at the P_2 positions (Rut et al., 2021). These preferences inform the development of specific peptide scaffolds for the inhibitors of these proteases. It is generally held that reversible covalent inhibition will afford inhibitors of higher selectivity and lower cytotoxicity than their irreversible counterparts, such as the vinyl sulfone warhead of K777 (Doyle et al., 2007; Kerr et al., 2009). Peptide aldehydes comprise a long-standing class of reversible covalent inhibitors of the cysteine protease (Lewis and Wolfenden, 1977; Woo et al., 1995; Peheré et al., 2019).

In addition to the essentiality of the 3CL protease to establish cellular infection by SARS-CoV-2, host-cell proteases are also involved, catalyzing the peptidolysis of the coronaviral spike protein (S), which is required for cellular uptake and intracellular trafficking of the coronavirus (Mellott et al., 2021;



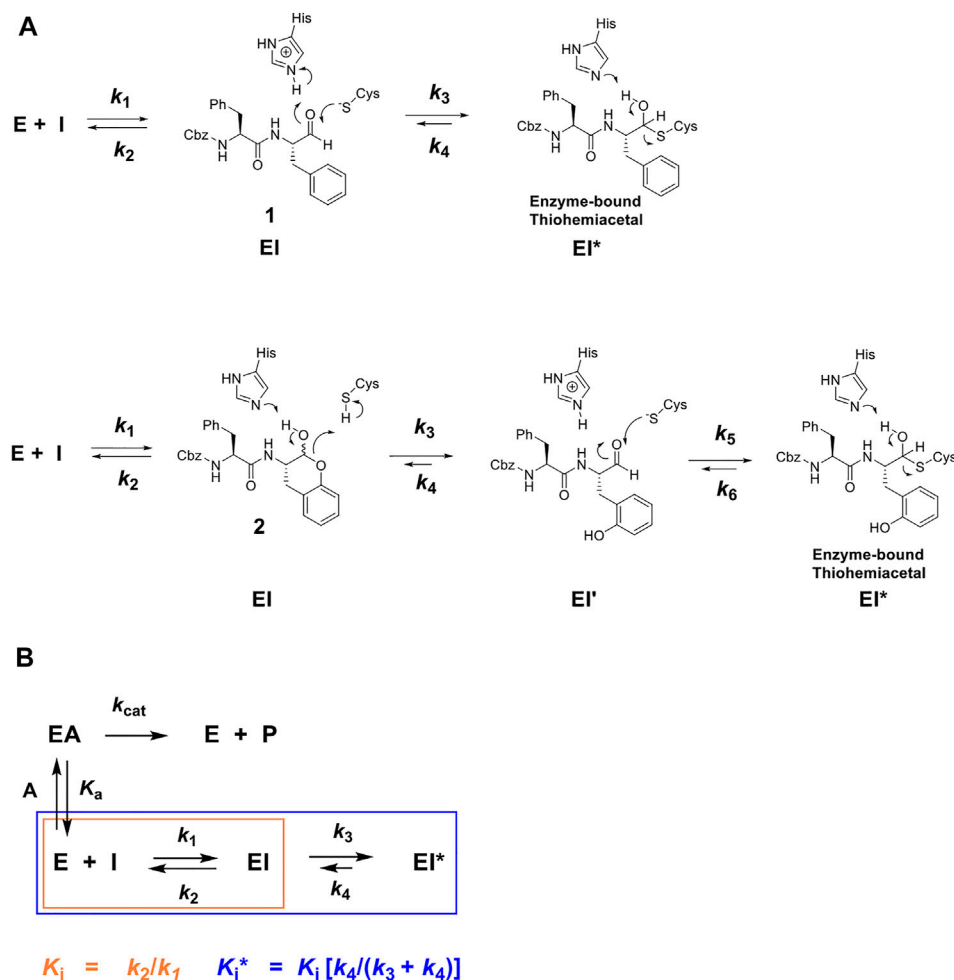


FIGURE 1 | (A) Putative chemical mechanisms of reversible covalent inhibition of a cysteine protease by Cbz-Phe-Phe-CHO (**1**) and its self-masked aldehyde analogue **2** (Li et al., 2021). Dipeptide aldehyde **1** binds to free enzyme **E** to form an **EI** complex, which apparently undergoes a reaction with the active-site to form a thiohemiacetal adduct (k_3), the **EI*** complex, which can slowly revert via the k_4 step to re-form the aldehyde. The self-masked aldehyde (**2**), is a *o*-tyrosinyl analogue of **1**, which exists in the solution as a δ -lactol; the form which binds to the protease. The cysteine protease apparently catalyzes the ring-opening of the lactol (The k_3 step), to afford the bound aldehyde (**EI'**), which proceeds to form the reversibly-covalent **EI*** complex (Li et al., 2021). **(B)** Kinetic scheme for time-dependent inhibitor **I** which competes with substrate **A** for free enzyme **E** to rapidly form complex **EI** (described by inhibition constant K_i , orange), which after minutes forms slowly-reversible complex **EI*** (described by inhibition constant K_i^* , blue), for which $K_i > K_i^*$.

Hoffmann et al., 2020). Accordingly, these host proteases may also provide additional drug targets for SARS-CoV-2 infection. We recently reported that **K777**, or **K11777**, a di-peptide vinyl sulfone inactivator of the trypanosomal cysteine protease, cruzain (Scheme 1), which had been a clinical candidate for Chagas disease (McKerrow et al., 2009), was an exceptionally potent anti-SARS-CoV-2 agent (Mellott et al., 2021). We used a propargyl analogue of **K777** to covalently label and characterize the cellular target of **K777** in SARS-CoV-2-infected Vero E6 cells. We showed that cathepsin L was specifically labeled by **K777**, and in addition, we demonstrated that purified human cathepsin L catalyzed a unique cleavage of the spike protein from SARS-CoV-2; an event that assists the coronaviral uptake. As a result, human cathepsin L comprises an additional cellular target for the development of anti-COVID-19 agents.

While peptidic aldehydes form reversible thiohemiacetal adducts with the active-site cysteines of cysteine proteases (Cianni et al., 2021; Lewis and Wolfenden, 1977; Peheré et al., 2019; and Woo et al., 1995), and thereby afford exceptionally potent inhibition, free aldehydes are in general too reactive to provide therapeutic agents (Kaplowitz, 2005; Gampe and Verma, 2020; and O'Brien et al., 2005). However, CAT811, a macrocyclic aldehyde which is an inhibitor of the cysteine protease calpain, may be applied topically to the eye leading to the reduction of cataract formation (Morton et al., 2013). Consequently, we developed a novel class of reversible covalent inhibitors of cruzain, known as self-masked aldehyde inhibitors (SMAIs). SMAIs exist in aqueous solutions as stable δ -lactols, and in our hands, cruzain catalyzed the opening of the lactol to provide the enzyme-bound aldehyde, which subsequently

formed a thiohemiacetal adduct with cruzain (**Figure 1**) (Li et al., 2021). These SMAIs provided potent inhibition of cruzain ($K_i = 18\text{--}350\text{ nM}$), and some of these compounds demonstrated potent anti-trypanosomal activity in cellular-infection models of Chagas disease (Li et al., 2021). Given that human cathepsin L and cruzain share 36% amino-acid identity, and consequently, similar peptide-substrate specificity, we sought to characterize these SMAIs as inhibitors of human cathepsin L, and then evaluate potent inhibitors as potential anti-SARS-CoV-2 agents in models of cellular infection. We describe the results of these studies herein. In the preparation of this article, we became aware that benzyl δ -lactols of structures similar to our SMAIs are found in the anti-bacterial, nature-products known as cordycepamides (Fan et al., 2020).

MATERIALS AND METHODS

Chemicals

Sodium acetate, disodium-EDTA, Tris-HCl, and NaCl were obtained from Millipore Sigma. CHAPS and dithiothreitol were obtained from BioGold. Cbz-Phe-Arg-7-amino-4-methylcoumarin (Z-FR-AMC) was purchased from EMD Millipore or GenScript. The methods for the synthesis and characterization of the FRET-based substrate for 3CL-PR, (Abz)HN-Ser-Ala-Val-Leu-Gln*Ser-Gly-Phe-Arg-Lys (ϵ -Dnp)-CONH₂ is described in Mellott *et al.* (2021). The synthesis and characterization of all self-masked aldehyde inhibitors described in this work may be found in Li *et al.* (2021).

Cathepsins

Recombinant proteases were obtained from the following vendors: recombinant human cathepsin L (Millipore Sigma, Athens Research and Technology, Inc.), and human liver cathepsin B (Millipore Sigma), which were used without further purification. The solid proteins were dissolved into a solution of 50 mM sodium acetate (pH 5.5), 1 mM Na₂EDTA, 1 mM CHAPS, 10% (v/v) DMSO, and 5 mM DTT to final protein concentrations of 1–10 μM in 20- μL aliquots, and stored at -80°C until needed. These samples were then diluted into the same buffer to concentrations of $\sim 100\text{ nM}$, and these dilutions were stored at 4°C and used daily until depletion.

Expression and Purification of SARS-CoV-2 3CL Protease (3CL-PR)

The expression and purification of the 3CL-PR have been previously described (Mellott *et al.*, 2021). In brief, an expression construct of SARS-CoV-2 3CL-PR contained a GST domain at the N-terminus of the 3CL-PR coding sequence, followed by the 3CL-PR cleavage sequence (SAVLQ*SGF) preceding the sequence encoding the remaining 303 amino acids of the 3CL-PR monomer, followed at its C-terminus by a modified PreScission protease sequence (SGVTFFQ*GP), that preceded a His₆ sequence (Zhang *et al.*, 2020; Mellott *et al.*, 2021). Upon expression, auto-proteolysis from 3CL-PR removed the N-terminal GST tag, yielding the authentic N-terminus (SGF).

After binding this processed protein to a nickel-NTA column, eluted fractions were pooled and dialyzed to remove imidazole. Proteolysis of the C-terminal H₆ tag was conducted by incubating with 3.5 units of HRV 3C Protease (Thermo Fisher Scientific) per mg of 3CL-PR (determined by Nanodrop) at 4°C overnight. Subsequently, the protein mixture was subjected to chromatography on a 5-ml GStrap HP column, and then a 5-ml HisTrap HP column (GE Healthcare), to remove, respectively, the GST-fused HRV 3C protease and undigested H₆-tagged protein. After chromatography on an anion exchange column and gel-filtration column, the tag-free 3CL-PR was pooled and concentrated (10 kDa molecular weight cutoff filter, GE Healthcare). The protein was deemed to be $\geq 95\%$ pure by SDS-PAGE, and was stored at -80°C in 12 mM Tris-HCl, 120 mM NaCl, 0.1 mM EDTA, and 2 mM DTT, (pH 7.5) with 50% glycerol (v/v). Analytical gel filtration indicated that native 3CL-PR was the expected homodimer (68 kDa).

Kinetic Assays and Characterization of Inhibition for Human Cathepsin B and L

For assays of cathepsin L and B, inhibitors were evaluated in 0.25-ml reaction mixtures containing a buffer of sodium acetate (pH 5.5), 1 mM CHAPS, 1 mM Na₂EDTA, and 5 mM DTT at 25°C . The fluorogenic substrate Cbz-Phe-Arg-7-amino-4-methylcoumarin (Z-FR-AMC) was dissolved in 100% DMSO, as were all inhibitors and aliquots of both substrates, and inhibitors were added to the reaction mixtures with final concentrations of DMSO of 10% (v/v). Reactions were initiated by addition of the proteases to final concentrations of 1–2 nM of either cathepsin L or cathepsin B. Michaelis constants for Z-FR-AMC were determined for cathepsin L ($K_m = 2.9\text{ }\mu\text{M}$) and cathepsin B ($K_m = 150\text{ }\mu\text{M}$), and fixed concentrations of Z-FR-AMC of 1x or 2x K_m were used to evaluate inhibitors. Formation of the fluorescent product AMC was monitored over 30–60-min time courses for reaction mixtures in 96-well black microplates (Greiner). Rates of peptidolysis of the dipeptide-AMC substrate(s) were measured on either a SpectraMax M2 (Molecular Devices) or a Synergy Mx (Biotek, Winooski, VT) microplate reader which measured the formation of fluorescence using an excitation wavelength of $\lambda_{\text{ex}} = 360\text{ nm}$, with detection of emission at $\lambda_{\text{em}} = 460\text{ nm}$ at $\geq 8\text{-s}$ intervals. Control samples excluded substrate. The measured relative fluorescence units (RFUs) of generated AMC were converted to reaction rates of $\mu\text{M/s}$ by use of a standard curve of known AMC concentrations obtained for both plate readers.

Kinetic Analysis of SARS-CoV-2 3CL-PR and Characterization of Its Inhibitors

In reaction mixtures containing 20 mM Tris-HCl (pH 7.5), 150 mM NaCl, 0.1 mM EDTA, 2 mM DTT, 10% (v/v) DMSO (a final concentration arising from addition of substrates and inhibitors added from 100% (v/v) DMSO solutions), and variable concentrations (10–175 μM) of the FRET-based substrate Abz-SAVLQ*SGFRK (DNP)-NH₂,⁵ the reaction was initiated by the addition of 3CL-PR to final concentrations of 25–50 nM in 96-

well plates (Greiner, flat-bottom half volume, clear black plates). Rates of peptidolysis of the Abz-SAVLQ*SGFRK (DNP)-NH₂ substrate were measured on either a SpectraMax M5 (Molecular Devices) or a Synergy HTX (Biotek, Winooski, VT) microplate reader with $\lambda_{\text{ex}} = 320$ nm, $\lambda_{\text{em}} = 420$ nm in 8–60 s intervals, and time courses of inhibition were obtained for either 30 or 60 min intervals. Control samples excluded the substrate. The measured relative fluorescence units (RFUs) of the generated Abz-SAVLQ-COOH were converted to reaction rates of $\mu\text{M/s}$ by use of a standard curve of known concentration of fully hydrolyzed substrates obtained for both plate readers.

Cell Culture and Evaluation of Efficacy in SARS-CoV-2 Infection

Vero E6 cells [CRL:1586, ATCC], derived from African green monkey cells were grown in an Eagle's minimal essential medium (EMEM) supplemented with standard doses of penicillin and streptomycin, and 10% fetal bovine serum (FBS), which we designate as the M-10 medium. Human A549 cells that had been stably transduced with human ACE2 viral receptor (A549/ACE2), and then selected for increased ACE2 receptor, were grown in M-10. SARS-CoV-2 (USA_WA1/2020 isolate), the 3rd passage in Vero E6 cells from the original CDC (Atlanta) material with a confirmed sequence, was used throughout the study. A modified Vero E6-based standard micro-neutralization assay was used to rapidly evaluate the drug efficacy against the SARS-CoV-2 infection. Briefly, confluent Vero E6 or A549/ACE2 cells grown in 96-wells microtiter plates were pre-treated with 78 nM to 20 μM of the SMAIs and K777 (2-fold serially diluted) for 2 h, before infection with ~ 100 or ~ 500 infectious SARS-CoV-2 particles, respectively, in 100 μL EMEM supplemented with 2% FBS (2-MEM). Cells pre-treated with 2-fold serially-diluted dimethyl sulfoxide (DMSO; final concentration = 1% (v/v)) with or without the virus were included as positive and negative controls, respectively. After cultivation at 37°C for 3 days (Vero E6) or 4 days (A549/ACE2), individual wells were observed by microscopy for the status of a virus-induced formation of the cytopathic effect (CPE). The efficacy of individual drugs was calculated and expressed as the lowest concentration capable of completely preventing virus-induced CPE in 100% of the wells. The values of EC₅₀ (the concentration of inhibitor that results in a 50% growth of the virus) were determined in two ways: 1) In duplicate samples of a single compound dilution in which 100% CPE was observed for both replicates, and in which no CPE was observed at the next highest concentration of the inhibitor in duplicates, we assigned the value of EC₅₀ as the average of these two concentrations. 2) In cases in which duplicate concentrations result in one sample displaying CPE while the other does not, the value of EC₅₀ was assigned to this concentration. All experiments using infectious viruses were conducted at the University of Texas Medical Branch under BSL-3 conditions.

Fitting of Kinetic Data

The time-course data for compounds which exhibited time-dependent inhibition were fitted to Eq. 1, for which P is the relative fluorescence units of the AMC product, where v_i and v_s are the initial ($t < 500$ s) and steady-state ($t > 3,000$ s)

velocities, respectively, and k_{obs} is the rate constant of conversion of v_i to v_s , t is time in seconds, and C is a background constant.

$$P = v_s t + \left(\frac{v_i - v_s}{k_{\text{obs}}} \right) (1 - e^{-k_{\text{obs}} t}) + C \quad (1)$$

Resulting values of k_{obs} vs. $[I]$ were re-plotted and fitted to Eq. 2, in which k_3 and k_4 represent the respective rates of formation and reversion of the EI* complex as shown in Figure 1B, in which $K_i = k_2/k_1$ and $K_i^* = (k_2/k_1) (k_4/(k_3 + k_4))$, and for which A is the fixed substrate concentration, and K_a is the Michaelis constant.

$$k_{\text{obs}} = k_4 + \frac{k_3 [I]}{K_i \left(1 + \frac{[A]}{K_a} \right) + [I]} \quad (2)$$

Linearity of k_{obs} vs. $[I]$ of the inhibitor compounds will be observed when $K_i \gg K_i^*$. Under these conditions, the concentration of inhibitors required to observe time-dependent inhibition would be much less than the value of K_i for the EI complex. In this case, Eq. 2 reduces to Eq. 3, which is a linear function with a slope = $k_3/[K_i (1 + [A]/K_a)]$ and a y -intercept = k_4 .

$$k_{\text{obs}} = k_4 + \frac{k_3 [I]}{K_i \left(1 + \frac{[A]}{K_a} \right)} \quad (3)$$

Inhibition constants (K_i and K_i^* values) were also obtained by fitting plots of v_i/v_0 and v_s/v_0 vs. [inhibitor] to Eqs 4 and 5, wherein v_i and v_s are velocities at the early and late stages of the time courses of inhibition, respectively, v_0 is v_i and v_s when no inhibitor is present, $[I]$ is variable concentrations of the inhibitor, and K_a is the Michaelis constant of the substrate.

$$\frac{v_i}{v_0} = \frac{1}{\left\{ 1 + \frac{[I]}{K_i \left(1 + \frac{[A]}{K_a} \right)} \right\}} \quad (4)$$

$$\frac{v_s}{v_0} = \frac{1}{\left\{ 1 + \frac{[I]}{K_i^* \left(1 + \frac{[A]}{K_a} \right)} \right\}} \quad (5)$$

RESULTS AND DISCUSSION

Inhibition of Cysteine Proteases

The time courses of the inhibition of human cathepsin L by the parent aldehyde inhibitor in this study, Cbz-Phe-Phe-CHO (1), demonstrated initial inhibition, arising from the immediate formation of an EI complex, that apparently isomerized to a tighter complex (EI*) in a concentration-dependent manner, after 1,000 s of incubation (Figures 1, 2A), in a manner nearly indistinguishable from that observed for cruzain (Li et al., 2021). By fitting the time course at each concentration of 1 to Eq. 1, we obtained values of k_{obs} , v_i , and v_s ; the latter two of which were normalized by the division of each value by the corresponding value of v_i and v_s in which $[I] = 0$, to provide values of v_i/v_0 and v_s/v_0 . A replot of the values of k_{obs} vs. $[I]$ (Figure 2A, inset) were fitted to both Eqs 2, 3. The apparent lack of a hyperbolic response

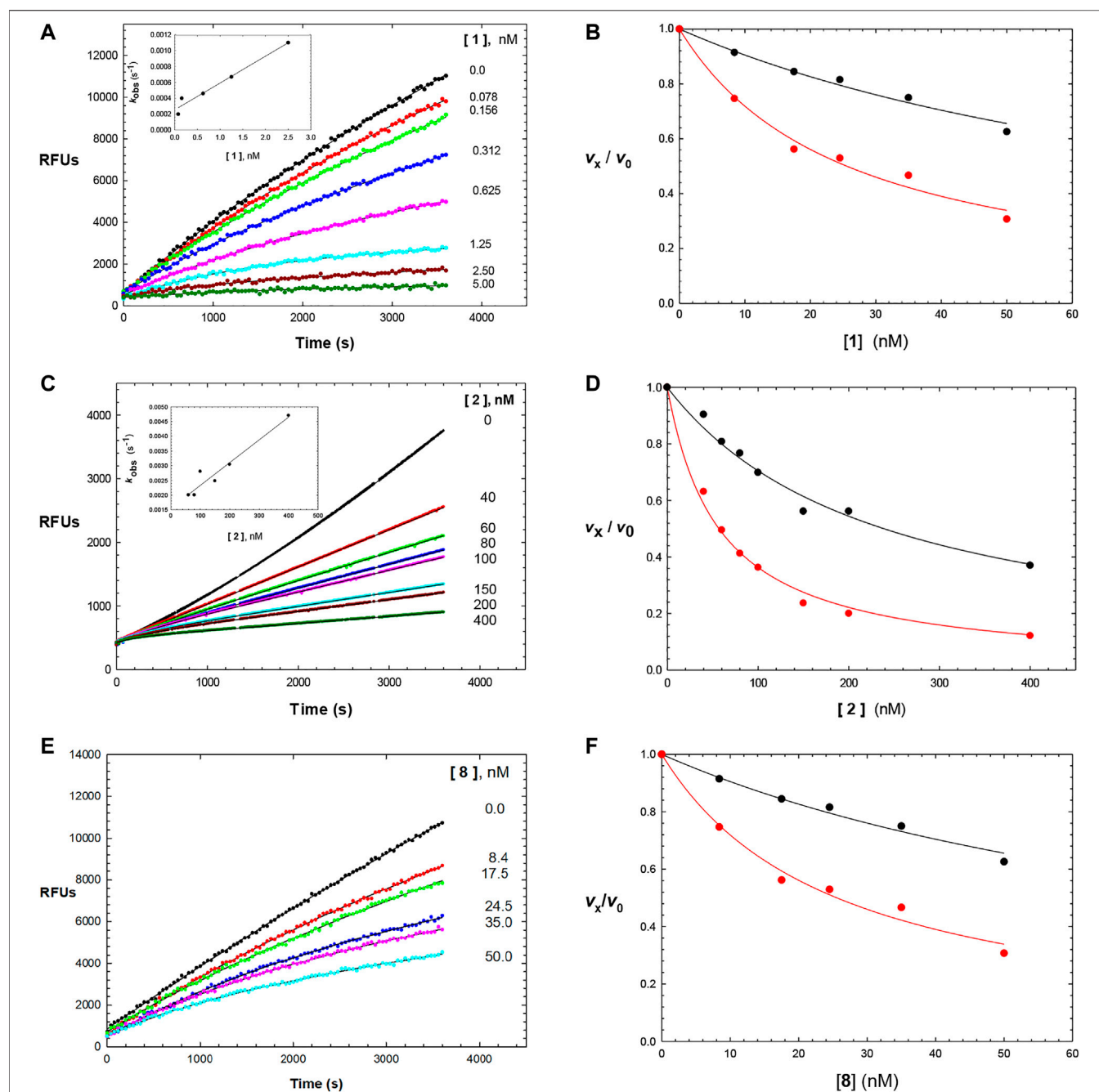


FIGURE 2 | Time courses (0–3600 s) of the inhibition of human cathepsin L by Cbz-Phe-Phe-CHO (**1**) (**A**); 0–5 nM of compound **1**, Cbz-Phe-o-Tyr-CHO (**2**) (**C**); 0–400 nM of compound **2**, and NMe-Pip-Phe-o-Tyr-CHO (**8**) (**E**); 0–50 nM of compound **8**. The measured RFUs (relative fluorescence units) were obtained upon cleavage of the fluorogenic peptide substrate Cbz-Phe-Arg-AMC (10 μ M; **3X** its apparent Michaelis constant with human cathepsin L). The lines drawn through the experimental points were from the plotting of each line to Eq. 1, and resulting values of v_i and v_s were normalized by dividing by v_i and v_s at $[I] = 0$ (v_0), to provide values of v_i/v_0 and v_s/v_0 , which were then replotted vs. each concentration of inhibitor as v_i/v_0 vs. [inhibitor] (black) and v_s/v_0 vs. [inhibitor] (red) in (**B,D,F**). Each plot was fitted to versions of the Cheng–Prusoff equation (Eq. 4 for v_i/v_0 , and Eq. 5 for v_s/v_0), to provide, the apparent inhibition constants of K_i and K_i^* , respectively. The insets in Figures 2A,C are replots of k_{obs} vs. [1] and k_{obs} vs. [2], from values of k_{obs} obtained from each time-course curve for each inhibitor from fitting to Eq. 1, respectively. The line drawn through the inset plots were from fitting to Eq. 3, resulting in values of $k_3/[K_i(1 + [A]/K_a)] = (1.5 \pm 0.2) \times 10^{-4} \text{ nM}^{-1} \text{ s}^{-1}$ and $k_4 = (2.6 \pm 0.5) \times 10^{-4} \text{ s}^{-1}$ (inhibitor **1**), and $k_3/K_i = (4 \pm 0.5) \times 10^{-6} \text{ nM}^{-1} \text{ s}^{-1}$ and $k_4 = 0.0016 \pm 0.0002 \text{ s}^{-1}$ (inhibitor **2**). Fitting of v_i/v_0 and v_s/v_0 vs. [8] resulted in values of K_i and K_i^* which are found in Table 1, along with all inhibition parameters.

of k_{obs} by **1** indicated that K_i was much greater than the applied concentrations of the aldehyde, and that Eq. 3 was the more appropriate equation for data fitting. Consequently, the use of Eq.

3 resulted in values of $k_3/[K_i(1 + [A]/K_a)] = (1.5 \pm 0.2) \times 10^{-4} \text{ nM}^{-1} \text{ s}^{-1}$ and $k_4 = (2.6 \pm 0.5) \times 10^{-4} \text{ s}^{-1}$, from which we may calculate $k_4K_i/k_3 \sim K_i^* = 13 \text{ nM}$. The rate constant for the

TABLE 1 | Self-masked aldehyde inhibitors of cysteine proteases and their effects on SARS-CoV-2 infected cells^a.

Compound	R ₄	R ₃	R ₂	R ₁ -A	K _i [*] (nM)				Anti-CoV-2 EC ₅₀ (μM)	
					hCatL	Cruzain ^b	hCatB	3CLpro ^b	Vero E6 Cells	A549/ACE2 Cells
1	H		Bz		0.14 ± 0.01	0.44 ± 0.02	ND	>10,000	0.47/7.5	>20
2	H	Cbz	Bz		12.6 ± 0.4	49 ± 2	4,500 ± 100	>10,000	10 ± 5	>20
3	OMe	Cbz	Bz	o-Tyr-CHO	17 ± 0.9	350 ± 30	5,500 ± 400	>10,000	ND	ND
4	Me	Cbz	Bz	o-Tyr-CHO	26 ± 0.9	103 ± 5	6,100 ± 900	>10,000	ND	ND
5	Cl	Cbz	Bz	o-Tyr-CHO	12.1 ± 0.3	70 ± 10	1400 ± 100	>10,000	ND	ND
6	F	Cbz	Bz	o-Tyr-CHO	10.3 ± 0.5	48 ± 2	2,300 ± 200	>10,000	4	ND
7	CO ₂ Me	Cbz	Bz	o-Tyr-CHO	4.8 ± 0.2	18.0 ± 0.5	670 ± 30	>10,000	2.5	ND
8	H		Bz	o-Tyr-CHO	9.0 ± 0.4	47 ± 2	1270 ± 70	>10,000	9 ± 2	ND
9	H				22 ± 4	ND	ND	9 ± 2 ^b	ND	3.75
10	H	Me-Pip	Bz		NA	NA	NA	NA	2.5	0.31
11	H	Me-Pip	Bz		NA	NA	NA	NA	2.5	0.62
12	H	Me-Pip	Bz		NA	NA	NA	NA	4	0.31
K777 ^c	NA	Me-Pip			k _{inact} /K _i = 3 ± 1 μM ⁻¹ ·s ⁻¹	k _{inact} /K _i = 1.0 ± 0.3 μM ⁻¹ ·s ⁻¹	k _{inact} /K _i = 0.009 ± 0.004 μM ⁻¹ ·s ⁻¹	>10,000	0.62 ^c / 0.15	<0.078 ^c
PF-07321332					>100mM ^d	ND	>100mM ^d	3.11 ^d	0.074 ^d / >20	0.077 ^d / 0.47

^aInhibition constants (K_i^{*} values) obtained after 30-min incubation of inhibitors with cysteine proteases as described in Methods.^bData for human cathepsins B and L were obtained at pH 5.5, and at neutral pH for cruzain (pH 7.5) (Zhai and Meek, 2018) and for 3CL protease (pH 7.2).^cKinetic parameters of inactivation for K777 are as reported in Mellott et al. (2021).^dData from Owen et al. (2021); NA, not applicable; ND, no data.

reversal of the EI* complex to EI is exceptionally slow ($k_4 = (2.6 \pm 0.5) \times 10^{-4} \text{ s}^{-1}$), and this is an important factor in the observed, sub-nanomolar value of K_i^{*}, and also reflects the apparent stability of the enzyme-thiohemiacetal complex of EI*. Fitting

of the plots of v_i/v_0 and v_s/v_0 vs. [1], Eqs. 4 and 5, resulted in respective inhibition constants of K_i = 0.18 ± 0.22 nM and K_i^{*} = 0.14 ± 0.01 nM (Figure 2B), respectively, demonstrating that Cbz-Phe-Phe-CHO is an exceptionally potent inhibitor of human

cathepsin L (**Table 1** and **Figure 2A**), and is 3-fold more potent than its inhibition of cruzain ($K_i^* = 0.44 \pm 0.04$ nM (Li et al., 2021), **Table 1**).

Its analogue, the self-masked aldehyde Cbz-Phe-*o*-Tyr-CHO (**2**) demonstrated less time-dependent inhibition compared to **1** (**Figure 2C**), and again, the replot of k_{obs} vs. **[2]** (**Figure 2C**, inset) was linear. Fitting of these data to **Eq. (3)** resulted in the values of $k_3/K_i = (8 \pm 1) \times 10^{-6}$ nM⁻¹ s⁻¹ and $k_4 = 0.0016 \pm 0.0002$ s⁻¹, leading to $k_4K_i/k_3 \sim K_i^* = 200$ nM. The conversion of the apparent EI* to EI (rate constant of $k_4 = 0.0016 \pm 0.0002$ s⁻¹) is ~5-fold faster than that of aldehyde **1**, which contributes to the 100-fold weaker inhibition of **2**, as exemplified by K_i^* (see below). As discussed in our study of compound **2** with cruzain, we ascribed this faster rate of reversion of the thiohemiacetal (EI* to EI) due to the facilitation of the phenoxide group of **2** to break the C–S bond of the thiohemiacetal to elicit reformation of the lactol of **2** (Li et al., 2021). Fitting of plots of v_i/v_0 and v_i/v_0 vs. **[2]** to, **Eqs 4** and **5**, resulted in respective inhibition constants of $K_i = 54 \pm 6$ nM and $K_i^* = 12.6 \pm 0.4$ nM. Also, as with cruzain, the self-masked aldehyde analogue of **1** (Cbz-Phe-*o*-Tyr-CHO (**2**)) was 100-fold less potent as an inhibitor of cathepsin L, but the value of K_i^* of **2** for cathepsin L was 3.9-fold more potent than that observed for cruzain (**Table 1**). The kinetic behavior of the inhibitors of **1** and **2** are very similar to that observed with cruzain (Li et al., 2021).

Addition of the electron-donating groups methoxy (**3**) and methyl (**4**) at the 4'-position of the *o*-Tyr group resulted in respective 1.4-fold and 2-fold increases in their K_i^* values compared to **2**, while the substitution of **2** at this position with the electron-withdrawing groups fluoro (**5**) and chloro (**6**) had little effect on the inhibition of cathepsin L compared to unsubstituted compound **2**. With the exception of compound **3**, these inhibitors were ≥ 2 -fold more potent for human cathepsin L than cruzain, which also indicated that substitution at the 4'-position had less of an effect on the inhibition of cathepsin L than that of cruzain. Like with cruzain, the 4'-methylcarboxylate substituent of compound **7** improved potency 2.6-fold over that of **2**, and afforded the most potent SMAI in this series of compounds. Substitution of the terminal Cbz group of **2** with an N-methyl-piperidinyl urea provided a more potent analogue of **2**: compound **8** (**Figures 2E and F**), for which values of $K_i = 22 \pm 1$ nM and $K_i^* = 9.0 \pm 0.4$ nM were obtained. Inhibitor **8** has greater aqueous solubility than **2** (Li et al., 2021), and was nearly twice as potent as **2** for human cathepsin L. In the earlier study, we showed that the [*aldehydic*-¹³C] form of compound **8**, as analyzed by ¹H-¹³C HSQC NMR, remained exclusively in its δ -lactol form in aqueous reaction buffer, but upon the addition of an equimolar amount of cruzain, changes to the chemical shifts in the NMR data were consistent with the formation of an enzyme-bound thiohemiacetal adduct (Li et al., 2021). The improved potency of compound **8** with cathepsin L suggests, but does not prove, that cathepsin L in kind, catalyzes the opening of the δ -lactol form leading to the formation of a thiohemiacetal with cathepsin L.

Where studied, the SMAIs in **Table 1** were 120–320-fold less potent inhibitors of human cathepsin B than with cathepsin L. This selectivity also underscores the 36% amino-acid identity between cruzain and human cathepsin L, while there is only a 29% amino-

acid identity between human cathepsins L and B. Expectantly, none of compounds **1–8** exhibited inhibition of the SARS-CoV-2 3CL protease at concentrations of 10 μ M or lower (**Table 1**).

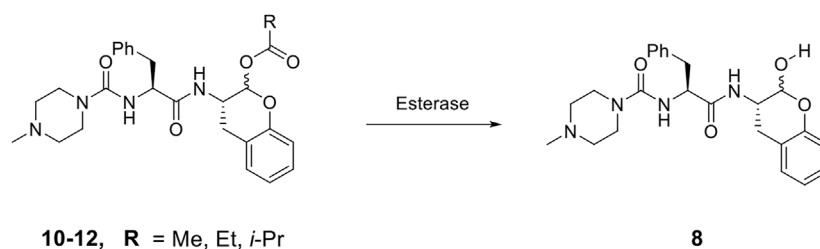
Modifications of SMAIs to Develop 3CL-PR Inhibitors That are Also Inhibitors of Human Cathepsin L

We sought to identify an amino-acid sidechain at the P₁ position of a peptide scaffold which would be recognized by both human cathepsin L and SARS-CoV-2 3CL PR. To date, only 2-oxopyrrolidinyl-alanyl groups (Op-Ala), in effect, glutaminyllactams, have afforded suitable sidechains at the P₁ position for inhibitors of SARS-CoV-2 3CL-PR (Dai et al., 2020; Zhang et al., 2020; and Owen et al., 2021). Given that the substituted or un-substituted phenylalanyl groups at the P₁ position within the peptidomimetic scaffolds of compounds **1–8** provide potent cathepsin L inhibitors that had no effect on purified 3CL protease, we sought to find an amino-acid group for the P₁ sidechain that would be accommodated by both human cathepsin L and SARS-CoV-2 3CL protease. Such bi-functional anti-CoV-2 agents would presage a novel class of COVID-19 drugs that might subvert the development of viral mutations that thwart the action of drugs that only target 3CL protease, or for that matter, cathepsin L.

We hypothesized that compound **9** would be an inhibitor of both 3CL protease and human cathepsin L. In this SMAI, the P₃ position contains a valyl group, the P₂ position contains the leucyl analogue cyclohexyl-alanyl, and the P₁ position contains the novel glutamine analogue, 2-pyridone (Li et al., 2021). We expected the 2-pyridone aldehyde to also form a δ -lactol, and also be recognized by both human cathepsin L and SARS-CoV-2 3CL protease, and this was indeed the case. Compound **9** is a low nanomolar inhibitor of both enzymes ($K_i = 22$ nM for human cathepsin L, and $K_i = 9$ nM for SARS-CoV-2 3CL protease), demonstrating the feasibility of designing an inhibitor to target both enzymes.

Prodrugs of SMAI 8

As compound **8**, an inhibitor with a peptidomimetic scaffold similar to that of the anti-chagasic compound K777 (common elements include the P₃ N-methyl-piperazinoyl group and the P₂ phenylalanyl group), demonstrated potent inhibition of human cathepsin L, we sought to protect the δ -lactol functionality of **8** by synthesizing pro-drug forms in which the secondary alcohol of **8** was acylated. (Li et al., 2021) (**Scheme 2**). Compounds **10–12**, respectively comprise the O-acetyl, O-*n*-propanoyl, and the O-isobutanoyl derivatives of lactol **8**. We previously demonstrated that treatment of pro-drugs **10–12** with porcine esterase *in vitro* generated inhibitor **8** (**Scheme 1**). Pro-drugs **10–12** exerted anti-trypanosomal activity at micromolar concentrations in infected-cell cultures which was superior to that of the free lactol **8** (Li et al., 2021). From these results we sought to evaluate these pro-drug forms of **8**



SCHEME 2 | De-acylation of Pro-drugs of Compound 8 as catalyzed by cellular esterases.

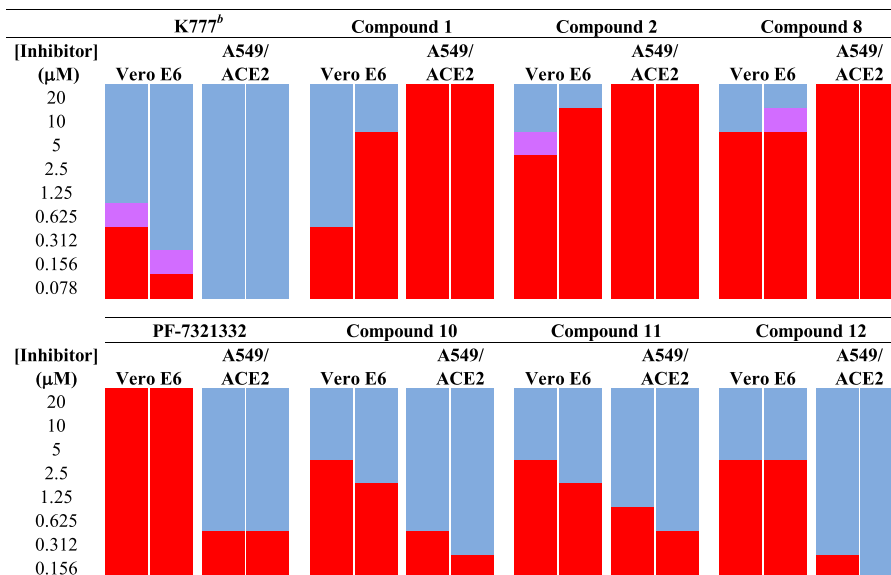


FIGURE 3 | Anti-SARS-CoV-2 activity of SMAIs, compared to that of **K777** and **PF-07321332**. SARS-CoV-2-infected Vero E6 and human A549/ACE2 cells were treated as described with **K777**, aldehyde **1**, SMAIs **2**, **8**, and the pro-drug forms of **8**, compounds **10-12**.

in SARS-CoV-2-infected mammalian cells, as described below.

Anti-SARS-CoV-2 Activities of the SMAIs

We tested aldehyde **1**, selected SMAIs (compounds **2**, **8**, **10-12**), and the approved drug **PF-07321332**, in two types of mammalian cells (Vero E6 and A549/ACE2) infected with SARS-CoV-2 (Figure 3 and Table 1), along with data for **K777** as previously reported (Mellott et al., 2021). Vero E6 are derived from African green monkeys, while A549/ACE2 cells are human adenocarcinoma cells that are stably transduced with the human ACE2 viral receptor. We previously found that **K777**, an irreversible inactivator of human cathepsin L blocked the SARS-CoV-2-induced cytopathic effect (CPE) in Vero E6 and A549/ACE2 cells at respective values of $EC_{50} = 625$ and <78 nM. In a second study, an EC_{50} of 156 nM was obtained in Vero E6 cells. These activities of **K777** are among the most potent yet observed for any inhibitor of SARS-CoV-2 cell infection. The anti-SARS-CoV-2 effects of **PF-07321332** in infected Vero and A549/ACE2 cells were reported as respective EC_{50} values of 74

and 77 nM. However, in our hands, **PF-07321332** had no anti-SARS-CoV-2 effects in Vero E6 cells at concentrations of ≤ 20 μM, while we measured a value of $EC_{50} = 470$ nM in A549/ACE2 cells, which is >6 -fold less potent than **K777**. Regardless of the reasons for these differences obtained in two different laboratories, we consider the results we report in our studies to serve as “benchmark” data for an approved drug to compare with our inhibitors.

Dipeptide aldehyde **1** was a potent anti-SARS-CoV-2 agent in Vero E6 cells ($EC_{50} = 470$ nM), but upon repeating this experiment with a different sample of **1**, we observed a value of $EC_{50} = 7.5$ μM. The cause of this discrepancy is unknown, as the experimental conditions are identical. Compound **1** exerted no inhibition of CPE in A549/ACE2 at concentrations of ≤ 20 μM, which may validate the higher of the two EC_{50} values observed in Vero E6 cells. The value of EC_{50} for SMAI **2** was found to be 10 ± 5 μM in Vero E6 cells, while in A549/ACE2 cells, there was no inhibition of CPE at concentrations of ≤ 20 μM. The 4'-benzyl-substituted SMAIs **6** and **7** displayed a slightly higher anti-CoV-2 activity in Vero E6 cells, with respective values of $EC_{50} = 4$ and

2.5 μM in infected Vero E6 cells (**Table 1**). The more soluble SMAI, compound **8**, had a slightly increased anti-SARS-CoV-2 activity compared to SMAI **2** in Vero E6 ($\text{EC}_{50} = 9 \pm 2 \mu\text{M}$), but again, no anti-viral effect in infected A549/ACE2 cells. We previously reported (Li et al., 2021) that the dual inhibitor of human cathepsin L and 3CL-PR, compound **9**, had no effect in SARS-CoV-2-infected Vero E6 cells, but demonstrated an $\text{EC}_{50} = 3.75 \mu\text{M}$ in SARS-CoV-2-infected A549/ACE2 cells (**Table 1**).

Two of the three pro-drug analogues of compound **8**, compounds (**10–12**) proved the most potent anti-SARS-CoV-2 agents in our study. These inhibitors differ structurally from compound **8** only in that the secondary alcohol of the lactol of **8** is now O-acylated with, acetyl, propanoyl, and iso-butanoyl groups, respectively. As previously proposed (Li et al., 2021), we expected that O-acylation of this hydroxyl group would provide protection of the lactol from opening to the requisite aldehyde, and subsequent reaction with electrophiles within cells. Indeed, pro-drugs **10–12** were highly effective in preventing CPE in both Vero E6 (respective EC_{50} values of 2.5, 2.5, and 3.75 μM) and especially in A549/ACE2 cells (respective EC_{50} values of 312, 625, and 156 nM). It is notable that in A549/ACE2 cells, the more sterically-hindered O-iso-butanoyl group provided the most potent inhibition of CPE, suggesting that this ester has the highest metabolic stability in cells of the three pro-drugs studied. It is noteworthy that these three pro-drugs of SMAI **8** are effectively equipotent with that of **PF-07321332** in A549/ACE2 cells, and demonstrated an activity at low micromolar concentrations in CoV-2-infected Vero E6 cells, in which **PF-07321332** was inactive.

SUMMARY

In this report we have described the expanded use of our novel class of cysteine protease inhibitors, the self-masked aldehydes, to the inhibition of human cathepsin L, in which these inhibitors were more potent than their inhibition of the highly similar cysteine protease, cruzain, from the parasitic protozoan *Trypanosoma cruzi*. While none of the SMAIs inhibited the 3CL protease of SARS-CoV-2, some nevertheless demonstrated inhibition of the cytopathic effect arising from SARS-CoV-2 infection of two mammalian cell lines. SMAI **8** exhibited a value of $K_i = 9 \text{ nM}$ vs. human cathepsin L, but with moderate anti-SARS-CoV-2 activity at micromolar concentrations in Vero E6 cells, and with no

effect in the SARS-CoV-2-infected A549/ACE2 cells. However, three O-acylated pro-drug forms of **8** blocked CoV-2-mediated CPE in infected A549/ACE2 cells with potencies equivalent to that of the FDA-approved, 3CL-PR inhibitor **PF-07321332**. As we have embarked on the discovery of a single SMAI that inhibits both hCatL and SARS-CoV-2 3CL protease, as exemplified here by the 2-pyridone analogue of alanine compound **9**, which, while a nanomolar inhibitor of both enzymes, the anti-CoV-2 effects of this dual inhibitor are no better than that of SMAIs discussed previously. However, based on the success of pro-drug forms of human cathepsin L inhibitor **8**, it would be circumspect to synthesize O-acylated analogues of SMAI **9**, and evaluate them in cellular models of the SARS-CoV-2 infection. This will be the focus of upcoming studies.

DATA AVAILABILITY STATEMENT

The raw data supporting the conclusion of this article will be made available by the authors, without undue reservation.

AUTHOR CONTRIBUTIONS

Compounds were prepared and analyzed by LL and BC. 3CL protease was expressed and purified by AK, ZT, and DM, with support from FR. The FRET-based peptide for 3CL protease was prepared by DM or JZ. Inhibition kinetics was performed by JZ and LL, with assistance from CG, AD, VT, and C-TT provided SARS-CoV-2-cell infectivity data. TM wrote the manuscript. LL and JZ are co-first authors of this work.

FUNDING

Financial support for the research was provided by NIH grants R21 AI127634, R01 GM129076, and Texas A&M AgriLife Research.

ACKNOWLEDGMENTS

We thank Prof. Frank M. Raushel for supporting this work. We also thank Hayley Boswell for assistance with acquiring data.

REFERENCES

- Bai, B., Arutyunova, E., Khan, M. B., Lu, J., Joyce, M. A., Saffran, H. A., et al. (2021). Peptidomimetic Nitrile Warheads as SARS-CoV-2 3CL Protease Inhibitors. *RSC Med. Chem.* 12, 1722–1730. doi:10.1039/d1md000247c
- Brömme, D., Bonneau, P. R., Lachance, P., and Storer, A. C. (1994). Engineering the S2 Subsite Specificity of Human Cathepsin S to a Cathepsin L- and Cathepsin B-like Specificity. *J. Biol. Chem.* 269, 30238–30242. doi:10.1016/s0021-9258(18)43803-3
- Cianni, L., Rocho, F. D. R., Bonatto, V., Martins, F. C. P., Lameira, J., Leitão, A., et al. (2021). Design, Synthesis and Stepwise Optimization of Nitrile-Based Inhibitors of Cathepsins B and L. *Bioorg. Med. Chem.* 29, 115827. doi:10.1016/j.bmc.2020.115827
- Cianni, L., Feldmann, C. W., Gilberg, E., Gütschow, M., Juliano, L., Leitão, A., et al. (2019). Can Cysteine Protease Cross-Class Inhibitors Achieve Selectivity? *J. Med. Chem.* 62, 10497–10525. doi:10.1021/acs.jmedchem.9b00683
- Dai, W., Zhang, B., Jiang, X.-M., Su, H., Li, J., Zhao, Y., et al. (2020/2020). Structure-based Design of Antiviral Drug Candidates Targeting the SARS-CoV-2 Main Protease. *Science* 368, 1331–1335. doi:10.1126/science.abb4489
- Doyle, P. S., Zhou, Y. M., Engel, J. C., and McKerrow, J. H. (2007). A Cysteine Protease Inhibitor Cures Chagas' Disease in an Immunodeficient-Mouse Model

- of Infection. *Antimicrob. Agents Chemother.* 51, 3932–3939. doi:10.1128/aac.00436-07
- Fan, W., Li, E., Ren, J., Wang, W., Liu, X., and Zhang, Y. (2020). Cordycepamides A–E and Cordyglycoside A, New Alkaloidal and Glycoside Metabolites from the Entomopathogenic Fungus *Cordyceps* Sp. *Fitoterapia* 142, 104525. doi:10.1016/j.fitote.2020.104525
- Gampe, C., and Verma, V. A. (2020). Curse or Cure? A Perspective on the Developability of Aldehydes as Active Pharmaceutical Ingredients. *J. Med. Chem.* 63, 14357–14381. doi:10.1021/acs.jmedchem.0c01177
- Hoffmann, M., Kleine-Weber, H., Schroeder, S., Krüger, N., Herrler, T., Erichsen, S., et al. (2020). SARS-CoV-2 Cell Entry Depends on ACE2 and TMPRSS2 and Is Blocked by a Clinically Proven Protease Inhibitor. *Cell* 181, 271–280. doi:10.1016/j.cell.2020.02.052
- Johns Hopkins University of Medicine. Coronavirus Resource Center. 2022. <https://coronavirus.jhu.edu/>.
- Kaplowitz, N. (2005). Idiosyncratic Drug Hepatotoxicity. *Nat. Rev. Drug Discov.* 4, 489–499. doi:10.1038/nrd1750
- Kerr, I. D., Lee, J. H., Farady, C. J., Marion, R., Rickert, M., Sajid, M., et al. (2009). Vinyl Sulfones as Antiparasitic Agents and a Structural Basis for Drug Design. *J. Biol. Chem.* 284, 25697–25703. doi:10.1074/jbc.m109.014340
- Lewis, C. A., Jr, and Wolfenden, R. (1977). Thiohemiacetal Formation by Inhibitory Aldehydes at the Active Site of Papain. *Biochemistry* 16, 4890–4895. doi:10.1021/bi00641a023
- Li, L., Chenna, B. C., Yang, K. S., Cole, T. R., Goodall, Z. T., Giardini, M., et al. (2021). Self-masked Aldehyde Inhibitors: A Novel Strategy for Inhibiting Cysteine Proteases. *J. Med. Chem.* 64, 11267–11287. doi:10.1021/acs.jmedchem.1c00628
- McKerrow, J. H., Doyle, P. S., Engel, J. C., Podust, L. M., Robertson, S. A., Ferreira, R., et al. (2009). Two Approaches to Discovering and Developing New Drugs for Chagas Disease. *Mem. Inst. Oswaldo Cruz.* 104 Suppl 1 (Suppl. 1), 263–269. doi:10.1590/s0074-02762009000900034
- Mellott, D. M., Tseng, C.-T., Drelich, A., Fajtová, P., Chenna, B. C., Kostomiris, D. H., et al. (2021). A Clinical-Stage Cysteine Protease Inhibitor Blocks SARS-CoV-2 Infection of Human and Monkey Cells. *ACS Chem. Biol.* 16, 642–650. doi:10.1021/acscchembio.0c00875
- Morton, J. D., Lee, H. Y. Y., McDermott, J. D., Robertson, L. J. G., Bickerstaffe, R., Jones, M. A., et al. (2013). A Macrocyclic Calpain Inhibitor Slows the Development of Inherited Cortical Cataracts in a Sheep Model. *Invest. Ophthalmol. Vis. Sci.* 54, 389–395. doi:10.1167/iovs.12-11088
- O'Brien, P. J., Siraki, A. G., and Shangari, N. (2005). Aldehyde Sources, Metabolism, Molecular Toxicity Mechanisms, and Possible Effects on Human Health. *Crit. Rev. Toxicol.* 35, 609–662. doi:10.1080/10408440591002183
- Owen, D. R., Allerton, C. M. N., Anderson, A. S., Aschenbrenner, L., Avery, M., Berritt, S., et al. (2021). An Oral SARS-CoV-2 M Pro Inhibitor Clinical Candidate for the Treatment of COVID-19. *Science* 374, 1586–1593. doi:10.1126/science.abl4784
- Peheré, A. D., Nguyen, S., Garlick, S. K., Wilson, D. W., Hudson, I., Sykes, M. J., et al. (2019). Tripeptide Analogues of MG132 as Protease Inhibitors. *Bioorg. Med. Chem.* 27, 436–441. doi:10.1016/j.bmc.2018.12.022
- Pfizer. Pfizer Receives U.S. FDA Emergency Use Authorization for Novel COVID-19 Oral Antiviral Treatment. Washington, DC: FDA Announcement. 2021. Retrieved 22 December 2021.
- Puzer, L., Cotrin, S. S., Alves, M. F. M., Egborge, T., Araújo, M. S., Juliano, M. A., et al. (2004). Comparative Substrate Specificity Analysis of Recombinant Human Cathepsin V and Cathepsin L. *Arch. Biochem. Biophys.* 430, 274–283. doi:10.1016/j.abb.2004.07.006
- Rut, W., Groborz, K., Zhang, L., Sun, X., Zmudzinski, M., Pawlik, B., et al. (2021). SARS-CoV-2 Mpro Inhibitors and Activity-Based Probes for Patient-Sample Imaging. *Nat. Chem. Biol.* 17, 222–228. doi:10.1038/s41589-020-00689-z
- Schechter, I., and Berger, A. (1967). On the Size of the Active Site in Proteases. I. Papain. *Biochem. Biophysical Res. Commun.* 27, 157–162. doi:10.1016/s0006-291x(67)80055-x
- Woo, J.-T., Sigeizumi, S., Yamaguchi, K., Sugimoto, K., Kobori, T., Tsuji, T., et al. (1995). Peptidyl Aldehyde Derivatives as Potent and Selective Inhibitors of Cathepsin L. *Bioorg. Med. Chem. Lett.* 5, 1501–1504. doi:10.1016/0960-894x(95)00236-m
- Zhai, X., and Meek, T. D. (2018). Catalytic Mechanism of Cruzain from *Trypanosoma Cruzi* as Determined from Solvent Kinetic Isotope Effects of Steady-State and Pre-steady-state Kinetics. *Biochemistry* 57, 3176–3190. doi:10.1021/acs.biochem.7b01250
- Zhang, L., Lin, D., Sun, X., Curth, U., Drosten, C., Sauerhering, L., et al. (2020). Crystal Structure of SARS-CoV-2 Main Protease Provides a Basis for Design of Improved α -ketoamide Inhibitors. *Science* 368, 409–412. doi:10.1126/science.abb3405

Conflict of Interest: The authors declare that the research was conducted in the absence of any commercial or financial relationships that could be construed as a potential conflict of interest.

Publisher's Note: All claims expressed in this article are solely those of the authors and do not necessarily represent those of their affiliated organizations, or those of the publisher, the editors, and the reviewers. Any product that may be evaluated in this article, or claim that may be made by its manufacturer, is not guaranteed or endorsed by the publisher.

Copyright © 2022 Zhu, Li, Drelich, Chenna, Mellott, Taylor, Tat, Garcia, Katzfuss, Tseng and Meek. This is an open-access article distributed under the terms of the Creative Commons Attribution License (CC BY). The use, distribution or reproduction in other forums is permitted, provided the original author(s) and the copyright owner(s) are credited and that the original publication in this journal is cited, in accordance with accepted academic practice. No use, distribution or reproduction is permitted which does not comply with these terms.



OPEN ACCESS

EDITED BY

Wenshe Ray Liu,
Texas A&M University, United States

REVIEWED BY

Asanga Bandara,
Pledge-Tx, United States
Sreedhar Ranganath Pai,
Manipal Academy of Higher Education,
India

*CORRESPONDENCE

Shuibing Chen,
shc2034@med.cornell.edu

SPECIALTY SECTION

This article was submitted to Chemical
Biology,
a section of the journal
Frontiers in Chemistry

RECEIVED 07 June 2022

ACCEPTED 11 July 2022

PUBLISHED 05 October 2022

CITATION

Duan X, Lacko LA and Chen S (2022),
Druggable targets and therapeutic
development for COVID-19.
Front. Chem. 10:963701.
doi: 10.3389/fchem.2022.963701

COPYRIGHT

© 2022 Duan, Lacko and Chen. This is
an open-access article distributed
under the terms of the [Creative
Commons Attribution License \(CC BY\)](#).
The use, distribution or reproduction in
other forums is permitted, provided the
original author(s) and the copyright
owner(s) are credited and that the
original publication in this journal is
cited, in accordance with accepted
academic practice. No use, distribution
or reproduction is permitted which does
not comply with these terms.

Druggable targets and therapeutic development for COVID-19

Xiaohua Duan, Laretta A. Lacko and Shuibing Chen*

Department of Surgery, Weill Cornell Medicine, New York, NY, United States

Coronavirus disease (COVID-19), which is caused by SARS-CoV-2, is the biggest challenge to the global public health and economy in recent years. Until now, only limited therapeutic regimens have been available for COVID-19 patients, sparking unprecedented efforts to study coronavirus biology. The genome of SARS-CoV-2 encodes 16 non-structural, four structural, and nine accessory proteins, which mediate the viral life cycle, including viral entry, RNA replication and transcription, virion assembly and release. These processes depend on the interactions between viral polypeptides and host proteins, both of which could be potential therapeutic targets for COVID-19. Here, we will discuss the potential medicinal value of essential proteins of SARS-CoV-2 and key host factors. We summarize the most updated therapeutic interventions for COVID-19 patients, including those approved clinically or in clinical trials.

KEYWORDS

SARS-CoV-2, main protease, papain-like protease, RNA-dependent RNA polymerase, neutralizing antibodies, host factors

Introduction

In the past 2 decades, there have been three coronavirus outbreaks, severe acute respiratory syndrome (SARS) in 2003, Middle East respiratory syndrome (MERS) in 2012, and coronavirus disease 2019 (COVID-19) in 2019. For COVID-19, it was identified that the novel coronavirus SARS-CoV-2 was the causative pathogen. SARS-CoV-2, a new member of the genus Betacoronavirus, was most closely related to three bat coronaviruses, BANAL-52, BANAL-103, and BANAL-236, of which the animal reservoir were *Laotian R. malayanus*, *R. pusillus*, and *R. marshalli*, respectively. Notably, BANAL-52 has the highest nucleotide conservation in the receptor-binding domain (RBD) and N-terminal domain (NTD) of the S1 domain in the spike protein (Temmam et al., 2022). It was evidenced that spike (S) protein of SARS-CoV-2 could mediate viral entry through binding to angiotensin converting enzyme 2 (ACE2) (Hoffmann et al., 2020b; Zhou P. et al., 2020). S protein has two subunits, S1 and S2. The 319–529 amino acid peptide of S1 was identified as the ACE2 binding domain, which is the target of neutralizing antibodies (Shang et al., 2020b). Compared with SARS-CoV, the binding domain of SARS-CoV-2 has stronger affinity to human angiotensin-converting enzyme 2 (hACE2). However, there are several additional receptors shown to mediate virus entry, such as CD147, Neuropilin-1, and Dipeptidyl peptidase 4 (DPP4) (Masre et al., 2021). Proteolytic

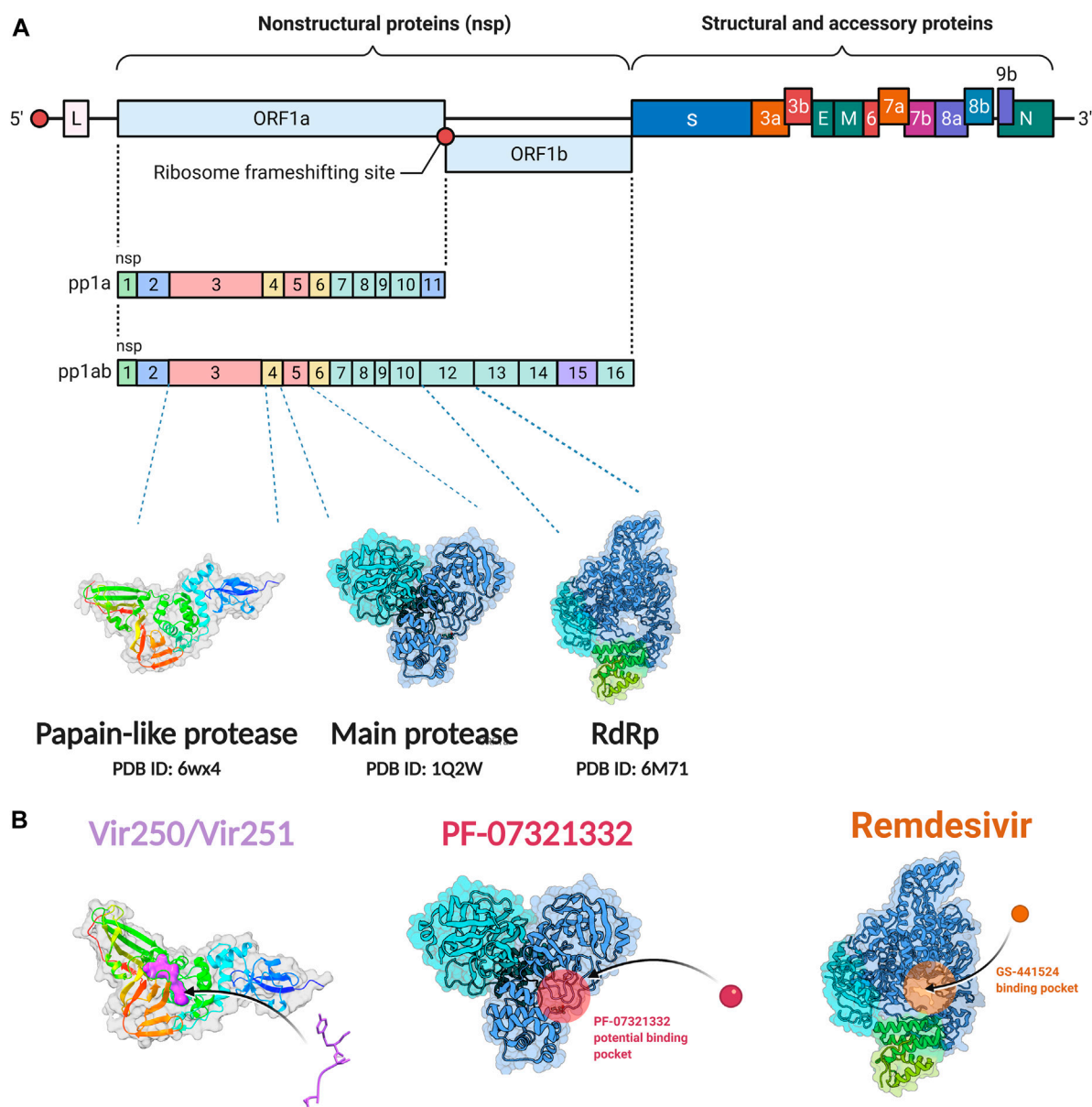


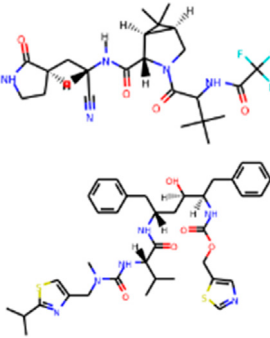
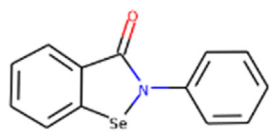
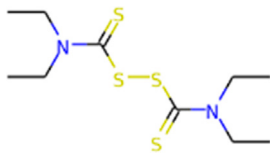
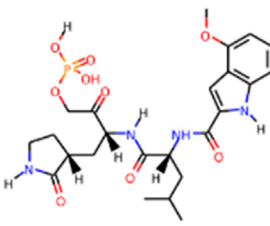
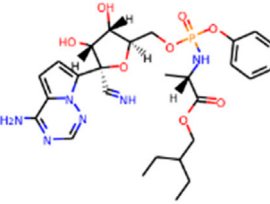
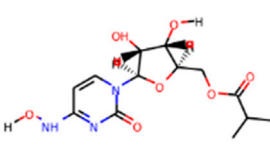
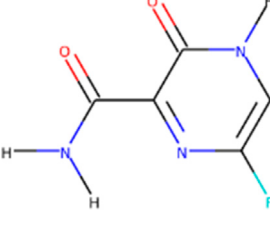
FIGURE 1

Non-structural protein as targets for antiviral drug development. (A) Genome organization of SARS-CoV-2. (B) The crystal structure of the non-structural proteins and their inhibitors. The crystal structure of VIR250 and VIR251 in complex with PLpro of SARS-CoV-2; the crystal structure of Mpro and its binding pocket of PF-07321332; the crystal structure of RdRp and its binding pocket of remdesivir. The crystal structures were obtained from RCSB Protein Data Bank. Figure was generated by BioRender.

processing of the SARS-CoV-2 S protein is required for activation. (Shang et al., 2020b). Host proteases, including transmembrane protease serine protease 2 (TMPRSS2), cathepsin L, and furin can cleave S protein and facilitate the entry of SARS-CoV-2 (Shang et al., 2020a; Ou et al., 2020). After the RNA genome of SARS-CoV-2 is released into the host cell, 16 non-structural proteins (nsp), four structural proteins, and several accessory proteins are transcribed and translated. The

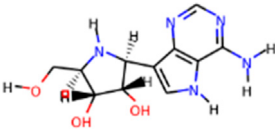
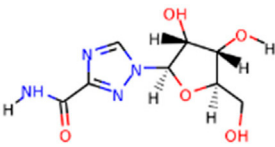
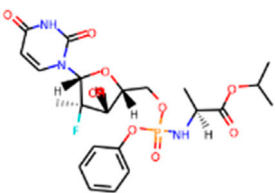
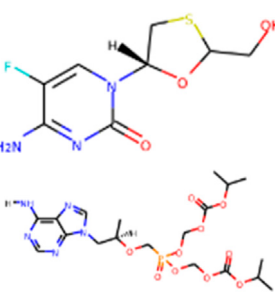
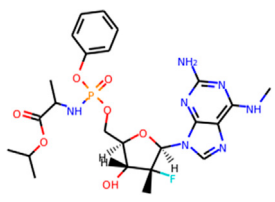
nsp are encoded by two open reading frames, ORF1a and ORF1b, which mediate the viral replication. The structural proteins include S, envelope (E), membrane (M) and nucleocapsid (N). The accessory proteins, which have not been well studied until now, are thought to play a critical role in SARS-CoV-2 pathogenicity and the regulation of the host immune response (Michel et al., 2020). Overall, every process during the viral life cycle relies heavily on the interactions

TABLE 1 Protease enzyme and RdRP inhibitors at or after clinical trials.

Target	Drug name	Structure	Clinical status	References
main protease (Mpro)	Nirmatrelvir/ritonavir		Emergency use authorization in COVID-19	Owen et al. (2021)
	Ebselen		Phase 2 in COVID-19	Jin et al. (2020)
	Disulfiram		Phase 2 in COVID-19	Jin et al. (2020)
	PF-07304814		Phase 1 in COVID-19	Boras et al. (2021)
RNA-dependent RNA polymerase (RdRp)	Remdesivir		Emergency use authorization in COVID-19	Beigel et al. (2020)
	Molnupiravir		Emergency use authorization in COVID-19	Jayk Bernal et al. (2021)
	Favipiravir		Phase 3 in COVID-19	Udwadia et al. (2021)

(Continued on following page)

TABLE 1 (Continued) Protease enzyme and RdRP inhibitors at or after clinical trials.

Target	Drug name	Structure	Clinical status	References
	Galidesivir		Phase 1 in COVID-19	Julander et al. (2021)
	Ribavirin		Phase 2 in COVID-19	Tong et al. (2020)
	Sofosbuvir		Phase 2 in COVID-19	Abbass et al. (2021)
	Emtricitabine/tenofovir disoproxil		Phase 3 in COVID-19	DeJong et al. (2021)
	AT-527		Phase 3 in COVID-19	Good et al. (2021)

between viral proteins and host factors. Each of these molecular proteins can be targeted for anti-SARS-CoV-2 drug development. In the current review, we will discuss the druggable targets and their potential therapeutic development.

The pathogenesis of most patients with COVID-19 is asymptomatic and mild, however, some patients will develop severe COVID-19 and even respiratory failure. At the initial stage, viral particles invade epithelial cells in the nasopharynx, where they replicate, migrate down to the airway, and then infect alveolar epithelial cells. Compared with other respiratory viruses, the inflammatory response to SARS-CoV-2 infection is significantly different. A delayed interferon response and high expression of IL-6 were defined as the features of COVID-19 ([Blanco-Melo et al., 2020](#)). Notably, the severe COVID-19 and death cases are mainly caused by acute respiratory distress

syndrome (ARDS), which is a consequence of the cytokine storm. ([Mehta et al., 2020](#); [Chen et al., 2021](#)). Here, we will also discuss the current drug development in targeting cytokine storm and ARDS.

Drug development against targets of SARS-CoV-2

Non-structural proteins as drug targets

SARS-CoV-2 is a single stranded and positive sense RNA virus ([Marra et al., 2003](#); [Chen Y. et al., 2020](#)). The ORF1a and ORF1b in the RNA genome encode two big polypeptides with a ribosomal frameshift, pp1a and pp1ab, which can be cleaved

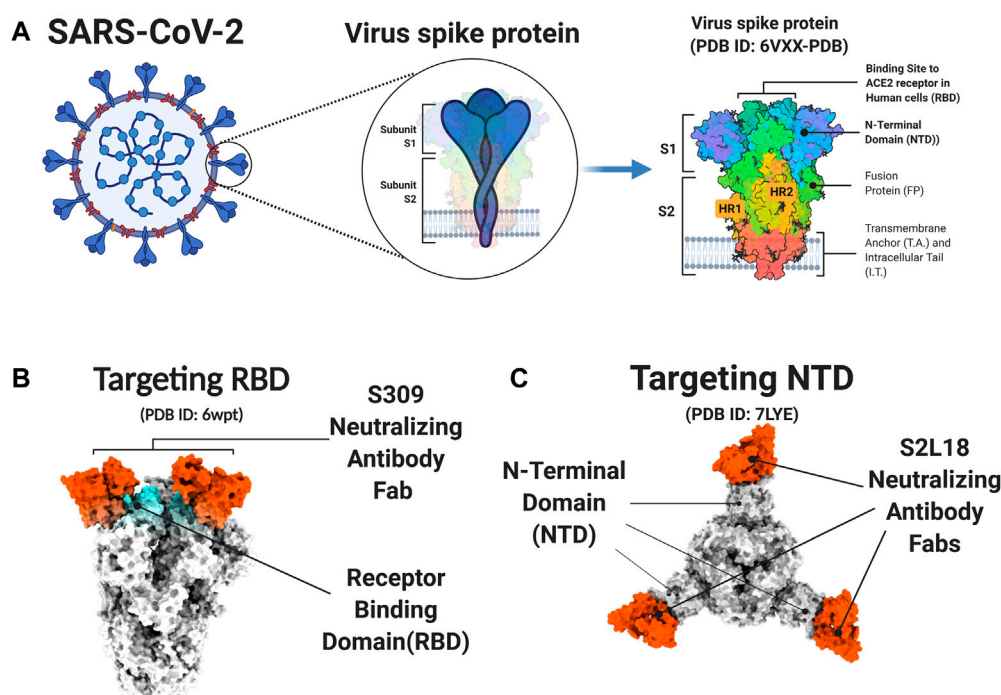


FIGURE 2

S protein and neutralizing antibody. (A) The Structure of the SARS-CoV2 S Glycoprotein. (B-C) The PDB model of S protein and neutralizing antibody. The S309 neutralizing antibody targets the receptor-binding domain (RBD) of S protein (B) The S2L18 neutralizing antibody targets the N-terminal domain (NTD) of S protein (C). Figure was generated by BioRender.

into 16 nsps by nsp3, papain-like protease (PLpro) and nsp5, main protease (Mpro) (Figure 1A). Another important nsp is nsp12, RNA-dependent RNA polymerase (RdRp), which is main component of RNA replication machinery catalyzing

the synthesis of RNA (Figure 1A). Due to their critical functions, PLpro, Mpro, and RdRp have been considered as the major drug targets for anti-viral drug development.

TABLE 2 Antibody treatments for COVID-19 at or after phase three clinical trial.

Target	Drug name	PDB ID	Clinical status	References
receptor-binding domain (RBD)	REGN-COV (REGN10933/casirivimab + REGN10987/imdevimab)	6XDG	Emergency use authorization in COVID-19	Weinreich et al. (2021)
	Bamlanivimab (LY3819253 or LY-CoV555) + etesevimab (LY3832479, LY-CoV016)	7KMG + 7F7E	Emergency use authorization in COVID-19	Tuccori et al. (2021)
	Sotrovimab (VIR-7831/GSK4182136)	7TLY	Emergency use authorization in COVID-19	Gupta et al. (2021)
	AZD7442 (AZD8895/tixagevimab + AZD1061/cilgavimab)	7L7E	Emergency use authorization in COVID-19	Mahase, (2021)
	Regdanvimab (CT-P59)	7CM4	Approved by European Commission and South Korea	(Lee et al., 2021; Syed, 2021)
	TY027	Not available	Phase 3	Kreuzberger et al. (2021)
	Amubarvimab + romlusevimab (BRII-196 + BRII-198)	Not available	Phase 3	Group, A.C.-T.f.I.w.C.-S. et al. (2021)
	Etesevimab (JS016, LY-CoV016, LY3832479)	7F7E	Phase 3	Kreuzberger et al. (2021)
	DZIF-10c, BI 767551	6XDG	Phase 2/3	Halwe et al. (2021)

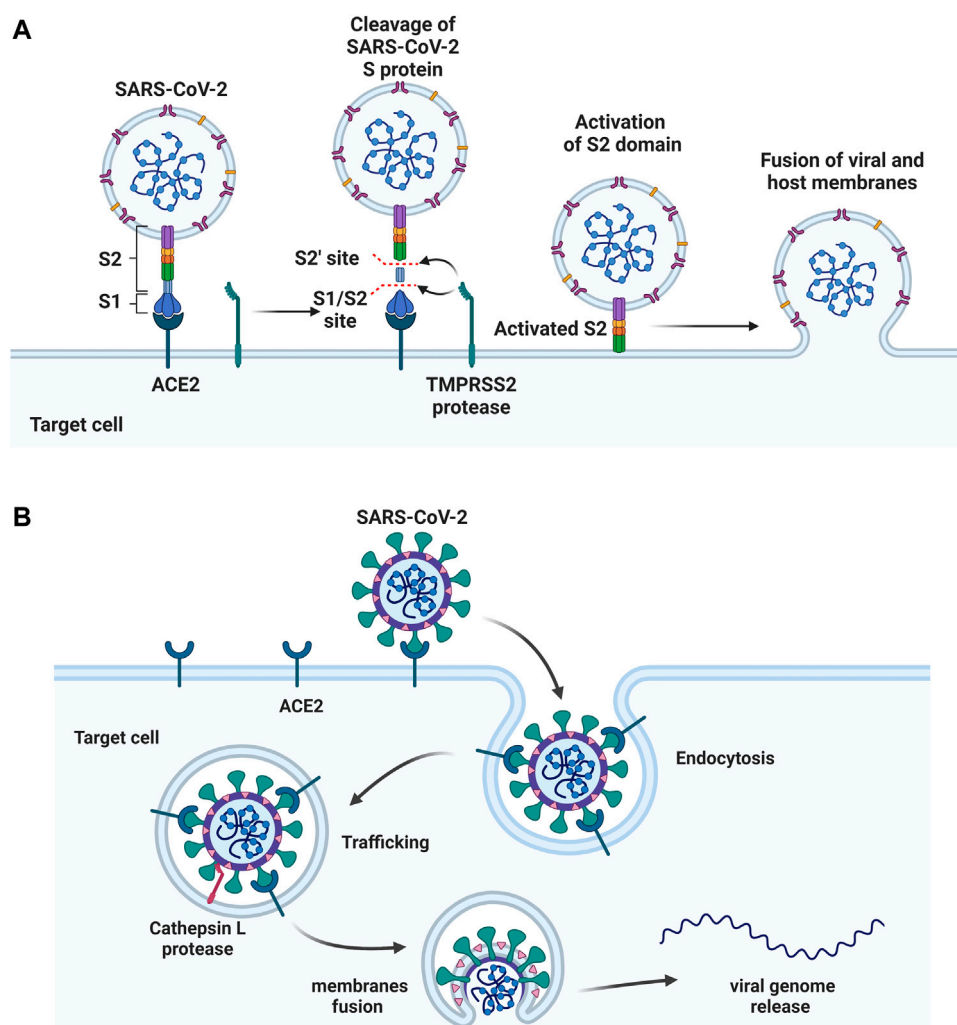


FIGURE 3

Two approaches of SARS-CoV-2 entry. (A) S protein binds to the host ACE2 receptor, followed by cleaving at S1/S2 and S2' sites by TMPRSS2 protease. S2 domain mediates the fusion of viral and host membranes. (B) The S protein binds to ACE2, followed by the receptor mediated endocytosis. The viral fusion occurs in cytoplasm after S activation by host protease cathepsin L. Figure was generated by BioRender.

PLpro and inhibitors

The PLpro of SARS-CoV-2 is an essential coronavirus enzyme encoded by nsp3 (Figure 1A), which cleaves the viral polypeptide to generate a functional replicase complex (Harcourt et al., 2004). PLpro also exhibits deubiquitinating activity on host proteins against host antiviral immune responses (Barretto et al., 2005; Shin et al., 2020). It has been well reported that type I interferons (IFNs) play a key role in the antiviral response through activating the expression of interferon-stimulated genes (ISGs), which could induce the antiviral states of host cells (McNab et al., 2015). Moreover, Type I IFNs can activate both adaptive and innate immune responses by affecting the functions of myeloid cells, B cells, T cells, and NK cells (McNab

et al., 2015). For patients with severe COVID-19, impaired type I IFNs response to SARS-CoV-2 infection have been observed (Hadjadj et al., 2020; Lei et al., 2020). SARS-CoV-2-PLpro can remove interferon stimulated gene 15 protein ubiquitylation, and may attenuate host type I IFNs response and promote viral escaping the immune surveillance. (Shin et al., 2020; Osipiuk et al., 2021). Overall, SARS-CoV-2-PLpro is a critical candidate for drug target to inhibit SARS-CoV-2 infection and activate host antiviral immune response.

Several drug screens have been performed against SARS-CoV-2-PLpro, but very few drug candidates have been found, and no clinical trials are currently under evaluation. The first two inhibitors, VIR250 and VIR251, were identified, and the

structural biological experiments showed that these inhibitors can bind to the pocket of PLpro of SARS-CoV-2, (Figure 1B; Table 1), providing a molecular basis for the substrate specificity and the inhibitory mechanisms (Rut et al., 2020; Patchett et al., 2021). Since SARS-CoV-2-PLpro has the similar catalytic preference and activity with SARS-CoV PLpro, the inhibitors that have been developed for SARS-CoV PLpro can be repurposed against SARS-CoV-2. Therefore, GRL0617, which was designed for SARS-CoV, showed inhibition of PLpro of SARS-CoV-2 (Ratia et al., 2008; Gao et al., 2021) (Table 1). Based on the structure of GRL0617, several new compounds were synthesized and are also capable of inhibiting SARS-CoV-2 viral replication in cells (Osipiuk et al., 2021).

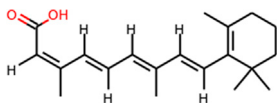
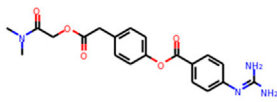
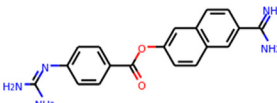
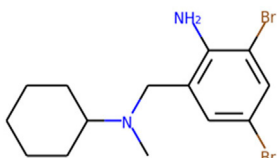
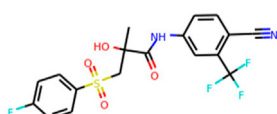
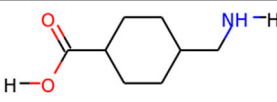
Main proteases and inhibitors

Mpro, also called 3C-like protease (3CL protease), is another major protease encoded by SARS-CoV-2 RNA genome. Mpro is encoded by nsp5 (Figure 1A), and cleaves polyproteins, pp1a and pp1ab to release nonstructural proteins that mediate the

assembly of the replication and transcription complex (Jin et al., 2020). The crystal structure of SARS-CoV-2 Mpro was reported soon after the identification of SARS-CoV-2 (Jin et al., 2020). Mpro contains three domains (Domains I, II, and III), which are conserved across coronaviruses. There is a substrate binding site under the gap of domain I and II, which has a catalytic dyad exerting proteolysis activity (Hegyi and Ziebuhr, 2002). In this dyad, Mpro forms a conserved binding pocket, and many drugs can bind to this site (Jin et al., 2020). In addition, Mpro is highly conserved and has no counterpart in host cells, which prompt targeting Mpro therapeutics will not induce the unnecessary side effect (Jin et al., 2020). Together, these make SARS-CoV-2 Mpro a promising virus-specific drug target.

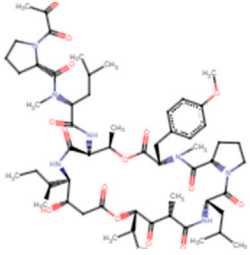
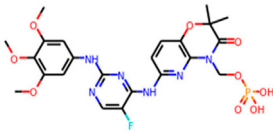
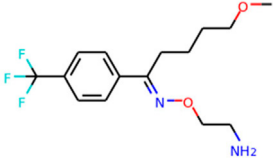
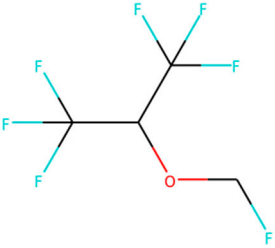
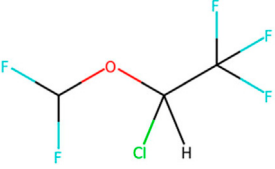
Recently, An Emergency Use Authorization (EUA) was issued by Food and Drug Administration (FDA) for Paxlovid (Figure 1B and Table 1), developed by Pfizer, for the treatment of mild-to-moderate COVID-19. Paxlovid is comprised of nirmatrelvir, a Mpro inhibitor, co-packaged with ritonavir. Ritonavir is not the active ingredient to

TABLE 3 Inhibitors targeting host factors at or after phase three trials.

Target	Drug name	Structure	Clinical status	References
ACE2	Isotretinoin		Phase 3	Demirel Ogut et al. (2021)
	Angiotensin Receptor Blockers	Not available	Phase 4	Hockham et al. (2021)
	Ensovibep	Not available	Phase 3	Tao et al. (2021)
TMPRSS2	Camostat Mesylate		Phase 3	Hoffmann M. et al. (2021)
	Nafamostat Mesilate		Phase 3	Zhuravel et al. (2021)
	Bromhexine		Phase 3	Ansarin et al. (2020)
	Bicalutamide		Phase 3	Welen et al. (2022)
Plasmin	Tranexamic acid		Phase 3	Ogawa and Asakura, (2020)

(Continued on following page)

TABLE 3 (Continued) Inhibitors targeting host factors at or after phase three trials.

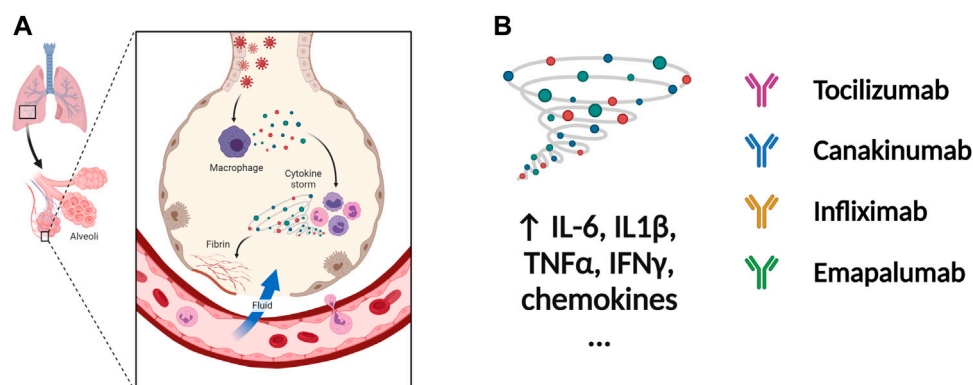
Target	Drug name	Structure	Clinical status	References
EEF1A1	Plitidepsin		Phase 3	Varona et al. (2022)
tyrosine kinase	Fostamatinib		Phase 3	Strich et al. (2021)
SIGMAR1	Fluvoxamine		Phase 3	Reis et al. (2022)
ATP2C1	Sevoflurane		Phase 3	Jabaudon et al. (2017)
	Isoflurane		Phase 3	Flinspach et al. (2020)

bind to Mpro, but functions as a regulator to prolong the duration of nirmatrelvir and increasing the drug plasma concentrations to inhibit SARS-CoV-2 replication ([Anastassopoulou et al., 2022](#)).

Significant efforts have been made to develop drugs targeting Mpro. Numerous inhibitors have exhibited binding activity to Mpro. Jin *et al.* ([Jin et al., 2020](#)) identified several lead compounds targeting Mpro, including disulfiram, carmofur, ebselen, shikonin, tideglusib, PX-12, N3 and TDZD-8. Disulfiram can strongly inhibit Mpro with a half effective concentration (EC₅₀) at 9.35 μ M. And ebselen also exhibited

a strong inhibition against Mpro. Both ebselen and disulfiram are under clinical trials for the patients with COVID-19 (NCT04485130 and NCT04484025). In addition, a computational docking analysis identified Bepridil, which displayed a huge potential for SARS-CoV-2 treatment in the *in vitro* assay. ([Vatansever et al., 2021](#)) (Table 1).

In addition, several studies reported a series of α -ketoamides that inhibit Mpro ([Zhang et al., 2020](#)). Another study presented two peptidomimetic aldehydes can inhibit Mpro activity through covalently binding to the C145 of the catalytic active center. Another two inhibitors labeled 11a and 11b, exhibited excellent

**FIGURE 4**

Potential therapeutic regimens targeting the immune system and cytokine storm. (A) The SARS-CoV-2 infected cells will secrete great amounts of chemokines or cytokines, which recruit immune cells including macrophages. The cytokine storm is caused by uncontrolled immune response that immune cells continuously activate, expand, and produce immense amounts of cytokines. The inflammation will damage the lung cells followed by the formation of fibrin and accumulation of fluid seeping into the lung cavities, leading to the failure of gas exchange. (B) The nAbs targeting IL-1β, IL-6, TNF-α, and IFN-γ among others have been tested in patients with severe COVID-19 inflammation. Figure was generated by BioRender.

TABLE 4 Inhibitors targeting the immune system and cytokine storm at or after phase three trials.

Target	Drug name	PDB or structure	Clinical status	References
C5a	IFX-1 (BDB-001)		Phase 3	Vlaar et al. (2020)
CCR5	Leronlimab (PRO-140)	Not available	Phase 3	Agresti et al. (2021)
Connective tissue growth factor	Pamrevlumab (FG-3019)	Not available	Phase 3	Richeldi et al. (2020)
DAMPs, Siglec G/10	CD24Fc (SACCOVID)	Not available	Phase 3	Song et al. (2022)
GM-CSF	Lenzilumab	Not available	Phase 3	Temesgen et al. (2021)
GM-CSF receptor	Mavrilimumab	Not available	Phase 3	Cremer et al. (2021)
IFN gamma	Emapalumab (Gamifant)	Not available	Phase 3	Cure et al. (2021)
IL-1	RPH-104	Not available	Phase 3	Valenzuela-Almada et al. (2021)
IL-1 β	Canakinumab	5BVJ	Phase 3	Caricchio et al. (2021)
IL-6	Siltuximab	Not available	Phase 3	Gritti et al. (2021)
IL-6 VEGF	Olokizumab	4CNI	Phase 3	Antonov et al. (2020)
	Clazakizumab	Not available	Phase 3	Vaidya et al. (2020)
	Bevacizumab	7V5N	Phase 3	Pang et al. (2021)
C5	Ravulizumab-cwvz	Not available	Phase 3	McEneny-King et al. (2021)
IL-6R	Tocilizumab	Not available	Emergency use authorization in COVID-19	Rosas et al. (2021)
IL-6R CD6	Sarilumab (SAR153191, Kevzara)	Not available	Phase 3	Investigators et al. (2021)
	Levilimab (BCD-089)	Not available	Approved in Russia	Lomakin et al. (2021)
	Itolizumab (EQ001, H-T1, T1-h)	Not available	Approved in India and Cuba	Atal et al. (2020)

inhibition of Mpro with low EC₅₀ at 0.053 and 0.040 μ M, respectively (Dai et al., 2020). Based on the strategy, there are a series of aldehyde derivatives that have been developed. MI-09 and MI-30, significantly reduced viral burden in the lungs of an *in vivo* model with good pharmacokinetic activity and safety in animals (Qiao et al., 2021). 6j was verified to reduce both SARS-CoV-2 infection in an *ex vivo* assay and the MERS-CoV viral titer of infected hDPP4-KI mice (Rathnayake et al., 2020). Guided by previous studies about Mpro of SARS-CoV, a panel of Mpro inhibitors reversibly bonding to the Mpro active-site cysteine C145 have been developed. Among these compounds, MPI5 and MPI8 could prevent SARS-CoV-2 infection in ACE2 expressing A549 and Vero cell lines. At the same time, MPI8 also showed high selectivity toward cathepsin L and high cellular and antiviral potency (Yang K. S. et al., 2021; Ma et al., 2022).

RNA-dependent RNA polymerase and inhibitors

Since SARS-CoV-2 is a positive sense RNA virus, RNA synthesis basing on RNA template is critical for SARS-CoV-2 viral transcription and replication (Naydenova et al., 2021). Nsp12, an RNA-directed RNA polymerase, is the key component of the replication and transcription complex (RTC) (Imbert et al., 2006). Nsp8 and nsp7 are two cofactors, which assist to the viral RNA transcription and production of viral particles in complex with nsp12 (Romano et al., 2020). There are three domains in the structure of SARS-CoV-2 RdRp, an interface domain connecting a core RdRp domain and a nidovirus-specific N-terminal domain (Gao et al., 2020). The core RdRp domain catalyzes RNA synthesis and maintains a relatively conserved architecture among the polymerase family of viruses (McDonald, 2013). It is comprised of three subunits, a finger, a palm and a thumb subdomain (Gao et al., 2020). The nidovirus-specific N-terminal domain contains a nidovirus RdRp-associated nucleotidyltransferase (NiRAN) structure. A new N-terminal b hairpin (residues D29 to K50) embeds into the pocket surrounded by the palm subdomain and NiRAN domain (Gao et al., 2020). The interface domain connects the right-hand RdRp domain and the NiRAN domain. The SARS-CoV-2 RdRp plays a similar role with cellular RNA polymerases and is also similar with SARS-CoV RdRp. These processes consist of RNA elongation, capping, and backtracking. (Dulin et al., 2015; Dulin et al., 2017; Chen J. et al., 2020; Malone et al., 2021). Another two nsps, nsp13 and nsp14, are also necessary to SARS-CoV-2 transcription and replication. The helicase nsp13 is an SF1B-family RNA helicase that could stably interact with the RTC of SARS-CoV-2. (Tanner et al., 2003; Ivanov et al., 2004; Lee et al., 2010; Malone et al., 2022). Nsp13 may participate in switching, backtracking, or disruption of the RNA genome template (Newman et al., 2021). Moreover, nsp14 could interact with RTC and play a role in proofreading activity. Since SARS-CoV-2 has a large RNA genome, replication fidelity is essential for maintaining genetic integrity. The backtracking function of nsp13 may assist nsp14 in approaching the mistake nucleotide and use its exonuclease activity

to maintain high fidelity during RNA transcription and replication (Chen J. et al., 2020; Malone et al., 2021).

Since its essential role in RNA replication and its lack of a human homolog, RdRp is an important druggable target for anti-SARS-CoV-2 drug development. There are two types of RdRp inhibitors: nucleoside analogue inhibitors (Hall et al., 2021) and nonnucleoside analogue inhibitors (Yin et al., 2021). Remdesivir and molnupiravir are two nucleoside analogue inhibitors, which have been issued EUA by the U.S. FDA (Beigel et al., 2020; Jayk Bernal et al., 2021) (Table 1). Remdesivir is an adenosine analogue and once incorporated, will induce immediate pausing of RNA synthesis (Gordon C. J. et al., 2020). The structure of pre-translocated catalytic RTC incorporated with remdesivir clearly demonstrates its mechanism (Figure 1B). Unlike classic chain terminators, delayed chain termination occurs when remdesivir proceeds to the i+3 position. The incorporated remdesivir will be at position -3 or -4 for the pre- or post-translocated state, respectively (Wang Q. et al., 2020; Kokic et al., 2021). As a prodrug, molnupiravir can be converted into a cytidine analogue in the human body. The cytidine analogue exerts transition mutations during viral replication through indiscriminately incorporating either A or G (Kabinger et al., 2021). In addition, there are several other nucleoside analogue inhibitors, including galidesivir, favipiravir, Ribavirin, and AT-527, that are currently being evaluated in clinical trials (Table 1).

Structural proteins as drug targets

The 3' one-third RNA genome encodes S, M, E, N viral structural proteins. In addition to these structural proteins, the accessory genes are also located on this region. Although the function of accessory genes in SARS-CoV-2 are still not completely understood, some of them can modulate host innate or adaptive immune response (Nelson et al., 2020; Redondo et al., 2021). The most studied and first reported was the S protein, which mediates viral entry, providing basic information for the development of a neutralizing antibody.

S protein and S protein-neutralizing antibodies

S protein is a trimers structure that forms a crown on the surface of the viral particle (Figure 2A). It mediates virus entry and determines host tropism and pathogenesis. The S protein has two subdomains, S1 and S2, which are cleaved by furin or TMPRSS2 protease. S1 mediates binding to the receptor of host cells and S2 is responsible for membrane fusion (Walls et al., 2020). The S1 subunit contains two functional domains, the C-terminal domain (CTD) and the N-terminal domain (NTD). Part of the S1 subunit is a receptor-binding domain (RBD), which is the core domain and contains a receptor binding motif (Figures 2B,C). To bind the human angiotensin-converting enzyme 2 (hACE2) receptor, the RBD of S1 exhibits the up conformational

movement, which enables RBD access to hACE2. When in the closed or “down” conformation, the RBD is hidden in the center (Wrapp et al., 2020). Due to the critical function of S protein, it is an attractive target of neutralizing antibodies (nAbs). The SARS-CoV-2 RBD is the main target of nAbs [6, 7]. Like the RBD, much of the S1 NTD is also exposed on the spike trimer surface and is targeted by neutralizing antibodies. The NTD plays a role in the conformation transition of the S protein. Many studies have proved that potent NTD antibodies confer protection against SARS-CoV-2 challenge, which highlights the importance of NTD-specific nAbs (Chi et al., 2020; McCallum et al., 2021).

Major effort has been devoted to leverage antibody therapeutics. Based on the targets on the SARS-CoV-2 S protein, the current antibody therapeutics can be classified into RBD targeted nAbs, NTD targeted nAbs and polyclonal antibodies. As shown in Table 2, there are several antibody therapeutics targeting RBD that have been granted emergency use authorization or are currently under clinical trials. Currently, four anti-SARS-CoV-2 nAb products or antibody cocktails have been issued EUAs by FDA, bamlanivimab plus etesevimab, casirivimab plus imdevimab, sotrovimab, and tixagevimab plus cilgavimab for the treatment of non-hospitalized mild to moderate patients with SARS-CoV-2 infection. However, according to the NIH COVID-19 Treatment Guidelines, the use of bamlanivimab plus etesevimab and casirivimab plus imdevimab have not been recommended, since the protective effect disappears against the B.1.1.529 variant (Cameroni et al., 2022; Cao et al., 2022; Liu et al., 2022). Sotrovimab, however, did exhibit antibody neutralizing activity against the Omicron variant in lab testing, and is therefore expected to retain its therapeutic efficacy against this variant. Moreover, another long-acting anti-SARS-CoV-2 mAb combination, tixagevimab plus cilgavimab, also maintained its effectiveness for neutralizing the Omicron variant. (Cameroni et al., 2022; Li et al., 2022; Liu et al., 2022). The nAbs under phase three trials still face the challenges of Omicron variant escape. Therefore, nAbs interventions must be adjusted in real time according to the evolutionary trajectory of SARS-CoV-2. (Table 2).

Drug development against host factors

SARS-CoV-2 receptors

As a major receptor of SARS-CoV-2 (Shang et al., 2020a; Hoffmann et al., 2020b), ACE2 is a carboxypeptidase that removes a single amino acid from the C terminus of angiotensin I to angiotensin II, which are generated by renin and ACE (Gheblawi et al., 2020). Protein structural analysis revealed that the peptidase domain of ACE2 could bind to the receptor binding motif of the SARS-CoV-2 S protein (Lan et al., 2020; Yan et al., 2020) (Figure 3A). Lack of ACE2 blocks SARS-CoV-2 infection in Huh7.5 (Hoffmann et al., 2021a; Schneider et al., 2021) and Caco-2 (Gordon et al., 2020b) cells. In addition

to ACE2, two groups reported neuropilin1 (NRP1) as another entry factor for SARS-CoV-2 (Cantuti-Castelvetri et al., 2020; Daly et al., 2020). TMPRSS2-mediated entry of wild-type SARS-CoV-2 could be enhanced by the presence of NRP1. Mutations at the furin cleavage site could decrease viral infection, which provides evidence that NRP1 requires a furin-cleaved substrate for its function (Cantuti-Castelvetri et al., 2020).

Multiple efforts have been pursued to exploit ACE2 as a therapeutic target. The fundamental principle of targeting ACE2 is to block the accessibility of virus to membrane-bound ACE2. The use of soluble ACE2 as a decoy receptor capable of trapping the virus to prevent membrane attachment is under investigation (Monteil et al., 2020; Zoufaly et al., 2020). Our study suggested that both imatinib and quinacrine dihydrochloride can bind with ACE2 and block the viral entry (Han et al., 2021). Other strategies target ACE2 using pseudoligands, blocking antibodies, or inhibitors downregulating ACE2 expression. Isotretinoin downregulates ACE2 expression (Sinha et al., 2020), and it also reduces dihydrotestosterone levels and downregulates TMPRSS2 (Table 3). Notably, ACE2 is a key enzyme of the renin-angiotensin-aldosterone system (RAAS), which is a commonly prescribed hypertension drug target. Studies suggested that they increase ACE2 expression (Ferrario et al., 2005) and may therefore worsen COVID-19 severity. However, clinical investigations revealed no adverse effects (Cohen et al., 2021; Williams, 2021). (Table 3). For the alternative receptors of SARS-CoV-2, corresponding therapeutics were also studied for reducing the burden of COVID-19. Meplazumab, which blocks the entry of SARS-CoV-2 by targeting CD147, was tested in a phase II clinical trial (NCT04275245) in China (Masre et al., 2021). Moreover, a potential monoclonal neutralizing antibody against NRP1 is currently under investigation for SARS-CoV-2 infection.

Proteases essential for SARS-CoV-2 entry

After binding, the S protein conformational transition depends on proteolytic cleavage, which depends on the types of target cell proteases. There are two cleavage sites, one is the S1/S2 boundary and the other is S2' site of S2 subunit. For SARS-CoV-2, the S1/S2 boundary is cleaved by furin, while the S2' site cleavage requires proteases in targeted cells. The other two proteases, TMPRSS2 and cathepsin L, activate S protein at different location of the cells. TMPRSS2-mediated S protein activation occurs at the cell surface (Figure 3A), whereas cathepsin-mediated activation occurs in the endo-lysosome (Figure 3B) (Hoffmann et al., 2020a; Sungnak et al., 2020; Zang et al., 2020).

Significant efforts have been applied to develop candidates targeting TMPRSS2 mediated S activation. The TMPRSS2 inhibitors camostat mesylate (Hoffmann M.

et al., 2021), namostat (Jang and Rhee, 2020) and aprotinin (Bojkova et al., 2020) are being investigated in multiple ongoing clinical trials. As androgens are involved in the TMPRSS2 expression (Clinckemalie et al., 2013), several studies also investigated androgen-directed therapy (Bhowmick et al., 2020) (Table 3).

Additional work has been applied to develop drug candidates targeting cathepsins, endosomal cysteine proteases required for pH-dependent endocytic entry (Yang and Shen, 2020). Chloroquine and hydroxychloroquine, which inhibit the activity of cathepsin L, have proven antiviral activity in cell culture (Liu et al., 2020). However, chloroquine and hydroxychloroquine failed to block SARS-CoV-2 infection in an *in vivo* assay (Kaptein et al., 2020; Park et al., 2020) (Table 3). The clinical outcome of chloroquine and hydroxychloroquine is disappointing. Based on RECOVERY and WHO SOLIDARITY, two highly pragmatic trials, hydroxychloroquine treatment may lead to increased mortality in patients with COVID-19 (Axfors et al., 2021).

Lipid and SARS-CoV-2 infection

Genetic screens have identified that several genes controlling fatty acid and cholesterol synthesis are involved in SARS-CoV-2 assembly and replication (Gordon et al., 2020a; Baggen et al., 2021; Chu et al., 2021; Schneider et al., 2021; Wang et al., 2021). Two P4-ATPase complex factors, TMEM30A and ATP8B1, can transport aminophospholipids and mediate the membrane communication between the ER and other membranes, which were related with viral replication. Sterol-regulatory-element-binding proteins (SREBPs) are the key transcription factors that regulate fatty acid and cholesterol synthesis, which were identified in several genetic screens (Schneider et al., 2021; Wang et al., 2021). Our recent work reported that the compounds inhibiting fatty acid biosynthesis can block SARS-CoV-2 infection (Duan et al., 2021). This suggests Fatty Acid synthase and Acetyl-CoA carboxylase Alpha are potential host targets for drug development, which were verified using animal studies (Chu et al., 2021; Duan et al., 2021). 25-hydrocholesterol could inhibit S protein mediated membrane fusion of SARS-CoV-2 by consuming cholesterol from the cell plasma membrane. (Wang S. et al., 2020). Moreover, TMEM41B is identified as another critical host factor required for infection of human coronaviruses SARS-CoV-2 and SARS-CoV (Baggen et al., 2021; Hoffmann et al., 2021b). Together, this suggests that cholesterol and other lipids participate in the viral life cycle, including viral entry, intracellular transport, and replication complex formation. Viruses interact with lipid membranes to infect a cell and reprogram lipid metabolism to fuel replication.

Potential therapeutic regimens targeting immune system and cytokine storm

The severity and modality of COVID-19 patients correlates with increased concentrations of circulating cytokines (de la Rica et al., 2020; De Virgiliis and Di Giovanni, 2020). The deaths of patients with COVID-19 are closely related with ARDS, which is often caused by an uncontrolled immune response. Continuous expansion and activation of inflammation and release of large amounts of inflammatory cytokines are the main characteristics of ARDS. (Del Valle et al., 2020). Recent cohort studies showed high circulating cytokine levels in patients with COVID-19 (Laing et al., 2020). Therefore, lowering the inflammatory response may be a potential therapeutic strategy for severe COVID-19. Anti-IL-6 receptor nAbs, such as sarilumab, tocilizumab, levilumab and anti-IL-6 mAb siltuximab, have been evaluated in several clinical (Zhou F. et al., 2020; Wang Z. et al., 2020; Huang et al., 2020) (Figures 4A,B and Table 4). An EUA of Actemra (tocilizumab) was issued by the FDA to treat the severe COVID-19 adults and children (more than 2 years old) patients. Moreover, other cytokines and growth factors, including TNF- α , IL-1 β , granulocyte-macrophage CSF, vascular endothelial growth factor, and IFN- γ , among others, were exploited as potential drug targets for COVID-19 patients. Our recent studies using an immune-cardiac co-culture platform identified a JAK inhibitor that blocks macrophage-mediated inflammation and myocardial injury (Yang L. et al., 2021). The FDA also issued an EUA for baricitinib (Olumiant), a JAK inhibitor, in combination with remdesivir for confirmed COVID-19 patients. Glucocorticoids are widely used for repressing inflammatory reactions, so theoretically glucocorticoids can reduce the progression to respiratory failure and death in patients with COVID-19. Although the use of glucocorticoids was debated at the beginning of the pandemic (Shang L. et al., 2020; Russell et al., 2020), a randomized clinical trial of dexamethasone reported that patients with severe COVID-19 can benefit from the use of dexamethasone, which could lower the 28-days mortality in patients with invasive mechanical ventilation or oxygenation alone (Group et al., 2021).

Prospective

In the last two and half years, SARS-CoV-2 continues to evolve. Recently, the omicron variant has developed into BA.1, BA.2, and BA.3.1 variants (Viana et al., 2022). Omicron variant BA.2 has become the dominant strain in many places (Chen and Wei, 2022). The BA.1 variant has shown substantial escape from neutralizing antibodies induced by vaccination (Cele et al., 2022; Liu et al., 2022; Schmidt et al., 2022). A recent study estimated that BA.2 is about 1.5 times as

contagious as BA.1, and 30% more capable than BA.1 to escape current vaccines (Chen and Wei, 2022). Overall, there is an urgent need to develop pan-effective antiviral drugs and nAbs. Here, we have summarized druggable targets and therapeutic development for SARS-CoV-2 infection. The potential treatment targets can be divided into two groups, essential viral proteins and host factors supporting the viral life cycle. The non-structural proteins, Mpro, PLpro, and RdRp, are attractive drug targets, since they play pivotal roles in mediating viral replication and transcription. The structural S protein, which mediates viral entry, is the main target of nAbs and vaccines. S protein is also a very challenging target due to the high variability that enhances immune escape. It is still challenging for the nAbs and vaccine development to keep up with the continuing viral mutations. Regarding host factors, ACE2, TMPRSS2, and cathepsins, which have critical roles in viral binding and membrane fusion, are promising drug targets to develop pan-inhibitors of SARS-CoV-2. A majority of genetic and drug screening, as well as protein interactome studies, have identified several host factors that play roles in viral replication, viral translocation, and assembly. Finally, COVID-19 can produce a systemic inflammatory reaction involving many organs, which is highly associated with the severity of the disease. Thus, blocking immune cell-mediated host damage and cytokine storm are also critical for anti-SARS-CoV-2 drug development. In summary, significant efforts have been

applied to understand SARS-CoV-2, which has provided insights into novel anti-SARS-CoV-2 drug development.

Author contributions

XD conceived the review, drafted the manuscript, and prepared figures. XD, LL and SC revised and edited the manuscript.

Conflict of interest

SC is a co-founder of Oncobeat LLC.

The remaining authors declare that the research was conducted in the absence of any commercial or financial relationships that could be construed as a potential conflict of interest.

Publisher's note

All claims expressed in this article are solely those of the authors and do not necessarily represent those of their affiliated organizations, or those of the publisher, the editors and the reviewers. Any product that may be evaluated in this article, or claim that may be made by its manufacturer, is not guaranteed or endorsed by the publisher.

References

- Abbass, S., Kamal, E., Salama, M., Salman, T., Sabry, A., Abdel-Razek, W., et al. (2021). Efficacy and safety of sofosbuvir plus daclatasvir or ravidasvir in patients with COVID-19: A randomized controlled trial. *J. Med. Virol.* 93 (12), 6750–6759. doi:10.1002/jmv.27264
- Agresti, N., Lalezari, J. P., Amodeo, P. P., Mody, K., Mosher, S. F., Seethamraju, H., et al. (2021). Disruption of CCR5 signaling to treat COVID-19-associated cytokine storm: Case series of four critically ill patients treated with leronlimab. *J. Transl. Autoimmun.* 4, 100083. doi:10.1016/j.jtauto.2021.100083
- Anastassopoulou, C., Hatziantoniou, S., Boufidou, F., Patrinos, G. P., and Tsakris, A. (2022). The role of oral antivirals for COVID-19 treatment in shaping the pandemic landscape. *J. Pers. Med.* 12 (3), 439. doi:10.3390/jpm12030439
- Ansarin, K., Tolouian, R., Ardalan, M., Taghizadieh, A., Varshochi, M., Teimouri, S., et al. (2020). Effect of bromhexine on clinical outcomes and mortality in COVID-19 patients: A randomized clinical trial. *Bioimpacts* 10 (4), 209–215. doi:10.34172/bi.2020.27
- Antonov, V. N., Ignatova, G. L., Pribytkova, O. V., Sleptsova, S. S., Strebkova, E. A., Khudyakova, E. A., et al. (2020). Experience of olokizumab use in COVID-19 patients. *Ter. arkhiv* 92 (12), 148–154. doi:10.26442/00403660.2020.12.200522
- Atal, S., Fatima, Z., and Balakrishnan, S. (2020). Approval of itolizumab for COVID-19: A premature decision or need of the hour? *BioDrugs* 34 (6), 705–711. doi:10.1007/s40259-020-00448-5
- Axfors, C., Schmitt, A. M., Janiaud, P., van't Hooft, J., Abd-Elsalam, S., Abdo, E. F., et al. (2021). Mortality outcomes with hydroxychloroquine and chloroquine in COVID-19 from an international collaborative meta-analysis of randomized trials. *Nat. Commun.* 12 (1), 2349. doi:10.1038/s41467-021-22446-z
- Baggen, J., Persoons, L., Vanstreels, E., Jansen, S., Van Looveren, D., Boeckx, B., et al. (2021). Genome-wide CRISPR screening identifies TMEM106B as a proviral host factor for SARS-CoV-2. *Nat. Genet.* 53 (4), 435–444. doi:10.1038/s41588-021-00805-2
- Barretto, N., Jukneliene, D., Ratia, K., Chen, Z., Mesecar, A. D., and Baker, S. C. (2005). The papain-like protease of severe acute respiratory syndrome coronavirus has deubiquitinating activity. *J. Virol.* 79 (24), 15189–15198. doi:10.1128/JVI.79.24.15189-15198.2005
- Beigel, J. H., Tomashek, K. M., Dodd, L. E., Mehta, A. K., Zingman, B. S., Kalil, A. C., et al. (2020). Remdesivir for the treatment of covid-19 - final report. *N. Engl. J. Med. Overseas. Ed.* 383 (19), 1813–1826. doi:10.1056/NEJMoa2007764
- Bhowmick, N. A., Oft, J., Dorff, T., Pal, S., Agarwal, N., Figlin, R. A., et al. (2020). COVID-19 and androgen-targeted therapy for prostate cancer patients. *Endocr. Relat. Cancer* 27 (9), R281–R292. doi:10.1530/ERC-20-0165
- Blanco-Melo, D., Nilsson-Payant, B. E., Liu, W. C., Uhl, S., Hoagland, D., Moller, R., et al. (2020). Imbalanced host response to SARS-CoV-2 drives development of COVID-19. *Cell* 181 (5), 1036–1045.e9. doi:10.1016/j.cell.2020.04.026
- Bojkova, D., Bechtel, M., McLaughlin, K. M., McGreig, J. E., Klann, K., Bellinghausen, C., et al. (2020). Aprotinin inhibits SARS-CoV-2 replication. *Cells* 9 (11), 2377. doi:10.3390/cells9112377
- Boras, B., Jones, R. M., Anson, B. J., Arenson, D., Aschenbrenner, L., Bakowski, M. A., et al. (2021). Preclinical characterization of an intravenous coronavirus 3CL protease inhibitor for the potential treatment of COVID19. *Nat. Commun.* 12 (1), 6055. doi:10.1038/s41467-021-26239-2
- Cameroni, E., Bowen, J. E., Rosen, L. E., Saliba, C., Zepeda, S. K., Culap, K., et al. (2022). Broadly neutralizing antibodies overcome SARS-CoV-2 Omicron antigenic shift. *Nature* 602 (7898), 664–670. doi:10.1038/s41586-021-04386-2
- Cantuti-Castelvetri, L., Ojha, R., Pedro, L. D., Djannatian, M., Franz, J., Kuivanen, S., et al. (2020). Neuropilin-1 facilitates SARS-CoV-2 cell entry and infectivity. *Science* 370 (6518), 856–860. doi:10.1126/science.abd2985

- Cao, Y., Wang, J., Jian, F., Xiao, T., Song, W., Yisimayi, A., et al. (2022). Omicron escapes the majority of existing SARS-CoV-2 neutralizing antibodies. *Nature* 602 (7898), 657–663. doi:10.1038/s41586-021-04385-3
- Caricchio, R., Abbate, A., Gordeev, I., Meng, J., Hsue, P. Y., Neogi, T., et al. (2021). Effect of canakinumab vs placebo on survival without invasive mechanical ventilation in patients hospitalized with severe COVID-19: A randomized clinical trial. *JAMA* 326 (3), 230–239. doi:10.1001/jama.2021.9508
- Cele, S., Jackson, L., Khoury, D. S., Khan, K., Moyo-Gwete, T., Tegally, H., et al. (2022). Omicron extensively but incompletely escapes Pfizer BNT162b2 neutralization. *Nature* 602 (7898), 654–656. doi:10.1038/s41586-021-04387-1
- Chen, J., Malone, B., Llewellyn, E., Grasso, M., Shelton, P. M. M., Olinares, P. D. B., et al. (2020). Structural basis for helicase-polymerase coupling in the SARS-CoV-2 replication-transcription complex. *Cell* 182 (6), 1560–1573.e13. doi:10.1016/j.cell.2020.07.033
- Chen, J., and Wei, G. W. (2022). Omicron BA.2 (B.1.1.529.2): High potential to becoming the next dominating variant. *J. Phys. Chem. Lett.* 13 (17), 3840–3849. doi:10.1021/acs.jpclett.2c00469
- Chen, R., Lan, Z., Ye, J., Pang, L., Liu, Y., Wu, W., et al. (2021). Cytokine storm: The primary determinant for the pathophysiological evolution of COVID-19 deterioration. *Front. Immunol.* 12, 589095. doi:10.3389/fimmu.2021.589095
- Chen, Y., Liu, Q., and Guo, D. (2020). Emerging coronaviruses: Genome structure, replication, and pathogenesis. *J. Med. Virol.* 92 (4), 418–423. doi:10.1002/jmv.25681
- Chi, X., Yan, R., Zhang, J., Zhang, G., Zhang, Y., Hao, M., et al. (2020). A neutralizing human antibody binds to the N-terminal domain of the Spike protein of SARS-CoV-2. *Science* 369 (6504), 650–655. doi:10.1126/science.abc6952
- Chu, J., Xing, C., Du, Y., Duan, T., Liu, S., Zhang, P., et al. (2021). Pharmacological inhibition of fatty acid synthesis blocks SARS-CoV-2 replication. *Nat. Metab.* 3 (11), 1466–1475. doi:10.1038/s42255-021-00479-4
- Clinckemalie, L., Spans, L., Dubois, V., Laurent, M., Helsen, C., Joniau, S., et al. (2013). Androgen regulation of the TMPRSS2 gene and the effect of a SNP in an androgen response element. *Mol. Endocrinol.* 27 (12), 2028–2040. doi:10.1210/me.2013-1098
- Cohen, J. B., Hanff, T. C., William, P., Sweitzer, N., Rosado-Santander, N. R., Medina, C., et al. (2021). Continuation versus discontinuation of renin-angiotensin system inhibitors in patients admitted to hospital with COVID-19: A prospective, randomised, open-label trial. *Lancet Respir. Med.* 9 (3), 275–284. doi:10.1016/S2213-2600(20)30558-0
- Cremer, P. C., Abbate, A., Hudock, K., McWilliams, C., Mehta, J., Chang, S. Y., et al. (2021). Mavrilimumab in patients with severe COVID-19 pneumonia and systemic hyperinflammation (MASH-COVID): An investigator initiated, multicentre, double-blind, randomised, placebo-controlled trial. *Lancet Rheumatol.* 3 (6), e410–e418. doi:10.1016/S2665-9913(21)00070-9
- Cure, E., Kucuk, A., and Cure, M. C. (2021). Can emapalumab be life saving for refractory, recurrent, and progressive cytokine storm caused by COVID-19, which is resistant to anakinra, tocilizumab, and Janus kinase inhibitors. *Indian J. Pharmacol.* 53 (3), 226–228. doi:10.4103/ijp.IJP_615_20
- Dai, W., Zhang, B., Jiang, X. M., Su, H., Li, J., Zhao, Y., et al. (2020). Structure-based design of antiviral drug candidates targeting the SARS-CoV-2 main protease. *Science* 368 (6497), 1331–1335. doi:10.1126/science.abb4489
- Daly, J. L., Simonetti, B., Klein, K., Chen, K. E., Williamson, M. K., Anton-Plagaro, C., et al. (2020). Neuropilin-1 is a host factor for SARS-CoV-2 infection. *Science* 370 (6518), 861–865. doi:10.1126/science.abd3072
- de la Rica, R., Borges, M., and Gonzalez-Freire, M. (2020). COVID-19: In the eye of the cytokine storm. *Front. Immunol.* 11, 558898. doi:10.3389/fimmu.2020.558898
- De Virgiliis, F., and Di Giovanni, S. (2020). Lung innervation in the eye of a cytokine storm: Neuroimmune interactions and COVID-19. *Nat. Rev. Neurol.* 16 (11), 645–652. doi:10.1038/s41582-020-0402-y
- DeJong, C., Spinelli, M. A., Okochi, H., and Gandhi, M. (2021). Tenofovir-based PrEP for COVID-19: An untapped opportunity? *AIDS* 35 (9), 1509–1511. doi:10.1097/QAD.0000000000002877
- Del Valle, D. M., Kim-Schulze, S., Huang, H. H., Beckmann, N. D., Nirenberg, S., Wang, B., et al. (2020). An inflammatory cytokine signature predicts COVID-19 severity and survival. *Nat. Med.* 26 (10), 1636–1643. doi:10.1038/s41591-020-1051-9
- Demirel Oğut, N., Kutlu, O., and Erbagci, E. (2021). Oral isotretinoin treatment in patients with acne vulgaris during the COVID-19 pandemic: A retrospective cohort study in a tertiary care hospital. *J. Cosmet. Dermatol.* 20 (7), 1969–1974. doi:10.1111/jocd.14168
- Duan, X., Tang, X., Nair, M. S., Zhang, T., Qiu, Y., Zhang, W., et al. (2021). An airway organoid-based screen identifies a role for the HIF1 α -glycolysis axis in SARS-CoV-2 infection. *Cell Rep.* 37 (6), 109920. doi:10.1016/j.celrep.2021.109920
- Dulin, D., Arnold, J. J., van Laar, T., Oh, H. S., Lee, C., Perkins, A. L., et al. (2017). Signatures of nucleotide analog incorporation by an RNA-dependent RNA polymerase revealed using high-throughput magnetic tweezers. *Cell Rep.* 21 (4), 1063–1076. doi:10.1016/j.celrep.2017.10.005
- Dulin, D., Vilfan, I. D., Berghuis, B. A., Poranen, M. M., Depken, M., and Dekker, N. H. (2015). Backtracking behavior in viral RNA-dependent RNA polymerase provides the basis for a second initiation site. *Nucleic Acids Res.* 43 (21), 10421–10429. doi:10.1093/nar/gkv1098
- Ferrario, C. M., Jessup, J., Chappell, M. C., Averill, D. B., Brosnihan, K. B., Tallant, E. A., et al. (2005). Effect of angiotensin-converting enzyme inhibition and angiotensin II receptor blockers on cardiac angiotensin-converting enzyme 2. *Circulation* 111 (20), 2605–2610. doi:10.1161/CIRCULATIONAHA.104.510461
- Flinspach, A. N., Zacharowski, K., Ioanna, D., and Adam, E. H. (2020). Volatile isoflurane in critically ill coronavirus disease 2019 patients-A case series and systematic review. *Crit. Care Explor.* 2 (10), e0256. doi:10.1097/CCE.0000000000000256
- Gao, X., Qin, B., Chen, P., Zhu, K., Hou, P., Wojdyla, J. A., et al. (2021). Crystal structure of SARS-CoV-2 papain-like protease. *Acta Pharm. Sin. B* 11 (1), 237–245. doi:10.1016/j.apsb.2020.08.014
- Gao, Y., Yan, L., Huang, Y., Liu, F., Zhao, Y., Cao, L., et al. (2020). Structure of the RNA-dependent RNA polymerase from COVID-19 virus. *Science* 368 (6492), 779–782. doi:10.1126/science.abb7498
- Gheblawi, M., Wang, K., Viveiros, A., Nguyen, Q., Zhong, J. C., Turner, A. J., et al. (2020). Angiotensin-converting enzyme 2: SARS-CoV-2 receptor and regulator of the renin-angiotensin system: Celebrating the 20th anniversary of the discovery of ACE2. *Circ. Res.* 126 (10), 1456–1474. doi:10.1161/CIRCRESAHA.120.317015
- Good, S. S., Westover, J., Jung, K. H., Zhou, X. J., Moussa, A., La Colla, P., et al. (2021). AT-527, a double prodrug of a guanosine nucleotide analog, is a potent inhibitor of SARS-CoV-2 *in vitro* and a promising oral antiviral for treatment of COVID-19. *Antimicrob. Agents Chemother.* 65 (4), e02479-20. doi:10.1128/AAC.02479-20
- Gordon, C. J., Tchesnokov, E. P., Woolner, E., Perry, J. K., Feng, J. Y., Porter, D. P., et al. (2020). Remdesivir is a direct-acting antiviral that inhibits RNA-dependent RNA polymerase from severe acute respiratory syndrome coronavirus 2 with high potency. *J. Biol. Chem.* 295 (20), 6785–6797. doi:10.1074/jbc.RA120.013679
- Gordon, D. E., Hiatt, J., Bouhaddou, M., Rezeli, V. V., Ulferts, S., Braberg, H., et al. (2020a). Comparative host-coronavirus protein interaction networks reveal pan-viral disease mechanisms. *Science* 370 (6521), eabe9403. doi:10.1126/science.abe9403
- Gordon, D. E., Jang, G. M., Bouhaddou, M., Xu, J., Obernier, K., White, K. M., et al. (2020b). A SARS-CoV-2 protein interaction map reveals targets for drug repurposing. *Nature* 583 (7816), 459–468. doi:10.1038/s41586-020-2286-9
- Gritti, G., Raimondi, F., Bottazzi, B., Ripamonti, D., Riva, I., Landi, F., et al. (2021). Siltuximab downregulates interleukin-8 and pentraxin 3 to improve ventilatory status and survival in severe COVID-19. *Leukemia* 35 (9), 2710–2714. doi:10.1038/s41375-021-01299-x
- Group, R. C., Horby, P., Lim, W. S., Emberson, J. R., Mafham, M., Bell, J. L., et al. (2021). Dexamethasone in hospitalized patients with covid-19. *N. Engl. J. Med. Overseas. Ed.* 384 (8), 693–704. doi:10.1056/NEJMoa2021436
- Gupta, A., Gonzalez-Rojas, Y., Juarez, E., Crespo Casal, M., Moya, J., Falcì, D. R., et al. (2021). Early treatment for covid-19 with SARS-CoV-2 neutralizing antibody sotrovimab. *N. Engl. J. Med. Overseas. Ed.* 385 (21), 1941–1950. doi:10.1056/NEJMoa2107934
- Hadjadi, J., Yatim, N., Barnabei, L., Corneau, A., Boussier, J., Smith, N., et al. (2020). Impaired type I interferon activity and inflammatory responses in severe COVID-19 patients. *Science* 369 (6504), 718–724. doi:10.1126/science.abc6027
- Hall, M. D., Anderson, J. M., Anderson, A., Baker, D., Bradner, J., Brimacombe, K. R., et al. (2021). Report of the national institutes of health SARS-CoV-2 antiviral therapeutics summit. *J. Infect. Dis.* 224 (1), S1–S21. doi:10.1093/infdis/jiab305
- Halwe, S., Kupke, A., Vanshylla, K., Libertà, F., Gruell, H., Zehner, M., et al. (2021). Intranasal administration of a monoclonal neutralizing antibody protects mice against SARS-CoV-2 infection. *Viruses* 13 (8), 1498. doi:10.3390/v13081498
- Han, Y., Duan, X., Yang, L., Nilsson-Payant, B. E., Wang, P., Duan, F., et al. (2021). Identification of SARS-CoV-2 inhibitors using lung and colonic organoids. *Nature* 589 (7841), 270–275. doi:10.1038/s41586-020-2901-9
- Harcourt, B. H., Jukneliene, D., Kanjanahaluethai, A., Bechill, J., Severson, K. M., Smith, C. M., et al. (2004). Identification of severe acute respiratory syndrome coronavirus replicase products and characterization of papain-like protease activity. *J. Virol.* 78 (24), 13600–13612. doi:10.1128/JVI.78.24.13600-13612.2004
- Hegyi, A., and Ziebuhr, J. (2002). Conservation of substrate specificities among coronavirus main proteases. *J. Gen. Virol.* 83 (3), 595–599. doi:10.1099/0022-1317-83-3-595
- Hockham, C., Kotwal, S., Wilcox, A., Bassi, A., McGree, J., Pollock, C., et al. (2021). Protocol for the controlled evaluation of angiotensin receptor blockers for COVID-19 respiraTorY disease (CLARITY): A randomised controlled trial. *Trials* 22 (1), 573. doi:10.1186/s13063-021-05521-0

- Hoffmann, H. H., Sanchez-Rivera, F. J., Schneider, W. M., Luna, J. M., Soto-Feliciano, Y. M., Ashbrook, A. W., et al. (2021a). Functional interrogation of a SARS-CoV-2 host protein interactome identifies unique and shared coronavirus host factors. *Cell Host Microbe* 29 (2), 267–280.e5. doi:10.1016/j.chom.2020.12.009
- Hoffmann, H. H., Schneider, W. M., Rozen-Gagnon, K., Miles, L. A., Schuster, F., Razoosky, B., et al. (2021b). TMEM41B is a pan-flavivirus host factor. *Cell* 184 (1), 133–148.e20. doi:10.1016/j.cell.2020.12.005
- Hoffmann, M., Hofmann-Winkler, H., Smith, J. C., Kruger, N., Arora, P., Sorensen, L. K., et al. (2021). Camostat mesylate inhibits SARS-CoV-2 activation by TMPRSS2-related proteases and its metabolite GBPA exerts antiviral activity. *EBioMedicine* 65, 103255. doi:10.1016/j.ebiom.2021.103255
- Hoffmann, M., Kleine-Weber, H., and Pohlmann, S. (2020a). A multibasic cleavage site in the spike protein of SARS-CoV-2 is essential for infection of human lung cells. *Mol. Cell* 78 (4), 779–784.e5. doi:10.1016/j.molcel.2020.04.022
- Hoffmann, M., Kleine-Weber, H., Schroeder, S., Kruger, N., Herrler, T., Erichsen, S., et al. (2020b). SARS-CoV-2 cell entry depends on ACE2 and TMPRSS2 and is blocked by a clinically proven protease inhibitor. *Cell* 181 (2), 271–280.e8. doi:10.1016/j.cell.2020.02.052
- Huang, C., Wang, Y., Li, X., Ren, L., Zhao, J., Hu, Y., et al. (2020). Clinical features of patients infected with 2019 novel coronavirus in Wuhan, China. *Lancet* 395 (10223), 497–506. doi:10.1016/S0140-6736(20)30183-5
- Imbert, I., Guillemot, J. C., Bourhis, J. M., Bussetta, C., Coutard, B., Egloff, M. P., et al. (2006). A second, non-canonical RNA-dependent RNA polymerase in SARS coronavirus. *EMBO J.* 25 (20), 4933–4942. doi:10.1038/sj.emboj.7601368
- Investigators, R.-C., Gordon, A. C., Mouncey, P. R., Al-Beidh, F., Rowan, K. M., Nichol, A. D., et al. (2021). Interleukin-6 receptor antagonists in critically ill patients with covid-19. *N. Engl. J. Med. Overseas. Ed.* 384 (16), 1491–1502. doi:10.1056/NEJMoa2100433
- Ivanov, K. A., Thiel, V., Dobbe, J. C., van der Meer, Y., Snijder, E. J., and Ziebuhr, J. (2004). Multiple enzymatic activities associated with severe acute respiratory syndrome coronavirus helicase. *J. Virol.* 78 (11), 5619–5632. doi:10.1128/JVI.78.11.5619-5632.2004
- Jabaudon, M., Boucher, P., Imhoff, E., Chabanne, R., Faure, J. S., Roszyk, L., et al. (2017). Sevoflurane for sedation in acute respiratory distress syndrome. A randomized controlled pilot study. *Am. J. Respir. Crit. Care Med.* 195 (6), 792–800. doi:10.1164/rccm.201604-0686OC
- Jang, S., and Rhee, J. Y. (2020). Three cases of treatment with nafamostat in elderly patients with COVID-19 pneumonia who need oxygen therapy. *Int. J. Infect. Dis.* 96, 500–502. doi:10.1016/j.ijid.2020.05.072
- Jayk Bernal, A., Gomes da Silva, M. M., Musungaie, D. B., Kovalchuk, E., Gonzalez, A., Delos Reyes, V., et al. (2021). Molnupiravir for oral treatment of covid-19 in nonhospitalized patients. *N. Engl. J. Med. Overseas. Ed.* 386, 509–520. doi:10.1056/NEJMoa2116044
- Jin, Z., Du, X., Xu, Y., Deng, Y., Liu, M., Zhao, Y., et al. (2020). Structure of M(pro) from SARS-CoV-2 and discovery of its inhibitors. *Nature* 582 (7811), 289–293. doi:10.1038/s41586-020-2223-y
- Julander, J. G., Demarest, J. F., Taylor, R., Gowen, B. B., Walling, D. M., Mathis, A., et al. (2021). An update on the progress of galidesivir (BCX4430), a broad-spectrum antiviral. *Antivir. Res.* 195, 105180. doi:10.1016/j.antiviral.2021.105180
- Kabinger, F., Stiller, C., Schmitzova, J., Dienemann, C., Kovic, G., Hillen, H. S., et al. (2021). Mechanism of molnupiravir-induced SARS-CoV-2 mutagenesis. *Nat. Struct. Mol. Biol.* 28 (9), 740–746. doi:10.1038/s41594-021-00651-0
- Kaptein, S. J. F., Jacobs, S., Langendries, L., Seldeslachts, L., Ter Horst, S., Liesenborghs, L., et al. (2020). Favipiravir at high doses has potent antiviral activity in SARS-CoV-2-infected hamsters, whereas hydroxychloroquine lacks activity. *Proc. Natl. Acad. Sci. U. S. A.* 117 (43), 26955–26965. doi:10.1073/pnas.2014441117
- Kovic, G., Hillen, H. S., Tegunov, D., Dienemann, C., Seitz, F., Schmitzova, J., et al. (2021). Mechanism of SARS-CoV-2 polymerase stalling by remdesivir. *Nat. Commun.* 12 (1), 279. doi:10.1038/s41467-020-20542-0
- Kreuzberger, N., Hirsch, C., Chai, K. L., Tomlinson, E., Khosravi, Z., Popp, M., et al. (2021). SARS-CoV-2-neutralising monoclonal antibodies for treatment of COVID-19. *Cochrane Database Syst. Rev.* 9, CD013825. doi:10.1002/14651858.CD013825.pub2
- Laing, A. G., Lorenc, A., Del Molino Del Barrio, I., Das, A., Fish, M., Monin, L., et al. (2020). A dynamic COVID-19 immune signature includes associations with poor prognosis. *Nat. Med.* 26 (10), 1623–1635. doi:10.1038/s41591-020-1038-6
- Lan, J., Ge, J., Yu, J., Shan, S., Zhou, H., Fan, S., et al. (2020). Structure of the SARS-CoV-2 spike receptor-binding domain bound to the ACE2 receptor. *Nature* 581 (7807), 215–220. doi:10.1038/s41586-020-2180-5
- Lee, J. Y., Lee, J. Y., Ko, J. H., Hyun, M., Kim, H. A., Cho, S., et al. (2021). Effectiveness of regdanvimab treatment in high-risk COVID-19 patients to prevent progression to severe disease. *Front. Immunol.* 12, 772320. doi:10.3389/fimmu.2021.772320
- Lee, N. R., Kwon, H. M., Park, K., Oh, S., Jeong, Y. J., and Kim, D. E. (2010). Cooperative translocation enhances the unwinding of duplex DNA by SARS coronavirus helicase nsP13. *Nucleic Acids Res.* 38 (21), 7626–7636. doi:10.1093/nar/gkq647
- Lei, X., Dong, X., Ma, R., Wang, W., Xiao, X., Tian, Z., et al. (2020). Activation and evasion of type I interferon responses by SARS-CoV-2. *Nat. Commun.* 11 (1), 3810. doi:10.1038/s41467-020-17665-9
- Li, M., Lou, F., and Fan, H. (2022). SARS-CoV-2 variant omicron: Currently the most complete "escapee" from neutralization by antibodies and vaccines. *Signal Transduct. Target. Ther.* 7 (1), 28. doi:10.1038/s41392-022-00880-9
- Liu, J., Cao, R., Xu, M., Wang, X., Zhang, H., Hu, H., et al. (2020). Hydroxychloroquine, a less toxic derivative of chloroquine, is effective in inhibiting SARS-CoV-2 infection *in vitro*. *Cell Discov.* 6, 16. doi:10.1038/s41421-020-0156-0
- Liu, L., Iketani, S., Guo, Y., Chan, J. F., Wang, M., Liu, L., et al. (2022). Striking antibody evasion manifested by the Omicron variant of SARS-CoV-2. *Nature* 602 (7898), 676–681. doi:10.1038/s41586-021-04388-0
- Lomakin, N. V., Bakirov, B. A., Protsenko, D. N., Mazurov, V. I., Musaev, G. H., Moiseeva, O. M., et al. (2021). The efficacy and safety of levilimab in severely ill COVID-19 patients not requiring mechanical ventilation: Results of a multicenter randomized double-blind placebo-controlled phase III CORONA clinical study. *Inflamm. Res.* 70 (10–12), 1233–1246. doi:10.1007/s00011-021-01507-5
- Ma, X. R., Alugubelli, Y. R., Ma, Y., Vatansever, E. C., Scott, D. A., Qiao, Y., et al. (2022). MP18 is potent against SARS-CoV-2 by inhibiting dually and selectively the SARS-CoV-2 main protease and the host cathepsin L. *ChemMedChem* 17 (1), e202100456. doi:10.1002/cmdc.202100456
- Mahase, E. (2021). Covid-19: AstraZeneca says its antibody drug AZD7442 is effective for preventing and reducing severe illness. *BMJ* 375, n2860. doi:10.1136/bmj.n2860
- Malone, B., Chen, J., Wang, Q., Llewellyn, E., Choi, Y. J., Olinares, P. D. B., et al. (2021). Structural basis for backtracking by the SARS-CoV-2 replication-transcription complex. *Proc. Natl. Acad. Sci. U. S. A.* 118 (19), e2102516118. doi:10.1073/pnas.2102516118
- Malone, B., Urakova, N., Snijder, E. J., and Campbell, E. A. (2022). Structures and functions of coronavirus replication-transcription complexes and their relevance for SARS-CoV-2 drug design. *Nat. Rev. Mol. Cell Biol.* 23 (1), 21–39. doi:10.1038/s41580-021-00432-z
- Marra, M. A., Jones, S. J., Astell, C. R., Holt, R. A., Brooks-Wilson, A., Butterfield, Y. S., et al. (2003). The Genome sequence of the SARS-associated coronavirus. *Science* 300 (5624), 1399–1404. doi:10.1126/science.1085953
- Masre, S. F., Jufri, N. F., Ibrahim, F. W., and Abdul Raub, S. H. (2021). Classical and alternative receptors for SARS-CoV-2 therapeutic strategy. *Rev. Med. Virol.* 31 (5), 1–9. doi:10.1002/rmv.2207
- McCallum, M., De Marco, A., Lempp, F. A., Tortorici, M. A., Pinto, D., Walls, A. C., et al. (2021). N-terminal domain antigenic mapping reveals a site of vulnerability for SARS-CoV-2. *Cell* 184 (9), 2332–2347.e16. doi:10.1016/j.cell.2021.03.028
- McDonald, S. M. (2013). RNA synthetic mechanisms employed by diverse families of RNA viruses. *WIREs. RNA* 4 (4), 351–367. doi:10.1002/wrna.1164
- McEneny-King, A. C., Monteleone, J. P. R., Kazani, S. D., and Ortiz, S. R. (2021). Pharmacokinetic and pharmacodynamic evaluation of ravulizumab in adults with severe coronavirus disease 2019. *Infect. Dis. Ther.* 10 (2), 1045–1054. doi:10.1007/s40121-021-00425-7
- McNab, F., Mayer-Barber, K., Sher, A., Wack, A., and O'Garra, A. (2015). Type I interferons in infectious disease. *Nat. Rev. Immunol.* 15 (2), 87–103. doi:10.1038/nri3787
- Mehta, P., McAuley, D. F., Brown, M., Sanchez, E., Tattersall, R. S., Manson, J. J., et al. (2020). COVID-19: Consider cytokine storm syndromes and immunosuppression. *Lancet* 395 (10229), 1033–1034. doi:10.1016/S0140-6736(20)30628-0
- Michel, C. J., Mayer, C., Poch, O., and Thompson, J. D. (2020). Characterization of accessory genes in coronavirus genomes. *Virol. J.* 17 (1), 131. doi:10.1186/s12985-020-01402-1
- Monteil, V., Kwon, H., Prado, P., Hagelkruys, A., Wimmer, R. A., Stahl, M., et al. (2020). Inhibition of SARS-CoV-2 infections in engineered human tissues using clinical-grade soluble human ACE2. *Cell* 181 (4), 905–913.e7. doi:10.1016/j.cell.2020.04.004
- Naydenova, K., Muir, K. W., Wu, L. F., Zhang, Z., Coscia, F., Peet, M. J., et al. (2021). Structure of the SARS-CoV-2 RNA-dependent RNA polymerase in the

- presence of fapiravir-RTP. *Proc. Natl. Acad. Sci. U. S. A.* 118 (7), e2021946118. doi:10.1073/pnas.2021946118
- Nelson, C. W., Ardern, Z., Goldberg, T. L., Meng, C., Kuo, C. H., Ludwig, C., et al. (2020). Dynamically evolving novel overlapping gene as a factor in the SARS-CoV-2 pandemic. *Elife* 9, e59633. doi:10.7554/eLife.59633
- Newman, J. A., Douangamath, A., Yadzani, S., Yosaatmadja, Y., Aimon, A., Brandao-Neto, J., et al. (2021). Structure, mechanism and crystallographic fragment screening of the SARS-CoV-2 NSP13 helicase. *Nat. Commun.* 12 (1), 4848. doi:10.1038/s41467-021-25166-6
- Ogawa, H., and Asakura, H. (2020). Consideration of tranexamic acid administration to COVID-19 patients. *Physiol. Rev.* 100 (4), 1595–1596. doi:10.1152/physrev.00023.2020
- Ospiuk, J., Azizi, S. A., Dvorkin, S., Endres, M., Jedrzejczak, R., Jones, K. A., et al. (2021). Structure of papain-like protease from SARS-CoV-2 and its complexes with non-covalent inhibitors. *Nat. Commun.* 12 (1), 743. doi:10.1038/s41467-021-21060-3
- Ou, X., Liu, Y., Lei, X., Li, P., Mi, D., Ren, L., et al. (2020). Characterization of spike glycoprotein of SARS-CoV-2 on virus entry and its immune cross-reactivity with SARS-CoV. *Nat. Commun.* 11 (1), 1620. doi:10.1038/s41467-020-15562-9
- Owen, D. R., Allerton, C. M. N., Anderson, A. S., Aschenbrenner, L., Avery, M., Berritt, S., et al. (2021). An oral SARS-CoV-2 M(pro) inhibitor clinical candidate for the treatment of COVID-19. *Science* 374 (6575), 1586–1593. doi:10.1126/science.abl4784
- Pang, J., Xu, F., Aondio, G., Li, Y., Fumagalli, A., Lu, M., et al. (2021). Efficacy and tolerability of bevacizumab in patients with severe Covid-19. *Nat. Commun.* 12 (1), 814. doi:10.1038/s41467-021-21085-8
- Park, S. J., Yu, K. M., Kim, Y. I., Kim, S. M., Kim, E. H., Kim, S. G., et al. (2020). Antiviral efficacies of FDA-approved drugs against SARS-CoV-2 infection in ferrets. *mBio* 11 (3), e01114-20. doi:10.1128/mBio.01114-20
- Patchett, S., Lv, Z., Rut, W., Bekes, M., Drag, M., Olsen, S. K., et al. (2021). A molecular sensor determines the ubiquitin substrate specificity of SARS-CoV-2 papain-like protease. *Cell Rep.* 36 (13), 109754. doi:10.1016/j.celrep.2021.109754
- Qiao, J., Li, Y. S., Zeng, R., Liu, F. L., Luo, R. H., Huang, C., et al. (2021). SARS-CoV-2 M(pro) inhibitors with antiviral activity in a transgenic mouse model. *Science* 371 (6536), 1374–1378. doi:10.1126/science.abf1611
- Rathnayake, A. D., Zheng, J., Kim, Y., Perera, K. D., Mackin, S., Meyerholz, D. K., et al. (2020). 3C-like protease inhibitors block coronavirus replication *in vitro* and improve survival in MERS-CoV-infected mice. *Sci. Transl. Med.* 12 (557), eabc5332. doi:10.1126/scitranslmed.abc5332
- Ratia, K., Pegan, S., Takayama, J., Sleeman, K., Coughlin, M., Baliji, S., et al. (2008). A noncovalent class of papain-like protease/deubiquitinase inhibitors blocks SARS virus replication. *Proc. Natl. Acad. Sci. U. S. A.* 105 (42), 16119–16124. doi:10.1073/pnas.0805240105
- Redondo, N., Zaldivar-Lopez, S., Garrido, J. J., and Montoya, M. (2021). SARS-CoV-2 accessory proteins in viral pathogenesis: Knowns and unknowns. *Front. Immunol.* 12, 708264. doi:10.3389/fimmu.2021.708264
- Reis, G., Dos Santos Moreira-Silva, E. A., Silva, D. C. M., Thabane, L., Milagres, A. C., Ferreira, T. S., et al. (2022). Effect of early treatment with flvoxamine on risk of emergency care and hospitalisation among patients with COVID-19: The TOGETHER randomised, platform clinical trial. *Lancet Glob. Health* 10 (1), e42–e51. doi:10.1016/S2214-109X(21)00448-4
- Richeldi, L., Fernandez Perez, E. R., Costabel, U., Albera, C., Lederer, D. J., Flaherty, K. R., et al. (2020). Pamrevlumab, an anti-connective tissue growth factor therapy, for idiopathic pulmonary fibrosis (PRAISE): A phase 2, randomised, double-blind, placebo-controlled trial. *Lancet Respir. Med.* 8 (1), 25–33. doi:10.1016/S2213-2600(19)30262-0
- Romano, M., Ruggiero, A., Squeglia, F., Maga, G., and Berisio, R. (2020). A structural view of SARS-CoV-2 RNA replication machinery: RNA synthesis, proofreading and final capping. *Cells* 9 (5), 1267. doi:10.3390/cells9051267
- Rosas, I. O., Brau, N., Waters, M., Go, R. C., Hunter, B. D., Bhagani, S., et al. (2021). Tocilizumab in hospitalized patients with severe covid-19 pneumonia. *N. Engl. J. Med. Overseas. Ed.* 384 (16), 1503–1516. doi:10.1056/NEJMoa2028700
- Russell, C. D., Millar, J. E., and Baillie, J. K. (2020). Clinical evidence does not support corticosteroid treatment for 2019-nCoV lung injury. *Lancet* 395 (10223), 473–475. doi:10.1016/S0140-6736(20)30317-2
- Rut, W., Lv, Z., Zmudzinski, M., Patchett, S., Nayak, D., Snipas, S. J., et al. (2020). Activity profiling and crystal structures of inhibitor-bound SARS-CoV-2 papain-like protease: A framework for anti-COVID-19 drug design. *Sci. Adv.* 6 (42), eabd4596. doi:10.1126/sciadv.abd4596
- Group, A.C.-T.f.I.w.C.-S.Sandkovsky, U., Reilly, C. S., Vock, D. M., Gottlieb, R. L., Mack, M., et al. (2021). Efficacy and safety of two neutralising monoclonal antibody therapies, sotrovimab and BRII-196 plus BRII-198, for adults hospitalised with COVID-19 (TICO): A randomised controlled trial. *Lancet Infect. Dis.* 22, 622–635. doi:10.1016/S1473-3099(21)00751-9
- Schmidt, F., Muecksch, F., Weisblum, Y., Da Silva, J., Bednarski, E., Cho, A., et al. (2022). Plasma neutralization of the SARS-CoV-2 omicron variant. *N. Engl. J. Med. Overseas. Ed.* 386 (6), 599–601. doi:10.1056/NEJMc2119641
- Schneider, W. M., Luna, J. M., Hoffmann, H. H., Sanchez-Rivera, F. J., Leal, A. A., Ashbrook, A. W., et al. (2021). Genome-scale identification of SARS-CoV-2 and pan-coronavirus host factor networks. *Cell* 184 (1), 120–132.e14. doi:10.1016/j.cell.2020.12.006
- Shang, J., Wan, Y., Luo, C., Ye, G., Geng, Q., Auerbach, A., et al. (2020a). Cell entry mechanisms of SARS-CoV-2. *Proc. Natl. Acad. Sci. U. S. A.* 117 (21), 11727–11734. doi:10.1073/pnas.2003138117
- Shang, J., Ye, G., Shi, K., Wan, Y., Luo, C., Aihara, H., et al. (2020b). Structural basis of receptor recognition by SARS-CoV-2. *Nature* 581 (7807), 221–224. doi:10.1038/s41586-020-2179-y
- Shang, L., Zhao, J., Hu, Y., Du, R., and Cao, B. (2020). On the use of corticosteroids for 2019-nCoV pneumonia. *Lancet* 395 (10225), 683–684. doi:10.1016/S0140-6736(20)30361-5
- Shin, D., Mukherjee, R., Grewe, D., Bojkova, D., Baek, K., Bhattacharya, A., et al. (2020). Papain-like protease regulates SARS-CoV-2 viral spread and innate immunity. *Nature* 587 (7835), 657–662. doi:10.1038/s41586-020-2601-5
- Sinha, S., Cheng, K., Schaffer, A. A., Aldape, K., Schiff, E., and Rupp, E. (2020). *In vitro* and *in vivo* identification of clinically approved drugs that modify ACE 2 expression. *Mol. Syst. Biol.* 16 (7), e9628. doi:10.15252/msb.20209628
- Song, N. J., Allen, C., Vilgelm, A. E., Riesenberger, B. P., Weller, K. P., Reynolds, K., et al. (2022). Treatment with soluble CD24 attenuates COVID-19-associated systemic immunopathology. *J. Hematol. Oncol.* 15 (1), 5. doi:10.1186/s13045-021-01222-y
- Strich, J. R., Tian, X., Samour, M., King, C. S., Shlobin, O., Reger, R., et al. (2021). Fostamatinib for the treatment of hospitalized adults with COVID-19 A randomized trial. *Clin. Infect. Dis.* 75 (1), e491–e498. doi:10.1093/cid/ciab732
- Sungnak, W., Huang, N., Becavin, C., Berg, M., Queen, R., Litvinukova, M., et al. (2020). SARS-CoV-2 entry factors are highly expressed in nasal epithelial cells together with innate immune genes. *Nat. Med.* 26 (5), 681–687. doi:10.1038/s41591-020-0868-6
- Syed, Y. Y. (2021). Regdanvimab: First approval. *Drugs* 81 (18), 2133–2137. doi:10.1007/s40265-021-01626-7
- Tanner, J. A., Watt, R. M., Chai, Y. B., Lu, L. Y., Lin, M. C., Peiris, J. S., et al. (2003). The severe acute respiratory syndrome (SARS) coronavirus NTPase/helicase belongs to a distinct class of 5' to 3' viral helicases. *J. Biol. Chem.* 278 (41), 39578–39582. doi:10.1074/jbc.C300328200
- Tao, K., Tzou, P. L., Nounin, J., Bonilla, H., Jagannathan, P., and Shafer, R. W. (2021). SARS-CoV-2 antiviral therapy. *Clin. Microbiol. Rev.* 34 (4), e0010921. doi:10.1128/CMR.00109-21
- Temesgen, Z., Burger, C. D., Baker, J., Polk, C., Libertin, C. R., Kelley, C. F., et al. (2021). Lenzilumab in hospitalised patients with COVID-19 pneumonia (LIVE-AIR): A phase 3, randomised, placebo-controlled trial. *Lancet Respir. Med.* 10, 237–246. doi:10.1016/S2213-2600(21)00494-X
- Temmam, S., Vongphayloth, K., Baquero, E., Munier, S., Bonomi, M., Regnault, B., et al. (2022). Bat coronaviruses related to SARS-CoV-2 and infectious for human cells. *Nature* 604 (7905), 330–336. doi:10.1038/s41586-022-04532-4
- Tong, S., Su, Y., Yu, Y., Wu, C., Chen, J., Wang, S., et al. (2020). Ribavirin therapy for severe COVID-19: A retrospective cohort study. *Int. J. Antimicrob. Agents* 56 (3), 106114. doi:10.1016/j.ijantimicag.2020.106114
- Tuccori, M., Convertino, I., Ferraro, S., Valdiserra, G., Cappello, E., Fini, E., et al. (2021). An overview of the preclinical discovery and development of bamlanivimab for the treatment of novel coronavirus infection (COVID-19): Reasons for limited clinical use and lessons for the future. *Expert Opin. Drug Discov.* 16 (12), 1403–1414. doi:10.1080/17460441.2021.1960819
- Udwadia, Z. F., Singh, P., Barkate, H., Patil, S., Rangwala, S., Pendse, A., et al. (2021). Efficacy and safety of favipiravir, an oral RNA-dependent RNA polymerase inhibitor, in mild-to-moderate COVID-19: A randomized, comparative, open-label, multicenter, phase 3 clinical trial. *Int. J. Infect. Dis.* 103, 62–71. doi:10.1016/j.ijid.2020.11.142
- Vaidya, G., Czer, L. S. C., Kobashigawa, J., Kittleson, M., Patel, J., Chang, D., et al. (2020). Successful treatment of severe COVID-19 pneumonia with clazakizumab in a heart transplant recipient: A case report. *Transpl. Proc.* 52 (9), 2711–2714. doi:10.1016/j.transproceed.2020.06.003
- Valenzuela-Almada, M. O., Putman, M. S., and Duarte-Garcia, A. (2021). The protective effect of rheumatic disease agents in COVID-19. *Best. Pract. Res. Clin. Rheumatol.* 35 (1), 101659. doi:10.1016/j.berh.2021.101659

- Varona, J. F., Landete, P., Lopez-Martin, J. A., Estrada, V., Paredes, R., Guisado-Vasco, P., et al. (2022). Preclinical and randomized phase I studies of plitidepsin in adults hospitalized with COVID-19. *Life Sci. Alliance* 5 (4), e202101200. doi:10.26508/lsa.202101200
- Vatansever, E. C., Yang, K. S., Drelich, A. K., Kratch, K. C., Cho, C.-C., Kempaiah, K. R., et al. (2021). Bepiridil is potent against SARS-CoV-2 *in vitro*. *Proc. Natl. Acad. Sci. U. S. A.* 118 (10), e2012201118. doi:10.1073/pnas.2012201118
- Viana, R., Moyo, S., Amoako, D. G., Tegally, H., Scheepers, C., Althaus, C. L., et al. (2022). Rapid epidemic expansion of the SARS-CoV-2 Omicron variant in southern Africa. *Nature* 603 (7902), 679–686. doi:10.1038/s41586-022-04411-y
- Vlaar, A. P. J., de Bruin, S., Busch, M., Timmermans, S., van Zeggeren, I. E., Koning, R., et al. (2020). Anti-C5a antibody IFX-1 (vilobelimab) treatment versus best supportive care for patients with severe COVID-19 (PANAMO): An exploratory, open-label, phase 2 randomised controlled trial. *Lancet Rheumatol.* 2 (12), e764–e773. doi:10.1016/S2665-9913(20)30341-6
- Walls, A. C., Park, Y. J., Tortorici, M. A., Wall, A., McGuire, A. T., and Veesler, D. (2020). Structure, function, and antigenicity of the SARS-CoV-2 spike glycoprotein. *Cell* 181 (2), 281–292.e6. doi:10.1016/j.cell.2020.02.058
- Wang, Q., Wu, J., Wang, H., Gao, Y., Liu, Q., Mu, A., et al. (2020). Structural basis for RNA replication by the SARS-CoV-2 polymerase. *Cell* 182 (2), 417–428.e13. doi:10.1016/j.cell.2020.05.034
- Wang, R., Simoneau, C. R., Kulsuptrakul, J., Bouhaddou, M., Travisano, K. A., Hayashi, J. M., et al. (2021). Genetic screens identify host factors for SARS-CoV-2 and common cold coronaviruses. *Cell* 184 (1), 106–119.e14. doi:10.1016/j.cell.2020.12.004
- Wang, S., Li, W., Hui, H., Tiwari, S. K., Zhang, Q., Croker, B. A., et al. (2020). Cholesterol 25-Hydroxylase inhibits SARS-CoV-2 and other coronaviruses by depleting membrane cholesterol. *EMBO J.* 39 (21), e106057. doi:10.15252/emboj.2020106057
- Wang, Z., Yang, B., Li, Q., Wen, L., and Zhang, R. (2020). Clinical features of 69 cases with coronavirus disease 2019 in wuhan, China. *Clin. Infect. Dis.* 71 (15), 769–777. doi:10.1093/cid/ciaa272
- Weinreich, D. M., Sivapalasingam, S., Norton, T., Ali, S., Gao, H., Bhoire, R., et al. (2021). REGN-COV2, a neutralizing antibody cocktail, in outpatients with covid-19. *N. Engl. J. Med. Overseas. Ed.* 384 (3), 238–251. doi:10.1056/NEJMoa2035002
- Welen, K., Rosendal, E., Gisslen, M., Lenman, A., Freyhult, E., Fonseca-Rodriguez, O., et al. (2022). A phase 2 trial of the effect of antiandrogen therapy on COVID-19 outcome: No evidence of benefit, supported by epidemiology and *in vitro* Data. *Eur. Urol.* 81 (3), 285–293. doi:10.1016/j.eururo.2021.12.013
- Williams, B. (2021). Renin-angiotensin system inhibitors in hospitalised patients with COVID-19. *Lancet Respir. Med.* 9 (3), 221–222. doi:10.1016/S2213-2600(21)00003-5
- Wrapp, D., Wang, N., Corbett, K. S., Goldsmith, J. A., Hsieh, C. L., Abiona, O., et al. (2020). Cryo-EM structure of the 2019-nCoV spike in the prefusion conformation. *Science* 367 (6483), 1260–1263. doi:10.1126/science.abb2507
- Yan, R., Zhang, Y., Li, Y., Xia, L., Guo, Y., and Zhou, Q. (2020). Structural basis for the recognition of SARS-CoV-2 by full-length human ACE2. *Science* 367 (6485), 1444–1448. doi:10.1126/science.abb2762
- Yang, K. S., Ma, X. R., Ma, Y., Alugubelli, Y. R., Scott, D. A., Vatansever, E. C., et al. (2021). A quick route to multiple highly potent SARS-CoV-2 main protease inhibitors. *ChemMedChem* 16 (6), 942–948. doi:10.1002/cmdc.202000924
- Yang, L., Han, Y., Jaffre, F., Nilsson-Payant, B. E., Bram, Y., Wang, P., et al. (2021). An immuno-cardiac model for macrophage-mediated inflammation in COVID-19 hearts. *Circ. Res.* 129 (1), 33–46. doi:10.1161/CIRCRESAHA.121.319060
- Yang, N., and Shen, H. M. (2020). Targeting the endocytic pathway and autophagy process as a novel therapeutic strategy in COVID-19. *Int. J. Biol. Sci.* 16 (10), 1724–1731. doi:10.7150/ijbs.45498
- Yin, W., Luan, X., Li, Z., Zhou, Z., Wang, Q., Gao, M., et al. (2021). Structural basis for inhibition of the SARS-CoV-2 RNA polymerase by suramin. *Nat. Struct. Mol. Biol.* 28 (3), 319–325. doi:10.1038/s41594-021-00570-0
- Zang, R., Gomez Castro, M. F., McCune, B. T., Zeng, Q., Rothlauf, P. W., Sonnek, N. M., et al. (2020). TMPRSS2 and TMPRSS4 promote SARS-CoV-2 infection of human small intestinal enterocytes. *Sci. Immunol.* 5 (47), eabc3582. doi:10.1126/sciimmunol.abc3582
- Zhang, L., Lin, D., Sun, X., Curth, U., Drosten, C., Sauerhering, L., et al. (2020). Crystal structure of SARS-CoV-2 main protease provides a basis for design of improved alpha-ketoamide inhibitors. *Science* 368 (6489), 409–412. doi:10.1126/science.abb3405
- Zhou, F., Yu, T., Du, R., Fan, G., Liu, Y., Liu, Z., et al. (2020). Clinical course and risk factors for mortality of adult inpatients with COVID-19 in wuhan, China: A retrospective cohort study. *Lancet* 395 (10229), 1054–1062. doi:10.1016/S0140-6736(20)30566-3
- Zhou, P., Yang, X. L., Wang, X. G., Hu, B., Zhang, L., Zhang, W., et al. (2020). A pneumonia outbreak associated with a new coronavirus of probable bat origin. *Nature* 579 (7798), 270–273. doi:10.1038/s41586-020-2012-7
- Zhuravel, S. V., Khmelitskiy, O. K., Burlaka, O. O., Gritsan, A. I., Goloshechkin, B. M., Kim, S., et al. (2021). Nafamostat in hospitalized patients with moderate to severe COVID-19 pneumonia: A randomised phase II clinical trial. *EClinicalMedicine* 41, 101169. doi:10.1016/j.eclinm.2021.101169
- Zoufaly, A., Poglitsch, M., Aberle, J. H., Hoepler, W., Seitz, T., Traugott, M., et al. (2020). Human recombinant soluble ACE2 in severe COVID-19. *Lancet Respir. Med.* 8 (11), 1154–1158. doi:10.1016/S2213-2600(20)30418-5



OPEN ACCESS

EDITED BY

Wenshe Ray Liu,
Texas A&M University, United States

REVIEWED BY

Michele Saviano,
Institute of Crystallography, Department
of Chemical Sciences and Materials
Technologies, National Research
Council (CNR), Italy
George Kokotos,
National and Kapodistrian University of
Athens, Greece

*CORRESPONDENCE

Gaetano T. Montelione,
monteg3@rpi.edu

SPECIALTY SECTION

This article was submitted to Medicinal
and Pharmaceutical Chemistry,
a section of the journal
Frontiers in Chemistry

RECEIVED 20 May 2022

ACCEPTED 08 August 2022

PUBLISHED 06 October 2022

CITATION

Bafna K, Cioffi CL, Krug RM and
Montelione GT (2022), Structural
similarities between SARS-CoV2 3CL^{pro}
and other viral proteases suggest
potential lead molecules for developing
broad spectrum antivirals.
Front. Chem. 10:948553.
doi: 10.3389/fchem.2022.948553

COPYRIGHT

© 2022 Bafna, Cioffi, Krug and
Montelione. This is an open-access
article distributed under the terms of the
Creative Commons Attribution License
(CC BY). The use, distribution or
reproduction in other forums is
permitted, provided the original
author(s) and the copyright owner(s) are
credited and that the original
publication in this journal is cited, in
accordance with accepted academic
practice. No use, distribution or
reproduction is permitted which does
not comply with these terms.

Structural similarities between SARS-CoV2 3CL^{pro} and other viral proteases suggest potential lead molecules for developing broad spectrum antivirals

Khushboo Bafna ^{1,2}, Christopher L. Cioffi ¹,
Robert M. Krug ³ and Gaetano T. Montelione ^{1,2*}

¹Department of Chemistry and Chemical Biology, Rensselaer Polytechnic Institute, Troy, NY, United States, ²Center for Biotechnology and Interdisciplinary Sciences, Rensselaer Polytechnic Institute, Troy, NY, United States, ³Department of Molecular Biosciences, John Ring LaMontagne Center for Infectious Disease, Institute for Cellular and Molecular Biology, University of Texas at Austin, Austin, TX, United States

Considering the significant impact of the recent COVID-19 outbreak, development of broad-spectrum antivirals is a high priority goal to prevent future global pandemics. Antiviral development processes generally emphasize targeting a specific protein from a particular virus. However, some antiviral agents developed for specific viral protein targets may exhibit broad spectrum antiviral activity, or at least provide useful lead molecules for broad spectrum drug development. There is significant potential for repurposing a wide range of existing viral protease inhibitors to inhibit the SARS-CoV2 3C-like protease (3CL^{pro}). If effective even as relatively weak inhibitors of 3CL^{pro}, these molecules can provide a diverse and novel set of scaffolds for new drug discovery campaigns. In this study, we compared the sequence- and structure-based similarity of SARS-CoV2 3CL^{pro} with proteases from other viruses, and identified 22 proteases with similar active-site structures. This structural similarity, characterized by secondary-structure topology diagrams, is evolutionarily divergent within taxonomically related viruses, but appears to result from evolutionary convergence of protease enzymes between virus families. Inhibitors of these proteases that are structurally similar to the SARS-CoV2 3CL^{pro} protease were identified and assessed as potential inhibitors of SARS-CoV2 3CL^{pro} protease by virtual docking. Several of these molecules have docking scores that are significantly better than known SARS-CoV2 3CL^{pro} inhibitors, suggesting that these molecules are also potential inhibitors of the SARS-CoV2 3CL^{pro} protease. Some have been previously reported to inhibit SARS-CoV2 3CL^{pro}. The results also suggest that established inhibitors of SARS-CoV2 3CL^{pro} may be considered as potential inhibitors of other viral 3C-like proteases.

KEYWORDS

COVID-19, drug discovery, structural bioinformatics, virtual docking, structure based dendrograms, topology diagrams, viral protease inhibitors, 3CL^{pro} (Mpro)

Introduction

Coronaviruses (CoVs) cause human respiratory diseases. While several human coronaviruses cause relatively mild respiratory infections, three coronaviruses cause severe respiratory diseases in humans: Severe Acute Respiratory Syndrome (SARS), Middle East Respiratory Syndrome (MERS), and Corona Virus Infectious Disease 2019 (COVID-19) (de Wit et al., 2016; Wu et al., 2020; Zhou et al., 2020). The current COVID-19 pandemic has had a devastating impact on public health and global economies. The etiologic cause of COVID-19 disease is the novel SARS-CoV2 virus (Wu et al., 2020; Zhou et al., 2020). While both vaccines and approved antiviral drugs (Mei and Tan, 2021; Burki, 2022) are now available, immuno- and antiviral-resistant viral variants continue to emerge, with severe ongoing public health consequences. Considering the high mutation rate of SARS-CoV2 (McLean et al., 2022), an important focus of current research is the development of therapeutic strategies and molecules that address and suppress antiviral resistance.

Coronaviruses, including SARS-CoV2, are enveloped positive-strand RNA viruses. Their genome comprises a single, large (27–34 kilobase) single-stranded RNA, which is directly translated by host cells. The SARS-CoV2 genome encodes 4 structural proteins, 16 non-structural proteins (NSPs) which carry out crucial intracellular functions, and 9 accessory proteins (Gordon et al., 2020; Wu et al., 2020). Many of these proteins, and their host binding partners (Gordon et al., 2020), are potential targets for development of antiviral therapeutics for COVID-19. Translation of the viral RNA results in the synthesis of two polyproteins that are processed by two virally-encoded cysteine proteases, the papain-like protease (PL^{pro}), a part of Non-Structural Protein 3 (NSP3), and a 3C-like protease (3CL^{pro}), which is also referred to as Non-Structural Protein 5 (NSP5), or as the main protease (M^{pro}). Both PL^{pro} and 3CL^{pro} proteases are required for virus replication and are targets for antiviral development.

Considering the urgency for identifying effective antiviral drugs for COVID-19, and the usually lengthy process involved in approving candidate drugs for safe human use, an important approach has been to identify existing drugs and inhibitors that can be optimized as potent and safe antivirals. Viral proteases have been successfully targeted for the development of antiviral drugs against human immunodeficiency virus-1 (HIV-1), hepatitis C virus (HCV) (Wlodawer and Vondrasek, 1998; Kwo and Vinayek, 2011; McGivern et al., 2015; Ghosh et al., 2016), and most recently for SARS-CoV2 (Beck et al., 2020; Nguyen et al., 2020; Boras et al., 2021; Dampalla et al., 2021; Liu

et al., 2022; Narayanan et al., 2022). Here we outline the potential of using existing inhibitors directed to other viral proteases as lead molecules for developing new drugs targeting the SARS-CoV2 3CL^{pro} protease.

Work over the past ~15 years on the SARS-CoV 3CL protease has provided an extensive understanding of structure-activity relationships of lead molecules suitable for drug discovery efforts (Anand et al., 2003; Yang et al., 2003; Yang et al., 2006; Akaji et al., 2011; Hilgenfeld and Peiris, 2013; Pillaiyar et al., 2016; Gordon et al., 2020). Although these drug development efforts have been focused on specific proteases, in some cases broad spectrum activities have been documented. We define broad spectrum protease inhibitors as molecules that effectively inhibit proteases from viral strain variants, or even proteases from different viral species. Particularly noteworthy are several hepatitis C virus (HCV) drugs developed as inhibitors of the HCV NS3/4A protease, which also have activity as micromolar inhibitors of SARS-CoV2 virus replication in cell culture (Bafna et al., 2020; Bafna et al., 2021; Gammeltoft et al., 2021; Lo et al., 2021). Another example, with a narrower target range, nirmatrelvir, a peptidomimetic developed as an inhibitor of the SARS-CoV2 virus and a key component of the Pfizer antiviral drug combination Paxlovid™, has good activity as an inhibitor of 3CL^{pro} from a wide range of SARS-CoV2 viral strains (Ullrich et al., 2022). Rupintrivir also has activity against a broad range of 3CL^{pro}—type viral proteases from corona viruses, coxsackie viruses, rhinoviruses, and enteroviruses (Lockbaum et al., 2021). Broad spectrum antiviral activity may be important for development of drugs that can suppress the evolution of viral resistance.

While in most cases broad spectrum activity of 3CL^{pro} inhibitors has been assessed by experimental screening using protease inhibition or antiviral activity assays, some success has also been achieved by using rational approaches and virtual screening. For example, several HCV protease inhibitor drugs were initially proposed as inhibitors of SARS-CoV2 3CL^{pro} based on structural bioinformatics studies which identified structural similarity in and around the active sites of these two proteases (Bafna et al., 2020). This hypothesis was subsequently validated by virtual docking studies, and experimental biochemical protease inhibition and cell-based viral inhibition assays (Bafna et al., 2021; Gammeltoft et al., 2021).

In this study, we expand our earlier structural bioinformatics analysis to identify more than 20 proteases from a wide range of positive single-stranded RNA viruses for which the 3D structures of the binding-site cleft is similar to SARS-CoV2 3CL^{pro}. These viral proteases belong to the well-recognized PA superfamily of chymotrypsin-like proteases (Bazan and Fletterick, 1988; Gorbalenya et al., 1989; Kanitz et al., 2019), which includes

TABLE 1 Viral proteases identified from DALI search.

PDB id	Z score	RMSD	Protein name ^a (Cys/Ser protease)	Organism
4WME	33.6	0.9	3C-Like protease (Cys)	Middle East respiratory syndrome (MERS) related coronavirus
6IJJ	34.3	0.8	Main protease (Cys)	Murine hepatitis virus (MHV) strain A59
4ZUH	33.9	0.9	3C-Like protease (Cys)	Porcine epidemic diarrhea virus (PEDV)
2Q6F	33.3	1.2	Main protease (Cys)	Infectious bronchitis virus (IBV)
5LAK	14.3	3.1	3C-Like protease (Cys)	Cavally virus (CV)
1LVM	14.0	3.1	3C-Like protease (Cys)	Tobacco etch virus (TEV)
3ZZ9	12.4	2.8	3C-Like protease (Cys)	Coxsackievirus (CAV) B3
5FX6	12.4	2.7	3C-Like protease (Cys)	Rhinovirus (RHV)
3Q3Y	12.4	2.8	3C-Like protease (Cys)	Human enterovirus (HEV) 93
2H9H	12.3	3.2	3C- proteinase (Cys)	Hepatitis A virus (HAV)
1MBM	12.2	2.7	NSP4 proteinase (Ser)	Equine arteritis virus (EAV)
5BPE	12.3	2.8	3C Protease (Cys)	Human enterovirus (HEV) A71
5Y4L	11.8	2.8	3C-Like protease (NSP4) (Ser)	Porcine reproductive and respiratory syndrome virus (PRRSV)
4INH	11.6	3.0	Protease (Cys)	Norwalk virus (NWV)
5E0H	11.6	2.9	3C-Like protease (Cys)	Norovirus (NOV)
4ASH	11.3	2.8	NS6 protease (Cys)	Murine norovirus 1 (MNOV)
6LO7	10.5	3.3	3C Protease (Cys)	Senecavirus A (SNV)
2WV4	10.7	3.0	3C Protease (Cys)	Foot-and-mouth disease virus (FMDV)
3L6P	9.0	2.8	NS2B/NS3 protease (Ser)	Dengue virus (DENV)
2GGV	9.0	2.8	NS2B/NS3 protease (Ser)	West Nile virus (WNV)
5LC0	8.5	2.9	NS2B/NS3 protease (Ser)	Zika virus (ZKV)
2P59	8.1	3.0	NS3/4A protease (Ser)	Hepatitis C virus (HCV)

^aBased on their structures, we consider all of these proteases as 3C-Like proteases; the name provided is a common name reported in the literature.

proteases from species across the tree of life (Laskar et al., 2012; Monttinen et al., 2019). Phylogenetic and structural topology analysis indicates that the proteins from these various viral protease clades have evolutionarily converged on similar active site structures. For many of these proteases, medicinal chemistry efforts have previously identified inhibitor molecules. Our virtual docking experiments suggest that many of these known protease inhibitors have potential as lead molecules for developing novel drugs directed to SARS-CoV2 3CL^{pro}. In a few cases, these inhibitors developed for these other viral proteases have already been shown to inhibit of SARS-CoV2 3CL^{pro} and/or viral replication in cell-based assays at micromolar concentrations.

Computational methods

Structural bioinformatics

Proteins that are structurally similar to SARS-CoV2 3CL^{pro} were identified using the DALI (Distance matrix ALignment) (Holm and Sander, 1995; Holm, 2020a) server (<http://ekhidna2.biocenter.helsinki.fi>). The first two domains of the SARS-CoV2 3CL^{pro} were used as a structural template to search for

structurally-similar viral proteases in the PDB25 database (Holm, 2020b). PDB25 is a non-redundant subset of the PDB, consisting of representative structures from clades clustered at 25% sequence identity. In addition, the all-against-all structure comparison option available on the DALI server was used to generate structure-based dendrograms of these viral proteases. Sequence based phylogenetic trees were generated using Clustal Omega (Madeira et al., 2022) available on the European Bioinformatics (EBI) website (<https://www.ebi.ac.uk/Tools/msa/clustalo/>). Clustal Omega uses the HHalign (Soding, 2005) algorithm with the Gonnet (Gonnet et al., 1992) transition matrix. Sequence information for each protein listed in Table 1 was obtained in FASTA format from the respective PDB entry.

Virtual docking

Virtual docking was done using the open source *Autodock* suite (Morris et al., 2009). *AutoDockTools* was used for coordinate preparation, docking, and analysis of results, as described previously (Bafna et al., 2021). SARS-CoV2 3CL^{pro} atomic coordinates were obtained from X-ray crystal structure PDB id 6Y2G (Zhang et al., 2020), and structural water molecules

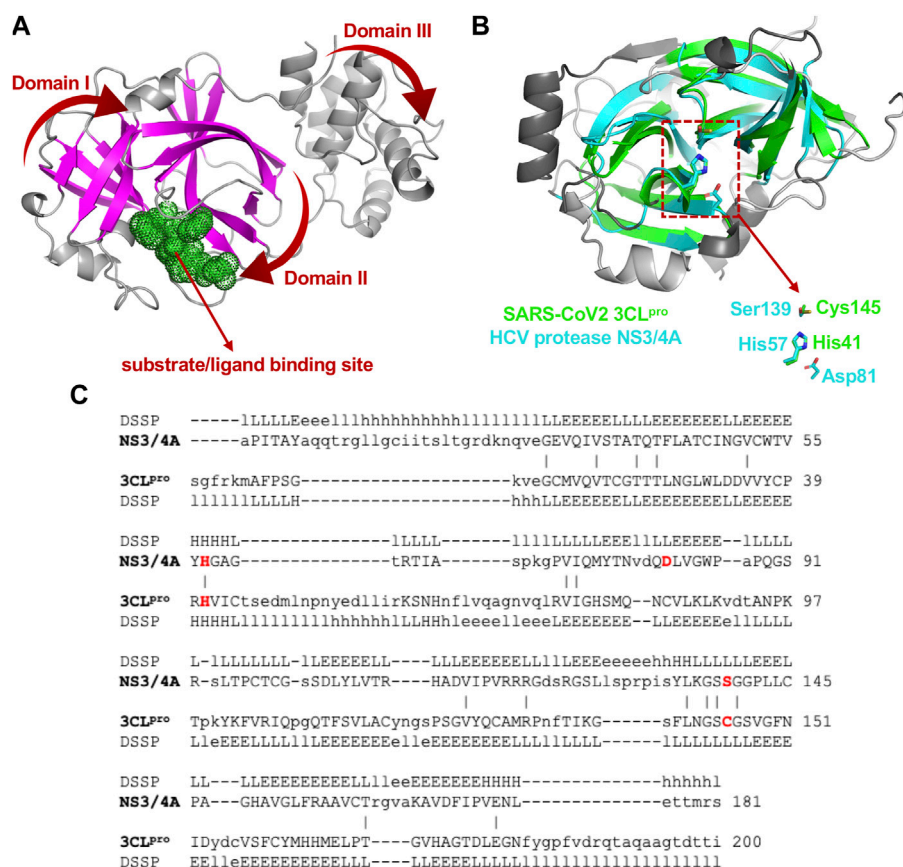


FIGURE 1

Structural superimposition and structure-based sequence alignments of SARS-CoV2 3CL^{pro} and HCV NS3/4A proteases. **(A)** Three-dimensional structures of SARS-CoV2 3CL^{pro}. The β -strands forming the characteristic β -barrels are colored in magenta. Other secondary structure elements are shown as cartoon representation colored in gray. **(B)** The backbone structure of the SARS-CoV2 3CL^{pro}, PDB 6Y2G (green) is superimposed on the backbone structure of hepatitis C virus protease HCV NS3/4A, PDB 2P59 (cyan). The regions identified by DALI server as structurally-analogous are shown in color (green and cyan), and the regions that are not structurally-analogous are shown in gray. This superimposition of backbone atoms results in superimposition of the catalytic residues Cys145 and His41 of the SARS-CoV2 3CL^{pro} with Ser139 and His57 of HCV NS3/4A protease. Residue Asp81 of the HCV protease catalytic triad is also shown. **(C)** Structure-based sequence alignment of HCV NS3/4A and SARS-CoV2 3CL^{pro}. Catalytic residues of HCV NS3/4A (His57, Asp81 and Ser139) and SARS-CoV2 3CL^{pro} (His41 and Cys145) are highlighted in bold red. Three-state secondary structure definitions (H = helix, E = sheet, L = coil) are shown for each amino acid sequence. Structurally equivalent residues are in uppercase, structurally non-equivalent residues (e.g. in loops) are in lowercase. Identical amino acids are marked by vertical bars. Adapted from Bafna et al., 2021.

were removed. Three-dimensional coordinates for ligand molecules were obtained from the PDB (<http://www.rcsb.org/>) or from chemical structure databases ChemSpider (<http://www.chemspider.com/>) and DrugBank (<https://www.drugbank.ca/>). Docking calculations were carried out using a cpu cluster at the Rensselaer Polytechnic Institute Center for Computer Innovations (CCI) (<https://cci.rpi.edu/>). Atomic coordinates for best-scoring conformation obtained in each docking simulation, for each drug-protein complex, were saved in PDB format for analysis. These protein - ligand complexes were analyzed in detail using the open source PyMol molecular visualization tool (DeLano, 2009) and fully automated Protein-Ligand Interaction Profiler (Salentin et al., 2015) (<https://projects.biotec.tu-dresden.de/plip-web/plip/>).

Results

Structural analogs of SARS-CoV2 3CL^{pro}

3CL^{pro} of SARS-CoV2 is a 67.6 kDa homodimeric cysteine protease. It has about 97% sequence identity with the corresponding 3CL^{pro} of the SARS-CoV virus responsible for the 2003 SARS pandemic. Not surprisingly, the 1.75 Å X-ray crystal structure of SARS-CoV2 3CL^{pro} protease (Jin et al., 2020; Zhang et al., 2020) demonstrates its structure is very similar to this SARS-CoV 3CL^{pro} protease (Anand et al., 2003; Yang et al., 2003). Both of these proteases contain three domains. Domains I and II adopt a double β -barrel fold, with the substrate binding site located in a shallow cleft between two antiparallel β -barrels

(Figure 1A). Both of these 3CL^{pro} proteases also have an additional C terminal helical-bundle domain, Domain III (also shown in Figure 1A), which stabilizes their homodimer forms (Shi and Song, 2006; Nashed et al., 2022).

The 3D structure of Domains I and II of SARS-CoV2 3CL^{pro}, including the double β -barrel fold and the substrate binding cleft, was used as input for searching for structurally-similar proteins in the PDB25 database using the DALI server. The DALI server compares superimposition-independent distance matrices, accounting for gaps, insertions, and rearrangements, to define a structural superimposition and a structure-based sequence alignment (Holm and Sander, 1993). Structural similarity is reported as Z-score, relative to the distribution of all-vs-all pair-wise structural similarity scores in the queried structural database. A higher Z-score means the structures have higher structural similarity in their ordered regions (Holm and Sander, 1995).

The fold architectures of Domains I and II of CoV 3CL^{pro} proteases are well known to be similar to those of chymotrypsin-like proteases and the 3C family of viral proteases (Anand et al., 2002; Monttinen et al., 2019). Using domains I and II of the SARS-CoV2 3CL^{pro} as a query, our DALI search of the PDB identified several 3C-like proteases, including the HCV NS3/4A protease, as structurally-similar (Bafna et al., 2020; Bafna et al., 2021). These SARS-CoV2 3CL^{pro} and HCV NS3/4A protease structures have a structural similarity Z score = +8.1, and overall backbone root-mean-squared deviation for structurally-similar regions of ~ 3.0 Å. Like all 3C-like proteases, the HCV NS3/4A protease has a double β -barrel fold, with relative domain orientations similar to those of the SARS-CoV and SARS-CoV2 3CL^{pro} proteases, with a substrate binding site located in a shallow cleft between its two six-to eight-stranded antiparallel β -barrels. Superimposition of the backbone structures of these two proteases results also in superimposition of their active-site catalytic residues, His41/Cys145 and His57/Ser139 of SARS-CoV2 3CL^{pro} and HCV NS3/4A proteases, respectively, with remarkable structural similarity in the substrate binding cleft (Figure 1B), despite very little sequence identity in the pair-wise structure-based sequence alignment (Figure 1C). Our observation of this structural similarity between SARS-CoV2 3CL^{pro} and HCV proteases led us to studies of known HCV NS3/4A protease inhibitors as inhibitors of SARS-CoV2 3CL^{pro} enzyme activity and virus replication (Bafna et al., 2021).

The DALI analysis identified 22 additional viral proteins (Table 1) to which SARS-CoV2 3CL^{pro} is more structurally-similar than it is to HCV NS3/4A protease. Although many other structurally-similar proteases across the PA superfamily (Monttinen et al., 2019) were also identified, in this analysis we focused on structural-similarity between the 3CL proteases of positive single-strand RNA viruses belonging to the virus Kingdom *Orthornavirae* (RNA viruses), and in the Phyla *Pisuviricota* and *Kitrinoviricota* which include eukaryotic viruses. Many of the proteins reported in Table 1 are 3C-like

proteases from important virus pathogens, including human hepatitis A, dengue, coxsackie, Norwalk, entero-, foot-and-mouth disease, West Nile, and Zika viruses. The DALI structural similarity Z scores, using domains I and II of SARS-CoV2 3CL^{pro} as a search template, on each of the proteases listed in Table 1 are all higher than (more structurally similar) the Z score to HCV NS3/4A protease; i.e. these Z scores are all $> +8$. As some inhibitors of HCV NS3/4A protease are now known to both inhibit SARS-CoV2 3CL^{pro} enzyme activity and to suppress the SARS-CoV2 virus replication in cell culture at 1–50 μ M concentrations (Bafna et al., 2021; Gammeltoft et al., 2021), these simple bioinformatics search results suggest a significant potential for repurposing the known inhibitors of these various proteases for treating COVID-19, as well as for using them as lead molecules for structure-based drug design efforts focused on developing novel inhibitors of SARS-CoV2 3CL^{pro}. These bioinformatics results also suggest the converse; using SARS-CoV2 3CL^{pro} inhibitors as lead molecules for developing drugs targeted to 3C-like proteases of these other viruses.

The viral proteases identified as structurally similar to SARS-CoV2 3CL^{pro} contain variations on the characteristic double β -barrel two-domain architecture (Figure 1A), with active sites located at the interface between the two domains. The 3D structures of some of representative viral proteases in Table 1, each having double β -barrel architectures similar to SARS-CoV2 3CL^{pro} domains I and II, are illustrated in Figure 2. The β -strands of the double β -barrel architecture, formed by 6–7 β -strands, respectively, are colored in magenta while the rest of these 3D structures (i.e., alpha helices and loops) are colored gray. The structure of one protomer of the dimeric SARS-CoV2 3CL^{pro} is also shown for comparison. These remarkable overall structural similarities across proteins from a wide taxonomic range of viral families supports the potential of developing broad spectrum inhibitors useful as lead molecules for developing new drugs targeting several viral 3CL proteases.

Viral taxonomy

The taxonomic lineages of the viruses associated with the proteins in Table 1 are summarized in Figure 3. They belong to two Phyla, *Pisuviricota* and *Kitrinoviricota*. Phylum *Pisuviricota* includes Classes (and Orders): *Pisoniviricetes* (Orders *Picornavirales* and *Nidovirales*), and *Stelpaviricetes* (Order *Patatavirales*). The *Picornavirales* viruses include the Families *Picornaviridae* [e.g., human hepatitis A virus (HAV)] and *Caliciviridae* [e.g., human Norwalk virus (NWV)]. The Order *Nidovirales* viruses includes the Families (or subfamilies) *Coronaviridae* [e.g., human SARS coronaviruses (SARS-CoV)], *Arteriviridae* [e.g., Equine Arteritis Virus (EAV)], and *Mesnidoviridae* [e.g., Cavally virus (CV)]. Tobacco etch mosaic virus (TEV), a common biotechnology reagent,

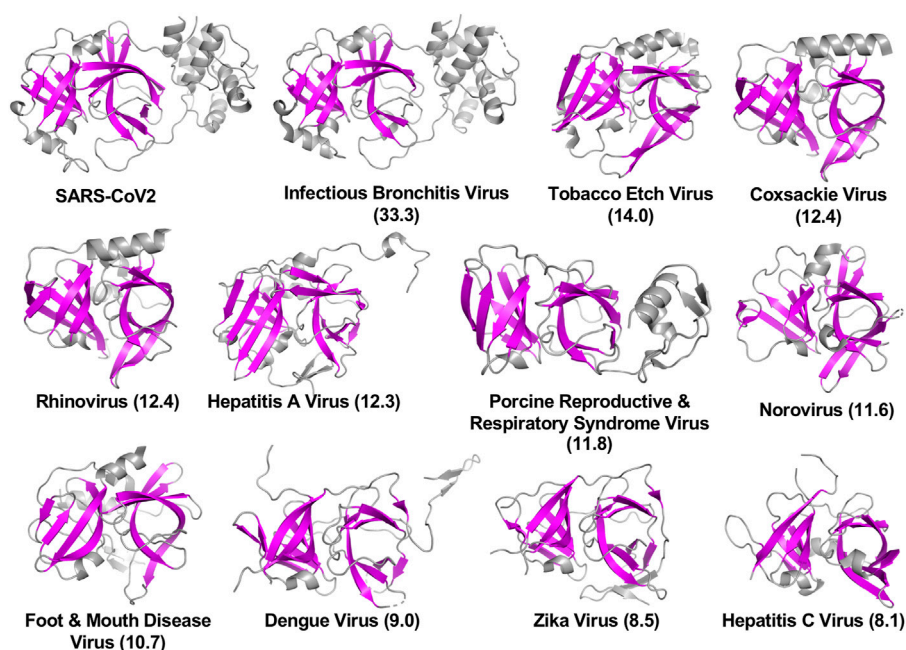


FIGURE 2

Three-dimensional structures of viral proteases that have the double β -barrel fold like the SARS-CoV2 3CL^{pro}. The β -strands forming the characteristic β -barrels are colored in magenta. Other secondary structure elements are shown as cartoon representation colored in gray. Dali Z scores to SARS-CoV2 3CL^{pro} are shown in parentheses.

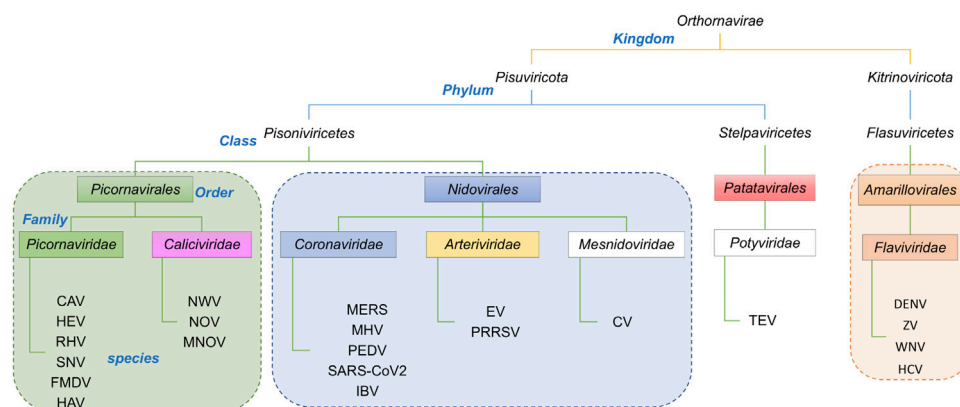


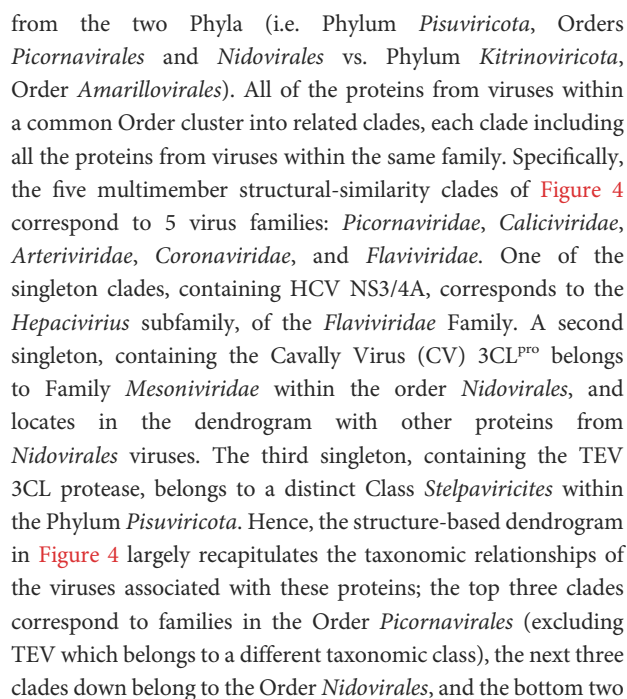
FIGURE 3

Taxonomic lineage of positive strand RNA viruses listed in Table 1. These viruses belong to two phyla in the Kingdom *Orthornavirae*. This evolutionary information is obtained from <https://www.ncbi.nlm.nih.gov/Taxonomy/Browser/wwwtax.cgi>.

belongs to the Class *Stelpaviricetes*, Order *Patatavirales*, of the Phylum *Pisuviricota*. The second phylum represented in the viral proteases returned by the DALI search (Table 1), *Kitrinoviricota*, includes the Family *Flaviviridae* of Class *Flasuiviricetes*, Order *Amarillovirales*. The viruses of this family include flaviviruses [e.g., human dengue virus (DENV)], and hepaciviruses [e.g., human hepatitis C virus (HCV)].

Structure- and sequence-based dendrograms

Despite these similarities in their double β -barrel architecture (Figure 2), there are also striking differences in the overall structures of many of these viral proteases. In order to assess these similarities and differences, the structurally-similar



clades belong to a distinct Phylum, *Kitrinoviricota*, and Order *Amarillovirales* (Family *Flaviviridae*, Genus *Flavivirus* and *Hepacivirus*). Since the three-dimensional structure of a protein is an important phenotypic feature with functional implications for evolutionary selection, it is not surprising that there is a close correlation between the structure-based dendrogram and the corresponding viral taxonomy.

Viral proteases that are structurally closest to the SARS-CoV2 3CL^{pro} (PDB id 6Y2G chain A) all come from viruses in the Order *Nidovirales* (Families *Coronaviridae*, *Mesoniviridae*, and *Arteriviridae*). These proteases all have a third domain, domain III, in addition to the two domains forming the double β -barrel fold. The third domain of the 3C-Like protease of Cavally Virus (CV) is quite similar to the third domain of SARS-CoV2 3CL^{pro}, while the third domains of the NSP4 proteinase from the Equine Arteritis Virus (EAV) (PDB id 1MBM) and the 3CL protease of Porcine Reproductive and Respiratory Syndrome Virus (PRRSV) (PDB id 5Y4L) are structurally different. The 3CL proteases from viruses of Order *Picornavirales* [e.g., human Rhinovirus (RHV), foot-and-mouth disease virus (FMDV), hepatitis A virus (HAV), and human Norovirus (NOV)] and Order *Amarillovirales* [e.g., dengue virus (DENV), West Nile virus (WNV), Zika virus (ZKV), and hepatitis C virus (HCV)] all have only domains I and II of the double beta-barrel fold, without the additional domain III.

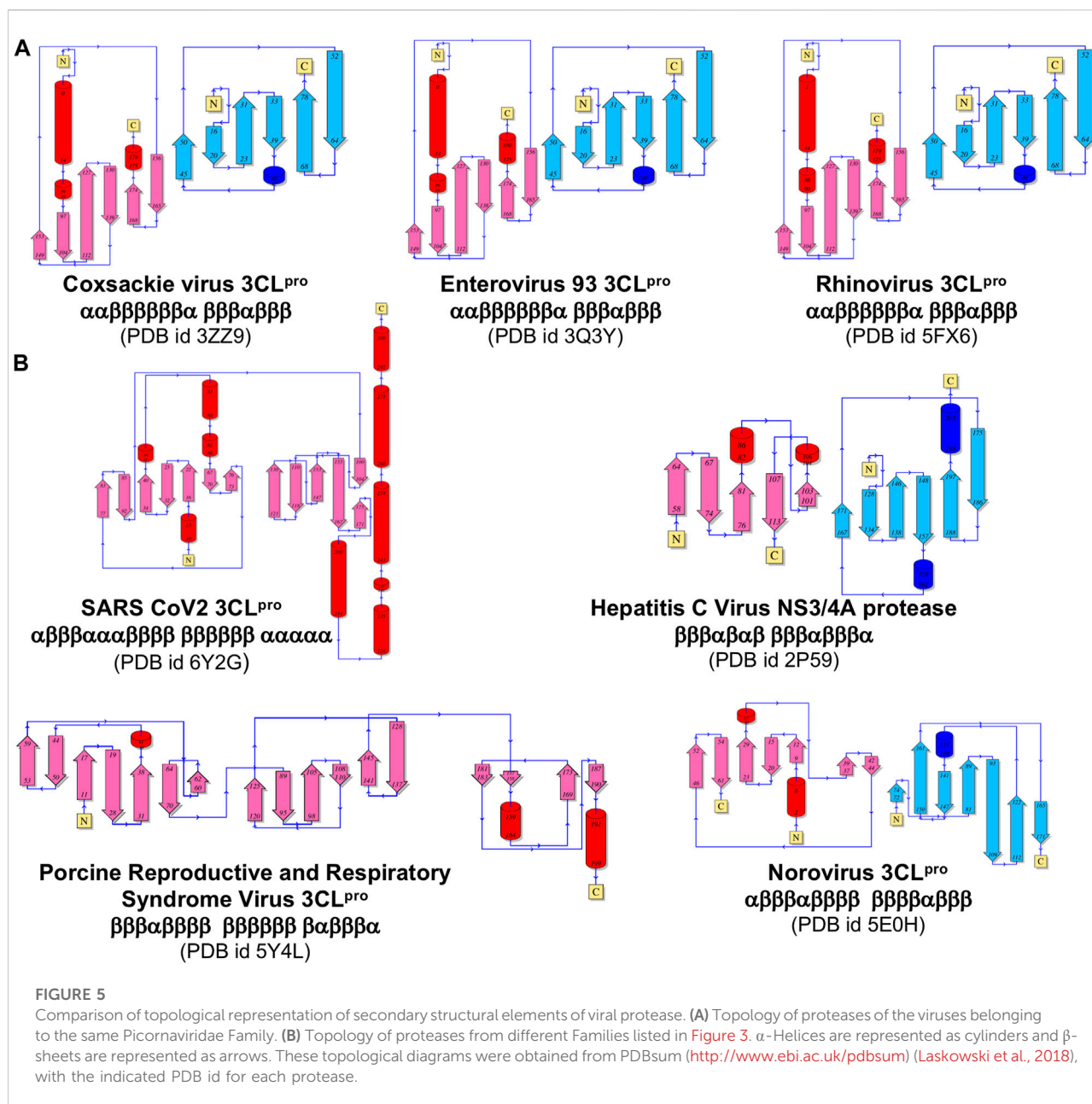
Figure 4 (right) also shows a sequence-based dendrogram of these viral proteases. Generally, the sequence-based dendrogram is similar to the structure-based dendrogram, identifying the same five multiprotein clades. However, in this case the neat relationships between clades and taxonomic classification is absent. Relative to the structure-based dendrogram, the sequence-based dendrogram mixes clades between taxonomic classes. For example, the top three clades, with some sequence similarity to one another, belong to the taxonomic Families *Caliciviridae* (pink) of Order *Picornavirales*, *Flaviridae* (orange) of Order *Amarillovirales*, and *Arteriviridae* (yellow) of Order *Nidovirales*. While the *Picornaviridae* and *Caliciviridae* families of Order *Picornavirales* are recognized as individual clades, they are remote in the sequence-based dendrogram. Similarly, the *Coronaviridae* and *Arteriviridae* families are recognized as clades of Order *Nidovirales* but are also remote in the dendrogram. HCV NS3/4A protein forms an independent clade, and its structural and taxonomic relationship to other proteins from viruses in the Family *Flaviridae* is not evident in this sequence-based dendrogram. In addition, the CV 3CL protease, a virus in the taxonomic Order *Nidovirales*, is classified as a singleton, with no indication of its taxonomic and structural relationship to proteins from other *Nidovirales* viruses.

This disconnect between taxonomy and sequence-based dendrograms is attributable in part to the very low sequence similarity of proteases between families. Considering this low sequence similarity, one explanation for the structural similarity

of substrate binding sites and superimposition of catalytic residues of these proteases from different taxonomic families is that they have converged in evolution on a common three-dimensional structure in order to achieve similar biochemical functions. For example, despite their common active site, substrate binding cleft, and sensitivity to several protease inhibitors, there is no phylogenetic evidence for common ancestors of HCV NS3/4A protease and SARS-CoV2 3CL^{pro}, or of HCV and SARS-CoV viruses. Indeed, these two viruses belong to different taxonomic Phyla (Figure 3). The HCV NS3/4A protease is a serine-protease, with catalytic triad His57, Asp81, and Ser139, while the SARS-CoV2 3CL^{pro} is a cysteine protease, with catalytic dyad residues His41, Cys145 (Figure 1), consistent with the concept of convergent evolution to achieve a similar proteolytic function.

Fold topology analysis

Similarities in overall fold, locations of substrate binding sites, and common positioning of active-site residues can result from either homologous (divergent) evolution, or by convergence of different lineages to a common structure in order to achieve similar functions. In order to test the hypothesis that the observed disconnect between the structure- and sequence-based dendrograms (Figure 4) is due to convergent evolution of these proteins, we carried out a detailed fold topology analysis (Figure 5). Fold topology refers to the order of secondary structure elements within super-secondary structure or domains, and how these secondary structures are connected along the protein polypeptide chain (Thornton et al., 1999). Evolutionary divergence generally preserves, or changes in simple ways (including circular permutations or chain swapping) the fold topology, while proteins with very different topologies but similar functions can arise from different evolutionary lineages. Supporting the convergent evolution hypothesis for these 3C-like protease families, we observe that the several proteins within each of the five multimember structure-based clades have very similar fold topologies (Figure 5A, and Supplemental Figures S2–S6), while structures in different clades (corresponding to different taxonomic families) have quite different fold topologies (Figure 5B). Proteins from clades/families of the same taxonomic order are more similar to one another. One interesting exception is the striking similarity in the fold topologies of domain II of 3C-like proteases from virus Orders *Picornavirales* (e.g., Cocksackie virus 3CL^{pro}) and *Amarillovirales* (e.g., Hepatitis C Virus NS3/4A protease) (Figure 5), which belong to different Phyla (Figure 4). Hence, for the 3C-like proteases, similarities in structural topology, like similarities in overall 3D structures, follow more closely the taxonomic classification of the corresponding viruses than sequence similarity metrics.



Docking simulations with HCV NS3/4A protease inhibitors

The results outlined above suggest that structural similarity across viral 3C-like proteases may provide a basis for broad spectrum activities of 3C-like protease inhibitors. In previous studies, we assessed the use of *AutoDock* with flexible ligand conformation and fixed protein receptor conformation for inhibitor docking studies with SARS-CoV2 3CL^{pro}. The aim of these docking studies is not to necessarily predict an accurate binding pose, but rather to provide supporting data on the feasibility for

proposed inhibitors to bind into the substrate binding and/or active site of SARS-CoV2 3CL^{pro}. Many of the molecules found to bind SARS-CoV2 3CL^{pro} with good *AutoDock* scores were subsequently observed to inhibit the enzyme activity *in vitro*, and in some cases to also inhibit viral replication in cell-based assays (Bafna et al., 2020; Ma et al., 2020; Bafna et al., 2021; Gammeltoft et al., 2021; Lo et al., 2021). For several cases where X-ray crystal structures of small molecule—3CL^{pro} complexes are available, we consistently observed *AutoDock* docking poses with an excellent match to the crystal structures among the best-scoring docked states (Bafna et al., 2021).

TABLE 2 Docking scores for HCV 3C/4A protease inhibitors with SARS-CoV2 3CL^{Pro}.

Inhibitor (Trade Name)	Identifier of protease inhibitor	Database id of protease inhibitor structure	AutoDock score (kcal/mol) Lowest “Energy”	Drug Status
SARS-CoV2 3CL^{Pro} inhibitor				
α -ketoamide inhibitor lowest “energy” pose pose most similar to X-ray structure	13b	6Y2G ^a	−10.69	Not Applicable
HCV NS3/4A Protease Inhibitor Drugs				
Paritaprevir (Veruprevir/ABT-450; Abbot)	PAR	32700634 ^b	−13.79	Prescription Drug
Narlaprevir (Arlansa; Merck/R-Pharm)	NAR	3LON ^c	−13.36 (−10.40) *	Prescription Drug
Boceprevir (Victrelis; Merck)	BOC	DB08873 ^d	−13.17 (−11.44) *	Prescription Drug
Sovaprevir (ACH-1625; Achillion)	SOV	28529313 ^b	−13.16	Investigational
Glecaprevir (Mavyret [®] /Maviret [®] ; AbbVie/Enanta)	GLE	35,013,015 ^b	−13.01	Prescription Drug
Simeprevir (Olysio; Medivir/Janssen)	SIM	3KEE ^c	−12.19	Prescription Drug
Telaprevir (Incivek/Incivo; Vertex/J&J)	TEL	3SV6 ^c	−12.02	Prescription Drug
Danoprevir (Ganovo; Array/Pfizer, Roche/Ascletis)	DAN	3M5L ^c	−11.65	Investigational
Faldaprevir (Fadaprevir, Boehringer-Ingelheim)	FAL	3P8N ^c	−11.49	Investigational
Asunaprevir (Sunvepra; Bristol-Myers Squibb)	ASU	4WF8 ^c	−11.46	Investigational
Grazoprevir (Zepatier; Merck)	GRZ	3SUD ^c	−10.77	Prescription Drug
Vaniprevir (MK-7009; Merck)	AN	3SU3 ^c	−10.36	Investigational

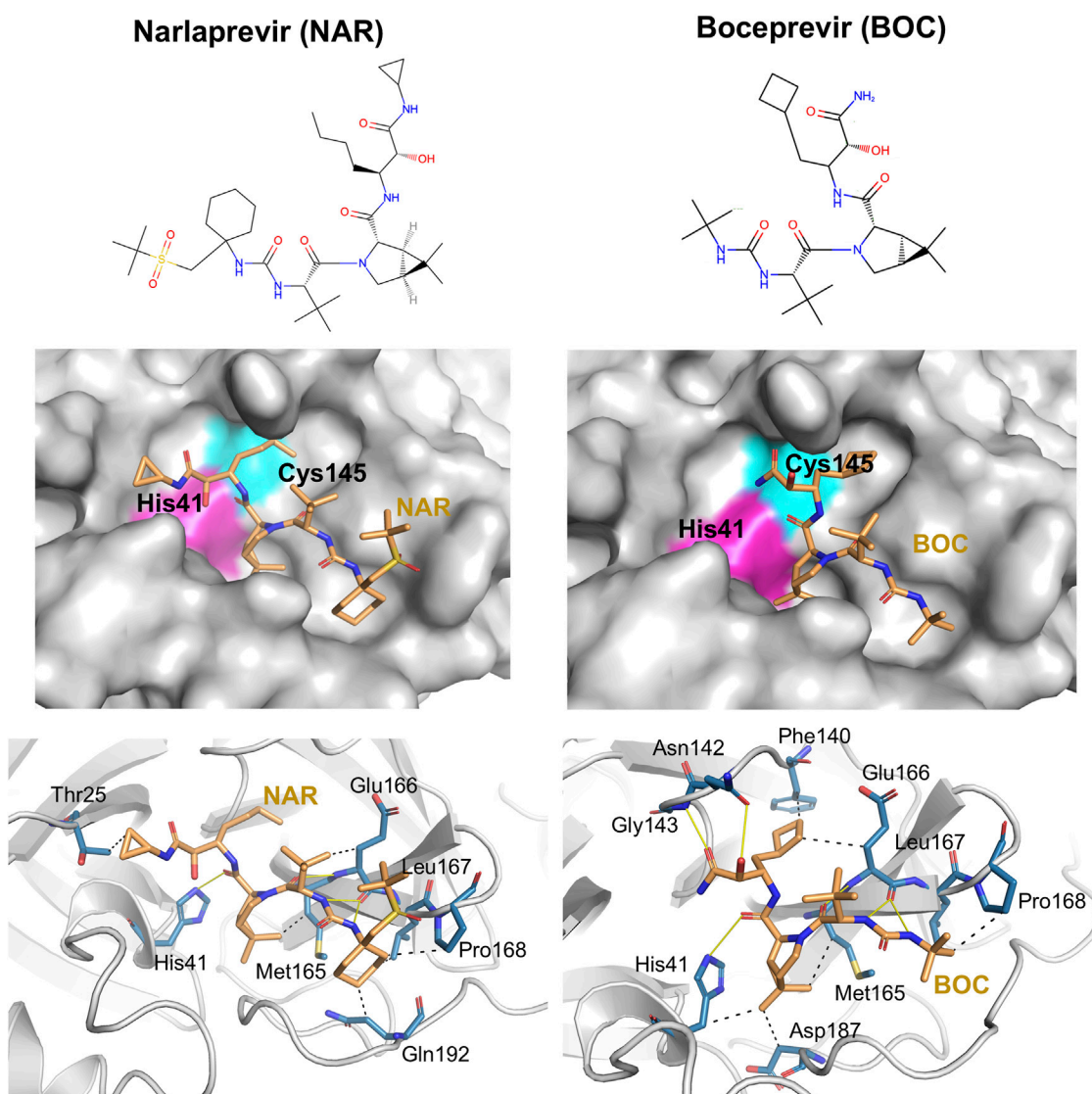
^aAtomic coordinates for the inhibitor taken from 6Y2G.^bAtomic coordinates for the inhibitor were taken from the ChemSpider database.^cAtomic coordinates for the inhibitor were taken from the PDB, coordinates of the corresponding complex of the inhibitor bound to HCV, 3C/4A protease.^dAtomic coordinates for the inhibitor were taken from the DrugBank database. * AutoDock score for pose most similar to the X-ray crystal structure.^eMavyret (or Maviret) is a multidrug formulation including glecaprevir and pibrentasvir.

Based on the bioinformatics analysis outlined above, additional docking simulation calculations were carried out for several HCV NS3/4A protease inhibitor drugs using a similar protocol, with a larger docking grid size that used in our previous work (Bafna et al., 2020; Bafna et al., 2021) to accommodate larger peptide-like inhibitor molecules. These molecules, summarized in Table 2, have all been approved for at least Phase 1 clinical trials; some are FDA approved prescription drugs useful in treating hepatitis C virus infection. Results are also provided in Table 2 for the SARS-CoV2 inhibitor 13b. The AutoDock scores of the best scoring pose (i.e., lowest AutoDock binding energy) for each of these 12 HCV NS3/4A protease inhibitors are also summarized in Table 2. All of these 12 molecules, with AutoDock scores ranging from −10.36 to −13.79 kcal/mol, have more favorable binding scores than the α -ketoamide inhibitor 13b known to inhibit SARS-CoV2 3CL^{Pro}; AutoDock score 10.69 kcal/mol for best-scoring pose which is also the pose that best matches to the crystal structure of this complex (PDB id 6Y2G) (Zhang et al., 2020).

While AutoDock scores (Table 2) are useful for assessing the feasibility of complex formation, they are not sufficiently accurate

to correctly rank the observed activities of these HCV drugs as inhibitors of SARS-CoV2 3CL^{Pro}. However, seven of these HCV proteases including narlaprevir (NAR), boceprevir (BOC), simeprevir (SIM), telaprevir (TEL), asunaprevir (ASU), grazoprevir (GRZ), and vaniprevir (VAN), do in fact inhibit SARS-CoV2 3CL^{Pro} enzyme activity with IC₅₀ of 2–50 μ M, and also inhibit viral replication in Vero or human cells in similar concentration ranges (Bafna et al., 2021; Gammeltoft et al., 2021). Hence, the AutoDock scores for HCV drugs binding and inhibiting SARS-CoV2 3CL^{Pro} have useful prognostic value in identifying lead molecules for testing and optimization. Surprisingly, three of these HCV drugs SIM, GRZ, and VAN, along with HCV protease inhibitor drug paritaprevir (PAR), also inhibit the SARS-CoV2 papain-like protease (PL^{Pro}), providing an alternative pathway for inhibition of SARS-CoV2 viral replication in cell culture (Bafna et al., 2021).

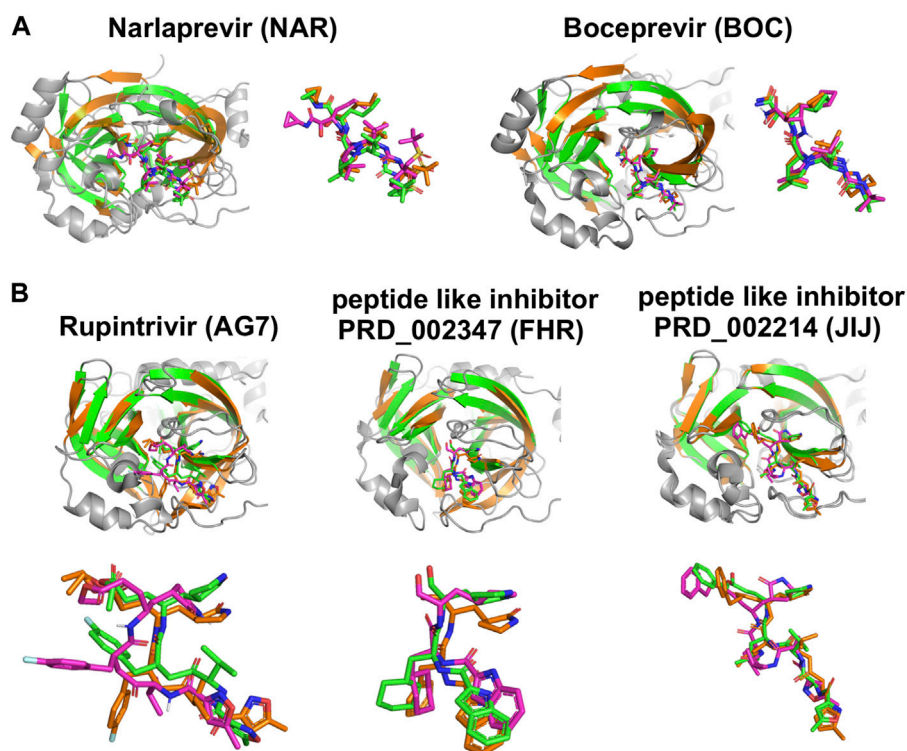
For all 12 drugs, the SARS-CoV2 3CL^{Pro} bound-state pose with best AutoDock score fits well in the active site of the enzyme and recapitulates many of the key ligand-protein interactions observed in the complex with α -ketoamide inhibitor 13b

**FIGURE 6**

Docking of HCV protease NS3/4A inhibitor drugs to SARS-CoV2 3CL^{Pro}. Top panels - Molecular structures of two HCV protease inhibitor drugs. Middle panels—Lowest energy *AutoDock* pose of these HCV protease inhibitors (orange sticks) in the SARS CoV2 3CL^{Pro} active site, Bottom panels—Details of atomistic interactions in the lowest energy *AutoDock* poses of these HCV protease inhibitors. Hydrogen bonds and hydrophobic interactions between the drug and the enzyme are shown with yellow solid lines and black dashed lines, respectively. Sidechains of catalytic residues His41 and Cys145 are labeled, along with other protein residues that form key interactions with these drugs.

(Supplementary Table S1). Some of these predicted drug—SARS-CoV2 3CL^{Pro} complexes are shown in Supplementary Figures S7, S8. In this analysis, we paid particular attention to key details of the docking conformations, including interactions with the side chains of catalytic dyad residues His41 and Cys145, and hydrogen-bonded interactions with the backbone amides of Gly143, Ser144, and Cys145, which form the oxyanion hole of this cysteine protease (13). X-ray crystal structures are also available for boceprevir (BOC), narlaprevir (NAR), and telaprevir (TEL) bound to SARS-CoV2 3CL^{Pro} (Fu et al., 2020;

Kneller et al., 2020; Oerlemans et al., 2020; Kneller et al., 2021a; Bai et al., 2021; Kneller et al., 2021b). Although the drug poses in these crystal structures are somewhat different than in the corresponding lowest-energy *AutoDock* poses, they include some of the same ligand—protein interactions (Supplementary Table S1). These modeling predictions further support the premise that inhibitors of one member of the viral PA superfamily (e.g., inhibitors of HCV protease) have the potential to function as lead molecules for development of inhibitors of other enzymes in this family (e.g., SARS-CoV2

**FIGURE 7**

Comparisons of experimentally-determined structures and predicted docking poses of drugs and inhibitors bound to SARS-CoV2 3CL^{pro} and other viral proteases. **(A)** Comparison of the HCV NS3/4A protease inhibitors NAR and BOC binding pose in *AutoDock* (magenta) with the X-ray crystal structure in complex with SARS-CoV2 3CL^{pro} (green, NAR (PDB: 6XQT) and BOC (PDB: 6XQU)) and X-ray crystal structure in complex with HCV NS3/4A protease (orange, NAR (PDB: 3LON) and BOC (PDB: 3LOX)). **(B)** Comparison of inhibitor binding poses in *AutoDock* (magenta) with X-ray crystal structures of complexes with SARS-CoV2 3CL^{pro} (green, AG7 (PDB: 7L8J), FHR (PDB: 6LZE), N3 (PDB: 7BQY)) and X-ray crystal structure in complex with other proteases (orange, HEV93-AG7 (PDB: 3RUO), HEV71-FHR (PDB: 7DCN), MHV-N3 (PDB: 6J1J)). *AutoDock* poses most similar to crystal structure pose are shown here.

3CL^{pro}), even though these enzymes do not appear to be homologs evolved by evolutionary divergence.

Details of intermolecular interactions for the *AutoDock* modes of NAR and BOC bound to SARS-CoV2 3CL^{pro} that are most similar to the corresponding X-ray crystal structures are illustrated in Figure 6. These binding poses exhibit extensive hydrogen-bonded and hydrophobic interactions within the substrate binding site and have relatively low *AutoDock* energies of -10.40 and -11.44 kcal/mol, for NAR and BOC complexes, respectively. These predicted poses are compared to the corresponding X-ray crystal structures of these same drugs bound to SARS-CoV2 3CL^{pro} and HCV NS3/4A proteases in Figure 7A. These binding modes of BOC and NAR in these two inhibitor—SARS-CoV2 3CL^{pro} complexes are also very similar to those observed in the crystal structures of the corresponding complexes with HCV NS3/4A protease (Bennett et al., 2010; Bai et al., 2021). The binding of TEL to SARS-CoV2 3CL^{pro} requires structural changes in the protease (Kneller et al., 2020), and this binding mode is not so well predicted by *AutoDock*.

Novel 3CL^{pro} inhibitor predictions

SARS-CoV2 3CL^{pro} is more structurally similar to each of the 22 viral proteases listed in Table 1 than it is to the HCV NS3/4A protease (Table 1 and Figure 2). Considering the high success in identifying SARS-CoV2 3CL^{pro} inhibitors based on its structural similarity with HCV NS3/4A protease (Bafna et al., 2021), and having established the value of these *AutoDock* protocols in predicting potential small molecule—3CL^{pro} complex structures and providing useful hypotheses for lead development, we carried out the same docking protocol on 51 known inhibitors of the 22 viral proteins listed in Table 1. These results are summarized in Table 3. Interestingly, 19 of these molecules have *AutoDock* scores equal to or better than the scores for the several HCV drugs and the 13b inhibitor previously shown to inhibit both SARS-CoV2 3CL^{pro} enzymatic activity and viral replication in cell culture at low micromolar concentrations (Zhang et al., 2020; Bafna et al., 2021; Gammeltoft et al., 2021), including VAN (*AutoDock* score -10.36 kcal/mol).

TABLE 3 Docking scores for viral protease inhibitors with SARS-CoV2 3CL^{PR}.

Inhibitor name	Database id of protease inhibitor structure	Identifier of protease inhibitor	AutoDock score (kcal/mol) Lowest “Energy”	Type of binding in crystal structure	Protease Target(s)
Nelfinavir	7DOZ (Bihani et al., 2021)	1UN	−13.16	non-covalent	Dengue virus NS2B/NS3 protease
Triazole-based macrocyclic inhibitor	5E0J (Weerawarna et al., 2016)	5LJ	−12.49	covalent ^a	Norovirus 3C-Like protease
Triazole-based macrocyclic inhibitor	6BID (Galasiti Kankanamalage et al., 2019)	DW4	−11.82	covalent	Norovirus 3C-Like protease
α,β -unsaturated ethyl ester inhibitor	3ZZA	G84	−11.57	covalent	Coxsackievirus B3 3C-Like protease
Compound 15	6KK5 (Braun et al., 2020)	DE6	−11.19	non-covalent	Zika virus NS2B/NS3 protease
Analog of Rupintrivir (γ-phenyl substitution)	5FX6 (Kawatkar et al., 2016)	6OY	−11.09	covalent	Rhinovirus 3C-Like protease
Compound 4	6KK3 (Braun et al., 2020)	DUU	−11.06	non-covalent	Zika virus NS2B/NS3 protease
AG7404	3Q3Y (Costenaro et al., 2011)	XNV	−10.98	covalent	Human Enteroviruses 3C-Like protease
Dipeptidyl inhibitor (Hexagonal form)	5T6G (Galasiti Kankanamalage et al., 2017)	N40	−10.96	covalent	Norovirus 3C-Like protease
Compound 8	6KPQ (Braun et al., 2020)	DT0	−10.91	non-covalent	Zika virus NS2B/NS3 protease
Bromocriptine	7JVR (Zhuang et al., 2021)	08Y	−10.77	non-covalent	Zika virus NS2B/NS3 protease
Rupintrivir (AG7088)	3RUO (Costenaro et al., 2011)	AG7	−10.60	covalent	Coxsackie virus A16 3C-Like protease Rhinovirus 3C-Like protease Human Enteroviruses 3C-Like protease
PRD_002347	6LZE (Dai et al., 2020)	FHR	−10.58	covalent	Human Enterovirus 71 3C-Like protease
Triazole-based macrocyclic inhibitor	6BIB (Galasiti Kankanamalage et al., 2019)	DW7	−10.55	covalent	Norovirus 3C-Like protease
α,β -unsaturated ethyl ester inhibitor	3ZZ9	G83	−10.48	covalent	Coxsackie virus B3 3C-Like protease
PRD_002214 (N3)	6IJ (Cui et al., 2019)	JIJ	−10.48	covalent	Murine hepatitis virus strain A59 Main protease Porcine epidemic diarrhea virus (PEDV) 3C-Like protease Infectious bronchitis virus (IBV) Main protease
Compound 9	6KK4 (Braun et al., 2020)	DE0	−10.48	non-covalent	Zika virus NS2B/NS3 protease
Novobiocin	6B89 (May et al., 2017)	NOV	−10.39	non-covalent	Zika virus NS2B/NS3 protease
α,β -unsaturated ethyl ester inhibitor	3ZZB	G85	−10.38	covalent	Coxsackie virus B3 3C-Like protease
Compound16	6KK6 (Braun et al., 2020)	DV0	−10.35	non-covalent	Zika virus NS2B/NS3 protease
PRD_001171 (peptide inhibitor)	2M9Q	2M9	−10.32	covalent	Dengue virus NS2B/NS3 protease
Dipeptidyl inhibitor (Hexagonal form)	5T6F (Galasiti Kankanamalage et al., 2017)	N38	−10.23	covalent	Norovirus 3C-Like protease
α,β -unsaturated ethyl ester inhibitor	3ZZ8	G82	−10.19	covalent	Coxsackie virus B3 3C-Like protease
E22	5BPE (Zhai et al., 2015)	E22	−10.06	non-covalent	Human Enteroviruses 3C-Like protease
PRD_001054 (peptide inhibitor, syc59)	4INH (Muhaxhiri et al., 2013)	4IN	−10.06	covalent	Norwalk Virus Protease
Triazole-based macrocyclic inhibitor	5E0G (Guo et al., 2016)	5LG	−9.99	covalent	Norovirus 3C-Like protease
PRD_000568 (TG-0204998/0,204,998)	2ZU3 (Lee et al., 2009)	ZU3	−9.96	covalent	Coxsackie virus B3 3C-Like protease
PRD_002189 (oxadiazole-based, cell permeable macrocyclic (20-mer) inhibitor)	5DGJ (Damalanka et al., 2016)	V64	−9.96	covalent	Norovirus 3C-Like protease
Compound 9	5DP9 (Wu et al., 2016)	5EX	−9.94	covalent	Human Enteroviruses 3C-Like protease
α,β -unsaturated ethyl ester inhibitor	3ZZ6	G75	−9.91	covalent	Coxsackie virus B3 3C-Like protease
Allosteric inhibitor	6MO2 (Yao et al., 2019)	JVM	−9.89	non-covalent	Dengue virus NS2B/NS3 protease

(Continued on following page)

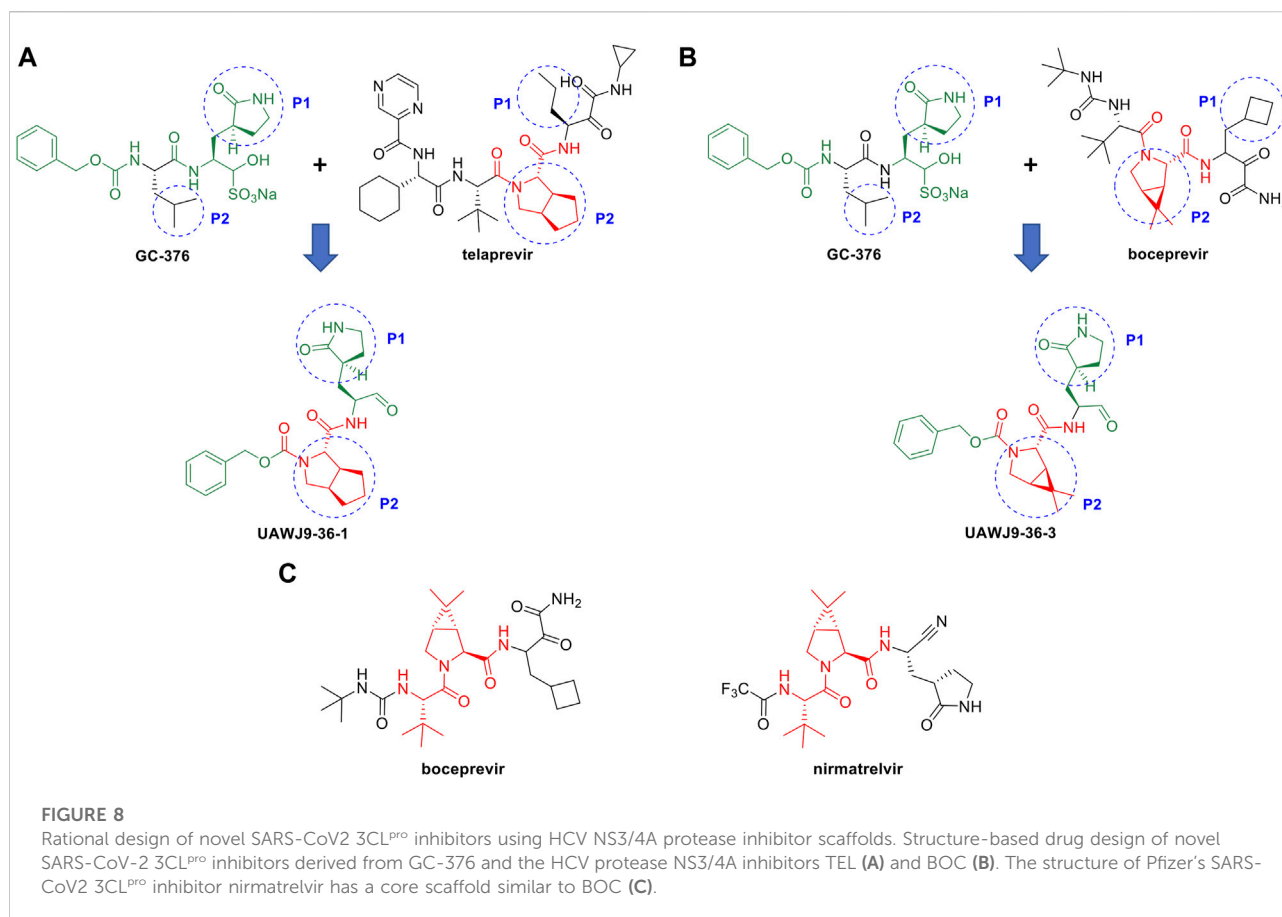
TABLE 3 (Continued) Docking scores for viral protease inhibitors with SARS-CoV2 3CL^{pro}.

Inhibitor name	Database id of protease inhibitor structure	Identifier of protease inhibitor	AutoDock score (kcal/mol) Lowest “Energy”	Type of binding in crystal structure	Protease Target(s)
Allosteric inhibitor	6MO0 (Yao et al., 2019)	JVJ	−9.79	non-covalent	Dengue virus NS2B/NS3 protease
PRD_000363 (Ace-LEALFQ-ethylpropionate inhibitor)	2B0F (Bjornndahl et al., 2007)	2B0	−9.74	covalent	Rhinovirus 3C-Like protease
Triazole-based macrocyclic inhibitor	6BIC (Galasiti Kankanamalage et al., 2019)	5LH	−9.67	covalent	Norovirus 3C-Like protease
Allosteric inhibitor	6MO1 (Yao et al., 2019)	I16	−9.63	non-covalent	Dengue virus NS2B/NS3 protease
PRD_001062 (peptide inhibitor, syc8)	4IMQ (Muhaxhiri et al., 2013)	4IM	−9.46	covalent	Norwalk Virus Protease
Compound 10	6Y3B (Braun et al., 2020)	O7N	−9.41	non-covalent	Zika virus NS2B/NS3 protease
Compound 2	6KK2 (Braun et al., 2020)	D9U	−9.31	non-covalent	Zika virus NS2B/NS3 protease
NK-1.8K	5GSO (Wang et al., 2017b)	5GI	−9.18	covalent	Coxsackie virus B3 3C-Like protease
Temoporfin	DB11630	TEM	−9.08	non-covalent	Zika virus NS2B/NS3 protease
macrocyclic inhibitor	6FFS (Namoto et al., 2018)	D8E	−9.06	covalent	Rhinovirus 3C-Like protease
α,β -unsaturated ethyl ester inhibitor	3ZZ7	G81	−8.81	covalent	Coxsackie virus B3 3C-Like protease
X77	6W81	X77	−8.79	non-covalent	Porcine epidemic diarrhea virus (PEDV) 3C-Like protease
dipeptidyl inhibitor (covalent)	4XBD (Galasiti Kankanamalage et al., 2015)	M40	−8.65	covalent	Norwalk Virus Protease
Carnosine	Pubchem 439,224	CAR	−8.11	non-covalent	Dengue virus NS2B/NS3 protease
MB21	88,296,444 Chempidder	MB2	−8.03	non-covalent	Dengue virus NS2B/NS3 protease
N-(iodoacetyl)-L-valyl-L-phenylalaninamide	1QA7 (Bergmann et al., 1999)	IVF	−7.66	covalent	Hepatitis A virus 3C proteinase
α,β-unsaturated ethyl ester inhibitor	3ZZ5	G74	−7.57	covalent	Coxsackie virus B3 3C-Like protease
2-phenylquinolin-4-ol (Non-covalent)	2XYA (Baxter et al., 2011)	7L4	−6.23	non-covalent	Rhinovirus 3C-Like protease
n-[(benzyloxy)carbonyl]-L-alanine (peptide-based ketone inhibitor)	2HAL (Yin et al., 2006)	BBL	−5.51	non-covalent	Hepatitis A virus 3C proteinase
NSC157058	Pubchem 423,738	NSC	−5.11	non-covalent	Zika virus NS2B/NS3 protease

^aMolecules with the potential to form covalent complexes may bind significantly more favorably than indicated by relative *AutoDock* scores.

Chemical structures of the 20 top scoring inhibitors are shown in [Supplementary Figure S9](#). Included in [Table 3](#) are several molecules previously reported to inhibit SARS-CoV2 3CL^{pro} enzyme activity; viz compound PRD_002347 (FHR; *AutoDock* Score −10.58 kcal/mol), first reported as an inhibitor of human enterovirus 71 (HEV) 3C-like protease (Dai et al., 2022), compound PRD_002214 (N3 or J1J; *AutoDock* Score −10.48 kcal/mol), reported as an inhibitor of murine hepatitis virus strain A59 (MHV) main protease (Cui et al., 2019), porcine epidemic diarrhea virus (PEDV) 3C-like protease (Wang F. et al., 2017), and avian infectious bronchitis virus (IBV) main protease (Wang F. et al., 2017), and compound X77 (*AutoDock* Score −8.79 kcal/mol) reported as an inhibitor of porcine epidemic diarrhea virus (PEDV) 3C-like protease

(Mesecar, 2021). Rupintrivir (compound AG7088 or AG7, *AutoDock* Score −10.60 kcal/mol), an inhibitor of Coxsackie virus (CAV) A16 3C-like protease (Lu et al., 2011), human rhinovirus (RHV) 3C-like protease (Matthews et al., 1999), and human enteroviruses (HEV) 3C-like protease (Costenaro et al., 2011; Hung et al., 2011) is also reported to weakly inhibit SARS-CoV2 3CL^{pro} (Liu et al., 2021), although another study found that rupintrivir is not active against SARS-CoV2 3CL^{pro} (Ma et al., 2022). Nelfinavir, the best scoring molecule in [Table 3](#), an inhibitor of the human dengue virus (DENV) NS2B/NS3 protease (Bhakat et al., 2015) is also a weak inhibitor of SARS-CoV2 3CL^{pro} (Ohashi et al., 2021). Comparisons of crystal structures determined for three of these inhibitors bound to SARS-CoV2 3CL^{pro} and one other viral 3C-like protease, together



with low-energy *AutoDock* docking poses, are shown in **Figure 7B**. Taken together, the results support the view that inhibitors of viral proteases that are structurally-similar to SARS-CoV2 3CL^{pro} are valuable candidates for exploration as potential lead molecules for SARS-CoV2 3CL^{pro} inhibitor drug discovery programs.

Discussion

The global health, economic, and social impact of the COVID-19 pandemic is enormous. Moreover, future pandemics, by coronaviruses or other pathogenic viruses, are inevitable. For example, disruptions to ecological niches due to global warming create the opportunity for emergent viruses to access new host ranges, increasing the prevalence of viral outbreaks. Although public health policies can slow the spread of a virus, effective control of viral diseases requires both vaccines and antivirals. In particular, antivirals are crucial for the present COVID-19 pandemic. Despite the initial success of the antiviral drug Paxlovid™, a combination of the 3CL^{pro} inhibitor nirmatrelvir and the P450 enzyme inhibitor ritonavir which improves the pharmacokinetics of nirmatrelvir, antiviral

resistance is anticipated. Hence, the identification and development of additional orally-bioavailable inhibitors of SARS-CoV2 3CL^{pro} is critical. More generally, it is important to proactively develop an arsenal of antiviral drugs which can be used either individually or in combinations to suppress virus infection and avoid viral resistance.

In this context, repurposing of existing antiviral drugs previously developed for other viral 3C-like proteases, like those listed in **Table 3**, is vitally important and can quickly add to the armamentarium of SARS-CoV2 3CL^{pro} inhibitors. These newly identified compounds can also serve as viable leads with which to execute hit-to-lead and lead optimization drug discovery efforts towards novel SARS-CoV2 3CL^{pro} inhibitor chemotypes. For example, Wang and coworkers reported the discovery of novel and potent SARS-CoV2 3CL^{pro} inhibitors derived from the reported SARS-CoV2 3CL^{pro} inhibitor GC-376 and the HCV NS3/4A protease inhibitors TEL and BOC (**Figures 8A,B**) (Xia et al., 2021). Guided by X-ray co-crystal structures, the team generated novel hybrid chemotypes that exploited the overlay of key structural motifs. Notably, the superimposed X-ray co-crystal structures showed that the GC-376 leucine, TEL octahydrocyclopenta[c]pyrrole, and BOC 6,6-dimethyl-3-azabicyclo[3.1.0]hexane structures all occupy the

hydrophobic S2 pocket, and it was anticipated that swapping the GC-376 leucine residue with the more lipophilic bicyclic core structures of TEL and BOC could potentially improve potency by engaging in additional hydrophobic interactions. These structural changes, along with incorporation of the GC-376 benzyl carbamate and other rational design modifications based on the overlaid structures, lead to the identification of two novel and promising SARS-CoV2 3CL^{pro} inhibitors (UAWJ9-36-1 and UAWJ9-36-3) that exhibit properties suitable for further development. Kneller et al., have also recently reported covalent hybrid inhibitors of 3CL^{pro} created by splicing components of hepatitis C protease inhibitors BOC and NAR, and known SARS-CoV1 protease inhibitors, which inhibit virus replication in cell culture (Kneller et al., 2022). Pfizer's FDA-approved SARS-CoV2 3CL^{pro} inhibitor nirmatrelvir also contains the 6,6-dimethyl-3-azabicyclo[3.1.0]hexane and 2-amino-3,3-dimethylbutanamide structural elements of BOC (Figure 8C) (Zhao et al., 2021). These reports clearly demonstrate the significant value that identifying leads from existing protease inhibitors of other viruses can have for future SARS-CoV2 3CL^{pro} inhibitor drug discovery efforts.

The 3C-like proteases of *Orthornavirae* viruses, the kingdom of viruses with RNA genomes encoding an RNA-dependent RNA polymerase (RdRp), are essential to the virus life cycle, and are important targets for antiviral drug development. Koonin et al. first predicted that coronaviruses contain a protein (later identified as the main protease, 3CL^{pro}) similar to the 3C proteases of picornaviruses (37), and Anand et al. (17) subsequently described the striking structural similarity between the active sites of transmissible gastroenteritis coronavirus (TGEV) 3CL^{pro} and the 3CL protease of picornavirus hepatitis A virus (HAV). Our initial structural bioinformatics analysis (Bafna et al., 2020; Bafna et al., 2021) demonstrated strong structural similarity between the active sites SARS-CoV2 3CL^{pro} and HCV NS3/4A, which was surprising as these two enzymes are in very distantly related viruses (coronaviruses and flaviviruses, respectively) from different Phyla (see Figure 3). Most importantly, we and others have observed that inhibitors of HCV NS3/4A are also inhibitors of SARS-CoV2 3CL^{pro}, and of SARS-CoV2 replication in cell culture (Bafna et al., 2020; Bafna et al., 2021; Gammeltoft et al., 2021; Lo et al., 2021).

Fold topology, overall fold, locations of substrate binding sites, and common positioning of active-site residues can result from homologous (divergent) evolutionary relationships between proteins. For example, 3C-like Cys proteases of picornaviruses have been proposed to be homologous to Ser proteases of the trypsin protease superfamily (Bazan and Fletterick, 1988). Both Koonin and co-workers (Gorbalenya et al., 1989) and James and co-workers (Allaire et al., 1994) have also proposed a divergent evolutionary relationship between the 3CL cysteine proteases of picornaviruses and chymotrypsin-

like serine proteases. Coronaviruses and picornaviruses are in the same Class, but in different Orders. However, convergent evolution can also occur, and apparent structural convergence of protease active sites is a classic structural bioinformatics observation (Robertus et al., 1972; Kester and Matthews, 1977). The wide range of structural topologies observed across the positive-strand RNA proteases of the PA superfamily (Figure 5; Supplementary Figures S2–S4) support the idea that their analogous three-dimensional structures arose by evolutionary convergence on a common biochemistry rather than divergence from a common ancestor. In particular, the structural similarity in and around the active sites of the evolutionarily-distant HCV NS3/4A and SARS-CoV2 3CL^{pro} proteases is striking, and appears to be the result of convergent evolution from different fold topologies to create a similar binding pocket. Interesting in this regard, recent marine metagenomic sequencing and phylogenetic studies suggest that ancient ancestors of the positive-strand RNA viruses, including highly mobile RNA retroelements that can readily move to new locations in the genome, predate even the Last Universal Cellular Ancestor (LUCA) (Zayed et al., 2022). Such a pre-cellular RNA ecology could potentially provide a source of structurally-variable ancient progenitors of the various clades of modern 3C-like proteases of positive-strand RNA viruses.

Molecular docking is a widely used tool for modern structure-based drug discovery. It is used not only to explore the binding conformations of lead molecules in the active site of drug targets, but also to estimate the strength of interaction between the ligand and target. The *AutoDock* program used in our study offers a variety of search algorithms to recursively evaluate ligand conformations and uses a force-field-based scoring function to rank the binding poses. The accuracy of the program has been tested with a diverse set of protein–ligand complexes of biological and medicinal interest (Forli et al., 2016). The predicted *AutoDock* binding energies may not be highly accurate, and even relative affinities within a series of ligands cannot generally be reliably determined. While the best-scored *AutoDock* complex does not always match the experimentally determined structure, the experimentally determined structure is generally among the best scoring poses (Kolb et al., 2009; Kolb and Irwin, 2009). Accordingly, the best-ranked predictions, illustrated for example in Supplementary Figures S7 and S8, should capture key features of the ligand–protein interaction, but they might not be the dominant pose observed in future experimental studies.

Some known inhibitors of 3CL^{pro} form covalent bonds upon complex formation, which are not accounted for in these *AutoDock* models. For several cases where the three-dimensional structures of these covalent complexes are known, including complexes with compound 13b (Zhang et al., 2020), boceprevir (Kneller et al., 2020), and narlaprevir (Kneller et al., 2020), covalent bond formation is in fact stabilizing one of the low energy *AutoDock* poses. As shown

in Figures 6, 7, *AutoDock* calculations predict the crystal structure poses of these inhibitors where the respective alpha-ketoamide warhead is positioned to form a co-valent bond with the active site Cys thiol. Failure to account for covalent bond formation would not contradict the conclusion, based on good non-covalent docking scores, that a molecule is a potential inhibitor. However, appropriate consideration of covalent stabilization could rule in candidates with poorer non-covalent *AutoDock* scores. In order to address this, we identify also in Table 3 the proposed 3CL^{pro} inhibitors which potentially form covalent complexes with the active-site Cys residue. If such covalent bond formation occurs, these inhibitors could have enhanced binding affinity than indicated by simple *AutoDock* scores.

Another important limitation of the *AutoDock* protocol used here is the inability to model the conformational flexibility of the protein target. This problem is typically approached through the generation of multiple conformations of the protein by molecular dynamics before docking, or by allowing the ligand active site residues to be flexible during the docking runs, which are both important future direction for this work.

In conclusion, our studies describe interesting structural similarity between the 3C-like proteases of Kingdom *Orthornavirae* that comprises positive-stranded RNA viruses from multiple Classes and Phyla. The fact that the same molecules can inhibit SARS-CoV2 3CL^{pro} and HCV NS3/4A proteases, spanning the structural similarity scores and taxonomic distribution of proteases from a wide range of viruses in the Kingdom *Orthornavirae*, strongly supports the potential for considering inhibitors of this wide range of 3C-like proteases as lead molecules for developing novel broad spectrum viral protease inhibitor drugs.

Data availability statement

The authors acknowledge that the data presented in this study must be deposited and made publicly available in an acceptable repository, prior to publication. Frontiers cannot accept a manuscript that does not adhere to our open data policies.

Author contributions

GM, RK and KB designed the research, KB carried out structural bioinformatics and computational docking studies,

GM, CC, RK, and KB interpreted the data, all authors contributed in writing the manuscript.

Funding

This research was supported by National Institutes of Health grants R01-GM120574 and 1R35-GM141818 awarded to GM, and grant 1U19 AI171443-01 to S. Chanda and A. García-Sastre, with subcontract to GM.

Acknowledgments

We thank T. Acton, S. Ciurli, A. DeFalco, N. Dube, A. Gibbs, Y. P. Huang, L. Ma, L. Mazzei, C. Sander, G. V. T Swapna, R. Greene-Cramer, A. Jovanovic, and J. Liu for helpful discussions, suggestions, and comments on the manuscript. Docking calculations were carried out using cpu clusters of the Rensselaer Polytechnic Institute Center for Computer Innovations (CCI) (<https://cci.rpi.edu/>).

Conflict of interest

GM is a founder of Nexomics Biosciences, Inc.

The remaining authors declare that the research was conducted in the absence of any commercial or financial relationships that could be construed as a potential conflict of interest.

Publisher's note

All claims expressed in this article are solely those of the authors and do not necessarily represent those of their affiliated organizations, or those of the publisher, the editors and the reviewers. Any product that may be evaluated in this article, or claim that may be made by its manufacturer, is not guaranteed or endorsed by the publisher.

Supplementary material

The Supplementary Material for this article can be found online at: <https://www.frontiersin.org/articles/10.3389/fchem.2022.948553/full#supplementary-material>

References

- Akaji, K., Konno, H., Mitsui, H., Teruya, K., Shimamoto, Y., Hattori, Y., et al. (2011). Structure-based design, synthesis, and evaluation of peptide-mimetic SARS 3CL protease inhibitors. *J. Med. Chem.* 54 (23), 7962–7973. doi:10.1021/jm200870n
- Allaire, M., Chernaia, M. M., Malcolm, B. A., and James, M. N. (1994). Picornaviral 3C cysteine proteinases have a fold similar to chymotrypsin-like serine proteinases. *Nature* 369 (6475), 72–76. doi:10.1038/369072a0
- Anand, K., Palm, G. J., Mesters, J. R., Siddell, S. G., Ziebuhr, J., and Hilgenfeld, R. (2002). Structure of coronavirus main proteinase reveals combination of a chymotrypsin fold with an extra alpha-helical domain. *EMBO J.* 21 (13), 3213–3224. doi:10.1093/emboj/cdf327
- Anand, K., Ziebuhr, J., Wadhwani, P., Mesters, J. R., and Hilgenfeld, R. (2003). Coronavirus main proteinase (3CLpro) structure: Basis for design of anti-SARS drugs. *Science* 300 (5626), 1763–1767. doi:10.1126/science.1085658
- Bafna, K., Krug, R. M., and Montelione, G. T. (2020). Structural similarity of SARS-CoV2 M(pro) and HCV NS3/4A proteases suggests new approaches for identifying existing drugs useful as COVID-19 therapeutics (Preprint). *ChemRxiv*. doi:10.26434/chemrxiv.12153615.v1
- Bafna, K., White, K., Harish, B., Rosales, R., Ramelot, T. A., Acton, T. B., et al. (2021). Hepatitis C virus protease that inhibit SARS-CoV-2 papain-like protease synergize with remdesivir to suppress viral replication in cell culture. *Cell Rep.* 35 (7), 109133. doi:10.1016/j.celrep.2021.109133
- Bai, Y., Ye, F., Feng, Y., Liao, H., Song, H., Qi, J., et al. (2021). Structural basis for the inhibition of the SARS-CoV-2 main protease by the anti-HCV drug nardaprevir. *Signal Transduct. Target. Ther.* 6 (1), 51. doi:10.1038/s41392-021-00468-9
- Baxter, A., Chambers, M., Edfeldt, F., Edman, K., Freeman, A., Johansson, C., et al. (2011). Non-covalent inhibitors of rhinovirus 3C protease. *Bioorg. Med. Chem. Lett.* 21 (2), 777–780. doi:10.1016/j.bmcl.2010.11.110
- Bazan, J. F., and Fletterick, R. J. (1988). Viral cysteine proteases are homologous to the trypsin-like family of serine proteases: Structural and functional implications. *Proc. Natl. Acad. Sci. U. S. A.* 85 (21), 7872–7876. doi:10.1073/pnas.85.21.7872
- Beck, B. R., Shin, B., Choi, Y., Park, S., and Kang, K. (2020). Predicting commercially available antiviral drugs that may act on the novel coronavirus (SARS-CoV-2) through a drug-target interaction deep learning model. *Comput. Struct. Biotechnol. J.* 18, 784–790. doi:10.1016/j.csbj.2020.03.025
- Bennett, F., Huang, Y., Hendrata, S., Lovey, R., Bogen, S. L., Pan, W., et al. (2010). The introduction of P4 substituted 1-methylcyclohexyl groups into boceprevir: A change in direction in the search for a second generation HCV NS3 protease inhibitor. *Bioorg. Med. Chem. Lett.* 20 (8), 2617–2621. doi:10.1016/j.bmcl.2010.02.063
- Bergmann, E. M., Cherney, M. M., McKendrick, J., Frommann, S., Luo, C., Malcolm, B. A., et al. (1999). Crystal structure of an inhibitor complex of the 3C proteinase from hepatitis A virus (HAV) and implications for the polyprotein processing in HAV. *Virology* 265 (1), 153–163. doi:10.1006/viro.1999.9968
- Bhakat, S., Delang, L., Kaptein, S., Neyts, J., Leyssen, P., and Jayaprakash, V. (2015). Reaching beyond HIV/HCV: Nelfinavir as a potential starting point for broad-spectrum protease inhibitors against dengue and chikungunya virus. *RSC Adv.* 5 (104), 85938–85949. doi:10.1039/c5ra14469h
- Bihani, S. C., Gupta, G. D., and Hosur, M. V. (2021). Molecular basis for reduced cleavage activity and drug resistance in D30N HIV-1 protease. *J. Biomol. Struct. Dyn.*, 1–9. doi:10.1080/07391102.2021.1982007
- Bjorn Dahl, T. C., Andrew, L. C., Semenchenko, V., and Wishart, D. S. (2007). NMR solution structures of the apo and peptide-inhibited human rhinovirus 3C protease (serotype 14): Structural and dynamic comparison. *Biochemistry* 46 (45), 12945–12958. doi:10.1021/bi7010866
- Boras, B., Jones, R. M., Anson, B. J., Arenson, D., Aschenbrenner, L., Bakowski, M. A., et al. (2021). Preclinical characterization of an intravenous coronavirus 3CL protease inhibitor for the potential treatment of COVID19. *Nat. Commun.* 12 (1), 6055. doi:10.1038/s41467-021-26239-2
- Braun, N. J., Quek, J. P., Huber, S., Kouretova, J., Rogge, D., Lang-Henkel, H., et al. (2020). Structure-based macrocyclization of substrate analogue NS2B-NS3 protease inhibitors of Zika, West Nile and dengue viruses. *ChemMedChem* 15 (15), 1439–1452. doi:10.1002/cmdc.202000237
- Burki, T. K. (2022). The role of antiviral treatment in the COVID-19 pandemic. *Lancet Respir. Med.* 10 (2), e18. doi:10.1016/S2213-2600(22)00011-X
- Costenaro, L., Kaczmarek, Z., Arnan, C., Janowski, R., Coutard, B., Sola, M., et al. (2011). Structural basis for antiviral inhibition of the main protease, 3C, from human enterovirus 93. *J. Virol.* 85 (20), 10764–10773. doi:10.1128/JVI.05062-11
- Cui, W., Cui, S., Chen, C., Chen, X., Wang, Z., Yang, H., et al. (2019). The crystal structure of main protease from mouse hepatitis virus A59 in complex with an inhibitor. *Biochem. Biophys. Res. Commun.* 511 (4), 794–799. doi:10.1016/j.bbrc.2019.02.105
- Dai, W., Jochmans, D., Xie, H., Yang, H., Li, J., Su, H., et al. (2022). Design, synthesis, and biological evaluation of peptidomimetic aldehydes as broad-spectrum inhibitors against enterovirus and SARS-CoV-2. *J. Med. Chem.* 65 (4), 2794–2808. doi:10.1021/acs.jmedchem.0c02258
- Dai, W., Zhang, B., Jiang, X. M., Su, H., Li, J., Zhao, Y., et al. (2020). Structure-based design of antiviral drug candidates targeting the SARS-CoV-2 main protease. *Science* 368 (6497), 1331–1335. doi:10.1126/science.abb4489
- Damalanka, V. C., Kim, Y., Alliston, K. R., Weerawarna, P. M., Galasiti Kankanamalage, A. C., Lushington, G. H., et al. (2016). Oxadiazole-based cell permeable macrocyclic transition state inhibitors of norovirus 3CL protease. *J. Med. Chem.* 59 (5), 1899–1913. doi:10.1021/acs.jmedchem.5b01464
- Dampalla, C. S., Zheng, J., Perera, K. D., Wong, L. R., Meyerholz, D. K., Nguyen, H. N., et al. (2021). Postinfection treatment with a protease inhibitor increases survival of mice with a fatal SARS-CoV-2 infection. *Proc. Natl. Acad. Sci. U. S. A.* 118 (29), e2101555118. doi:10.1073/pnas.2101555118
- de Wit, E., van Doremalen, N., Falzarano, D., and Munster, V. J. (2016). SARS and MERS: Recent insights into emerging coronaviruses. *Nat. Rev. Microbiol.* 14 (8), 523–534. doi:10.1038/nrmicro.2016.81
- DeLano, W. L. (2009). *The PyMOL molecular graphics system*. Palo Alto: Schrödinger, LLC. Version 1.2r3pre.
- Forli, S., Huey, R., Pique, M. E., Sanner, M. F., Goodsell, D. S., and Olson, A. J. (2016). Computational protein-ligand docking and virtual drug screening with the AutoDock suite. *Nat. Protoc.* 11 (5), 905–919. doi:10.1038/nprot.2016.051
- Fu, L., Ye, F., Feng, Y., Yu, F., Wang, Q., Wu, Y., et al. (2020). Both Boceprevir and GC376 efficaciously inhibit SARS-CoV-2 by targeting its main protease. *Nat. Commun.* 11 (1), 4417. doi:10.1038/s41467-020-18233-x
- Galasiti Kankanamalage, A. C., Kim, Y., Rathnayake, A. D., Damalanka, V. C., Weerawarna, P. M., Doyle, S. T., et al. (2017). Structure-based exploration and exploitation of the S4 subsite of norovirus 3CL protease in the design of potent and permeable inhibitors. *Eur. J. Med. Chem.* 126, 502–516. doi:10.1016/j.ejmech.2016.11.027
- Galasiti Kankanamalage, A. C., Kim, Y., Weerawarna, P. M., Uy, R. A., Damalanka, V. C., Mandadapu, S. R., et al. (2015). Structure-guided design and optimization of dipeptidyl inhibitors of norovirus 3CL protease. Structure-activity relationships and biochemical, X-ray crystallographic, cell-based, and *in vivo* studies. *J. Med. Chem.* 58 (7), 3144–3155. doi:10.1021/jm5019934
- Galasiti Kankanamalage, A. C., Weerawarna, P. M., Rathnayake, A. D., Kim, Y., Mehzabeen, N., Battaile, K. P., et al. (2019). Putative structural rearrangements associated with the interaction of macrocyclic inhibitors with norovirus 3CL protease. *Proteins* 87 (7), 579–587. doi:10.1002/prot.25682
- Gammeltoft, K. A., Zhou, Y., Duarte Hernandez, C. R., Galli, A., Offersgaard, A., Costa, R., et al. (2021). Hepatitis C virus protease inhibitors show differential efficacy and interactions with remdesivir for treatment of SARS-CoV-2 *in vitro*. *Antimicrob. Agents Chemother.* 65 (9), e0268020. doi:10.1128/AAC.02680-20
- Ghosh, A. K., Osswald, H. L., and Prato, G. (2016). Recent progress in the development of HIV-1 protease inhibitors for the treatment of HIV/AIDS. *J. Med. Chem.* 59 (11), 5172–5208. doi:10.1021/acs.jmedchem.5b01697
- Gonnet, G. H., Cohen, M. A., and Benner, S. A. (1992). Exhaustive matching of the entire protein sequence database. *Science* 256 (5062), 1443–1445. doi:10.1126/science.1604319
- Gorbalenya, A. E., Donchenko, A. P., Blinov, V. M., and Koonin, E. V. (1989). Cysteine proteases of positive strand RNA viruses and chymotrypsin-like serine proteases. A distinct protein superfamily with a common structural fold. *FEBS Lett.* 243 (2), 103–114. doi:10.1016/0014-5793(89)80109-7
- Gordon, D. E., Jang, G. M., Bouhaddou, M., Xu, J., Obernier, K., White, K. M., et al. (2020). A SARS-CoV-2 protein interaction map reveals targets for drug repurposing. *Nature* 583, 459–468. doi:10.1038/s41586-020-2286-9
- Guo, Y., Wang, W., Sun, Y., Ma, C., Wang, X., Wang, X., et al. (2016). Crystal structure of the core region of hantavirus nucleocapsid protein reveals the mechanism for ribonucleoprotein complex formation. *J. Virol.* 90 (2), 1048–1061. doi:10.1128/JVI.02523-15
- Hilgenfeld, R., and Peiris, M. (2013). From SARS to MERS: 10 years of research on highly pathogenic human coronaviruses. *Antivir. Res.* 100 (1), 286–295. doi:10.1016/j.antiviral.2013.08.015

- Holm, L. (2020a). DALI and the persistence of protein shape. *Protein Sci.* 29 (1), 128–140. doi:10.1002/pro.3749
- Holm, L., and Sander, C. (1995). Dali: A network tool for protein structure comparison. *Trends biochem. Sci.* 20 (11), 478–480. doi:10.1016/s0968-0004(00)89105-7
- Holm, L., and Sander, C. (1993). Protein structure comparison by alignment of distance matrices. *J. Mol. Biol.* 233 (1), 123–138. doi:10.1006/jmbi.1993.1489
- Holm, L. (2020b). Using Dali for protein structure comparison. *Methods Mol. Biol.* 2112, 29–42. doi:10.1007/978-1-0716-0270-6_3
- Hung, H. C., Wang, H. C., Shih, S. R., Teng, I. F., Tseng, C. P., and Hsu, J. T. (2011). Synergistic inhibition of enterovirus 71 replication by interferon and rupintrivir. *J. Infect. Dis.* 203 (12), 1784–1790. doi:10.1093/infdis/jir174
- Jin, Z., Du, X., Xu, Y., Deng, Y., Liu, M., Zhao, Y., et al. (2020). Structure of M(pro) from SARS-CoV-2 and discovery of its inhibitors. *Nature* 582 (7811), 289–293. doi:10.1038/s41586-020-2223-y
- Kanitz, M., Blanck, S., Heine, A., Gulyaeva, A. A., Gorbalenya, A. E., Ziebuhr, J., et al. (2019). Design and structure-activity relationships of novel inhibitors of a 3C-like cysteine protease from a mosquito mesonivirus. *Virology* 533, 21–33. doi:10.1016/j.virol.2019.05.001
- Kawatkar, S. P., Gagnon, M., Hoesch, V., Tiong-Yip, C., Johnson, K., Ek, M., et al. (2016). Design and structure-activity relationships of novel inhibitors of human rhinovirus 3C protease. *Bioorg. Med. Chem. Lett.* 26 (14), 3248–3252. doi:10.1016/j.bmcl.2016.05.066
- Kester, W. R., and Matthews, B. W. (1977). Comparison of the structures of carboxypeptidase A and thermolysin. *J. Biol. Chem.* 252 (21), 7704–7710. doi:10.1016/s0021-9258(17)41025-8
- Kneller, D., Li, H., Phillips, G., Weiss, K., Zhang, Q., Arnould, M., et al. (2022). Covalent naltrexone- and boceprevir-derived hybrid inhibitors of SARS-CoV-2 main protease: Room-temperature X-ray and neutron crystallography, binding thermodynamics, and antiviral activity. *Res. Sq.* doi:10.21203/rs.3.rs-1318037/v1
- Kneller, D. W., Galanie, S., Phillips, G., O'Neill, H. M., Coates, L., and Kovalevsky, A. (2020). Malleability of the SARS-CoV-2 3CL M(pro) active-site cavity facilitates binding of clinical antivirals. *Structure* 28 (12), 1313–1320.e3. doi:10.1016/j.str.2020.10.007
- Kneller, D. W., Phillips, G., Weiss, K. L., Zhang, Q., Coates, L., and Kovalevsky, A. (2021a). Direct observation of protonation state modulation in SARS-CoV-2 main protease upon inhibitor binding with neutron crystallography. *J. Med. Chem.* 64 (8), 4991–5000. doi:10.1021/acs.jmedchem.1c00058
- Kneller, D. W., Zhang, Q., Coates, L., Louis, J. M., and Kovalevsky, A. (2021b). Michaelis-like complex of SARS-CoV-2 main protease visualized by room-temperature X-ray crystallography. *IUCr* 8 (6), 973–979. doi:10.1107/S2052252521010113
- Kolb, P., Ferreira, R. S., Irwin, J. J., and Shoichet, B. K. (2009). Docking and chemoinformatic screens for new ligands and targets. *Curr. Opin. Biotechnol.* 20 (4), 429–436. doi:10.1016/j.copbio.2009.08.003
- Kolb, P., and Irwin, J. J. (2009). Docking screens: Right for the right reasons? *Curr. Top. Med. Chem.* 9 (9), 755–770. doi:10.2174/156802609789207091
- Kwo, P. Y., and Vinayek, R. (2011). The therapeutic approaches for hepatitis C virus: Protease inhibitors and polymerase inhibitors. *Gut Liver* 5 (4), 406–417. doi:10.5009/gnl.2011.5.4.406
- Laskar, A., Rodger, E. J., Chatterjee, A., and Mandal, C. (2012). Modeling and structural analysis of PA clan serine proteases. *BMC Res. Notes* 5, 256. doi:10.1186/1756-0500-5-256
- Laskowski, R. A., Jablonska, J., Pravda, L., Varekova, R. S., and Thornton, J. M. (2018). PDBsum: Structural summaries of PDB entries. *Protein Sci.* 27 (1), 129–134. doi:10.1002/pro.3289
- Lee, C. C., Kuo, C. J., Ko, T. P., Hsu, M. F., Tsui, Y. C., Chang, S. C., et al. (2009). Structural basis of inhibition specificities of 3C and 3C-like proteases by zinc-coordinating and peptidomimetic compounds. *J. Biol. Chem.* 284 (12), 7646–7655. doi:10.1074/jbc.M807947200
- Liu, C., Boland, S., Scholle, M. D., Bardiot, D., Marchand, A., Chaltin, P., et al. (2022). Dual inhibition of SARS-CoV-2 and human rhinovirus with protease inhibitors in clinical development. *Antivir. Res.* 187, 105020. doi:10.1016/j.antiviral.2021.105020
- Liu, H., Iketani, S., Zask, A., Khanizeman, N., Bednarova, E., Forouhar, F., et al. (2022). Development of optimized drug-like small molecule inhibitors of the SARS-CoV-2 3CL protease for treatment of COVID-19. *Nat. Commun.* 13 (1), 1891. doi:10.1038/s41467-022-29413-2
- Lo, H. S., Hui, K. P. Y., Lai, H. M., He, X., Khan, K. S., Kaur, S., et al. (2021). Simeprevir potentially suppresses SARS-CoV-2 replication and synergizes with remdesivir. *ACS Cent. Sci.* 7 (5), 792–802. doi:10.1021/acscentsci.0c01186
- Lockbaum, G. J., Henes, M., Lee, J. M., Timm, J., Nalivaika, E. A., Thompson, P. R., et al. (2021). Pan-3C protease inhibitor rupintrivir binds SARS-CoV-2 main protease in a unique binding mode. *Biochemistry* 60 (39), 2925–2931. doi:10.1021/acs.biochem.1c00414
- Lu, G., Qi, J., Chen, Z., Xu, X., Gao, F., Lin, D., et al. (2011). Enterovirus 71 and coxsackievirus A16 3C proteases: Binding to rupintrivir and their substrates and anti-hand, foot, and mouth disease virus drug design. *J. Virol.* 85 (19), 10319–10331. doi:10.1128/JVI.00787-11
- Ma, C., Sacco, M. D., Hurst, B., Townsend, J. A., Hu, Y., Szeto, T., et al. (2020). Boceprevir, GC-376, and calpain inhibitors II, XII inhibit SARS-CoV-2 viral replication by targeting the viral main protease. *Cell Res.* 30, 678–692. doi:10.1038/s41422-020-0356-z
- Ma, C., Tan, H., Choza, J., Wang, Y., and Wang, J. (2022). Validation and invalidation of SARS-CoV-2 main protease inhibitors using the Flip-GFP and Protease-Glo luciferase assays. *Acta Pharm. Sin. B* 12 (4), 1636–1651. doi:10.1016/j.apsb.2021.10.026
- Madeira, F., Pearce, M., Tivey, A. R. N., Basutkar, P., Lee, J., Edbali, O., et al. (2022). Search and sequence analysis tools services from EMBL-EBI in 2022. *Nucleic Acids Res.* 50, W276–W279. doi:10.1093/nar/gkac240
- Matthews, D. A., Dragovich, P. S., Webber, S. E., Fuhrman, S. A., Patick, A. K., Zalman, L. S., et al. (1999). Structure-assisted design of mechanism-based irreversible inhibitors of human rhinovirus 3C protease with potent antiviral activity against multiple rhinovirus serotypes. *Proc. Natl. Acad. Sci. U. S. A.* 96 (20), 11000–11007. doi:10.1073/pnas.96.20.11000
- May, J. M., Owens, T. W., Mandler, M. D., Simpson, B. W., Lazarus, M. B., Sherman, D. J., et al. (2017). The antibiotic novobiocin binds and activates the ATPase that powers lipopolysaccharide transport. *J. Am. Chem. Soc.* 139 (48), 17221–17224. doi:10.1021/jacs.7b07736
- McGivern, D. R., Masaki, T., Lovell, W., Hamlett, C., Saalau-Bethell, S., and Graham, B. (2015). Protease inhibitors block multiple functions of the NS3/4A protease-helicase during the hepatitis C virus life cycle. *J. Virol.* 89 (10), 5362–5370. doi:10.1128/JVI.03188-14
- McLean, G., Kamil, J., Lee, B., Moore, P., Schulz, T. F., Muik, A., et al. (2022). The impact of evolving SARS-CoV-2 mutations and variants on COVID-19 vaccines. *mBio* 13 (2), e0297921. doi:10.1128/mbio.02979-21
- Mei, M., and Tan, X. (2021). Current strategies of antiviral drug discovery for COVID-19. *Front. Mol. Biosci.* 8, 671263. doi:10.3389/fmolb.2021.671263
- Mesecar, A. (2021). Structure of PEDV main protease bound to potent broad-spectrum non-covalent inhibitor X77. PDB ID, 6W81. doi:10.2210/pdb6W81/pdb
- Monttinen, H. A. M., Ravaniti, J. J., and Poranen, M. M. (2019). Structural comparison strengthens the higher-order classification of proteases related to chymotrypsin. *PLoS One* 14 (5), e0216659. doi:10.1371/journal.pone.0216659
- Morris, G. M., Huey, R., Lindstrom, W., Sanner, M. F., Belew, R. K., Goodsell, D. S., et al. (2009). AutoDock4 and AutoDockTools4: Automated docking with selective receptor flexibility. *J. Comput. Chem.* 30 (16), 2785–2791. doi:10.1002/jcc.21256
- Muhaxhiri, Z., Deng, L., Shanker, S., Sankaran, B., Estes, M. K., Palzkill, T., et al. (2013). Structural basis of substrate specificity and protease inhibition in Norwalk virus. *J. Virol.* 87 (8), 4281–4292. doi:10.1128/JVI.02869-12
- Namoto, K., Sirockin, F., Sellner, H., Wiesmann, C., Villard, F., Moreau, R. J., et al. (2018). Structure-based design and synthesis of macrocyclic human rhinovirus 3C protease inhibitors. *Bioorg. Med. Chem. Lett.* 28 (5), 906–909. doi:10.1016/j.bmcl.2018.01.064
- Narayanan, A., Narwal, M., Majowicz, S. A., Varricchio, C., Toner, S. A., Ballatore, C., et al. (2022). Identification of SARS-CoV-2 inhibitors targeting Mpro and PLpro using in-cell-protease assay. *Commun. Biol.* 5 (1), 169. doi:10.1038/s42003-022-03090-9
- Nashed, N. T., Aniana, A., Ghirlando, R., Chiliveri, S. C., and Louis, J. M. (2022). Modulation of the monomer-dimer equilibrium and catalytic activity of SARS-CoV-2 main protease by a transition-state analog inhibitor. *Commun. Biol.* 5 (1), 160. doi:10.1038/s42003-022-03084-7
- Nguyen, D. D., Gao, K., Chen, J., Wang, R., and Wei, G. W. (2020). Potentially highly potent drugs for 2019-nCoV. bioRxiv. doi:10.1101/2020.02.05.936013
- Oerlemans, R., Ruiz-Moreno, A. J., Cong, Y., Dinesh Kumar, N., Velasco-Velazquez, M. A., Neochoritis, C. G., et al. (2020). Repurposing the HCV NS3-4A protease drug boceprevir as COVID-19 therapeutics. *RSC Med. Chem.* 12 (3), 370–379. doi:10.1039/d0md00367k
- Ohashi, H., Watashi, K., Saso, W., Shionoya, K., Iwanami, S., Hirokawa, T., et al. (2021). Potential anti-COVID-19 agents, cepharanthine and nelfinavir, and their usage for combination treatment. *iScience* 24 (4), 102367. doi:10.1016/j.isci.2021.102367

- Pillaiyar, T., Manickam, M., Namasivayam, V., Hayashi, Y., and Jung, S. H. (2016). An overview of severe acute respiratory syndrome-coronavirus (SARS-CoV) 3CL protease inhibitors: Peptidomimetics and small molecule chemotherapy. *J. Med. Chem.* 59 (14), 6595–6628. doi:10.1021/acs.jmedchem.5b01461
- Robertus, J. D., Alden, R. A., Birktoft, J. J., Kraut, J., Powers, J. C., and Wilcox, P. E. (1972). X-ray crystallographic study of the binding of peptide chloromethyl ketone inhibitors to subtilisin BPN. *Biochemistry* 11 (13), 2439–2449. doi:10.1021/bi00763a009
- Salentin, S., Schreiber, S., Haupt, V. J., Adasme, M. F., and Schroeder, M. (2015). Plip: Fully automated protein-ligand interaction profiler. *Nucleic Acids Res.* 43 (W1), W443–W447. doi:10.1093/nar/gkv315
- Shi, J., and Song, J. (2006). The catalysis of the SARS 3C-like protease is under extensive regulation by its extra domain. *FEBS J.* 273 (5), 1035–1045. doi:10.1111/j.1742-4658.2006.05130.x
- Soding, J. (2005). Protein homology detection by HMM-HMM comparison. *Bioinformatics* 21 (7), 951–960. doi:10.1093/bioinformatics/bti125
- Thornton, J. M., Orengo, C. A., Todd, A. E., and Pearl, F. M. (1999). Protein folds, functions and evolution. *J. Mol. Biol.* 293 (2), 333–342. doi:10.1006/jmbi.1999.3054
- Ullrich, S., Ekanayake, K. B., Otting, G., and Nitsche, C. (2022). Main protease mutants of SARS-CoV-2 variants remain susceptible to nirmatrelvir. *Bioorg. Med. Chem. Lett.* 62, 128629. doi:10.1016/j.bmcl.2022.128629
- Wang, F., Chen, C., Yang, K., Xu, Y., Liu, X., Gao, F., et al. (2017a). Michael acceptor-based peptidomimetic inhibitor of main protease from porcine epidemic diarrhea virus. *J. Med. Chem.* 60 (7), 3212–3216. doi:10.1021/acs.jmedchem.7b00103
- Wang, Y., Cao, L., Zhai, Y., Yin, Z., Sun, Y., and Shang, L. (2017b). Structure of the enterovirus 71 3C protease in complex with NK-1.8k and indications for the development of antienterovirus protease inhibitor. *Antimicrob. Agents Chemother.* 61 (7), e00298-17. doi:10.1128/AAC.00298-17
- Weerawarna, P. M., Kim, Y., Galasiti Kankanamalage, A. C., Damalanka, V. C., Lushington, G. H., Alliston, K. R., et al. (2016). Structure-based design and synthesis of triazole-based macrocyclic inhibitors of norovirus protease: Structural, biochemical, spectroscopic, and antiviral studies. *Eur. J. Med. Chem.* 119, 300–318. doi:10.1016/j.ejmech.2016.04.013
- Wlodawer, A., and Vondrasek, J. (1998). Inhibitors of HIV-1 protease: A major success of structure-assisted drug design. *Annu. Rev. Biophys. Biomol. Struct.* 27, 249–284. doi:10.1146/annurev.biophys.27.1.249
- Wu, C., Zhang, L., Li, P., Cai, Q., Peng, X., Yin, K., et al. (2016). Fragment-wise design of inhibitors to 3C proteinase from enterovirus 71. *Biochimica Biophysica Acta - General Subj.* 1860 (6), 1299–1307. doi:10.1016/j.bbagen.2016.03.017
- Wu, F., Zhao, S., Yu, B., Chen, Y. M., Wang, W., Song, Z. G., et al. (2020). A new coronavirus associated with human respiratory disease in China. *Nature* 579 (7798), 265–269. doi:10.1038/s41586-020-2008-3
- Xia, Z., Sacco, M., Hu, Y., Ma, C., Meng, X., Zhang, F., et al. (2021). Rational design of hybrid SARS-CoV-2 main protease inhibitors guided by the superimposed cocrystal structures with the peptidomimetic inhibitors GC-376, telaprevir, and boceprevir. *ACS Pharmacol. Transl. Sci.* 4 (4), 1408–1421. doi:10.1021/acspstsci.1c00099
- Yang, H., Yang, M., Ding, Y., Liu, Y., Lou, Z., Zhou, Z., et al. (2003). The crystal structures of severe acute respiratory syndrome virus main protease and its complex with an inhibitor. *Proc. Natl. Acad. Sci. U. S. A.* 100 (23), 13190–13195. doi:10.1073/pnas.1835675100
- Yang, S., Chen, S. J., Hsu, M. F., Wu, J. D., Tseng, C. T., Liu, Y. F., et al. (2006). Synthesis, crystal structure, structure-activity relationships, and antiviral activity of a potent SARS coronavirus 3CL protease inhibitor. *J. Med. Chem.* 49 (16), 4971–4980. doi:10.1021/jm0603926
- Yao, Y., Huo, T., Lin, Y. L., Nie, S., Wu, F., Hua, Y., et al. (2019). Discovery, X-ray crystallography and antiviral activity of allosteric inhibitors of Flavivirus NS2B-NS3 protease. *J. Am. Chem. Soc.* 141 (17), 6832–6836. doi:10.1021/jacs.9b02505
- Yin, J., Cherney, M. M., Bergmann, E. M., Zhang, J., Huitema, C., Pettersson, H., et al. (2006). An episulfide cation (thiiranium ring) trapped in the active site of HAV 3C proteinase inactivated by peptide-based ketone inhibitors. *J. Mol. Biol.* 361 (4), 673–686. doi:10.1016/j.jmb.2006.06.047
- Zayed, A. A., Wainaina, J. M., Dominguez-Huerta, G., Pelletier, E., Guo, J., Mohssen, M., et al. (2022). Cryptic and abundant marine viruses at the evolutionary origins of Earth's RNA virome. *Science* 376 (6589), 156–162. doi:10.1126/science.abm5847
- Zhai, Y., Zhao, X., Cui, Z., Wang, M., Wang, Y., Li, L., et al. (2015). Cyanohydrin as an anchoring group for potent and selective inhibitors of enterovirus 71 3C protease. *J. Med. Chem.* 58 (23), 9414–9420. doi:10.1021/acs.jmedchem.5b01013
- Zhang, L., Lin, D., Sun, X., Curth, U., Drosten, C., Sauerhering, L., et al. (2020). Crystal structure of SARS-CoV-2 main protease provides a basis for design of improved alpha-ketoamide inhibitors. *Science* 368 (6489), 409–412. doi:10.1126/science.abb3405
- Zhao, Y., Fang, C., Zhang, Q., Zhang, R., Zhao, X., Duan, Y., et al. (2021). Crystal structure of SARS-CoV-2 main protease in complex with protease inhibitor PF-07321332. *Protein Cell* 13, 689–693. doi:10.1007/s13238-021-00883-2
- Zhou, P., Yang, X. L., Wang, X. G., Hu, B., Zhang, L., Zhang, W., et al. (2020). A pneumonia outbreak associated with a new coronavirus of probable bat origin. *Nature* 579 (7798), 270–273. doi:10.1038/s41586-020-2012-7
- Zhuang, Y., Xu, P., Mao, C., Wang, L., Krumm, B., Zhou, X. E., et al. (2021). Structural insights into the human D1 and D2 dopamine receptor signaling complexes. *Cell* 184 (4), 931–942.e18. doi:10.1016/j.cell.2021.01.027

Frontiers in Chemistry

Explores all fields of chemical science across the periodic table

Advances our understanding of how atoms, ions, and molecules come together and come apart. It explores the role of chemistry in our everyday lives - from electronic devices to health and wellbeing.

Discover the latest Research Topics

[See more →](#)

Frontiers

Avenue du Tribunal-Fédéral 34
1005 Lausanne, Switzerland
frontiersin.org

Contact us

+41 (0)21 510 17 00
frontiersin.org/about/contact

